

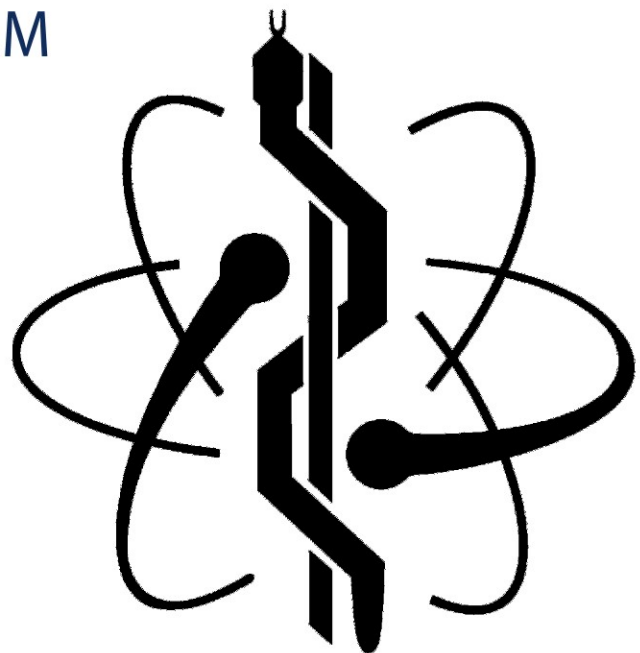
IFMBE Proceedings

Vo Van Toi · Truong Quang Dang Khoa (Eds.)

Volume 27

The Third International Conference
on the Development of Biomedical Engineering
in Vietnam

BME 2010 January 11 - 14th, 2010
Ho Chi Minh City, VIETNAM



The International Federation for Medical and Biological Engineering, IFMBE, is a federation of national and transnational organizations representing internationally the interests of medical and biological engineering and sciences. The IFMBE is a non-profit organization fostering the creation, dissemination and application of medical and biological engineering knowledge and the management of technology for improved health and quality of life. Its activities include participation in the formulation of public policy and the dissemination of information through publications and forums. Within the field of medical, clinical, and biological engineering, IFMBE's aims are to encourage research and the application of knowledge, and to disseminate information and promote collaboration. The objectives of the IFMBE are scientific, technological, literary, and educational.

The IFMBE is a WHO accredited NGO covering the full range of biomedical and clinical engineering, healthcare, healthcare technology and management. It is representing through its 58 member societies some 120.000 professionals involved in the various issues of improved health and health care delivery.

IFMBE Officers

President: Makoto Kikuchi, Vice-President: Herbert Voigt, Former-President: Joachim H. Nagel

Treasurer: Shankar M. Krishnan, Secretary-General: Ratko Magjarevic

<http://www.ifmbe.org>

Previous Editions:

IFMBE Proceedings ICDBME 2010, "The Third International Conference on the Development of Biomedical Engineering in Vietnam", Vol. 27, 2010, Ho Chi Minh City, Vietnam, CD

IFMBE Proceedings MEDITECH 2009, "International Conference on Advancements of Medicine and Health Care through Technology", Vol. 26, 2009, Cluj-Napoca, Romania, CD

IFMBE Proceedings WC 2009, "World Congress on Medical Physics and Biomedical Engineering", Vol. 25, 2009, Munich, Germany, CD

IFMBE Proceedings SBEC 2009, "25th Southern Biomedical Engineering Conference 2009", Vol. 24, 2009, Miami, FL, USA, CD

IFMBE Proceedings ICBME 2008, "13th International Conference on Biomedical Engineering", Vol. 23, 2008, Singapore, CD

IFMBE Proceedings ECIFMBE 2008 "4th European Conference of the International Federation for Medical and Biological Engineering", Vol. 22, 2008, Antwerp, Belgium, CD

IFMBE Proceedings BIOMED 2008 "4th Kuala Lumpur International Conference on Biomedical Engineering", Vol. 21, 2008, Kuala Lumpur, Malaysia, CD

IFMBE Proceedings NBC 2008 "14th Nordic-Baltic Conference on Biomedical Engineering and Medical Physics", Vol. 20, 2008, Riga, Latvia, CD

IFMBE Proceedings APCMBE 2008 "7th Asian-Pacific Conference on Medical and Biological Engineering", Vol. 19, 2008, Beijing, China, CD

IFMBE Proceedings CLAIB 2007 "IV Latin American Congress on Biomedical Engineering 2007, Bioengineering Solution for Latin America Health", Vol. 18, 2007, Margarita Island, Venezuela, CD

IFMBE Proceedings ICEBI 2007 "13th International Conference on Electrical Bioimpedance and the 8th Conference on Electrical Impedance Tomography", Vol. 17, 2007, Graz, Austria, CD

IFMBE Proceedings MEDICON 2007 "11th Mediterranean Conference on Medical and Biological Engineering and Computing 2007", Vol. 16, 2007, Ljubljana, Slovenia, CD

IFMBE Proceedings BIOMED 2006 "Kuala Lumpur International Conference on Biomedical Engineering", Vol. 15, 2004, Kuala Lumpur, Malaysia, CD

IFMBE Proceedings WC 2006 "World Congress on Medical Physics and Biomedical Engineering", Vol. 14, 2006, Seoul, Korea, DVD

IFMBE Proceedings BSN 2007 "4th International Workshop on Wearable and Implantable Body Sensor Networks", Vol. 13, 2006, Aachen, Germany

IFMBE Proceedings ICBMEC 2005 "The 12th International Conference on Biomedical Engineering", Vol. 12, 2005, Singapore, CD

IFMBE Proceedings Vol. 27

Vo Van Toi · Truong Quang Dang Khoa (Eds.)

The Third International Conference on the Development of Biomedical Engineering in Vietnam

BME2010

11–14 January, 2010

Ho Chi Minh City, Vietnam

 Springer

Editors

Vo Van Toi
Chair of Biomedical Engineering Department
International University - Vietnam National
Universities at HCM
Quarter 6, Linh Trung, Thu Duc Dist.
Ho Chi Minh City, Vietnam
E-mail: vvtoi@hcmiu.edu.vn

Truong Quang Dang Khoa
Biomedical Engineering Department
International University - Vietnam National
Universities at HCM
Quarter 6, Linh Trung, Thu Duc Dist.
Ho Chi Minh City, Vietnam
E-mail: tqdkhoa@hcmiu.edu.vn

ISSN 1680-0737

ISBN 978-3-642-12019-0

e-ISBN 978-3-642-12020-6

DOI 10.1007/978-3-642-12020-6

Library of Congress Control Number: 2010922304

© International Federation for Medical and Biological Engineering 2010

This work is subject to copyright. All rights are reserved, whether the whole or part of the material is concerned, specifically the rights of translation, reprinting, reuse of illustrations, recitation, broadcasting, reproduction on microfilm or in any other way, and storage in data banks. Duplication of this publication or parts thereof is permitted only under the provisions of the German Copyright Law of September 9, 1965, in its current version, and permissions for use must always be obtained from Springer. Violations are liable to prosecution under the German Copyright Law.

The use of general descriptive names, registered names, trademarks, etc. in this publication does not imply, even in the absence of a specific statement, that such names are exempt from the relevant protective laws and regulations and therefore free for general use.

The IFMBE Proceedings is an Official Publication of the International Federation for Medical and Biological Engineering (IFMBE)

Typesetting: Scientific Publishing Services Pvt. Ltd., Chennai, India.

Cover Design:

Printed on acid-free paper

9 8 7 6 5 4 3 2 1

springer.com

About IFMBE

The International Federation for Medical and Biological Engineering (IFMBE) was established in 1959 to provide medical and biological engineering with a vehicle for international collaboration in research and practice of the profession. The Federation has a long history of encouraging and promoting international cooperation and collaboration in the use of science and engineering for improving health and quality of life.

The IFMBE is an organization with membership of national and transnational societies and an International Academy. At present there are 52 national members and 5 transnational members representing a total membership in excess of 120000 worldwide. An observer category is provided to groups or organizations considering formal affiliation. Personal membership is possible for individuals living in countries without a member society. The International Academy includes individuals who have been recognized by the IFMBE for their outstanding contributions to biomedical engineering.

Objectives

The objectives of the International Federation for Medical and Biological Engineering are scientific, technological, literary, and educational. Within the field of medical, clinical and biological engineering its aims are to encourage research and the application of knowledge, and to disseminate information and promote collaboration.

In pursuit of these aims the Federation engages in the following activities: sponsorship of national and international meetings, publication of official journals, cooperation with other societies and organizations, appointment of commissions on special problems, awarding of prizes and distinctions, establishment of professional standards and ethics within the field, as well as other activities which in the opinion of the General Assembly or the Administrative Council would further the cause of medical, clinical or biological engineering. It promotes the formation of regional, national, international or specialized societies, groups or boards, the coordination of bibliographic or informational services and the improvement of standards in terminology, equipment, methods and safety practices, and the delivery of health care.

The Federation works to promote improved communication and understanding in the world community of engineering, medicine and biology.

Activities

Publications of IFMBE include: the journal *Medical and Biological Engineering and Computing*, the electronic magazine *IFMBE News*, and the Book Series on Biomedical Engineering. In cooperation with its international and regional conferences, IFMBE also publishes the IFMBE Proceedings Series. All publications of the IFMBE are published by Springer Verlag. The Federation has two divisions: Clinical Engineering and Health Care Technology Assessment.

Every three years the IFMBE holds a World Congress on Medical Physics and Biomedical Engineering, organized in cooperation with the IOMP and the IUPESM. In addition, annual, milestone and regional conferences are organized in different regions of the world, such as Asia Pacific, Europe, the Nordic-Baltic and Mediterranean regions, Africa and Latin America.

The administrative council of the IFMBE meets once a year and is the steering body for the IFMBE: The council is subject to the rulings of the General Assembly, which meets every three years. Information on the activities of the IFMBE can be found on the web site at: <http://www.ifmbe.org>.

Preface

Vietnam is a rapidly developing, socially dynamic country, where interest in biomedical engineering activities has grown considerably in recent years. The leadership of the Vietnamese government, and of research and educational institutions, are well aware of the importance of this field for the development of the country and have instituted policies to promote its development. The political, economic and social environment within the country offers unique opportunities for the international community and this conference was intended to provide a vehicle for the sharing of experiences; development of support and collaboration networks for research; and exchange of ideas on how to improve the educational and entrepreneurial environment to better address the urgent needs of Vietnam.

In January 2004, under the sponsorship of the U.S. National Science Foundation, a U.S. delegation that consisted of Biomedical Engineering professors from different universities in the United States, visited several universities and research institutions in Vietnam to assess the state of development of this field. This delegation proposed a five year plan that was enthusiastically embraced by the international scientific communities to actively develop collaborations with Vietnam.

Within this framework, in July 2005, the First International Conference on the Development of Biomedical Engineering in Vietnam was held in Ho Chi Minh City. From that conference a Consortium of Vietnam-International Universities was created to advise and assist the development of Biomedical Engineering in Vietnamese universities.

In July 2007, the Second International Conference on the Development of Biomedical Engineering in Vietnam was held in Hanoi. During this event the Vietnamese Association of Biomedical Science and Engineering was endorsed by the Asia-Pacific International Molecular Biology Network (AIMBN), Biomedical Engineering Society Singapore (BESS), International Federation for Medical and Biological Engineering (IFMBE), Société Française de Génie Biologique et Médical (SFGBM) and IFMBE Asia-Pacific Working Group.

In March 2009, International University (IU), a member of Vietnam National Universities – Ho Chi Minh City (VNU-HCM), one of the two most famous university networks in Vietnam established its Biomedical Engineering Department and the first accredited Biomedical Engineering degree in Vietnam (code: 52.42.02.04). IU is the first public university in Vietnam that teaches all courses in English and was created as a new model to modernize the higher education in Vietnam.

The Third International Conference on the Development of Biomedical Engineering in Vietnam was organized on January 11–14, 2010, by IU in Ho Chi Minh City, Vietnam and had the theme of: “**New frontiers in Biomedical Engineering**”. It reflected the steady growth of the activities in this field in Vietnam, and featured the contributions of researchers of 21 countries, including: Australia, Belgium, Canada, Denmark, France, India, Japan, Korea, Malaysia, New Zealand, Philippines, Poland, Russia, Singapore, Spain, Switzerland, Taiwan, Thailand, United Kingdom, the United States and Vietnam. The main keynote speaker was Dr. John C. Gore, University Professor of Radiology and Radiological Sciences, Biomedical Engineering, and Physics, and Director of Vanderbilt University Institute of Imaging Science (U.S.). The special topic keynote speakers were Dr. Robert E. Burrell, Professor and Canada Research Chair in Nano-structured Biomaterials (Canada); Dr. K. Kirk Shung, Professor and Director of National Institutes of Health Resource on Medical Ultrasonic Transducer Technology of University of Southern California, (U.S.); and Dr. Regis B. Kelly, Professor and Director of California Institute for Quantitative Biosciences (QB3) (U.S.). Besides the invited, oral and poster presentations there were tutorial lectures to educate junior researchers in different subfields of Biomedical Engineering. This volume summarizes those presentations and was provided as an education foundation and scientific reference. The Conference constituted a kick-off event to celebrate the 15 Anniversary of the establishment of VNU-HCM and also hosted the Clinical Engineering Workshop of the IFMBE Asia Pacific Working Group.

The editors would like to thank the leadership of VNU-HCM and IU, and the staff of Biomedical Engineering Department and of difference offices of IU for their valuable support for the conference and their assistance in the editing and publication of this volume.

Vo Van Toi and Truong Quang Dang Khoa
Biomedical Engineering Department
International University of the Vietnam National Universities – Ho Chi Minh
www.hcmiu.edu.vn/bme
bme@hcmiu.edu.vn

Table of Contents

Keynote Speakers

Challenges and Opportunities of Ultra-High Field MRI	1
<i>A.N. Dula, E.B. Welch, J.L. Creasy, J.C. Gatenby, E.A. Stringer, L.M. Chen, A.W. Anderson, M.J. Avison, J.C. Gore</i>	
Nanocrystalline Silver: Novel Structure and Activity	6
<i>Robert E. Burrell, Patricia Nadworny</i>	
Ultrasound: Past, Present and Future	10
<i>K. Kirk Shung</i>	
Bioengineering in Vietnam	14
<i>Regis B. Kelly</i>	

Invited Speakers

Detection and Treatment of Diseases Using Light	19
<i>W. Pham</i>	
Magnetic Resonance Imaging of Schizophrenia and Alzheimer's Disease	23
<i>A.W. Anderson, X. Hong, L.R. Arlinghaus, M. Tumuklu, Thornton-Wells, R.E. Hoffman, S. Park, H.Y. Meltzer</i>	
Current Development of Neuroimaging Using PET Techniques	27
<i>A.L. Brownell</i>	
Peanut Agglutinin-Immobilized Fluorescent Nanospheres with Surface Poly(N-vinylacetamide) Chains as a Novel Colonoscopic Imaging Agent	31
<i>S. Sakuma, K. Hiwatari, T. Yano, K. Iwata, Y. Masaoka, M. Kataoka, H. Tachikawa, Y. Shoji, R. Kimura, K. Nakamura, H. Ma, Z. Yang, L. Tang, R.M. Hoffman, S. Yamashita</i>	
Techniques for the Incorporation of Fluorine-18 and Carbon-11	35
<i>Nickels, W. Pham</i>	

Modeling

Dynamic Model Identification of PAM-Based Rehabilitation Robot Using Neural MIMO NARX Model	39
<i>Ho Pham Huy Anh, Le Tan Loi</i>	
Simulation of the Gait of a Patient Specific Model of Post Polio Residual Paralysis (PPRP): Effect of the Orthosis	44
<i>T.T. Dao, P. Pouletaut, F. Marin, P. Aufaure, F. Charleux, M.C. Ho Ba Tho</i>	
Mechanical Behavior of Muscles during Flexion and Extension of Lower Limb on Variable Age Group by Using BRG.LifeMod	48
<i>Nitin Sahai, Ravi P. Tewari, Lokesh Singh</i>	

Biomechanics of Index Finger during Mouse Click	51
<i>P. Chivapornthip, E.L.J. Bohez, S. Nanthavanij, K. Sitthiseripratip, E. Lorprayoon</i>	
Numerical Study of Deformation-Induced Fluid Flows in Osteonal Matrix	55
<i>V.-H. Nguyen, T. Lemaire, S. Naili</i>	
Evaluation Spatial-temporal and Pressure Parameters of Normal Cats at Walk, Using a Pressure Walkway	59
<i>T. LeQuang, P. Maitre, A. Colin, E. Viguier</i>	
Gait Analysis for Sound Dogs at a Walk by Using a Pressure Walkway	62
<i>T. LeQuang, P. Maitre, A. Colin, T. Roger, E. Viguier</i>	
Robust Design with Time-Oriented Responses for Regenerative Medicine Industry	67
<i>N.K.V. Truong, S.M. Shin, Y.S. Choi, S.H. Jeong, B.R. Cho</i>	
Cerebral Palsy Classification Using Heuristics and Belief Decision Tree: A Preliminary Study	71
<i>T.T. Dao, F. Marin, F. Mégrot, M.C. Ho Ba Tho</i>	
Test for Determinism and Nonlinearity in Near Infrared Spectroscopy Data	75
<i>N.T. Dzung</i>	
Multifractality in NIRS Data of Brain Activity	80
<i>N.T. Dzung</i>	
Instrumentation	
Design, Fabrication and Analysis of Silicon Microneedles for Transdermal Drug Delivery Applications	84
<i>D.W. Bodhale, A. Nisar, N. Afzulpurkar</i>	
Heat-Stress Relationships of Rat Cardiac Trabeculae Determined Using a Micromechanocalorimeter	90
<i>J.-C. Han, A.J. Taberner, P.M.F. Nielsen, R.S. Kirton, D.S. Loisselle</i>	
About the Operating Principles of System DDFAO “(Dépistage et Diagnostique Fonctionnel Assisté Par Ordinateur)”	94
<i>Huynh Luong Nghia, Nguyen Van Tiep</i>	
A Design of Renal Dataflow Control and Patient Record Management System for Renal Department Environment in Vietnam	98
<i>Hai D. Vu, Thuan D. Nguyen, Ngoc P. Pham, Huy Q. Hoang, Thanh V. Pham</i>	
Anisotropy of Longitudinal Wave Velocity in Spherically Shaped Bovine Cortical Bone	102
<i>K. Yamamoto, T. Nakatsuji, M. Indo, T. Yanagitani, M. Matsukawa, K. Yamazaki</i>	
Calculating the Dosimetry Distribution of Leksell Gamma Knife in Phantom Zupal Head by Using MCNP5	106
<i>Dang Truong Ka My, Dang Nguyen Phuong, Truong Thi Hong Loan, Mai Van Nhon</i>	
A Program for Locating Possible Breast Masses on Mammograms	110
<i>Viet Dzung Nguyen, Duc Thuan Nguyen, Tien Dzung Nguyen, Thom Thao Nguyen Thi, Duc Hoa Tran</i>	

Retrospective Study of Biomechanical Factors Influencing Early Clinical Results of the Munting Stemless Hip Prosthesis	114
<i>F. Boucher, P. Pouletaut, E. Munting, M.C. Ho Ba Tho</i>	
Integrated Approaches for Personalised Cranio-Maxillofacial Implant Design and Manufacturing	119
<i>L.C. Hieu, E. Bohez, J.V. Sloten, L.T. Hung, L. Khanh, N. Zlatov, P.D. Trung</i>	
Current Medical Product Development for Diagnosis, Surgical Planning and Treatment in the Areas of Neurosurgery, Orthopaedic and Dental-Cranio-Maxillofacial Surgery in Vietnam	123
<i>L.C. Hieu, L.H. Quoc, V.V. Thanh, T.D. Nguyen, P.V. An, L.T. Hung, L. Khanh</i>	
Glass Nanopipette: Fabrication and Application for Studying Living Cells	127
<i>Duong Chi Dung, Huynh Luong Nghia, V.P. Veiko, A.O. Golubok, E.B. Yakovlev</i>	
Resolution Study of Ultrasound Reflections in Bovine Vertebral Bones <i>In-Vitro</i>	130
<i>L.H. Le, C. Zhang, E. Lou</i>	
Light-Emitting Diodes (LEDs): An Artificial Lighting Source for Biological Studies	134
<i>Duong Tan Nhut, Nguyen Ba Nam</i>	
A Novel Electronic Cervical Range of Motion Measurement System	140
<i>E. Lian, J. Hachadorian, Ngo Thanh Hoan, Vo Van Toi</i>	
Measurement of the Range of Neck Motion: A Comparative Study	144
<i>J. Hachadorian, A. Lugo, E. Lian, Truong Quang Dang Khoa, Vo Van Toi</i>	
Molecular/Cell	
Extract an Irregular Structure of an Echinocytes Using Morphological Operations	148
<i>Hoang Manh Ha, Thai Thanh Nga</i>	
Study on Artificial Scaffold from Cancellous Bone	152
<i>To Minh Quan, Thai Tu Thanh, Phan Kim Ngoc, Tran Le Bao Ha</i>	
Report Case: Cultured Keratinocyte Autograft on Collagen from Amniotic Membrane for Treatment the Injured Human Skin	155
<i>Tran Le Bao Ha, Huynh Minh Tuan, Tran Thi Thanh Thuy, Tran Cong Toai, Hoang Nghia Son</i>	
Doxorubicin Delivery by Copolymeric Nanoparticle for Treatment of Breast Cancer	159
<i>N.V. Cuong, J.L. Jiang, M.F. Hsiesh</i>	
Regeneration of Pancreatic β Cells of Type 1 Diabetic Mouse by Stem Cell Transplantation ..	163
<i>Pham Van Phuc, Pham Le Buu Truc, Duong Thanh Thuy, Truong Hai Nhung, Doan Chinh Chung, Nguyen Khac Toan, Ma Kien Phuc, Phan Kim Ngoc</i>	
Results of Curing Some Diseases by Stem Cell Transplantation at Stem Cell R&D Laboratory	167
<i>Phan Kim Ngoc, Pham Van Phuc</i>	
Regulations of Cell Division from Streptomyces That May Play an Important Role in Drug Resistance	171
<i>Nguyen H.K. Tu</i>	

Cellular Bio-corrosion of Metal Implants and Effects of Metal Ions on Bone Cells and Immune Cells	175
<i>Filgueira, E. Chan, D. Cadosch</i>	
Chitosan Hydrogel as an Immunoisulative Barrier for Xenogeneic Islet Transplantation	179
<i>K.C. Yang, Z. Qi, F.H. Lin, C.C. Wu, S. Sumi</i>	
The Method to Encourage Biological Cell Division with Vibration and Circulation Technique Using Optical Manipulating	182
<i>N. Watanabe, K. Taguchi</i>	
Imaging	
Adaptive Cross-Point Regions for Lossless Images Compression	186
<i>T.T. Dang, T.D. Vu, T.P. Vo</i>	
Cortical Bone Microelasticity Assessed with Scanning Acoustic Microscopy: Relationship to Nanostructural Characteristics across a Human Osteon	190
<i>Mathilde Mouchet, Aurélien Gourrier, Fabienne Rupin, Kay Raum, Françoise Peyrin, Amena Saïed, Pascal Laugier</i>	
The Overview of Tomographic Algorithms Used in Medical Imaging Equipments	193
<i>Huynh Luong Nghia, Tran Anh Quang</i>	
Adaptive Complex Wavelet Technique for Medical Image Denoising	196
<i>Nguyen Thanh Binh, Ashish Khare</i>	
Three Dimensional Medical Image Processing and Analysing Software	200
<i>Tran Phan Son Giang</i>	
Biomaterial	
Formation of Biodegradable Copolymeric Nanoparticles for Anticancer Drug Delivery	203
<i>N.T.H. Anh, N.V. Cuong, N.K. Hoang</i>	
Synthesis and in <i>Vitro</i> Cell Compatibility of α-Tricalcium Phosphate-Based Apatite Cement Containing Tricalcium Silicate	207
<i>L.J. Cardenas, A. Takeuchi, K. Tsuru, S. Matsuya, K. Ishikawa</i>	
In Vitro Culture and Differentiation of Osteoblasts on Coral Scaffold from Human Bone Marrow Mesenchymal Stem Cells	211
<i>C. Gargiulo, H.D. Thao, H.M. Tuan, T.T.T. Thuy, P.H. Van, L. Filgueira, T.C. Toai</i>	
Evaluation of Novel Carbon Nano-tube Particles in the Bacterial and Viral DNA and RNA Extraction from the Clinical Samples	216
<i>S.T. Pham, K.C. Nguyen, D.X.A. Vo, H.N. Hoang, L.T.T. Ho, H.V. Pham</i>	
Stem Cell Origin and Microenvironment Contribution for NF1-Associated Neurofibromas ...	219
<i>L.Q. Le, T. Shipman, D.K. Burns, L.F. Parada</i>	
Green Tea Epigallocatechin Gallate Exhibits Anticancer Effect in Human Pancreatic Carcinoma Cells via Inhibition of Both FAK and IGF-1R	223
<i>H.A. Vu, Y. Beppu, H.T. Chi, K. Sasaki, H. Yamamoto, P.T. Xinh, T. Tanii, Y. Hara, T. Watanabe, Y. Sato, I. Ohdomari</i>	

Application of Shrimp Chitosan Solution as Additive and Supplementing Ingredient in Culturing 3T3 Fibroblast Cells	227
<i>Nguyen Van Toan, Nguyen Duc Tam</i>	
Preparation of Size-Controlled BSA Nanoparticles by Intermittent Addition of Desolvating Agent	231
<i>Hoang Hai Nguyen, Sanghoon Ko</i>	
Mechanical Properties of a Single Trabecula in Bovine Femur by the Three Point Bending Test	235
<i>Kazuto Tanaka, Yusuke Kita, Tsutao Katayama, Mami Matsukawa</i>	
Ultrasonic Characterization of Bovine Bone Marrow	239
<i>Tomohiro Kubo, Nicolas Cazier, Takashi Saeki, Mami Matsukawa</i>	
Tribological Response of Cobalt-Chromium Femoral Head under Lubrication of Bovine Serum Albumin	243
<i>Cong-Truyen Duong, Seonghun Park</i>	
Educational Model	
VEF-Sponsored HUT Biomechanics Course	247
<i>B.S. Kelley, B.R. Rigby, H.D. Vu</i>	
Building an Elearning Website for Biomedical Engineering Education	251
<i>H.Q. Huy, N.D. Thuan, V.D. Hai</i>	
Others	
Ethnic Differences in Dietary Intake and the Association between Dietary Intake and Gastric Cancer Risk in Chinese Subjects Resident in Malaysia	255
<i>D.M. Ha, D. Forman, K.L. Goh, K.M. Fock, H.M. Mitchell</i>	
Phylogenetic Analysis the 5'-Noncoding Sequences of the Hepatitis C Virus Detected from the Patient with HCV Infection	259
<i>Nguyễn Thái Sơn, Phạm Hùng Vân</i>	
A Study of Mean Glandular Dose during Diagnostic Mammography in Hospitals in Hanoi, Vietnam	263
<i>Nguyen Thai Ha, Nguyen Duc Thuan, Nguyen Thu Van</i>	
Relationship between Dental Occlusion and Arm Strength	266
<i>Lê Minh Hòa, Đặng Nam Huân, Nguyễn Hồng Thảo, Ngô Thanh Hoàn, Truong Quang Dang Khoa, Nguyễn H.M. Tâm, Võ Văn Tới</i>	
Eyestrain, Blink Rate and Dry Eye Syndromes of Video Display Terminal Users	270
<i>B. Dumery, P.A. Grounauer, Vo Van Toi</i>	
A Laser Headset for Measuring Cervical Range of Motion	274
<i>Gustavo Lugo, Tran Anh Vu, Nguyen Huynh Minh Tam, Vo Van Toi</i>	
Engineering Resistance in Brinjal against Nematode (Meloidogyne Incognita) Using cry1Ab Gene from <i>Bacillus Thuringiensis</i> Berliner	278
<i>Phan Dinh Phap, Hoang Thi Lan Xuan, D. Sudhakar, P. Balasubramanian</i>	

Removing Noise and Artifacts from EEG Using Adaptive Noise Cancelator and Blind Source Separation	282
<i>Nguyen T.K. Cuong, Vo Q. Ha, Nguyen T.M. Huong, Truong Quang Dang Khoa, Nguyen Huynh Minh Tam, Huynh Q. Linh, Vo Van Toi</i>	
Removing Electroencephalographic Artifacts by Independent Components Analysis	287
<i>Nguyen Thi Minh Huong, Truong Quang Dang Khoa, Nguyen Thi Kim Cuong, Vo Quang Ha, Nguyen Huu Pho, Le Tu Quoc Tuan, Ngo Thanh Hoan, Huynh Quang Linh, Vo Van Toi</i>	
Lab-On-A- Chip - Applied Micro and Nanotechnology in Life Sciences	
A Trip from a Tube to a Chip Applied Micro and Nanotechnology in Biotechnology, Veterinary and Life Sciences	291
<i>Dang Duong Bang, Raghuram Dhumpa, Cao Cuong, Laouenan Florian, Javier Berganzo, Rafal Walczak, Yuliang Liu, Mingiang Bu, Sun Yi, Jan Dzuiban, Jesus Miguel Rruano, Anders Wolff</i>	
Au Nanoparticles for Applications in Analysis of Cellular and Biomolecular Recognitions	295
<i>Cuong Cao, Anders Wolff, Dang Duong Bang</i>	
A Total Integrated Biochip System for Detection of SNP in Cancer	299
<i>Ivan R. Perch-Nielsen, Monica Brivio, Eva Schaeffer, Klaus S. Drese, Frederica Rampf, Dang Duong Bang, Henrik Bruus, Anders Wolff</i>	
Lab on a Chip Application in Life Sciences	303
<i>N.T. Nguyen, Y. Sun, Y.C. Kwok, H.Y. Tan, W.K. Loke</i>	
A Lab-on-Chip for Separating and Focusing Bioparticles via Dielectrophoresis	308
<i>Ngoc-Duy Dinh, Cheng-Hsien Liu</i>	
Nanotechnology at SHTP LABS in Vietnam	312
<i>Khe Nguyen, Pham Hung Van</i>	
Microparticle Encoding Technologies for High-Throughput Multiplexed Suspension Assays	316
<i>S.W. Birtwell, H. Morgan</i>	
Author Index	321
Keyword Index	325

Challenges and Opportunities of Ultra-High Field MRI

A.N. Dula^{1,2}, E.B. Welch³, J.L. Creasy², J.C. Gatenby^{1,2}, E.A. Stringer¹, L.M. Chen^{1,2}, A.W. Anderson^{1,2,4}, M.J. Avison^{1,2},
and J.C. Gore^{1,2,4}

¹ Vanderbilt University Institute of Imaging Science, Nashville, USA

² Department of Radiology and Radiological Sciences, Vanderbilt University, Nashville, USA

³ Philips Healthcare Inc., Cleveland, USA

⁴ Department of Biomedical Engineering, Vanderbilt University, Nashville, USA

Abstract— **Magnetic resonance imaging (MRI) and spectroscopy (MRS) have contributed considerably to our understanding of the structure and function of the human brain, and are essential in modern radiological practice. The development and applications of MRI systems at fields of 7 Tesla and above provide many new opportunities and technical challenges. The increased signal strength at higher fields may be used to obtain higher resolution images, faster images and/or images with greater contrast to noise. These can be used to improve detection of lesions, for more accurate assessment of the structural anatomy of the brain (including higher resolution tractography of white matter), and improved sensitivity in functional MRI. However, high field MR imaging is also affected by macroscopic field variations caused by inhomogeneities of magnetic susceptibility within the body, and these can degrade spectra and introduce image distortions. Moreover, the performance of radiofrequency (RF) coils is also affected at higher fields, and it is more difficult to create uniform RF fields within large objects. These challenges are being met using various technical innovations such as dynamic shimming, the use of parallel arrays of coils, novel spectral-spatial excitation methods, novel pulse sequences and post-acquisition digital processing. In combination these efforts promise to allow ultra-high field imaging and spectroscopy to contribute significantly to our understanding of brain structure and function in various conditions.**

Keywords— **MRI, MRS, ultra-high field, neuroimaging.**

I. INTRODUCTION

Magnetic resonance imaging has contributed considerably to our ability to study and understand the structure and function of the human brain, including the anatomic and functional changes that accompany development, degeneration, diseases and disorders. MRI was introduced into clinical practice in the early 1980's, and since then multiple technological advances have been made that have dramatically improved image quality. The earliest commercial MRI scanners operated at field strengths of 0.15 Tesla or below, but these low field

systems were rapidly replaced as superconducting magnets were introduced. The most common field in use quickly rose to 1.5 Tesla, which remained the mainstay for human MRI for almost 20 years. In the past five years many medical centers and neuroscience research groups have adopted MRI scanners operating at 3 Tesla, and this promises to be the state-of-the-art field strength for brain studies for the foreseeable future. However, accelerated by the interest of major equipment vendors in exploring higher fields, in the past few years approximately 30+ scanners operating at a field strength of 7 Tesla (or even higher) have been installed in major medical centers throughout the world, and there is considerable interest and effort in developing successful MRI techniques for clinical and research applications at these high fields.

These efforts are motivated by the observation that, over the past 25 years, each substantive increase in field strength has in time led to dramatic improvements in the quality of images and spectra obtainable, and to “quantum increases” in the information available about brain structure and function. Each major increase in field has also introduced new technical challenges and problems that have required creative scientific and engineering solutions in order to realize the potential of improved image quality. Image quality in MRI is always limited by the relative strengths of the available signal and the “noise” - those random fluctuations in images that are unavoidable but which obscure details and make the detection of small signal differences more difficult. The strength of MRI signal increases quadratically with field strength, and in principle the higher signal to noise ratio available at 7 Tesla compared to lower fields can be used to make images with finer spatial resolution, or in less time, or in which small signal differences are easier to detect. In addition, some specific intrinsic properties of tissues are field dependent so that at high field they contribute significantly more to image contrast. For example, variations in tissue magnetic susceptibility, which themselves may be dominated by blood volume and oxygenation or levels of iron in tissue,

give rise to MRI signal differences that increase dramatically at high field. This implies, for example, that differences in image signal induced by functional activation via the BOLD (blood oxygen level dependent) effect, or because of the presence of venous structures, will be much larger at higher fields and therefore can be detected with greater sensitivity.

In this report we describe our early experience with human brain imaging at 7 Tesla, and show convincing evidence that higher field strength systems can offer new capabilities over what can be achieved at lower fields. We show how high field MRI can be used and provide superior information in clinical studies of pathology, for high-resolution anatomic and functional imaging, and for *in vivo* MR spectroscopy. We also discuss some of the new technical challenges that must be overcome to realize the full potential of 7T imaging, and briefly describe some approaches to meeting these challenges.

II. ANATOMIC IMAGING AT 7T

The finer resolution and higher signal to noise ratio is important for numerous types of applications but is especially valuable for quantitative morphometry of small brain structures such as the hippocampus [1]. Excellent soft tissue contrast between grey and white matter can be obtained at high field after appropriate adjustments are made to standard pulse sequences. In our preliminary work we have implemented a standard 3D gradient echo pulse sequence that provides excellent delineation of the cortex in less than 9 minutes with isotropic voxels of dimension 0.7mm. Compared to the isotropic 1 mm voxel commonly used at lower fields, the voxel volume obtained at high field strength is only 35% as large as the lower field. With appropriate segmentation algorithms the ability to measure fine detail, such as cortical thickness or nuclear volumes, is markedly improved. Moreover, partial volume effects at boundaries are also reduced so that some features become much clearer. For example, Figure 1 shows a comparison of a section through the hippocampus at both 3T and 7T, both obtained in approximately five minutes. 7T MRI clearly provides improved anatomic clarity of the fine hippocampal structures due to the increased signal to noise ratio and a smaller voxel volume.

As mentioned above, high field images are very sensitive to variations in the magnetic susceptibility of tissues. This

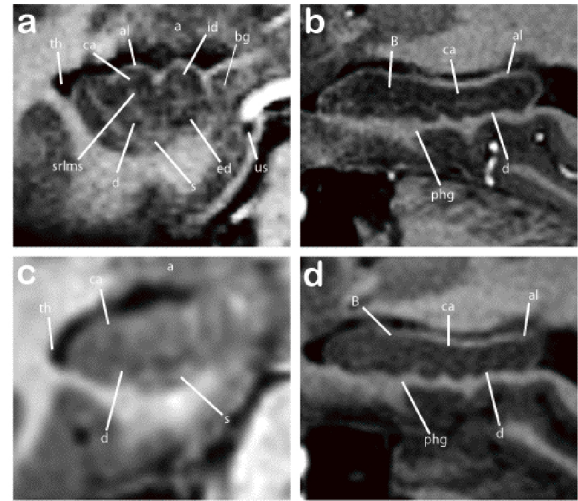


Fig. 1 7 Tesla T1W 3D TFE coronal imaging through the hippocampal head (a) and sagittal imaging through the hippocampal body (b) with comparable slices of the same subject at 3 Tesla (c & d). The 7 Tesla image demonstrates the increased conspicuity at this field strength showing the temporal horn of lateral ventricle (th), Cornu Ammonis (ca), alveus (al), amygdala (a), internal digitations of hippocampal head (id), band of Giacomini (bg), uncus sulcus (us), external digitations of hippocampal head (ed), subiculum (s), dentate gyrus (d), composite of strata radiatum, lacunosum, moleculare, and vestigial hippocampal sulcus (srlms), and parahippocampal gyrus (phg)

sensitivity can be exploited using specialized methods generically termed susceptibility weighted imaging, in which the image intensity is modulated directly by the magnitude of the deviation of the local field strength compared to the average background field. This deviation can be estimated by analysing the phase of the MR signal in addition to the magnitude, and overlaying this phase distribution as a mask after performing an appropriate spatial filter [2-5]. At high field the phase differences between regions evolve more rapidly than at lower field with the result that susceptibility weighted images can be obtained at shorter echo times and higher signal to noise values than at lower field. Figure 2 shows the appearance of normal brain vasculature obtained using this approach with control minimum intensity projections (mIP's, top row) for sections of 5, 10 and 20 mm thickness. The corresponding mIP's using the positive phase mask (bottom row) exhibit noticeably enhanced vessel conspicuity. Quite small venous structures can be readily imaged by this method, which has considerable promise also for studies involving hemorrhage, iron deposition, calcium or other pathological conditions.

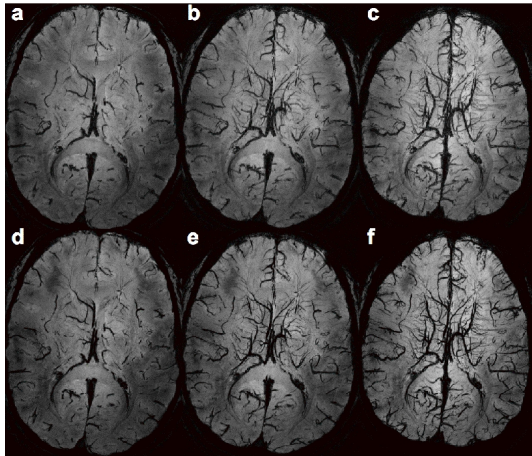


Fig. 2 Susceptibility weighted image (SWI) of healthy control acquired at 7 Tesla. mIP's of thickness 5, 10, and 20 mm (left to right) using original magnitude data (a,b,c) and positive-phase -weighted magnitude data (d,e,f). SWI was performed using a 3D velocity compensated and RF spoiled gradient echo sequence with scan time=7.3 minutes. Complex image data were processed using MATLAB (Natick, MA)

Even without specific masking of areas of increased susceptibility, higher field images are more sensitive to signal losses induced by the presence of susceptibility variations that reduce the time constant $T2^*$. For example, the iron-laden nuclei within the basal ganglia are easily identifiable with increased conspicuity due to this relaxation enhancement at high field. High field images with $T2^*$ weighting (Fig. 3) show clear delineation of the deep brain structures which are typically difficult to distinguish at lower field strengths.

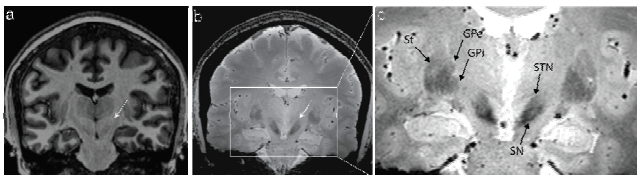


Fig. 3 MR imaging of deep brain nuclei a) 3 Tesla T1 weighted image 1.0 mm³ isotropic resolution, the subthalamic nucleus (STN) and substantia nigra (SN) are indistinguishable b) 7 Tesla $T2^*$ -weighted image with 0.5 mm² in-plane resolution with increased contrast to noise compared to the 3T image. c) Zoomed-in on region of deep brain nuclei, arrows indicate location of STN and SN showing clear delineation between the two, as well as the striatum (St), internal globus pallidus, (GPi), and external globus pallidus

The greater MR signal strength available at high fields facilitates the visualization of neurological pathology.

Higher spatial resolution is achievable while maintaining grey-white matter contrast and soft tissue differentiation. This increased signal to noise ratio at high field can be utilized to examine multiple sclerosis (MS) patients [6-8].

Susceptibility weighted imaging provides unique conspicuity of blood vessels at 7T and highlights the perivascular location typical of most MS lesions. Figure 4 is an example of the unique contrast achieved at 7T on MS pathology. Visualization of tissue detail achieved with 7T provides the ability to detect smaller MS lesions as well as novel pathological phenomena.

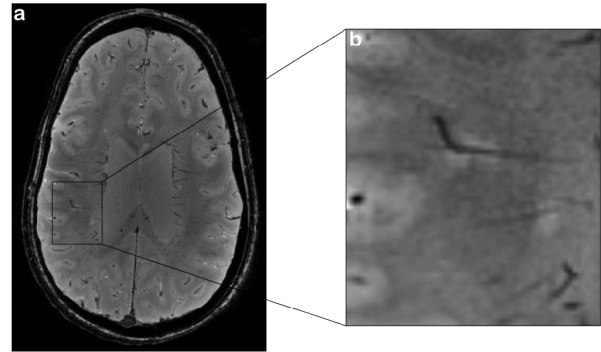


Fig. 4 Perivascular distribution of multiple sclerosis lesions at 7 Tesla. $T2^*$ -weighted image with 0.5 mm x 0.5 mm x 1.0 mm resolution and scan duration equal to 4 minutes (a). Zoomed in region of signal enhancement around centrally coursing vein (b)

III. FUNCTIONAL IMAGING AT 7T

Functional MRI based on the blood oxygen level dependent (BOLD) effect has added considerably to our ability to study the organization and functional architecture of the brain at a “systems” level. With appropriate experimental designs and analyses, the neural circuits underlying specific behaviors and cognitive processes may be evaluated in individual subjects. Most functional imaging studies use “snapshot” imaging techniques of which echo-planar imaging (EPI) is a prime example, in which complete cross sectional images that are sensitive to BOLD effects and that are obtained in very short times, substantially less than one second. These methods are of lower resolution than more conventional images, so that activation maps are typically acquired with voxels on the order of 30-40 mm³.

At 7 Tesla the BOLD signals themselves, which correspond to subtle changes in the tissue susceptibility, are much stronger and the spatial resolution can be pushed to much smaller voxels. For example, Figure 5 shows an activation map comparing the sensory responses to stimulation (by air puffs) of different single digits. These maps are acquired in less than five minutes with voxel dimensions 1 x 1 x 2 mm. The limits on spatial resolution of fMRI at 7T have not been well explored, but clearly there is the possibility of resolving the functional architecture of the cortex at sub-millimeter resolution.

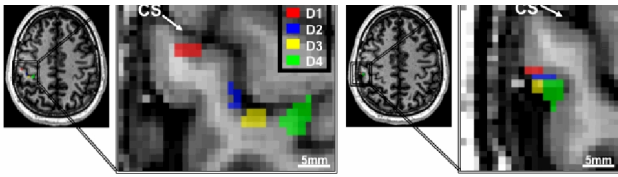


Fig. 5 Composite map of the digit representations in SI of an individual subject overlaid on the axial plane of the subject's anatomical image; with D1 red, D2 blue, D3 yellow, and D4 green. (a) Topographical organization of digits along the posterior bank of the central sulcus (CS). (b) Topographical organization of digits along the crest of the postcentral gyrus

One additional advantage of using higher resolution is that partial volume averaging effects are reduced. This means that very small focal activations are less likely to be averaged out to a lower value by being included in a voxel containing non-activated tissues. A similar argument applies to the use of higher field and higher resolution images for diffusion tensor imaging (DTI) of white matter tracts. DTI data are also usually acquired using single-shot imaging, and tensor information can then be used to depict white matter tracts in the brain. The ability to delineate tracts is diminished when voxels are so large that they contain more than one tract with different orientations, such as when tracts cross within a voxel. Higher spatial resolution, and the acquisition of data from multiple angles is key to being able to follow tracts over many voxels in white matter with complex architecture.

IV. MRS AT 7T

Magnetic resonance spectroscopy (MRS) provides information on the chemical composition of the brain. Proton MRS in particular has been widely explored to obtain information on local concentrations of neural metabolites and some neurotransmitters. Measurements of the major inhibitory neurotransmitter GABA along with the major excitatory neurotransmitter glutamate may have a practical role in various neuropsychiatric conditions. The higher field strength at 7T increases the dispersion of the resonant frequencies from different metabolites, while the higher signal to noise ratio implies that voxel dimensions can again become smaller or acquisition times may be reduced. At 7T spectral images of the distributions of major neural metabolites such as choline, creatine, and N-acetyl aspartate can be obtained in times of order 10 minutes with spatial resolution substantially under 1 ml and excellent signal to noise.

V. TECHNICAL CHALLENGES OF 7T

All major advances in magnet field strength have provided challenges as well as opportunities. Many technical limitations arise when the field strength increases including specific absorption rate (SAR), field inhomogeneities, and susceptibility artifacts. When imaging at high field, it is necessary to modify those sequences that require high peak RF power due to SAR limitations. Prolonging the duration of the pulses, using modified pulses in spin-echo based imaging, or modifying the acquisition can all be applied to reduce SAR at 7T. Although clinical imaging at field strengths of 3T is now routine practice translation of imaging protocols to 7T is not straightforward. Some sequences translate well but others are more difficult and it is necessary to adjust the imaging parameters due to prolongation of T1 and shortening of T2.

Sequences that rely on B1 uniformity are compromised when operating at 300MHz, where the RF pulse wavelength becomes smaller than the dimensions of the head. In this regime standing wave and "near-field" phenomena give rise to large variations in the RF field achieved in an object being imaged. Multi-channel transmit and receive elements can be used to mitigate the observed central brightening pattern resulting from the coil transmission and reception profiles. Advanced pulse designs and image excitation techniques such as spatial-spectral encoding or the use of parallel transmitters are in development to overcome the B1 inhomogeneities at 7T and to excite complicated spatial profiles to cancel the expected dielectric pattern. These techniques are effective in reducing major B1 inhomogeneities.

The problems of inhomogeneity and susceptibility artifacts become ever more severe at higher field strengths, which strengthens the requirement for dynamic shimming. When imaging at 7T, distortion and dephasing arise at tissue/air interfaces due to susceptibility-induced perturbation of B_0 . The substantial phase differences and dielectric effects are exacerbated at high field but can be overcome with better shimming techniques such as dynamic shimming. This technique obtains optimal B_0 field homogeneity for a multi-slice region by updating the shim coil currents slice by slice in real time during interleaved data acquisitions. With the use of dynamic shimming, signal losses and geometric distortions due to differences in magnetic susceptibility can be reduced. This technique can be especially useful in fast T2* based imaging sequences like echo planar imaging (EPI). This fast imaging technique is very sensitive to the effects of inhomogeneities of the

main magnetic field, which cause image distortions and signal losses that are worse at higher fields. At 7T more advanced imaging methods and post-processing corrections for field variations are needed to overcome these challenges.

VI. SUMMARY

Magnetic resonance imaging at 7 Tesla has already proven effective for research purposes and has promise for routine applications in a clinical setting. The experiences to date have validated the expected increase in SNR and favorable increases in contrast, susceptibility effects, and spectral dispersion. With exploitation of the sensitivity increase and consequent increase in resolution, 7T imaging will yield new insights into the diagnosis and management of neurological conditions such as multiple sclerosis, stroke, brain neoplasm, and degenerative diseases. Many technical problems are yet to be addressed and methods to be refined before 7T imaging can be routinely implemented clinically.

Nonetheless, these technical issues are being overcome by creative engineering and physics so that the full potential of high field MRI and MRS can be realized.

REFERENCES

1. Thomas BP, Welch EB, Niederhauser BD, et al. (2008) High-Resolution 7T MRI of the Human Hippocampus In Vivo. *Journal of Magnetic Resonance Imaging*. 28(5): 1266-1272.
2. Haacke EM, Xu YB, Cheng YCN, Reichenbach JR. (2004) Susceptibility weighted imaging (SWI). *Magnetic Resonance in Medicine*. 52:612-618.
3. Reichenbach JR, Haacke EM. (2001) High-resolution BOLD venographic imaging: a window into brain function. *NMR in Biomedicine*. 14:453-467.
4. Reichenbach JR, Venkatesan R, Schillinger DJ, Kido DK, Haacke EM. (1997) Small vessels in the human brain: MR venography with deoxyhemoglobin as an intrinsic contrast agent. *Radiology*. 204:272-277.
5. Wang Y, Yu Y, Li D, et al. (2000) Artery and vein separation using susceptibility-dependent phase in contrast-enhanced MRA. *Journal of Magnetic Resonance Imaging*. 12:661-670.
6. Kollia K, Maderwald S, Putzki N, et al. (2009) First clinical study on ultra-high-field MR imaging in patients with multiple sclerosis: comparison of 1.5T and 7T. *American Journal of Neuroradiology*. 30:699-702.
7. Tallantyre EC, Morgan PS, Dixon JE, et al. (2009) 7-Tesla MRI Improves the Detection of Cortical Lesions in Multiple Sclerosis. *Neurology*. 72:A269-A269.
8. Tallantyre EC, Morgan PS, Dixon JE, et al. (2009) A comparison of 3T and 7T in the detection of small parenchymal veins within MS lesions. *Investigative Radiology*. 44:491-494.

Nanocrystalline Silver: Novel Structure and Activity

Robert E. Burrell¹ and Patricia Nadworny²

¹ Professor and Chair, Department of Biomedical Engineering, Faculties of Engineering and of Medicine & Dentistry, University of Alberta

² Professor and Canada Research Chair in Nanostructured Biomaterials, Department of Chemical and Materials Engineering, Faculty of Engineering, University of Alberta

Abstract—Silver, as Ag^+ , is a well known antimicrobial agent. Depending upon the delivery vehicle the single silver ion may be proinflammatory which could delay wound healing. Further, the Ag^+ ion is chemically very active forming complexes with CF and proteins which reduces its antimicrobial efficacy. The advent of nanostructured silver has solved the antimicrobial issues by controlling the release of silver and generating new silver species. These new species have introduced a host of unexpected benefits around wound healing. Of particular importance is the anti-inflammatory activity which dramatically improves healing.

Keywords—Nanomedicine, Antimicrobial, Anti-inflammatory, Nanosilver, Wound healing.

I. INTRODUCTION

Historically, the use of silver as a medical treatment dates to the 1880s when Crede used a 1% silver nitrate solution to treat and prevent ophthalmia neonatorum. Von Behring soon demonstrated that dilute forms of silver nitrate were effective against typhoid and anthrax bacilli (<http://www.burnsurgery.org/Modules/silver/index.htm>). It was the activity of the dilute forms of silver nitrate that led von Nägeli to coin the term oligodynamic activity. Through the middle 20th century, silver fell into disuse as the medical world concentrated on antibiotics for the control of infection. The sixties saw a resurgence in silver usage as burn physicians searched for more effective broad spectrum antimicrobial agents. Silver nitrate (0.5% solution) and silver sulfadiazine (1% cream) became the standard forms of silver used in burn treatment. These treatments all released one form of silver, the single valent silver ion (Ag^+) (<http://www.burnsurgery.org/Modules/silver/index.htm>). In the mid-1990s, the use of nanotechnology allowed for the development of a new delivery system that released biologically active species other than Ag^+ . This technical innovation has changed the spectrum of biological activity found in silver-releasing products. The single valent silver ion was noted only as an antimicrobial agent and when it was delivered to a wound it was thought to be pro-inflammatory and potentially detrimental to wound healing. Nanocrystalline

silver releases multiple species of silver into solution and these new species have very different biological properties than Ag^+ . It has clearly been demonstrated *in vitro*, *in vivo*, and clinically that this new form of silver has unique anti-inflammatory and antimicrobial properties.

II. SILVER CHEMISTRY

Silver and gold, along with platinum and palladium, are noble metals. Some properties of silver and gold, which are structurally very similar, are shown in Table 1. Interestingly, the cell parameters for gold (407.82) and silver (408.53) are very similar even though the atomic weights are significantly different, which may be an important clue to the anti-inflammatory activity discussed later. Silver is most commonly found in the form of bulk silver metal, $\text{Ag}^{(0)}$, which is chemically inert. Ionic silver is most commonly found in the form of Ag^+ (ionization energy: 731 kJ/mol), but it can also be ionized to Ag^{2+} (ionization energy: 2070 kJ/mol) and Ag^{3+} (ionization energy: 3361 kJ/mol) (<http://www.webelements.com/silver/atoms.html>)

Table 1 Characteristics of Silver and Gold
(data from www.webelements.com)

Metal	Atomic Number	Atomic Weight	Group in Periodic Table	Period in Periodic Table	Structure	Cell Parameters (pm)
Ag	47	107.8	11	5	Face Centered Cubic	$a=b=c=408.53$ $\alpha=\beta=\gamma=90^\circ$
Au	79	197.0	11	6	Face Centered Cubic	$a=b=c=407.82$ $\alpha=\beta=\gamma=90^\circ$

While the structures of silver and gold are similar, they are very different chemically. Silver chloride is very water insoluble (with a K_{sp} of 1.8×10^{-10}) as is gold (I) chloride, while gold (III) chloride is highly soluble (68 g/100g water). It is the insolubility of silver chloride in aqueous media that limits silver uses in wound care. Tables 2 and 3 show what happens to silver when 1 or 50 ppm Ag^+ is placed in a 0.98 molar solution of sodium chloride (equivalent to the

chloride level in serum). Silver chloride precipitates leaving less than 0.21 ppb of the free silver ion. This loss of Ag^+ to AgCl reduces its antimicrobial efficacy dramatically, and is the reason that large amounts of silver were used in the past to treat and prevent wound infections.

Table 2 ICE table for $\text{Ag}^+ = 1$ ppm

	$[\text{Ag}^+_{\text{aq}}]$	$[\text{Cl}^-_{\text{aq}}]$
I	$9.25926 \times 10^{-6} \text{ M}$	$9.85915 \times 10^{-2} \text{ M}$
C	$-X$	$-X$
E	$9.25926 \times 10^{-6} - X \text{ M}$	$9.85915 \times 10^{-2} - X \text{ M}$

$$K_{\text{sp}} = [\text{Ag}^+][\text{Cl}^-]$$

$$1.8 \times 10^{-10} = (9.25926 \times 10^{-6} - X)(9.85915 \times 10^{-2} - X)$$

$$X = 9.25743 \times 10^{-6} \text{ mol/L} \rightarrow \text{Ag}^+ \text{ at equilibrium} = 1.8259 \times 10^{-9} \text{ M or } 0.1981 \text{ } \mu\text{g/L}$$

Table 3 ICE table for $\text{Ag}^+ = 50$ ppm

	$[\text{Ag}^+_{\text{aq}}]$	$[\text{Cl}^-_{\text{aq}}]$
I	$4.62962 \times 10^{-4} \text{ M}$	$9.85915 \times 10^{-2} \text{ M}$
C	$-X$	$-X$
E	$4.62962 \times 10^{-4} - X \text{ M}$	$9.85915 \times 10^{-2} - X \text{ M}$

$$K_{\text{sp}} = [\text{Ag}^+][\text{Cl}^-]$$

$$1.8 \times 10^{-10} = (4.62962 \times 10^{-4} - X)(9.85915 \times 10^{-2} - X)$$

$$X = 4.62778 \times 10^{-4} \text{ mol/L} \rightarrow \text{Ag}^+ \text{ at equilibrium} = 1.849 \times 10^{-9} \text{ M or } 0.2006 \text{ } \mu\text{g/L}$$

III. NANOCRYSTALLINE SILVER CHEMISTRY

Nanocrystalline silver has a grain or crystallite size less than about 25 nm. It may be created as a single crystal or as a polycrystal. As a polycrystalline structure, it is very unstable and will undergo room temperature annealing in a few hours unless it is stabilized. If trace levels of oxygen are incorporated into a polycrystalline silver material as it is created using a process such as physical vapor deposition, it can be stabilized. This is achieved through the incorporation of silver oxide molecules into the growing structure which limit silver atom migration, thus limiting crystal growth. These stable forms of nanocrystalline silver have a very unique chemistry that changes their biological properties. The uniqueness of the structure is evident in the data obtained from low temperature (<110°C) thermal treatments (Taylor *et al.*, 2005). These heat treatments altered many of the material properties. Grain growth occurred at temperatures above 75°C, when both the atomic oxygen and Ag-O bond concentrations in the film dropped precipitously. Similarly the water solubility and antimicrobial activity levels all dropped at the same point.

Nanocrystalline silver releases unique species of silver when it placed in an aqueous environment. Fan and Bard (2002) showed that along with the single valent ion, Ag^+ , a reduced species was also released. They concluded that the species released was Ag^0 . This form of silver is most likely

released as a cluster of silver atoms. Nadworny *et al.* (submitted, 2009) have shown that small clusters of silver atoms are present in the epidermis of pigs treated with nanocrystalline silver, which would support the view of Fan and Bard (2002).

Not only are unique species released, but the concentration of total silver released is very high relative to bulk metallic silver. Bulk silver releases silver at concentrations less than 1 ppm, while nanocrystalline silver releases concentrations over 70 ppm (Wright *et al.*, 1998). This high level of release combined with the unique species released may be responsible for the unusual biological properties of nanocrystalline silver.

Importantly, single silver nanocrystals were unable to generate any bactericidal activity (0 log reduction) against *P. aeruginosa*, unlike polynanocrystalline silver dressings, which produced excellent bactericidal activity, (log reductions of >6) for the same weight of silver (Shrum *et al.*, 2005). This suggest that the structure (polycrystalline) is important as well as the size of the crystals.

An examination of the structure of the poly-nanocrystalline material shows what happens during the thermal destabilization process. Taylor *et al.* (2005) showed that the silver oxide component disappeared as the temperature of heat treatment increased while the silver peaks increased in size, indicating that the oxide decomposed and reduced to metallic silver. In its bulk form, silver oxide decomposes at about 100°C. In the nanostructured form of silver oxide, decomposition occurs at room temperature with a significant increase in rate occurring above 75°C (Landry *et al.*, 2009). This decomposition of the oxide allowed the grains to grow (Taylor *et al.*, 2005). This occurred because the silver oxide acts as a barrier to adatom diffusion. Once the silver oxide is removed, silver atoms are free to move and re-crystallize, which is apparent as grain growth.

Grain growth and changes in the physical structure were also apparent in analyses performed using scanning electron microscopy. At 23°C and 37°C, Taylor *et al.* (2005) found little change in the structure of the material. At 50°C, there was an apparent rounding of the edges of the grains, which was more pronounced at 65°C. The SEM pictures taken after the 90°C heat treatments showed that the nanostructure had completely changed. Further, x-ray diffraction analysis by Taylor *et al.* (2005) showed that the grain size had more than doubled and the oxide component had clearly declined. At 100°C and 110°C, the structure had radically changed, while the oxide component had disappeared. The crystal size increased by factors of four and ten at the two highest thermal treatments, 100°C and 110°C (Taylor *et al.*, 2005). Concomitant with all the physical changes described, Taylor *et al.* (2005) showed that the antimicrobial activity was negatively affected by grain growth. Clearly, the nanostructured material is thermally unstable, and the antimicrobial activity is related to the structure.

IV. ANTIMICROBIAL ACTIVITY OF NANOCRYSTALLINE SILVER

Poly-nanocrystalline silver has unique antimicrobial activity relative to other sources of silver. In Table 4, the data for 30 minute bactericidal assays (log reductions) for a variety of silver wound dressing products are compared. In these assays, the organisms are added directly to the test article (dressing, solution, or cream) in a chloride-containing growth medium, incubated for thirty minutes under appropriate conditions of atmosphere and temperature, and then recovered in a sodium thioglycolate/saline solution (STS) (Gallant-Behm *et al.*, 2005). The STS binds free silver, reducing the carryover problem often associated with antimicrobial silver assays. The recovered solutions are enumerated using a standard plating technique on appropriate growth media and incubated at appropriate temperatures for 24 hours. Colonies are counted and log reductions determined by subtracting the log of the number of recovered organisms from the initial number of bacteria added to the test article. A three log reduction in the microbial population is considered bactericidal, based upon antibiotic assay methods (Hall *et al.*, 1987).

Table 4 A 30 minute bactericidal (log reduction) assay comparison of a poly-nanocrystalline silver dressing (Acticoat™), against 7 other silver containing wound treatments. Silver nitrate and silver sulfadiazine (SSD) are a 0.5% solution and a 1% cream, respectively

	Acti-coat	Aquacel Ag	Arglaes	Actisorb 220	Avan ce	Silver-lon	AgN O ₃	SSD
<i>S.aureus</i>	4	0	0.1	0.8	0	0	1.2	0.2
<i>P.aeruginosa</i>	4.7	0	0.1	0.6	0	0.8	1.3	1.2
<i>B. cepacia</i>	6.1		<0.6	0.9	0.2	0.4	1.4	3.1
<i>MRSA</i>	3.7	0	0.2	0.6	0	0	0.9	1.6
<i>VRE</i>	5	0.2	<0.5	0	0	0	<0.1	0.2
<i>C.albicans</i>	4.7	0.2	0	0.7	0	0	1.1	5.1
<i>C.glabrata</i>	5.4		0.1	0.7	0	2.7	<0.7	<0.7
<i>B.fragilis</i>	3.1	0.3	0.4	0.5	1.2	3.1	2	3.4
<i>MDR.P.a.</i>	5	0	0.4	0.5	0	0.6	0.1	0.3
<i>S.epidermidis</i>	4.9		0	0.3	0.2	0.2	1.8	0
<i>K.pneumoniae</i>	5.8		1.1	0.8	0.2	1.6	1.5	1.1
<i>E.coli</i>	6.1		0.6	1.1	0.2	0.9	0.9	2.1
<i>Alcaligenes sp.</i>	5.6	0.1	0	0.4	0	2.3	0.7	0.7
<i>C.koseri</i>	5	1.2	0.7	2.7		1.6	2.4	2.4
<i>Acinetobacter sp.</i>	7.9	0.6	0.7	0.5	0.1	2.8	1.8	7.9
<i>Mucor sp.</i>	6.7	0.2	0.1	0.2	0.1	0.3	0.1	0.3
<i>Aspergillus sp.</i>	2.9	0	0	0.2	0.1	0.2	0	0.2

The data clearly shows that the nanocrystalline silver dressing was bactericidal against all test organisms, while none of the other test articles were effective against more than 1 organism. This result was initially confusing as the SSD and silver nitrate contain and release over 3000 ppm of Ag⁺, while the nanocrystalline silver releases about 70ppm (Wright *et al.*, 1998). However, the work of Fan and Bard (2002) showed that the nanocrystalline material releases multiple species of silver including Ag⁺ and Ag⁰, and it is believed that the multiple species of silver released changes the antimicrobial activity of the nanostructured silver.

Similar results were shown in log reduction assays performed over time. The data in Figure 1 shows that MRSA was controlled by the nanocrystalline silver in 30 minutes, while the other silver technologies were not considered bactericidal (>3 log reduction) over the 2 hours of the test.

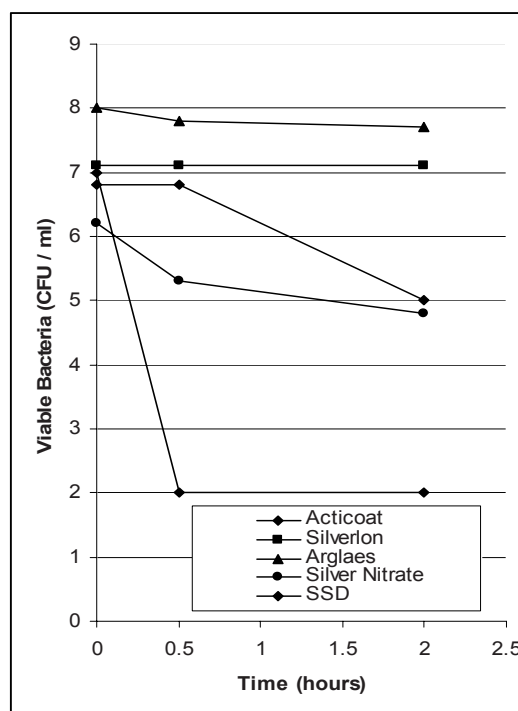


Fig. 1 Bactericidal assays (log number of survivors vs. time) for various silver dressing treatments tested against MRSA. The organisms were grown in, and the tests were performed in, Trypticase Soy Broth at 37°C. Note: The limit of detection is 2

In clinical use, the nanostructured silver dressing has shown excellent antimicrobial activity. In a clinical study performed by Tredget *et al.* (1998), they found that the frequency of burn wound sepsis was a factor of three lower

in the nanocrystalline silver treated wounds versus those treated with 0.5% silver nitrate. They also found that the nanocrystalline silver dressing reduced bacteremias by a factor of 5 when compared to silver nitrate. Similar antimicrobial activity was shown for wounds contaminated with MRSA that were treated with nanocrystalline silver (Strohal *et al.* 2005).

V. ANTI-INFLAMMATORY ACTIVITY OF NANOCRYSTALLINE SILVER

Early clinical feedback suggested that nanocrystalline silver dressings were positively affecting wound healing in a way that seemed greater than just excellent antimicrobial control. Demling (<http://www.burnsurgery.org/Modules/silver/index.htm>) postulated that the nanocrystalline silver dressing may have some anti-inflammatory activity based upon his observation of wound healing in burn patients treated with the dressing. To examine this hypothesis, Wright *et al.* (2002) undertook a porcine wound healing study. In this study, there were no significant differences in matrix metalloproteinase (MMP) activity between the samples on Days 1 and 2. However, the MMP activity of wound fluid recovered from the nanocrystalline silver treated wounds on Day 3 was significantly less ($p < 0.05$) than for the controls. Similarly, on Day 4, nanocrystalline silver-treated wounds showed significantly less gelatinolytic activity than silver nitrate-treated wounds ($p < 0.05$) or the control wounds ($p < 0.01$). On Day 5, the MMP activity of the nanocrystalline silver treated wounds was significantly less ($p < 0.0001$) than either of the other treatments. This data suggested that the dressing was anti-inflammatory; however, the inclusion of bacteria in the wounds did not allow a definitive conclusion to be drawn.

To determine definitively if the dressing was anti-inflammatory, Nadworny *et al.* (2008) undertook a study of chemically inflamed dermal tissue. They found that the nanocrystalline silver dressing resolved inflammation much faster than did Ag^+ provided from a 0.5% silver nitrate solution. There were differences in erythema and oedema scores suggesting this outcome, but the histological analyses clearly showed the positive impact of the nanocrystalline silver on the resolution of severe chemical inflammation. In their study, the negative control showed no inflammation, while the positive control (treated with saline soaked gauze) remained highly inflamed for the 3 days of the study. Silver nitrate had no positive impact on the healing process, while the nanocrystalline silver-treated tissues were virtually normal after 3 days of treatment. It is

believed that this was a result of the release of multiple species of silver during dissolution by the nanocrystalline silver dressing.

The mechanism behind this remarkable anti-inflammatory effect appeared to be related to the induction of apoptosis in the inflammatory cells. Nadworny *et al.* (2008) showed that there was no apoptosis in the negative control and only limited apoptosis in the positive controls. Silver nitrate induced apoptosis in the keratinocytes, while the nanostructured silver induced it primarily in inflammatory cells in the dermis. The silver nitrate result suggests that Ag^+ may slow re-epithelialization, while the nanostructured silver clearly resolved inflammation by removing the inflammatory cells safely.

In the same study the authors looked at the impact of the treatments on various cytokines. The data showed that these markers for inflammation were predominately found in the positive controls and silver nitrate-treated wounds, as would be expected based upon the histology. The nanocrystalline silver-treated tissues were comparable to the negative controls.

VI. CONCLUSIONS

By controlling the nanostructure of silver, new important biological properties can be created, including antimicrobial and anti-inflammatory activity. The activity generated is not a result of the simple release of Ag^+ , nor can it be achieved by simply making nanoparticles of silver. The activity, which is closely associated with a polycrystalline structure with an average grain size between 10 and 15 nm, is responsible for improved wound healing. Improvements include more rapid closure and reduced scarring.

REFERENCES

1. Fan & Bard *J Phys Chem B* 2002;106:279-87
2. Gallant-Behm *et al.* *Wound Rep Reg* 2005;13:412-421
3. Hall *et al.* *J Oral Maxillofac Surg* 1987;45:779-84
4. <http://www.burnsurgery.org/Modules/silver/index.htm>
5. <http://www.webelements.com/silver/atoms.html>
6. <http://www.webelements.com>
7. Landry *et al.* *Biomaterials* 2009;30:6929-6939
8. Nadworny *et al.* *Nanomedicine: Nanotech, Biol, and Med.* 2008; 4:241-251
9. Shrum *et al.* *ICMENS 2005 Conference, Banff, Alberta*
10. Strohal *et al.* *Journal of Hospital Infection* 2005 60, 226-230
11. Taylor *et al.* *Biomaterials* 2005 26:7230-7240
12. Tredget *et al.* *(J Burn Care Rehabil* 1998;19:531-537
13. Wright *et al.* *Wounds* 1998;10(6):179-188
14. Wright *et al.* *Wound Rep Reg* 2002;10:141-151

Ultrasound: Past, Present and Future

K. Kirk Shung

Department of Biomedical Engineering, University of Southern California, Los Angeles, CA, USA

Abstract—Ultrasound has been used as a diagnostic tool for more than 40 years. Many medical applications have been found, mostly notably in obstetrics and cardiology. It had a humble beginning, started by a few curious scientists and clinicians in different parts of the world in early 1950s and did not become an established diagnostic tool until early 1970s when grey scale ultrasonography was introduced. Modern ultrasound scanners are capable of producing images of anatomical structures in great detail in grey scale and of blood flow in a color scale in real-time. State of the art 4D scanners yielding 3D volumetric images in real-time are pushing the technical envelope further. Today ultrasound is the second-most used clinical imaging modality next only to conventional x-ray radiography. Although ultrasound is considered to be a mature technology, technical advances are still constantly being made. The most significant achievements in ultrasound recently have been in the developments of approaches capable of quantitative measurement of tissue elastic properties, namely ultrasound elastography and radiation force imaging, high frequency imaging yielding improved spatial resolution and therapeutic applications in drug delivery and high intensity focused ultrasound surgery. In this paper, the history and current state of medical ultrasound will be reviewed and future developments discussed.

Keywords—Ultrasound, ultrasonic imaging, color Doppler, elastography, radiation force imaging.

I. PAST

The potential of ultrasound as an imaging modality was realized as early as in late 1940's when several groups of investigators around the world utilizing sonar and radar technology developed during World War II started exploring diagnostic capabilities of ultrasound [1](Goldberg and Kimmelman, 1988). John Wild, a clinician and John Reid, an engineer, at University of Minnesota Medical School, USA, developed a prototype 15 MHz B-mode ultrasonic mechanical scanner with components borrowed from a naval laboratory. They were able to demonstrate the capability of ultrasound for imaging and characterization of cancerous tissues. John Wild's pioneering effort and accomplishment were recognized with the Japan prize in 1991. At the same time, Douglas Howry and Joseph

Holms at University of Colorado at Denver, apparently unaware of the effort by Wild and Reid, also built an ultrasonic imaging device with which they produced cross-sectional images of the arm and leg. In Japan starting in the late 1940's medical applications of ultrasound were explored by Kenji Tanaka and Toshio Wagai. Two Japanese investigators, Shigeo Satomura and Yasuhara Nimura were credited for the earliest development of ultrasonic Doppler devices for monitoring tissue motion and blood flow in 1955. Virtually simultaneously with the work going on in Japan and in the U.S., Inge Edler and Hellmuth Hertz at University of Lund in Sweden worked on echocardiography, an ultrasound imaging technique for imaging cardiac structures and monitoring cardiac functions. In parallel with these developments in the diagnostic front, William Fry and his colleagues at the University of Illinois at Urbana worked on applying high intensity ultrasound beam to treat neurological disorders in the brain. Fig. 1 shows an early ultrasonic scanner and an image of a fetus obtained by such a scanner. There are many modes of ultrasonic imaging [2 shung]. The primary form of ultrasonic imaging however to date has been that of a pulse-echo mode. The principle is very similar to that of sonar and radar. In essence, following an ultrasonic pulse transmission, echoes from the medium being interrogated are detected and used to form an image. Many terminologies used in ultrasound are imported from the field of sonar and radar. Although pulse-echo ultrasound had been used to diagnose a variety of medical problems since 1950's, it did not become a widely accepted diagnostic tool until early 1970's when gray-scale ultrasound in which non-linear echo amplitude to gray level mapping was introduced [2,3]. Continuous wave (CW) and pulsed Doppler (PW) ultrasound devices for measuring blood flow also became available during that time. Duplex ultrasound scanners that combined both functions allowing the imaging of anatomy and the measurement of blood flow with one single instrument soon followed. In 1985 color Doppler flow mapping system that combined Doppler flow imaging in color with B-mode imaging in gray scale was 1st introduced by Aloka in Japan.

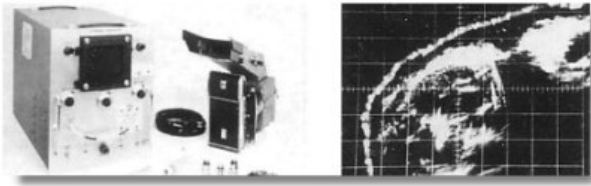


Fig. 1 An early scanner and an image obtained by such a scanner from website: <http://www.ob-ultrasound.net/>

II. PRESENT

Today all high end ultrasonic scanners are capable of color Doppler flow imaging and performing CW and pulsed Doppler flow measurements. A color Doppler image is shown in Fig. 2 where the blood flow information is depicted in color. A “BART” (blue away red toward) system is used to depict blood flow direction. Red means toward the transducer whereas blue away from the transducer. Shades of a color indicate the magnitude of flow velocity. The anatomy information or B-mode image is displayed in gray scale. The development of non-toxic contrast agents, primarily encapsulated gas bubbles has opened new avenues for ultrasonic imaging including harmonic imaging which increases contrast and perfusion imaging [2,4]. Tissue displacement imaging enables assessment of elastic properties of tissues and distinguishing lesions unseen in standard B-mode images. Multidimensional imaging that utilizes multidimensional arrays e.g. 1.5D and 2D allows for improvement in image contrast resulted from better control of slice thickness and 3D volumetric imaging in real-time or 4D imaging. Figs. 3 and 4 show respectively a 3D image of a fetus in utero and an image obtained by ultrasound elastography where a volume of tissue is disturbed and estimation of elastic properties of the tissue is estimated by measuring tissue displacement from correlating the speckle patterns prior and after the mechanical disturbance [2,5].



Fig. 2 Color Doppler image of a fetus and an umbilical cord (Courtesy of Philips)

Today ultrasound is the second most utilized diagnostic imaging modality in medicine, next only to conventional x-ray, and is a critically important diagnostic tool of any medical facility. Ultrasound not only complements the more traditional approaches such as x-ray but also possesses unique characteristics that are advantageous in comparison to other competing modalities such as x-ray computed tomography (CT), radionuclide emission tomography, and magnetic resonance imaging (MRI). More specifically, (1) ultrasound is a form of non-ionizing radiation and is considered safe to the best of present knowledge, (2) it is less expensive than imaging modalities of similar capabilities, (3) it produces images in real time, unattainable at the present time by any other methods, (4) it has a resolution in the millimeter range for the frequencies being clinically used today, which may be made better if the frequency is increased, (5) it can yield blood flow information by applying the Doppler principle, and (6) it is portable and thus can be easily transported to the bedside of a patient.

Ultrasound also has several drawbacks. Chief among them are that (1) organs containing gases and bony structures cannot be adequately imaged without introducing specialized procedures, (2) only a limited window is available for ultrasonic examination of certain organs such as heart and neonatal brain, (3) it is operator skill-dependent, and (4) it is sometimes impossible to obtain good images from certain types of patients including obese patients.

The many advantages that ultrasound can offer have allowed it to become a valuable diagnostic tool in such medical disciplines as cardiology, obstetrics, gynecology, surgery, pediatrics, radiology, and neurology, to name just a few. The relationship among ultrasound and other imaging modalities is a dynamic one. Ultrasound is the tool of choice in obstetrics primarily because of its non-invasive nature, its cost-effectiveness, and its real-time imaging capability. This role will not change in the foreseeable future. Ultrasound also enjoys similar success in cardiology, demonstrated by the fact that echocardiography is a training that every cardiologist must have. The future of ultrasound in cardiology however is not as rosy as in obstetrics because while ultrasound is progressing at a rapid rate, other competing imaging modalities such as multi-slice spiral CT and MR are also making great strides in improving the image acquisition rate and image quality. Ultrasound may lose ground in certain areas but it may gain in other areas. Ultrasound mammography is an example of gradually gaining importance in breast cancer imaging. Nevertheless at the time of heightened public concern with health care costs,

the cost-effectiveness of an imaging tool is a crucial factor in planning diagnostic strategies. Diagnostic ultrasound is particularly attractive in this respect and has been anticipated by many, clinicians and manufacturers alike, to be a major modality of the future.



Fig. 3 A 3D image of a 10-week old fetus in utero (courtesy of Philips)

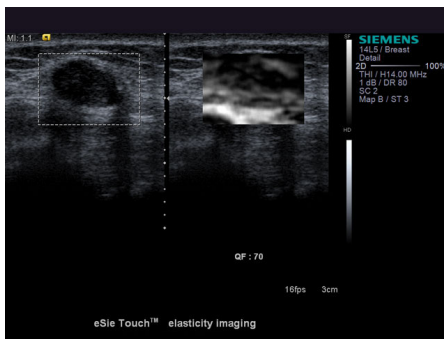


Fig. 4 B-mode image (left) and ultrasound elastogram (right) of a breast cancer (courtesy of Siemens)

III. FUTURE

Despite that ultrasound has been in existence for more than 40 years and is considered a mature technology by many, the field is constantly evolving. Technical advances are still constantly being made. The developments of portable scanners, miniature pocket size scanners, and high frequency scanners are just a few examples.

High frequency (higher than 20 MHz) scanners are being developed for eye, skin and small animal imaging in addition to intravascular imaging because of the improved spatial resolution while paying the price of a reduced depth of penetration [2]. There are at least more than half a dozen of

eye scanner manufacturers around the world. The basic design has been a mechanical sector scanner in which a high frequency single element transducer is mechanically rotated to form an image. The electronics is relatively simple consisting of a single radio frequency channel. The novelty lies in the probe and transducer design [6,7]. Fig. 5 shows an image of the anterior segment of the eye at 40 MHz obtained such a scanner. Detailed anatomy can be clearly seen. Such a system has also been used to image small animals and skin lesions. Mechanical scanners suffer from a slow frame rate and non-uniform image quality. As a result high frequency linear arrays and scanners have been developed [2,8,9]. Fig. 6 shows a 256 element 35 MHz element linear arrays made from 2-2 composites with a bandwidth better than 50%.

40 MHz US Image of excised eye

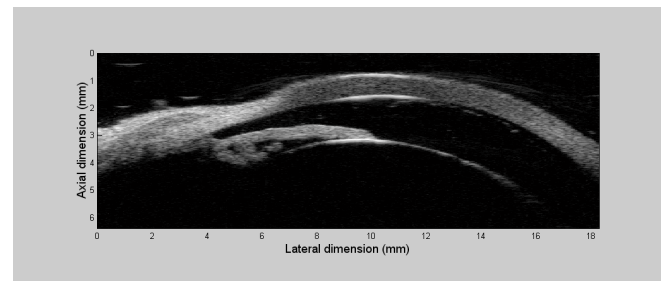


Fig. 5 Image of the anterior segment of an excised eye obtained by a mechanical high frequency scanner

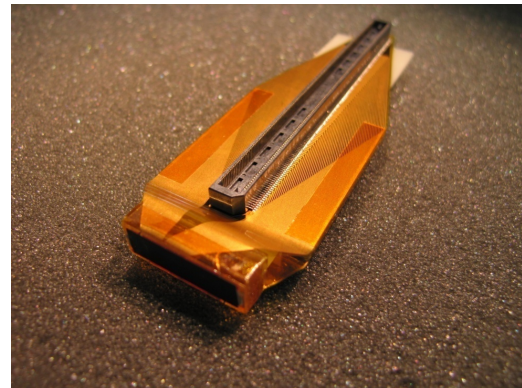


Fig. 6 Photo of a 256 element 30 MHz linear array showing the aperture in the front and the flex circuit for interconnection

Although the pace of development in therapeutic ultrasound has not been as striking as diagnostic ultrasound,

there has been an intense recent interest in imaging guided ultrasound therapy for hyperthermia and for high intensity focused tissue ablation. A MR guided ultrasound therapy system is now commercially available for treating uterine fibroids and being clinically evaluated for treating bone, liver, and breast cancer.

IV. CONCLUSION

Ultrasound has come a long way since its humble beginning in early 1950s. It is one of the most important tools in diagnostic medicine today. Although it is now considered a mature technology, technical advances are still constantly being made. It is conceivable in the not too distant future that every physician's office may have one just like a stethoscope and it may find applications in areas that can never be imagined.

REFERENCES

1. Goldberg B, Kimmelman B. (1998) Medical diagnostic ultrasound : a retrospective on its 40th anniversary. Eastman Kodak Company, New York.
2. Shung K. (2005) Diagnostic ultrasound: imaging and blood flow measurements. CRC Press, Boca Raton, FL.
3. Szabo T. (2004) Diagnostic ultrasound imaging: inside out. Elsevier Press, Burlington, MA.
4. Finking P, Bouakaz A, Kirkhorn J, Ten Carte F, de Jong N (2000) Ultrasound contrast imaging: current and new potential methods. *Ultrasound Med Biol* 26: 965-975.
5. Nightingale K, Soo M, Nightingale R, Trahey G (2002) Acoustic radiation force impulse imaging: in vivo demonstration of clinical feasibility. *Ultrasound Med Biol* 28: 227-235.
6. Foster F, Zhang Y, Zhou YQ et al. (2002) A new ultrasound instrument for in vivo imaging of mice. *Ultrasound Med Biol* 28: 1165-1172.
7. Cannata J, Ritter T, Chen W, et al. (2003) Design of efficient broadband single element (20-80 MHz) ultrasonic transducers for medical imaging. *IEEE Trans Ultras Ferroelect Freq Cont* 50: 1548-1557.
8. Foster F, Mehi J, Lukacs M et al (2009) A new 15-50 MHz based micro-ultrasound scanner for preclinical imaging. *Ultrasound Med Biol* 35: 1700-1708.
9. Cannata J, Williams J, Zhou Q et al. (2005) Development of a 35 MHz piezo-composite ultrasound array for medical imaging. *IEEE Trans Ultras Ferroelect Freq Cont* 52: 224-236.

Bioengineering in Vietnam

Regis B. Kelly

The California Institute for Quantitative Biosciences (QB3), USA

Summary—**Biologists seek an accurate description of the biological world. Engineers do not describe things. Instead they design devices that they then build and test. Bioengineers bring these disparate disciplines together in two ways that are conceptually very different. In the past, bioengineering has meant designing, building and testing mechanical devices that operate on biological tissue. A rapidly growing branch of bioengineering, however, applies biological principles to design, build and test novel forms of cells that execute reliably a desired function. We offer a brief review of recent developments in both forms of bioengineering and examine their potential value for Vietnamese bioengineers.**

I. BIOLOGICAL DEVICE ENGINEERING

When discussing the impact of bioengineering on human health it is convenient to distinguish four stages in disease progression, (1) a genetic predisposition to a certain disease, (2) environmental factors that trigger disease, (3) diagnosis of the disease that is causing symptoms and (4) treatment.

Genetic predispositions to disease have been discovered by genome wide analyses that link genomic DNA markers, usually single nucleotide polymorphisms, to the probability of developing a disease such as Diabetes, or Alzheimer's. Very, very rarely is that probability 100%. The current commercial devices that recognize DNA variations usually involve hybridizing a person's DNA to known oligonucleotides in a microarray. An important new technology, high throughput DNA sequencing, might replace microarray analyses. The new DNA sequencing techniques are driving up the speed of DNA sequencing while driving down the cost dramatically. Bioengineers are rushing to find ways of taking full advantage of this dramatic development and are finding that device development must go hand-in-hand with software development and bioinformatic analyses.

Fifty percent of disease is believed to be due to **environmental factors**, which often trigger disease onset preferentially in patients who are genetically predisposed. A class of environmental factors of major interest to bioengineers are the pathogens. Human health could be greatly improved if we had pathogen detectors that could unequivocally recognize dangerous pathogens. Until recently, unknown pathogens have been recognized by

hybridizing their nucleic acids to DNA microarrays (Chiu et al). An exciting application of the new high throughput sequencing capacity appearing in leading university research labs has been the use of DNA sequencing to identify pathogens either in patients tissues, or in the sewage generated by large towns and cities. The goal in this case it to build robust devices that can alert public health authorities to the impending emergence of a serious epidemic.

Bioengineers wishing to improve health outcomes invest considerable creativity into **diagnostic devices**. Here it is important to distinguish two classes of diagnostic device, those that provide early detection of disease before symptoms arise and those that accurately identify the disease that is causing the symptoms when they arise.

Early diagnostic devices screen apparently healthy populations to identify patients that have diabetes, cancer or heart disease for example but are not yet displaying symptoms. It is essential that early diagnostic devices use patient material, blood, saliva, breath, that is easily available, and that the cost per test and the incidence of false positives be very low. A test that gave 1% false positives for a disease that has an incidence on one in a thousand would have limited value. In practice this means that early diagnosis devices have had poor market penetration. Bioengineers are pushing down the cost per test by using microfluidic strategies to eliminate the need for expensive technicians and to reduce the amounts of material needed. To reduce the false positive problem, more and more tests are multiplexed, measuring five to twenty parameters simultaneously. An illustrative example of an early diagnostic is a screen for Type II diabetes developed by Tethys Diagnostics. Interest is emerging in linking early diagnostic screening to patients who have a high genetic predisposition to a particular disease (Kohlberg et al).

Once a patient displays symptoms, and **disease diagnosis** is the primary concern there is less emphasis on diminishing the cost of the test. The goal becomes accuracy and the concern is missing the correct diagnosis through false negatives or a test that lacks adequate specificity. The physician's physical exam is usually complemented nowadays by a molecular, physiological or imaging

verification. Molecular verification can involve measuring levels of metabolites, proteins or nucleic acids. An exciting new development that could have great value is the use of high throughput sequencing to measure protein synthesis rates with great accuracy (Ingolia et al). Another is in magnetic resonance spectroscopy to measure metabolites in a tissue of a living patient. This technique is proving to be of value in distinguishing benign from malignant cancers and to identifying damaged disc vertebrae that are causing back pain (Zuo et al). The appeal of such non-invasive diagnostic procedures is that they take away the need to biopsy patients, a procedure which is usually uncomfortable and often induces damaging side effects, including death, in the patient being diagnosed.

Once a disease is accurately diagnosed the bioengineer has to devote attention to optimizing the therapeutic response. Usually the preferred, most cost-effective therapeutic intervention involves prescribing therapeutic drugs for the sick patient. Pharmacology may appear to be outside the domain of a bioengineers' expertise but that is not so. Diagnosis is fraught with errors and so markers of disease progression, molecular, physiological and imaging are needed to verify that the patient is responding appropriately to the chosen therapeutic regimen. Even when the diagnosis is correct, it is essential to match the drug provided to the particular patient, the area now known as pharmacogenomics (Kroetz et al). This brings us back to the need to know a patient's particular genotype to be able to tailor an appropriate physician response. A well known case involves the response to warfarin. Finally the bioengineer's skills are of major importance in drug delivery. The conventional regimen or ingestion by mouth and non-specific delivery to the whole body, healthy as well as diseased, is slowly being replaced by drug delivery devices, often based on nanotechnology, that selectively deliver the therapeutic drug to the diseases tissue (Ainslie et al).

When a drug cannot cure a sick patient, the physician must often turn to the more expensive and risky strategy of surgery. Bioengineering again has major roles to play. Perhaps the most valuable is to show that surgery will not in fact be beneficial. By using sophisticated diagnostic measures the bioengineers device can show that this particular class of patient will not benefit by the surgical intervention. Patient stratification of this type is proving particularly valuable in common diseases such as breast and prostate cancer. Once surgery has been decided upon, there is a great need to bring quantitation to the process of anesthetizing the patient. The way surgeons estimate the depth of anesthesia is almost medieval. After surgery, devices designed by bioengineers monitor a patient's vital signs. Here we are faced with the challenge of setting alarm monitors appropriately so that

frequent false alarms do not negate the value of the monitor, a frequent clinical occurrence.

II. CELL BIOENGINEERING

A new sub-field within bioengineering, often called synthetic biology in analogy with synthetic chemistry, designs, builds and tests devices that use biological materials to deliver the desired result. Synthetic biologists think like engineers, not biologists. They view a cell as the combination of a set of functional sub-routines, each executed by a set of gene products interacting with each other in a coordinated fashion. An engineering parallel might be the way mechanical elements interact to produce, for example, a computer hard drive. Like engineers, synthetic biologists want each biological sub-routine to be a standardized, off-the-shelf component, that can be combined seamlessly with other subroutines, the way hard drives are combined with CPUs, keyboards, etc to create a computer. The Parts Lab based at MIT has a library of over 2,000 such subroutines, each encoded in a stretch of DNA that specifies the needed set of gene products at the appropriate levels.

Consider an example to show how elements can be combined to give a bacterium that acts as photographic film. One MIT part turns on gene products when a bacterium is exposed to light. Another creates a dark pigment. If both sub-routines are introduced into bacteria appropriately then the bacteria produce pigment when exposed to light, producing a photographic image. If pigment production requires light and a chemical signal bacteria can produce an edge detector (Tabor et al).

The ability to tailor the properties of microbial cells to engineer a desired function opens the door to a new field of engineering that is inexpensive, simple and environmentally attractive, or "green" as it is now called. Consider an example. Gasoline can be made commercially from methane using large industrial plants that employ zeolite catalysts to add halides to produce methyl halides. This step is however very energy demanding. Yeast that have been engineered to contain high levels of the enzyme, methyl halide transferase, can generate volatile fuels when provided a carbohydrate energy source (Bayer et al). To get the carbohydrate energy source the yeast are co-cultured with a bacterium that secretes cellulases that break down biomass waste to simple sugars.

Cellular engineering of this type is attracting a great deal of interest from investors. Products being made in this way include not only biofuels, but also expensive pharmaceuticals, precursors to plastics and other biomaterials.

III. LESSONS FOR VIETNAM

Vietnam is growing rapidly in many ways but is not currently viewed as an international leader in biological research. This is understandable. Vietnam has to spend its resources wisely and it is hard to compete with countries that have been investing billions of dollars annually into biomedical research for several decades and have, as a consequence, a huge reservoir of trained human capital and expertise. Vietnam, however, has an enviable record of creativity in engineering, with a talent for designing simple but clever and robust devices that perform reliably. In my opinion, the country should take advantage of its engineering capacity to build its reputation in the biological sciences by focusing on bioengineering.

Two opportunities within bioengineering seem particularly attractive to Vietnam. Just over a year ago I spent almost two weeks touring hospitals within Vietnam. What impressed me was the lack of simple devices such as respirometers, ultrasound monitors and microtomes. Furthermore, medical monitoring devices, purchased from or donated by foreign countries were sitting unused because they had no service contracts or lacked appropriate instructions in their use. This seems to provide an attractive opening for Vietnamese bioengineers. Hospital monitoring devices created by rich countries are often more complicated than they need to be, because expensive devices can generate more income for the manufacturer. Besides increasing the price this complexity makes the equipment difficult to use without extensive training sessions and liable to frequent break-down. Engineers in Vietnam might be able to use their ingenuity to design and build simple, but robust devices that serve the needs of the Vietnamese medical population but also those of other countries at equivalent state of economic development.

The second opportunity lies in the area of cellular engineering, or synthetic biology. Conventional engineering products are built of metals, plastics, etc. but Vietnam is not richly endowed with the materials that are needed. In contrast, synthetic biology requires biomass. Vietnam is richly endowed with sunlight, water and coastline and so has an advantage when engineering uses biologically based materials. Synthetic biology has other advantages for Vietnam. Although a new field it is basically very simple and does not require huge investments in sophisticated equipment. High school students can do it! It is a new field, and so Vietnam would not be as far behind as it is, for example, in pharmaceutical discovery and development. Finally, product manufacture requires mainly fermentation technologies, an area in which Vietnam already has a trained workforce.

Whatever direction Vietnamese bioengineers choose to take, the principles behind the decision remain the same. Since no one can be an expert in everything, and Vietnam has limited resources, it has to identify the areas of bioengineering on which it should focus? Choosing the correct focus means identifying the unique strengths of Vietnam, matching those strengths to scientific areas that are not already overpopulated internationally, and giving preference to areas that could generate income growth for Vietnam. The Vietnamese government is most likely to provide its scarce resources for scientific research to those areas that will improve the economic status of its citizens.

REFERENCES

1. Chiu CY, Urisman A, Greenhow TL, Rouskin S, Yagi S, Schnurr D, Wright C, Drew WL, Wang D, Weintrub PS, Derisi JL, Ganem D. Department of Biochemistry and Biophysics, University of California San Francisco, San Francisco, CA, USA. Utility of DNA microarrays for detection of viruses in acute respiratory tract infections in children. *J Pediatr.* 2008 Jul;153(1):76-83. Epub 2008 Mar 7.
 OBJECTIVE: To assess the utility of a panviral DNA microarray platform (Virochip) in the detection of viruses associated with pediatric respiratory tract infections (RTIs). STUDY DESIGN: The Virochip was compared with conventional direct fluorescent antibody (DFA)- and polymerase chain reaction (PCR)-based testing for the detection of respiratory viruses in 278 consecutive nasopharyngeal aspirate samples from 222 children. RESULTS: The Virochip was superior in performance to DFA, showing a 19% increase in the detection of 7 respiratory viruses included in standard DFA panels, and was similar to virus-specific PCR (sensitivity, 85% to 90%; specificity, $\geq 99\%$; positive predictive value, 94% to 96%; negative predictive value, 97% to 98%) in the detection of respiratory syncytial virus, influenza A, and rhinoviruses/enteroviruses. The Virochip also detected viruses not routinely tested for or missed by DFA and PCR, as well as double infections and infections in critically ill patients that DFA failed to detect. CONCLUSIONS: Given its favorable sensitivity and specificity profile and expanded spectrum for detection, microarray-based viral testing holds promise for clinical diagnosis of pediatric RTIs.
2. Kolberg JA, Jørgensen T, Gerwien RW, Hamren S, McKenna MP, Moler E, Rowe MW, Urdea MS, Xu XM, Hansen T, Pedersen O, Borch-Johnsen K. Tethys Bioscience, Emeryville, California, USA. jkolberg@tethysbio.com Development of a type 2 diabetes risk model from a panel of serum biomarkers from the Inter99 cohort. *Diabetes Care.* 2009 Jul;32(7):1207-12.
 OBJECTIVE: The purpose of this study was to develop a model for assessing the 5-year risk of developing type 2 diabetes from a panel of 64 circulating candidate biomarkers. RESEARCH DESIGN AND METHODS: Subjects were selected from the Inter99 cohort, a longitudinal population-based study of approximately 6,600 Danes in a nested case-control design with the primary outcome of 5-year conversion to type 2 diabetes. Nondiabetic subjects, aged ≥ 39 years, with BMI ≥ 25 kg/m² at baseline were selected. Baseline fasting serum samples from 160 individuals who developed type 2 diabetes and from 472 who did not were tested. An ultrasensitive immunoassay was used to measure of 58 candidate biomarkers in multiple diabetes-associated pathways, along with six routine clinical variables. Statistical learning methods and permutation testing were

used to select the most informative biomarkers. Risk model performance was estimated using a validated bootstrap bias-correction procedure. RESULTS: A model using six biomarkers (adiponectin, C-reactive protein, ferritin, interleukin-2 receptor A, glucose, and insulin) was developed for assessing an individual's 5-year risk of developing type 2 diabetes. This model has a bootstrap-estimated area under the curve of 0.76, which is greater than that for A1C, fasting plasma glucose, fasting serum insulin, BMI, sex-adjusted waist circumference, a model using fasting glucose and insulin, and a noninvasive clinical model. CONCLUSIONS: A model incorporating six circulating biomarkers provides an objective and quantitative estimate of the 5-year risk of developing type 2 diabetes, performs better than single risk indicators and a noninvasive clinical model, and provides better stratification than fasting plasma glucose alone.

3. Ingolia NT, Ghaemmaghami S, Newman JR, Weissman JS. Department of Cellular and Molecular Pharmacology, Howard Hughes Medical Institute, University of California, San Francisco, and California Institute for Quantitative Biosciences, San Francisco, CA 94158, USA. *ingolia@cmp.ucsf.edu* Genome-wide analysis in vivo of translation with nucleotide resolution using ribosome profiling. *Science*. 2009 Apr 10;324(5924):218-23. Epub 2009 Feb 12.

Techniques for systematically monitoring protein translation have lagged far behind methods for measuring messenger RNA (mRNA) levels. Here, we present a ribosome-profiling strategy that is based on the deep sequencing of ribosome-protected mRNA fragments and enables genome-wide investigation of translation with subcodon resolution. We used this technique to monitor translation in budding yeast under both rich and starvation conditions. These studies defined the protein sequences being translated and found extensive translational control in both determining absolute protein abundance and responding to environmental stress. We also observed distinct phases during translation that involve a large decrease in ribosome density going from early to late peptide elongation as well as widespread regulated initiation at non-adenine-uracil-guanine (AUG) codons. Ribosome profiling is readily adaptable to other organisms, making high-precision investigation of protein translation experimentally accessible.

4. Zuo J, Saadat E, Romero A, Loo K, Li X, Link TM, Kurhanewicz J, Majumdar S. Department of Radiology and Biomedical Imaging, University of California, San Francisco, San Francisco, California, USA. *jzuo@radiology.ucsf.edu* Assessment of intervertebral disc degeneration with magnetic resonance single-voxel spectroscopy. *Magn Reson Med*. 2009 Nov;62(5):1140-6.

This study examined the feasibility of using short-echo water-suppressed point-resolved spectroscopy (PRESS) on a clinical 3T magnetic resonance (MR) scanner for evaluating biochemical changes in degenerated bovine and cadaveric human intervertebral discs. In bovine discs (N = 17), degeneration was induced with papain injections. Degeneration of human cadaveric discs (N = 27) was assessed using the Pfirrmann grading on T(2)-weighted images. Chemicals in the carbohydrate region (Carb), the choline head group (Cho), the N-acetyl region (N-acetyl), and the lipid and lactate region (Lac+Lip) were quantified using (1)H PRESS, and were compared between specimens with different degrees of degeneration. The correlation between the spectroscopic findings and glycosaminoglycan (GAG) quantification using biochemical assays was determined. Significant differences were found between the ratios (N-acetyl/Cho, N-acetyl/Lac+Lip) acquired before and after papain injection in bovine discs. For human cadaveric discs, significant differences in the ratios (N-acetyl/Carb, N-acetyl/Lac+Lip) were found between discs having high and low Pfirrmann scores. Significant correlations were found between N-acetyl/Lac+Lip and GAG content in bovine discs

(R = 0.77, P = 0.0007) and cadaveric discs (R = 0.83, P < 0.0001). Significant correlation between N-acetyl/Cho and GAG content was also found in cadaveric discs (R = 0.64, P = 0.0039). This study demonstrates for the first time that short-echo PRESS on a clinical 3T MR scanner can be used to noninvasively and can reproducibly quantify metabolic changes associated with degeneration of intervertebral discs. (c) 2009 Wiley-Liss, Inc.

5. Kroetz DL, Ahituv N, Burchard EG, Guo S, Sali A, Giacomini KM. Department of Bioengineering and Therapeutic Sciences, Schools of Pharmacy and Medicine, University of California San Francisco, San Francisco, CA, USA. Institutional Profile: The University of California Pharmacogenomics Center: at the interface of genomics, biological mechanisms and drug therapy. *Pharmacogenomics*. 2009 Oct;10(10):1569-76.

The Pharmacogenomics Center of the University of California, San Francisco (CA, USA) fosters research and educational activities focused on the genomic basis for variation in drug response. Investigators in the Center conduct multidisciplinary and multicenter research on a diverse array of clinically used drugs with the goal of understanding the genetic factors that contribute to variation in therapeutic and adverse drug response. The Center houses the large NIH-supported Pharmacogenomics of Membrane Transporters Project, which is a leader in understanding genetic variation in membrane transporters that are important in clinical drug response. Center investigators study racially and ethnically diverse populations, are pioneers in the education of PharmD, MD and PhD students in pharmacogenomics, and have led the establishment of unique graduate and postdoctoral training programs focused on pharmacogenomics. A key emphasis of the Center is on biological mechanisms with a goal of facilitating the development of safer and more effective medications.

6. Ainslie KM, Lowe RD, Beaudette TT, Petty L, Bachelder EM, Desai TA. Therapeutic Micro and Nanotechnology Laboratory Departments of Bioengineering and Therapeutic Sciences, and Physiology Division of Bioengineering University of California, San Francisco San Francisco, CA 94158 (USA). Microfabricated Devices for Enhanced Bioadhesive Drug Delivery: Attachment to and Small-Molecule Release Through a Cell Monolayer Under Flow. *Small*. 2009 Sep 28. [Epub ahead of print]

The development of a novel microfabricated device for oral drug delivery that overcomes many of the common barriers present in the gastrointestinal tract is reported. Specifically, the attachment of targeting ligands, subsequent device binding, and small molecule release from the microdevices in flow are investigated. A diffusion chamber that permits the simultaneous study of particle binding and small-molecule release under physiologically relevant shear conditions is developed. It is observed that once the particles bind to the cell surface, they remain attached. A small fraction of the devices detach in flow; however, most of these devices readily reattach to the cell layer in a new location. This steady-state density of microdevices is most likely the result of larger order microdevice clusters releasing their loose interactions with nearby microdevices, shifting slightly downstream, and subsequently reattaching to the cell monolayer. The release of a model small molecule from microdevices over time is roughly linear and approximately ten times greater than that observed with the small molecule alone. Overall, the preparation and characterization of an oral drug-delivery microdevice system capable of both targeting and asymmetric release in flow is reported.

7. Tabor JJ, Salis HM, Simpson ZB, Chevalier AA, Levskaya A, Marcotte EM, Voigt CA, Ellington AD. Department of Pharmaceutical Chemistry, School of Pharmacy, University of California San Francisco, San Francisco, CA 94158, USA. A synthetic genetic edge detection program. *Cell*. 2009 Jun 26;137(7):1272-81.

Edge detection is a signal processing algorithm common in artificial intelligence and image recognition programs. We have constructed a genetically encoded edge detection algorithm that programs an isogenic community of *E. coli* to sense an image of light, communicate to identify the light-dark edges, and visually present the result of the computation. The algorithm is implemented using multiple genetic circuits. An engineered light sensor enables cells to distinguish between light and dark regions. In the dark, cells produce a diffusible chemical signal that diffuses into light regions. Genetic logic gates are used so that only cells that sense light and the diffusible signal produce a positive output. A mathematical model constructed from first principles and parameterized with experimental measurements of the component circuits predicts the performance of the complete program. Quantitatively accurate models will facilitate the engineering of more complex biological behaviors and inform bottom-up studies of natural genetic regulatory networks.

8. Bayer TS, Widmaier DM, Temme K, Mirsky EA, Santi DV, Voigt CA. Department of Pharmaceutical Chemistry, University of California, San Francisco, MC 2540, Room 408C, 1700 4th Street, San Francisco, California 94158-2330, USA. Synthesis of methyl halides from biomass using engineered microbes. *J Am Chem Soc.* 2009 May 13;131(18):6508-15.

Methyl halides are used as agricultural fumigants and are precursor molecules that can be catalytically converted to chemicals and fuels. Plants and microorganisms naturally produce methyl halides, but these organisms produce very low yields or are not amenable to industrial production. A single methyl halide transferase (MHT) enzyme transfers the methyl group from the ubiquitous metabolite S-adenosyl methionine (SAM) to a halide ion. Using a synthetic metagenomic approach, we chemically synthesized all 89 putative MHT genes from plants, fungi, bacteria, and unidentified organisms present in the NCBI sequence database. The set was screened in *Escherichia coli* to identify the rates of CH₃Cl, CH₃Br, and CH₃I production, with 56% of the library active on chloride, 85% on bromide, and 69% on iodide. Expression of the highest activity MHT and subsequent engineering in *Saccharomyces cerevisiae* results in productivity of 190 mg/L-h from glucose and sucrose. Using a symbiotic co-culture of the engineered yeast and the cellulolytic bacterium *Actinotalea fermentans*, we are able to achieve methyl halide production from unprocessed switchgrass (*Panicum virgatum*), corn stover, sugar cane bagasse, and poplar (*Populus* sp.). These results demonstrate the potential of producing methyl halides from non-food agricultural resources.

Detection and Treatment of Diseases Using Light

W. Pham

Institute of Imaging Science/Department of Radiology, Vanderbilt University, Nashville, Tennessee, USA

Abstract— Fluorescence light is a natural phenomenon that has been employed recently in medical imaging and therapy. The implication of this technology in clinical studies is largely dependent on the chemical design of organic dyes or photosensitizers. The novel design and application of the probes is the subject of this discussion. In the past decade, significant improvements have yielded innovative dyes for in vivo imaging of numerous diseases in a mouse model while improvements in distribution enable photosensitizers to be used in photodynamic therapy.

Keywords— fluorescence, molecular imaging, near-infrared.

I. INTRODUCTION

Humans have recognized the emission of light among natural species for thousands of years. However, medical applications of this phenomenon began a little more than a decade ago when scientists initially demonstrated the ability to detect the molecular signatures of cancers in mouse models.

Given the subsequent advancements in chemistry methodologies, several fluorescence probes have been developed for in vivo optical imaging. One of the requirements of this work is the use of near-infrared (NIR) dyes. Imaging in the NIR window offers several advantages compared to blue-shift dyes, including deep tissue penetration and an enhanced signal-to-noise ratio. The two major types of fluorescence probes that dominate this field at present are targeted imaging probes and enzyme-activated probes. Targeted imaging probes involve the labeling of specific ligands to the dyes, while enzyme-activated probes, sometimes called “smart” activated probes, involve the use of fluorescence resonance energy transfer (FRET) to sense the activities of proteases associated with diseases. Since activation is specific to the molecular expression level of the measured biological pathway, this technique is more quantitative and real time in nature.

In addition to imaging, the fluorescence technique can be used to sensitize intrinsic molecules of the tumor microenvironment to generate radicals intended to kill cancers. This technique is called photodynamic therapy and thus far, it has proven remarkably effective for the treatment of surface tumors in clinical studies.

In this paper, we will discuss the development of probes for the imaging and treatment of cancers.

II. PROBE DEVELOPEMENT

A. Fundamental of Light

When a small organic chromophore receives light, its electrons will excite from the ground state to the higher energy level excited state. Immediately, the electrons will relax and return to the ground state via several mechanisms depending upon the structure of the molecule. In general, the cascade of electrons to the S_0 state follows a radiation or radiationless mechanism. In the latter, the delivery of electrons from the S_1 energy level to S_0 via internal conversion or intersystem crossing generates heat. One of the applications of this mechanism can be found in photochemistry where the delivered excited molecule to the ground state associated with new bond formation due to the change of the molecule's electronic configuration. In the radiation mechanism, the direct return of the excited electrons from the S_1 to the S_0 energy state emits fluorescence light. In some dyes, the excited electrons cascade to the triplet state and emit light from T_1 to S_0 generate phosphorescence. There is a fundamental difference between fluorescence and phosphorescence. The former emits light over the course of nanoseconds while the latter can last several minutes.

The excited electrons in the triplet state from some dyes, for instance porphyrin, can sensitize the triplet ground state of oxygen into excited state singlet oxygen, which thus becomes toxic for cells. The reactive oxygen species (ROS) have been utilized for the eradication of tumor cells, a process called photodynamic therapy (PDT).

B. Fluorescence Dyes

The chemistry development of colorants has been studied exhaustively in the past century. As a general rule, any extended conjugation compound can absorb light in the visible region and produce color. This is explained by the molecular orbital theory, in which the electrons in the highest occupied molecular orbital (HOMO) (2×10^{-7} m) undergo a transition to the lowest unoccupied molecular orbital

(LUMO) (4×10^{-7}). The longer the conjugation system, the greater the shift to the red region, as a consequence the energy difference between HOMO and LUMO decreases. Fluorescence dyes used for molecular imaging not only contain large π -conjugated systems, but other requirements associated with the intrinsic characteristics of optical imaging and tissue penetration are also taken into account. Although none of the dyes can meet all of the requirements, the ideal colorant would include in the design (i) NIR absorption; (ii) light emission; (iii) water solubility; (iv) chemical stability; (v) and last but not least, the availability of a function group for bioconjugation. Currently, cyanine and rhodamine are the most popular family of fluorescence dyes used in molecular imaging.

Cyanine dyes. Cyanine dyes are comprised of a large family of colorants that have been used in textiles, optical media, the Xerox industry, guest-host liquid crystal displays, and recently in molecular imaging and other medical avenues. The chemical structure of cyanine dyes includes either one or two heterocyclic aromatic ring systems joined by an unsaturated chain of carbon atoms called the polymethine bridge (Fig. 1). The elements of oxygen or nitrogen on those rings act as an electron sink where absorbance of the dye relies on the electrons' propagation forward and backward along the methine chain. What makes cyanine dyes stand out uniquely compared to other dyes is the flexible chemistry that enables modifications through many possible positions on the backbones for numerous applications such as, (i) the absorbance wavelengths can be tuned as precisely as possible; (ii) solubility; (iii) stability; and (iv) functionalization.

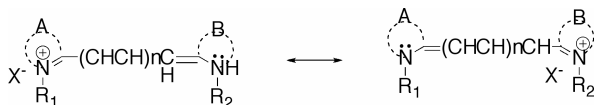


Fig. 1 A general chemical structure of cyanine dyes

Tuning near-infrared (NIR) cyanine dyes can be achieved through modulation of the methine carbons or the electronic effect in the end groups. For every additional methine carbon, the wavelength will enhance 100 nm versus 20 nm for an additional phenyl ring. This approach has particular implication when designing dyes for molecular imaging; while the dyes have extended wavelengths, the design retains compactness and hydrophilicity, which represents another advantage of methine group modification.

Another approach to designing a stable dye with NIR capability, although not particularly popular but seemingly feasible is the compromise of long polymethine carbons for shorter ones while optimizing the electronic effect of the aromatic rings. Possible rings are benz[c,d]indolium,

telluropyrylium, and cyclohepta pyrrolium salts. This strategy is exemplified by comparing the absorbance bands between indole-based ring and its counterpart, benz[c,d]indole-based ring. Both of the dyes have the trimethine bridge but the latter excels 180 nm to the red shift compared to the other. This suggests that designing unique heterocyclic end groups is critical in the quest to make NIR dyes.

Overall, cyanine dyes have good physical properties; they have a unique, mirror image between absorbance and emission profiles, and the dyes have an acceptable quantum yield for imaging applications. The Stokes shifts of cyanine dyes are narrow, with most in the range of 30 nm. However, this is not always the case. Recently, chemists have been able to develop cyanine dyes with large Stokes shifts, similar to that of quantum dots. The underlying mechanism of this design focuses on perturbation of the electronic propagation along the polymethine bridge. The intramolecular charge transfer mechanism is attributed to a change of geometry in the emitting and absorbing profiles.

Rhodamine dyes. Rhodamine and oxazine dyes are considered as honeycomb dyes, since they have architectural clusters of hexagonal frameworks formed by the conjugated π -system.

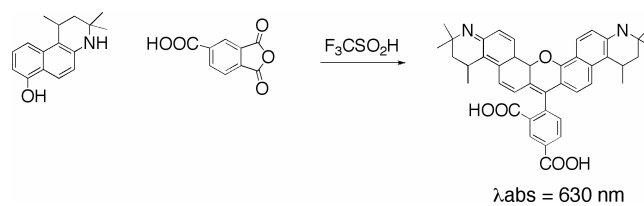


Fig. 2 Tuning a rhodamine dye to NIR window

Rhodamine dyes are perhaps the most popular in terms of their biological applications in view of their stability. For instance, they are comprised of a family of dyes used in microscopy, histology, and imaging such as Alexa dyes, Fluorescein and Texas Red. The simplest synthesis of rhodamine dye is the condensation of *m*-diethylaminophenol with formaldehyde, followed by oxidation with ferric chloride in hydrochloric acid. In order to create the dye with a longer wavelength, a few choices are available: (i) enhancement of the ring size or (ii) electronic manipulation on the backbone of the molecule. In the first case, the condensation reaction between large ring structures of *m*-aminophenol with phthalic anhydride can provide the dye product with emission near the NIR range (Fig. 2). In the second case, NIR rhodamine dyes are achieved by replacing the carboxylphenyl moiety with an electron-withdrawing group at the central carbon. For example, the addition of a

CF2 moiety in place of an aromatic ring resulted in an apparent bathochromic shift.

One of the superior characteristics of rhodamine dyes is their high quantum yield. No other family of dyes can provide such high quantum yield. In general, the quantum yield of rhodamine dyes can reach from 50 to 90%. This may partially be attributed to the stability of the dyes.

Rhodamine dyes that have hydroxyl groups at the end rings are very sensitive to physiological pH change and are used as intracellular pH indicators. For example Vita Blue 9, an amphiphilic dye designed for cell membrane permeable. The deprotonation of the dye in basic condition switches the excitation/emission from 524/609 nm to 570/665 nm.

Oxazine dyes. By replacing the central carbon of a rhodamine with a nitrogen atom, an oxazine dye forms. Because of this replacement, the molecule exhibits longer wavelength (1). The central nitrogen atom serves as an electron sink for the π electrons of the quarternary amine in the indole ring. This design contributes to a wavelength shift of about 80-100 nm toward the NIR region. There are a number of oxazine dyes emit light in the NIR region (2). Furthermore, several lines of research demonstrated that oxazine dyes are photochemically more stable than rhodamine dyes (3).

FRET. Fluorescence resonance energy transfer (FRET) has been used widely in biophysics over the past several years since its discovery four decades ago by Stryer and Haugland. Since the underlying mechanism involves energy transfer from the donor fluorescence molecules to the acceptor dyes when they are in proximity to each other, the dynamic characteristics of this interaction are considered to be the molecular ruler used to determine the spatial distance between two entities. The initial use of FRET between fluorescence proteins revealed crucial information regarding the intracellular interaction, unfolding protein function, and dynamic biochemical signals in living cells.

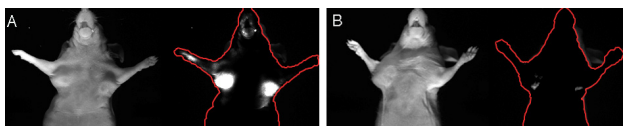


Fig. 3 (A) Imaging MMP7-associated tumor using a FRET probe; (B) control mice

Another recent scientific employment of FRET focuses on the *in vivo* detection of protease activity. The advent of optical devices, especially the CCD camera and computer-based imaging technology, has provided a straightforward method to detect the dequenching photons from the FRET activation. One typical design of a FRET probe for imaging

application can be found in the recent development of fluorescence-activated molecular beacon to detect MMP7 (matrix metalloproteinase). In this construct, the specific peptide backbone for MMP7 was modified to accommodate a FRET pair on the peptide ends. This can be achieved through an orthogonal chemical maneuver in which the acceptor dye was conjugated to the terminal aminated peptidic resin. While the donor was conjugated in solution phase. During FRET, the transfer of electronic excitation energy from a donor chromophore to an acceptor dye located in a close distance via a through-space dipole-dipole coupling mechanism between the donor-acceptor pair. Treatment of this probe in the presence of MMP-7 afforded a specific enzyme-activation fluorescence that was seven fold higher than the control experiment. *In vivo* imaging of MMP7-associated cancer in a xenograft mouse model confirms the specificity and sensitivity of this design (Fig. 3).

Using a similar strategy, the activity of BACE (β -site of APP-cleaving enzyme), which is an aspartic protease that cleaves the amyloid precursor protein (APP), the β -secretase site was detected at nanogram scale. The activated fluorescence signal was detected conveniently using an optical imaging instrument (Fig. 4).

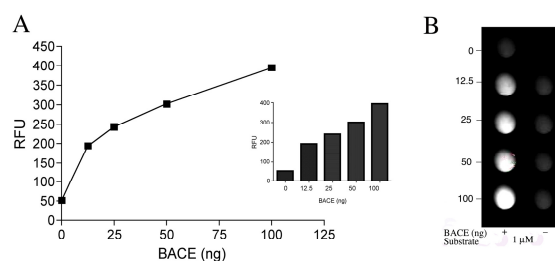


Fig. 4 Activation of a peptide-based NIR FRET probe with BACE. (A) A fixed concentration of probe was treated with increasing concentration of BACE. (B) Optical imaging of the activation

The selection of a pair of dyes for FRET probes would be more effective if the acceptor dye could act as a dark hole quencher. In this capacity, the dye's exclusive role is to absorb the emission photons from the donor, but would not emit fluorescence light. For example, a few years ago, we developed such quenchers using an azulene backbone. As a matter of fact, it has been known for a while that azulene derivatives have anomalous fluorescence due to the large S1-S2 gap, which thus prevents excited photons from equilibrating to the S1 energy level. However, the short absorbance wavelength of individual azulene hampers its role in imaging application. To overcome this, we tuned the absorbance of dyes from visible to NIR by extending the conjugated π system utilizing the polymethine carbons. Another interesting aspect of this work is that the dye can

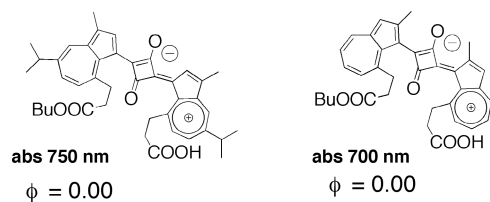


Fig. 5 Tuning the absorbance wavelength of azulene-based quenchers

be tuned to exert bathochromic shift using the molecular orbital perturbation theory, with particular applicability to the π -electrons of the aromatic end rings (Fig. 5).

Photodynamic therapy. Three components are involved in PDT (i) photosensitizers; (ii) light; and (iii) reactive oxygen species. Organic dyes with unique excitation photons that cascade in the triplet state have profound implications for therapy to eradicate tumor cells because of their specificity and sensitivity. Similar to the imaging approach, one of the requirements in PDT is that light must reach all of the cancer tissue for successful therapy. This is a challenging, since light may either scatter or be absorbed by intrinsic tissue chromophores. Therefore, the photosensitizers used in PDT must have a long absorbance wavelength that permits deep tissue penetration, with minimum scattering and maximum photosensitizer activation, and the greatest tissue destruction (4). The super family of porphyrin dyes were one of the earliest photosensitizers used in PDT. Although there is no ideal photosensitizers available currently, porphyrin compounds seems to be the best candidates given the ease in modification on the compounds for in vivo study. The dyes also have acceptable triplet excited state long-live enough to produce high quantum yields of singlet oxygen. To extend the absorbance of porphyrin, several works have demonstrated that hydrogenation of one of the pyrrole rings of an porphyrin, which generates a reduced form known as chlorins, have a highly absorbent band in the red region of the spectrum, specifically in the 630-715 nm range. These sensitizers populate in the triplet state with excellent lifetimes of greater than 100 μ s, which are efficiently quenched by ground state oxygen to produce singlet oxygen with a quantum yield of approximately 0.6 (5).

One of the challenges in using porphyrin-based photosensitizers in clinical study is their hydrophobicity. Therefore, the design of photosensitizers for in vivo study would include a technique for distribution either by carriers using liposomes or through the incorporation of intrinsic hydrophilic moiety, such as sulfonate groups. Sometimes, a balance control to keep the compounds to be amphiphilic is the key to optimizing cancer treatment (6). Other techniques that are available to improve tissue availability include metal chelator or cationization to increase cellular uptake through the electrostatic interaction.

Currently, PDT has become an FDA-approved procedure for the treatment a number of cancers. In clinical work, the photosensitizer (Photofrin®) is injected into the bloodstream of the patient. The compounds will traverse to the whole body, but will eventually distribute and reside in the tumor longer than in other tissues. Light will be used to illuminate the photosensitizer a day post injection in order to generate ROS for killing tumor cells. What makes PDT more appealing than other techniques for treatment of tumor is that the production of ROS not only damages tumor cells but also their surrounding network. Tumor growth is associated with angiogenesis, ROS generated in the tumor mass damages the blood vessels, will help to kill tumor cells indirectly due to their lack of nutrients.

Since light absorption is limited in tissue penetration, PDT is suitable for the treatment of surface tumors like melanoma, or on the lining of internal organs such as the lungs or esophagus cancer. The technique is still limited to large tumors.

III. CONCLUSION

It is increasingly recognized that the development of molecular probes for imaging and PDT plays an important role in modern medicine and research. Besides enhancing our capability to detect the diseases, these probes can be used to monitor and assess therapy in preclinical animal models. There is still enormous opportunity related to research into optical imaging and PDT. Successful implementation of the design of physical and biologically advanced probes, combined with the detection capability, could produce an imaging modality that is more effective and safer than the other modalities currently available.

ACKNOWLEDGEMENT

This work is supported by a grant from NIA (AG026366).

REFERENCES

1. Kanitz A, Hartmann H. Preparation and characterization of bridged naphthoxazinium salts. *European Journal of Organic Chemistry* 1999:923-930.
2. Sens R, Drexhage KH. Fluorescence quantum yield of oxazine and carbazine laser dyes. *J Luminesc* 1981; 24/25:709-712.
3. Kuznetsova NA, Marinina LE, Alekseeva VI, Lukyanets EA. *Zhurnal Prikladnoi Spektroskopii* 1977; 29:315-317.
4. Ochsner M. Light scattering of human skin: a comparison between zinc (II)-phthalocyanine and photofrin II. *J Photochem Photobiol B* 1996; 32:3-9.
5. Spikes JD. Chlorins as photosensitizers in biology and medicine. *J Photochem Photobiol. B: Biol.* 1990; 6:259-274.
6. Wohrle D, Iskander N, Grasczew G, et al. Synthesis of positively charged phthalocyanines and their activity in the photodynamic therapy of cancer cells. *Photochem Photobiol* 1990; 51:351-356.

Magnetic Resonance Imaging of Schizophrenia and Alzheimer's Disease

A.W. Anderson^{1,2,6,7}, X. Hong^{1,7}, L.R. Arlinghaus⁷, M. Tumuklu³, Thornton-Wells⁶, R.E. Hoffman⁵,
S. Park⁴, and H.Y. Meltzer³

¹ Biomedical Engineering, School of Engineering, Vanderbilt University, Nashville, USA

² Radiology and Radiological Sciences, Vanderbilt University, Nashville, USA

³ Department of Psychiatry, Vanderbilt University, Nashville, USA

⁴ Department of Psychology, Vanderbilt University, Nashville, USA

⁵ Department of Psychiatry, Yale University, New Haven, USA

⁶ Kennedy Center, Vanderbilt University, Nashville, USA

⁷ Institute of Imaging Science, Vanderbilt University, Nashville, TN, USA

Abstract— **Magnetic resonance imaging (MRI) can be used to quantify brain morphology, tissue microstructure, and function. These measurements can be used to identify the tissue changes that accompany brain injury and disease. For example, high spatial resolution structural images can be analyzed to map local reductions in cortical volume. Diffusion weighted imaging can be used to reconstruct axonal fiber pathways in brain white matter and to assess fiber integrity. Functional imaging provides maps of neuronal activity during rest and task performance, and hence can identify the cortical networks that underlie sensation, memory, emotion, and cognition. These imaging techniques have been applied to a wide range of neurological and psychiatric diseases to shed light on the role different brain regions play in the pathophysiology of each disease. This talk will focus on the specific examples of schizophrenia and Alzheimer's disease. Key imaging studies will be described that implicate specific brain regions in the development of disease symptoms. Prospects for identifying imaging endophenotypes of these diseases will be discussed. Finally, imaging biomarkers will be described that may be useful for monitoring disease progression and treatment.**

Keywords— **MRI, DTI, fMRI, schizophrenia, Alzheimer's disease.**

I. INTRODUCTION

Advanced imaging methods provide a unique window on changes in the brain that accompany normal development, aging, injury and disease. Magnetic resonance imaging (MRI), in particular, has proved useful in assessing brain tissues across a wide range of distance scales, from the level of molecules to organ systems. The information gained from imaging studies can be used to understand the origins of disease symptoms, to guide therapy, and to monitor treatment efficacy. Sophisticated image acquisition and analysis methods now provide quantitative measurements of tissue microstructure, anatomical structure, and function.

II. TISSUE MICROSTRUCTURE

Magnetic resonance imaging can be used to measure the molecular diffusion of water in body tissues [1]. Since cell membranes hinder the diffusive motion of water, the net diffusivity of water indirectly reflects the density of membranes and other structural elements of cells [2]. On the time scale of the diffusion measurement (typically ~30 ms for human scanners), the diffusive movement of both intra- and extracellular water is larger parallel to nearby cell membranes than perpendicular to those membranes, because molecules encounter fewer obstructions moving parallel to the membranes. This implies that a tissue with a preferred orientation of cells also has a preferred orientation for diffusion, i.e., diffusion is anisotropic. In brain white matter, diffusion imaging reveals the orientation of large bundles of axons [3], because diffusion is fast parallel to axons and slower in the perpendicular direction. The anisotropy of diffusion in these fiber bundles reflects axon myelination, diameter, packing density, and directional dispersion. Hence, diffusion anisotropy has been adopted as a biomarker for fiber integrity. The anisotropy of diffusion is conveniently described by a diffusion tensor [4]—hence this technique is called Diffusion Tensor Imaging (DTI).

Since diffusion is fastest in the direction parallel to axons in a fiber bundle, diffusion measurements can be used to estimate fiber orientation in each voxel in an MRI data set. If these orientations are interpreted as the local tangent to fiber pathways, then the pathways can be reconstructed by following the fast diffusion direction from point to point along a fiber bundle [5-6]. Fiber tracking based on diffusion data, known as MR tractography, is used to visualize and segment specific anatomical fiber bundles in the brain (Figure 1). This kind of analysis makes it possible to characterize individual fiber bundles and identify those that are affected by disease.

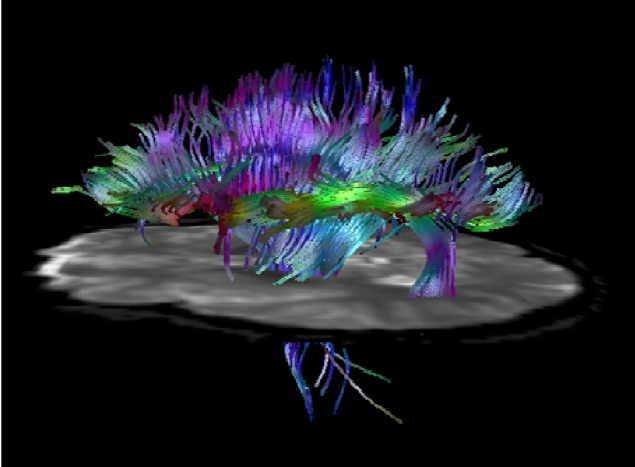


Fig. 1 Fiber pathways in the brain visualized using diffusion MRI data. Fibers are colored according to orientation (*red* indicates a left-right orientation, *green* indicates anterior-posterior, and *blue* indicates superior-inferior). Displayed fibers include the corpus callosum, cingulum, internal capsule, and arcuate fasciculus

III. ANATOMICAL STRUCTURE

High resolution anatomical imaging can reveal subtle changes in the volume of brain structures. Such volume changes can result from abnormal development or degeneration of neurons, and can be used, for example, to determine which gray matter regions are affected by specific diseases and what the typical time course is for those effects. Measurements of cortical folding and thickness [7] can be used to quantify variations in shape and volume between individuals. Another approach, Voxel Based Morphometry (VBM), provides statistical maps of local gray matter volume changes between groups of individuals [8]. In this method, images are segmented to produce gray and white matter masks, which are spatially normalized to facilitate voxel-wise analysis. The gray matter volume within a certain distance of each voxel (the local ‘density’) is calculated and compared across groups to detect differences in cortical shape and volume and their associations with specific disease phenotypes.

IV. NEURONAL FUNCTION

Changes in blood oxygenation are detectable using MRI [9]. This is due to the magnetic properties of deoxyhemoglobin, which make hemoglobin act as an endogenous, oxygen-sensitive contrast agent. Since blood oxygenation changes in response to neuronal activity, MRI

signal variations reflect changes in neuronal activity. So-called Blood Oxygenation Level Dependent (BOLD) signal contrast can be used to map neuronal activity while subjects perform a wide range of tasks, from passive sensation to higher level cognitive processing. Measurements of the location and level of activation can then be used to identify specific regions in which activation is abnormal. Functional magnetic resonance imaging (fMRI) is the collection of methods for mapping brain activity in this way.

V. SCHIZOPHRENIA

Schizophrenia is a severe brain disorder that affects approximately 1% of the adult population each year. A great deal of effort has been devoted to trying to understand the causes and effective treatments of the disease. Imaging studies can help to determine the regions of the brain most affected by the disease and to monitor the effects of medication on the brain. Structural MRI studies have found significant reductions in gray and white matter volume in patients with schizophrenia. These changes are evident at the earliest stages of the disease, since volume deficits are apparent even in first-episode, never-medicated subjects [10]. The volume reductions are correlated with disease symptoms: sub-syndromes of schizophrenia have distinct patterns of regional brain volume deficits [11]. Focusing on white matter changes, diffusion MRI measurements have shown that anisotropy is abnormally low in several large fiber bundles even in first-episode, never-medicated patients [12]. We have found that diffusion anisotropy in specific fiber pathways is strongly correlated with patient symptoms, for example frequency of hallucinations and global measures of psychopathology (Figure 2). These structural studies suggest that symptoms of the disease can be understood in terms of changes to specific brain regions.

Functional MRI (fMRI) has been used to study changes in brain activity associated with schizophrenia. Significant reductions in activity have been measured in patients performing working memory [13] and executive function tasks [14], which are core cognitive deficits associated with the disease. fMRI has also been used to localize brain activity during auditory hallucinations [15]. The activated regions appear to be part of the normal auditory pathway and include the middle and superior temporal gyrus (Figure 3). In patients with frequent hallucinations, activated regions were used as targets for repetitive transcranial magnetic stimulation (rTMS), which transiently reduces neuronal excitability. This treatment decreased hallucination frequency relative to rTMS applied to control sites [16]. Hence, fMRI can localize abnormal brain function in schizophrenia.

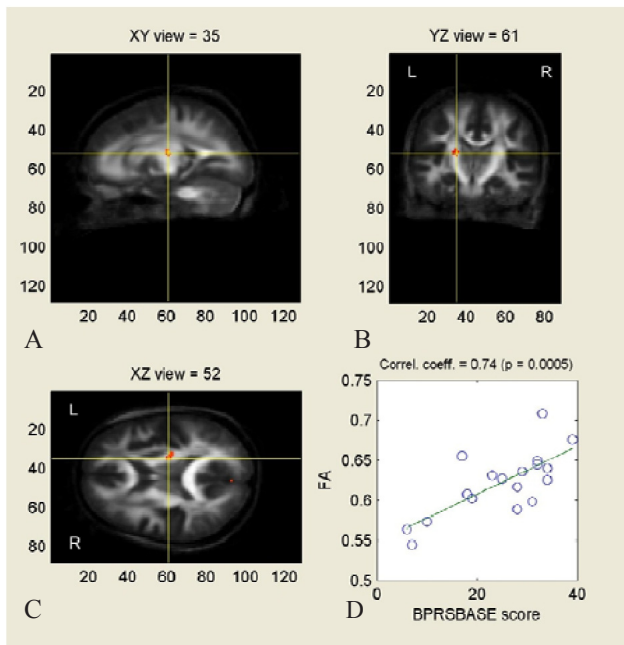


Fig. 2 Correlation between diffusion anisotropy and psychopathology in schizophrenia. Three orthogonal views of the mean anisotropy map for 32 schizophrenia patients and 20 age-matched controls (A-C). A cluster of voxels (red) under the cross-hairs displays a significant correlation between fractional anisotropy (FA) and psychopathology, assessed with the Brief Psychiatric Rating Scale (D)

VI. ALZHEIMER'S DISEASE

Alzheimer's disease is an age-related brain disorder which, over a period of years, can lead to severe loss of cognitive function. MRI has proved useful in understanding progressive changes in the brain caused by Alzheimer's disease. Voxel-based morphometry has been used to show that the earliest and largest volume changes occur in the hippocampus [17], which agrees with the clinical presentation of early loss of memory function. Longitudinal measurements of tissue volume have shown that progression from mild cognitive impairment (MCI) to Alzheimer's disease (AD) was related to volume loss in the entorhinal cortex, which forms the main input to the hippocampus.

Diffusion MRI has been used to study the impact of AD on specific white matter fiber tracts [18]. The observed loss of diffusion anisotropy in white matter is distinguishable from the patterns of change found in normal aging [19]. Functional MRI has demonstrated that brain activity in specific brain regions (e.g., left superior temporal and prefrontal lobes) during an associative memory task is significantly correlated with patient score on neuropsychological tests of verbal memory and global cognition [20]. fMRI has

also shown increases in frontoparietal brain activity during working memory tasks as a result of medication [21]. The measured increases in activity correlated significantly with improvements in cognitive tests, suggesting that fMRI can localize the clinically relevant treatment effects.

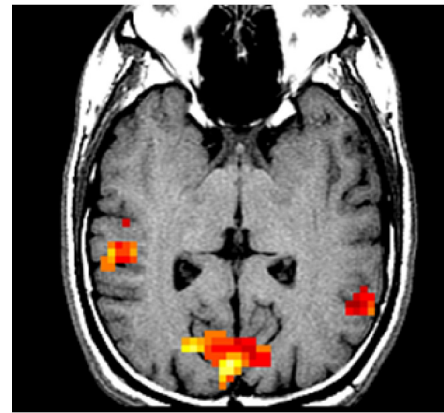


Fig. 3 Functional MRI map of neuronal activity during auditory hallucinations in a patient with schizophrenia. Areas of increased activity during hallucinations (color) are superimposed on an anatomical image (gray). Activity in the right and left temporal and occipital lobes match the qualitative description given by the patient of his hallucinations (both auditory and visual components)

VII. CONCLUSIONS

Improvements in MR imaging and analysis techniques are making possible more specific and informative measurements of the effects of diseases on the brain. Creative application of these techniques promises to improve our understanding of important diseases and ultimately provide improved treatments to those affected both now and in the future.

ACKNOWLEDGMENT

The authors would like to acknowledge support from the National Alliance for Research on Schizophrenia and Depression.

REFERENCES

1. Le Bihan, D., *Molecular diffusion, tissue microdynamics and microstructure*. NMR Biomed, 1995. **8**(7-8): p. 375-86.
2. Beaulieu, C., *The basis of anisotropic water diffusion in the nervous system - a technical review*. NMR Biomed, 2002. **15**(7-8): p. 435-55.

3. Moseley, M.E., et al., *Diffusion-weighted MR imaging of anisotropic water diffusion in cat central nervous system*. Radiology, 1990. **176**(2): p. 439-45.
4. Basser, P.J., J. Mattiello, and D. LeBihan, *Estimation of the effective self-diffusion tensor from the NMR spin echo*. J Magn Reson B, 1994. **103**(3): p. 247-54.
5. Conturo, T.E., et al., *Tracking neuronal fiber pathways in the living human brain*. Proc Natl Acad Sci U S A, 1999. **96**(18): p. 10422-7.
6. Basser, P.J., et al., *In vivo fiber tractography using DT-MRI data*. Magn Reson Med, 2000. **44**(4): p. 625-32.
7. Acosta, O., et al., *Automated voxel-based 3D cortical thickness measurement in a combined Lagrangian-Eulerian PDE approach using partial volume maps*. Med Image Anal, 2009. **13**(5): p. 730-43.
8. Wright, I.C., et al., *A voxel-based method for the statistical analysis of gray and white matter density applied to schizophrenia*. Neuroimage, 1995. **2**(4): p. 244-52.
9. Ogawa, S., et al., *Brain magnetic resonance imaging with contrast dependent on blood oxygenation*. Proc Natl Acad Sci U S A, 1990. **87**(24): p. 9868-72.
10. Chua, S.E., et al., *Cerebral grey, white matter and csf in never-medicated, first-episode schizophrenia*. Schizophr Res, 2007. **89**(1-3): p. 12-21.
11. Nenadic, I., H. Sauer, and C. Gaser, *Distinct pattern of brain structural deficits in subsyndromes of schizophrenia delineated by psychopathology*. Neuroimage, 2009.
12. Cheung, V., et al., *A diffusion tensor imaging study of structural dysconnectivity in never-medicated, first-episode schizophrenia*. Psychol Med, 2008. **38**(6): p. 877-85.
13. Barch, D.M., et al., *Selective deficits in prefrontal cortex function in medication-naive patients with schizophrenia*. Arch Gen Psychiatry, 2001. **58**(3): p. 280-8.
14. Broome, M.R., et al., *Neural correlates of executive function and working memory in the 'at-risk mental state'*. Br J Psychiatry, 2009. **194**(1): p. 25-33.
15. Lennox, B.R., et al., *Spatial and temporal mapping of neural activity associated with auditory hallucinations*. Lancet, 1999. **353**(9153): p. 644.
16. Hoffman, R.E., et al., *Probing the pathophysiology of auditory/verbal hallucinations by combining functional magnetic resonance imaging and transcranial magnetic stimulation*. Cereb Cortex, 2007. **17**(11): p. 2733-43.
17. Chetelat, G., et al., *Three-dimensional surface mapping of hippocampal atrophy progression from MCI to AD and over normal aging as assessed using voxel-based morphometry*. Neuropsychologia, 2008. **46**(6): p. 1721-31.
18. Hess, C.P., *Update on diffusion tensor imaging in Alzheimer's disease*. Magn Reson Imaging Clin N Am, 2009. **17**(2): p. 215-24.
19. Damoiseaux, J.S., et al., *White matter tract integrity in aging and Alzheimer's disease*. Hum Brain Mapp, 2009. **30**(4): p. 1051-9.
20. Diamond, E.L., et al., *Relationship of fMRI activation to clinical trial memory measures in Alzheimer disease*. Neurology, 2007. **69**(13): p. 1331-41.
21. Saykin, A.J., et al., *Cholinergic enhancement of frontal lobe activity in mild cognitive impairment*. Brain, 2004. **127**(Pt 7): p. 1574-83.

Current Development of Neuroimaging Using PET Techniques

A.L. Brownell

Massachusetts General Hospital, Department of Radiology, Harvard Medical School, Boston, USA

Abstract— Positron emission imaging was developed more than 50 yrs ago, when Dr. Gordon Brownell did the first clinical brain imaging with his scanner in 1951 on 8-year old girl to detect a brain tumor. Detection and localization of brain tumors was the main application area of the positron emission imaging for the following 20 years. The isotopes like ^{72}As , ^{64}Cu and ^{68}Ga were used as imaging agents. When the cyclotrons came available in the hospital environment in 1970s, ^{15}O and ^{11}C labeled gases replaced the long-lived isotopes. These studies were based on blood flow and oxygen metabolism and are still used in a variety of neurological applications. New area of neuroimaging started, when radiolabeling techniques developed to produce compounds to investigate metabolic and specific biochemical (receptor and/or enzyme) functions in the brain. This development established in vivo neurochemistry, which is presently one of the most active research areas in neuroimaging. Presently the mostly used radiolabels in PET imaging are ^{11}C and ^{18}F , which can be attached to the imaging ligand through radiosyntheses. The main application areas of PET imaging for diagnosis and research include neurodegeneration, stroke, drug addiction, brain activation, epilepsy, inflammation, cancer, and drug development. The application area is continuously increasing based on radiopharmaceutical development. The first significant breakthrough in in vivo neuroimaging happened after introducing of radioligands to image dopamine transporters. Even these ligands are not generally approved for clinical diagnosis; they are used world wide as research tools in neurodegenerative disorders, especially in Parkinson's diseases (PD) as well as drug abuse. Presently world wide interest is to develop specific ligands for diagnosis of Alzheimer's disease and several imaging ligands are in clinical trials. Other active radiopharmaceutical developments include ligands for serotonergic and metabotropic glutamate receptor systems.

Keywords— PET, blood flow, metabolism, receptor, dopamine.

I. INTRODUCTION

Recent developments in instrumentation and imaging techniques have revolutionized neuroimaging. Images obtained from different imaging modalities can be fused and overlaid to combine anatomical and physiological information. Molecular imaging has been introduced to follow functional processes in the brain and obtain specific information to be used in tailoring individual therapies.

Development of neurological PET imaging as well as the whole PET imaging has been dependent on two factors; development of imaging instrumentation and development of radiopharmaceuticals. The concept of positron emission based imaging was developed already in 1951 [1] by Dr. Gordon Brownell and the first human studies were published in 1953 [2]. After that fundamental technical development has taken place in all scientific fields including electronics, computer science, biology and biochemistry. These developments have also significantly advanced the development of positron emission based imaging techniques. The most important aspect has been the development of mathematical algorithms, which turned positron imaging to positron emission tomographic imaging (PET) [3-7]. Further development of image reconstruction including filtering techniques has followed the advances in computer science. Even though, positron imaging technology is more than 50 years old, its use in the clinical environment has been recognized only in the past 20 years.

PET imaging techniques have high sensitivity, and only tracer amounts of radiolabeled ligand or drug is needed for imaging. Thus the homeostasis of the biological system is not changed and it is possible to quantitate tracer amounts of ligands. These techniques can be used to investigate physiological functions related to blood flow, metabolism or receptor binding; and to test drug candidates for accumulation, distribution, binding and latency. Radiolabeled biomarkers have significantly enhanced the role of PET imaging especially in drug development as well as in developing new sensitive diagnostic methods and/or techniques to follow the response of therapeutic regimen.

II. METHODS

A. PET Imaging Instrumentation

Technical development of positron emission imaging had many steps after starting as 2-dimensional imaging using one pair of single detectors [2]. The major developments have been in detector design including crystal material, crystal size and light detection, which directly effect on the resolution of the device. In addition development of photomultipliers and overall detection geometry effect on

the sensitivity of the imaging system. Recently, an application driven development of PET instrumentation has been an object of interest. In addition to self-standing head and whole body PET scanners, combined PET and x-ray computed tomographic (CT) as well as magnetic resonance imaging (MRI) systems are commercially available. These systems can combine high resolution anatomical information provided by CT or MRI to the functional information of PET. PET imaging gains also from the high resolution of CT or MRI to obtain correct boundaries for activity distribution (Fig. 1).

There are only four installed human brain PET-MR imagers in the world at this moment. The PET insert is inside the magnet covered by the gradient coil. Data acquisition can be done separately or simultaneously by using two separate computers. The platform of the PET insert is the same as in the latest version of Siemens Inveon animal PET system. The MR imager is Siemens 3T TRIO.

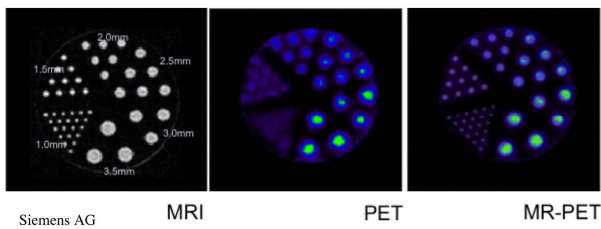


Fig. 1 The Derenzo phantom study with $[^{18}\text{F}]$ water solution using the combined PET-MR imager installed at the Martinos Biomedical Imaging Center, Massachusetts General Hospital, Boston, USA demonstrates that with the combined PET and MRI system activity distribution can be localized even in 1 mm diameter phantom holes

B. Radiopharmaceutical Development for Neuroimaging

Development of radiopharmaceuticals has been application and technology dependent. The early brain imaging by PET techniques relied on the changes in the blood brain barrier and was used mainly for tumor detection [2]. After the radiolabeled gases came available, neuroimaging with PET techniques expanded significantly, since it was possible to quantitatively image blood flow and apply these imaging techniques to a variety of neurological diseases and conditions. Development of radiopharmaceutical for neuroimaging can be divided into several classes; substrates for blood flow, perfusion, metabolism, receptors, enzymes etc.

a) Blood flow: The mostly used blood flow agents comprise $\text{C}[^{15}\text{O}]_2$ -gas and $[^{15}\text{O}]$ -water [8]. Detection of hemodynamic changes in brain blood flow has been one of earliest clinical application of PET techniques [8]. These techniques were used intensively in stroke studies to localize a site and extension of the lesion as well as to follow up the recovery

[9]. PET studies have been also done to evaluate stimulation induced hemodynamic changes to evaluate the activation and connectivity in different brain circuitries. These stimulations can be introduced through all the senses, but visual stimulation is the most commonly used technique combined with different tasks [10].

b) Metabolism: Concerning metabolism the mostly used radioligand $[^{18}\text{F}]$ FDG is used to investigate glucose metabolism, $[^{15}\text{O}]_2$ for oxygen metabolism and $[^{11}\text{C}]$ methionine for protein metabolism.

The availability of fluorine-18 labeled 2-fluoro-2-deoxy-D-glucose [11] has enhanced PET studies to the level of the concept of FDG-PET. Glucose is the main source of energy in the brain. So therefore all the changes in functionality create some changes in regional glucose metabolism. Even though glucose metabolism is a sensitive indicator of changed metabolism it is not a selective method, and the clinical relevance has to be obtained with other additional studies.

Glucose metabolic rate can be used as an index of malignancy in the brain tumors [12] as well as to predict the response for the therapy.

c) Receptors: Imaging of receptor function has significantly enhanced understanding of the underlying pathophysiological mechanisms in many neurological disorders. There are a number of specific ligands to investigate dopaminergic receptor functions. PET studies of dopaminergic function have enabled an early diagnosis of Parkinson's disease [13] as well as to develop and test therapeutic regimens for repairing the function via either pharmacological or surgical methods, including deep brain stimulation or cell transplantation. Dopaminergic function is related in addition to neurodegenerative disorders also to schizophrenia and drug addiction and is proposed to be part of many psychological conditions like anger, anxiety, and hyperactivity [14].

The dopamine D2 receptor system was the first receptor to be examined by PET in humans [15]. The involvement of this receptor system in numerous brain-related disorders such as schizophrenia, Parkinson's disease and other movement disorders has prompted an intense research in this field. Although high affinity PET ligands exist for imaging the postsynaptic dopamine D1 and D2 receptors, there are no selective radioligands for the dopamine D3, D4 or D5 receptor subtypes. For the presynaptic dopamine transporters (DAT)s, a series of cocaine congeners labeled with either ^{11}C or ^{18}F have been developed. Some of these compounds are used in routine applications in hospitals to investigate Parkinson's disease. They have also application as surrogate markers in the development of novel drugs for therapeutic use of brain disorders.

We have studied extensively the imaging characteristics of DAT-ligand, (2 β -carbomethoxy-3 β -(4-fluorophenyl) tropane ($[^{11}\text{C}]\text{CFT}$) in normal and MPTP-treated primates [16]. Our group was the first to demonstrate, that $[^{11}\text{C}]\text{CFT}$ binding correlated closely with onset and progression of behavioral symptoms in a primate model of Parkinson's disease [17]. This has been verified in a larger series of primates and also in early Parkinson's disease in humans [13]. $[^{11}\text{C}]\text{CFT}$ accumulation shows the extension and magnitude of the binding to dopamine transporter sites and provides anatomical information of the striatum based on the high contrast (receptor density in a normal striatum is higher than in the surrounding tissue) (Fig. 2).

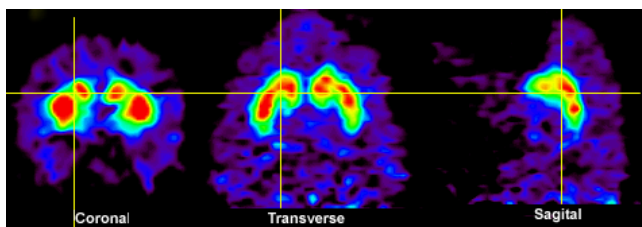


Fig. 2 Coronal, transverse and sagittal view of $[^{11}\text{C}]\text{CFT}$ distribution in a normal monkey 40 min after administration of 10 mCi of the ligand (P4, Concord Microsystems, Inc). The cross lines demonstrate the location of the same voxel in 3-dimensions. The slice thickness is 1.2 mm

After our early experiments, several variations of phenyltropane ligands have been developed for imaging of dopamine transporter function. One of these ligands, β -CIT (2 β -carbomethoxy-3 β -(4-iodophenyl)tropane, a potent halogenated phenyltropane analog has been tested both in PET and SPECT imaging [18]. This compound has a high specific binding ratio in the striatum and a high binding ratio for midbrain. However, it takes 4 hrs for the ligand to clear, before a difference of 30-40% between normal and Parkinson's diseased brains become apparent [18]. Recently, several ligands have been developed with radiolabeled fluorine-18, since the half-life of fluorine-18 (110 min) allows transportation of the radiolabeled ligand to research centers, which do not have their own isotope production facility. Of these fluorinated ligands the mostly used is N-3-(^{18}F -fluoropropyl)-2 β -carbomethoxy-3 β -(4-iodophenyl) nortropane.

Before specific ligands for dopamine transporters were developed, $[^{18}\text{F}]\text{6-L-fluorodopa}$ was used to assess presynaptic dopaminergic function. $[^{18}\text{F}]\text{6-L-fluorodopa}$, is a fluorinated analog of natural body constituent, L-dopa (L-3,4-dihydroxyphenylalanine) [15]. $[^{18}\text{F}]\text{6-L-fluorodopa}$ is metabolized to 3-O-methyl-6-fluoro-L-dopa (3-OMFD), which enters the brain with nonspecific binding mechanism and complicates kinetic modeling of dopamine synthesis.

There are several physiological functions, which are related to kinetics of ^{18}F -6-L-fluorodopa; dopamine synthesis, turnover and storage.

As compared with the dopaminergic system, there are only a handful of PET ligands available for the serotonergic system. Although more than 16 receptor subtypes for this system are known, PET ligands exist only for the 5-HT_{1A} and 5-HT_{2A} receptor subtypes. For the imaging of the SERT, the first promising tracer developed was (+)- ^{11}C -McN 5652 [19]. Although (+)- ^{11}C -McN 5652 labels the SERT in the human brain, it exhibits also high non-specific binding and slow kinetics. More recently, a highly promising new class of compounds, namely ^{11}C -3-amino-4-(2-dimethylaminomethylphenylsulfanyl) benzonitrile (^{11}C -DASB) and ^{11}C -MADAM [20] have been developed as putative PET ligands for the *in vivo* imaging of the SERT in humans.

Metabotropic glutamate receptors (mGluR)s belong to Class C of a superfamily of G protein coupled receptors (GPCRs). Class C GPCRs possess a large extracellular domain that is responsible for ligand recognition, in addition to the seven strand transmembrane domain that is for G protein activation, which is characteristic of all GPCRs. The mGluRs possess a large bi-lobed extracellular N-terminus of ~560 amino acids which has been shown by mutagenesis studies to confer glutamate binding, agonist activation of the receptor, and subtype specificity for group selective agonists [21].

Starting from 1996 [22], a number of structural types of non-competitive negative, positive and neutral allosteric modulators have been developed as mGluR ligands. These ligands modulate mGlu receptor activity by binding to allosteric binding sites that are located in the seven strand transmembrane domain. The allosteric binding sites are structurally distinct from the classical agonist orthosteric binding site. Positive and negative modulators thus offer the potential for improved selectivity for individual mGluR family members compared to competitive agonists and antagonists at the glutamate site. These ligands are not amino acid derivatives and are structurally diversified. They are lipophilic and have much better penetration ability in the central nervous system. Thus, positive and negative modulators with high binding affinity, high subtype selectivity, and appropriate lipophilicity are good candidates for mGluR radiotracer development. There will be no competitive binding of this kind of tracers with endogenous glutamate, which increases the tracer's sensitivity.

During the last decade modulators have been identified for mGluR1, mGluR2, mGluR4, mGluR5 and mGluR7. Based on these modulators, several PET radiotracers have been developed for *in vivo* imaging of mGluR1 and mGluR5 [23].

d) Drug development: PET has a potential to be a powerful tool in drug discovery and development. PET imaging technology is able to non-invasively assess drug distribution and action at the molecular level. Positron emitters can be introduced to the drug candidates and used as radiolabeled ligands. It has been well established that substituting a stable atom with a radioisotope of the same element does not affect the physicochemical, pharmacokinetic or biological properties of a drug. Longitudinal dynamic PET imaging can be used to determine time course of accumulation and retention of the drug candidates.

III. CONCLUSIONS

Current development of neuroimaging using PET techniques relies presently on the development of radiopharmaceuticals. Especially for targeted therapy, more selective and sensitive imaging ligands are needed to investigate modulation of neurotransmission in different pathological conditions. PET imaging is the key to obtain in depth information of the brain functions.

ACKNOWLEDGEMENT

The experimental work was supported by NIH grants NIBIB-EB001850 and NINDS-NS39793.

REFERENCES

- Sweet WH (1951) The use of nuclear disintegration in diagnosis and treatment of brain tumors. *N Engl J Med*. 245: 875-8
- Brownell GL, Sweet WH (1953) Localization of brain tumors with positron emitters. *Nucleonics* 11: 40-45
- Chesler DD (1971) Three-dimensional activity distribution from multiple positron scintigraphs. *J Nucl Med* 12: 347-348
- Chesler DA (1973) Positron emission tomography and three-dimensional reconstruction technique. In *Tomographic Imaging in Nuclear Medicine*. Freedman GS, Ed. The Society of Nuclear Medicine, New York, 1973, pp 176-83
- Ambrose J (1973) Computerized transverse axial scanning (tomography): Part II. Clinical application. *Br J Radiol* 46: 1023-47
- Hounsfield GN (1973) Computerized transverse axial scanning (tomography). Part I: Description of system. Part II: Clinical applications. *Br J Radiol* 46: 1016-22.
- Cormack AM (1973) Representation of a function by its line integrals, with some radiological applications. *J Appl Phys* 34: 2722-27
- Jones T, Chesler DA, Ter-Pogossian MM (1976) The continuous inhalation of oxygen-15 for assessing regional oxygen extraction fraction in the brain of man. *Br J Radiol* 49: 339-45
- Lenzi GL, Frackowiak RS, Jones T (1982) Cerebral oxygen metabolism and blood flow in human cerebral ischemic infarction. *J Cereb Blood Flow Metab* 2: 321-35
- Ito H, Takahashi K, Hatazawa J, Kim SG, Kanno I (2001) Changes in human regional cerebral blood flow and cerebral blood volume during visual stimulation measured by positron emission tomography. *J Cereb Blood Flow Metab* 21: 608-12.
- Gallagher BM, Ansari A, Atkins H, et al (1977) Radiopharmaceuticals XXVII. 18F-labeled 2-deoxy-2-fluoro-d-glucose as a radiopharmaceutical for measuring regional myocardial glucose metabolism in vivo: tissue distribution and imaging studies in animals. *J Nucl Med* 18: 990-6.
- Di Chiro G, DeLaPaz RL, Brooks RA, et al. (1982) Glucose utilization of cerebral gliomas measured by [18F]fluoro-deoxyglucose and positron emission tomography. *Neurology* 32: 1323-9
- Frost JJ, Rosier AJ, Reich SG, et al (1993) Positron emission tomographic imaging of the dopamine transporter with 11C-WIN 35,428 reveals marked decline in mild Parkinson's disease. *Ann Neurol* 34: 423-31
- Frankle WG, Laruelle M (2002) Neuroreceptor imaging in psychiatric disorders. *Ann Nucl. Med.* 16: 437-46.
- Garnett ES, Firnau G, Nahmias C. (1983) Dopamine visualized in the basal ganglia of living man. *Nature* 305: 137-8
- Brownell A-L, Elmaleh DR, Meltzer P, et al. (1996) Cocaine congeners as PET imaging probes for dopamine terminals in normal and MPTP induced parkinsonism in nonhuman primate brain. *J Nucl Med* 37: 1186-92
- Wullner U, Pakzaban P, Brownell A-L, et al (1994) Dopamine terminal loss and onset of motor symptoms in MPTP-treated monkeys: A positron emission tomography study with 11C-CFT. *Exp Neurol* 126: 305-9
- Marck K, Innis R, van Dyck C, et al (2001) [123I]beta-CIT SPECT imaging assessment of the rate of Parkinson's disease progression. *Neurology* 57: 2089-94
- Szabo Z, Kao PF, Scheffel U, et al (1995) Positron emission tomography imaging of serotonin transporters in the human brain using [¹¹C](+)-McN5652. *Synapse* 20: 37-43
- Bischof Delaloye A (2002) Progress in the diagnosis and treatment of disease by nuclear medicine and molecular imaging. *Eur J Nucl Med.* 29:139-159
- Johnson BG, Wright WA, Arnold MB, et al (1999) [3H]-LY341495 as a novel antagonist radioligand for group II metabotropic glutamate (mGlu) receptors: characterization of binding to membranes of mGlu receptor subtype expressing cells. *Neuropharmacology*, 38:1519-1529
- Annoura H, Fukunaga A, Uesugi M, et al (1996) A novel class of antagonists for metabotropic glutamate receptors, 7-(hydroxyimino) cyclopropachromen-1 α -carboxylates. *Bioorg Med Chem Lett* 6: 763-766
- Wang J, Tueckmantel W, Zhu A, et al (2007) Synthesis and preliminary biological evaluation of 3-[(18F)fluoro-5-(2-pyridinylethynyl)benzotrile as a PET radiotracer for imaging metabotropic glutamate receptor subtype 5. *Synapse* 61: 951-61

Peanut Agglutinin-Immobilized Fluorescent Nanospheres with Surface Poly(N-vinylacetamide) Chains as a Novel Colonoscopic Imaging Agent

S. Sakuma¹, K. Hiwatari², T. Yano¹, K. Iwata¹, Y. Masaoka¹, M. Kataoka¹, H. Tachikawa², Y. Shoji², R. Kimura², K. Nakamura², H. Ma³, Z. Yang³, L. Tang³, R.M. Hoffman^{3,4}, and S. Yamashita¹

¹ Setsunan University, Hirakata, Osaka, Japan

² ADEKA Co., Arakawa-ku, Tokyo, Japan

³ AntiCancer Inc., San Diego, CA, USA

⁴ University of California at San Diego, La Jolla, CA, USA

Abstract— A goal of our research is to develop a colonoscopic imaging agent that enables real-time and accurate diagnosis of small-sized colorectal cancer. Colorectal cancer first develops in the mucous membrane of the large intestine. We designed an imaging agent that can recognize tumor-derived changes on the mucosal side of epithelial cells in the large intestine with high affinity and specificity. The agent is peanut agglutinin (PNA)-immobilized polystyrene nanospheres with surface poly(N-vinylacetamide) (PNVA) chains encapsulating coumarin 6. PNA is a targeting moiety that binds to β -D-galactosyl-(1-3)-N-acetyl-D-galactosamine, which is the terminal sugar of the Thomsen-Friedenreich antigen that is specifically expressed on the mucosal side of colorectal cancer cells. The tumor-derived change in the large intestinal mucosa is very small throughout the entire large intestine. To detect such a small change accurately, the imaging agent should have a strong affinity for targets with minimal nonspecific interactions with nontargets. PNVA is also immobilized on the nanosphere surface to enhance the specificity of PNA by reducing the nonspecific interactions between the imaging agent and normal tissues. Coumarin 6 is used as the fluorescent dye that provides an endoscopically detectable fluorescence intensity. It is anticipated that intracolonic (enema) administration of the imaging agent leads to the specific accumulation on the mucosal surface of tumor tissues in the large intestine with resulting fluorescence. Real-time and accurate diagnosis of small-sized early colorectal cancer can be then achieved through observations of a clear fluorescence contrast between the normal and tumor tissues using the standard fluorescence endoscopy.

Keywords— Endoscopic imaging agent, Colonoscopy, Colorectal cancer, Peanut agglutinin, Poly(N-vinylacetamide).

I. INTRODUCTION

Colorectal cancer is primarily treated by surgical resection, and early detection is critical for successful treatment [1]. A fecal occult blood test is widely used as the easiest way of screening for colorectal cancer [2]. Patients with positive findings need to be diagnosed by subsequent endoscopy in

order to visually confirm the existence of cancer. Colorectal cancer first develops in the mucous membrane of the large intestine, and invasion and metastasis are observed as the cancer progresses. Colonoscopy performed for the above-mentioned purpose is often accompanied by the resection of cancer that remains in the mucous membrane or only minimally invades the submucosal tissues without vessel invasion [3]. This minimally invasive operation, known as endoscopic mucosal resection (EMR), can serve as an alternative to surgical resection in the early stage of cancer.

Colonoscopy is the preferred screening method for colorectal cancer because it provides a definitive diagnosis in such cases. While the colonoscopy procedure is critically important, standard white-light colonoscopy has a major limitation: it can only detect tumor tissues that are larger than ca. 1 cm in size. Tumors of this size have a relatively high probability of metastasis [4]. Magnifying endoscopy contributes to the early detection of small-sized colorectal cancer; however, real-time and accurate differentiation of neoplastic mucosal changes remains a significant challenge. Advances in bioengineering have provided promising revolutionary imaging strategies for endoscopic diagnosis [5-6]. Narrow band imaging is a novel technique that enhances the visualization of surface mucosal and vascular patterns. Autofluorescence imaging is another new technique that involves the use of blue endoscopic light to induce mucosal autofluorescence. Some studies suggest the clinical usefulness of these techniques for the diagnosis of early colorectal cancer.

There is also a great need for developing an endoscopic imaging agent that can provide early detection of small-sized colorectal cancer [7]. We have been investigating a novel endoscopic imaging agent for the early detection of small-sized colorectal cancer [8-9]. We noted the mechanism of the cancer development, and designed the colonoscopic imaging agent that can recognize tumor-derived changes in the large intestinal mucosa with high affinity and specificity. As illustrated in Fig. 1, the agent comprises submicron-sized

fluorescent polystyrene nanospheres with two functional groups- peanut (Arachis hypogaea) agglutinin (PNA) and poly(N-vinylacetamide) (PNVA) -on their surfaces. The Thomsen-Friedenreich (TF) antigen is expressed specifically on the mucosal side of colorectal cancer cells [10]. Its terminal sugar is β -D-galactosyl-(1-3)-N-acetyl-D-galactosamine (Gal- β (1-3)GalNAc), and this sugar is masked by oligosaccharide side chain extension or sialylation in normal cells. Lectins are proteins that recognize and bind reversibly to specific carbohydrate residues expressed on the cell surface [11]. PNA was immobilized on the nanosphere surface as a targeting moiety that binds to the TF antigen specifically through the recognition of Gal- β (1-3)GalNAc. PNVA is a nonionic polymer with strong hydrophilicity. Our past research has indicated that hydrophilicity-induced thick water layers prevented the materials that were surface-coated with PNVA from interacting with the mucous membrane of the gastrointestinal tract [12]. Since the tumor-derived change in the large intestinal mucosa is very small throughout the entire large intestine, the imaging agent should have a strong affinity for targets (i.e., cancer tissues) with minimal nonspecific interactions with nontargets (i.e., normal tissues) to detect such a small change accurately. PNVA was immobilized on the nanosphere surface to enhance the specificity of PNA by reducing the nonspecific interaction between the imaging agent and normal tissues. Coumarin 6, which is a commercial product with high fluorescence quantum efficiency, was used as the fluorescent dye that provides an endoscopically-detectable fluorescence intensity. It was encapsulated into the polystyrene cores of the nanospheres through their strong hydrophobic interactions.

In this paper, we summarize characters of our imaging agent.

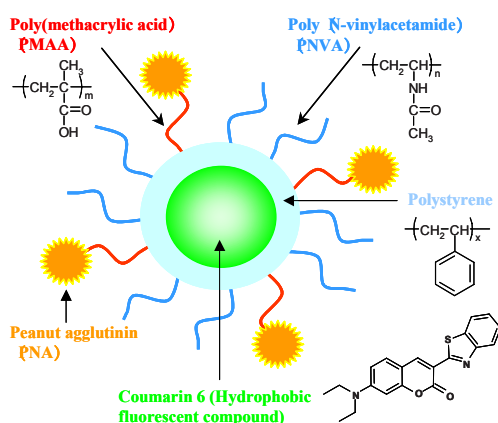


Fig. 1 Schematic representation of an imaging agent

II. MATERIALS AND METHODS

A. Synthesis of the Imaging Agent

Vinylbenzyl group-terminated PNVA and vinylbenzyl group-terminated poly(methacrylic) acid (PMAA) were radically copolymerized with styrene in an ethanol/water mixture dissolving coumarin 6 to obtain fluorescent nanospheres with surface PNVA and PMAA chains. PNA was immobilized on the nanosphere surface by coupling the amino groups of PNA with the carboxyl groups of PMAA. Standard instrumental analysis was performed to evaluate the characteristics of the resulting PNA-immobilized fluorescent nanospheres with surface PNVA chains encapsulating coumarin 6 (imaging agents). The imaging agent was dispersed in PBS at a concentration of 4 mg/mL.

B. Measurement of the PNA Activity

The PNA activity of the imaging agent was measured with a conventional hemagglutination test. Untreated rabbit erythrocytes were used with neuraminidase-treated ones in which Gal- β (1-3)GalNAc was presented. The minimum agglutination concentration (MAC) was defined as the minimum concentration of PNA on the nanosphere surface that caused erythrocyte agglutination. The same test was performed by substituting intact PNA for the imaging agent.

C. In vitro Biorecognition of the Imaging Agent for Human Colorectal Cancer Cells

Human colorectal adenocarcinoma cell lines, HT-29, HCT-116, LS174T, HCT-15, Caco-2, and SW-480, were cultured under conditions reported widely. Cultured epithelial cells of the small intestine in humans were used as negative control without the TF antigen. The dispersion of the imaging agent was mixed with an equivalent volume of cell suspension (1×10^7 cells/mL). After incubation at 37°C for 30 min, the mixture was centrifuged to separate the cells from free imaging agents. Fluorescence microphotographs of cells re-suspended in PBS were measured using a fluorescence microscope (excitation: 470-495 nm; emission: 510-550 nm; exposure: 1/60 of a second). Fluorescence intensity of the imaging agent bound to cells was quantitatively estimated using an image analysis tool.

D. In vivo Biorecognition of the Imaging Agents for Tumor Tissues

A red fluorescent protein (RFP)-expressing orthotopic human colorectal cancer model was constructed as follows. A tumor stock of RFP gene-transduced HT-29 was

established by subcutaneously injecting HT-29-RFP cells (1×10^6 cells/mL, 0.05 mL) into the flank of nude mice. The tumor was maintained in the nude mice subcutaneously as tumor stock prior to being used. On the day of implantation, the tumor was harvested from the subcutaneous site, necrotic tissues were removed, and viable tissues were cut into 1 mm^3 pieces. Two fragments of the RFP-expressing HT-29-derived tumor tissues were implanted orthotopically in the serosa of the ascending colon of other nude mice. The mice were maintained for a predetermined period after the implantation until cancer cells invaded the mucosal side of epithelial cells. Under ether anesthesia, the abdomen was opened and the ascending colon, in which tumor tissues were implanted, was observed. An approximately 3-cm loop of the colon bearing the tumors was prepared in the abdomen by ligating both ends of the colon after washing its luminal side with saline. The dispersion of the imaging agent (1.0 mL) was injected into the loop. After 30 min, the loop was removed and its luminal side was washed with ≥ 1.0 mL of PBS. The colon was cut longitudinally and the mucosal surface was observed with a fluorescence microscope under experimental conditions that were free from tissue autofluorescence (excitation: 470–495 nm; emission: 510–550 nm; exposure: 1/60 of a second).

III. RESULTS AND DISCUSSION

In a series of research, the hemagglutination test was first performed to optimize the chemical structure of the imaging agent. The MAC of intact PNA was $0.39 \text{ }\mu\text{g/mL}$ for neuraminidase-treated erythrocytes and $5.7 \text{ }\mu\text{g/mL}$ for untreated ones, respectively. The ratio of MAC was 15 ($5.7/0.39$). Data proved that the PNA was bound to Gal- β (1-3)GalNAc expressed on the erythrocyte surface with high affinity. Imaging agents with different chemical structures on their surface were prepared, and the affinity and specificity of immobilized PNA for Gal- β (1-3)GalNAc was examined. Agglutination of normal and Gal- β (1-3)GalNAc-expressing erythrocytes in the presence of the imaging agent showed that PNA was immobilized actively on the nanosphere surface. Among parameters that influenced the surface structure, molecular weights of PNVA and PMAA affected the PNA activity most strongly. When there was no difference in weight-average molecular weights between PNVA and PMAA on the nanosphere surface, the average MAC was 1.0 and $125 \text{ }\mu\text{g/mL}$ for neuraminidase-treated and untreated erythrocytes, respectively, indicating that the affinity for Gal- β (1-3)GalNAc was as strong as that of intact PNA; the specificity for the carbohydrate residues was higher than that of the

PNA. Results indicated that PNVA enhanced the specificity of PNA through the reduction of nonspecific interactions between PNA and carbohydrates other than Gal- β (1-3)GalNAc on the erythrocyte surface without a significant decrease of the affinity.

Since the chemical structure of the imaging agent was optimized, *in vitro* biorecognition of the imaging agent for human colorectal cancer cells was subsequently evaluated. The TF antigen-positive HT-29 cells were clearly observed with strong fluorescence after incubating them with the imaging agent. The image analysis estimated that the intensity was 30.4 ± 4.1 (mean \pm s.d., $n=5$). When HT-29 cells were substituted with epithelial cells of the small intestine that had not exposed Gal- β (1-3)GalNAc, the fluorescence intensity was significantly reduced (8.72 ± 0.56). The average fluorescence intensity of any type of colorectal cancer cell used in this study was higher than that of small intestinal epithelial cells. *In vitro* studies demonstrated that the imaging agent bound to human colorectal cancer cells with high affinity and specificity. This was due to the recognition of Gal- β (1-3)GalNAc by the imaging agent.

The *in vivo* performance of imaging agents was finally evaluated using a human colorectal cancer orthotopic animal model. In this study, animals with tumors on the mucosa of the large intestine are required because the imaging agent has been designed to recognize tumor-derived changes on the mucosal side of cells. Two types of human colorectal cancer orthotopic animal models have been reported [9]: the implantation of cultured cancer cells in the intestine of immune-deficient animals such as nude mice, and the implantation of tumor tissues in the intestine. In the latter model, cultured cancer cells are first xenografted onto the flank of the animals, and then matured tumor tissues are transplanted in the intestine of other animals by surgical orthotopic implantation. However, since cancer cells and tumor tissues are implanted on the serosal side of the intestine, the animals are required to be maintained until the implanted cells invade the mucosal side. Therefore, we examined the period that is required for the mucosal invasion of tumor tissues implanted on the large intestinal serosa by using the latter model. Histological examination showed that tumor tissues invaded the mucosal side of the epithelial cells when mice were maintained for at least 2 weeks after implantation. *In vivo* biorecognition of the imaging agent for tumor tissues was evaluated using this orthotopic model. As shown in Fig. 2, imaging agent-derived strong fluorescence was observed at several sites of the large intestinal mucosa in the tumor tissues-implanted nude mice after the luminal side of the colonic loop was contacted with imaging agents. In contrast, when mice that

did not undergo tumor implantation were used, the fluorescence intensity on the mucosal surface was extremely low. This observation indicated that the imaging agent recognized the mucosal invasion of HT-29-derived tumors implanted orthotopically in the large intestinal serosa of nude mice.

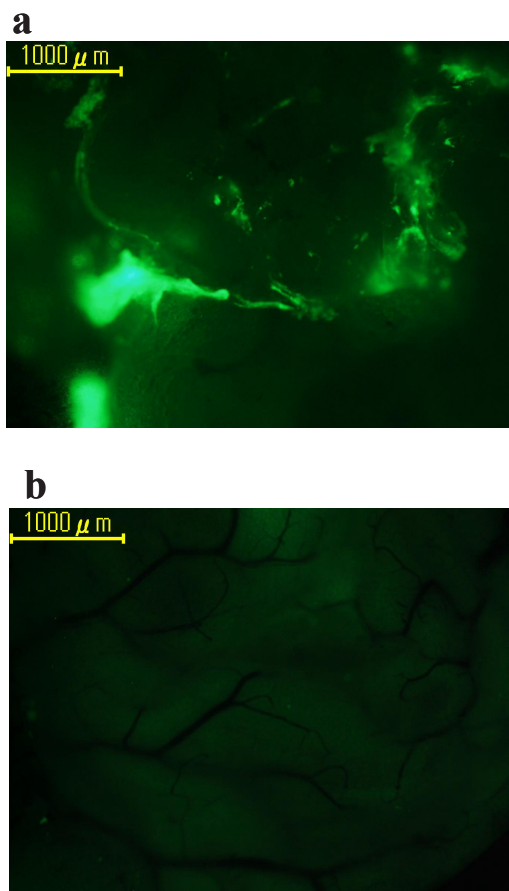


Fig. 2 Fluorescence microphotographs of the colonic mucosa treated with the imaging agent in RFP gene-transduced HT-29-derived tumor tissues-implanted nude mice (a) and normal nude mice (b). Tumor tissues-implanted mice were sacrificed at 48th day after the surgical orthotopic implantation

IV. CONCLUSIONS

It is anticipated that real-time and accurate diagnosis of small-sized colorectal cancers can be realized through the observation of a clear fluorescence contrast between the normal and tumor tissues after intracolonic administration of the imaging agent under a standard fluorescence endoscope with or without magnification.

ACKNOWLEDGMENTS

This work was financially supported in part by a grant-in-aid for scientific research from the Ministry of Education, Culture, Sports, Sciences and Technology of Japan (MEXT), a grant-in-aid for a research for promoting technological seeds from Japan Science and Technology Agency (JST), a grant-in-aid from The Japanese Foundation for Research and Promotion of Endoscopy (JFE), a grant-in-aid from Japan Interaction in Science & Technology Forum (JIST), and a grant-in-aid from the Sagawa foundation for promotion of cancer research. The authors thank Showa Denko Co. for the gift of NVA monomers.

REFERENCES

- Balch GC, De Meo A, Guillem JG (2006) Modern management of rectal cancer: a 2006 update. *World J Gastroenterol* 12:3186-3195.
- Harford WV (2006) Colorectal cancer screening and surveillance. *Surg Oncol Clin N Am* 15:1-20.
- Kudo S, Tamegai Y, Yamano H et al. (2001) Endoscopic mucosal resection of the colon: the Japanese technique. *Gastrointest Endosc Clin N Am* 11:519-535.
- Kashida H, Kudo S (2006) Early colorectal cancer: concept, diagnosis, and management. *Inter J Clin Onco* 1:11-8.
- Tischendorf JJ, Wasmuth HE, Koch A et al. (2007) Value of magnifying chromoendoscopy and narrow band imaging (NBI) in classifying colorectal polyps: a prospective controlled study. *Endoscopy* 39:1092-1096.
- Anandasabapathy S (2008) Endoscopic imaging: emerging optical techniques for the detection of colorectal neoplasia. *Curr Opin Gastroenterol* 24:64-69.
- Kelly K, Alencar H, Funovics M et al. (2004) Detection of invasive colon cancer using a novel, targeted, library-derived fluorescent peptide. *Cancer Res* 64:6247-6251.
- Hiwatari K, Sakuma S, Iwata K et al. (2008) Poly(N-vinylacetamide) chains enhance lectin-induced biorecognition through the reduction of nonspecific interactions with non-targets. *Eur J Pharm Biopharm* 70:453-461.
- Sakuma S, Yano T, Masaoka Y et al. (2009) In vitro/in vivo biorecognition of lectin-immobilized fluorescent nanospheres for human colorectal cancer cells. *J Control Release* 134:2-10.
- Campbell BJ, Finnie IA, Hounsell EF et al. (1995) Direct demonstration of increased expression of Thomsen-Friedenreich (TF) antigen from colonic adenocarcinoma and ulcerative colitis mucin and its concealment in normal mucin. *J Clin Invest* 95:571-576.
- Sakuma S, Lu ZR, Kopečková P et al. (2001) Biorecognizable HPMA copolymer-drug conjugates for colon-specific delivery of 9-aminocamptothecin. *J Control Release* 75:365-379.
- Sakuma S, Hayashi M, Akashi M (2001) Design of nanoparticles composed of graft copolymers for oral peptide delivery. *Adv Drug Deliv Rev* 47:21-37.

Author: Shinji Sakuma
 Institute: Setsunan University
 Street: 45-1, Nagaotoge-cho
 City: Hirakata Osaka
 Country: Japan
 Email: sakuma@pharm.setsunan.ac.jp

Techniques for the Incorporation of Fluorine-18 and Carbon-11

Nickels and W. Pham

Vanderbilt University/VUIIS, Research Fellow, Nashville, TN, USA

Abstract— Molecular imaging is an attractive modality that has been widely employed in many aspects of biomedical research, especially those aimed at the early detection of diseases such as cancers, inflammation and neurodegenerative disorders. One specific type of molecular imaging, which has shown a renewed interest in recent years, comes in the form of positron emission tomography (PET). This type of imaging relies on the formation of small molecule drugs that have been selectively labeled with a positron emitting radionuclide. Ideally, the small molecule will have a high affinity for the molecular target, cell line or physiological process to be imaged, which allows for the accumulation of the agent. The predictable mode and rate of decay associated with the chosen nuclide allows for both spatial and quantitative imaging of the tissues associated with the small molecule radiotracer when contrasted against the surrounding tissue that lacks the characteristic radioactive decay. Over the many years of radiotracer development, various methods for the incorporation of the radionuclide have been discovered and utilized. Much of this experimentation has shed light on the types of reaction substrates, solvents, temperatures and reactant forms that allow for the most efficient and repeatable labeling of a given class of molecule. This paper will highlight many of the previously attempted, currently used and potential reactions for the incorporation of either fluorine-18 or carbon-11 radionuclides onto both small molecule and macromolecular drugs. This will include both aliphatic and aromatic labeling techniques and the types of products and potential by-products one may observe.

Keywords— PET, Radiochemistry, Molecular Imaging, Fluorine-18, Carbon-11.

I. INTRODUCTION

Positron emission tomography (PET) is a non-invasive, *in vivo* imaging technique that uses relatively short-lived positron-emitting radioisotopes at a tracer level. The introduced radionuclides are intended to probe physiological processes, such as diseases, in living organisms, which allows for a real time understanding of how these processes are affecting or progressing within the organism [1]. In addition to disease states, PET has become an important imaging modality for both tumor and normal tissue pharmacokinetics,

tumor responses, cell proliferation, gene expression, and the status of receptors or tumors [2], along with the diagnoses of heart disease, epilepsy, and stroke [3].

Strategic design and synthesis of radiolabeled imaging agents presents a daunting task for even the most experienced synthetic organic chemist. Synthetic design of a novel radiolabeled drug must take into account both the hazardous nature of the radioisotope and the limited timeframe the synthesis, purification and formulation can occur over. Typically, positron emitting radionuclides have short half-lives (Table 1) which requires incorporation of the isotope as late in the synthetic route as possible with as short of reaction time as can be obtained. With this fact in mind, the usual synthetic approach used for radiolabeling has no more than one additional step after incorporation of the radionuclide and this step is most commonly a highly efficient deprotection step. Working against the clock in a multi-step operation with a large amount of radioisotope requires the combination of the latest apparatus technologies, such as automated module systems, and the latest reaction methodologies in order to achieve the necessary precision and address the ever present safety concerns. In the following sections, both the traditional methodologies, which have been used with great reliability in a wide variety of studies, and the most recently reported advances in this field will be discussed for fluorine-18 and carbon-11.

Table 1 Typical positron emitting radionuclides

Isotope	Half-Life (min)	Positron Energy (MeV)	Positron Range (mm)	Production Source
⁸² Rb	1.26	3.15	1.7	generator
¹⁵ O	2.03	1.70	1.5	cyclotron
¹³ N	9.97	1.19	1.4	cyclotron
¹¹ C	20.3	0.96	1.1	cyclotron
¹⁸ F	109.8	0.64	1.0	cyclotron
⁶⁴ Cu	768	0.66	n/a	cyclotron

II. DISCUSSION

A. Fluorine-18 Methodologies

Fluorine-18 is an attractive positron-emitter for three main reasons; first, fluorine-18 possesses a longer half-life

when compared to other tracers used in clinical PET studies, second, fluorine-18 decay produces a positron of relatively low energy providing a low average distance travelled before the annihilation event, and lastly, steric similarity to a hydrogen atom can potentially convert any active therapeutic agent into a PET probe without severely hindering the affinity for the target. A low average distance travelled before the annihilation event enables qualitative imaging with a high spatial resolution [4].

Formation of fluorine-18 containing molecules can be divided into two main reaction classifications; the first is the formation of aliphatic or sp^3 hybridized carbon bonded to fluorine bonds and the second is aromatic or non- sp^3 hybridized carbons bonded to fluorine. Within these two different types of reaction classifications, one can consider a wide range of different fluorine displacement reaction precursors. In terms of the aliphatic subclass, which will be discussed first, the type of reaction that fluoride undertakes is referred to as a nucleophilic substitution or an S_N2 reaction. This type of reaction relies on the presence of a functional group that has a strong ability to be displaced by the weakly nucleophilic fluoride ion. The main functionality used is that of the sulfonic esters.

a) Sulfonic Esters as Leaving Groups

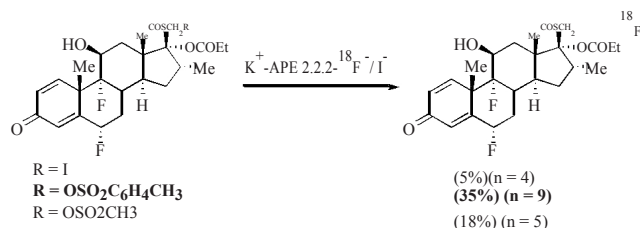


Fig. 1 Fluorine-18 labeling of an aliphatic carbon bearing different leaving groups

A successful fluorine-18 labeling can be defined by both reproducibility and a high radiochemical yield (RCY), which can both be obtained via the proper design of the precursor. In terms of obtaining a radiochemical tracer with an aliphatic carbon fluorine bond, the best choice of leaving groups come in the form of the sulfonic esters, which include but are not limited to methane sulphonate (mesylate), trifluoromethylsulphonate (triflate), 2- or 4-nitrobenzenesulphonate (nosylate) and 4-methylbenzenesulphonate (tosylate). In an effort to compare the reactivity of various sulphonate and halide precursors towards fluorine-18 displacement, Aigbirhio and coworkers developed a small library of compounds that possessed these various leaving groups [5]. They then performed the same displacement reaction on each of the precursors, which allowed for a quantitative comparison of the labeling efficiency

(Figure 1). Results showed that there is a clear advantage to using the tosylate leaving group when compared to both the mesylate and iodo precursors.

The ideal choice of the leaving group varies between chemical species, meaning that the ideal choice for one type of chemical species will be different for another chemical species. Typically, the rate of fluoride displacement is greatest among the sulfonate family for the triflate, however, it generally has low stability resulting in low RCYs [6]. As a result, triflates are not favored as fluorination precursors.

b) Trimethylammonium Salts as Leaving Groups

Formation of aromatic or non- sp^3 hybridized carbon fluorine bonds require a different type of reaction precursor, namely, a precursor with a suitable leaving group found on either an aromatic ring or unsaturated carbon. In addition to the proper choice of leaving groups, the electronics of the ring must also be taken into account. Nucleophilic fluoride displacement typically requires a substantially electron deficient ring, whereas electrophilic aromatic substitution requires an electron rich ring. Nearly a decade ago, aryl-fluorine-18 fluorinations, via nitro precursors, were considered to be the most popular method used in PET chemistry [7]. More recently, aryltrimethyl ammonium salts have been more heavily focused on due to the groups excellent leaving group ability and the emergence of more demanding chemical targets for which nitro leaving groups did not prove to be adequate. It's been found that the choice of ammonium counter ion plays a crucial role in the outcome of the fluorination reaction. The two most prevalent counterion examples are perchlorate and triflate, with triflate being favored due to lower fluoride displacement temperatures and ease of preparation [8].

As an alternative to fluoride displacements directly on the compound of interest, many researchers opt for the development of molecules that have the ability be linked to a molecule that has efficiently been labeled with fluorine-18. Probably the most well known example of this class of fluorine-18 labeled linker capable molecules is the N-succinimidyl-4- ^{18}F fluorobenzoate (^{18}F SFB). The preparation of this reagent comprises a total of three steps beginning with the initial two step preparation of 4- ^{18}F fluorobenzoic acid (^{18}F FBA) [9] and then finished off with the formation of the desired succinimidyl ester (Figure 2) [10].

An alternative to the use of ^{18}F SFB, which limits the identity of the final product, comes in the form of fluorine-18 labeled molecules specifically designed to possess a terminal alkyne, which allows for the use of so-called "click chemistry" to link the labeled molecule with either an azide containing peptide or an azide containing small molecule

[11]. The reaction of an azide and alkyne in the presence of a catalytic amount of Cu(I) results in the diastereospecific formation of a 1,4-disubstituted 1,2,3-triazole.

In addition to the two linkers already discussed, a large variety of additional linkers have been developed and shown to be useful for the formation of labeled small molecule drugs or peptides [12]. Further discussion on the additional types of molecules is out of the scope of this paper.

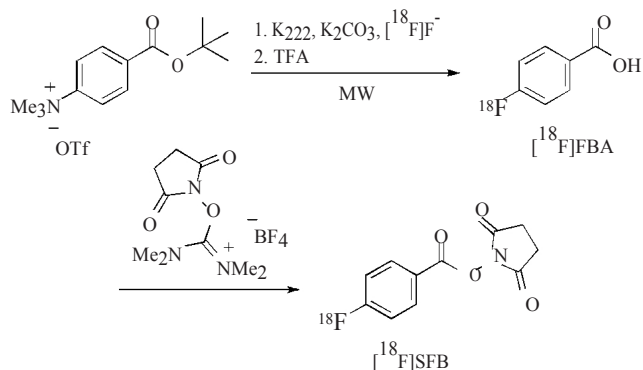


Fig. 2 Production of $[^{18}\text{F}]\text{SFB}$ via production of $[^{18}\text{F}]\text{FBA}$

c) Aromatic Nitro Groups as Leaving Groups

As has already been discussed in the previous section, aromatic nitro precursors have traditionally been the most commonly used functionality for the production of aromatic fluorine products [7]. With this fact in mind, one can imagine that a huge variety of fluorine-18 labeled imaging agents have been synthesized since the discovery of this methodology. Due to the large amount of research that has been done on this type of system, many new discoveries into the fundamentals of this class of reaction have been reported. One of the most fundamental discoveries pertains to the displacement yields in a variety of solvents. Typically, a nucleophilic aromatic substitution is best carried out in polar aprotic solvents. The most common examples of these solvents are DMSO, DMF, sulfolane and acetonitrile. Studies have shown that the RCY for reactions carried out in DMSO or sulfolane are much higher than for reactions carried out in DMF or acetonitrile [13]. However, since sulfolane is a solid at room temperature, DMSO has been found to be an ideal solvent candidate. It is important to note that the reaction will be deactivated in the presence of water. Therefore, it is important to azeotropically remove water from the mixture of kryptofix/potassium carbonate/ $[^{18}\text{F}]\text{fluoride}$ (from cyclotron) before introducing the precursor, pre-dissolved in a suitable anhydrous solvent. As an alternative to polar aprotic solvents, initial studies have shown that hindered tertiary alcohols, such as tert-butyl

alcohol and tert-amyl alcohol, can be used to obtain high RCY in fluorine-18 displacements [14].

d) Diaryliodonium Salts as Aromatic Fluorination Precursors

The use of diaryliodonium salts represents the newest method for fluorine-18 labeling of aromatic compounds when compared to previously discussed methods. What stands for this class of compounds is the excellent nucleofugality of the phenyliodonio group, which has shown a leaving group ability of about 10^6 times greater than that of an alkenyltriflate [15]. Generally, diaryliodonium salts are air stable, crystalline solids, with slight sensitivity to light. Counterions associated with the salts are typically triflates or tosylates, but a wide variety of anions can be employed (Figure 3).

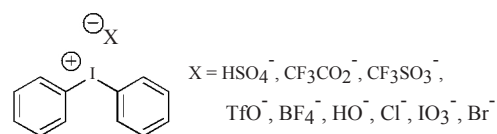


Fig. 3 Diaryliodonium salt with representative known counterions

B. Carbon-11 Methodologies

Carbon-11 labeled molecules are the next most popular nuclide used in PET imaging, but due to the short half-life, only a small selection of chemical processes have successfully been reported. One of the most common is $[^{11}\text{C}]\text{methyl iodide}$ which is frequently used as a carbon-11 precursor due to the ease of production, handling and the fact that biologically active compounds typically have multiple positions that can be functionalized with a $[^{11}\text{C}]\text{methyl}$ group. When radiochemical reaction timing and yield are critical, a more reactive source of carbon-11 is necessary. This comes in the form of $[^{11}\text{C}]\text{methyl triflate}$, which can be synthesized by combining $[^{11}\text{C}]\text{methyl iodide}$ and silver triflate [16]. Several biologically active compounds have been developed in high radioactive quantities (80-170 mCi), allowing for multiple human PET studies [17].

In addition to the labeling of molecules via a carbon-11 methyl containing reagent, a large amount of research has gone into the development and utilization of gaseous carbon-11 in the form of either carbon dioxide or carbon monoxide. Use of these reagents allows for the formation of aldehydes, ketones, esters and amides with the central carbonyl carbon possessing the desired label. Usually, $[^{11}\text{C}]\text{carbon dioxide}$ is reacted with a suitable Grignard reagent then transformed into the desired functionality [18]. Alternatively, the use of $[^{11}\text{C}]\text{carbon monoxide}$ allows for the direct formation of functionalities, such as amides, via

a palladium mediated condensation between a suitable halide, [^{11}C]carbon monoxide and the desired primary or secondary amine [19].

III. CONCLUSIONS

In recent years, a renewed interest into the development of imaging agents has emerged due to a wide variety of factors, such as advances in computer technology. Over the last couple of decades, there has been an explosion in the field of computer technology and, as a direct benefit; there has also been a huge advancement in the accompanying instrumentation. These advances have allowed scientists and medical doctors to gain unprecedented clarity in the images they have been obtaining, which directly lead to the need for new more selective or sensitive agents. Whether these agents are intended for human imaging, mouse or rat studies, drug development, or metabolic studies, there is always a need for skilled chemists capable of producing these agents both on tracer level and/or large-scale GMP type preparations. Understanding both the chemical possibilities and the potential targets requires multidisciplinary chemists and biologists working together towards identification and preparation of these new targets. Efforts towards achieving this type of synergistic relationship have produced new programs at research institutions all over the world, albeit most have been created as drug discovery programs. In reality, drug discovery is just one step away from becoming an imaging agent development program and with all of these programs running at full speed, the future of imaging probe development looks bright.

ACKNOWLEDGMENT

We would like to thank the organizing committee for inviting us to present this material at the 3rd International Conference on the Development of Biomedical Engineering. We would also like to thank the faculty and staff of the Vanderbilt University Institute of Imaging Sciences especially Director John C. Gore.

REFERENCES

1. Phelps M (2000) Inaugural article: positron emission tomography provides molecular imaging of biological processes. *Proc Natl Acad Sci USA* 97:9226-9233
2. Brady F, Luthra SK, Brown GD, Osman S, Aboagye E, Saleem A, Price PM (2001) Radiolabelled tracers and anticancer drugs for assessment of therapeutic efficacy using PET. *Curr Pharm Des* 7:1863-1892
3. Mandelkern MA (1995) Nuclear techniques for medical imaging: positron emission tomography. *Annu Rev Nucl Part Sci* 45:205-254

4. Jalilian AR, Tabatabai SA, Shafiee A, Afarideh H, Najafi R, Bineshmarvasti M (2000) One-step, no-carrier-added, synthesis of a ^{18}F -labeled benzodiazepine receptor ligand. *J Labelled Compd & Radiopharm* 43:545-555
5. Aigbirhio FI, Carr RM, Pike VW, Steel CJ, Sutherland DR (1997) Automated radiosynthesis of no-carrier added [S-fluoromethyl- ^{18}F]fluticasone propionate as a radiotracer for lung deposition studies with PET. *J Labelled Compd & Radiopharm* 39:567-584
6. Jeong JM, Lee DS, Chung JK, Lee MC, Koh CS, Kang SS (1997) Synthesis of no-carrier-added [^{18}F]fluoroacetate. *J Labelled Compd & Radiopharm* 39:395-399
7. Kilbourn MR, Haka MS (1988) Synthesis of [^{18}F]GBR13119, a presynaptic dopamine uptake antagonist. *Int J Rad Appl Instrum [A]* 39:279-282
8. Haka MS, Kilbourn MR, Watkins GL, Toorongian SA (1989) Aryl-trimethylammonium trifluoromethanesulfonates as precursors to aryl[^{18}F]fluorides: improved synthesis of [^{18}F]GBR-13119. *J Labelled Compd & Radiopharm* 27:823-833
9. Ding YS (2000) ^{18}F -Labeled biomolecules for PET studies in the neurosciences. *J Fluorine Chem* 101:291-295
10. Wüst F, Hultsch C, Bergmann R, Johannsen B, Henle T (2003) Radiolabelling of isopeptide N^ε-(γ -glutamyl)-L-lysine by conjugation with N-succinimidyl-4-[^{18}F]fluorobenzoate. *Appl Radiat Isot* 59:43-48
11. Inkster JH, Guérin B, Ruth TJ, Adam MJ (2008) Radiosynthesis and bioconjugation of [^{18}F]FPy5yne, a prosthetic group for the ^{18}F labeling of bioactive peptides. *J Labelled Compd & Radiopharm* 51:444-452
12. Kuhnast B, Hinnen F, Tavitian B, Dollé F (2008) [^{18}F]FPyKYNE, a fluoropyridine-based alkyne reagent designed for the fluorine-18 labelling of macromolecules using click chemistry. *J Labelled Compd & Radiopharm* 51:336-342
13. Makosza M, Jagusztyn-Grochowska M, Ludwikow M, Jawdosiuik M (1974) Reactions of organic anions. I. Reactions of phenylacetone nitrile derivatives with aromatic nitro compounds in basic media. *Tetrahedron* 30:3723-3735
14. Kim DW, Ahn DS, Oh YH, Lee S, Kil HS, Oh SJ, Lee SJ, Kim JS, Ryu JS, Moon DH, Chi DY (2006) A new class of Sn2 reactions catalyzed by protic solvents: facile fluorination for isotopic labeling of di-agonistic molecules. *J Am Chem Soc* 128:16394-16397
15. Okuyama T, Takino T, Sueda T, Ochiai M (1995) Solvolysis of cyclohexenylidonium salt, a new precursor for the vinyl cation: remarkable nucleofugality of the phenyliodonio group and evidence for internal return from an intimate ion-molecule pair. *J Am Chem Soc* 117:3360-3367
16. Jewett DM (1992) A simple synthesis of [^{11}C]methyl triflate. *Int J Rad Appl Instrum [A]* 43:1383-1385
17. Chakroborty PK, Gildersleeve DL, Jewett DM, Toorongian SA, Kilbourn MR, Schwaiger M, Wieland DM (1993) High yield synthesis of high specific activity R-(-)-[^{11}C]epinephrine for routine PET studies in humans. *Nucl Med Biol* 20:939-944
18. Kawashima H, Yajima K, Kuge Y, Hashimoto N, Miyake Y (1997) Synthesis of 1-[^{11}C]-2-octynoic acid, 1-[^{11}C]-2-decyloic acid and 1-[^{11}C]-3-(R,S)-methyloctanoic acid as potential markers for PET studies of fatty acid metabolism. *J Labelled Compd & Radiopharm* 39:181-193
19. Kihlberg T, Langstroem B (1999) Biologically active ^{11}C -labeled amides using palladium-mediated reactions with aryl halides and [^{11}C]carbon monoxide. *J Org Chem* 64:9201-9205

Author: Michael Nickels
 Institute: Vanderbilt University
 Street: 1161 21st Ave. South MCN AA-1105
 City: Nashville, TN
 Country: USA
 Email: michael.l.nickels@vanderbilt.edu

Dynamic Model Identification of PAM-Based Rehabilitation Robot Using Neural MIMO NARX Model

Ho Pham Huy Anh² and Le Tan Loi¹

¹ Nguyen Trai Hospital, HCM City, Viet Nam

² Ho Chi Minh City University of Technology, Viet Nam

Abstract— In this paper, a novel Forward Dynamic MIMO Neural NARX model is used for simultaneously modeling and identifying both joints of the 2-axes PAM robot arm's forward dynamic model. The contact force variation and highly nonlinear cross effect of both links of the 2-axes PAM robot arm are modeled thoroughly through a Forward Neural MIMO NARX Model-based identification process using experiment input-output training data. Consequently the proposed Forward Dynamic Neural MIMO NARX model scheme of the nonlinear 2-axes PAM robot arm has been investigated. The results show that the novel Forward Dynamic Neural MIMO NARX Model trained by Back Propagation learning algorithm yields outstanding performance and perfect accuracy.

Keywords— Rehabilitation Robot, Modeling, Neural MIMO NARX Model, Forward Dynamic Identification.

I. INTRODUCTION

The nonlinear n-DOF robot arm used in rehabilitation robot is belonged to highly nonlinear systems where perfect knowledge of their parameters is unattainable by conventional modeling techniques because of the time-varying inertia, external force variation, cross-effect between the joints and other joint friction model uncertainties. To guarantee a good force/position tracking performance, lots of researches have been carried on. Jatta *et al.* in [1] applied hybrid force/velocity control of industrial manipulator considering friction compensation. In [2], Khayati *et al.* realized a multistage position/force control for constrained robotic system using multi-objective observer. Katsura *et al.* in [3] installed an adaptive model used as a disturbance observer for force control of robotic manipulator.

Recently, robust-adaptive control approaches combining conventional methods with new learning techniques are realized. During the last decade several neural network models and learning schemes have been applied to offline and online learning of manipulator dynamics [4-8]. Ahn and Anh in [9-10] have successfully optimized a NARX fuzzy model of the PAM robot arm using genetic algorithm. These authors in [11] have identified the PAM manipulator based on recurrent neural networks. The drawback of all these results is related to

consider the n -DOF robot arm as n independent decoupling joints and the external force variation like negligible effect. Consequently, all intrinsic cross-effect features of the n -DOF robot arm have not represented in its recurrent neural model.

To overcome these disadvantages, in this paper, a new approach of intelligent dynamic model, namely Forward Dynamic Neural MIMO NARX model, firstly utilized in simultaneously modeling and identification both joints of the 2-axes pneumatic artificial muscle (PAM) robot arm system used as 2-axes PAM-based wrist and elbow rehabilitation robot. The results show that the novel Forward Dynamic Neural MIMO NARX Model trained by Back Propagation learning algorithm yields outstanding performance and perfect accuracy.

The rest of paper is organized as follows. Section 2 introduces to BP learning algorithm applied to the modeling and identification of the 2-axes PAM robot arm. Section 3 presents the experimental set-up configuration for Forward Dynamic Neural MIMO NARX model-based identification. The results from the Forward Dynamic Neural MIMO NARX model-based identification are presented in Section 4. Finally, in Section 5 a conclusion remark is made for this paper.

II. BACK PROPAGATION (BP) LEARNING ALGORITHM IN FORWARD MIMO NARX MODEL IDENTIFICATION

Forward Dynamic Neural MIMO NARX model used in this paper is a combination between the Multi-Layer Perceptron Neural Networks (MLPNN) structure and the *Auto-Regressive with eXogenous input* (ARX) model. Due to this combination, Forward MIMO NARX model possesses both of powerful universal approximating feature from MLPNN structure and strong predictive feature from nonlinear ARX model.

Consider a 2nd order ARX model with noisy input, which can be described as

$$A(q^{-1})y(t) = B(q^{-1})u(t-T) + C(q^{-1})e(t) \quad (1)$$

with

$$A(q^{-1}) = 1 + a_1q^{-1} + a_2q^{-2}$$
$$B(q^{-1}) = b_1 + b_2q^{-1}$$
$$C(q^{-1}) = c_1 + c_2q^{-1} + c_3q^{-2}$$

where $e(t)$ is the white noise sequence with zero mean and unit variance; $u(t)$ and $y(t)$ are input and output of system respectively; q is the forward shift operator and T is the time delay.

From equation (1), not consider noise component $e(t)$, we have the general form of the discrete ARX model in domain z (with the time delay $T=n_k=1$)

$$\frac{y(z^{-1})}{u(z^{-1})} = \frac{b_1 z^{-1} + b_2 z^{-2} + \dots + b_{n_b} z^{-n_b}}{1 + a_1 z^{-1} + a_2 z^{-2} + \dots + a_{n_a} z^{-n_a}} \quad (2)$$

in which n_a and n_b are the order of output $y(z^{-1})$ and input $u(z^{-1})$ respectively.

By embedding a 3-layer MLPNN (with number of neurons of hidden layer = 5) in a 2nd order ARX model with its characteristic equation derived from (2) as follows:

$$\begin{aligned} y_{1hat}(k) &= b_1 u_1(k-1) + b_2 u_2(k-1) - a_1 y_1(k-1) - a_2 y_2(k-1) \\ y_{2hat}(k) &= b_2 u_1(k-1) + b_{22} u_2(k-1) - a_2 y_1(k-1) - a_{22} y_2(k-1) \end{aligned} \quad (3)$$

We will obtain the resulting MIMO Neural NARX11 model ($n_a = 1$, $n_b = 1$, $n_k = 1$) with 6 inputs ($u_{11}(t)$, $u_{21}(t)$, $y_1(t-1)$, $u_{12}(t)$, $u_{22}(t)$ and $y_2(t-1)$), 2 outputs (y_{1hat} , y_{2hat}) and its structure shown in Fig. 1.

The class of MLPNN-networks considered in this paper is furthermore confined to those having only one hidden layer and using sigmoid activation function:

$$\hat{y}_i(w; W) = F_i \left(\sum_{j=1}^q W_{ij} O_j(w) + W_{i0} \right) = F_i \left(\sum_{j=1}^q W_{ij} f_j \left(\sum_{l=1}^n w_{jl} z_l + w_{j0} \right) + W_{i0} \right) \quad (4)$$

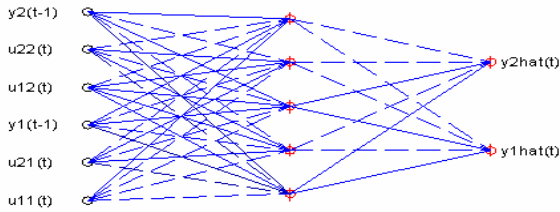


Fig. 1 Structure of MIMO Neural NARX11 model

The weights (specified by the matrices w and W) are the adjustable parameters of the network, and they are determined from a set of *examples* through the process called *training*. The examples, or the training data as they are usually called, are a set of inputs, $u(t)$, and corresponding desired outputs, $y(t)$.

The prediction error approach, which is the strategy applied here, is based on the introduction of a measure of closeness in terms of a mean sum of square error (MSSE) criterion:

$$E_N(\theta, Z^N) = \frac{1}{2N} \sum_{t=1}^N [y(t) - \hat{y}(t|\theta)]^T [y(t) - \hat{y}(t|\theta)] \quad (5)$$

Based on the conventional error Back-Propagation (BP) training algorithms, the weighting value is calculated as follows:

$$W(k+1) = W(k) - \lambda \frac{\partial E(W(k))}{\partial W(k)} \quad (6)$$

with k is k^{th} iterative step of calculation and λ is the learning rate which is often chosen as a small constant value.

Concretely, the weights W_{ij} and w_{jl} of neural NARX model are then updated as:

$$\begin{aligned} W_{ij}(k+1) &= W_{ij}(k) + \Delta W_{ij}(k+1) \\ \Delta W_{ij}(k+1) &= \lambda \delta_i O_j \\ \delta_i &= \hat{y}_i (1 - \hat{y}_i) (y_i - \hat{y}_i) \end{aligned} \quad (7)$$

with δ_i is search direction value of i^{th} neuron of output layer ($i=[1 \rightarrow m]$); O_j is the output value of j^{th} neuron of hidden layer ($j=[1 \rightarrow q]$); y_i and \hat{y}_i are truly real output and predicted output of i^{th} neuron of output layer ($i=[1 \rightarrow m]$), and

$$\begin{aligned} w_{jl}(k+1) &= w_{jl}(k) + \Delta w_{jl}(k+1) \\ \Delta w_{jl}(k+1) &= \lambda \delta_j u_l \\ \delta_j &= O_j (1 - O_j) \sum_{i=1}^m \delta_i W_{ij} \end{aligned} \quad (8)$$

in which δ_j is search direction value of j^{th} neuron of hidden layer ($j=[1 \rightarrow q]$); O_j is the output value of j^{th} neuron of hidden layer ($j=[1 \rightarrow q]$); u_l is input of l^{th} neuron of input layer ($l=[1 \rightarrow n]$).

III. EXPERIMENT CONFIGURATION OF THE 2-AXES PAM REHABILITATION ROBOT

A general configuration and the schematic diagram of the 2-axes PAM rehabilitation robot and the photograph of the experimental apparatus are shown in Fig.2 and Fig.3, respectively.

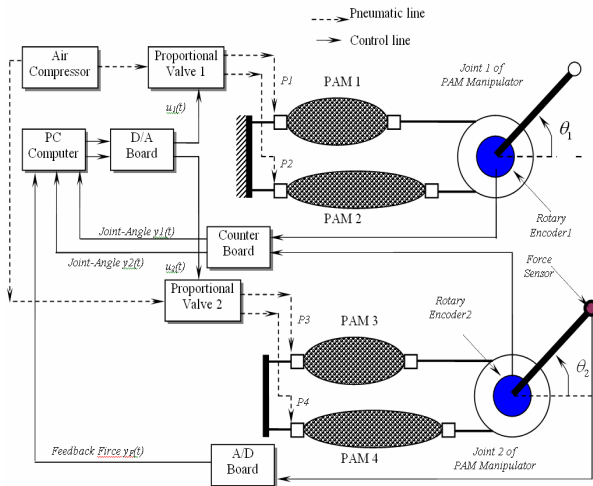


Fig. 2 Block diagram for working principle of 2-axes PAM rehabilitation robot

The hardware includes an IBM compatible PC (Pentium 1.7 GHz) which sends the voltage signals $u_1(t)$ and $u_2(t)$ to control the two proportional valves (FESTO, MPYE-5-1/8HF-710B), through a D/A board (ADVANTECH, PCI 1720 card) which changes digital signals from PC to analog voltage $u_1(t)$ and $u_2(t)$ respectively. The rotating torque is generated by the pneumatic pressure difference supplied from air-compressor between the antagonistic artificial muscles. Consequently, the both of joints of the 2-axes PAM robot arm will be rotated to follow the desired joint angle references ($Y_{REF1}(k)$ and $Y_{REF2}(k)$) respectively.

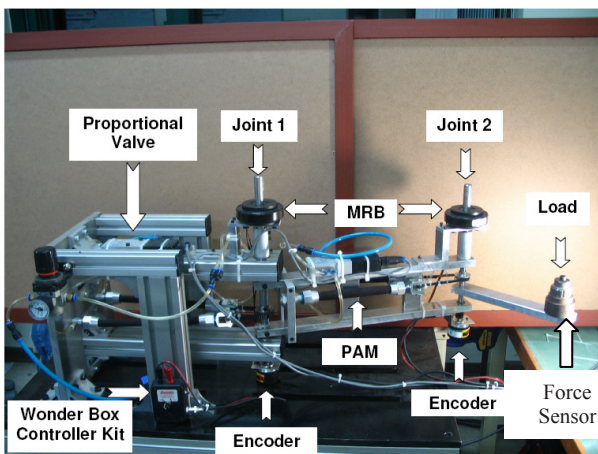


Fig. 3 Photograph of the experimental 2-axes PAM rehabilitation robot

IV. RESULTS OF FORWARD NEURAL MIMO NARX MODEL IDENTIFICATION

In general, the procedure which must be executed when attempting to identify a dynamical system consists of four basic steps.

- STEP 1 (Getting Training Data)
- STEP 2 (Select Model Structure)
- STEP 3 (Estimate Model)
- STEP 4 (Validate Model)

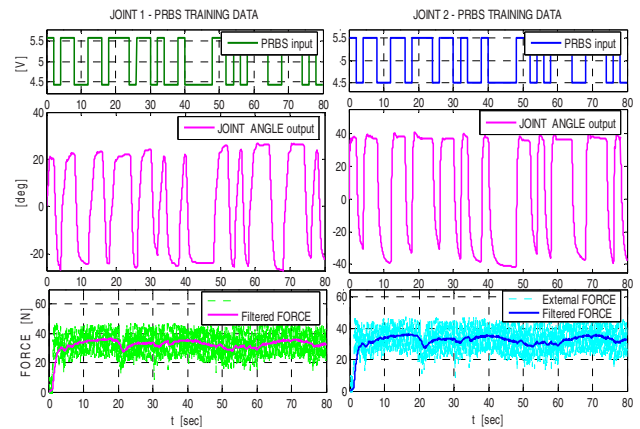


Fig. 4 Forward Neural MIMO NARX Model Training data

To realize Step 1, Fig.4 presents the PRBS input applied simultaneously to the 2 joints of the tested 2-axes PAM robot arm and the responding joint angle and feedback force outputs. This experimental PRBS input-output data is used for training and validating the Forward neural MIMO NARX model.

The 2nd step relates to select model structure. A nonlinear neural NARX model structure is attempted. The full connected Multi-Layer Perceptron (MLPNN) network architecture composes 3 layers with 5 neurons in hidden layer is selected (results derived from Ahn *et al.*, 2007 [15]). The final structure of proposed Forward neural MIMO NARX11 used in proposed neural MIMO NARX FNN-PID hybrid force/position control scheme is shown in Fig.5.

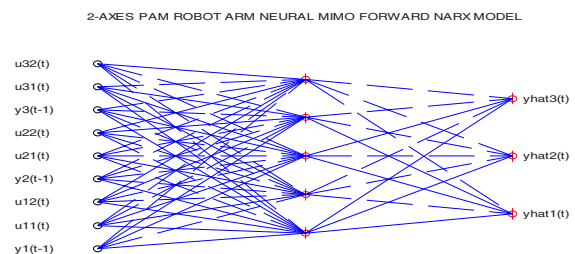


Fig. 5 Structure of proposed Forward neural MIMO NARX11 models of 2-axes PAM rehabilitation robot

The proposed neural MIMO NARX11 model structure is defined as a nonlinear neural MLPNN integrated a 1st order ARX model (with $n_A=1$; $n_B=1$ and $n_K=1$) possessed 5 neurons in hidden layer. The activating function applied in

neurons of hidden Layer and of output layer is hyperbolic tangent function and linear function respectively.

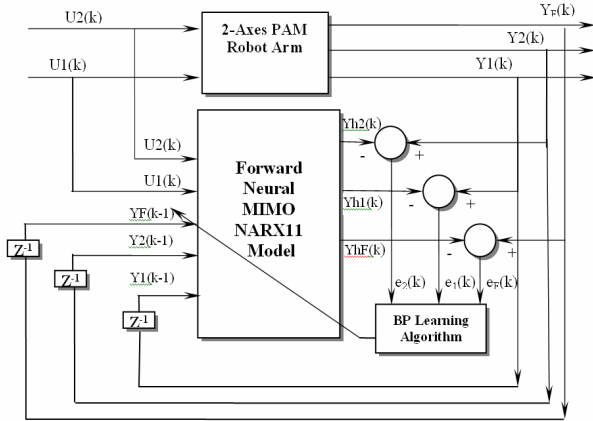


Fig. 6 Block diagram of Forward Neural MIMO NARX model identification

Fig.6 represents the block diagram for identifying Forward neural MIMO NARX11 model of the 2-axes PAM rehabilitation robot.

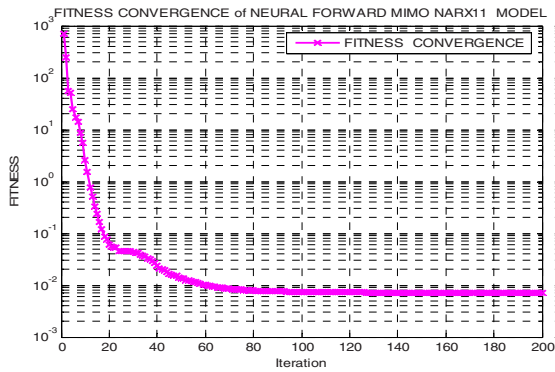


Fig. 7 Fitness convergence of Forward neural MIMO NARX Model

The 3rd step estimates trained Forward neural MIMO NARX11 model. A good minimized convergence is shown in Fig.7 with the minimized Mean Sum of Scaled Error (MSSE) value is equal to 0.003659 after number of training 200 iterations with the proposed forward neural MIMO NARX model. An excellent estimating result, which proves the perfect performance of resulted Forward Neural MIMO NARX model, is shown in Fig.8.

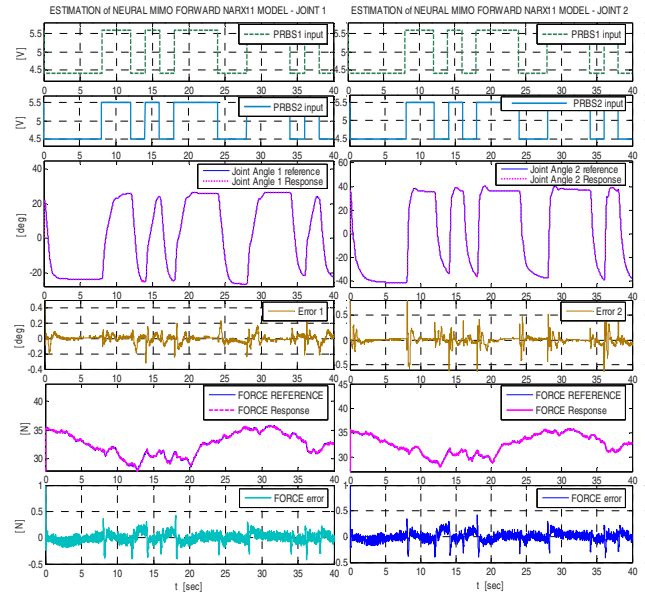


Fig. 8 Estimation of proposed Forward neural MIMO NARX Model

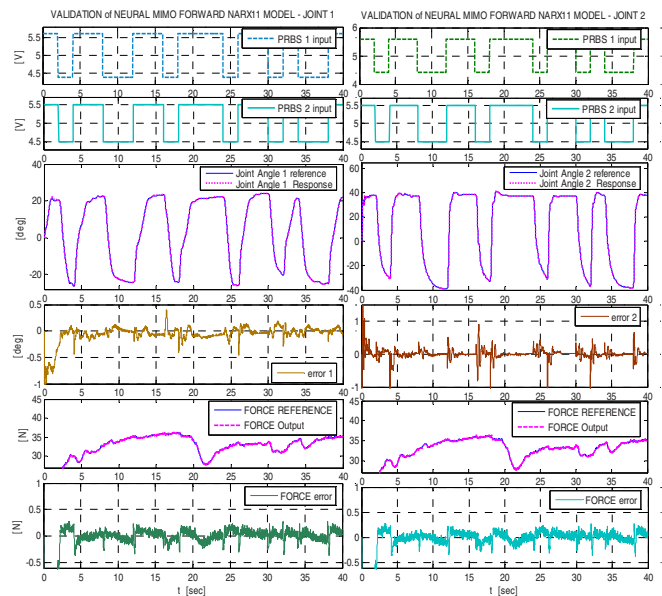


Fig. 9 Validation of proposed Forward neural MIMO NARX Model

The last step relates to validate resulting nonlinear neural Forward MIMO NARX models. Applying the same experimental diagram in Fig.6, an excellent validating result, which proves the performance of resulted Forward Neural MIMO NARX model, is shown in Fig.9. A good minimized convergence is shown in Fig.9 with the

minimized Mean Sum of Scaled Error (MSSE) value is equal to 0.005577 after a number of training equal 200 iterations.

V. CONCLUSIONS

In this paper, a new approach of Forward Dynamic Neural MIMO NARX model firstly utilized in modeling and identification of the 2-axes PAM-based rehabilitation robot. Training and testing results show that the newly proposed Forward Dynamic MIMO NARX model presented in this study can be used in online control with better dynamic property and strong robustness. This resulting proposed intelligent model is quite suitable to be applied for the modeling, identification and control of various MIMO plants, including linear and nonlinear MIMO process without regard greatly change of external environments.

REFERENCES

1. F. Jatta, G. Legnani and A. Visioli, Friction compensation in hybrid force/velocity control of industrial manipulators, *IEEE Trans. on Industrial Electronics*, Vol. 53, No.2, (2006), pp.604 – 613.
2. K. Khayati, P. Bigras and L.A. Dessaint, A Multistage Position/Force Control for Constrained Robotic Systems With Friction: Joint-Space Decomposition, Linearization, and Multiobjective Observer/Controller Synthesis Using LMI Formalism, *IEEE Trans. on Industrial Electronics*, Vol. 53, No.5, (2006), pp.1698 – 1712.
3. S. Katsura, Y. Matsumoto, K. Ohnishi, Modeling of Force Sensing and Validation of Disturbance Observer for Force Control, *IEEE Trans. on Industrial Electronics*, Vol. 54, No.1, (2007), pp.530 – 538.
4. W. Gueaieb, F. Karray and S. Al-Sharhan, A Robust Hybrid Intelligent Position/Force Control Scheme for Cooperative Manipulators, *IEEE/ASME Trans. Mechatronics*, vol. 12, no. 2, pp. 109–125, (2007).
5. J.Y. Sung, B. P. Jin and H.C. Yoon, Adaptive Dynamic Surface Control of Flexible-Joint Robots Using Self-Recurrent Wavelet Neural Networks, *IEEE Trans. on syst. man and cybern.*, vol. 36, no. 6, pp. 1342–1355, Dec. 2006.
6. A. Karakasoglu, and M.K. Sundareshan, Identification and decentralized adaptive control using dynamical neural networks with application to robotic manipulators, *IEEE Trans. on neural networks*, Vol. 4, No. 6, (1993), pp. 919-930.
7. D.M. Katic, and M.K. Vukobratovic, Highly efficient robot dynamics learning by decomposed connectionist feed-forward control, *IEEE Trans. on syst. man and cybern.*, Vol. 25, No. 1, (1995), pp. 145-158.
8. F.L. Lewis and A. Yesildirek, Neural network control of robot manipulators and nonlinear systems, Taylor & Francis, (1999).
9. K.K. Ahn, and H.P.H. Anh, System modeling and identification of the two-link pneumatic artificial muscle (PAM) manipulator optimized with genetic algorithm, *Proceedings 2006 IEEE-ICASE Int. Conf.*, Busan, Korea, (2006), pp. 4744-4749.
10. H.P.H. Anh and K.K. Ahn, Identification of the pneumatic artificial muscle manipulators by MGA-based nonlinear NARX fuzzy model, *IFAC Journal of MECHATRONICS*, Vol. 19, Issue 1, (Feb. 2009), pp. 106-133.
11. K.K. Ahn, and H.P.H. Anh, A new approach of modeling and identification of the pneumatic artificial muscle (PAM) manipulator based on neural networks, *IMechE, Part I: Journal of Systems and Control Engineering*, (2007), 221(18), 1101-1122.

Simulation of the Gait of a Patient Specific Model of Post Polio Residual Paralysis (PPRP): Effect of the Orthosis

T.T. Dao¹, P. Pouletaut¹, F. Marin¹, P. Aufaure², F. Charleux², and M.C. Ho Ba Tho¹

¹ UTC – CNRS UMR 6600, Biomécanique et Bioingénierie, Compiègne, France

² Polyclinique St Côme, Compiègne, France

Abstract— The aim of this present study was to develop a patient specific 3D musculoskeletal model to post polio residual paralysis (PPRP) subject. This model allows the effects of the lower limbs orthosis on the gait kinematics and kinetics to be quantified objectively. CT scan data were used to personalize the geometrical model and its inertial properties. Gait-based experimental protocol based on David's protocol was performed. Kinematics data were measured using VICON motion system with six infrared cameras. Ground reaction force and moments were acquired simultaneously using two AMTI forces platforms. A direct/inverse algorithm of BRB.LifeMod software was used to simulate healthy (standard model provided by LifeMod) and pathological gaits (PPRP). The comparison of healthy and PPRP subjects was carried out. The biomechanics effects of the orthosis device were studied on simulated joint angles and torques, muscle force, and experimental ground reaction forces. The results showed that the orthosis device reduces the amplitude of movement of PPRP subject. It increases the ground contact time of the PPRP subject. However, a strategy of compensation exhibits a greater joint angle of the PPRP subject. Moreover, PPRP subject supports greater joint torques and lower muscle force due to the blocked knee joint device. The biomechanic effects of the lower limb orthosis helps to prevent long-term the injuries and damages of the biological structures involved of the PPRP paralysis. Furthermore, the personalization of the inertial properties of segmental bodies was taken in account to improve the accuracy of the patient specific biomechanics modelling.

Keywords— Patient Specific Model, Poliomyelitis, Orthosis, Orthopaedics, Gait Kinematics and Kinetics, Lower Limbs.

I. INTRODUCTION

Poliomyelitis is an infectious disease caused by poliovirus. This pathology has been appeared nearly 6000 years ago [1]. The morbidity was concentrated in third world countries such as India, Vietnam, Pakistan, Afghanistan, Nigeria, Egypt, etc. But developing countries such as the United States, France, Canada, etc. were also indispensable targets of this pathology [2]. At the moment, global polio eradication is almost achieved [3]. However, PPRP syndrome of hard and soft tissue deformities reminded one of the most occupations for the health care

system of each country involved and especially for the quality of life of the Polio individual and his family [4], [5].

Gait analysis aims to gather quantitative information about the interactive mechanism of musculoskeletal system during its movement [6], [7], [8]. Kinematics and kinetics parameters were used recently to determinate the pathological gait pattern [9], [10]. The results reported from gait analysis become commonly objective data during clinical diagnosis and treatment. Furthermore, the combination between biomechanics modeling and gait analysis allow to develop patient specific 3D musculoskeletal model and to quantify its kinematics and kinetics during gait simulation.

In fact, computer-aided biomechanics modeling aims to understand and simulate the human body during its movement. Musculoskeletal 3D models have been developed recently to healthy subject [11] and to clinical applications such as crouch gait [12], stiff knee gait [13]. However, the modeling parameters such as anthropometrical and geometrical of the bones and muscles were extracted and used usually from literature data. In our previous study [14], we showed that these parameters influenced strongly on the kinematics and kinetics simulation results. Subsequently, the personalization of these parameters, especially inertial properties of segmental bodies, should be considered and determined experimentally for patient specific model.

The aim of this present study was to develop a patient specific 3D musculoskeletal model of the Post Polio Residual Paralysis (PPRP) subject. This model will allow the effects of the lower limb orthosis on the gait kinematics and kinetics of the patient with PPRP syndrome to be quantified objectively. A healthy 3D musculoskeletal model was also developed as a reference model to pick out pathological disorders of post-polio subject.

II. MATERIALS AND METHODS

A. Subjects

Two subjects were proposed for the present study. The first subject is a healthy subject (man, 29 years old, 1m68

height, and 65kg weight). Another is a patient with PPRP syndrome (man, 26 years old, 1m70 height, and 66kg weight). Both of the subjects signed the agreement for human experimentation ethics.

The healthy subject had no historical injuries and damages on the lower limbs whereas the PPRP subject had a muscular tendon surgery in order to align the vatus lateralis muscle and tendon of the left lower limb. The PPRP subject performed rehabilitation procedure daily during 2 years to reinforce the muscle activation and joint flexibility. An orthosis device has been attached on the left lower limb with blocked knee joint to support and compensate the body of PPRP subject during its movement.

B. CT Scan-Based Experimental Protocol

Computed tomography (CT) was performed using a spiral-imaging scanner (GE Light Speed VCT 64, Polyclinique St Côme, Compiègne, France). Imaging medical protocol was set up by the radiologist to ensure lower effective radiation dose (less than 2 mSv) in order to protect the PPRP subject during experimental acquisition. The slice interval was set to 1.25 mm. The image matrix was 512×512, and the number of slices was 384. The duration time of the full images acquisition was about 30 seconds. The collected images were stored in DICOM format to further segmentation and reconstruction processing

C. Personalization of Inertial Properties of Segmental Bodies

The 3D Slicer software (Surgical Planning Laboratory, MIT, 1998) was used to perform 3D segmentation and reconstruction of segmental bodies such as pelvis, thigh, leg, and foot. To determinate the mass, the positions of center of mass, and moments of inertia of each segment, anatomical axes using the parallel axis theorem were used [15]. VTK/ITK programming library [16] was used to develop the related algorithm.

D. Gait-Based Experimental Protocol

First of all, the Helen Hayes protocol based on Davis biomechanical model [17] was used to define marker's positions on the lower limb of PPRP subjects (Figure 1). This protocol has become a standard clinical protocol used to set and track the 3D motion of markers on the lower limbs.

Then, experimental 3D marker's trajectories were measured using a VICON Motion Capture system with six

infrared cameras. The ground reaction forces and moments were measured simultaneously using two AMTI forces platforms at 100 Hz (Watertown, USA).

Finally, the 3D trajectories of the cutaneous markers were corrected by a low-pass filter (Butterworth, fourth-order, cut-off frequency of 5 Hz). A trajectory superposition procedure was performed to fill in the missing positions during experimental acquisition.

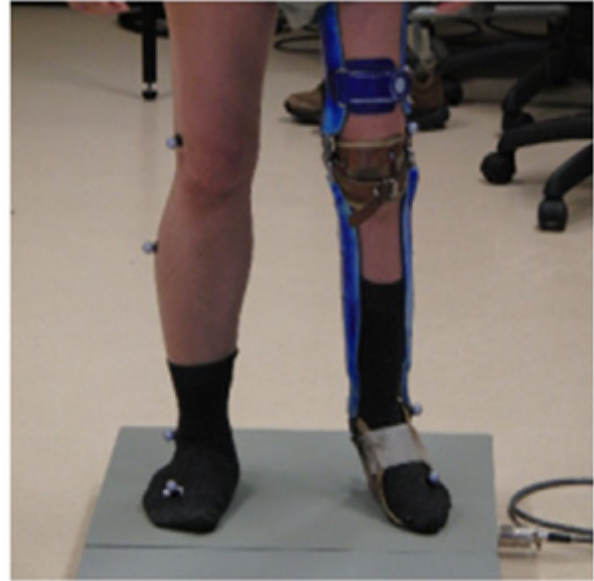


Fig. 1 Marker's positions based on Davis's protocol on the PPRP subject with lower limb orthosis

E. Musculoskeletal Models and Inverse/Forward Dynamics Analysis

Musculoskeletal models of the lower limb were developed using BGR.LifeMod software. Each model consisted of 7 segments (pelvis, left and right thigh, left and right leg, and left and right foot), 3 joints (hip, knee, and ankle), and 10 significant muscles for movement analysis of the lower limbs such as biceps femoris, semitendinosus, soleus, gastronemius, anterior tibialis, rectus femoris, vastus lateralis, vastus medialis, anterior gluteus medius, posterior gluteus medius.

The gait was simulated using direct/inverse dynamics algorithms of the BGR.LifeMod software. The comparison of healthy and PPRP subjects was carried out to study physiological disorders of PPRP subject. The biomechanics effects of the orthosis were studied on the simulated joint angles and torques, muscle forces and experimental ground reaction forces.

III. RESULTS

The patient-specific musculoskeletal model of the lower limb of PPRP subject is illustrated in Fig. 2.

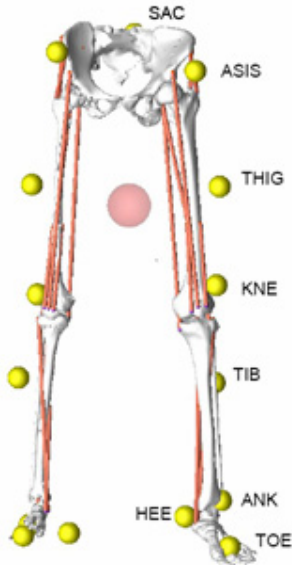


Fig. 2 Patient-specific musculoskeletal model of the lower limb of PPRP subject

The personalized inertial properties of all segments of PPRP subject were reported in Table 1. The segment mass and moments of inertia were standardized by body weight of the PPRP subject.

Table 1 Inertial properties of the PPRP subject

Segments	Segment Mass (% BW)	Ixx (kg m ²)	Iyy (kg m ²)	Izz (kg m ²)
Pelvis	16.17	0.059	0.086	0.089
Right thigh	7.65	0.033	3.242	1.337
Left thigh	3.58	0.016	1.544	0.428
Right leg	4.12	1.307	1.33	0.4
Left leg	1.44	0.005	0.488	0.072
Right foot	1.41	0.002	0.001	0.002
Left foot	0.77	0.001	0	0.001

Gait kinematics and kinetics such as simulated joint angles and torques, muscle force, and experimental ground reaction forces are presented as below.

At the right hip angle, the PPRP subject showed greater amplitude of movement and slower movement time than the healthy subject (Fig. 3). The right hip torque generated from the direct analysis demonstrated a significant difference during the stance phase between healthy and PPRP subjects. Furthermore, the maximum peak torque occurred at the end of the stance phase (Fig. 4).

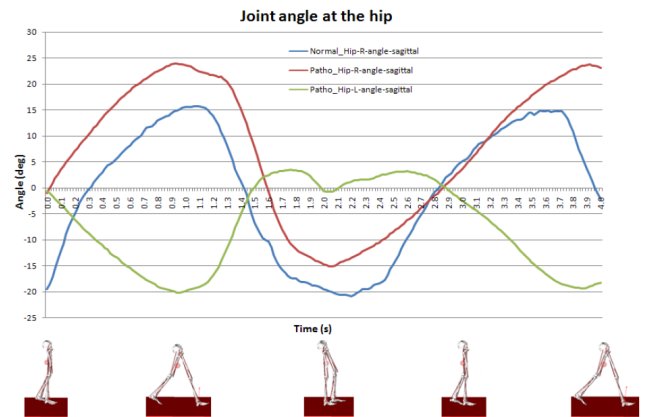


Fig. 3 Comparison of right hip angle between healthy and PPRP subjects

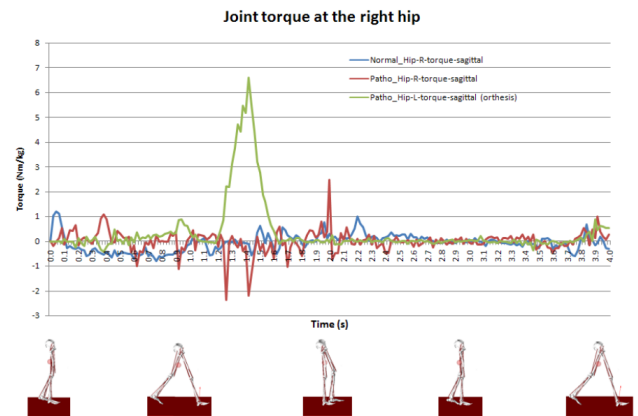


Fig. 4 Right hip torques: healthy vs. PPRP subjects

Concerning the muscle forces, the healthy subject showed greater force than the PPRP subject (e.g. about twice higher for the semitendinosus muscle).

The experimental ground reaction forces of PPRP subject are greater than the ground reaction forces of healthy subject. The qualitative comparison showed a longer contact time for PPRP subject. The maximal peak force happened at the heel strike phase during the contact between the foot and the ground. Furthermore, the heel off and toe off phases are not occurred for PPRP subject (Fig. 5).

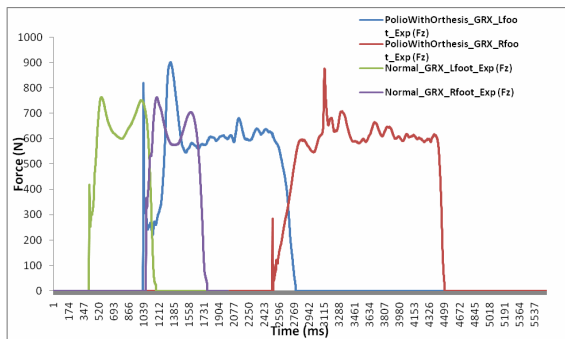


Fig. 5 Experimental ground reaction forces: healthy vs. PPRP subjects

IV. DISCUSSION

The comparison of healthy subject and PPRP subject showed substantial disorders of gait kinematics and kinetics of the PPRP subject. Due to the rigidity of the left lower limb with orthosis, the PPRP subject supports larger amplitude of rotation in the sagittal plane and greater joint torques at the hip and knee joints. Moreover, the orthosis device reduces the acceleration of movement and it increases the ground contact time.

When observing the PPRP subject separately, the orthosis device reduces substantially the amplitude of movement of the left lower limb with orthosis, thus it is necessary that the contralateral limb compensates this reduction by increasing its amplitude of rotation during its movement.

One of the limitations of the present study involves the contact model between the foot and the ground of the PPRP subject. The morphological deformities of the foot cannot be modeled physiologically due to limitations of software development technologies. Furthermore, the missing orthosis modelling influences the reality of developed model.

V. CONCLUSION

A patient specific 3D musculoskeletal model was developed to study the effects of the lower limb orthosis on the gait kinematics and kinetics. The comparison of PPRP and healthy subjects was presented and discussed. Clinical findings of the orthosis effects during gait analysis were reported. The development of such models would be of help to prevent the injuries and damages of the biological structures of the PPRP subject or other lower limbs pathologies. Such models would also be of help for orthosis designer to improve, predict the mechanical behaviour of the personalized orthosis on the subject.

REFERENCES

- Adnan AF (2006) Poliomyelitis: Orthopaedic management, *Current Orthopaedics*, 20, pp. 41–46.
- Bunimovich-Mendrazitsky S, Stone L (2005) Modeling polio as a disease of development, *Journal of Theoretical Biology*, 237, pp. 302–315.
- Hull HF, Aylward RB, (2001) Progress towards global polio eradication, *Vaccine*, 19, pp. 4378–4384.
- Stuifbergen AK, Seraphineb A (2005) Tracie Harrisona, Eishi Adachi, An explanatory model of health promotion and quality of life for persons with post-polio syndrome, *Social Science & Medicine*, 60, pp. 383–393.
- Katz SL (2006) Polio—New challenges in 2006, *Journal of Clinical Virology*, 36, pp. 163–165.
- Wilson DR, O'Connor JJ (1997) A three-dimensional geometric model of the knee for the study of joint forces in gait, *Gait & Posture*, 5, pp. 108–115.
- Cheze L (2000) Comparison of different calculations of three-dimensional joint kinematics from video-based system data. *J Biomech*, 33, pp. 1695–9.
- Cappozzo A, Croce UD, Leardini A, Chiari L (2005) Human movement analysis using stereophotogrammetry: Part 1: theoretical background, *Gait and Posture*, 21, pp. 186–196.
- Chau T (2001a) A review of analytical techniques for gait data. Part 1: Fuzzy, statistical and fractal methods. *Gait & Posture*, 13, pp. 49–66
- Chau T (2001b) A review of analytical techniques for gait data. Part 2: neural network and wavelet methods. *Gait & Posture*, 13, pp. 102–120
- Arnold AS, Thelen DG, Schwartzd MH, Andersona FC, Delp SL (2007) Muscular coordination of knee motion during the terminal-swing phase of normal gait, *Journal of Biomechanics*, 40, pp. 3314–3324.
- Hicks JL, Schwartz MH, Arnold AS, Delp SL (2008) Crouched postures reduce the capacity of muscles to extend the hip and knee during the single-limb stance phase of gait, *Journal of Biomechanics*, 41, pp. 960–967
- Jonkers I, Stewart C, Desloovere K, Molenaers G, Spaepen A (2006) Musculo-tendon length and lengthening velocity of rectus femoris in stiff knee gait, *Gait & Posture*, 23, pp. 222–229.
- Dao TT, Marin F, Ho Ba Tho MC. 2009. Influence of anthropometrical and geometrical parameters of the bones and muscles on musculoskeletal model of the lower limbs, *Computer Methods in Biomechanics and Biomedical Engineering* 12, Supplement 1, 2009, pp.91-92.
- Cheng CK, Chen HH, Chen CS, Lee CL, Chen CY (2000) Segment inertial properties of Chinese adults determined from magnetic resonance imaging, *Clinical Biomechanics*, 15, pp. 559–566.
- Schroeder W, Martin K, Lorensen B (1993) The Visualization Toolkit An Object-Oriented Approach to 3D Graphics. Available from: <http://www.itk.org> (accessed 01 May 2009)
- Davis RB, Ounpuu S, Tyburski D, Gage JR (1991) A gait analysis data collection and reduction technique. *Hum Movement Sci*, 10, pp. 575–87.

Corresponding author:

Author: Tien Tuan DAO
 Institute: Université de Technologie de Compiègne
 Street: Centre de Recherches de Royallieu
 City: Compiègne
 Country: France
 Email: tien-tuan.dao@utc.fr

Mechanical Behavior of Muscles during Flexion and Extension of Lower Limb on Variable Age Group by Using BRG.LifeMod

Nitin Sahai, Ravi P.Tewari, and Lokesh Singh

Applied Mechanics Department, Motilal Nehru National Institute of Technology, Deemed University, Allahabad, India

Abstract— The main objective of this paper is to find out the muscle which plays a major role during flexion and extension on models of different age groups and the extent of mechanical deformation which takes place in the muscles of lower limb with the help of BRG.Life Mod software which works in ADAM's environment. The muscles moment is obtained with the help of inverse and forward dynamics simulation of human model that shows us which muscle is active during flexion and extension and how much moment (torque) that muscle is exerting, which causes muscle deformation. According to Hill's mechanical model of muscle, it consists of three elements: one contractile element attached in series with an elastic element and both of these attached in parallel to an elastic element. During muscles contraction and expansion the deformation of muscles takes place and during one complete gait cycle it regains its original shape and size due to its viscoelastic nature. The deformation in the muscles is obtained by finding the change in the length of muscles during extended flexion and extension in complete gait cycle on different age group models. After conducting the simulation on models of different age group, it is observed that deformation in the muscles of lower limb is maximum obtained in Rectus femoris which is one of the four quadriceps muscles of the human body, the others being Vastus medialis, Vastus intermedius, and Vastus lateralis. On the basis of our experiment the conclusion is made that Rectus femoris plays a major role in regulating knee flexion and extension.

Keywords— Flexion & Extension, Hill Muscle Model, Gait cycle.

I. INTRODUCTION

Muscles provide two kinds of forces, active and passive, which compose a muscles total force. Though actin and myosin "ratching" mechanism muscles will provide the active force while with the help of non contractile element the muscle will provide passive forces, muscles are called as parallel elastic element that contributes to its passive forces. In 1922 A.V. Hill(Hill 1970) first noted that activated muscles produce more force when held isometrically (at a length fixed) then when they shorten.

Muscles co-ordinate muscle joints motion by generating forces that causes reaction forces throughout the body [1].

The motion of walking in human being is divided in to two phases swing phase and support phase. The swing phase is the behavior that the foot leaves the ground surface and the leg swing forward. The support phase is the behavior that the foot stays in the contact with the ground surface and the body is supported by leg [2] as shown in Fig. 2,3,4,5. In this paper the activity of the muscle rectus femoris of lower limb is observed during walking motion of human body of different age in inverse dynamics [3]. The change in the length of rectus femoris is find out during the normal Gait cycle of human being and compared with other muscle activity which helps in finding the strain in particular muscle. The amount of rectus femoris activity is related to walking speed [4] as it plays a crucial role in knee flexion and extension during the Gait cycle of human being [5,6,7,8]. For rectus femoris, the relative work contribution done in knee extension was 21% in jumping and 31% in sprinting[9].The paper's main focus is given to plot the length v/s time graph of muscle during the gait cycle.

II. MECHANICAL MUSCLE MODELHILL'S MODE

The Hill model is composed of three elements: two of which are arranged in series which, in turn, are in parallel with the third element. The contractile element is freely extendable when at rest, but capable of shortening when activated by an electrical stimuli. The contractile element is connected to an elastic serial element.

The serial element accounts for the muscle elasticity during isometric (constant muscle length) force conditions. The muscle elasticity during isometric contraction is due in a large part to the elasticity of the cross-bridges in the muscle [Fung 93]. These two elements are then joined in parallel with another elastic element used to account for the elasticity of the muscle at rest. The parallel element accounts for the inter-muscular connective tissues surrounding the muscle fibers [5]. Force-Length Properties

The properties of the three elements in the Hill model which are responsible for force generation are defined in terms of force-length properties and force-velocity properties. The force-length property is based on isometric muscle contraction, that is, the force generated within the muscle as the length of the muscle remains constant. During an isometric contraction, the series element lengthens while the contractile element shortens [10]. The lengthening of the serial element must be equal to the shortening of the contractile element for the overall length of the muscle to remain unchanged. As the serial element lengthens, the parallel element no longer remains slack and develops tension in a non-linear manner. The total force developed within the muscle is then the sum of the forces in both the active and passive muscle tissue. An example of the force-length curve common to skeletal muscles is shown in Fig.1.

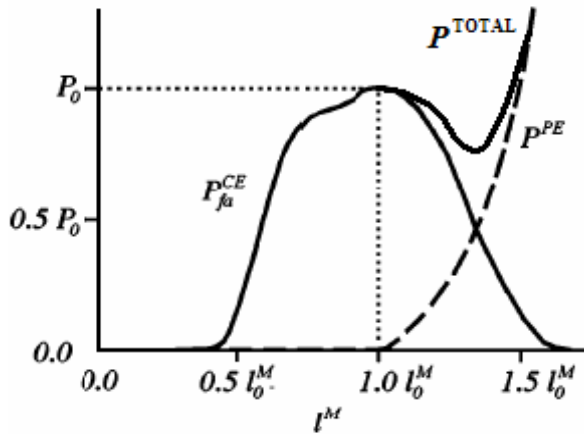


Fig. 1 Force-length property of muscle a) fully activated force length properties

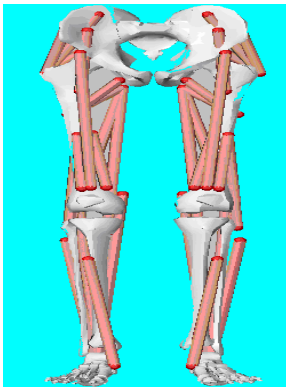


Fig. 2 Lower body model with muscle

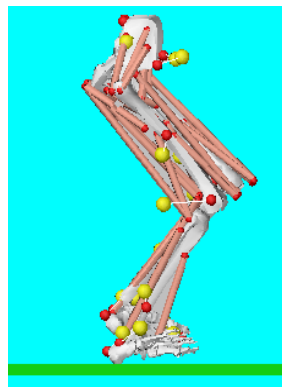


Fig. 3 Initial Swing Phase

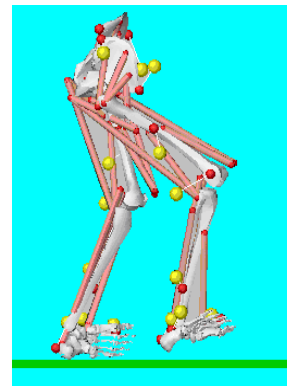


Fig. 4 Mid stance Phase

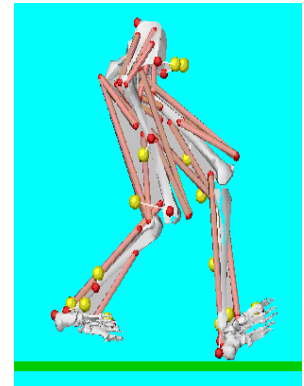


Fig. 5 Terminal Swing Phase

III. METHOD

Model is generated in BRG LifeMod of lower limb, It will generate the groups of main muscle which are responsible for the control of large motions of body segment in humans, in case flexion, extension LifeMOD assigns muscle tissue properties, which include the maximum allowable stress in each muscle and the physiological cross-sectional area (pCSA), from its database which is obtained from various in vivo experiment on various subjects. Each muscle contains a contractile element in series with a spring-damper element, storing the input motion and effectively ‘training’ the muscles to reproduce the necessary force to recreate the desired motion.[12]. Age,

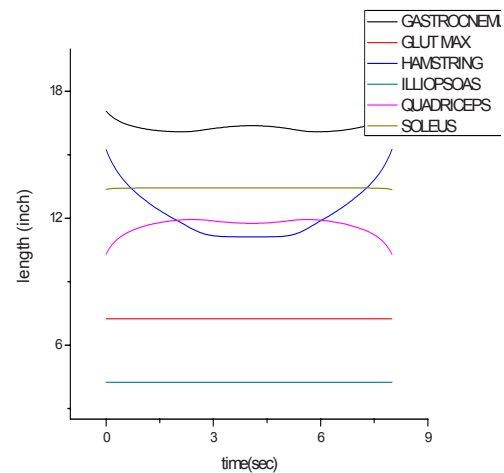


Fig. 6 Mechanical behavior of muscles during Flexion & Extension

height and region of the model is assign in the LifeMOD then according it will generate the model of lower limb then the formation of joint will takes place which is followed with the attachment of muscles. In the end the simulation is run for 9 sec and then the change in the length of the muscles during flexion and extension is obtained which is represented in Fig. 6. The EMG were taken of rectus femoris were taken of a subject during gait cycle[12] as shown in Fig. 7 which reflects activity of rectus femoris during flexion & extension.

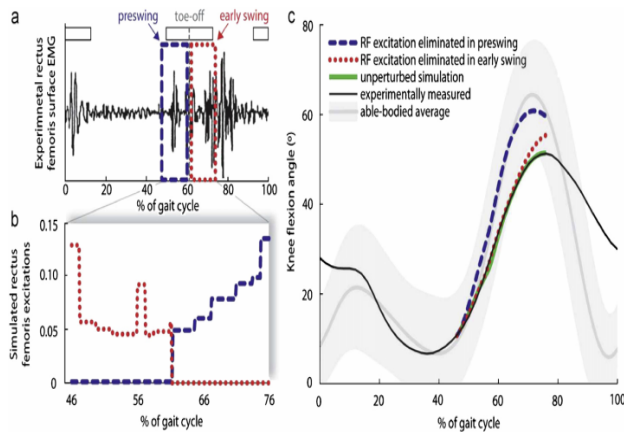


Fig. 7 [11] Example of methods used to determine increase in peak knee flexion when rectus femoris activity was eliminated during preswing and separately during early swing. (a) Rectus femoris surface EMG of a subject with stiff-knee gait was recorded over an entire gait cycle. Normal rectus femoris EMG timing is indicated by horizontal white bars (Bleck, 1987). Toe-off is indicated by a vertical dashed line at 61% of the gait cycle. Two time periods were selected for analysis: early swing (i.e., period from toe-off to peak knee flexion) and preswing (i.e., period before toe-off equal in duration to early swing). (b) Two simulation experiments were conducted by eliminating rectus femoris activity during preswing (dashed line) and separately during early swing (dotted line) to determine the muscle's effect on peak knee flexion. (c) Simulated changes in knee flexion angles were different when rectus femoris activity was eliminated during preswing (dashed line) or early swing (dotted line). The unperturbed simulation (thick solid line) and experimentally measured (thin solid line) knee angles are shown for comparison. Normal knee flexion (shaded line) and two standard deviations of the normal curve (shaded region) are shown as well.

IV. RESULTS

From the graphs as shown in Figure 6 & 7 we can obtain the activity of different muscles during flexion and extension of different muscles during the Gait cycle. As we can observe that Hamstring muscle shows more deviation during flexion & extension (Fig. 6). In figure 7 the enhance activity of the rectus femoris is shown during flexion and extension through EMG.

V. CONCLUSION

From the above it is conclude that during the flexion and extension of lower limb the deformation of muscles will occur and as the gait cycle proceeds and the activity of the Hamstring and the rectus femoris is enhanced. The models of different age group with abnormalities in their gait should be simulated in LifeMod and then the results will be compared with the in vivo experimental data.

REFERENCES

1. Flix E., Zajac, *et al.*(2002) ,"Understanding muscle coordination of human leg with dynamical simulation, journal of biomechanics", Vol. 35, pp 1011-1018.
2. Hui He, Kazuo Kiguchi, Etsuo Horikawa (2007), "A Study on Lower-Limb Muscle Activities during Daily Lower-Limb Motions", Vol. 9 No. 2.
3. Winter DA *et al*(1991), "The biomechanics and motor control of human gait normal, elderly and pathological", university of waterloo press, Ontario
4. Anand nene, R.Mayagortia *et al*(1999)., "Assessment of Rectus Femoris function during initial swing phase", Gait & Posture, Vol 9, pp 1-9.
5. A. Nene *et al.*(2004)., "Is Rectus Femois really a part of quadriceps: Assessment of rectus femoris function during Gait in able bodied adults", Gait & Posture, Vol. 20, issue , pp 1-13.
6. Jeffrey A. Rembolt *et al.* (2008), "Importance of pre-swing rectus femoris activity in stiff- Knee gait, Journal of Biomechanics", Vol 41, Issue 11, pp. 2362-2369.
7. Antonio Hernandez *et al.*(2002), "In vivo measurement of dynamic rectus femoris function at postures representative of early swing phase", Journal of Biomechanics Vol. 35, pp. 1029-1037
8. T.M. Annaswamy *et al.*, (1999), "Rectus femoris: Its role in normal gait, archives of physical medicine and rehabilitation", Vol. 80, issue 8, pp. 930-934.
9. Ron Jacobs, Maarten F. Bobbert and Gerrit Jan van Ingen Schena (1996), J. Biomeckpnics, Vol. 29, No. 4, pp. 513-523,
10. Michael S. Orendurff, Michael D. Aiona and Robin D. Dorociak,(2005) "Triceps Surae Force, Length and Velocity during Walking", Journal of Gait & Posture , Vol. 21, pp. 157-163
11. Jeffrey A. Reinbolt, Melanie D. Fox, Allison S. Arnold, Sylvia O unpuu, Scott L. Delp, (2008),"Importance of preswing rectus femoris activity in stiff-knee gait", Journal of Biomechanics Vol. 41, pp. 2362-2369
12. C.U.deJongh, A.H.Basson, C.Scheffer (2008),"Predictive modelling of cervical disc implant wear", Journal of Biomechanics Vol. 41 pp. 3177-3183.

Author : Nitin Sahai
 Institute : Motilal Nehru National Institute of Technology,
 Deemed University, Allahabad
 Street : 1
 City : Allahabad
 Country : India
 Email : nitinbiomedical@gmail.com

Biomechanics of Index Finger during Mouse Click

P. Chivapornthip¹, E.L.J. Bohez¹, S. Nanthavanij², K. Sitthiseripratip³, and E. Lorprayoon⁴

¹ Asian Institute of Technology/School of Engineering and Technology, Phatumthani, Thailand

² Sirindhorn International Institute of Technology/School of Management Technology, Phatumthani, Thailand

³ National Metal and Materials Technology Center/Medical Rapid Prototyping Lab, Phatumthani, Thailand

⁴ Chulalongkorn University/Department of Anatomy, Bangkok, Thailand

Abstract— In this paper, the biomechanics model of index finger flexion-extension during mouse click was formulated to analyze the force applied on the mouse button change throughout the duration of mouse click. The biomechanics model was formulated by solving nonlinear differential equations consisting of nonlinear mouse spring equation and Newton-Euler dynamic equation of three links open-chain. The model was successfully solved. The fingertip force-time characteristics of index finger during switch compression obtained from the mathematical model followed the similar trend as the fingertip force over time of keyboard switch. Nevertheless, the duration of click based on such model is significantly less than the survey data. This may be due to the fact that the model does not take the viscoelastic properties of fingertip pulp during switch compression into account. Moreover, the result obtain from such model has not been successfully validated by the real experiment. Hence, the model validation with the experiment on the force applied on the mouse switch during activation must be further investigated.

Keywords— Mouse click, Mouse switch, Fingertip, Biomechanics, Nonlinear Spring.

I. INTRODUCTION

A computer mouse is one of the most widely used computer input devices. The intensive use of computer mouse was directly concerned with several musculoskeletal symptoms in the upper extremities [1]. The posture of hand on the mouse is one of the significant factors that can lead computer users to encounter with carpal tunnel syndrome [2]. Several researchers studied the use of computer mouse in term of the users' behavior and the musculoskeletal symptoms occurring among the computer users reported in statistical data. The study of mouse use in the view of dynamics is not widely focused. Understanding the relationship between mouse activation force and time of the finger during click is an important component linking to the understanding of the energy used by different mouse users and the improvement of mouse architecture and characteristics

of mouse switch. It was reported that the change of the force-displacement characteristics of computer keyswitches directly affected the dynamic loading of the intrinsic muscle during tapping [3]. Moreover, the flexed posture of finger during tapping keyswitches produces the lowest net joints torque relative to the other finger postures [4]. Likewise in the case of mouse switch, the switch characteristics and finger posture on the mouse may have similar effect on the finger dynamics. Based on the statistical data reported by Lee et al. (2008), most mouse users had neutral posture during mouse execution [5]. Sex, age and especially mouse activation force corresponded to the mouse click duration [6]. Wu et al. (2008) presented the model to determine mass moment of inertia of finger [7]. Such model can be applied to determine the dynamics of finger flexion-extension together with the Newton-Euler inverse dynamics model of three links open-chain presented by Kuo et al. (2006) [8]. The research of Thom et al. (2005) showed that there was no significantly evidence proving that the double click increased the risk of having musculoskeletal symptoms in the upper extremities than that of single click [9]. However, we hypothesize that the double click may require higher energy to activate than single click. The characteristics of feedback force during the keyswitch compression were observed [10]. Also, there was time delay observed when the fingertip pulp was being compressed after switch reached the maximum displacement [10]. Hence, dynamics of finger during tapping is also concerned with the viscoelastic properties of finger pulp. The profile of fingertip force changed over time due to viscoelastic properties of finger pulp was presented by Jindrich et al. (2003) [11]. The experiment showed that average energy was absorbed during tapping [11]. In this paper, we present the mathematical model to study the dynamics of index finger flexion-extension during mouse click. The model consists of nonlinear mouse spring force as function of angular position and the applied Newton-Euler inverse dynamics equations. We hypothesize that the profile of fingertip force changed over time during mouse click is similar to the case of keyswitch activation.

II. MATERIALS AND METHODS

To formulate the mathematical model representing the dynamics of index finger during mouse click, the force-displacement characteristics of mouse spring must firstly be obtained. The force-displacement characteristics of mouse spring experiment apparatuses consist of OKION optical mouse circuit board model TIO, EMCO F1 3 axis CNC machine, boring bit diameter of 1 mm and UME digital balance series SC with resolution of 0.1 grams. The boring bit mounted on the arbor of 3 axes CNC machine was moved down to compress the left switch of the mouse circuit board lying on the digital balance. During switch compression, the digital balance displayed the weight (compression force) at every spring displacement of 0.01 mm. As we expected the hysteresis effect during the spring was bouncing back to its initial position, the compression force was once again measured during the boring bit was released from mouse switch 0.01 mm respectively until it returned to its original position. The raw data of force-displacement characteristics of mouse spring is illustrated in Fig. 1. The force-displacement characteristics of mouse spring can be approximated as 23rd order polynomial equation.

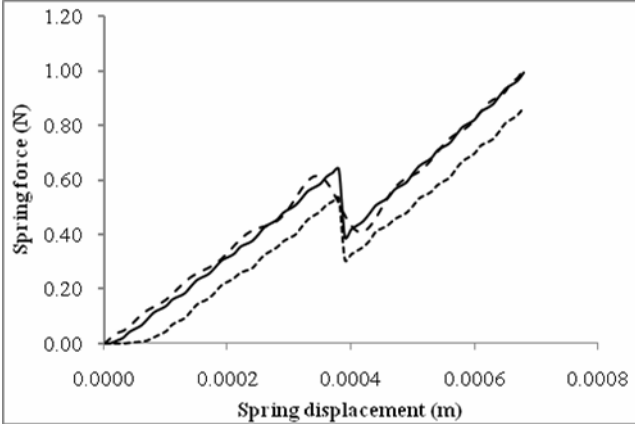


Fig. 1 Nonlinear force-displacement characteristics of OKION optical mouse spring. The solid line represents the spring force over spring displacement when the switch is compressed. The second dash line is the spring force approximated by 23rd order polynomial equation. The last dash line (the lowest) is the spring force over spring displacement when the switch is released

The dynamics model of index finger flexion-extension was mathematically formulated based on the Jacobian's principle [12] and Newton-Euler inverse dynamic of three links open-chain [8]. We made the assumption that most computer users click the mouse with rotation of metacarpophalangeal joint (MCP), while the other joints were fixed throughout the operation (PIP and DIP joints). Thus, the

matrix representing acceleration based on Jacobian is reduced to:

$$\begin{bmatrix} a_x \\ a_y \\ a_z \end{bmatrix} = \begin{bmatrix} -\dot{\theta}_1 L_1 C_1 - \dot{\theta}_1 L_2 C_{12} - \dot{\theta}_1 L_3 C_{123} \\ -\dot{\theta}_1 L_1 S_1 - \dot{\theta}_1 L_2 S_{12} - \dot{\theta}_1 L_3 S_{123} \\ 0 \end{bmatrix} \dot{\theta}_1 + \begin{bmatrix} -(L_1 S_1 + L_2 S_{12} + L_3 S_{123}) \\ L_1 C_1 + L_2 C_{12} + L_3 C_{123} \\ 1 \end{bmatrix} \ddot{\theta}_1 \quad (1)$$

where L_1 , L_2 and L_3 are the length of proximal, middle and distal phalanges respectively. S_1 , S_{12} , S_{123} are the sine of angle at MCP joint, sum of angles at MCP and PIP joints, sum of angles at MCP, PIP and DIP joints, respectively. Likewise, the cosine terms C_1 , C_{12} , C_{123} represent the cosine of angles in the same manner. $\dot{\theta}_1$ and $\ddot{\theta}_1$ are the angular velocity and acceleration at MCP joint. The left matrix a_x , a_y and a_z are the acceleration at the fingertip in x, y and z direction. By applying Eq. (2) to Newton's second law; the sum of the moments about MCP joint is equal to the total mass moment inertia of finger multiplied with angular acceleration of MCP joint:

$$\left[\sum_{i=1}^n (I_i + m_i r_i^2) \right] \ddot{\theta}_1 = M_E(\theta_1) \pm M_{ms}(\theta_1) \quad (2)$$

where I_i is the mass moment inertia at the center of mass of i th link (finger segments). The terms m_i and r_i represent the mass of i th link and effective length from center of mass of i th link to the center of MCP joint. $M_E(\theta_1)$ and $M_{ms}(\theta_1)$ are the external torque produced by the musculoskeletal system and gravity over the MCP joint angle and the torque from the mouse spring during depressing button as a function of MCP joint angle respectively. The latter term is 23rd order polynomial equation of mouse spring characteristics multiply with the horizontal moment arm from the spring location to center of MCP joint. The positive and negative signs in between both torque function represent the button depressing and releasing respectively. We predicted the external torque function as second order polynomial equation by assuming that the net torque at the maximum angular displacement of MCP joint for both finger depressing and lifting was equal to zero. The external torque function for depressing button is:

$$M_E^D(\theta_1) = -2143.186\theta_1^2 + 28.442\theta_1 - 0.0049 \quad (3)$$

and for lifting finger is:

$$M_E^L(\theta_1) = -4123.2\theta_1^2 + 35.9589\theta_1 - 0.0062 \quad (4)$$

Using the chain rule to solve Eq. (3) in order to obtain angular velocity at MCP joint, Eq. (3) becomes:

$$\dot{\theta} = \sqrt{2 \int_{\theta_i}^{\theta_f} \frac{M_E(\theta_1) \pm M_{ms}(\theta_1)}{\sum_{i=1}^n [(I_i) + m_i r_i^2]} d\theta_1} = F(\theta_1) \quad (5)$$

where $F(\theta_1)$ represents the angular velocity at MCP joint as a function of angle at MCP joint. Eq. (3) is further solved to obtain the relationship between the MCP joint angles changed and click time as follows:

$$\int_{\theta_i}^{\theta_f} \frac{1}{F(\theta)} d\theta = \int_0^t dt \quad (6)$$

The input parameters substituted into all these six equations to determine the index finger dynamics during mouse click are illustrated in Table. 1. The finger dimension, mass and mass moment of inertia of index finger are based on Wu et al. (2008) [7]. The angular position of MCP, PIP and DIP joints are obtained by graphical method. Fig. 2 illustrates the initial angular position of index finger posture on mouse.

Table 1 Mass, mass moment of inertia and posture angles of index finger during mouse activation

Finger segments	Length (mm)	Mass (grams)	I_{zz} (kg·m ²)
Distal	19.67	3.91	1.70E-07
Middle	24.67	6.79	4.51E-07
Proximal	43.57	15.5	2.83E-06

Finger joints	Angle (degrees)
DIP	3.732
PIP	22.849
MCP	6.618

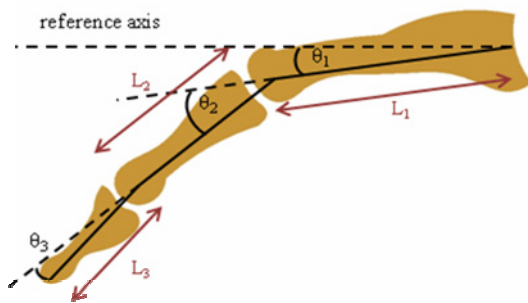


Fig. 2 Initial angular position of index finger posture on mouse

III. RESULTS

According to the graph illustrated in Fig. 3, the switch displaces from its initial position to the first trough which is point of the activation force within 15.75 ms. The first peak at time 16.26 ms is point where the click sound occurs or the mouse switch is completely activated. The fingertip at this position is 0.61 N. The graph then drops sharply to zero at the spring maximum displacement of 0.00068 mm and time of 17.45 ms. This is due to the fact that, we assume that net joint torque at the spring maximum displacement is zero prior to the finger swings back. The graph showed within the time range of 17.45 to 192.8 ms is the fingertip force during releasing finger from the button. The force is negative as it acts in opposite direction the compression force. The mouse switch reaches the click position at the time of 18.33. Then, the switch is completely deactivated at time of 18.56 ms as can be observed in the lowest point of the graph. Once again, the force suddenly drops to zero as we assume that the zero net torque at the end.

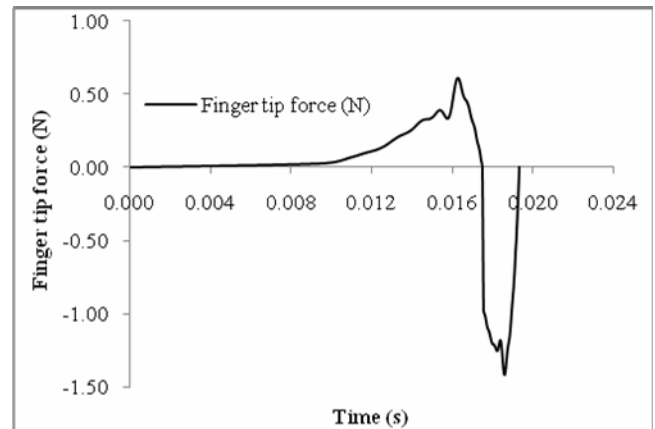


Fig. 3 Fingertip force changed over time during mouse activation and deactivation

IV. DISCUSSION

The fingertip force profile of switch activation graph (graph above horizontal axis) is similar to the case of key-switch [10]. However, the trend of switch deactivation is significantly different from the literature of Jindrich et al. (2004) [10]. This is because the deactivation trend from the literature is the fingertip force on force sensor anchored to the table. While, our model determines the fingertip force that pull the finger back to its initial position. According to the survey of Johnson et al. (2008), the duration of mouse button activation for adult on the mouse switch having similar activation force to our mouse is 100 ms approximately

[13]. Our model shows the activation time less than the literature almost 80 ms. The first assumption is that our model does not calculate the time delay during fingertip pulp compression. Based on the research of Jindrich et al. (2004), the pulp compression increases the activation time of keyswitch almost 50 ms [10]. The peak fingertip force at the click position is slightly different from literature of Johnson et al. (1996) which is 0.65 N [14]. The prediction of external torque trend based on Eq. (4) seems to be quite reliable. Based on Fig. 3, it can be seen that the characteristics of mouse switch affects the fingertip force profile. In order to improve the design of switch in which facilitates the mouse users to use less activation force, the overall force-displacement characteristics of switch should be lower than that of our tested mouse. However, the lower force-displacement characteristics of mouse switch means the lower force to push finger back during deactivation. Hence, it cannot be strongly concluded that the mouse with lower activation force will require less total energy during activation and deactivation than the mouse with higher activation force. The further investigation on the energy used during mouse click should be conducted. Moreover, our model should be validated with the real experiment like the experimental configuration of Jindrich et al. (2004). Also, the fingertip force should be obtained directly from the real experiment rather than prediction. The future work will be concerned with determination of energy and force used during mouse click of different finger posture and dimension of users' hands in order to understand how energy during mouse use relates to the anthropometry of human hand posture; thereby corresponding the improvement of mouse design and mouse use ergonomics.

V. CONCLUSIONS

The biomechanics model of index finger during mouse click was developed in order to study the characteristics of force over time during mouse click. The trend of fingertip force during switch activation is similar to the force-time characteristics of keyswitch. Nevertheless, the profile of fingertip force during switch deactivation is still questioning as there are no literatures support. Hence, the model is not successfully validated. The further validation based on real experiment should be conducted.

REFERENCES

1. Jensen C, Finsen L, Christensen H et al (2002) Musculoskeletal symptoms and duration of computer and mouse use. *International Journal of Industrial Ergonomics* 30: 265–275
2. Keir P, Bach J, Rempel D (1999) Effects of computer mouse design and task on carpal tunnel pressure. *Ergonomics* 42: 1350–1360
3. Lee D, Kuo P, Jindrich D et al. (2008) Computer keyswitch force-displacement characteristics affect muscle activity patterns during index finger tapping. *Journal of Electromyography and Kinesiology* :DOI 10.1016/j.jelekin.2008.03.011
4. Jindrich D, Balakrishnan A, Dennerlein J (2004) Effects of keyswitch design and finger posture on finger joint kinematics and dynamics during tapping on computer keyswitches. *Clinical Biomechanics* 19: 600–608
5. Lee D, McLoone H, Jindrich D (2008) Observed finger behaviour during computer mouse use. *Applied Ergonomics* 39:107-113
6. Komandur S, Johnson P, Storch R.L (2008) Relation between mouse button click duration and muscle contraction time. 30th Annual International IEEE EMBS Conference
7. Wu J, An K-N, Cutlip R et al. (2008) Analysis of musculoskeletal loading in an index finger during tapping. *Journal of Biomechanics* 41: 668–676
8. Kuo P-L, Lee D, Jindrich D et al. (2006) Finger joint coordination during tapping. *Journal of Biomechanics* 39: 2934–2942
9. Thorn S, Forsman M, Hallbeck S (2005) A comparison of muscular activity during single and double mouse clicks. *Eur J Appl Physiol* 94: 158–167
10. Jindrich D, Balakrishnan A, Dennerlein J et al. (2004) Finger joint impedance during tapping on a computer keyswitch. *Journal of Biomechanics* 37: 1589–1596
11. Jindrich D, Zhou Y, Becker Theodore (2003) Non-linear viscoelastic models predict finger tip pulp force-displacement characteristics during voluntary tapping. *Journal of Biomechanics* 36: 497-503
12. Zatsiorsky V (1998) Kinematics of human motion. Human kinetics, United State of American
13. Komandur S, Johnson P, Storch R.L (2008) Relation between mouse button click duration and muscle contraction time. 30th Annual International IEEE EMBS Conference Vancouver, British Columbia, Canada, August 20-24, 2008
14. Johnson P, Lehman S, Rempel D (1996) Measuring muscle fatigue during computer mouse use. 18th Annual International Conference of the IEEE Engineering in Medicine and Biology Society, Amsterdam 1996

Author: Prapol Chivapornthip
 Institute: Asian Institute of Technology
 Street: 58 Moo 9, Km. 42 Paholyothin Highway
 City: Phatumthani
 Country: Thailand
 Email: prapol_c@hotmail.com

Numerical Study of Deformation-Induced Fluid Flows in Osteonal Matrix

V.-H. Nguyen, T. Lemaire, and S. Naili

Laboratoire de Modélisation et Simulation Multi Echelle (CNRS 3160), Université Paris-Est, Créteil, France

Abstract— It is well-known that shear stress effects induced by bone fluid flows on the bone cells are important factors in triggering and signaling bone formation and remodeling. The aim of this work is to study how a mechanical stimulus involved in bone remodeling process changes with various loading conditions and geometrical/physical bone matrix parameters. Moreover, we also study the influence of a microcrack appeared in interstitial bones, which may act as a stimulus for bone remodeling by altering the fluid flow and convective transport through the bone tissue.

A mechanical model has been developed for this purpose. The model consists of a group of osteons surrounded by their cement lines and interstitial bone matrix which are all modeled as three-dimensional fully-saturated poroelastic media. The idealized structure is assumed to be homogenous in the longitudinal direction. We modeled also an individual microcrack located in the interstitial bone matrix that runs along the direction of osteons. Under uniform cyclic axial loading, an equivalent two-dimensional problem may be deduced. This problem is solved by using the finite element method in the frequency domain.

Keywords— cortical bone, poroelasticity, microcrack, fluid flow, finite element.

I. INTRODUCTION

Cortical tissue is the dense part of bone. As a living entity, this material is able to maintain and adapt its structure to external physical *stimuli* [1]. The seat of bone remodeling mechanisms corresponds to cylindrical structural elements called osteons. Each osteon is surrounded by a thin layer (cement line) and is centered on Haversian canal which runs primarily in the bone longitudinal axis. The Haversian canals contain the vasculature, the nerves and interstitial fluid. There are also Volkmann canals which are similar to Haversian canals except that they run along the transverse direction of the bone. At a smaller scale, other extravascular pores exist in the solid matrix of the bone forming the lacuno-canalicular system. This porous network irrigates the mechano-sensitive osteocytes which are believed to play an important role in bone adaptation as stated in recent experimental studies [2,3,4].

It has been shown that the fluid flow-induced shear stress applied on bone cells is an important factor bone formation and remodeling [5]. Moreover, targeted remodeling that is

activated by fatigue microcracks is also believed to be triggered and signaled by the fluid flow-induced shear stress [6].

In this paper we use a mechanical model to study the behavior the interstitial flows in cortical bone tissues under cyclic loading. The proposed model allows investigating the influence of different factors like strain rate, load's frequency, permeability and possibly presence of a microcrack on the interstitial fluid velocity which strictly related to shear stress acting on osteon cells.

II. MODELS

A. Description of Geometry

In osteonal bone matrix, Haversian canals run longitudinally through the bone cortex and are transversely inter-connected through Volkmann canals. Each osteon is developed concentrically around one Haversian canal and has cylinder-like form. In scope of this study, we are only interested on hydraulic behavior in zones that are assumed to be far enough from the Volkmann canals. As a consequence, the influence of Volkmann canals may be neglected. Figure 1-A shows a representative matrix of osteons in which one can find Haversian canals that run following the vertical direction \mathbf{x}_3 . As a first approximation, the osteons are assumed to be identical and parallel. Moreover, they are assumed to be arranged periodically in the horizontal plane ($\mathbf{x}_1, \mathbf{x}_2$) (Fig. 1-B). The osteons (denoted by the domain Ω_o in Fig. 1-C) are depicted as thick-walled hollow cylinders of which the inner cylinder represents Haversian canal. Each osteon is coated by a thin layer called the cement line (domain Ω_c). The tissues found outside of the cement lines, *i.e.* tissues that fill the space between the osteons, are called interstitial bone (domain Ω_i).

Assume that a linear microcrack exist within interstitial bone domain. According to *in vivo* observations presented in the literature [7, 8, 9], microcracks have elliptical shapes and they tend run along longitudinal direction of osteons. In this work, the microcrack is modeled by an elliptical domain (domain Ω_{ck} in Fig. 1-C). For simplification purposes, we assume that the microcrack is located on the symmetrical axis between two adjacent osteons.

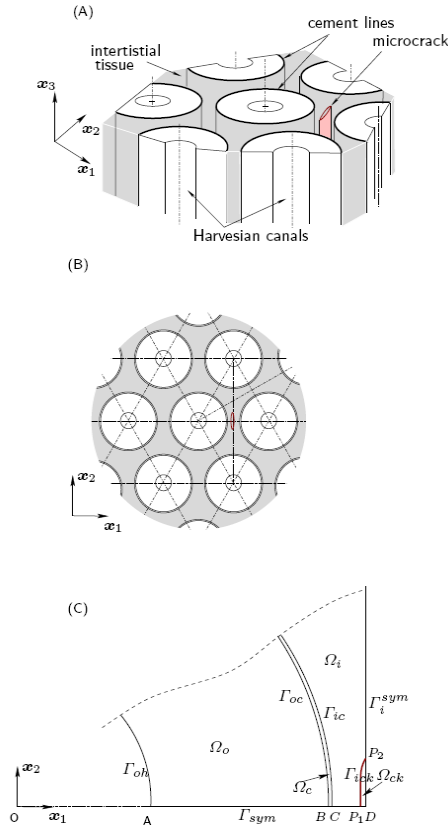


Fig. 1 Periodical matrix of osteons with a possible crack

B. Mechanical Modeling

The bone tissue materials (osteons, cement lines, and interstitial tissues) are all considered as saturated orthotropic poroelastic media. Neglecting the body forces, the linear anisotropic poroelastic equations in low-frequency range are given by [10]:

$$\rho \ddot{\mathbf{u}} - \text{div} \boldsymbol{\sigma} = \mathbf{0}, \quad (1)$$

$$\frac{1}{M} \dot{p} - \text{div}(\mathbf{k} \text{grad} p) + \boldsymbol{\alpha} : \boldsymbol{\varepsilon} = 0, \quad (2)$$

where $\rho = \rho_f + (1-\phi)\rho_s$ is the mixture density which is defined from the porosity ϕ and the densities ρ_f and ρ_s of the fluid and solid phases, respectively; \mathbf{u} and $\boldsymbol{\varepsilon}$ are the displacement vector and the strain tensor of the solid skeleton, respectively; $\boldsymbol{\sigma}$ is the total stress tensor; p is the fluid pressure in full-filled pores; \mathbf{k} is the anisotropic permeability tensor; $\boldsymbol{\alpha}$ is the Biot's tensor and M is the Biot's modulus. The relationship between the stress and strain tensor is given by the generalized Hooke's law:

$$\boldsymbol{\sigma} = \mathbf{C} \boldsymbol{\varepsilon} - \boldsymbol{\alpha} p, \quad (3)$$

where \mathbf{C} is the elastic stiffness tensor of drained material.

The permeability \mathbf{k} is the textural parameter allowing to quantifying the ability of a porous material to transmit fluids through the Darcy law:

$$\mathbf{v} = -\mathbf{k} \text{grad} p, \quad (4)$$

where \mathbf{v} is the filtration velocity vector defined by $\mathbf{v} = \phi(\mathbf{u}^f - \mathbf{u})$ where \mathbf{u}^f is the velocity vector of the interstitial fluid. The tensor \mathbf{k} may be evaluated by $\mathbf{k} = \boldsymbol{\kappa}/\eta$ where $\boldsymbol{\kappa}$ and η denote the intrinsic permeability and the pore fluid dynamic viscosity, respectively.

Here, as the orthotropic assumption were used, \mathbf{C} is defined by 9 independent constants and $\boldsymbol{\alpha}$ is a diagonal 3×3 matrix and is defined by 3 constants. The tensor \mathbf{k} is also assumed to be a diagonal matrix that defined by 3 constants.

The mechanical solicitation is described by an imposed cyclic strain that maintain uniform vertical strains in the whole system. The imposed strain is given by $\varepsilon_{33} = \varepsilon_0 \exp(2i\pi f_0 t)$ where ε_0 and f_0 are the amplitude and frequency of the strain.

C. Method of Resolution

Since only stationary responses are interested, it would be more convenient to convert the system described earlier (Eqs. 1-4) into the frequency domain. Moreover, using plane strain assumption in vertical direction allows deducing the three-dimensional problem into an equivalent two-dimensional one. In the scope of this paper, we will not present all detailed mathematical developments to obtain the equivalent two-dimensional problem due to the lack of space. However, one may refer to [11] for a more detailed description about this development as well as the weak formulations used for finite element implementation in the finite element software COMSOL Multiphysics [12].

III. NUMERICAL RESULTS

In this section we present some numerical tests to investigate the hydraulic sensibility of the system by considering the influences of: (i) the amplitude and the frequency of the loading; (ii) the distance between the osteons; (iii) the presence of a microcrack. In what follows, all results will be presented in terms of maximal fluid field in compressional phase of loading.

A. Parameters

The parameters used for geometry description are given as follows: inner radius (Haversian canal radius) of an osteon $r_i = 50\mu m$ and its outer radius $r_o = 150\mu m$; the cement line thickness $\delta = 1\mu m$; the center-to-center distance between two adjacent osteons is defined by $2r_o + d$. In what follows, the material properties of the different parts (osteons, cement, interstitial osteon) are given in the Tab. 1. Only the permeability of the cement line $\kappa^{(c)}$ is not as same (less permeable) as the ones of its neighboring osteonal tissues ($\kappa^{(o)}$, $\kappa^{(i)}$).

Table 1 Physical parameters

Parameter	Unit	Values
Mass density of the solid matrix ρ_s	kg.m ⁻³	2000
Young moduli [E_1, E_2, E_3]	GPa	[15.9, 15.9, 20.3]
Shear moduli [G_{12}, G_{13}, G_{23}]	GPa	[6.0, 6.9, 6.9]
Poisson's ratios [$\nu_{12}, \nu_{13}, \nu_{23}$]	-	[0.328, 0.25, 0.25]
Mass density of the fluid ρ_f	kg.m ⁻³	1000
Porosity ϕ	-	0.05
Biot's coefficients [$\alpha_1, \alpha_2, \alpha_3$]	-	[0.132, 0.132, 0.092]
Biot's modulus M	GPa	38.0
Intrinsic permeabilities [$\kappa_1, \kappa_2, \kappa_3$] ^(o,i)	m ²	[10 ⁻¹⁸ , 10 ⁻¹⁸ , 10 ⁻¹⁸]
Intrinsic permeabilities [$\kappa_1, \kappa_2, \kappa_3$] ^(c)	m ²	[10 ⁻¹⁹ , 10 ⁻¹⁹ , 10 ⁻¹⁹]
Pore fluid dynamic viscosity	Pa.s	10 ⁻³

Basing on the statement that bone cells *in vitro* actually respond to fluid shear stresses about 0.2 - 6 Pa over their surface [5], it would be able to determine a fluid velocity bound valued in range $2 \cdot 10^{-8} - 5 \cdot 10^{-8} \mu s^{-1}$ that correspond to the shear stress range (see [13] for the detail procedure to evaluate flow-induced shear stress in canaliculi from pore fluid velocity). As a result, the fluid velocity fields obtained in following tests will be compared with these values.

B. Osteonal Matrix without Microcracks

We first assume that there are no micro-cracks in the domain. The distance between osteons is determined with $d = 10\mu m$. Thanks to the periodical condition, only one Representative Elementary Volume (REV) (see Fig. 2) is needed to be modeled. Fig. 2 depicts the response of fluid velocity field when applying a frequency of loading $f_0 = 1Hz$ and a strain rate $\dot{\epsilon}_o = 0.003s^{-1}$ that were taken to mimic a typical daily activities. In the compressional phase, the fluid is pumped to flow toward to the Haversian edge and tend to nearly vanish at the vertical symmetric boundary.

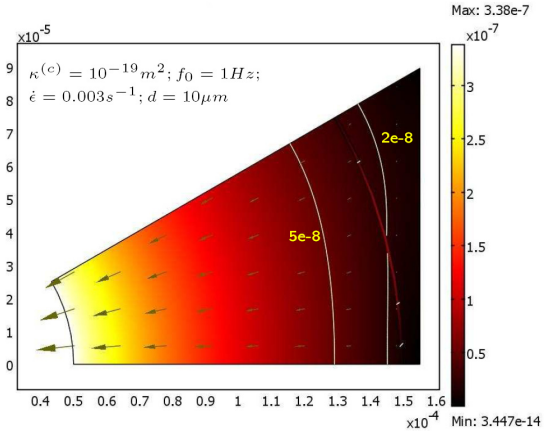


Fig. 2 No-crack case: interstitial fluid velocity field

In comparing with the fluid velocity bound $2 \cdot 10^{-8} - 5 \cdot 10^{-8} \mu s^{-1}$ proposed below, we may suggest that the interstitial flows may not sufficient to stimulate cells in zone outside of the osteon.

In the test presented in Fig. 3, the frequency is kept as in previous case ($f_0 = 1Hz$) whereas a smaller strain rate is applied ($\dot{\epsilon}_o = 0.001s^{-1}$). The strain rate reduction causes fluid velocity field strongly slowing down. It implies that the hydraulic “dead zone” spreads into inside the osteon volume since osteon cells are only stimulated in the vicinity of the Haversian canal.

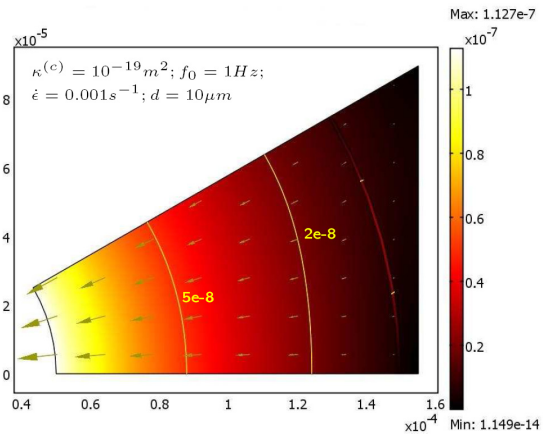


Fig. 3 No-crack case: effect of the strain rate

The next simulation is to consider the geometrical effect by keeping all parameters as same as the reference case (Fig. 2) except for the inter-Haversian distance that is now extended with $d = 50\mu m$. Comparing Fig. 2 and Fig. 4, one may state that the fluid velocity tends to increase with a larger inter-osteon distance. As a result, the stimulated zone is actually extended outside the cement line limit.

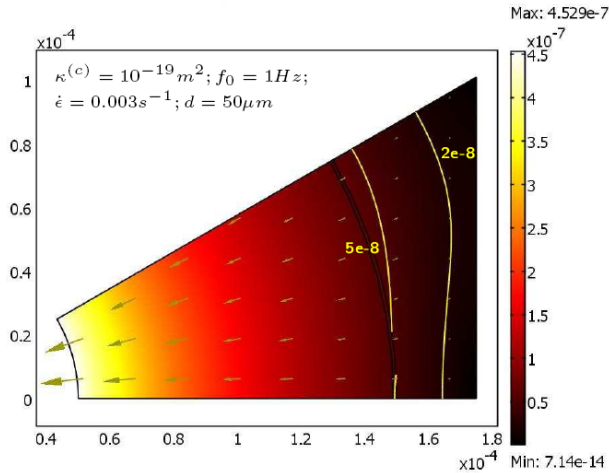


Fig. 4 No-crack case: effect of the distance between Haversian canals

C. Osteonal Matrix with One Microcrack

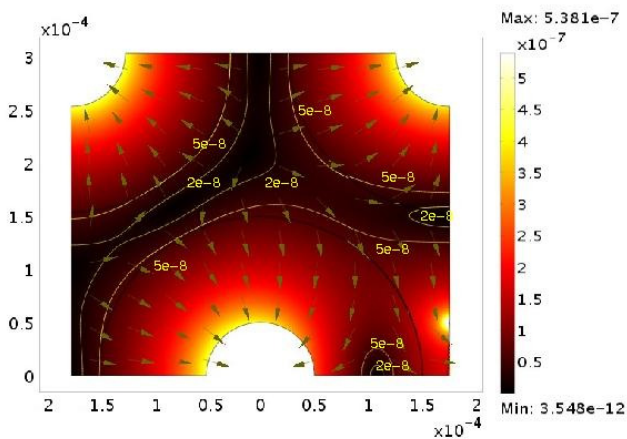


Fig. 5 Effect of the presence microcrack

Assume that there is a vertical microcrack (of which the dimension $100 \times 4 \mu\text{m}$) existing in the interstitial osteon domain. The same parameters as the case presented in Fig. 2 were used. Fig. 5 shows that the fluid velocity field is significantly modified due to the presence of the microcrack. During the compressional phase, the fluid may escape from osteon tissue not only by Haversian canal but also by the microcrack. This implies a “dead zone” inside osteon in which the fluid flows may not be sufficiently strong to stimulate osteon cells. Hence, the communication between osteocytes in this zone may actually be lost. This mechanism

might allow explaining how microcrack would be detected and acts as a factor that initiate bone remodeling.

IV. CONCLUSIONS

We have investigated the behavior of the interstitial fluid flow in osteons by considering the effects of strain rate, interaction between neighboring osteons and apparition of a microcrack. The results suggest that the strain rate as well the geometrical distribution osteons have significant effects on pore fluid velocity field. Moreover, the presence of the microcrack modifies strongly the fluid flow velocities in the osteon matrix. It may generate an area inside the osteon wherein the mechanotransduction signals might be insufficient to active the communication between osteocytes. This mechanism might explain how a microcrack may be detected even though it is located in the interstitial bone domain which is known as “dead tissue” zone.

REFERENCES

1. Lanyon L. E. and Rubin C. T. (1984). Static vs dynamic loads as an influence on bone remodelling. *J. Biomech.*, 17(12): 897–905.
2. Tatsumi S., Ishii K., Amizuka N., Li M. et al. (2007). Targeted ablation of osteocytes induces osteoporosis with defective mechanotransduction. *Cell Metabolism*, 5: 464 – 475.
3. Robling A. G., Niziolek P. J., Baldrige, L. A. et al. (2008). Mechanical stimulation of bone *in vivo* reduces osteocyte expression of sost/sclerostin. *J. Biol. Chem.*, 283(9):5866–5875.
4. You L., Temiyasathit S., Lee P. et al. (2008). Osteocytes as mechanosensors in the inhibition of bone resorption due to mechanical loading. *Bone*, 42:172 – 179.
5. Cowin S. C. (2002) Mechanosensation and fluid transport in living bone, *J. Musculokel. Neutron Interaction*, 2(3):256-260.
6. O’Brien F. J. (2005). Microcracks in cortical bone: How do they affect bone biology? *Current Osteoporosis Reports*, 3(2):39-45.
7. Mohsin S., O’Brien F., Lee T.C. (2006). Microcracks in compact bone: a three-dimensional view. *J. Anat.* 209: 119–124.
8. Taylor D., Lee C.T. (1998) Measuring the shape and size of microcracks in bone. *J. Biomech.*, 31(12): 1177–1180.
9. Wasserman N., Brydges B., Searles S. et al. (2008). *In vivo* linear microcracks of human femoral cortical bone remain parallel to osteons during aging. *Bone* 43: 856–861.
10. Biot M. (1956) Theory of propagation of elastic waves in a fluid saturated porous solid. I. Low-frequency range. *J. Acoust. Soc. Am.*, 28:168–178.
11. Nguyen V.-H., Lemaire T., Naili S. (2009) Numerical study of deformation-induced fluid flows in periodic osteonal matrix under harmonic axial loading. *Comptes Rendus Mecanique*, 337:268-276.
12. COMSOL Multiphysics (2008). User’s Guide.
13. Lemaire T., Boricin F., Naili S. (2008). Mechanotransduction of bone remodelling: role of micro-cracks at the periphery of osteons. *Comptes Rendus Mecanique*, 336:354-362.

Evaluation Spatial-temporal and Pressure Parameters of Normal Cats at Walk, Using a Pressure Walkway

T. LeQuang^{1,2}, P. Maitre^{1,3}, A. Colin^{1,3}, and E. Viguier^{1,3}

¹ UPSP 2007-03-135 RTI2B: Réparation Tissulaire, Interactions Biologiques et Biomatériaux, Université de Lyon, Ecole Nationale Vétérinaire de Lyon BP 83, 1 avenue Bourgelat, 69280 Marcy l'Etoile, France

² Department of Anatomy and Surgery Faculty of Medicine Veterinary and Animal Science Nong Lam University, KP6, Linh Trung, Thu Duc District., Ho Chi Minh City, Viet Nam

³ Service de chirurgie, Département des animaux de compagnie Université de Lyon, Ecole Nationale Vétérinaire de Lyon BP 83, 1 avenue Bourgelat, 69280 Marcy l'Etoile, France

Abstract— Quadrupedal locomotion is nowadays well known for dogs and horses; kinetic and kinematic systems allow sensitive and reliable gait analysis. On the other hand, cat locomotion has been less studied and data remain still confused and restricted.

The purpose of this study is to measure and evaluate spatio-temporal parameters and pressure data at walk in normal cats using a new pressure walkway adapted for cat. Gaitcat system is a pressure walkway of 2.4 m long with 28672 sensors. The system allows collecting of the spatio-temporal and pressure data, for each paw on consecutive strides. Data include: stride time, stance time, relative stance time (stance time/stride time), stride length, peak pressure, number of activated sensors by each paw and walking velocity. Symmetry left/right and ratio fore/hind limbs are also estimated. Twelve clinically healthy cats (mean weight: 5.0 and age: 2.1) were used in this study. Food or kennels were used to stimulate the cat cross the walkway.

The velocity average is 0.67 ± 0.22 m/s. No significant differences between the left and right forelimbs or the left and right hind limbs for all of the parameters. The ratio fore/hind limbs of the number of sensors is approximately one.

Stance distribution at walk seems to be equal between front and hind limbs. The ratio for relative stance time is 1.07 ± 0.04 ; the cats use the forelimbs slightly longer than the hind limbs during stance phase. For the peak pressure, it is 1.12 ± 0.15 ; its distribution is more important on the forelimbs, with 52.8% of the pressure reports on the front at walk.

This system enables measurement of the tempo-spatial parameters and pressure data of the cat at a walk. Stance distribution still seems to be more important on forelimbs although this dissymmetry is less important than in dogs and horses.

Keywords— Cat, pressure walkway, gait analysis, GAITRite® system, ratio fore/hind.

I. INTRODUCTION

Quadrupedal locomotion is nowadays well known for dogs and horses, and kinetic and kinematic systems allow sensitive and reliable analysis for these species such as force platform, treadmill with force platform integrated, system video sensor, pressure walkway. Force platforms were mainly used for dogs and horse to obtain sensitive and reliable data: the ground reaction forces (vertical and horizontal forces, acceleration, velocity, impulse, etc). On the other hand, cat locomotion has been less studied and, at the present time, data remain still confused and restricted. Force platform cannot easily be used for cat because it is difficult to concentrated cat to put their leg in the right position of the plate and their size is not enough to analyze. Romans et al. (2004) used a pressure platform to determine kinetic parameters in cats that had or had not undergone bilateral onychectomy [1] then in 2007 Lascelles et al. used a pressure-sensitive walkway to evaluation kinetic parameters of healthy cat at walk and jump [2].

The pressure walkway system also called pressure sensors system, most were designed to measure spatio-temporal gait analysis and built around pressure sensors included in a walkway. Data collection and analysis was performed by specific software. Pressure walkway was used recently in some research for humans [3], but still very little in animals such as dogs [4, 5], cats [1, 2], rat [6] and sheep [7].

The purpose of this study is to measure and evaluate spatio-temporal parameters and the pressure data associated with the walk in normal cats using a new gait analysis system adapted for cat.

II. MATERIALS AND METHODS

GAITCat system is a portable walkway composed by a combination of seven sections connected together to form a 2.4 m long walkway with 28672 sensors, ($\frac{1}{4}$ inch square sensor). Two plastic walls are fixed along each side of the walkway (figure 1).



Fig. 1 Cat across the GAITCat walkway

The system allows the simultaneous collect of the spatio-temporal and pressure data, for each four paws on consecutive strides. Data include: stride time, stance time, relative stance time (stance time/stride time), stride length, peak vertical pressure, mean number of activated sensors (surface of the foot print) by each paw and walking velocity. Symmetry left/right and stance distribution (ratio fore/hind limb) are also estimated.

Twelve clinically healthy cats of various breeds and shape (weight average: 5.0 ± 1.1 kg and age average: 2.1 ± 1.4 years old) were recruited from the staff of the National Veterinary School of Lyon. All cats underwent an orthopedic examination showing neither visible lameness nor appendicular and vertebral joint or muscle pain. No history of orthopedic disease was recorded before for any cat.

The cats have to cross the walkway by their own. To stimulate the cat, food or kennels are placed at the opposite of the starting walkway. A trial was considered valid when all of four paws were in contact with the surface of the walkway for each walk cycle; the cats maintained a steady-state, straight line gait pattern without stop or turning their heads; and there were at least three consecutive regular strides to analyze. Five valid trials were recorded for each cat.

The statistical paired t-test was used in order to make a comparison in gait parameters between left and right forelimbs, and the left and right hind limbs. The Mann-Whistney

Wilcoxon tests were performed to determine if difference in measurement of each gait parameter between two groups was significant. Difference was considered significant if p was under 0.05.

III. RESULTS

Cats walk freely from five to eight times and acceptable walks (regular and continuous) are analyzed (figure 2).

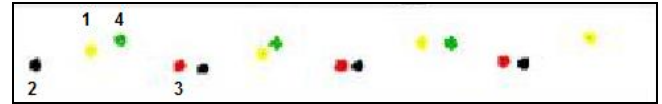


Fig. 2 Regular walk Pattern of cat obtained with GAITCat system (1: left front; 2: right hind; 3: right front and 4: left hind)

Despite the diversity of the shape and weight, all paws could be easily and efficiently analyzed. The velocity average is 0.67 ± 0.22 m/s.

There are no significant differences between the left and right forelimbs or the left and right hind limbs for all of the parameters (table 1).

Table 1 Values of parameters of normal cats at walk

	Left front	Right front	Left back	Right back
Stance time	0.50 ± 0.11	0.50 ± 0.11	0.49 ± 0.12	0.48 ± 0.10
Stride time	0.76 ± 0.13	0.76 ± 0.13	0.77 ± 0.14	0.78 ± 0.14
Stride length	49.6 ± 6.4	49.0 ± 7.0	49.4 ± 6.9	50.0 ± 5.9
Number of activated sensors	16.4 ± 3.1	16.9 ± 3.3	16.4 ± 2.7	16.3 ± 3.0

The ratio forelimbs/hind limbs of the number of sensors is approximately one (table 2).

Table 2 Symmetries and ratio of parameters of normal cats at walk

	Ratio Front/Hind	Symmetry Left/Right forelimb	Symmetry Left/Right hind limb
Relative stance time	1.07 ± 0.04	1.02 ± 0.04	1.00 ± 0.06
Stride time	0.98 ± 0.04	0.99 ± 0.04	1.00 ± 0.04
Stride length	0.99 ± 0.04	1.00 ± 0.03	1.00 ± 0.03
Peak vertical pressure	1.12 ± 0.15	0.99 ± 0.16	1.02 ± 0.16
Number of activated sensors	1.02 ± 0.10	0.98 ± 0.11	1.01 ± 0.10

IV. DISCUSSION

Our results were collected from 12 of 22 client-owned cats by encouraging them to walk freely across a pressure walkway.

Data were accepted only if the cats traversed the entire walkway in a straight line, nonstop. This may explain the failure to obtain data from all the cats, it being more difficult to get the cats to traverse the whole of the walkway in a straight line. Whereas dogs can be led across a force plate or pressure walkway, cats are not usually trained to a lead. Several methods were used to encourage the cats to traverse the mat, with toys, food and kennel being the most successful. Two plastic walls were used and fixed along each side of the walkway to help cat walk in a straight line.

Our result velocity is similar to the study of Romans et al. (2004): 0.66 - 0.69 m/s; or the study of Lascelles et al. (2007): 0.6 ± 0.1 m/s.

Stance distribution at walk seems to be equal between front and hind limbs for this parameter. This ratio for relative stance time is 1.07 ± 0.04 ; the cats use the forelimbs slightly longer than the hind limbs during stance phase. For the peak vertical pressure, it is 1.12 ± 0.15 ; its distribution is more important on the forelimbs, with 52.8% of the pressure reports on the anterior at walk. This result is very similar to report of Romans et al. (2004): 53-56%; and higher than the study of Lascelles et al. (2007): 48.2%.

But in the previous study of LeQuang et al. 2009 using the pressure walkway, which very similar to the one used in this study, for healthy large-breed dog, the ratio fore/hind limb of stance time relative and peak vertical pressure were 1.10 and 1.47, respectively [4]. In another report using the pressure walkway also in normal Greyhound, this ratio for peak vertical force was 1.38 [5]; and for the healthy sheep, body weight distribution was 59% for the forelimb [7]. The stance distribution in cat was less importance than in dog and sheep.

V. CONCLUSION

This system enables measurement of the tempo-spatial parameters and pressure data of the cat at a walk. Preliminary results confirm that the cat walk is a symmetric gait,

even if some slightly differences exist from other species. Stance distribution still seems to be more important on forelimbs although this dissymmetry is less important than in dogs and horses.

ACKNOWLEDGMENTS

Special thanks to all of owners of cats which were used in this study.

REFERENCES

1. Romans C.W., Conzemius M.G., Horstman C. L., Gordon W. J. and Evans R. B. (2004), Use of pressure platform gait analysis in cats with and without bilateral onychectomy. *American Journal of Veterinary Research*, 65: 1276-1278.
2. Lascelles B.D., Findley K., Marcellin-Little D. and Roe S. (2007), Kinetic evaluation of normal walking and jumping cats, using a pressure-sensitive walkway. *The Veterinary record*, 160: 512-516.
3. Cutlip RG, Mancinelli C, Huber F et al. (2000) Evaluation of an instrument walkway for measurement of the kinematic parameters of gait. *Gait Posture* 12: 134-138.
4. LeQuang T., Maitre P., Roger T., Viguier E. (2009) Is a pressure walkway system able to highlight a lameness in dog? *J Ani and Vet Adv*. 8: 1936-1944
5. Besancon MF, Conzemius MG, Derrick TR et al. (2003) Comparison of vertical forces in normal greyhounds between force platform and pressure walkway measurement system. *Vet Comp Orthop Traumatol* 16: 153-157.
6. Bozkurt A., Deumens R., Scheffel J., O'Dey D.M., Weis J., Joosten E.A., T. Führmann, Brook G.A., Pallua N. (2008) CatWalk analysis in assessment of functional recovery after sciatic nerve injury. *J neurosci. Meth*, 173: 91-98.
7. Kim J, Breur GJ (2008) Temporospacial and kinetic characteristics of sheep walking on a pressure sensing walkway. *Can J Vet Res* 72: 50-55.

Author: Thong LEQUANG
 Institute: Nong Lam University
 Street: KP6, Linh Trung, Thu Duc District
 City: Ho Chi Minh City
 Country: Viet Nam
 Email: lequangthong@gmail.com

Gait Analysis for Sound Dogs at a Walk by Using a Pressure Walkway

T. LeQuang^{1,2}, P. Maitre^{1,3}, A. Colin^{1,3}, T. Roger¹, and E. Viguier^{1,3}

¹ UPSP 2007-03-135 RTI2B: Réparation Tissulaire, Interactions Biologiques et Biomatériaux,
Université de Lyon, Ecole Nationale Vétérinaire de Lyon
BP 83, 1 avenue Bourgelat, 69280 Marcy l'Etoile, France

² Anatomy and Surgery Department

Faculty of Medicine Veterinary and Animal Science
Nong Lam University, KP6, Linh Trung, Thu Duc District., Ho Chi Minh City, Viet Nam

³ Service de chirurgie, Département des animaux de compagnie
Université de Lyon, Ecole Nationale Vétérinaire de Lyon
BP 83, 1 avenue Bourgelat, 69280 Marcy l'Etoile, France

Abstract— The purpose of this study was to evaluate spatio-temporal and pressure parameters in two different sized dogs: large-breed (Retriever) and small-breed dogs (Beagle), by using a pressure sensors walkway. 55 healthy adult dogs from 1 to 4.5 years old: 28 Retriever (mean weight: 29.7 kg) and 27 Beagle (mean weight: 10.8 kg) were tested by GAITRite® system. It is a portable pressure walkway of 4.3 meters long and 16128 sensors, which measures spatio-temporal and pressure parameters. Data collected included: stance time; relative stance time (stance time/stride time), stride time; stride length; peak vertical pressure, number of activated sensors by each paw; cadence and walking velocity. Symmetry left/right and ratio fore/hind limbs were also calculated. No significant difference for mean of velocity for Retriever (1.09 m/s) and Beagle dogs (1.14 m/s), but a significant different for the cadence between large (1.6) and small dogs (2.09) stride/s. No significant difference between the left and right forelimbs or left and right hind limbs for any parameters in either group. But the differences were significantly for all parameters between two groups.

The values of fore/hind limb ratio in both groups showed a more significant distribution on the forelimb than the hind limb for stance time; relative stance time; the peak vertical pressure and were significantly difference between large and small dogs (1.07 versus 1.12; 1.08 versus 1.15 and 1.60 versus 1.45, respectively). The GAITRite® analysis system enables measurement of the spatial-temporal parameters of the dog at walk. The study of symmetry and ratio allow an easier and quicker gait analysis. The size of dogs influenced the fore/hind ratio and significant difference; however the left and right symmetry did not seem to be modified. Pressure, relative stance time and number of activated sensors were more important in the forelimb than for the hind limb.

Keywords— Pressure walkway, gait analysis, healthy dog, GAITRite® system, ratio.

I. INTRODUCTION

Scientific gait analysis of canines has evolved over the past 25 years, most dramatically over the past decade thanks

to improvements in computer technology. Gait analysis may be realized by many different techniques: kinematic and kinetic analysis.

Kinetic analysis is an analysis of the forces acting on a system motion and has been described by many authors [1-8] using several devices such as force platforms, treadmill associated with force platforms, pressure mats....

Force platforms were mainly used to obtain sensitive and reliable data: the ground reaction forces (peak vertical and horizontal forces, vertical impulse, acceleration, symmetry, etc). Nevertheless the force platform presents several limits. The system is complex, hardly portable and requires a specific environment and conditions of use. Moreover, data cannot be collected from all four limbs during one cycle using a single force platform [7]. Consecutive strides cannot be assessed without an associated treadmill [8]. Several trials were necessary to obtain correct placement of the foot on the plate.

Because of those limits, other systems have been developed recently such as the pressure walkway system also called pressure sensors system. Most were designed to measure spatio-temporal gait analysis and built around pressure sensors included in a walkway. Data collection and analysis was performed by specific software. Pressure walkway was used recently in some research for humans [9-14] but still very little in animals such as dogs [6, 15-17], cats [18] and sheep [19].

Locomotion in healthy dogs has been characterized in several experimental force platform studies [1-8], but rarely, to the author's knowledge, with a pressure sensor system [6, 15, 16]. However the influence of the size has never been assessed with that system.

The purpose of this prospective study was to evaluate spatio-temporal and pressure parameters in two different sized dogs: healthy large-breed and small-breed dogs, by using a 4.3 meter pressure sensors walkway.

II. MATERIALS AND METHODS

Fifty-five adult dogs were included in this study: 28 healthy Retrievers (average aged: 2.3 years, SD 1 and average weight: 29.7 kg, SD 3.9) owned by the National association for training dogs for the disabled and 27 healthy adult Beagles (average aged: 1.7 years, SD 1.1 and average weight: 10.8 kg, SD 0.8) were recruited from Institute Claude Bourgelat of the National Veterinary School of Lyon. All dogs underwent an orthopedic examination showing neither visible lameness nor appendicular and vertebral joint or muscle pain. No history of orthopedic disease was recorded before for any dog.

The GAITrite® system (CIR Systems, Inc.) includes a portable walkway 4.3 meters long, which has seven sensor pads with an active area of 61 cm wide and 427 cm long. The active area contains 16,128 sensors arranged in a grid pattern which measure spatiotemporal aspects of gait. The spatial resolution of the device is 1.27 cm and the sampling frequency is 80 Hz. The data was collected by the activated sensors and transferred to a portable computer through a serial port where it was calculated by specialized quadruped-adapted software (GAITFour) and this data was then exported for further processing and analysis.

Before collecting data, six to eight practice trials were performed across the walkway to familiarize the dogs with their environment and the protocol. The dogs walked with an experienced handler (the same handler for each dog for all trials) across the walkway utilizing a loose leash. The dogs walked at their preferred and constant velocity while an observer evaluated and confirmed the validity of each trial. A trial was considered valid when all of four paws were in contact with the surface of the walkway for each walk cycle; the dogs maintained a steady-state, straight line gait pattern without pulling on the leash or turning their heads; and there were at least three consecutive regular strides to analyze. Five valid trials were recorded for each dog.

This system collected spatio-temporal (stride length, stance time, relative stance time or stance time %, stride time, cadence and walking velocity) and pressure data: peak vertical pressure and number of sensors activated during the stance.

In addition to the data/parameters collected directly by GAITrite®, we calculated for all the parameters the ratio of the fore/hind limbs and the symmetry of left/right limbs; left/right forelimbs and left/right hind limbs.

The statistical paired t-test was used in order to make a comparison in gait parameters between left and right forelimbs, and the left and right hind limbs. The Mann-Whitney Wilcoxon tests were performed to determine if difference in measurement of each gait parameter between

two groups was significant. Difference was considered significant if p was under 0.05.

III. RESULTS

The velocity of Retrievers was 1.09 (SD 0.18) m/s versus 1.14 (SD 0.36) m/s for Beagles group.

A significant difference was observed for the value of cadence between breeds: Retrievers = 1.6 (SD 0.2) strides/s; Beagles = 2.09 (SD 0.22) strides/s.

We did not detect significant difference between the left and right forelimbs or left and right hind limbs for any parameters in either group.

There were significant differences for all spatio-temporal parameters; peak pressure and number of activated sensors between Retrievers and Beagles group. These data from Beagle group were consistently lower than those of group of Retriever.

The symmetry of left/right limbs; left/right forelimbs and left/right hind limbs for all of spatio-temporal parameters; peak pressure and number of activated sensors in either group were not significantly different by 1 and there were no significant differences between two groups (table 1).

Table 1 The symmetry values for variables collected in healthy Retrievers and Beagles dogs at walk (Mean±SD)

Parameters	Symmetry	Retrievers	Beagles
Stance time (s)	Symmetry L/R	1.00±0.03	1.00±0.10
	Symmetry LF/RF	1.00±0.04	0.99±0.11
	Symmetry LH/RH	1.00±0.07	1.01±0.19
Relative stance time (% of cycle)	Symmetry L/R	1.00±0.03	0.99±0.12
	Symmetry LF/RF	1.00±0.04	0.99±0.12
	Symmetry LH/RH	1.01±0.05	1.01±0.26
Stride time (s)	Symmetry L/R	1.00±0.01	1.00±0.02
	Symmetry LF/RF	1.00±0.02	0.99±0.03
	Symmetry LH/RH	1.00±0.02	1.01±0.04
Stride length (cm)	Symmetry L/R	1.00±0.01	1.00±0.01
	Symmetry LF/RF	1.00±0.01	1.00±0.02
	Symmetry LH/RH	1.00±0.01	0.99±0.02
Peak pressure	Symmetry L/R	0.99±0.11	1.02±0.15
	Symmetry LF/RF	1.00±0.13	1.03±0.19
	Symmetry LH/RH	0.99±0.14	1.04±0.25
Number of activated sensors	Symmetry L/R	1.00±0.09	1.01±0.12
	Symmetry LF/RF	1.01±0.11	1.01±0.18
	Symmetry LH/RH	1.00±0.13	1.04±0.20

L/R = left fore and hind limbs/right fore and hind limbs; LF = left forelimb; RF = right forelimb; LH = left hind limb; RH = right hind limb

No significant differences were detected between Beagles and Retrievers dogs.

The fore/hind limb ratio of stance time was 1.07 (SD 0.07) for large breed dogs and 1.12 (SD 0.17) for Beagles, this ratio for relative stance time was 1.08 (SD 0.05) for Retrievers and 1.15 (SD 0.14) for small-breed. The fore/hind limb ratio for

stride time and stride length were not significantly different by 1.

For the peak pressure parameter, the fore/hind limb ratio were 1.60 (SD 0.15) and 1.45 (SD 0.28) and for activated sensors were 1.38 (SD 0.13) and 1.32 (SD 0.23) for Retrievers and Beagles, respectively (figure 1).

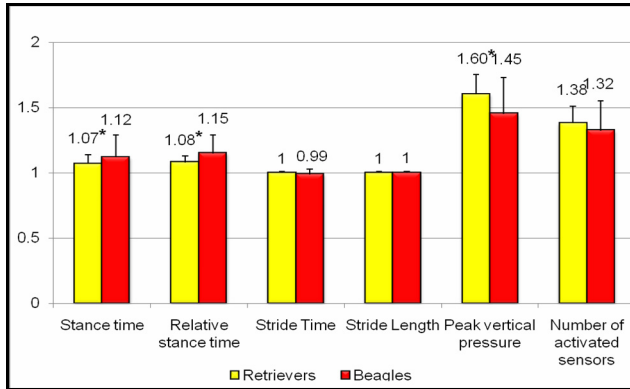


Fig. 1 The fore/hind limb ratio of the spatio-temporal parameters, the peak vertical pressure and the number of activated sensors of healthy large-breed adult and small-breed adult dogs at walk

Significant differences were observed in this ratio between the two groups for data values of stance time, relative stance time and peak pressure.

IV. DISCUSSION

Recently, a human gait analysis tools have introduced GAITRite® system, a pressure mat, which measure spatio-temporal parameter, peak vertical pressure and velocity of walk. Combined with specialized quadruped-adapted software, this system can calculate these parameters for each limb at the same time and in the same conditions at one walk.

This portable system allowed recording the data of the four foot collateral, consecutive in a single pass so that an adequate amount of data for statistical comparisons can be collected by fewer passes over the walkway to compare with the force plate [6].

Studies recently assessed the concurrent validity of the GAITRite® system in humans with video-based analysis system [9]; paper-and-pencil and video-based methods [10]; a footswitch system [11]; a three-dimensional motion analysis system: Vicon-512 [12] and stopwatch-footfall count method [14], all of these reports demonstrated that the results of validity and reliability of this system for gait analysis were excellent. The same procedures had been done in dogs [20].

According the operator, tests were more difficult to perform on small breed dogs; large dogs seemed to be more quiet and regular than small dogs during walking over the walkway. Analysis of data seemed also easier and quicker for large dogs.

Using a 4.3 m long walkway, allowed numerous data to be collected even with large dogs (at least three and maximum five strides for a regular retriever) or small breed dogs (at least three and maximum eight strides for a beagle). Contrary to the force platform where data collection could be limited by the size of the dog: a large-breed dog with long stride tended to frequently contact the wrong place and the small-breed dogs were difficult to centre properly [8].

Most studies concerning gait analysis have been realized in large-breed dogs but very rarely in small-breed dogs especially for walking of healthy dogs so we did not find value references at walk for our study. In this study, the mean walking velocity was 1.09 (SD 0.18) m/s for the healthy large-breed dogs. This value corresponded well with the results of former studies for walking velocities that were around 1 m/s [2, 6, 8, 15, 21]. In the healthy small-breed dogs, the velocity was slightly higher than in the large-breed dogs (1.14; SD 0.36 m/s) but it was not significantly different.

The cadence for the small dogs was greater than for the large dogs (2.09; SD 0.22 strides/s and 1.60; SD 0.24 strides/s, respectively). Because of shorter legs smaller dogs, have small stride length and need to generate a greater limb frequency to achieve the same velocity as the larger dogs.

Titianova in 2004, had showed in humans, which the spatial and temporal parameters of gait closely related to the speed of walking, so the cadence and stride length were directly related with the velocity, meanwhile stance time and stride time were inversely related to velocity [13].

Mean stance times in forelimbs and hind limbs for large dogs were 0.45 (SD 0.08) s and 0.42 (SD 0.09) s, respectively. Our results were very close to Roush's kinetic results and Hottinger's kinematic results [2, 21].

The stance time and the relative stance time between both groups were significantly different. The research of Budsberg et al. (1987) has proven that stance time and body size were directly related [1]. Moreover, in other studies, stance time in the forelimbs and hind limbs had been shown to have a negative linear correlation with velocity [2-5].

Difference in body size and body weight explain significant differences when observed of the values of stride time; stride length; peak pressure and number of activated sensors between two groups. Budsberg in 1987 has shown that the ground reaction forces, stance phase and morphometric measurements were significant correlations [1].

The values of fore/hind limb ratio in both groups showed a more significant distribution on the forelimb rather than

the hind limb for the stance time and relative stance time the peak pressure and the number of activated sensors. It corresponded well with the previous studies in healthy dogs at walk published by other authors [2, 5, 8, 15].

The ratio of fore/hind limb of the stance time was 1.07 (SD) for the large-breed. This result was slightly higher than ratio calculated from previous studies of Bockstahler (2007) and Hottinger (1996): 1.04 and 1.03, respectively.

The fore/hind limb ratio of maximal pressure was 1.60 (SD) for large dogs. Our values in large dogs were higher than the recent reports in healthy large-breed dogs were 1.38 [1] or 1.42 [15] or 1.46 for system platform and 1.38 for system pressure mat [6]. But this value in our study was similar to result 1.61 of Bockstahler (2007) [8].

Comparison of fore/hind limb ratio showed a significant difference between both sized groups for the stance time, relative stance time, and peak of pressure. And it seemed almost significantly different for the number of activated sensors. The forelimbs of small-breed adult dogs presented a fore/hind limbs distribution with less pressure (1.45/1.60) on forelimbs, but longer stance time (1.15/1.08) than the large-breed dogs, at walk.

To the author's knowledge, it has never been demonstrated before. Fore/hind limb ratio could be interesting to assess front or hind limb lameness but needs to be compared with same sized healthy dogs.

Symmetry between left and right legs was present in both groups for all parameters, and no significant variation in symmetry was found with size and weight variation for almost all parameters. However, authors noted that the standard variation for left and right symmetry in small breeds was slightly higher than large breed dogs for almost all parameters. Once again, difference in training could be advocated to explain such variation.

V. CONCLUSION

The GAITRite[®] system was proved to provide useful data: spatio-temporal parameters, maximal pressure and number of activated sensors of the dog at walk; and allowed quick analysis.

On the basis of the data obtained in this study and compared with the previous studies, it could be concluded that the results were similar to those found in literature for large breed dogs which used other gait analysis devices.

For small dogs, with no previous study available, we have established a normative database for future pathologic study.

We observed in this study that large dogs seemed to be more regular, easier and quicker to analyse. Moreover small dogs parameters variation seemed slightly higher. In the

first approach, the study of large dogs seems more reliable than small ones, but had required an adapted analysis device such as this long walkway.

The fore/hind limb ratio could be significantly modified with the size of the dog and needs to be taken into account for various sized dog gait analysis. This preliminary study needs to be followed by the establishment of a specific database for each breed and size.

However, the left and right symmetry did not seem to be modified by the size of the dogs, and were systematically present.

As already published, every lameness induces a modification of the symmetric pattern of the gait and according to this study, the use of the left/right limb symmetry and fore/hind limb ratio could help the clinician not only to determine and qualify the lameness but also allow reliable and accurate follow-up.

REFERENCES

1. Budsberg SC, Verstraete MC, Soutas-Little RW. (1987) Force plate analysis of the walking gait in healthy dogs. *Am J Vet Res* 48: 915-918.
2. Roush JK, McLaughlin MJ. (1994) Effects of subject stance time and velocity on ground reaction force in clinically normal Greyhounds at the walk. *Am J Vet Res* 55: 1672-1676.
3. McLaughlin RM, Roush JK. (1994) Effects of subject stance time and velocity on ground reaction force in clinically normal Greyhounds at the trot. *Am J Vet Res* 55: 1666-1671.
4. McLaughlin RM, Roush JK. (1995) Effects of increasing velocity on braking and propulsion times during force plate gait analysis in Greyhounds. *Am J Vet Res* 56: 159-161.
5. Renberg WC, Johnston SA, Ye K et al. (1999) Comparison of stance time and velocity as control variables in force plate analysis of dogs. *Am J Vet Res* 60: 814-819.
6. Besancon MF, Conzemius MG, Derrick TR et al. (2003) Comparison of vertical forces in normal greyhounds between force platform and pressure walkway measurement system. *Vet Comp Orthop Traumatol* 16: 153-157.
7. Brebner NS, Moens NMM, Runciman JR. (2006) Evaluation of a treadmill with integrated force plates for kinetic gait analysis of sound and lame dogs at a trot. *Vet Comp Orthop Traumatol* 19: 205-212.
8. Bockstahler BA, Skalicky M, Peham C et al. (2007) Reliability of ground reaction forces measured on a treadmill system in healthy dogs. *The Veterinary Journal* 173: 373-378.
9. Cutlip RG, Mancinelli C, Huber F et al. (2000) Evaluation of an instrument walkway for measurement of the kinematic parameters of gait. *Gait Posture* 12: 134-138.
10. McDonough AL, Batavia M, Chen FC et al. (2001) The validity and reliability of the GAITRite[®] system's measurements: a preliminary evaluation. *Arch Phys Med Rehabil* 82: 419-425.
11. Bilney B, Morris M, Webster K (2003) Concurrent validity of the GAITRite[®] walkway system for quantification of the spatial and temporal parameter of gait. *Gait Poster* 17: 68-74.
12. Webster KE, Wittwer JE, Feller JA (2004) Validity of the GAITRite[®] walkway system for the measurement of averaged and individual step parameters of gait. *Gait posture* 22: 317-321.
13. Titianova EB, Mateev PS, Tarkka IM (2004) Footprint analysis of gait using a pressure sensor system. *J Electromyogr kinesiol* 14: 275-281.

14. Youdas JW, Hollman JH, Aabers MJ et al. (2006) Agreement between the GAITRite® walkway system and a stopwatch-footfall count method for measurement of temporal and spatial gait parameters. *Arch Phys Med Rehabil* 87: 1648-1652.
15. Besancon MF, Conzemius MG, Evans RB et al. (2004) Distribution of vertical forces in the pads of Greyhounds and Labrador Retrievers during walking. *Am J Vet Res* 65: 1497-1501.
16. Lascelles BDX, Roe SC, Smith E et al. (2006) Evaluation of a pressure walkway system for measurement of vertical limb forces in clinically normal dogs. *Am J Vet Res* 67: 277-282.
17. Kim J, Blevins WE, Breur GJ (2006) Morphological and functional evaluation of a dog with dimelia. *Vet Comp Orthop Traumatol*, 19: 255-258.
18. Lascelles BD, Findley K, Correa M et al. (2007) Kinetic evaluation of normal walking and jumping in cats, using a pressure-sensitive walkway. *Vet Rec* 160: 512-516.
19. Kim J, Breur GJ (2008) Temporospatial and kinetic characteristics of sheep walking on a pressure sensing walkway. *Can J Vet Res* 72: 50-55.
20. Viguier E, LeQuang T, Maitre P et al. (2006) The validity and reliability of the GAITRite® system's measurement of the walk in dog. 2nd world veterinary orthopaedic and 33rd annual VOS meeting. Keystone (USA): 245.
21. Hottinger HA, Decamp CE, Olivier B et al. (1996) Noninvasive kinematic analysis of the walk in healthy large breed dogs. *Am J Vet Res* 57: 381-388.

Use macro [author address] to enter the address of the corresponding author:

Author: Thong LEQUANG
 Institute: Nong Lam University
 Street: KP6, Linh Trung, Thu Duc District
 City: Ho Chi Minh City
 Country: Viet Nam
 Email: lequangthong@gmail.com

Robust Design with Time-Oriented Responses for Regenerative Medicine Industry

N.K.V. Truong¹, S.M. Shin^{1,*}, Y.S. Choi¹, S.H. Jeong², and B.R. Cho³

¹ Department of Systems Management & Engineering, Inje University, Gimhae, 621-749, South Korea

² College of Pharmacy, Pusan National University, Busan, 609-735, South Korea

³ Department of Industrial Engineering, Clemson University, Clemson, SC 29643, U.S.A.

Abstract— In regenerative medicine industry, one of the key problems is to reduce variation of output characteristics so that a generic drug can pass the statistical criteria for bioequivalence tests. Quality by design (QbD) is a set of offline tools in which robust design (RD) plays significant role in controlling variance in the pharmaceutical process recently. The conventional RD approach basically deals with static data while the bioequivalence tests require dynamic (time-oriented) data. The primary objective of this paper is to develop a new RD approach with time-oriented responses to bioequivalence tests for generic drug. Because the responses are a function of control factors and time, it is reasonable that the tentative relationship can be analyzed according to both vertical and horizontal directions in which the response surface methodology (RSM) is utilized. For seeking the optimal control factors setting, a mean squared error (MSE) robust design model is chosen and optimized by utilizing Matlab package. A experimental study is conducted to demonstrate how to apply proposed RD approach in practice and how can it be used to improve the quality of generic drug for meeting statistical criteria of bioequivalence tests.

Keywords— Robust design, Quality by Design, Regenerative Medicine, Time-oriented Responses, Response surface methodology.

I. INTRODUCTION

Robust design (RD) is an enhanced process/product design methodology for determining the best factor settings while minimizing process variability and bias (i.e., the deviation from the target value of a product). The primary procedure of RD includes experimental design, model parameters estimation, and optimization to obtain the optimal factor settings. By exploiting the information about the relationships between input factors and output responses from an experimental design, RD methods determine the robust solutions which are less sensitive to input variations.

As an early attempt to the RD research, Vining and Myers (1990) introduced the dual response approach based on response surface methodology (RSM) in which the response functions of process mean and variance are estimated separately. By this way, it may achieve the primary

goal of robust design by minimizing the process variability while adjusting the process mean at the target. However, Lin and Tu (1995), pointing out that the robust design solutions obtained from the dual response model may not necessarily be optimal, since this model forces the process mean to locate at the target value, proposed the mean-squared error (MSE) model by relaxing the zero-bias assumption. While allowing some process bias, the resulting process variance is less than or at most equal to the variance obtained from the Vining and Myers' model. Hence, the MSE model may provide better (at least equal) robust design solutions unless the zero-bias assumption must be met. Further modifications to the mean-squared error model have been discussed by Cho et al. (2000) and Shin and Cho (2005). Recently, Kovach et al. (2008) studied on optimal robust design solutions by using the indirect optimization algorithm and physical programming, respectively. Shin and Cho (2009) proposed a biobjective RD optimization model using a lexicographic weighted Tchebycheff approach. This model might provide a more comprehensive set of solutions than the conventional dual-response and MSE models.

Even though the development of RD marks an obvious progress so far, it would seem that all solved RD problems based on static data sets in which all observed mean and variance values are obtained over experimental runs at a given time. This paper aims to apply robust design techniques to pharmaceutical time-oriented responses to bioequivalence tests for generic drug. At each experimental runs, mean and variance values are measured over time. New models for mean and variance functions were also developed. Intrinsically, the responses are a function of control factors and time. So, it is reasonable that the tentative relationship can be analyzed according to both vertical and horizontal directions. The response surface methodology (RSM) is utilized for both directions of analysis. For seeking the optimal control factor settings, a MSE robust design model is chosen and optimized by using Matlab package. The remainder of this paper is organized as follows: Mathematical model development is presented in section II. In Sections III, experiments and results are performed based on an experimental study in pharmaceutical industry. Finally, conclusions are addressed in Section IV.

$$\mathbf{Y}_c = [1 \ x_1 \ x_2 \ \dots] \times \mathbf{m}_c \quad (3)$$

where \mathbf{m}_c can be estimated by normal equation:

$$\mathbf{m}_c = (\mathbf{X}^T \mathbf{X})^{-1} \mathbf{X}^T \mathbf{Y}_c \quad (4)$$

Once the model for each column is established, the vertically general form of the relationship between \mathbf{Y} and \mathbf{X} can be expressed as:

$$\mathbf{Y} = [1 \ x_2 \ x_3 \ \dots] \times \mathbf{M}_c \quad (5)$$

in which \mathbf{M}_c is a matrix of parameters vertical analysis:

$$\mathbf{M}_c = [\mathbf{m}_{c1} \ \mathbf{m}_{c2} \ \dots \ \mathbf{m}_{cm}] = (\mathbf{X}^T \mathbf{X})^{-1} \mathbf{X}^T \mathbf{Y} \quad (6)$$

While vertical analysis can express the relationship between responses \mathbf{Y} and control factors \mathbf{x} represented by design matrix \mathbf{X} , horizontal analysis also proposed to build the relationship between responses \mathbf{Y} and time t . In horizontal direction, let $\mathbf{Y} = [\mathbf{Y}_{r1}; \mathbf{Y}_{r2}; \dots; \mathbf{Y}_{rm}]$ is the matrix of mean responses in which $\mathbf{Y}_{r1}, \mathbf{Y}_{r2}, \dots$ and \mathbf{Y}_{rm} are row vectors in the Table 1. Choosing the models for rows of \mathbf{Y} (\mathbf{Y}_r), each row \mathbf{Y}_r will be a function of t :

$$\mathbf{Y}_r = \mathbf{m}_r \times [1 \ t \ \dots]^T \quad (7)$$

in which \mathbf{m}_r can be estimated by normal equation:

$$\mathbf{m}_r = (\mathbf{X}^T \mathbf{X})^{-1} \mathbf{X}^T \mathbf{Y}_r \quad (8)$$

Once the model for each row is built, the horizontally general form of the relationship can be derived as:

$$\mathbf{Y} = \mathbf{M}_{r_mean} \times [1 \ t \ \dots]^T \quad (9)$$

where $\mathbf{M}_{r_mean} = [\mathbf{m}_{r1} \ \mathbf{m}_{r2} \ \dots \ \mathbf{m}_{rm}]^T$ is the matrix of parameters for horizontal analysis.

The results of two directions analysis from Equations (5), (6) and (9) can be combined into the following general relationship of \mathbf{Y} as a function of \mathbf{x} and t can be showed:

$$\mathbf{Y}(\mathbf{x}, t) = [1 \ x_1 \ x_2 \ \dots] \times (\mathbf{X}^T \mathbf{X})^{-1} \mathbf{X}^T \mathbf{M}_{r_mean} [1 \ t \ \dots]^T \quad (10)$$

In Table 1, both of time oriented-mean and variance responses are available. Similarly, the empirical relationships between variance and control factors are developed. The functional form of variance model can be expressed as:

$$\mathbf{S}(\mathbf{x}, t) = [1 \ x_1 \ x_2 \ \dots] \times (\mathbf{X}^T \mathbf{X})^{-1} \mathbf{X}^T \mathbf{M}_{r_var} [1 \ t \ \dots]^T \quad (11)$$

C. Proposed Time-Oriented Responses Robust Design Models and Optimization

Once the general relationship is established, the next stage of robust design procedure is choosing the robust design model in order to perform optimization in stage 3 to obtain the optimal setting of control factors \mathbf{x}^* . A norm p – MSE robust design model is proposed as follows:

$$\begin{aligned} & \text{minimize} \quad \sum_{i=1}^m (|\mathbf{Y}(\mathbf{x}, t_i) - \mathbf{T}_{ii}|)^p + \sum_{i=1}^m (|\mathbf{S}(\mathbf{x}, t_i)|)^p \quad (12) \\ & \text{S.t. } \mathbf{x} \in \Omega \end{aligned}$$

in which \mathbf{T}_{ii} 's are the targets of responses.

In this paper, norm $p = 2$ is chosen for MSE robust design model optimization.

III. EXPERIMENTS AND RESULTS

A. Experiments and Data Collection

To illustrate the proposed methodology, a gelation study of medicine was conducted in which two control factors of PEO (x_1) and PEG (x_2) were chosen. The time-oriented responses are gelation measurements of medicine collected from 0.5 hour to 5 hour (as described in Table 1). At each time, there are 6 experimental runs and four replications for each experimental run (as described in Table 2). In the **Error! Reference source not found.** below, the data y_i is the column of mean values and s_i^2 is the column of variance values of experimental runs. The main purpose of study is finding the optimal setting of control factors so that the mean responses \mathbf{y} (gelation measurements) are near the targets and the variances \mathbf{s} can be reduced as much as possible. For somewhat reasons, the experimental data cannot be published.

B. Results

With available data, interaction model (first order for x_1 and x_2 and their interaction x_1x_2) is applied for vertical analysis and second order model is applied for horizontal analysis for both mean and variance response models. With available data, the R-square values of mean functions for both of direction analysis range from 0.735 to 0.999 while those of variance functions range from 0.07 to 0.98.

After obtaining model parameters for mean and variance functions, The results hereafter are applied to the proposed time-oriented responses robust design models in Equation (12). After optimizing, the control settings and optimal solutions can be obtained as Table 3 follows:

Table 3 Optimal solutions for gelation study

RD model	x_1	x_2	PEO (%)	PEG (%)	Y_1 opt	Y_2 opt	Y_3 opt	Y_4 opt	Y_5 opt	Y_6 opt	Y_7 opt
MSE	94.26	140.04	67.31	148.57	38.06	48.25	57.34	65.32	77.99	86.25	90.10
Targets					37.75	47.61	56.71	65.54	77.55	88.42	88.81

Following figures illustrates the results gelation study. Figure 1 shows the mean responses and targets over time, the Figure 2 represents targets and optimal responses obtained by applying proposed methodology.

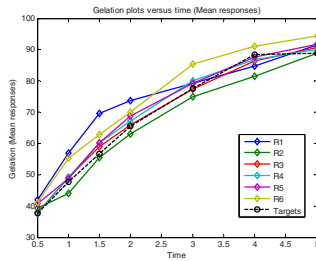


Fig. 1 Mean responses and targets versus time of gelation study

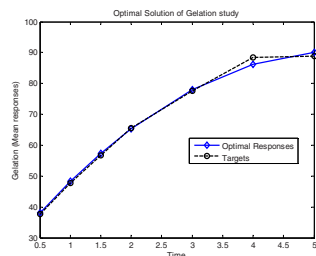


Fig. 2 Optimal solution of gelation study

IV. CONCLUSIONS

In this paper, a new RD model is proposed to apply on time-oriented responses in pharmaceutical industry. This RD model provides a useful tool to deal with time-oriented data that frequently happen in practice. For illustration, a experimental study from pharmaceutical industry is performed to show how to apply the improved methodology on the real situation. By using new RD model, an optimal control setting can be obtained so that the optimal responses are as close as the targets possible while the variances are reduced.

ACKNOWLEDGMENT

This work was supported by the Korea Science and Engineering Foundation (KOSEF) grant funded by the Korea government (MOST) (No. R01-2007-000-21070-0).

REFERENCES

1. Box and Draper, 1987. Empirical model building and response surface. New York: John Wiley & son.
2. Cho, B.R., Kim, Y.J., Kimber, D.L. and Phillips, M.D., 2000. An integrated joint optimization procedure for robust and tolerance design. *International Journal of Production Research*, 38(10), 2309-2325.
3. Khuri, A.I. and Cornell, J. A., 1987. *Response Surface: Design and Analyses*. New York: Marcel Dekker.
4. Kovach, J., Cho, B.R. and Antony, J., 2008. Development of an experiment based robust design paradigm for multiple quality characteristics using physical programming, *International Journal of Advanced Manufacturing Technology*, 35, 1100-1112.
5. Lin, D.K.J. and Tu, W., 1995. Dual response surface optimization: A fuzzy modeling approach. *Journal of Quality Technology*, 27, 34-39.
6. Myers and Montgomery, 2002. Response surface methodology, process and product optimization using design experiments. A Wiley-Interscience Publication.
7. Myers, R.H., 1999. Response Surface methodology current status and future direction (with discussions), *Journal of Quality Technology*, 31, 30-74.
8. Shin, S.M. and Cho, B.R., 2005. Bias-specified robust design optimization and an analytical solutions. *Computers & Industrial Engineering*, 48, 129-148.
9. Vining and Myers, 1990. Combining Taguchi and response surface philosophies: a dual response design. *Journal of quality technology*, 22(1), 38-45.

Cerebral Palsy Classification Using Heuristics and Belief Decision Tree: A Preliminary Study

T.T. Dao¹, F. Marin¹, F. Mégrot², and M.C. Ho Ba Tho¹

¹ UTC – CNRS UMR 6600, Biomécanique et Bioingénierie, France

² UCAMM - Centre de Médecine Physique et de Réadaptation pour Enfants de Bois-Larris, 60260 LAMORLAYE, France

Abstract— The objective of this present study was to classify two types of spastic cerebral palsy pathology such as diplegia and hemiplegia with belief labels. The discrimination process aims to predict new issues of cerebral palsy in case of uncertain classification. The Belief theory was applied to perform uncertain and imprecise classification. Following data were provided by the Bois Larris Center: Clinical kinematics, kinetics, and muscle activity parameters of the cerebral palsy were acquired motion analysis, forces platforms and Electromyography (EMG) system. An extraction parameter process was developed to reveal significant characters from kinematics, kinetics, and EMG curves. A heuristics-based belief assignment method was developed to distribute the mass function of each subject based on their extracted parameters. Belief decision tree method was used to develop uncertain classification model. A preliminary clinical application of 10 subjects (5 diplegias and 5 hemiplegias) was performed. Significant kinematics and kinetics parameters of the cerebral palsy such as ground reaction forces, contact time between the ground and the foot, maximal tension muscle and EMG-based average rectified voltage of the muscles were reported and discussed. Preliminary clinical findings of cerebral palsy classification were addressed in order to help clinicians in their diagnosis, decision-makings, and communications. We showed that Belief formalism was a universal formalism to classify cerebral palsy subjects with belief level.

Keywords— Classification, Discrimination, Cerebral Palsy, Belief Decision Tree, Heuristics, Diplegia, Hemiplegia.

I. INTRODUCTION

Cerebral palsy (CP) is an orthopaedics disease of children. The diagnosis and treatment are performed in early childhood to improve the clinical treatment quality. CP children support an abnormality of the immature brain due to a non-progressive brain's lesion [1].

The theory of belief functions or the theory of evidence has been known as Dempster–Shafer theory [2], [3]. The interpretation of belief theory as generalization of probability has been published in the 1990s [4], [5]. Many real-world problems were solved using this universal formalism such as valuation-based systems for the oil

wildcatter problem [6], the estimation of future climate change [7], the image fusion under imprecision [8], the confidence of telecommunication expert [9], the stochastic ordering [10], the postal address recognition [11]. However, there are few applications of belief functions in biomechanics fields, except for the classification of knee function [12].

Belief decision tree method is a classification method which has been developed recently based on belief functions [13], [14]. This method deals with a universal formalism for classifying uncertain classes with belief level. Furthermore, its promising applications are welcome to any field of sciences when performing uncertain discrimination [15].

CP children were classified clinically based on morphological deformities into three main types as spastic diplegia, hemiplegia, and quadriplegia. Classification of cerebral palsy aims to help the clinicians in their clinical diagnosis, decision-makings (as physical therapy steps and surgery planning) and communications. In literature, clinical studies related to classification and/or clustering of cerebral palsy were developed recently such as the discrimination between dynamic tightness and fixed contracture [16], and the discrimination between healthy and spastic diplegia form of CP [17]. A systematic review of different types of kinematics and kinetics data and analysis methods used to classify and/or cluster the cerebral palsy such as qualitative and quantitative pattern recognition, Hidden Markov models, support vector machine, etc. was also performed [18]. However, there is no study related to classify the cerebral palsy with uncertain classes. This means that each subject must be classified with a belief level according to used subjects, measurement tool, type of gait kinematics, kinetics, and EMG variables, anatomical level.

The present study aims to develop an uncertain classification process of cerebral palsy using a heuristics-based belief assignment method and belief decision tree method. This helps clinicians to classify two main types of cerebral palsy (diplegia and hemiplegia) with belief label automatically based on gait kinematics, kinetics, and EMG parameters.

II. MATERIALS AND METHODS

A. Methodology

A computational diagram of cerebral palsy classification process using belief functions is presented in Fig 1. First of all, kinematics parameters were measured by VICON motion system. Ground reaction forces and moments were acquired simultaneously using AMTI forces platforms at 100 Hz. Muscle activities were measured using Electromyography (EMG) system. All acquisitions were stored in C3D format to further processing. Then, a parameter extraction process was performed to extract significant parameters from kinematics, kinetics, and EMG curves. A heuristics-based belief assignment method was developed in order to distribute the belief level of each cerebral palsy subject. Belief level based on significant parameters extracted from kinematics, kinetics, and EMG acquisitions. Finally, a belief decision tree was developed to classify the cerebral palsy into two groups as Diplegia and Hemiplegia with belief labelled classes.

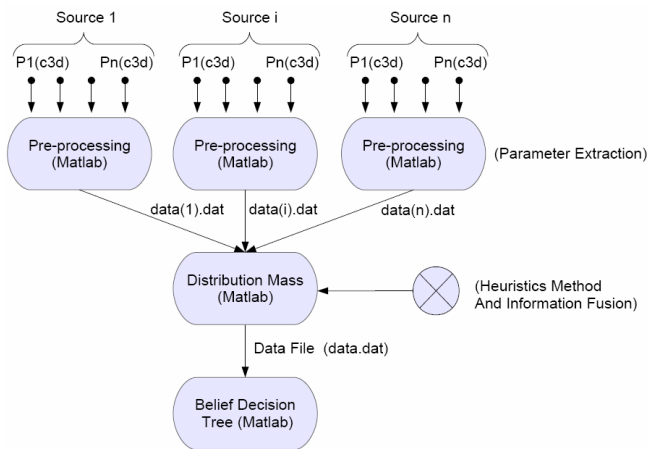


Fig. 1 Computational diagram of cerebral palsy classification using belief functions (each source i corresponds to kinematics or kinetics or EMG acquisition)

B. Extraction Parameter Process

Gait analysis deals with different kinds of data such as kinematics, kinetics, and EMG data. However, acquired data were always in form of temporal curves which are difficult to be interpreted clinically. Consequently, parameter extraction is necessary in order to select significant characters of temporal curves of kinematics, kinetics, and EMG data.

The extraction of kinetics parameters such as contact forces and contact times in heel strike and toe off phases of ground reaction forces was proposed (Fig. 2). Maximal

EMG and average rectified voltage (AFV) were selected as EMG parameters (Fig. 3).

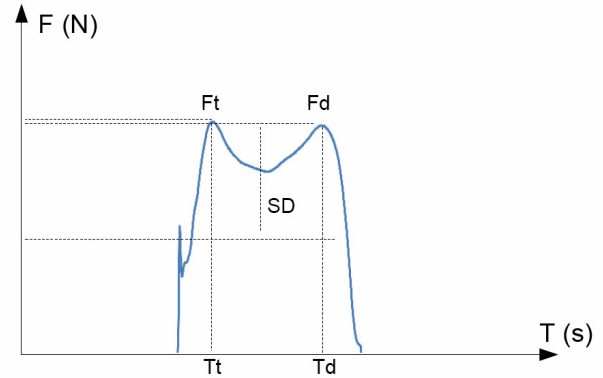


Fig. 2 Selected parameters extracted from kinetics curves: F_t (T_t), F_d (T_d) are forces (times) in heel strike and toe off phases respectively

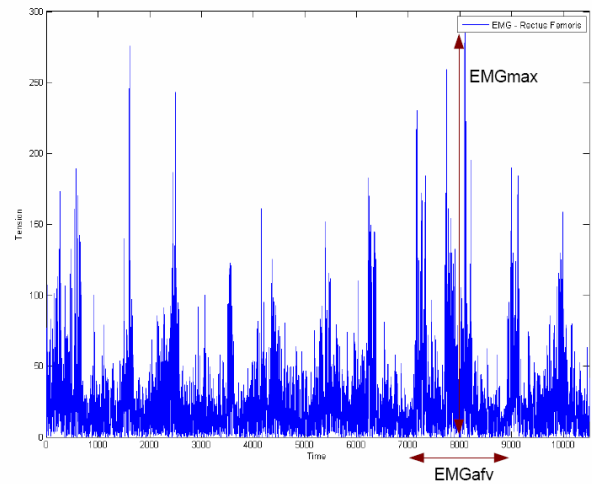


Fig. 3 Selected parameters extracted from EMG temporal curves: EMG_{max} and EMG_{afv} are maximal EMG and average rectified voltage of rectus femoris muscle

C. Heuristics-Based Belief Assignment Method

In order to quantify the belief level of each classification, a heuristics-based belief assignment method was developed. Two criteria were defined based on parameters extracted from ground reactions forces and EMG curves. The former deals with the difference between ground reactions forces in heel strike and toe off phases whereas the latter deals with the magnitude of EMG-based average rectified voltage of muscle. These parameters were standardized by the maximal value of all acquisitions. More precisely, the greater this difference and this magnitude are, the greater

the belief of cerebral palsy pathology is. Note that C is defined as the belief in the case of pathology; not C is defined as the belief in the case of normal; θ is defined as the belief in the case of unknown decision.

D. Belief Decision Tree Method

Belief decision tree is the combination of standard decision tree and belief functions. Basic elements of a belief decision tree consisted of a decision node, an edge, and a leaf with uncertain label. Averaging approach was selected to define the attributes selection measures based on extended gain criterion of the information theory of Shannon. A mean value was used as partitioning strategy. The growth process of belief decision tree was stopped when there are no more attributes to be tested [13].

E. Experimental Data

Ten cerebral palsy subjects (5 diplegia and 5 hemiplegia subjects) were participated in kinematics, kinetics, and EMG acquisitions.

III. RESULTS

Extracted parameters of kinetics and EMG data are presented in Table 1. Ground reaction forces were measured in Newton whereas contact time was measured in second. EMG-based average rectified voltage was measured in mV.

Table 1 Extracted parameters of kinetics and EMG data: example of spastic diplegia (Ft and Fd are the ground reaction forces in heel strike and toe off phases respectively; Tt and Td are the times in heel strike and toe off phases respectively; L and R are left and right sides; EMGafv is average rectified voltage)

Parameters	Subject 1	Subject 2	Subject 3	Subject 4	Subject 5
FtL	521	366	463	424	563
TtL	3598	4238	5842	3173	5129
FdL	465	333	256	294	412
TdL	4164	4934	6432	3827	6565
FtR	582	336	279	358	428
TdR	2607	5188	6781	2202	6641
FdR	498	262	200	293	290
TdR	3193	5747	7231	2883	7549
EMGafvR	35	33	87	57	74
EMGafvL	23	30	74	61	74
Class	Dip	Dip	Dip	Dip	Dip

The mass distributions of all subjects based on the difference of ground reactions forces of heel strike and toe off phases (Table 2) and EMG-based average rectified voltage were calculated. The mass distribution of the combination of the difference of ground reactions forces of heel strike and toe off phases and EMG-based average rectified voltage was carried out as input data in order to develop the belief decision tree of the cerebral palsy.

Table 2 The mass distributions based on the difference of ground reactions forces of heel strike and toe off phases: some examples

Diplegia			Hemiplegia		
C	Not C	θ	C	Not C	θ
0.6087	0	0.3913	0.3108	0	0.6892
0.5362	0	0.4638	0.4054	0	0.5946
1	0	0	1	0	0
0.6280	0	0.372	0.6552	0	0.3448
1	0	0	1	0	0
0.0145	0	0.9855	0.5811	0	0.4189
0.0362	0	0.9638	0.8514	0	0.1486
0.0435	0	0.9565	0.527	0	0.473
0.087	0	0.923	0.5946	0	0.4054
0.0507	0	0.9493	0.7568	0	0.2432

Based on the gain ratio of all attributes, the most significant parameters were calculated such as ground reaction force during heel strike phase of the right foot, ground reaction force during toe off phase of the left foot, and EMG-based average rectified voltage of the right rectus femoris muscle. Belief decision tree of the cerebral palsy is presented in Fig 4.

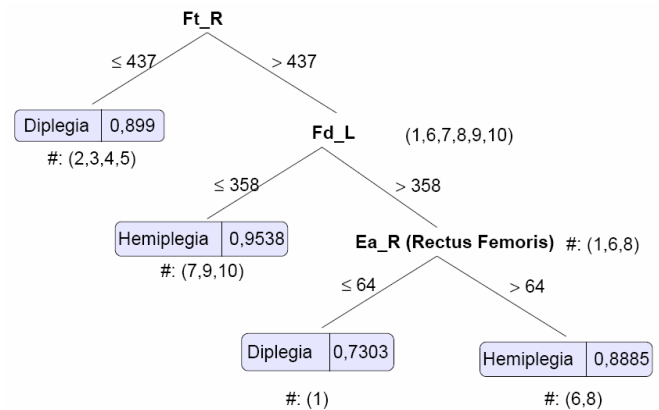


Fig. 4 Belief decision tree of cerebral palsy

IV. DISCUSSION

The methodology showed flexible development architecture of the uncertain classification model. Each data source was treated separately and it is easy to add others sources data without changing the development architecture.

The combination of two proposed criterions increased considerably the mass function distribution of each criterion, so others significant criterions should be added in order to improve the accuracy of classification model.

The belief decision tree of cerebral palsy showed an impact of the ground reactions forces and EMG-based average rectified voltage for classifying two types of cerebral palsy such as spastic diplegia and hemiplegia. The combination of belief functions and standard decision tree permitted to develop a universal formalism in case of uncertain classification.

In this preliminary study, kinetics and EMG data were only used to perform uncertain classification. However, kinematics data are necessary to be taken into account, especially for the joint angles due to morphological deformities of cerebral palsy subjects.

One of the limitations of this present study is the smaller quantity of computed data. Consequently, the validation may not be performed to calculate the sensitivity and the specificity of developed classification model.

V. CONCLUSIONS AND PERSPECTIVES

The uncertain classification of two types of cerebral palsy was developed using belief functions and decision tree method. A heuristics-based belief assignment method was developed in order to distribute the mass function of all subjects according to their kinetics and EMG acquisitions. A preliminary belief decision tree of cerebral palsy was performed. Clinical findings were discussed based on significant parameters such as ground reaction force during heel strike and toe off phases and EMG-based average rectified voltage of the rectus femoris muscle.

In perspectives, more pathological subjects will be required to improve the accuracy of the uncertain classification model. Clinical validation will be performed before the development of a belief-based computer-aided decision system to help clinicians in their decision-makings and communications.

REFERENCES

- Blair E, Watson L (2005) Epidemiology of cerebral palsy. *Semin Fetal Neonatal Med*, pp. 1–9.
- Dempster, A (1967) Upper and lower probabilities induced by multivalued mapping. *Annals of Mathematical Statistics*, 38, pp. 325–339.
- Shafer, G (1976) *A mathematical theory of evidence*. Princeton: Princeton University Press, 1976.
- Smets, P, (1990) The combination of evidence in the transferable belief model. *IEEE Transaction on Pattern Analysis and Machine Intelligence*, 12, pp. 447–458.
- Smets, P (1997) The normative representation of quantified beliefs by belief functions, *Artificial Intelligence*, 92, pp. 229–242.
- Xu, H (1997) Valuation-based systems for decision analysis using belief functions, *Decision Support Systems*, 20, pp. 165–184.
- Kriegler, E, Held, H (2005) Utilizing belief functions for the estimation of future climate change, *International Journal of Approximate Reasoning*, 39, pp. 185–209.
- Bloch, I (2008) Defining belief functions using mathematical morphology. Application to image fusion under imprecision, *International Journal of Approximate Reasoning*, 48, pp. 437–465.
- Yang, SL, Fu, C, (2009) Constructing confidence belief functions from one expert, *Expert Systems with Applications*, 36, pp. 8537–8548.
- Denoeux, T (2009) Extending stochastic ordering to belief functions on the real line, *Information Sciences*, 179, pp. 1362–1376.
- Mercier, D, Cron, G, Denoeux, T, Masson, MH, (2009) Decision fusion for postal address recognition using belief functions, *Expert Systems with Applications*, 36, pp. 5643–5653.
- Jones, L, Beynon, MJ, Holt, CA, Roy, S (2006) An application of the Dempster–Shafer theory of evidence to the classification of knee function and detection of improvement due to total knee replacement surgery, *Journal of Biomechanics*, 39, pp. 2512–2520
- Elouedi, Z, Mellouli, K, Smets, P (2001) Belief decision trees: theoretical foundations, *International Journal of Approximate Reasoning*, 28, pp. 91–124.
- Vannoorenberghe, P (2004) On aggregating belief decision trees, *Information Fusion*, 5, pp. 179–188.
- Trabelsi, S, Elouedi, Z, Mellouli, K, (2007) Pruning belief decision tree methods in averaging and conjunctive approaches, *International Journal of Approximate Reasoning*, 46, pp. 568–595.
- Zwick, EB, Leistriz, L, Milleit, B, Saraph, V, Zwick, G, Galicki, M, Witte, H, Steinwender, G (2004) Classification of equinus in ambulatory children with cerebral palsy – discrimination between dynamic tightness and fixed contracture, *Gait and Posture*, 20, pp. 273–279.
- Zhang, BL, Zhang, Z, Begg, R (2009) Gait classification in children with cerebral palsy by Bayesian approach, *Pattern Recognition*, 42, pp. 581–586.
- Dobson, F, Morris, ME, Baker, R, Graham, HK (2007) Gait classification in children with cerebral palsy: A systematic review, *Gait & Posture*, 25, pp. 140–152.

Corresponding author:

Author: Tien Tuan DAO
 Institute: Université de Technologie de Compiègne
 Street: Centre de Recherches de Royallieu
 City: Compiègne
 Country: France
 Email: tien-tuan.dao@utc.fr

Test for Determinism and Nonlinearity in Near Infrared Spectroscopy Data

N.T. Dzung

Department of Electronics and Informatics, Faculty of Electronics and Telecommunications,
Hanoi University of Technology, Hanoi, Vietnam

Abstract— In this study, dynamical properties in brain activity have been analyzed by means of observed near infrared spectroscopy (NIRS) data at the area of brain of primary motor. Nonlinear properties are investigated by using the methods of delay vector variance (DVV) and data surrogate. The result shows that the underlying processes of the change of oxygenated-hemoglobin and deoxygenated-hemoglobin concentration are highly stochastic. The number of NIRS time series exhibiting nonlinearity in the task of imagery of movement is larger than that in the task of relax. In addition, the level of nonlinearity in such the dynamical processes is rather low.

Keywords— nonlinear analysis, surrogate, near infrared spectroscopy (NIRS).

I. INTRODUCTION

Understanding the detail of an underlying process is very important in any signal processing applications. The information about such processes helps to choose appropriate modeling and techniques for processing. In some cases of the biomedical field, especially concerned in the brain activity, the information of underlying processes may provide the health condition [1,2], physiological states [3,4] of a subject, or support for diagnostic purposes [5,6,7,8], etc. In addition, the brain activity can be observed by various kinds of methods, i.e. electroencephalographic (EEG), event-related potentials (ERP), functional magnetic resonance imaging (fMRI), positron emission tomography (PET), single positron emission computed tomography (SPECT), magneto encephalography (MEG), and near infrared spectroscopy (NIRS). Recently, NIRS is developed and used for recording the changes in human brain. It is a noninvasive optical method with advantages over the other ones in terms of low noise, portability, safety, and low cost. Thus, NIRS is seen as a good candidate for future applications [9], especially for brain-computer interface [10,11].

In particular, NIRS enables to measure concentration change in oxygenated hemoglobin (Oxy-Hb), deoxygenated hemoglobin (DeOxy-Hb) (see [12] and therein) during functional brain activation. The sum of Oxy-Hb and DeOxy-Hb concentration is related to human cortical activation. Accordingly, the relationship between brain oxygen metabolic and brain activation can be interpreted [12,14]. In other

words, several types of brain activities can have been accessed, including motor activity, visual activation, auditory stimulation, and the performance of cognitive tasks [15] through analysis on measured NIRS signals.

To my best knowledge, most of research on NIRS signals, to date, focuses on photons interact with the tissue under the modified Beer-Lambert Law [15], blood flow effect impacts on NIRS ([16] and therein), homodynamic changes in the cerebral cortex [17], etc. Some of them consider brain activation corresponding to human physical movements via NIRS signals, for example, finger tapping task [14], blood oxygenation levels in the case of complex task with workload [12,13], and so on. However, so far, the change in Oxy-Hb and DeOxy-Hb concentration has not been investigated under viewpoints of dynamical theory, by which there is the possibility of unveil dynamical properties of systems generating signals [18].

In the present paper, NIRS data measured from human brain is used for testing nonlinearity and determinism of underlying processes by means of method of data surrogate. This can be seen as the primitive step for further investigation of the underlying system, for example, model building. The discrimination of variance of delay vector is calculated and used in the analysis. The aim of this study is to find the answer for the question that the change in Oxy-Hb and DeOxy-Hb concentration is caused by linear or nonlinear and deterministic or stochastic processes at the area of brain of primary motor. The result shows that the underlying processes of the change of Oxy-Hb and DeOxy-Hb concentration are highly stochastic. The number of NIRS time series exhibiting nonlinearity in the task of imagery is larger than that in the task of relax. In addition, the level of nonlinearity in such the dynamical processes is rather low.

II. MATERIALS AND METHODS

A. The NIRS Data

The equipment, subject and recording of the NIRS Data

The available NIRS instrument (OMM-3000 from Shimadzu Corporation, Japan) for acquiring Oxy-Hb and DeOxy-Hb concentration changes during cognitive tasks. This

instrument operates at three different wavelengths of 780nm, 805nm and 830nm. The data will be acquired at the sampling rate of up to 40Hz and digitalized by 16-bit analog to digital converters.

In this study, three healthy people are chosen to provide NIRS data. Different tasks done by subjects are of rest and imagery of movement. Each subject is in the status of relax in the task of rest, and looking at a walking body on the screen in the task of imagery of movement. According to functional brain map [19], the positions of emitters and receivers should be placed in the area of primary motor. NIRS data is recorded from twenty two channels as displayed in Fig. 1. The purpose of taking these tasks is to check nonlinearity for underlying processes at the corresponding activated area of brain. There, the red and blue circular points are for emitters and receivers, respectively. The channels are numbered between pairs of emitters and receivers. In addition, the sampling interval is set at 130ms, and recording is taken around over twenty minutes for each cognitive task. The number of 9385 data points in every channel is used for analysis.

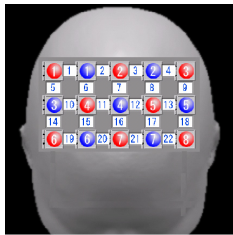


Fig. 1 Location of emitters and receivers

B. The Mathematical Tools

In this section, tools employed in the analysis are briefly presented. They are surrogate algorithms and the DVV method.

a) Surrogate Data

Surrogate data techniques can be used for accessing the presence of nonlinearity [4], non-stationary [21,20] as well as determinism versus stochastic [25] in the time series by means of testing specific hypotheses. In general, to apply the surrogate techniques to test if a time series possesses the interested properties P, null hypothesis is selected, which assumes that time series has a property Q opposite to P. Specifically, a set of surrogate time series is artificially generated such that some statistical properties of original time series, which belong to Q, are preserved in the surrogate ones while destroying all others. Then, suitable discriminating statistic(s) is computed for both the surrogates and original time series. If the discriminating statistic of

original time series significantly deviates from that of surrogate time series, the null hypothesis is rejected. In other words, the test time series possesses the property P other than Q. In practical, there are many methods existing for the generation of surrogate time series [22]. In this study, nonlinearity and determinism are tested, thus, three successful algorithms are employed to generate surrogate data, i.e. Fourier Transform (FT) [4], Fourier Shuffle (FS) [23] and iterative Amplitude Adjusted Fourier Transform (iAAFT) [24]. The algorithm of iAAFT is an improvement of Amplitude Adjusted Fourier Transform (AAFT) [4]. In addition, the FT surrogate preserves power spectrum but does not preserve the empirical histogram. In contrast to the FT surrogate, the FS surrogate preserves the empirical histogram but does not preserve power spectrum. The iAAFT generated surrogates have amplitude spectra similar and amplitude distributions identical to those of the original time series. It preserves both the empirical histogram and power spectrum. The steps to generate surrogate time series in each algorithm can be briefly described below.

The steps in the FT algorithm are:

- (1) The Fourier transform is applied to the original data to obtain amplitude and a phase at each frequency.
- (2) At each frequency, the phase is randomized by Gaussian random numbers.
- (3) The result surrogate data is obtained by applying the inverse Fourier transform to the data at the second step.

The steps in the FS algorithm are:

- (1) The FT surrogate data is generated.
- (2) The original data is shuffled in such a way that its rank order is identical to that of the FT surrogate data. The rank order is the order of the state values in the time series.

The steps in the iAAFT algorithm are:

- (1) The power spectrum of original time series is estimated by Fourier transform.
- (2) The FS surrogate data of original time series is generated.
- (3) The Fourier transform is applied to the FS surrogate data. Here, at each frequency, the amplitude is replaced by that of the result time series in the first step, while the phase is preserved.
- (4) The inverse Fourier transform is applied to the time series obtained at the third step.
- (5) The original time series is reordered to obtain the same rank order as that of time series resulted by the fourth step. The reordered time series is the iAAFT surrogate.
- (6) Above steps are repeated by replacing the FS surrogate with the iAAFT in the third step until the discrepancy between the amplitude of the original and the iAAFT from fifth step is sufficiently small.

In fact, surrogate is a statistic test, thus, the confidence in the test is proportional to the number of generated surrogate time series.

b) The Method of Delay Vector Variance

Recently, the delay vector variance (DVV) [25,26] has been considered as a good method in detecting nonlinearity and determinism of underlying process from time series. In other words, DVV give a unified analysis of the predictability and the degree of nonlinearity, and the analysis result can be visually straightforward interpreted. The DVV used for testing some benchmark models, and it has presented an advantage (see [25] for comparison) over other nonlinearity methods such as Casdagli's Deterministic versus Stochastic (DVS) [28], Kaplan's $\delta-\epsilon$ [29] or traditional nonlinearity metrics [30]. For such the reason, DVV is chosen to test nonlinearity and determinism in NIRS data in this study. A given time series is represented in the form of delay embedding of $X = \{x(k) | k = 1, \dots, N\}$, where $x(k) = [x_{k-(m-1)\tau}, x_{k-(m-2)\tau}, \dots, x_k]$ is a delay vector (DV) with a given embedding m [31] and delay τ [32], and x_i is data point from the time series. The DVV method is summarized as follows.

(1) The mean, μ_d , and standard deviation, σ_d , are computed over all pairwise distance between DVs, $\|x(i) - x(j)\| (i \neq j)$.

(2) The sets $\Omega_k(d)$ is established such that $\Omega_k(d) = \{x(i) | \|x(i) - x(j)\| \leq d\}$. d is a certain distance taken from $[\mu_d - n_d \sigma_d; \mu_d + n_d \sigma_d]$; n_d is a bound parameter controlling the span where the DVV performs analysis. The d chosen to calculate variance is $d(n) = \mu_d - n_d \sigma_d + \frac{2n_d \sigma_d n}{N_d - 1}$, $n = 1 \dots N_d$. N_d is the number of evaluation points such that $N_d = kn_d$, and k is set at 30 in this research.

(3) For every Ω_k , the variance σ_k^2 is calculated. The average over all sets Ω_k , normalized by the variance of time series σ_x^2 , that yields the measure of unpredictability σ^{*2} .

Note that, the variance estimates will be reliable only if the $\Omega_k(d)$ set contains at least 30 DVs. s is chosen to test for determinism and nonlinearity.

The DVV plot is of normalized distance d versus the variance σ^{*2} . The DVV scatter diagram is the combination of the DVV plot of original and surrogate time series. These visual result are directly used for interpreting the

characteristics of underlying process. In addition, indication of nonlinearity can be quantified by root mean squared error (RMSE) between σ^{*2} of the original time series and the σ^{*2} averaged over the DVV plots of the surrogate time series. This degree of unpredictability can be computed as

$$t^{DVV} = \sqrt{\left\langle \left(\sigma^{*2}(d) - \frac{\sum_{i=1}^M \sigma_{s,i}^{*2}}{2} \right)^2 \right\rangle_{\text{valid } d}}$$

Note that, *valid* d is the value of d by which the $\Omega_k(d)$ set contains at least 30 delay vectors.

III. RESULTS AND DISCUSSIONS

In this section, the NIRS data from twenty two channels of different tasks is analyzed to identify characteristics of the change in concentration of Oxy-Hb and DeOxy-Hb in the human brain. The embedding time delay and embedding dimension are computed and they are chosen at 6 and 520ms for embedding dimension and embedding delay, respectively. Shown in Figure 2 is the result for rank test of nonlinearity for three subjects with the tasks of relax and imagery of movement. Note that, the test static of original time series is ranked among totally 200 time series, and a is the rank of test static of original time series in the notion of $\frac{a}{200}$. Because this test is the right-tailed one with the

rejection significance of 0.01, null hypothesis is rejected as the rank a is greater or equal to 199. In the case of rejection, the test result is displayed in a square bracket, “[” and “]”. For the task of relax on a certain subject, the number of NIRS time series exhibiting nonlinearity in task of movement imagery is larger than that in task of relax. Especially, some Oxy-Hb and DeOxy-Hb concentration, there is no channel of NIRS data presenting nonlinearity for the case of task of relax.

In the DVV method, the level of nonlinearity intuitively is higher as the increase in the deviation of a DVV scatter plot of variances of original and surrogate data from the bisector line (see [26]). The level of nonlinearity in both the tasks of Subject 1 is considered by the DVV scatter diagrams only for nonlinear NIRS time series of Oxy-Hb and DeOxy-Hb concentration. The result is obtained for the DVV scatter diagrams of the time series from Oxy-Hb NIRS of Channels 11 and 19 with the task of relax, Channels 4, 10, 11, and 18 with the task of imagery of movement, and from DeOxy-Hb NIRS of Channels 1, 4 13 and 18 with the task of imagery of movement exhibits the low

Channel	Subject 1				Subject 2				Subject 3			
	Relax		Movement Imaginary		Relax		Movement Imaginary		Relax		Movement Imaginary	
	Oxy-Hb	DeOxy-Hb	Oxy-Hb	DeOxy-Hb	Oxy-Hb	DeOxy-Hb	Oxy-Hb	DeOxy-Hb	Oxy-Hb	DeOxy-Hb	Oxy-Hb	DeOxy-Hb
1	132/200	97/200	192/200	[199/200]	77/200	151/200	197/200	172/200	33/200	138/200	191/200	183/200
2	97/200	146/200	193/200	135/200	109/200	142/200	187/200	109/200	97/200	101/200	[200/200]	8/200
3	97/200	78/200	193/200	19/200	79/200	63/200	174/200	176/200	197/200	148/200	136/200	197/200
4	52/200	183/200	[199/200]	[200/200]	192/200	152/200	190/200	[200/200]	133/200	190/200	186/200	196/200
5	110/200	97/200	182/200	76/200	195/200	189/200	167/200	[200/200]	61/200	55/200	[200/200]	[200/200]
6	12/200	33/200	192/200	142/200	108/200	146/200	[199/200]	169/200	187/200	129/200	[200/200]	132/200
7	93/200	15/200	52/200	96/200	45/200	64/200	143/200	128/200	194/200	98/200	83/200	32/200
8	69/200	127/200	97/200	147/200	195/200	48/200	[200/200]	[200/200]	131/200	184/200	[199/200]	197/200
9	34/200	106/200	195/200	155/200	87/200	161/200	175/200	135/200	167/200	111/200	[200/200]	197/200
10	56/200	193/200	[199/200]	109/200	144/200	19/200	105/200	[199/200]	61/200	117/200	[200/200]	196/200
11	[200/200]	148/200	[200/200]	36/200	185/200	[200/200]	141/200	6/200	[199/200]	147/200	198/200	77/200
12	82/200	15/200	186/200	19/200	82/200	78/200	198/200	113/200	141/200	50/200	[200/200]	195/200
13	39/200	74/200	119/200	[200/200]	23/200	5/200	[200/200]	195/200	79/200	85/200	[200/200]	196/200
14	173/200	126/200	186/200	156/200	196/200	13/200	197/200	192/200	[200/200]	15/200	196/200	194/200
15	180/200	91/200	70/200	3/200	112/200	27/200	[199/200]	127/200	60/200	85/200	[199/200]	[199/200]
16	178/200	152/200	189/200	16/200	120/200	87/200	[200/200]	127/200	189/200	135/200	[199/200]	180/200
17	161/200	90/200	35/200	93/200	57/200	186/200	32/200	85/200	105/200	66/200	147/200	[200/200]
18	124/200	74/200	[200/200]	[200/200]	197/200	11/200	[200/200]	198/200	132/200	76/200	[200/200]	[200/200]
19	[200/200]	103/200	185/200	118/200	180/200	142/200	[199/200]	196/200	178/200	166/200	[200/200]	198/200
20	172/200	159/200	42/200	124/200	152/200	85/200	188/200	172/200	23/200	130/200	[200/200]	194/200
21	108/200	197/200	181/200	71/200	114/200	141/200	152/200	114/200	197/200	173/200	[200/200]	70/200
22	163/200	130/200	87/200	5/200	126/200	94/200	196/200	[199/200]	1/200	51/200	198/200	[200/200]

Fig. 2 Test for nonlinearity of NIRS data

level of nonlinearity. The low level of nonlinearity also presents in the NIRS data of the other two subjects.

In addition, the variance σ^{*2} in the DVV method illustrates for the unpredictability, thus, the level of determinism can be interpreted by observing the DVV plots. The DVV plots for Oxy-Hb and DeOxy-Hb concentration of NIRS data of Subject 1 from twenty two channels in the task of relax and movement imagery is with low predictability or most NIRS data is generated by stochastic processes. The analysis on NIRS data of the other two subjects gives the similar result, low predictability.

IV. CONCLUSIONS

In this paper, we have presented the result of nonlinear analysis for search concerning to the dynamical brain activity which has been observed through measured NIRS signals. The result has shown that the changes in concentration of Oxy-Hb and DeOxy-Hb in the tasks of relax and of movement imagery is highly stochastic. Most of NIRS data are generated by linear processes. In addition, the number of NIRS time series exhibiting nonlinearity in the task of movement imagery is larger than in the task of relax. In addition, the level of nonlinearity in such the dynamical processes is rather low.

REFERENCES

- Jells B., van Birgelen J.H, et al. (1999) Decrease of non-linear structure in the EEG of Alzheimer patients compared to healthy controls, *J. Clin. Neurophysiol.* 110:1159-1167.
- Jeong J., Chae T.H., et al. (2001) Nonlinear Dynamic Analysis of the EEG in Patients with Alzheimer's Disease and Vascular Dementia, *J. Clin. Neurophysiol.* 18:58-67.
- Stam C.J., van Woerkom T.C.A.M., et al. (1996) Use of non-linear EEG measures to characterize EEG changes during mental activity, *Electroencephalogr. Clin. Neurophysiol.* 99:214-224.
- Theiler J., Rapp P.E. (1996) Re-examination of the evidence for low-dimensional, nonlinear structure in the human electroencephalogram, *Electroencephalogr. Clin. Neurophysiol.* 98:213-222.
- Lehnertz K., Elger C.E. (1995) Spatio-temporal dynamics of the primary epileptogenic area in temporal lobe epilepsy characterized by neuronal complexity loss, *Electroencephalogr. Clin. Neurophysiol.* 95:108-117.
- Casdagli M.C., Iasemidis L.D., et al. (1997) Non-linearity in invasive EEG recordings from patients with temporal lobe epilepsy, *Electroencephalogr. Clin. Neurophysiol.* 102:98-105.
- Pijn J.P.M., Velis D.N., et al. (1997) Nonlinear dynamics of epileptic seizures on basis of intracranial EEG recordings, *Brain Topogr* 9:249-270.
- Andrzejak R.G., Widman G., et al. (2001) The epileptic process as nonlinear deterministic dynamics in a stochastic environment-An evaluation on mesial temporal lobe epilepsy. *Epilepsy Res.*44:129-140.
- Bunce S.C., Izzetoglu M., et al. (2006) Functional Near-Infrared Spectroscopy, *IEEE Engineering in Medicine and Biology Magazine*, 25:54-62.
- Coyle S.M., Ward T.E., et al. (2007) Brain-computer interface using a simplified functional near-infrared spectroscopy system, *J. Neural Engineering*, 4:219-226.
- Sitaram R., Zhang H., et al. (2007), Temporal classification of multichannel near-infrared spectroscopy signals of motor imagery for developing a brain-computer interface, *NeuroImage*, 34:1416-1427.
- Wobst P., Wenzel R., et al. (2001) Linear aspects of changes in deoxygenated hemoglobin concentration and cytochrome oxidase oxidation during brain activation, *Neuroimage*, 13:520-530.
- Izzetoglu K., Bunce S., et al. (2004) Functional optical brain imaging using near-infrared during cognitive tasks, *Int. J. Human-Computer Interaction* 17:211-231.
- Sato H., Fuchino Y., et al. (2005) Intersubject variability of near-infrared spectroscopy signals during sensor motor cortex activation, *J. Biomed. Optics* 10:044001.1-044001.10.

15. Villringer A., Chance B. (1997) Non-invasive optical spectroscopy and imaging of human brain function, *Trends in Neuroscience* 20:435-442.
16. Tomita M. (2006) Flow effect impacts NIRS, jeopardizing quantification of tissue hemoglobin, *NeuronImage* 33:13-16.
17. Schreiber T. (1999) Interdisciplinary application of nonlinear time series methods, *Phys. Rep.* 308:2-64.
18. Joseph R. (1996) *Neuropsychiatry, Neuropsychology, and Clinical Neuroscience: Emotion, Evolution, Cognition, Language, Memory, Brain Damage, and Abnormal*, Lippincott Williams & Wilkins.
19. Van T.V., Hammer P.E. et al. (2007) Mathematical model for the hemodynamic response to venous occlusion measured with near-infrared spectroscopy in the human forearm, *IEEE Trans. Biomed. Engin.* 54:573-584.
20. Timmer J. (1998) Power of surrogate data testing with respect to non-stationarity, *Phys. Rev. E* 58:5153-5156.
21. Schmitz A., Schreiber T. (1999) Surrogate data for non-stationary signals, Wuppertal preprint WUB-99-9.
22. Schreiber T., Schmitz A. (2000) Surrogate time series, *Physica D* 142:346-382.
23. Chang T., Schifi S.J., et al. (1994) Stochastic versus deterministic variability in simple neuronal circuits: I. Monosynaptic spinal cord reflexes, *Biophys. J.* 67:671-683.
24. Schreiber T., Schmitz A. (1996) Improved surrogate data for nonlinearity tests, *Phys. Rev. Lett.* 77: 635-638.
25. Gautama T., Mandic D.P., et al. (2004) The delay vector variance method for detecting determinism and nonlinearity in time series, *Physica D* 19:167-176.
26. Gautama T., Mandic D.P., et al. (1992) Indications of nonlinear structure in brain electrical activity, *Physical Review E* 67: 046204.
27. Theiler J., Eubank S., et al. (1992) Testing for nonlinearity in time series: the method of surrogate data, *Physica D* 58:77-94.
28. Casdagli M. (1991) Chaos and deterministic versus stochastic nonlinear modelling, *J.R. Statist. Soc. B* 54:303-328.
29. Kaplan D.T. (1994) Exceptional Events as Evidence for Determinism, *Physica D* 73:38-48.
30. Schreiber T., Schmitz A. (1997) Discrimination power of measures for nonlinearity in a time series, *Phys. Rev. E* 55:5443-5447.
31. Takens F. (1981) Detecting strange attractors in turbulence, *Lectures Notes in Mathematics* 898:366381.
32. Fraser A. M., Swinney H. L. (1986) Independent coordinates for strange attractors from mutual information, *Phys. Rev. A* 33:1134-1140.

Author: Nguyen Tien Dzung
Institute: Hanoi University of Technology
Street: 1 Dai Co Viet street
City: Hanoi
Country: Vietnam
Email: dungnt-fet@mail.hut.edu.vn

Multifractality in NIRS Data of Brain Activity

N.T. Dzung

Department of Electronics and Informatics, Faculty of Electronics and Telecommunications,
Hanoi University of Technology, Hanoi, Vietnam

Abstract— We present the evidence that multifractals existing in the near-infrared spectroscopy (NIRS) recorded during imagery tasks of brain. Left- and right-arrow imagery tasks of brain are considered in this study. The method of wavelet transform modulus maxima (WTMM) is employed in the estimation. The result shows that the local Hurst exponent h is in the range from 0 to 0.4 with the maximum around 0.1 in all the trials.

I. INTRODUCTION

Biological signals are generated by complex self-regulating systems with a broad range of characteristics [1,2]. Physiological time series recorded from living body usually have inhomogeneous, non-stationary and fluctuating in an irregular and complex manner. Considering properties of biological signals is essentially necessary for any further treatment. Multifractal formalism provides a scale invariant mechanism of complex systems for the analysis and generation of biological signals. In contrast to monofractal signals, multifractal ones have the different scaling properties and are characterized by a local Hurst exponent h . Multifractality has been found in living systems such as heartbeat dynamics [3], cerebral blood flow [4], etc. In other words, living systems have more than one scaling parameter and therefore those belong to a class of more complex processes.

Recently, near-infrared spectroscopy (NIRS) is developed and used for recording the changes in human brain. It is a non-invasive optical method with advantages over the other ones in terms of low noise, portability, safety, and low cost, thus, NIRS is seen as a good candidate for future applications [5], especially for brain-computer interface [6,7]. In particular, NIRS enables to measure concentration change in oxygenated hemoglobin (Oxy-Hb), deoxygenated hemoglobin (DeOxy-Hb) [8] during functional brain activation in humans. The sum of Oxy-Hb and DeOxy-Hb concentration is related to human cortical activation. Accordingly, the relationship between brain oxygen metabolic and brain activation can be interpreted [8,9,10]. In other words, several types of brain activity can have been accessed, including motor activity, visual activation, auditory

stimulation, and the performance of cognitive tasks [12] through analysis on measured NIRS signals.

NIRS is utilized to monitor the operation of brain areas [7] by means of measures of the change in Oxy-hemoglobin (Oxy-Hb) and DeOxy-hemoglobin (DeOxy-Hb) concentration. Most of research on NIRS signals, to date, focuses on photons interact with the tissue under the modified Beer-Lambert Law [11], blood flow effect impacts on NIRS ([12] and there in), homodynamic changes in the cerebral cortex [13], etc. Some of them consider brain activation corresponding to human physical movements via NIRS signals, for example, finger-tapping task [9], blood oxygenation levels in the case of complex task with workload [8,10], and so on. However, so far, the change in Oxy-Hb and DeOxy-Hb concentration has not been investigated under viewpoints of dynamical theory, by which there is the possibility of unveil dynamical properties of systems generating signals [14].

In this work, multifractality in NIRS data measured during imagery tasks of human brain is reported. This investigation on multifractality of NIRS data helps further development to identify the imagery tasks of brain. In this study, subjects look at left and right arrows on the screen, and NIRS data is measured from two channels as shown in the Figure 1. The emitters and receivers are positioned on the brain area of primary motor.

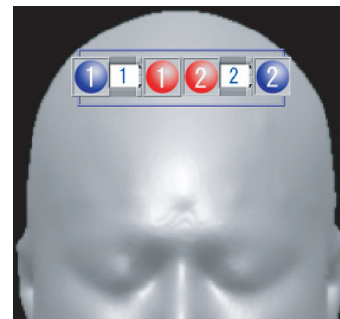


Fig. 1 Position of emitters and receivers

II. DATA AND METHOD

Experiment is carried out on healthy subjects in two minutes. The first and last thirty seconds are relaxing tasks,

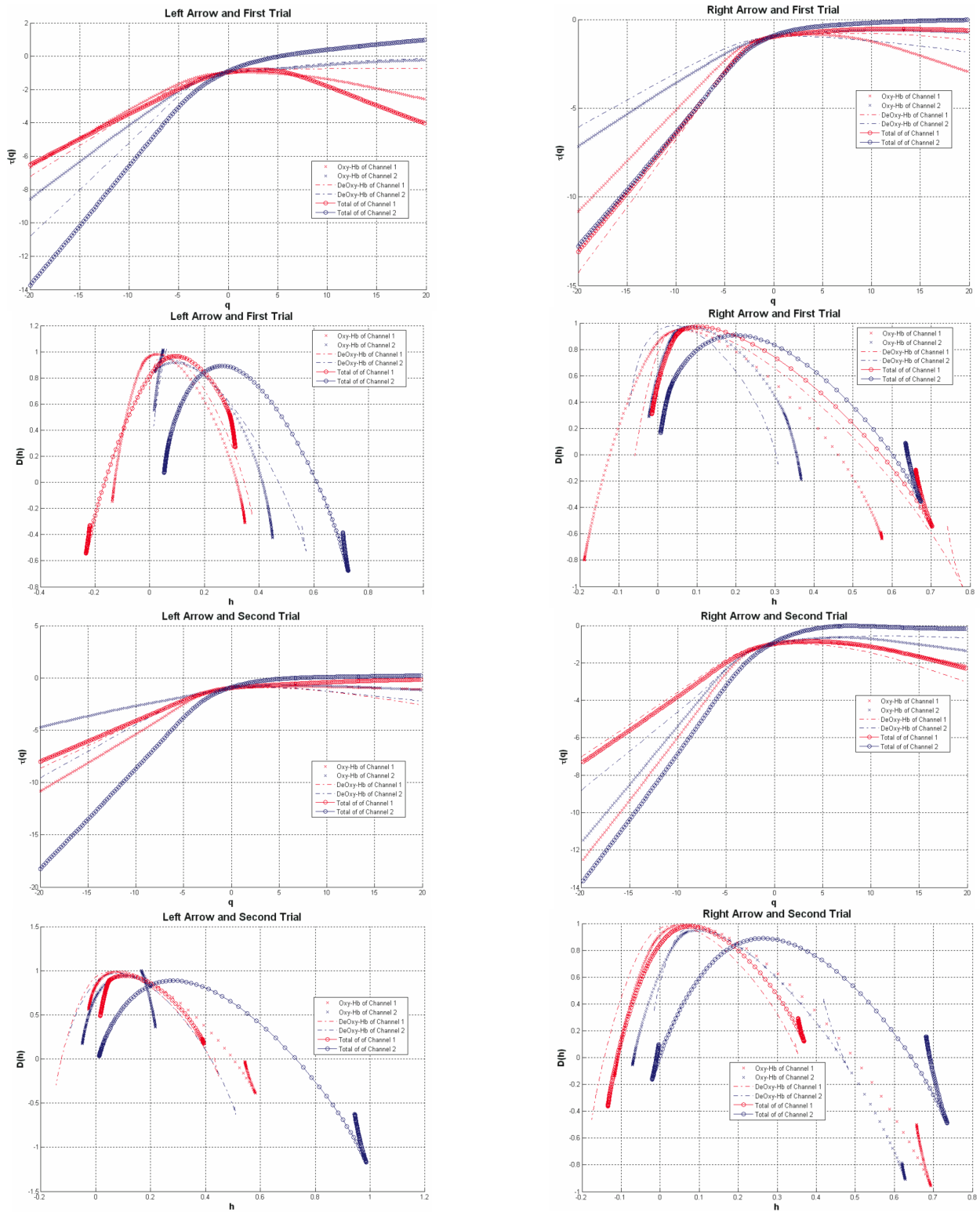


Fig. 2 Multifractal measures

the imagery task is in sixty seconds as illustrated in Fig. 3. The available NIRS instrument (OMM-3000 from Shimadzu Corporation, Japan) for acquiring Oxy-Hb and DeOxy-Hb concentration changes during imagery tasks. This instrument operates at three different wavelengths of 780nm, 805nm and 830nm. The data is sampled at the rate of up to 40Hz and digitalized by 16-bit analog to digital converters. In this experiment, data is acquired from two channels at the sampling rate of 40Hz, and 2405 data points of each channel are collected during imagery tasks for estimating fractal measures.

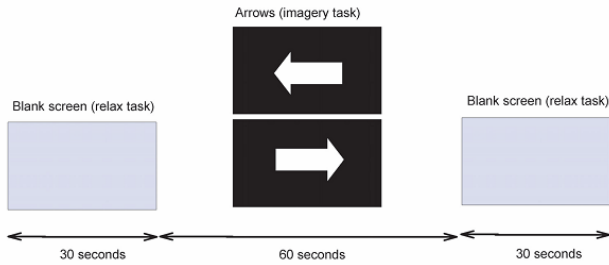


Fig. 3 Duration of relax and imagery tasks

In this study, the method of wavelet transform modulus maxima (WTMM) is based on the wavelet analysis. The method was proposed to deal with strongly non-stationary signals. Therefore, it is predicted to be suitable with biological signals. In the method, the local exponent h is evaluated via the modulus of maxima values of the wavelet transform at each point t in the time series. The partition function $Z(q, a)$ is defined as the sum of the q^{th} powers of local maxima of the modulus of the wavelet transform coefficients at scale a [15], i.e.,

$$Z(q, a) \sim a^{\tau(q)} \quad (1)$$

The quantity $\tau(q)$ is related to the singularity spectrum $D(h)$ by the Legendre transform $D(h) = \min_q [qh - \tau(q)]$. By varying q in Eq. (1), it is possible to characterize selectively the fluctuations of a time series: positive q s accentuate the strong inhomogeneities of the signal, while negative q s accentuate the smoothest ones. With monofractal signals, the relation of $t(q) = qH - 1$ (H is global Hurst exponent) is obtained, whereas $\tau(q)$ is nonlinear. Depending on the value of h , the input series could be long-range correlated ($h > 0.5$), uncorrelated ($h = 0.5$) or anti-correlated ($h < 0.5$).

III. RESULTS

We estimate multifractal for the NIRS data of Oxy-Hb, DeOxy-Hb and Total-Hb concentrations collected from two channels. Two trails of imagery tasks are done on both left- and right-arrow. The result of estimation of multifractal in Figure 2 is the relation of $\tau(q)$ versus q and of $D(h)$ versus h of NIRS data. It is clear that $\tau(q)$ is nonlinear with respect to q for all the NIRS data, i.e., of Oxy-Hb, DeOxy-Hb and Total-Hb concentrations from both channels. In other words, NIRS data measured during brain activity is multifractal. In addition, from the plot of $D(h)$ versus h , the local Hurst exponent h is in the range from 0 to 0.4 with the maximum around 0.1 in all the trials. This means that NIRS data is anti-correlated signals.

REFERENCES

1. Shlesinger M.F. (1987) Fractal time and $1/f$ noise in complex systems, Ann. NY Acad. Sci. 504:214-228.
2. Bassingthwaite J., Liebovitch L., et al (1994) Fractal Physiology Oxford University Press, Oxford.
3. Ivanov P., Amaral L., et al. (2003) Multifractality in Human Heart-beat Dynamics, Nature 399: 453-465.
4. B. West, M. Latka, et al. (2003) Statistical Mechanics and its Applications, Physica A 318:453460.
5. Bunce S., Izzetoglu M. et al., (2006) Functional Near-Infrared Spectroscopy, IEEE Engineering in Medicine and Biology Magazine 25:54-62.
6. Coyle S., Ward T., et al., (2007) Brain computer interface using a simplified functional near-infrared spectroscopy system, J. Neural Engineering 4:219- 226.
7. Sitaram R., Zhang H., et al., (2007) Temporal classification of multichannel near-infrared spectroscopy signals of motor imagery for developing a brain-computer interface, NeuroImage 34 1416:1427.
8. Wobst P., Wenzel R., et al., (2001) Linear aspects of changes in deoxygenated hemoglobin concentration and cytochrome oxidase oxidation during brain activation, NeuroImage 13:520:530.
9. Sato H., Fuchino Y., et al. (2005) Intersubject variability of near-infrared spectroscopy signals during sensorimotor cortex activation, J. Biomedical Optics 10:044001.
10. Izzetoglu K., Bunce S, et al. (2004) Functional Optical Brain Imaging Using NIR during Cognitive Tasks, Int.J.Human-Computer Interaction 17:211-227.
11. Villringer A., Chance B. (1997) Non-invasive optical spectroscopy and imaging of human brain function, Trends in Neuroscience 20:435-442.
12. Tomita M., (2006) Flow effect impacts NIRS, jeopardizing quantification of tissue hemoglobin, NeuroImage 33:13-16.
13. Van T., Hammer P., (2007) Mathematical Model for the Hemodynamic Response to Venous Occlusion Measured With Near-Infrared Spectroscopy in the Human Forearm, IEEE Trans. Biomed. Engineering 54:573-584.
14. Schreiber T. (1999) Interdisciplinary application of nonlinear time series methods, Phys. Rep. 308:2:64.
15. J. Muzy, E. Bacry, Multifractal formalism for fractal signals: The structure-function approach versus the wavelet-transform modulus-maxima method, Phys. Rev. E 47 (1993) 875-884.

Author: Nguyen Tien Dzung
Institute: Hanoi University of Technology
Street: 1 Dai Co Viet street
City: Hanoi
Country: Vietnam
Email: dungnt-fet@mail.hut.edu.vn

Design, Fabrication and Analysis of Silicon Microneedles for Transdermal Drug Delivery Applications

D.W. Bodhale, A. Nisar, and N. Afzulpurkar

Asian Institute of Technology, School of Engineering and Technology, Bangkok, Thailand

Abstract— One of the major drawbacks of transdermal drug delivery (TDD) systems has been their inability to deliver the drugs through the skin at therapeutically desirable range. To overcome this limitation, use of microneedles is gaining popularity. In this paper, the use of microneedles has been proposed for the transdermal drug delivery applications. By using the processes developed by microelectronics industry, the hollow cylindrical silicon microneedles array has been fabricated with microneedles having the tapered tip for easy skin insertion. Mask layout design and fabrication steps involving deep reactive ion etching (DRIE) using silicon wafers is first presented. The process is followed by actual fabrication of silicon hollow microneedles by a series of combined isotropic and anisotropic etching processes using inductively coupled plasma (ICP) etching technology. The performance of the microneedles is numerically characterized by using structural and coupled multifield analysis. To predict the stress distribution and model fluid flow in coupled multifield analysis, finite element (FE) and computational fluid dynamic (CFD) analysis using ANSYS has been used. Flow rate through the microneedles is investigated at different voltages and frequencies using multiple codes coupling method. The analysis of the flow behavior by coupled field method and structural characteristics provides useful data to fabricate optimized design of the hollow silicon microneedle based drug delivery device for transdermal drug delivery applications.

Keywords— Computational fluid dynamic (CFD) analysis, Deep reactive ion etching (DRIE), Drug delivery, Hollow silicon microneedle, Transdermal drug delivery (TDD).

I. INTRODUCTION

Transdermal drug delivery (TDD) is refers to the movement of pharmaceutical compound across the skin to reach the systemic circulation for subsequent distribution in the human body. Transdermal drug delivery systems cover a wide range of non-invasive and minimally invasive technologies for delivering drugs and vaccines across the skin [1], [2], [3]). One of the major drawbacks of TDD systems has been their inability to deliver the drugs through the skin within the desired therapeutic range. To overcome this limitation, many studies have been conducted on new drug delivery methods using emerging micro and nanotechnologies. The major focus of MEMS for drug delivery has been towards the

development of microneedles for minimally invasive TDD applications. Using MEMS technology, microneedles with various sizes, shapes, and materials have been fabricated. A MEMS based microneedle is a needle with diameter and length in micrometers. A microneedle is different from standard hypodermic needles used in medical applications as generally the length of the MEMS based microneedles is less than 1 mm. Thus microneedles are significantly smaller in length than ordinary needles. There are two types of microneedles. One is solid and other is hollow. Hollow microneedles have an internal bore or lumen which allows flow of fluid or drug through the microneedles. [4] reported one of the earliest out-of-plane microneedle array. [5] demonstrated sampling of body fluids by capillary action achieved with 350 μm long hollow out-of-plane microneedles. [6] fabricated microneedles for microdialysis applications.

Fabrication process plays an important role in design and development of the MEMS devices. Among all available microrfabrication processes Photolithography is the most common and powerful technique in fabrication technologies. With the help of anisotropic etching process, high aspect ratio structures can be easily fabricated and this process is generally referred to as deep reactive ion etching (DRIE) process. Silicon is anisotropically etched by DRIE process in a commercially available etching machine called inductively coupled plasma (ICP) etcher. [7] reported fabrication of 150 μm long solid microneedles in silicon using DRIE process. [8] fabricated biodegradable polymer microneedles by vacuum casting of polyglycolic acid in a silicon mold. Hollow microneedles with reservoirs have been developed for TDD to eliminate problem of fluctuation in daily dosage reduced side effects. [9] fabricated out-of-plane hollow metallic microneedles with SU-8 needles mold and backside exposure by metal deposition technology ([9], [10]) developed inclined LIGA process to fabricate microneedle array using PMMA. [11] fabricated out-of-plane hollow microneedles with inclined structure. With the development of dry etching technology in silicon, [12] used dots arrays as a mask to fabricate hollow needles.

The microneedle design and analysis involves strength modeling and CFD analysis. Many research studies have been conducted for structural and microfluidics (flow) analysis of the microneedles. [13] conducted numerical and

experimental studies for mechanical stability analysis of hollow cylindrical microneedle using silicon dioxide (SiO₂) material. [14] used numerical analysis for fluidic system to ensure uniform release of the fluid from each hollow microneedle. [15] used finite element modeling (FE) analysis for prediction of various forces acting on the microneedle during skin insertion. [16] used FEM simulation and confirmed that the stress concentration occurred severely at the tip area of the microneedle and sharp tip angle of the microneedle could be easily inserted into skin. [17] used in-plane single crystal silicon microneedle array for drug delivery and performed FEM simulation and experiments on microneedle for stress analysis by applying bending load at the tip of the microneedle. [18] performed the CFD simulation using CFD ACE+ Software to calculate shear rate in the flow for the appropriate scaling of the stepped internal lumen diameters.

In this paper, design and fabrication of silicon hollow microneedles is presented. Then an in-depth numerical analysis of a microneedle based piezoelectrically actuated microfluidic device is reported. The simulation involving transient multifield analysis using multiple code coupling method is conducted on three dimensional model of the microneedle based microfluidic device.

II. FABRICATION OF MICRONEEDLES

The proposed fabrication process of microneedles and reservoir involves isotropic and anisotropic etching processes using standard silicon wafers. The desired shape of microneedle structures is controlled is achieved by controlling the etching timings at various processing steps. Three set of chrome masks were fabricated. Microneedle Mask MN1 has been used to fabricate microneedle outside shape. Microneedle mask MN2 has been used to fabricate inner hole called lumen while the third microneedle Mask has been used for backside reservoir etching.

The fabrication process involves many steps. The step-wise fabrication process is shown in Fig.1.

III. ANALYSIS OF HOLLOW SILICON MICRONEEDLE

A. Mechanical Design Specifications

Design layout with I.D = 60 μm, O.D = 150 μm and center-to-center spacing = 1000 μm was chosen for numerical analysis. A schematic illustration of the design of microneedle with dimensions is shown in Fig. 3.

B. Theoretical Analysis

The design of the cylindrical hollow silicon microneedle considered for strength modeling and CFD analysis is

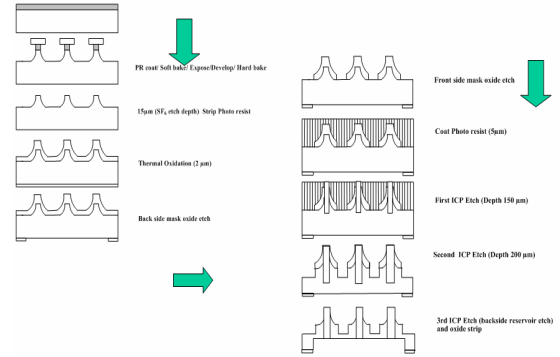


Fig. 1 Fabrication process of hollow silicon out-of-plane microneedles

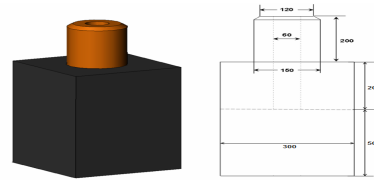


Fig. 2 Design specification of hollow silicon microneedle (all dimensions are in μm)

shown in Fig. 3. p_1 and p_2 is the inlet and outlet pressures of the microneedle.

D_1 and D_2 represent tip and outer diameter respectively. L is the length of the microneedle; Q is the flow rate in the lumen section.

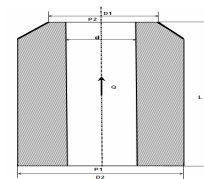


Fig. 3 Cross section of the microneedle

C. Microneedle Mechanics

During skin insertion, the possible failure of the microneedle may occur due to bending or buckling. An axial force acts on the microneedle tip during insertion. This axial force is compressive and causes buckling of the microneedle. The microneedle experiences resistive force exerted by skin during insertion, hence in order to pierce the microneedle into skin, the applied axial force has to be greater than skin resistance force. The axial force (compressive force), which the microneedle can withstand without breaking is given by:

$$F_{compressive} = \sigma_y A \tag{1}$$

Where, σ_y is the yield strength of the material and A is cross-sectional area of the microneedle tip.

The buckling force acting on the hollow microneedle during skin insertion is given by,

$$F_{Buckling} = \frac{\pi^2 E I}{L^2} \quad (2)$$

Where, E is young's modulus of material, I (m^4) is moment of inertia of cylindrical section and L (m) is length of the microneedle.

Moment of inertia for hollow cylindrical section for Eq. 2 is $I = \frac{\pi}{64}(D^4 + d^4)$.

Where, D is outer diameter and d is inner diameter of hollow cylindrical section.

As microneedle penetrates the human skin, it experiences resistive forces exerted by the human skin. To penetrate the human skin, the outside force or pressure must be greater than the resistive skin force. The resistive force offered by the skin before the skin is punctured is given by the following equation:

$$F_{resistance} = P_{pierce} A \quad (3)$$

Where, P_{pierce} is the required pressure to pierce the microneedle into skin.

The bending force, which the microneedle can withstand without breaking is given by:

$$F_{Bending} = \frac{\sigma_y I}{cL} \quad (4)$$

Where, c is the distance from vertical axis to the outer edge of the section [15].

D. Microfluidic Analysis

To determine fluid flow through the microneedle, Poiseuille's law of fluid flow in a cylinder is considered:

$$Q = \frac{\pi d^4 (\nabla P)}{128 \mu (L)} \quad (5)$$

Where, d is the inner diameter of the microneedle and is constant throughout the lumen, Q is the flow rate, ∇P is the pressure drop across the microneedle lumen. μ is the viscosity of fluid for water at 25^o C, and L is the length of the lumen of the microneedle.

The Reynolds number indicates the type of flow and is given as:

$$Re = \frac{\rho d V}{\mu} \quad (6)$$

Where, ρ is a density of the fluid and V is the fluid velocity in lumen. At micron level, the flow becomes laminar. The flow is considered as laminar if Re is less than 2100, otherwise the flow is considered as turbulent.

The microneedle section shown in Fig. 3 is modeled by using Modified Bernoulli equation [19]. By considering the friction losses, the pressure loss by the fluid is calculated:

$$\frac{P_1}{\rho g} + \frac{V_1}{2g} + Z_1 = \frac{P_2}{\rho g} + \frac{V_2}{2g} + Z_2 + \frac{fL}{d} + \frac{V^2}{2g} + \sum \frac{KV^2}{2g} \quad (7)$$

Where, P_1 is the inlet pressure, P_2 is the outlet pressure, V_1 is the inlet velocity, V_2 is the outlet velocity, ρ is the density of water, Z_1 and Z_2 is the distance from datum ($Z_1 = 0$ and $Z_2 = L$), f is the friction factor.

The pressure drop can be calculated from Eq. 7.

$$\nabla P = \mu \frac{128Q(L)}{\pi d^4} + \rho \frac{8Q^2}{\pi^2 d^5} (k) \quad (8)$$

Where, k is the loss coefficient factor for the square edge inlet and outlet. The value of loss coefficient for the microneedle design is taken as 0.5. The friction factor for laminar flow is given as $f = \frac{64}{Re}$. The first term of right hand side in Eq. (8) describes the pressure drop due to viscous shear force [20] and second term describes inertial effect at the inlet and exit [12].

IV. NUMERICAL SIMULATION

A. Structural Analysis

The structural analysis of the microneedle is performed using finite element (FE) method. During skin insertion, microneedle experiences axial force, bending force, shear force etc. It was found in the numerical solution that the maximum stress of 6.78 GPa occurs at the bottom of the microneedle for the applied bending force of 8.5 N, which is below the yield strength limit of the material as shown in fig. 4a.

The skin offers resistance of 3.18 MPa. ([14], [21]) during microneedle penetration into human skin. Hence, to overcome this skin resistance the microneedle must withstand the load more than 3.18 MPa. Hence, to show the effect of this resistance force on the structure of the microneedle, FE analysis was performed. The effect of applied axial load on the free end of the microneedle is shown in Fig. 4b. The result shows that the microneedle design is enough strong to penetrate into the human skin without failure.

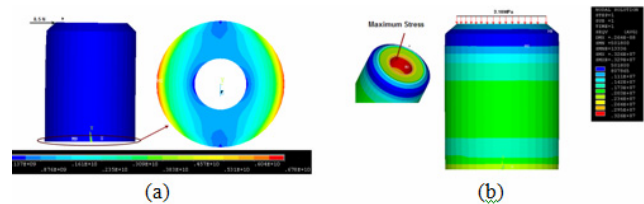


Fig. 4 a) Bending stress analysis b) Axial stress analysis

B. CFD Analysis Using Transient Multi-field Code Coupling

For the electromechanical coupling of piezoelectric actuator and fluid-membrane coupling, the multifield analysis using multiple code coupling has been conducted in ANSYS. The piezoelectric and fluid models are shown in Fig. 5a. The Multifield simulation results were obtained using MFX-ANSYS/CFX simulation environment. The modal boundary conditions for the fluid-structure interface are shown in Fig. 5b.

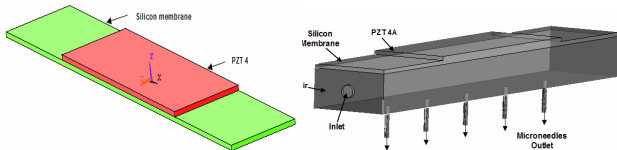


Fig. 5 a) Piezoelectric membrane b) CFD model using multi-field code coupling

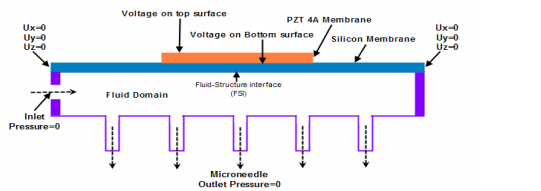


Fig. 6 Modal boundary conditions

V. RESULTS AND DISCUSSION

A. Fabrication of Microneedles

Microneedles with high aspect ratio have been fabricated using a series of combined isotropic and anisotropic etching processes in ICP etching machine. The SEM images of the fabricated microneedles are shown in Fig. 7 and 8 respectively.

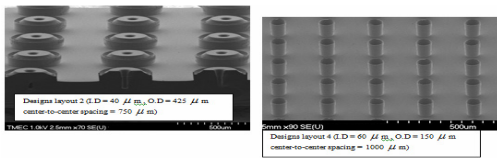


Fig. 7 SEM images of the fabricated Microneedle array

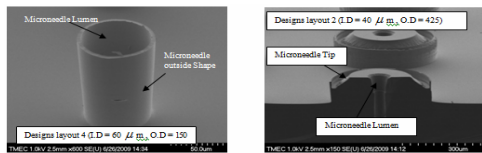


Fig. 8 SEM images of the fabricated hollow microneedles

Two microneedle designs, layout 2 (I.D. = 40 μm, O.D. = 425 μm center-to-center spacing = 750 μm) and layout 4 (I.D. = 60 μm O.D. = 150 μm center-to-center spacing = 1000 μm) as mentioned in Table 1 and shown in Fig. 8 and 10 above were successfully fabricated.

B. Stress Analysis

The stress analysis of the designed microneedle is done in the first set of the simulation. The deflection and stress of the microneedle is measured for the applied transverse force and is shown in Fig. 9 a. The deflection of the microneedle along its length is shown in Fig. 9b. The deflection of the microneedle gradually increases with increase in distance from root of the microneedle. As the bending force is applied directly at the microneedle tip, therefore maximum deflection occurs at the tip of the microneedle. For the applied bending force of 8.5 N at the tip, the maximum stress at the bottom of the microneedle is found to be 6.78 GPa with deflection of 36.6 μm. As the stress is below the yield stress (7 GPa) of the material hence, the microneedle is able to withstand the force of 8.5 N. The designed microneedle is strong due to its cylindrical section.

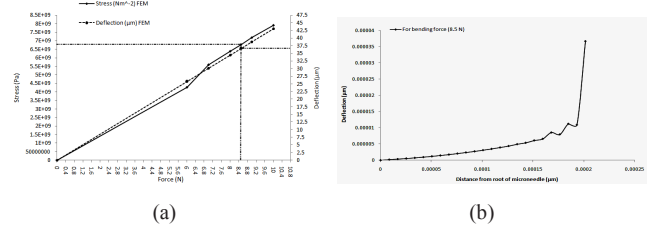


Fig. 9 a) Variation in stress and deflection of microneedle for applied force b) Deflection of the microneedle along its length due to applied bending force

The microneedle can puncture the human skin with applied skin piercing pressure of 3.18 MPa ([14], [21]) at the tip of the microneedle without failure. From the above results, it is predicted that the proposed microneedle design can withstand the bending as well as axial forces during skin insertion.

C. Transient Multifield Analysis

The deformation of the silicon membrane at sinusoidal voltage of 200 V at constant actuating frequency of 250 Hz is shown in Fig. 10 a. The deformation is measured along the length of the membrane. The maximum displacement of 4.76 μm. occurs at the centre of the membrane.

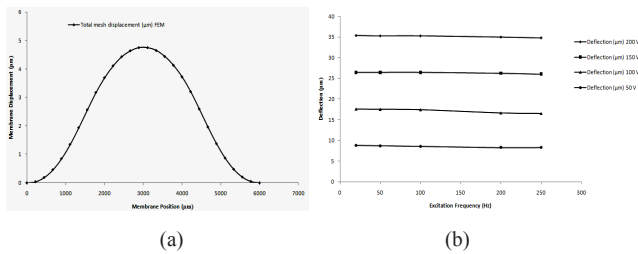


Fig. 10 a) Membrane deflection from FEM solution b) Deflection of the piezoelectric actuator at various excitation voltages

Fig. 10b shows the relationship between piezoelectric membrane deflection and excitation frequency for different excitation voltages. The deflection of the piezoelectric membrane is strongly affected by excitation voltage but not effected by varying excitation frequency if varied from 20 to 250 Hz.

The variation in flow rate with the excitation frequency for different excitation voltages is shown in Fig. 11a. The flow rate increases gradually with increase in excitation frequency. The maximum flow rate is obtained at 100 volt and is increases with the excitation frequency. For the current design of piezoelectric actuator, maximum flow rate of 83.99 $\mu\text{L}/\text{min}$ is obtained at maximum frequency of 250 Hz at 100 Volt with deflection of 16.48 μm .

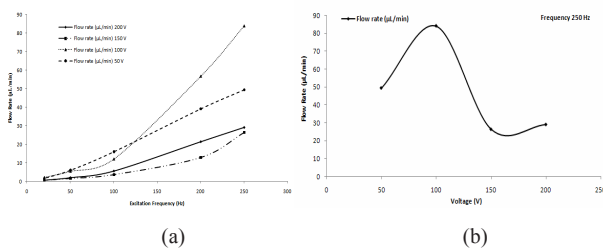


Fig. 11 a) Effect of excitation frequencies on flow rates at the different excitation voltages. b) Net flow rate for the applied voltages at fixed frequency

Fig. 11b shows the result for flow rate obtained at various voltages at fixed frequency. The flow rate is maximum at low voltages than high voltages.

VI. CONCLUSION

This paper presents a design, fabrication and analysis of hollow silicon microneedle for TDD applications. The microneedles fabrication is done using isotropic and anisotropic etching processes. The Standard silicon wafers were used for the fabrication purpose. The theoretical design and analysis of new hollow cylindrical microneedle is presented.

Theoretical calculations are done to validate numerical results.

The structural and CFD characteristics of the microneedle is analyzed with the help of simulation. The structural analysis of the designed microneedle shows that the microneedle is enough strong to penetrate into human skin without buckling. CFD analysis is done using multifield code coupling. The piezoelectric material is used to actuate the silicon membrane. The flow rates are compared with the various exciting voltages and frequencies. The simulation result shows that the flow rate is maximum at low voltages than high voltages. The maximum flow rate obtained is 83.99 $\mu\text{L}/\text{min}$ at frequency of 250 Hz at 100 Volt. The flow rate can be varied according to the requirement of the drug delivery into human body. Many studies have been performed to develop the drug delivery devices but still need to be incorporated in the practical use. Our future work will involve the integration of microneedle array with the micropump and control circuitry to form a complete TDD MEMS device.

REFERENCES

- Barry BW (2001) Novel mechanisms and devices to enable successful transdermal drug delivery. *Eur J Pharm Sci* 14:101–114
- Prausnitz MR (2004) Microneedles for transdermal drug delivery. *Adv Drug Deliv Rev* 56: 581–587
- Schuetz YB, Naik A et al (2005) Emerging strategies for the transdermal delivery of peptide and protein drugs. *Expert Opin Drug Deliv* 2:533–548
- Campbell PK et al (1991) A silicon-based, three-dimensional neural interface: manufacturing processes for an intracortical electrode array. *IEEE Trans Biomed Eng* 38(8):758–768
- Mukherjee EV et al (2004) Microneedle array for transdermal biological fluid extraction and in situ analysis. *Sens Actuators A* 114:267–275
- Zahn et al (2005) Microdialysis Microneedles for Continuous Medical Monitoring. *Biomedical Microdevices*, 10.1007/s10544-005-6173-9, pp. 59-69
- Henry S et al (1998a) Micro machined needles for the transdermal drug delivery of drugs. In: proceedings of IEEE Workshop MEMS, 494–498
- Park JH et al (2005) Biodegradable polymer microneedles: fabrication, mechanics and transdermal drug delivery. *J control release* 104:51–66
- Kim et al. (2004) A tapered hollow metallic microneedle array using backside exposer of SU-98. *J. Micromechanics and microengineering*, 14, 597-603.
- Moon et al. (2003) Fabrication of microneedle array using inclined LIGA process, 12th International Conference on, TRANSDUCERS, Solid-State Sensors, Actuators and Microsystems, 1546- 1549 vol.2
- Gardeniers HJGE et al (2003) Silicon micromachined hollow microneedles for transdermal liquid transport. *J Microelectro-998 mechan Syst* 12(6)
- Stoerber B and Liepmann D (2000) Fluid injection through out-of-plane microneedles. In: *Microtechnologies in Medicine and Biology*, 1st Annual International, Conference, Berkeley, CA 94704, USA
- Shibata T et al (2007) Fabrication and mechanical characterization of microneedle array for cell surgery. In: *Actuators and Microsystems Conference*, pp. 719–722

14. Wilke N et al (2006a) Silicon microneedle electrode array with temperature monitoring for electroporation. *Sens Actuators A*, 1090: 123–124: 319–325
15. Aggarwal P and Johnston CR (2004) Geometrical effects in mechanical characterizing of microneedle for biomedical applications. *Sens Actuators B* 102: 226–234
16. Aoyagi S et al (2007) Biodegradable polymer needle with various tip angles and consideration on insertion mechanism of mosquito's proboscis. *Sens Actuators A* 143: 20–28
17. Paik SJ et al (2004) In-plane single-crystal-silicon microneedles for minimally invasive microfluidic systems. *Sens Actuators A* 114: 276–284
18. Stoeber B and Liepmann D (2002) Design, fabrication and testing of a MEMS syringe. In: *Proceedings of Solid state sensor and actuator workshop*
19. Janna WS (1998) *Design of fluid thermal system*, 2nd edn. PWS Publications, Boston
20. Batchelor GK (1967) *An introduction to fluid dynamics*. University of Cambridge, Cambridge
21. Fan et al. (2005) Simulation of piezoelectrically actuated valveless micropump. *J. Smart Materials and Struct*, 14, 400–405.
22. Wang X et al (2006) A novel fabrication approach for microneedles using silicon micromachining technology. In: *1st IEEE International Conference on NEMS*, pp. 545–549

Heat-Stress Relationships of Rat Cardiac Trabeculae Determined Using a Micromechanocalorimeter

J.-C. Han¹, A.J. Taberner^{1,2}, P.M.F. Nielsen^{1,2}, R.S. Kirton¹, and D.S. Loisel^{1,3}

¹ Auckland Bioengineering Institute, The University of Auckland, Auckland, New Zealand

² Department of Engineering Science, The University of Auckland, Auckland, New Zealand

³ Department of Physiology, The University of Auckland, Auckland, New Zealand

Abstract— In order to study the physiology and pathophysiology of the heart, it is insightful to employ isolated cardiac muscle preparations. To that end, we have recently constructed a micromechanocalorimeter for measuring simultaneously the heat rate and force production of superfused cardiac trabeculae. In the microcalorimeter component of the micromechanocalorimeter, two arrays of non-contact thermopile sensors measure the temperature of superfusate upstream and downstream of a centrally-located respiring trabecula. The increment in temperature of superfusate downstream, relative to that upstream, is proportional to the heat liberated by the trabecula. Using the micromechanocalorimeter, we have determined the relationship between heat and force production of rat cardiac trabeculae ($n = 10$), in 1 mM and 2 mM extracellular calcium concentration ($[Ca^{2+}]_o$) at room temperature (20-22°C). Muscle force was varied by reducing muscle length below optimal value (L_o). Muscle force and rate of heat production were measured simultaneously at two stimulus frequencies: 0.2 Hz and 2.0 Hz. In healthy superfused cardiac trabeculae, we found that heat production was linearly correlated with stress (normalized force) production. The heat-stress regression lines were not significantly different between 0.2 Hz and 2.0 Hz at either value of $[Ca^{2+}]_o$. Activation heat values, which are the heat extrapolated to the zero-stress intercepts of the heat-stress regression lines, did not differ between stimulus frequencies, but were significantly higher in 2 mM than in 1 mM $[Ca^{2+}]_o$. We conclude that the heat-stress relationships are independent of stimulus frequency, but dependent on $[Ca^{2+}]_o$. To our knowledge, our micromechanocalorimeter is unique, and has allowed the first determination of the heat-stress relationships of cardiac trabeculae.

Keywords— Muscle Energetics, Cardiac Trabeculae Carneae, Microcalorimetry.

I. INTRODUCTION

As an isolated cardiac muscle, held fixed at both ends, is electrically stimulated, twitch force is produced. A metabolic consequence of this mechanical contraction is the

liberation of heat. In order to gain insight into the complex thermo-mechanical processes occurring within the muscle, both the mechanical and metabolic events, i.e. the twitch force and heat production, should ideally be measured simultaneously.

Using our recently described micromechanocalorimeter [1], we have measured simultaneously the heat rate and force production of right-ventricular trabeculae ($n = 10$) from rat undergoing fixed-end contractions in the presence of 1 mM and 2 mM $[Ca^{2+}]_o$ at room temperature (20-22°C). Trabeculae were electrically stimulated at 0.2 Hz and 2.0 Hz, at various muscle lengths (77-100% L_o). This has allowed us to determine the relationship between the heat liberation and the stress production of cardiac trabeculae.

II. MATERIALS AND METHODS

A. Muscle Preparation and Solutions

Wistar rats were anaesthetized using isoflurane prior to decapitation, thoracotomy and cardiectomy (as approved by The University of Auckland Animal Ethics Committee). The hearts were quickly excised and plunged into a cold dissection solution to induce arrest. The aortae were cannulated, and the coronary vasculatures Langendorff-perfused with dissection solution, vigorously bubbled with 100% O_2 , at 20-22°C. The dissection solution contained (in mM): 130 NaCl, 6 KCl, 1 $MgCl_2$, 0.5 NaH_2PO_4 , 0.3 $CaCl_2$, 10 HEPES, 10 glucose, and 20 2,3-butanedione monoxime (BDM). The pH of the dissection solution was adjusted to 7.4 using Tris.

An unbranched and geometrically-uniform trabecula was dissected from the right-ventricular inner wall. It was then transferred to the micromechanocalorimeter containing superfusate of composition identical to that of the dissection solution except for the absence of BDM and the increase in Ca^{2+} concentration to either 1 mM or 2 mM.

B. Micromechanocalorimeter

The principle of operation of the micro-mechanocalorimeter has been described in detail elsewhere [1]. Briefly, it consists of (i) a flow-through, open-ended, microcalorimeter [2], (ii) a compound muscle-length actuator, (iii) a silicon-beam force transducer, and (iv) two J-shaped platinum hooks, each glued to a quartz arm. The upstream arm is connected to the compound muscle-length actuator, while the downstream arm is attached to the force transducer. The microcalorimeter comprises an open-ended measurement chamber with two externally-mounted arrays of non-contact thermopile sensors and an open-topped muscle-mounting chamber. A trabecula is maneuvered onto the hooks in the mounting chamber before being translated into the measurement chamber and positioned between the two thermopile arrays. The two thermopile arrays sense the temperature of superfusate upstream and downstream of the trabecula. As the superfusate flows over the trabecula, the downstream thermopile array senses a higher temperature in proportion to the rate of heat production by the trabecula. The micromechanocalorimeter is enclosed in an optically-isolated and thermally-insulated enclosure during experiments.

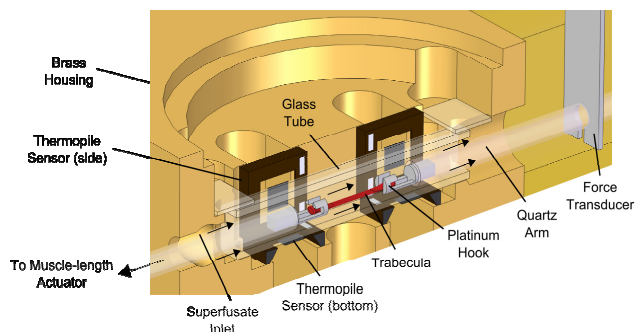


Fig. 1 Cut-away diagram of the micromechanocalorimeter architecture. A trabecula is mounted onto two J-shaped platinum hooks, each of which attaches to a quartz arm. The upstream arm attaches to the compound muscle-length actuator, while the downstream arm attaches to the force transducer. Two externally-mounted thermopile arrays (each consisting of thermopile sensors on both sides and bottom of the glass tube), which are 4 mm apart, measure the temperature of the flowing superfusate. The solid arrows indicate the direction of superfusate flow. Figure adapted from [1] with permission from the American Physiological Society

C. Experimental Protocol

At steady superfusate flow rate (nominally $1 \mu\text{L s}^{-1}$), the trabecula was field-stimulated using 3 V, 5 ms pulses at 0.2 Hz, delivered via the platinum electrode (located in the muscle-mounting chamber), for at least 1 hour to allow equilibration, during which time it was gradually stretched to its optimal length (L_0 : the length at which active force

production is maximal). Muscle length was then reduced stepwise from L_0 . At each length step, muscle force and heat rate were measured at 0.2 Hz and 2.0 Hz. Of the ten trabeculae, five received 1 mM prior to 2 mM $[\text{Ca}^{2+}]_o$, while the other five received 2 mM $[\text{Ca}^{2+}]_o$ first. Stimulus heat was quantified at the end of each experiment and the rate of heat production by the trabecula corrected retrospectively.

D. Data Acquisition

Force data were acquired at 50 kHz and heat rate data at 6.5 Hz using LabVIEW 8.5 (National Instruments). Both data streams were recorded using LabVIEW SignalExpress 2.5 (National Instruments).

E. Normalization

By approximating the geometry of each trabecula as a cylinder, its rate of heat production was normalized to its wet volume and expressed in kW m^{-3} . Heat production was computed by dividing the heat rate by stimulus frequency (and was expressed in kW m^{-3} per twitch). Stress is the force normalized to muscle cross-sectional area (expressed in kPa).

F. Statistical Analysis

Data were fitted by linear regression, employing the Random Coefficient Model of PROC MIXED [3] in SAS (SAS Inst. Inc.). Differences between regression lines were examined for statistical significance at the 95% level of confidence.

III. RESULTS

A. Simultaneous Measurements

The typical response of heat rate and stress production of a trabecula (210 μm in diameter and 3.7 mm in length) upon varying stimulus frequency, muscle length and $[\text{Ca}^{2+}]_o$ is shown in Fig 2. Steady-state twitch stress at 0.2 Hz stimulation is shown on the left hand side of the record. As can be seen, at 1 mM $[\text{Ca}^{2+}]_o$ and at 100% L_0 , the stress production at steady-state reduced slightly upon increasing stimulus frequency from 0.2 Hz to 2.0 Hz. When stimulus frequency was reduced back to 0.2 Hz, the stress increased back to the control value. The heat rate, on the other hand, increased from 0.2 Hz to 2.0 Hz. Reduction of muscle length decreased both the stress and the rate of production of heat. Similar responses were observed at 2 mM $[\text{Ca}^{2+}]_o$.

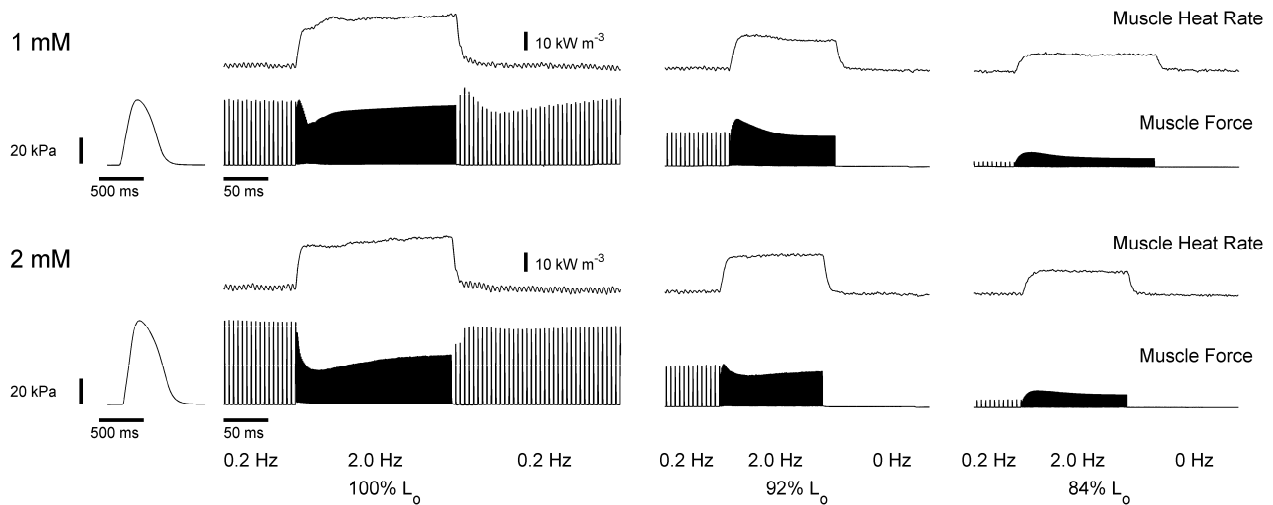


Fig. 2 Effects of stimulus frequency (0.2 Hz and 2.0 Hz), muscle length (100% L_o , 92% L_o and 84% L_o) and $[Ca^{2+}]_o$ (1 mM and 2 mM) on the heat rate and stress production of a representative trabecula. The left side of the record shows a single twitch stress at 0.2 Hz

B. Heat-Stress Relationships Are Frequency-Independent

The upper panel of Fig 3 illustrates two relationships between heat and stress production of a representative trabecula (the same as in Fig 2). The lower panel shows the average results of ten trabeculae (198 \pm 20 μ m in diameter and 3.0 \pm 0.3 mm in length).

For each of the ten trabeculae, separate least-squares regression lines were fitted to the data from each of the four $[Ca^{2+}]_o$ -frequency groups. Within each group, the ten regression lines were averaged using the Random Coefficient Model [3].

At 1 mM $[Ca^{2+}]_o$, the average regression line at 0.2 Hz was not significantly different from the average regression line at 2.0 Hz. At 2 mM $[Ca^{2+}]_o$, the average regression line at 0.2 Hz was also not significantly different from the average regression line at 2.0 Hz. These results imply that the heat-stress relationships are independent of stimulus frequency.

C. Heat-Stress Relationships Are $[Ca^{2+}]_o$ -Dependent

Statistical analysis revealed that the average regression lines at 1 mM and 2 mM $[Ca^{2+}]_o$ had the same slopes but different intercepts. This demonstrates that the heat-stress relationships are $[Ca^{2+}]_o$ -dependent.

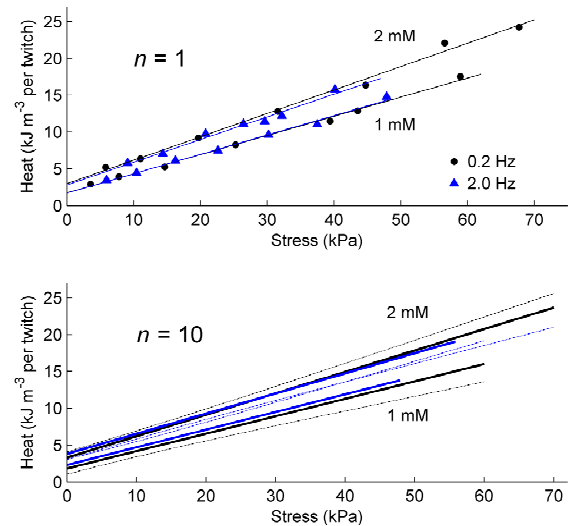


Fig. 3 *Upper panel*: the heat-stress relationships of a representative trabecula. Data were grouped by 0.2 Hz (black) and 2.0 Hz (blue) at 1 mM and 2 mM $[Ca^{2+}]_o$ and each fitted by a linear regression line. *Lower panel*: the heat-stress relationships of ten trabeculae. Each line in each stimulus frequency and $[Ca^{2+}]_o$ group is the average of 10 linear regression lines. The solid lines are the fitted regression lines, and the dotted lines are their 95% confidence intervals. At 1 mM $[Ca^{2+}]_o$, the intercepts are 1.8 ± 0.4 and 2.3 ± 0.4 kW m^{-3} per twitch and the slopes are 0.237 ± 0.015 and 0.240 ± 0.015 kW m^{-3} per twitch kPa^{-1} for 0.2 Hz and 2.0 Hz, respectively. At 2 mM $[Ca^{2+}]_o$, the intercepts are 3.3 ± 0.4 and 3.8 ± 0.4 kW m^{-3} per twitch and the slopes are 0.291 ± 0.015 and 0.273 ± 0.015 kW m^{-3} per twitch kPa^{-1} for 0.2 Hz and 2.0 Hz, respectively

IV. DISCUSSION

Prior to this study, the heat-stress relationship of cardiac muscle has been determined only on papillary muscles [4-11]. Although papillary muscles have roughly axially-aligned myocytes, they typically have cross-sectional areas about 10 times those of cardiac trabeculae. The smaller radial dimension of trabeculae greatly minimizes the risk of anoxia, especially under high rates of energy expenditure. Furthermore, the energetics of papillary muscle has traditionally been measured using the myothermic technique. This technique, in contrast to our micromechanocalorimetric approach, requires the temporary absence of flow of bathing medium when measurements are made. This disturbs the delivery of nutrients to the muscle, while allowing accumulation of the waste metabolites produced by the muscle.

With their axially-aligned myocytes and small radial dimensions, and under continuous superfusion, the heat-stress relationships of healthy trabeculae are linear. This finding is in accord with the heat-stress relationships in rat [10, 11] and in rabbit [7-9] papillary muscles. Also in accord with previous results, we find that the heat-stress relationships are independent of stimulus frequency [4-6] but are dependent on $[Ca^{2+}]_o$ [7].

The slopes of the linear heat-stress regression lines depend on neither stimulus frequency nor $[Ca^{2+}]_o$, reflecting a consistent economy of crossbridge cycling with increasing mechanical output. That is, the heat liberated is linearly correlated with the net twitch stress developed by cycling crossbridges.

The extrapolated zero-stress intercept of the heat-stress regression line is termed the activation heat. It represents the metabolic expenditure associated with the pumping of Ca^{2+} into the sarcoplasmic reticulum by its Ca^{2+} -ATPase at zero macroscopic force production by the crossbridges. We found that the activation heat values are independent of stimulus frequency but are dependent on $[Ca^{2+}]_o$, being greater, on average, at 2 mM than at 1 mM $[Ca^{2+}]_o$. Our activation heat values are ~30-50% greater than values reported in the literature [4-11]. We presume that this discrepancy reflects the combined advantages of continuous superfusion and the more favorable radial dimensions of trabeculae for oxygen diffusion into muscle tissue core.

We are now equipped to extend our micro-mechanocalorimetric technique to the study of the energetics of cardiac pathophysiology.

V. CONCLUSIONS

We have determined, for the first time, the heat-stress relationships of rat cardiac trabeculae. The heat-stress relationships are linear, independent of stimulus frequency, but dependent on $[Ca^{2+}]_o$.

ACKNOWLEDGMENT

We gratefully acknowledge funding received from the Royal Society of New Zealand through Marsden Fund Contract UOA0607.

REFERENCES

1. Han J-C, Taberner AJ, Kirton RS et al. (2009) A unique micromechanocalorimeter for simultaneous measurement of heat rate and force production of cardiac trabeculae carnea. *J Appl Physiol* 107: 946-951.
2. Taberner AJ, Hunter IW, Kirton RS et al. (2005) Characterization of a flow-through microcalorimeter for measuring the heat production of cardiac trabeculae. *Review of Scientific Instruments* 76: 104902-1:7.
3. Littell RC, Miliken GA, Stroup WW et al. (2006) SAS for mixed models. 2nd edition. SAS Institute Inc, Cary, NC.
4. Gibbs CL and Gibson WR (1970) Effect of alterations in the stimulus rate upon energy output, tension development and tension-time integral of cardiac muscle in rabbits. *Circ. Res.* XXVII: 611-618.
5. Loiselle DS and Gibbs CL (1979) Species differences in cardiac energetics. *Am J Physiol* 237(1): H90-H98.
6. Loiselle DS (1979) The effects of temperature on the energetics of rat papillary muscle. *Pflugers Arch* 379: 173-180.
7. Gibbs CL, Loiselle DS, and Wendt IR (1988) Activation heat in rabbit cardiac muscle. *J. Physiol* 395: 115-130.
8. Gibbs CL, Wendt IR, Kotsanas G et al. (1990) Mechanical, energetic, and biochemical changes in long-term pressure overload of rabbit heart. *Am. J. Physiol* 259: H849-H859.
9. Kiriiazis H, Gibbs CL, Kotsanas G et al. (1992) Mechanical and energetic changes in short-term volume and pressure overload of rabbit heart. *Heart Vessels* 7: 175-188.
10. Kiriiazis H and Gibbs CL (2001) Effects of ageing on the activation metabolism of rat papillary muscles. *Clin Exp Pharmacol Physiol* 28: 176-183.
11. Kiriiazis H and Gibbs CL (1995) Papillary muscles split in the presence of 2,3-butanedione monoxime have a normal energetic and mechanical properties. *Am J Physiol* 269: H1685-H1694.

Corresponding author:

Author: June-Chiew Han
 Institute: Auckland Bioengineering Institute
 Street: 70 Symonds Street
 City: Auckland
 Country: New Zealand
 Email: j.han@auckland.ac.nz

About the Operating Principles of System DDFAO “(Dépistage et Diagnostique Fonctionnel Assisté Par Ordinateur)”

Huynh Luong Nghia and Nguyen Van Tiep

Le Quy Don Technical University /Biomedical electronic Department -100 Hoang Quoc Viet, Hanoi, Vietnam

Abstract— At present, one of advanced noninvasive techniques for medical diagnostics is the system electrosonatograph (ESG- DDFAO), which is estimated playing equivalent role of whole polyclinic. The paper treats the basics of this technique and define operating principles and structures for typical system ESG - DDFAO - Pro MEDISCAN M3D now firstly used in Vietnam.

Keywords— electrosonatograph, expert-like system, algorithm, bio-electroimpedance. Identify.

I. INTRODUCTION TO SYSTEM DDFAO [2]

A. What Is DDFAO ?

DDFAO has been invented in France and is an French acronym for **Dépistage et Diagnostique Fonctionnel Assisté par Ordinateur** to designate the first “Computer-Aided Screening and Functional Diagnosis” non-invasive investigation tool for the entire human body.

DDFAO is an imaging medical device but, unlike conventional scanners or MRI, which are expensive imaging devices looking for any possible lesion in the body and therefore require extensive computer power in order not to miss any detail, DDFAO is looking for the functional state of the different organs and systems of the human body.

B. The Applications of DDFAO

Screening and early detection

By pinpointing any discrepancy between the expected values measured in the different areas of the body which are linked together through the different body’s regulation systems modeled into DDFAO, all disorders in the organs and systems are highlighted, suggesting sensitivity to possible future pathologies and actions to be taken even before external symptoms have yet appeared. The operator-independent simple and quick procedure allows a high throughput for quick screening of large batches of population under scrutiny.

Functional diagnosis

DDFAO expert-like system analyzes the possible risks related to the current alkalosis or acidosis state of the organs and tissues of the patient, suggesting conventional examinations to assert the patient’s condition. DDFAO allows the doctor to look for the origin of a problem, not just treat the external symptoms.

It is to be noted that, like in a normal medical practice, knowing the clinical context of a patient is of a particular importance, since DDFAO is not looking for lesions. If the body is used to function with a particular lesion with no harm, DDFAO will not show a disorder. Similarly, if a treatment is appropriate and suppress the initial disorder, DDFAO will only show that, as a result of the good treatment, the body returned in an homeostatic (i.e. well balanced) state.

Treatment follow-up

Dynamic comparisons between the patient’s functional states, as recorded during two different visits. The values are instantly compared and DDFAO will pinpoint all the areas which have come closer to the homeostatic state, also highlighting the areas where the disorders have increased, allowing the doctor to take immediate corrective actions, before new external symptoms even appeared. Ultimately, DDFAO will allow to assert the return to the homeostatic state of a patient, thus indicating if the treatment must be continued even when the external symptoms have disappeared.

C. The Feature of DDFAO Technology

DDFAO is not representing these data on a hard-to-read list of numbers or hard-to-interpret graphics, but in a similar way that the data collected by mean of ultrasounds are displayed after calculations in an echography, DDFAO generates several reconstituted color graphic images in its unique easy-to-read yet comprehensive way.

DDFAO’s embedded expert-like system instantaneously proposes to the doctor its own analysis of the risks related to the current condition of the patient, suggesting possible complementary conventional examinations and actions related to several possible therapies.

II. SCIENTIFIC BASE AND OPERATING PRINCIPLES [2]

A. Scientific Base [1]

DDFAO is based on next sciences:

- a. The quantum theory
- b. Measurements of resistances of human body systems and organs
- c. Colloidal Properties of a material
- d. Perturbing foci and fields
- e. Measurement of biological microcurrents
- f. Somaesthesia
- g. Use of the principle of nuclear magnetic resonance in biology
- h. Information theory

B. Operating Principles [2]

DDFAO is a true medical device which reliably measures bio-electroimpedances by mean of 6 convenient large flat pods and determines accurately body parameters like pH and blood pressures, thanks to its highly integrated electronic circuitry.

DDFAO's integrated expert-like patented technology is also able to interpret these data by applying the neurophysiology principles and to propose automatically its own analysis of the patient's risks in less than 3 minutes (measuring time included), instead of simply printing out the measurements results as a set of raw data which require significant time of a trained person for the analysis !

DDFAO expert-like system is able to deliver a full analytical report on the detailed functioning of the complete body with organs and systems (down to the hormones), along with quantifying the risks for pathologies, giving recommendations for conventional examinations, and suggestions for therapies.

DDFAO is measuring the human body's electrical activity, actually using the same principles which are behind the well-known EEG and ECG, but instead of focusing on brain or heart activities, DDFAO applies the technique to the entire body, to record an ElectroSomatoGram (ESG).

DDFAO is simply sending a harmless low DC-voltage (1.28V) to the patient's body, by the mean of 6 electrodes in contact with his skin : two on his feet, two on his hands and two on his foreheads. By sequentially applying the positive polarity on each one of these electrodes while every other one is sequentially receiving the negative polarity, DDFAO initiates a migration of H⁺ and HC03⁻ ions in the different tissues traversed, thus creating a very low DC-current which is measured on each of the 22 branches under analysis.

The bio-electroimpedance of each branch is then simply calculated by the application of Ohm's Law and recorded as

the ESG. Of course, each branch is composed of many organs and tissues but DDFAO's patented cross-analysis algorithms allow to calculate the bio-electroimpedance of more than 69 different volumes (organs and surrounding tissues) in the human body and ultimately to determine the pH of each one of these volumes, whose pH is representative of their alkalosis or acidosis state, which is significative of trends or pathologies, according to the importance of this pH value.

The correlation between an organ's bio-electroimpedance and its pH or blood pressure is not new : it was actually proved by numerous electro-physiological research that started as early as the middle of the 19th century (E. Du Bois Reymond, 1857). But at that time, this experimental work had no applicable usage in common practice because it would take way too long to manually make all the measurements and calculations needed to make a proper diagnosis : only the modern understanding of the neuro-physiology principles and the affordable and extensive power of today's computers allowed fast calculations and the neurophysiology systems to be modeled into DDFAO.

III. THE DDFAO'S ALGORITHMS USED TO IDENTIFY DISEASES [5]

Analysing above described scientific base and operating principles of DDFAO enables to propose it's the algorithms used to identify the functional state of the different organs and systems of the human body (diseases) in figure 1. In this figure:

- The block “Preliminary processing” receives the signals from 6 electrodes and patient's medical file (the data about patient's age, sex and BMI). Then, this block prepares data to calculate the parameters named as parameter set to norms (N) and parameter of permeability called automatic (A).

- The block “Calculating parameters” estimates two parameters

1-Norm Na: this parameter depends on the body's water content and, after taking into account the above factors of variation, corresponds to functional norms of optimal concentration of the interstitium;

-Automatic Aa : The 0 point for this parameter is calculated relative to the mean electrical resistance of cell membranes or their permeability (electrochemical gradient of diffusion and activity). This will demonstrate the relationship between electrical membrane conductivity and ionic concentration of the interstitium;

- The blocks “Identifying ... diseases “ compare estimated parameters Aa and Na with standard parameters corresponding to diseases of the different organs and systems of the human body, and propose the diagnosis.

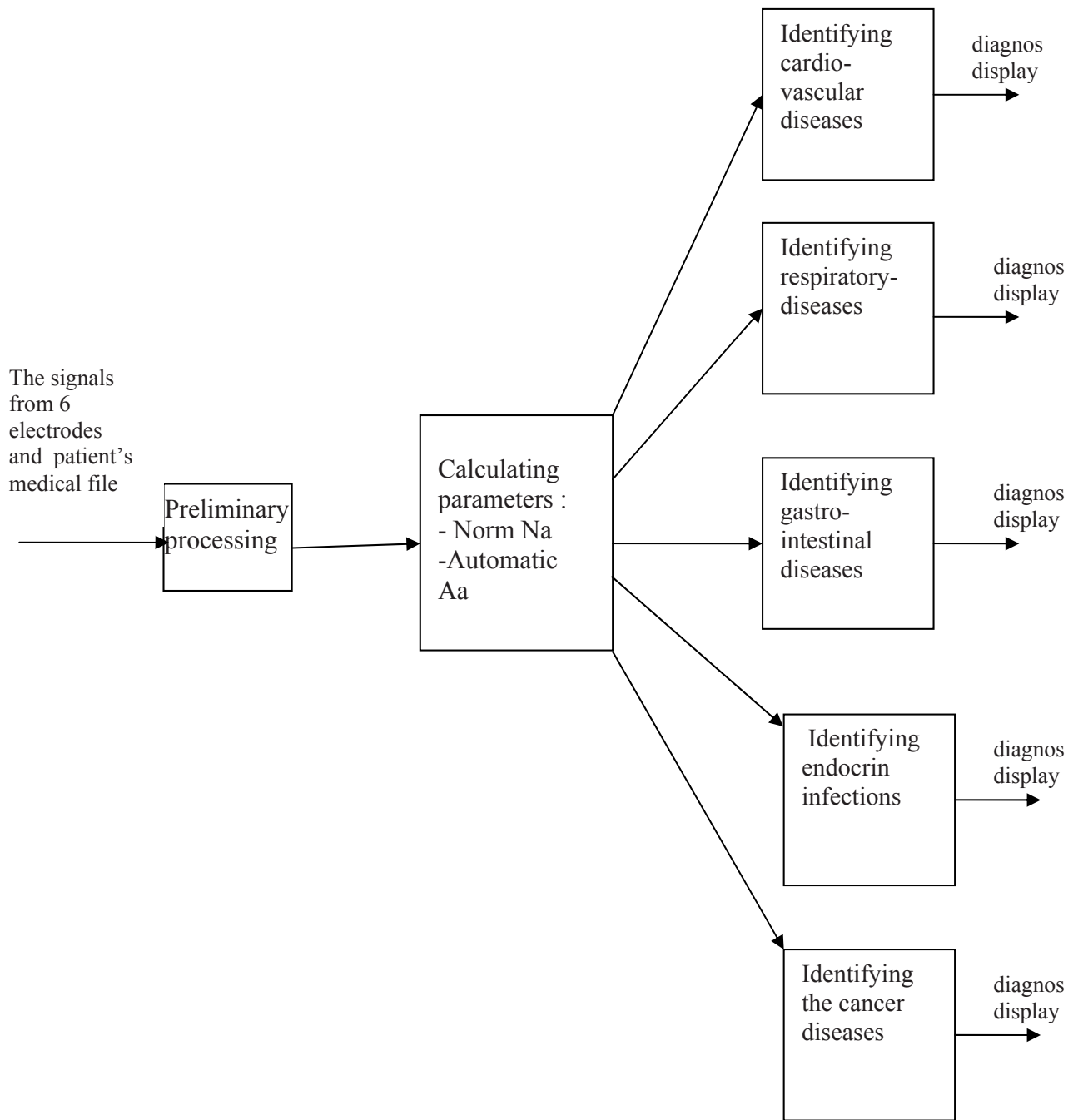


Fig. 1 Structure Scheme of diseases identifying algorithms used in DDFAO-PROMEDISCAN-M3D

IV. CONCLUSIONS

At the time of testing the DDFAO system's ability to detect the pathologies recorded is defined at 79.7%. Of the 1163 pathologies recorded, there were noted: False positives: 63 , False negatives: 112.

Sensitivity was 89% with a confidence interval of 9% for a remarkable specificity of 84% with a confidence interval of 11% (calculated at 95%).

REFERENCES

1. www.ddfao.ro/information.html
2. pagesperso-orange.fr/ms-tek/documents/DDFAO_FAQs.doc
3. www.medild.nl/Docs/Botkin_tests202003.pdf
4. www.helse1.no/dokumenter/DDFAO_T50_Synthesis.pdf
5. Huynh Luong Nghia, Nguyen Van Tiep, “The Study for Exploring the system DDFAO-PROMEDISCAN-M3D” , Thesis, Le Quy Don Technical University, Hanoi, 2009.

A Design of Renal Dataflow Control and Patient Record Management System for Renal Department Environment in Vietnam

Hai D. Vu¹, Thuan D. Nguyen¹, Ngoc P. Pham¹, Huy Q. Hoang¹, and Thanh V. Pham²

¹ Department of Biomedical Engineering, Hanoi University of Technology, Hanoi, Vietnam

² Viet Nhat Medical Equipments Co., Ltd., Hanoi, Vietnam

Abstract— According to Vietnam Ministry of Health report [1], kidney failure therapy is mainly depend on haemodialysis method (about 95%). This long-term method has to be used continuously to sustain patient life. Data extracted from the systems and patient records are greatly produced consequently. However, paper records are now major storage means that hold a big amount of the above data in almost renal departments in Vietnam. As the result, these state many inadequate settlements when dealing with patient records during treatment, monitoring and evaluating process. In corporation with Renal Department in Bach Mai Hospital and E Hospital, our research team has designed a renal dataflow control and patient record management system used in renal department environment.

The BK-HDmanager system combine hardware and software design to extract data from haemodialysis machine and transmit this information to computer, which has installed control software, via RS232 port. Main functions of this system include: Automatic control and management renal therapy - related parameters (NIBP, flow-out water, serum Urea and Creatinine concentration, electric dialysis parameters such as Na^+ , K^+ , Ca^+ , Cl^- concentration; check the availability of renal machines automatically, automatic change blood pressure measurement modes, HL7 standard data formation, data statistics... in our hardware design, controllable dataflow is tagged with ID, therefore, allow us to work with each separated module in haemodialysis. This hardware and software combination design is effectively support medical doctors and nurses during renal therapy process.

Keywords— Hemodialysis System, NIBP, Urea, Creatinine, HL7 standard, EMRs, e-Hospital, Patient ID.

I. INTRODUCTION

Based on recent reports from Vietnam Ministry of Health, Vietnam has over 72,000 patients who suffer kidney failure at their last stage every year. The only chance for them, which contribute up to 95% among other therapies, is to use hemodialysis for its advantages. Meanwhile, there are only 20 clinical centers that have been equipped haemodialysis machines but mostly are in Hanoi and HCM city. That means every year, only 5,000 patients, account for 7%, receives treatment. And 90% of kidney failure patient have to wait for their treatment and may end up with decease if

waiting time is too long [1]. For those who luckily receive treatments, they have to spent rest of their lives with hemodialysis machines with a minimum of 3 times per week. Data creation, therefore, has gradually become big [2]. A large number of patient has lead to overcrowding in hospital but doctors have to used paper-based management system with a minimum supports from computers [3]. Following research at several hospitals and clinics, we have designed a control and manage system, which is applied in kidney failure therapy. This system is connected to measuring devices through hardware interfaces (measuring devices and blood pressure monitoring) and automatically control, acquire data and monitor blood pressure parameters during therapy; manage therapy parameters, collect test parameters before and after treatment; establish thresholds; automatically locate the availability of machine for new patients. Besides, the program also has statistics function, reports and graphs, which are useful for doctors, reduce works for clinicians, and eliminate the overcrowding within hospital.

II. ANALYSIS AND DESIGN SYSTEM

A. Analyze Facts at Clinics

The operation in many hospitals as we researched is mostly manual works especially in data storage and management. Almost patient-related information as well as management procedures are relies on paper-based system. That is main reason for weak responses of clinics to patient demands and always witnesses the over-crowded circumstances. A few departments use computers to manage information but rather simple and un-uniform. Test results are manually extracted from machines by doctors or nurses, then printed out and attached to patient health record books [4,5].

Depend on scale of hospital, there are from a few to 10s haemodialysis machines to treat patient simultaneously. Patients take turn to use machine, which last 3 hours for each patient per treatment [1]. During therapy, due to its importance to patient's life, measuring and monitoring parameters need to be collected by clinicians continuously. It eats up a lot of time as hands do most of works.

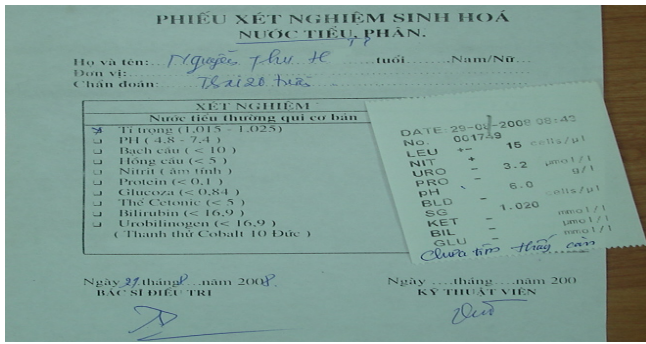


Fig. 1 Test results are printed out and clamped to paper-based patient record in laboratory

B. Design BK-HDmanager System

A system model has been designed following researches and analyzing facts at haemodialysis centers. In this model, to overcome internal problems in managing healthcare information, each patient will have an unique PID, which, in turn, allows system to acquire all information from patient processed that ID. This system controls patients by their IDs and treatment duration. When a patient comes for treatment, based on the availability of machines displayed on screen, clinician will guide patient to suitable machine. Then relevant information, from blood pressure measuring devices, will be recorded and sent to our system automatically. Data is stored in system database through IC interfacing board. Besides, other test parameters such as water output each treatment, Urea and Creatinine concentrations, electro dialysis parameters (Na⁺, K⁺, Ca⁺, Cl⁻...) is manually inputted and stored by controller program. From which, doctors can referenced all relevant information of patient to support their decisions in diagnosis, therapy or to trace patient's status.

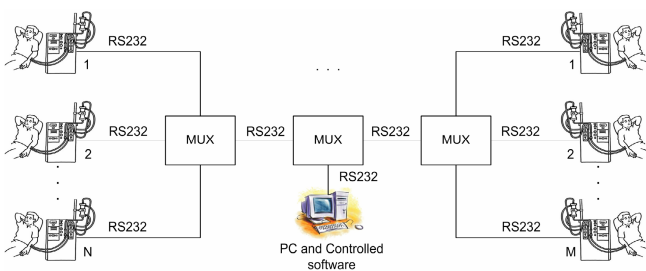


Fig. 2 The BK-HDmanager system model

C. Designing Hardware Interfacing Module

Main function of interfacing module in our system is to connect blood pressure measurement devices with computers, which therefore help program in computer, can automatically control and acquire data. According to our survey,

output port standard in most blood pressure devices is COM so we choose RS232 as our mean of interfacing.

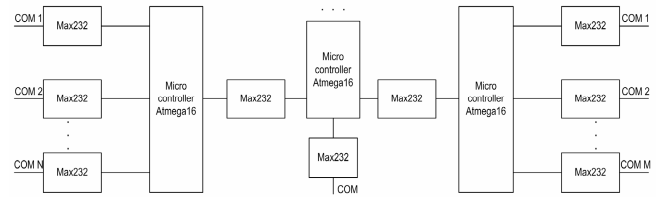


Fig. 3 Flow chart of hardware interfacing module

A critical point in controlling and acquiring data from measuring devices is to identify structure of data frames at the output. With references in technical manual supplied by manufacturer, IC board will encode data frames and sent reassembled data to computers [5,6]. In some cases where we could not get data formation from suppliers, we had to analyze device outputs by using software program to extract data from COM ports (such as Terminal, Collect, Virtual Serial Port Kit...), then compare with displayed data on screen to find out data formation of that devices [7]. In this design, blood pressure module is CSN602 from Beijing Choice. Meanwhile, data frame formations extracted from COM port is summarized follow [8]:

Reception protocol:

- Start bit + 8 data bit +1 stop +no parity
- <STX> ab; cd<ETX>
- <STX>: ASCII code, first byte is 0x02
- “ab”: commod code is changed to ASCII code
- “cd”: code to check error while changing to ASCII
- Error code is caculated:
- Sum = (a(hex) + b(hex) + c(hex) + d(hex)) %256
- <ETX>: ASCII code, last byte is 0x03

Transmission Protocol:

- Create: <STX> abc;d;e<ETX><CR>, which:
- <STX> (02): first value of frame
- “abc”: Current presure value
- “d”: Cuff errors
- “0”: Nomal cuff
- “1”: Change kind of patient
- “e”: Measurement status:
- “3”: Measuring
- “4”: Change mode
- <ETX>(03): Last value of frame
- <CR>(13): ASCII code, finish mesurement

Output data:

- <STX>a;b;cd;ef;ghijklmno;pqr; <ETX><CR>, which:
- <STX>(02): First value
- “a”: ASCII code of current status
- “0”: Finish self-test
- “1”: Normal system

- “b”: Kind of the patient
 - “0”: Adult
 - “1”: Infant
- “cd”: measurement modes:
 - “00”: Manual
 - “01”-“90”: Automation
- “ef”: Errors
- “ghi”: Systolic presure value ASCII code (mmHg)
- “jkl”: Diastolic presure value ASCII code (mmHg)
- “mno”: Mean presure value ASCII code (mmHg)
- “pqr”: Pulse Rate value ASCII code (bpm)

D. Design Controller Program

To increase the efficiency in implementation of Kiney Departments, controller program accompanied with the above interfacing module will automatically measure and monitor blood pressure parameters according to requirements from doctors, patient demographic and relevant information, automatic indentify location of available machine for next patients, supply searching, statistic, reporting, printing tools... which aids operations and help doctors in diagnosis, monitoring, treating patient with convenience, precise and fast [9,10].

As mentioned in previous paragraph, interfacing standard between computer and peripheral devices is RS232, hence transmitted and received data will in sequence form of packets. Each packet will be tagged at the beginning with <STX> and at the end by <ETX>, each packets are seperated by <CR> character. Data in each packet is sent successively from start character to end character. From what, operation chart implemented by program to receive and aquire data from devices will be as follow Fig. 4:

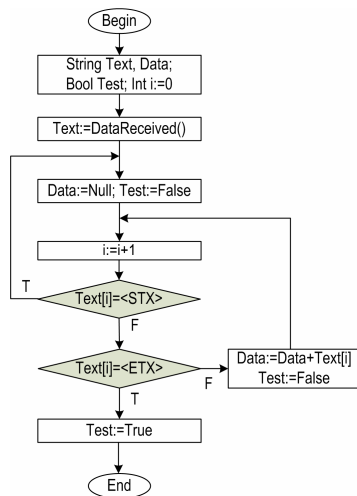


Fig. 4 Operation chart for controlling and acquiring data via COM port

Full control system design flow chart: Based on operation model existed in many departments, a program has supplied automatic control, adminstrate; manage patient information and personal health record and other tools to improve the effecitveness and efficiency. Algorithm for this program is shown in figure 5:

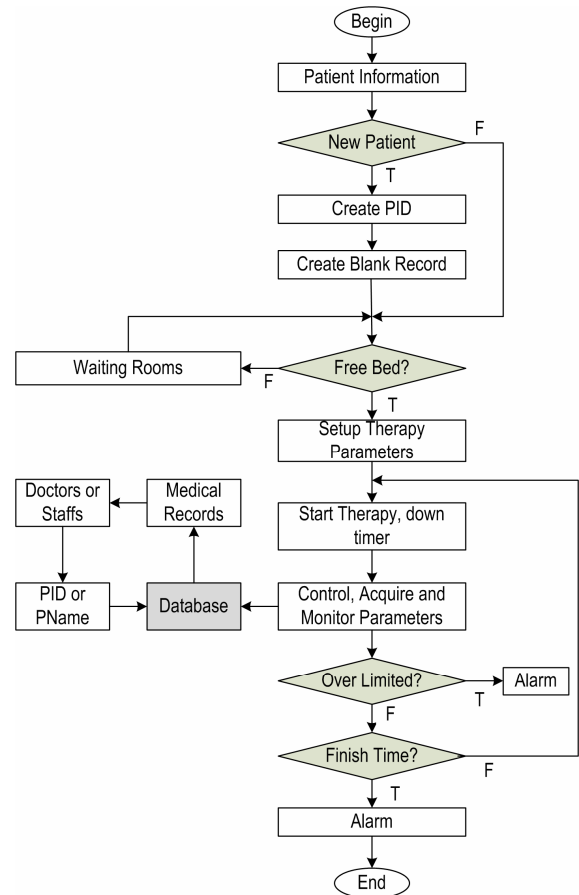


Fig. 5 Algorithm of the cotrolled software

III. CONCLUSIONS

The BK-HDmanager system has been fully designed with combination of hardware and software. Microcontroller Atmega16 is responsible for interfacing with machines through RS232 standard. Control software are written on .Net platform and use Microsoft SQL Server 2005 as database system. Interface of our software are displayed in Vietnam language, which therefore facilitate doctors and nurses usage. Our system is currently trialed at our Lab to calibrate parameters, and then plan to implement at Renal Department in Bach Mai hospital. Here are some results from our system design.

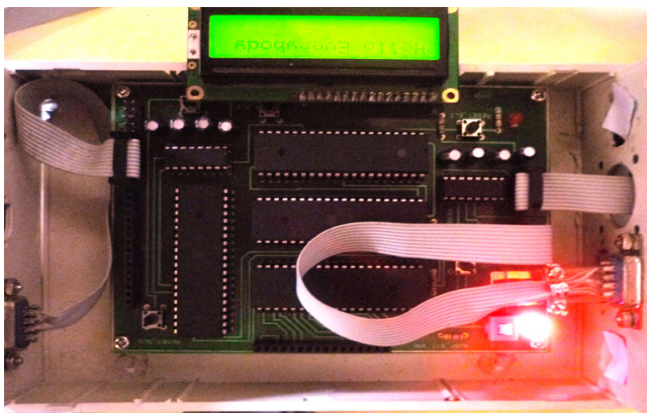


Fig. 6 Circuit to connect PC and hemodialysis machine

In our design, we use RS232 standard to interface PC with machine to control and acquire data. This contributes several problems when applied in hospitals. Therefore, we are developing alternative ways by using latest communication standards such as Wifi or Bluetooth, which helps our devices free from bundle of wires.

ACKNOWLEDGMENT

We would like to thank the Department of Biomedical Engineering, Hanoi University of Technology. We would like to thank the Bach Mai hospital, Khanh Luong hospital for their support and encouragement. The system was designed and developed by the Biomedical Engineering faculties and students at the Hanoi University of Technology.

REFERENCES

1. Nguyen N. Khoi, Tran V. Chat (2001) Hemodialysis, Journal of Medicine, Bach Mai Hospital 1:152-167.
2. Nguyen H. Phuong, Nguyen M. Anh, Hoang H. Anh (2008) Electronic Medical Record. Ministry of Health, Vietnam. Hanoi Medical Publisher.
3. Duong H. Lieu, Truong V. Dung (2006) Health Management. Ministry of Health, Vietnam - WHO. Hanoi Medical Publisher.
4. Nguyen D. Thuan, Vu D. Hai (2009) Building a Hospital Information processing System model in Vietnam. Journal of Science and Technology, Hanoi 69:6-10.
5. Vu D. Hai, Nguyen D. Thuan (2008) Acquiring and managing Laboratory data to apply in e-Hospital base on webserver. Journal of Science and Technology, Hanoi 68:28-34.
6. Vu D. Hai, Nguyen D. Thuan, Pham M. Hung, Nguyen T. Ha, Chu D. Hoang, Pham V. Thanh (2007) Designing Home - Care patient monitoring equipment, Proc. of the second International conference on the development of Biomedical engineering in Vietnam, Hanoi, 2007, pp 97-104.
7. Chu D. Hoang, Nguyen D. Thuan, Nguyen V. Dung, Vu D. Hai (2006) Measurement, analysis data flow of patient monitor and building program to display on PC, Journal of Science and Technology, Hanoi 58:45-50.
8. <http://www.choicemmed.com>
9. Vu D. Hai, Nguyen D. Thuan, Nguyen T. Ha (2006) Designing program to control and display biomedical parameters on computer, proc. of the 20th scientific conference - Biomedical Engineering section, Hanoi University of Technology, Hanoi, Vietnam, 2006, pp 55-60
10. Nguyen D. Thuan, Vu D. Hai, Nguyen T. Ha, Nguyen V. Dung, Nguyen S. Dung, Dinh T. Nhung, Nguyen T. Van, Pham V. Thanh (2008) Designing program to manage ultrasonography, proc. of the VN-HISMANAG'08, Ministry of Health, Hanoi, 2008, pp 167-172.



Fig. 7 User interfaces of control and manage software on PC, we have a plan to implement at Renal Department in Bach Mai hospital



Fig. 8 Connecting to PC and trial testing in our Laboratory

Author: Vu Duy Hai
 Institute: BME Department, Hanoi University of Technology
 Street: No. 1 Dai Co Viet str., Hai Ba Trung, Hanoi
 City: Hanoi
 Country: Vietnam
 Email: haivd-fet@mail.hut.edu.vn

Anisotropy of Longitudinal Wave Velocity in Spherically Shaped Bovine Cortical Bone

K. Yamamoto¹, T. Nakatsuji², M. Indo², T. Yanagitani³, M. Matsukawa², and K. Yamazaki¹

¹ Department of Orthopaedic Surgery, Hamamatsu University School of Medicine, Hamamatsu, Japan

² Laboratory of Ultrasonic Electronics, Doshisha University, Kyotanabe, Japan

³ Nagoya Institute of Technology, Nagoya, Japan

Abstract— Quantitative ultrasound (QUS) is a good method for measuring elastic properties of bone *in vivo*, because the obtained ultrasound wave properties directly reflect the longitudinal elasticity. Bone tissue is composed of minerals like hydroxyapatite (HAp) and collagen matrix. HAp crystallites orientation is thus one parameter of bone quality. In this study, we made spherically shaped specimens from anterior part of the cortical bone of three bovine femurs. By using these specimens, we experimentally investigate the anisotropy of ultrasonic wave velocity and the HAp crystallites orientation in axial-radial, axial-tangential and radial-tangential planes in detail. Longitudinal ultrasonic wave propagation was investigated by using a conventional ultrasonic pulse system. Wave velocity anisotropy was clear in each plane. The direction of the fastest wave velocity showed a small tilt from the bone axis in axial-radial and axial-tangential plane. Moreover, X-ray pole figure measurement indicated that there were also small tilts of the HAp crystallites orientation from the axial direction. The tilts were similar with the tilts of fastest velocity direction. There were actually good correlation between velocity and HAp crystallites orientation in axial-radial and tangential plane. But there was no correlation in radial-tangential plane.

Keywords— 1. Quantitative ultrasound (QUS), 2. hydroxyapatite (HAp), 3. cortical bone.

I. INTRODUCTION

In this aging society, nondestructive and safe assessment of bone is strongly expected to prevent elderly people from osteoporotic fracture risk. The present gold standard for the evaluation of osteoporosis is the dual-energy X-ray absorptiometry (DXA). DXA enables to measure bone mineral density (BMD). The X-ray measurements, however, have several problems. The measurement apparatus is large, expensive and not suitable for group screening. In addition, BMD only gives us the amount of mineral, which does not directly reflect the elastic properties of bone. On the other hand, quantitative ultrasound (QUS) is a good method for measuring elastic properties of bone *in vivo*, because the obtained ultrasound wave properties directly reflect the longitudinal elasticity. QUS techniques are usually low cost,

portability and always without the ionizing radiation, which is considered to be especially suitable for the assessment of children and pregnant women. Currently, two main parameters measured by QUS techniques are wave velocity (speed of sound, SOS) and slope of the frequency-dependent attenuation curve (broadband ultrasonic attenuation, BUA) [1]. These parameters can give us important information related to the bone elasticity and strength. One problem of this QUS method is the comparatively low measurement accuracy, which results from the complicated structure and elastic properties of bone. Actually, bones are usually heterogeneous and anisotropic [2, 3]. In the larger level, bones show anisotropic structure with the size of several 100 micron meters. For example, we can see haversian and brick-like (plexiform) structure in the cortical part of bone. At the nanoscopic level, bone consists of bone matrix, which includes type I collagen, polysaccharide and calcium phosphate. Calcium phosphate is 70% of total bone mass and forms an incomplete HAp crystal [4, 5]. Then, the orientation of HAp crystallites seems to affect the elastic properties of bone, as Young's modulus of HAp is about 80 times larger than that of collagen [6].

We have then tried to investigate the bone, especially focusing on the anisotropy and distribution of wave properties [7, 8]. We have reported the interesting wave velocity behavior in the bovine cortical bone, showing the strong effects of microstructures, direction of propagation, location of the measured parts. We have also pointed the relation between BMD and velocity [9]. However, despite the similar density, structure and BMD, in some bovine cortical bone specimens, the longitudinal wave velocities were often different. Therefore, we next focused on the effects of bone properties in much smaller level, for example, the crystallites orientation of HAp [9 - 11]. In these study, we found that velocities and HAp crystallites do mainly orientation in bone axis direction, and there are good correlation with them. Therefore we decided to do more detailed examination of bovine cortical bone.

In this study, we made spherically shaped specimens obtained from anterior part of the cortical bone of three bovine

femurs. By using these specimens, we experimentally investigate the anisotropy of ultrasonic wave velocity and the HAp crystallites orientation in axial-radial, axial-tangential and radial-tangential planes in detail.

II. MATERIALS AND METHODS

1. Materials

Figure 1 illustrates the preparation steps of the spherical bone samples. Three left femurs were obtained from 29, 30 and 30-month-old female bovines. The muscle and periosteum and bone marrow were removed from the cortical bone using surgical instruments. A ring-shaped cortical bone specimen was obtained from the mid-shaft. We made spherically shaped specimens obtained from anterior part of the cortical bones. The diameter of each spherical specimen was 10 mm. We defined each specimen as specimen 1, 2 and 3.

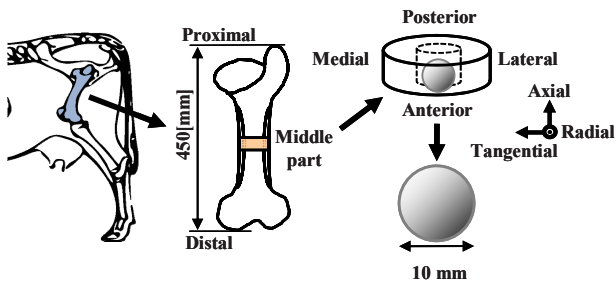


Fig. 1 Preparation steps of the spherical bone specimens

2. Ultrasonic Measurement

Measurements of longitudinal wave velocities were performed using a conventional ultrasonic pulse technique as shown Fig. 2. A PVDF focus transmitter (Custom made, TORAY, Yokohama, diameter 20 mm, focal length 40 mm) and a self-made PVDF receiver (diameter 10 mm) were used in this experiment. The beam width at the half maximum values of the wave amplitude was approximately 1.5 mm at the focal point [12]. Both PVDF transducers were mounted coaxially with distance of 60 mm in degassed water at 22.0 ± 0.1 °C. A function generator (Agilent, Colorado, 33250A) delivered electrical pulses to the transmitter, which was converted into ultrasonic waves. A single sinusoidal signal with a center frequency of 1 MHz, and amplitude of $50 V_{p-p}$ was applied to the transmitter. The longitudinal wave propagated through water, specimen and water. The other transducer received the wave, and converted it into the electrical signal. The signal was amplified by a 40-dB preamplifier (NF, Yokohama, 5307) and visualized in an oscilloscope (Tektronix, Tokyo, TDS524A). The measured specimen was placed in the focal zone of the

sound field. The direction of the ultrasound incident wave was perpendicular to the side surface of the cylindrical specimen. By changing the incident angle, we obtained velocity distribution of longitudinal waves. The measurements were performed at each rotation angle of 5 degrees.

The wave velocity was calculated by the difference of the arrival time Δt of longitudinal wave fronts which passed through the water with or without the specimen. The wave velocity in the specimen can be derived from the equation.

$$v = dv_0 / (d - \Delta tv_0) \quad (1)$$

where d is the specimen diameter and v_0 is the wave velocity in water.

By using this method, we measured the anisotropy of ultrasonic wave velocity in axial-radial, axial-tangential and radial-tangential planes in detail (Fig. 3).

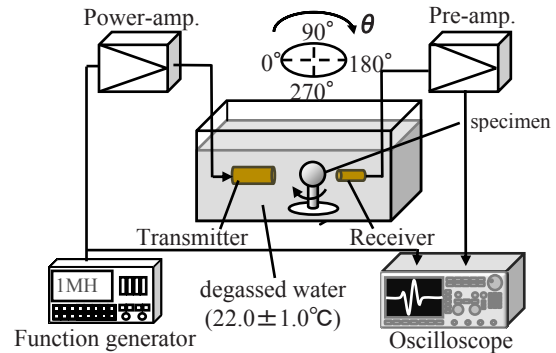


Fig. 2 Ultrasonic measurement system

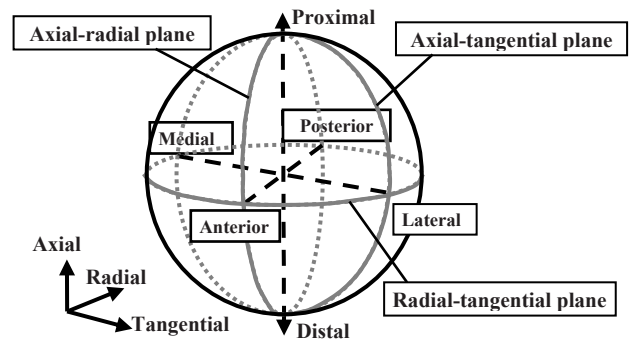


Fig. 3 The measurement planes in each specimen

3. X-ray Pole Figure Measurement

X-ray pole figure analysis was employed to evaluate crystallite alignment in the out-of-plane and in-plane direction. In previous study we used X-ray diffractometry [7,8], by using an X-ray diffractometer (PANalytical X-Pert Pro MRD). This measurement gives quantitative information on the crystallite

orientation, however, only in the equator plane. X-ray pole figure analysis reveals the extent of crystallite alignment in the out-of-plane and in-plane direction quantitatively. If the crystallites are unidirectionally aligned in the specific direction, the summation of poles diffracted by each crystallite forms a high concentration spots in the pole figure.

The configuration of the pole figure measurement system is shown in Fig. 4. Sample angle q and X-ray detector angle $2q$ were kept stationary. The angle in the sample rotation plane normal to the scanning plane is called the f - or y -angle. The f -angle is defined as the in-plane rotation angle. The y -angle is the elevation angle of the substrate plane. The pole figure is measured by scanning the f -angle and y -angle at a fixed q -angle under the Bragg condition.

As shown in Fig. 4, the y - and f -angles are indicated as the radial and circumferential directions in the pole figure, respectively. The X-ray intensity of the pole is represented in contour.

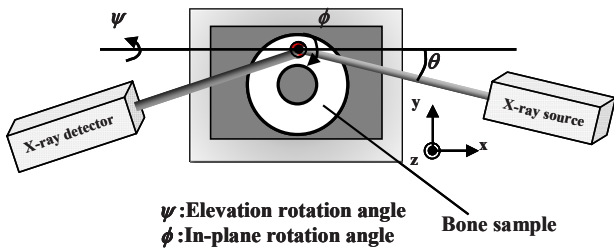


Fig. 4 Configuration of the pole figure measurement

III. RESULTS AND DISCUSSION

Figure 5 shows the velocity data in each plane of specimen 1. The velocity clearly changed due to the rotation angle. The maximum and minimum velocity values changed due to the specimens. Velocity anisotropy was present in a bone axis direction in axial-tangential and axial-radial plane mainly. In the radial-tangential plane, anisotropy was present in tangential direction. Three specimens showed similar tendency of velocity. However, the direction where the fastest wave velocity was observed was inclined 5 to 10 degrees from the axial direction. In addition, we could not find the common anisotropic tendency among three specimens.

Figure 6 shows (0002) pole figure measured from radial-tangential plane of sample 1. High pole concentration was clearly observed. This pole concentration indicates that the HAp crystalline c-axis are oriented to the similar direction.

Figure 6 shows (0002) pole figure measured from radial-tangential plane of sample 1. High pole concentration was clearly observed. This pole concentration indicates that the HAp crystalline c-axis are oriented to the similar direction.

We also found the small tilt of c-axis direction from the bone axis, which was similar with the velocity data. However, the HAp crystalline c-axis was not oriented to the other planes.

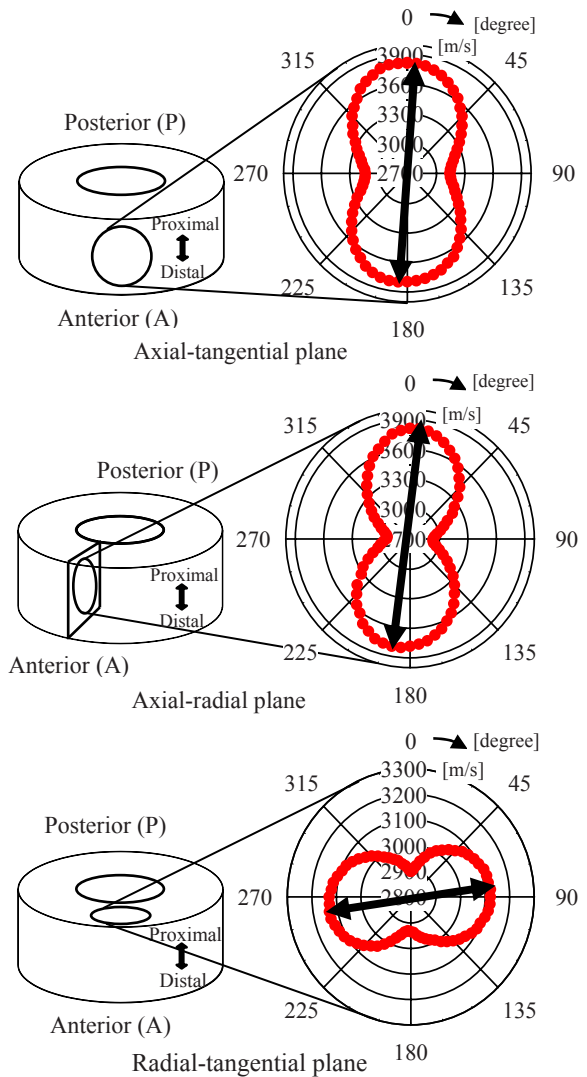


Fig. 5 Anisotropy of the velocity data of specimen 1 (A central value is not 0)

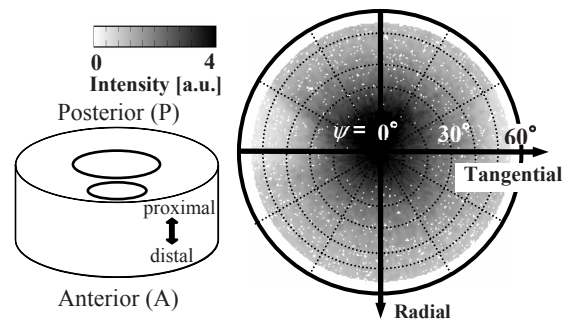


Fig. 6 (0002) pole figure in the radial-tangential plane of specimen 1

Considering the small tilt of HAp crystallites alignment and the fastest velocity angle, we next focused on the off-axis characteristics. The relationship between velocity and intensity of (0002) peaks in axial-tangential, axial-radial and radial-tangential planes are shown in Fig. 7. A significant correlation between the velocity and intensity was observed in axial-tangential and axial-radial direction ($R^2=0.88$, $P<0.001$ and $R^2=0.89$, $P<0.001$). There was no correlation in radial-tangential direction. This tells us that the small tilt of the fastest velocity angle seems to be dependent of the HAp crystallites orientation.

One reason for the anisotropic wave velocity in the radial - tangential plane, where few HAp crystallites align, seems to come from the microstructure. The anterior part of bovine cortical bone has plexiform structure, which is formed from bricklike bone lamellae sandwiched with vascular plexuses and grows parallel to the outer bone surface.

These present data tell us that the longitudinal wave velocity reflects HAp orientation in the nanoscopic level as well as the structure in the microscopic level.

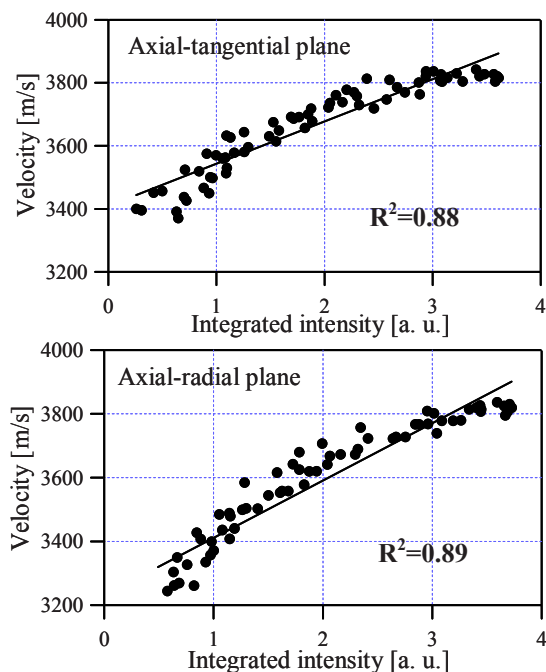


Fig. 7 The relationships between velocity and HAp crystallites orientation

IV. CONCLUSION

By using spherically shaped bovine cortical bone samples, we experimentally investigate the anisotropy of ultrasonic wave velocity and the HAp crystallites orientation in axial-radial, axial-tangential and radial-tangential planes in

detail. Ultrasonic wave velocity and HAp crystallites were mainly orientated in a bone axis direction. There were actually good correlation between velocity and HAp crystallites orientation in axial-radial and tangential plane. But there was no correlation in radial-tangential plane.

These results tell us the velocity seems to be an indicator of HAp crystallites orientation, which is strongly connected to the bone quality.

ACKNOWLEDGMENT

This study was partly supported by the Academic Frontier Research Project of the "New Frontier of Biomedical Engineering Research" by Doshisha University and the Ministry of Education, Culture, Sports, Science and Technology, a bilateral joint project between the Centre National De La Recherche Scientifique (CNRS) and the Japan Society for promotion of Science supported by the Japan Society for Promotion of Science and Grant-in-aid for Scientific Research (B) supported by Japan Society for Promotion of Science.

REFERENCES

1. C. M. Langton, S. B. Palmer, R. W. Porter: Eng. Med., Vol. 13, pp.89-91, 1984.
2. F. Padilla, E. Bossy and P. Laugier: Jpn. J. Appl. Phys., Vol. 45, No. 8A, pp.6496-6500, 2006.
3. Y. Nagatani, H. Imaizumi, T. Fukuda, M. Matsukawa, Y. Watanabe and T. Otani: Jpn. J. Appl. Phys., Vol. 45, pp.7186-7190, 2006.
4. R. B. Martin and D. B. Burr, New York: Springer-Verlag, 1980.
5. N. Sasaki, N. Matsushima, T. Ikawa, H. Yamamura and A. Fukuda: J. Biomech., Vol. 22, pp.157-164, 1989.
6. R. S. Gilmore and J. L. Katz: J. Mater. Sci., Vol. 17, pp.1131-1141, 1982.
7. Y. Yamato, H. Kataoka, M. Matsukawa, K. Yamazaki, T. Otani and A. Nagano: Jpn. J. Appl. Phys., Vol. 44, pp.4622-4624, 2005.
8. Y. Yamato, M. Matsukawa, T. Otani, K. Yamazaki and A. Nagano: Ultrasonics, Vol. 44, pp.227-233, 2006.
9. K. Yamamoto, Y. Yaoi, Y. Yamato, H. Mizukawa, T. Yanagitani, M. Matsukawa and K. Yamazaki: Jpn. J. Appl. Phys., Vol.47, pp.4096-4100, 2008.
10. Y. Yamato, M. Matsukawa, T. Yanagitani, K. Yamazaki, H. Mizukawa and A. Nagano: Calcif. Tissue Int., Vol.82, pp.162-169, 2008.
11. Y. Yaoi, K. Yamamoto, T. Nakatsuji, T. Yanagitani, M. Matsukawa, K. Yamazaki and A. Nagano: Jpn. J. Appl. Phys., Vol.48, 2009. 07GK06
12. T. Otani, Jpn. J. Appl. Phys., Vol.44, pp.4578-4582, 2005.

Author: Kazufumi YAMAMOTO
 Institute: Department of Orthopaedic Surgery, Hamamatsu University School of Medicine
 Street: 431-3192, 1-20-1 Handayama
 City: Hamamatsu
 Country: Japan
 Email: kazyama@hama-med.ac

Calculating the Dosimetry Distribution of Leksell Gamma Knife in Phantom Zupal Head by Using MCNP5

Dang Truong Ka My¹, Dang Nguyen Phuong², Truong Thi Hong Loan², and Mai Van Nhon²

¹ PET-CT & Cyclotron Unit, Cho Ray Hospital, Vietnam

² Faculty of Physics - University of Natural Sciences, VNU-HCMC, Vietnam

Abstract— Leksell Gamma Knife (LGK) is one of the most modern radiosurgery equipment in treating small volume brain cancer by using gamma-rays emitted by Co60 sources. In this paper, the MCNP5 code was used to calculate the absorbed dose distribution of LGK with 201 sources in different collimators diameters (4; 8; 14 and 18 mm) to Zupal head phantoms (a human-head contain more than 15 kinds of material about cerebral cortex, spinal cord, cartilage, orbit, bone...). The depth-dose was investigated. Zupal phantom was used to compare if there is any difference between doses estimated by using water phantoms and doses in real radiosurgery. The results showed that the dosimetry concentrated in center area of the Zupal phantom. These results were compared with the Gamma Plan at FWHM, there was no large difference between absorbed doses. Gamma Plan program was used accompany with the Leksell Gamma Knife Unit. Thus, it requires another program to verify the accuracy of the Gamma Plan. Calculating the absorbed dose in Zupal head phantom using MCNP5 code was considered to another method for testing the accuracy of the Gamma Plan. MCNP5 code was used for calculating absorbed dose in phantom Zupal head. These results were appropriate to real treatments. Simultaneously, MCNP5 is first used for calculating absorbed dose and treatment planning.

Keywords— Leksell Gamma Knife, Gamma Plan, dose distribution, Zupal head phantom, MCNP.

I. INTRODUCTION

LGK is an instrument that permits a precise external irradiation to treat intracranial lesions. This is the most modern device using high radioactive dose concentrated in small volume (less than 3.5mm) in patient's head. This effect on the benign tissue around is the lowest respectively [1]. LGK contain 201 Co⁶⁰ sources (approximately 30Ci) in a hemispherical arrangement. The size and shape of the final beam (gamma ray) can be achieved by combining different treatment helmets (4, 8, 14, 18mm) with an appropriate configuration of plugged sources. The LGK is used together with the Gamma Plan, a planning system which uses semi-empirical algorithms with various approximations to calculate the dose.



Fig. 1 Leksell Gamma Knife – Model C

To ensure the quality of the planning system, MCNP simulation is a good complementary tool to achieved this purpose. In this paper, we used MCNP5 to simulate LGK device for calculation dose distribution in Zupal head phantom. This result was calculated through tally FMESH [2]. We got the graph to display the dose distribution on x, z axis.

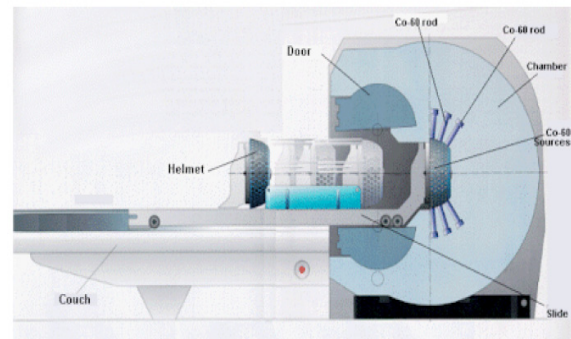


Fig. 2 Cross sectional view of LGK

II. MATERIALS AND METHODS

LGK Unit uses Co⁶⁰ sources for emitting gamma ray through the collimators with various material include in lead, tungsten and iron. The configuration of a single source and 201 sources in LGK are shown in figure 3a and 3b [4].

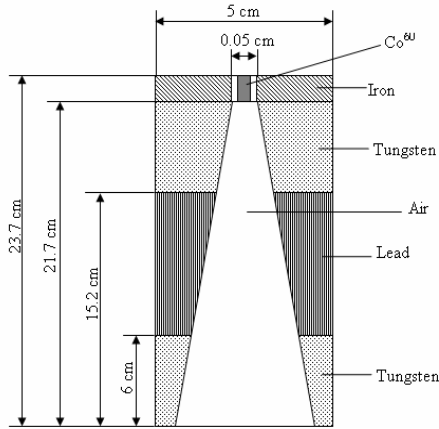


Fig. 3a Configuration of a single source in LGK

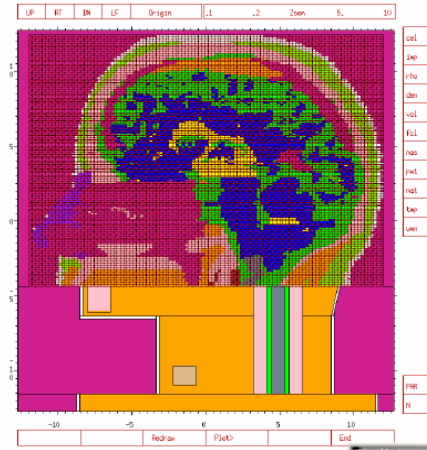


Fig. 4 Zupal head phantom

In the present study, we used MCNP5 to calculate the absorbed dose distribution in phantom Zupal head from 201 sources. The phantom Zupal head is similar with the real head, which was simulated with more than 15 kinds of various materials (including cerebral cortex, spinal cord, cartilage, orbit, bone...) [2]. Configuration of the Zupal head is divided in $85 \times 109 \times 120$ lattice of voxels, each voxel is $2.2 \times 2.2 \times 1.4 \text{ mm}^3$. After that we compared this result with the one from water phantom [3]. The energy of photon is 1.25 MeV.

The simulating process was divided into two stages [3]. First, we simulated the whole single-beam channel. Second, each source was modeled as a disk without any source and capsule filtration. Tally FMESH was used for calculating the absorbed dose in the phantom. The dose was investigated in four collimators 4, 8, 14, 18 mm. The total history is 1×10^7 .

III. RESULTS

Dose distribution with different size of collimators along x and z axis was shown in Fig 5, 6, 7, 8.

It can be seen from these figures that dose distribution is symmetric, concentrating at the center of the phantom and maximum absorbed dose in 1cm radius. Dose distribution along z axis dropped faster than x axis. The horizontal axis is shown the depth dose measured in cm. The vertical axis is shown the relative percentage dose (%).

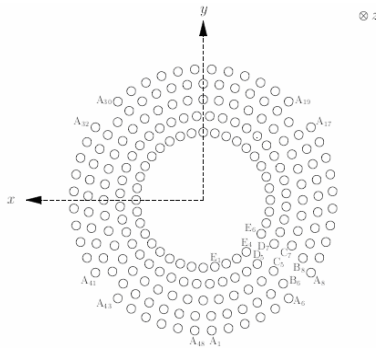


Fig. 3b The configuration of 201 sources

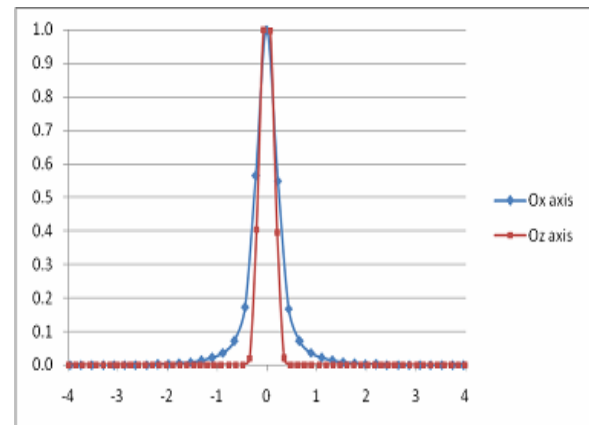


Fig. 5 Dose distribution on Ox, Oz axis with collimator 4mm

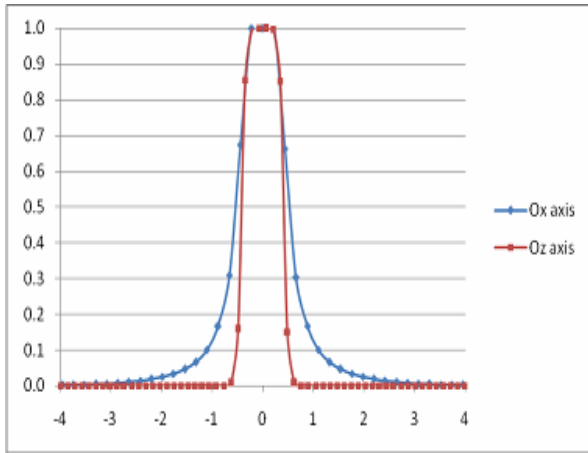


Fig. 6 Dose distribution on Ox, Oz axis with collimator 8mm

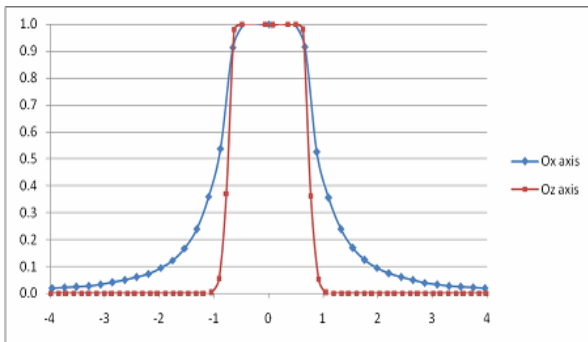


Fig. 7 Dose distribution on Ox, Oz axis with collimator 14mm

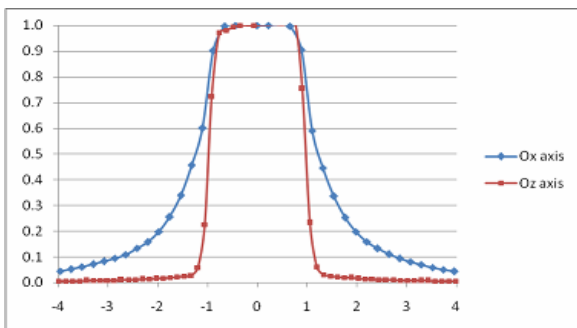


Fig. 8 Dose distribution on Ox, Oz axis with collimator 18mm

After that, we compared to water phantom. There is suitable between MCNP5 simulating results and the planning treatment.

IV. COMPARISON WITH GAMMA PLAN

To verify these results, we compared it to the Gamma Plan in FWHM through two tables below.

Table 1 Compare the results with Gamma Plan on Ox axis

The collimator diameter (mm)	FWHM (mm)	
	Gamma Plan	Results
4	6.0	5.0
8	11.2	10.0
14	19.1	17.9
18	24.4	22.7

Table 2 Compare the results with Gamma Plan on Oz axis

The collimator diameter (mm)	FWHM (mm)	
	Gamma Plan	Results
4	4.8	3.0
8	9.2	7.0
14	15.8	14.0
18	20.0	19.1

V. CONCLUSION

The results calculated by MCNP5 code in phantom Zubal head show that they are appropriate to the real treatment. Therefore, MCNP5 is the first used for calculating absorbed dose and treatment planning.

ACKNOWLEDGEMENTS

We are all grateful to doctors, physicists of Gamma Knife Unit in Cho Ray hospital for providing documentaries and ideas to finish this research.

REFERENCES

- [1] Introduce Leksell Gamma Knife – Cho Ray hospital 2006.
- [2] X-5 Monte Carlo Team, MCNP – A General Monte Carlo N-Particle Transport Code, Version 5, Los Alamos National Laboratory, 2003.
- [3] Dang Truong Ka My, Dang Nguyen Phuong, Truong Thi Hong Loan, Mai Van Nhon, Investigate the absorbed dose of Leksell Gamma Knife with 201 sources by using MCNP5 program, Congress of Medical Physics (The 8th AOCMP & 6th SEACOMP, 29 Oct. – 01 Nov. 2008).
- [4] Yipeng Li, Absorbed dose measurements and MCNP modeling for the Leksell Gamma Knife, Master Thesis, Ohio State University, 2002.

Author: Dang Truong Ka My
Institute: PET-CT & Cyclotron Unit, Cho Ray Hospital, Vietnam
Street: 790 Nguyen Chi Thanh St, Dist 5
City: HCM
Country: Vietnam.

A Program for Locating Possible Breast Masses on Mammograms

Viet Dzung Nguyen, Duc Thuan Nguyen, Tien Dzung Nguyen, Thom Thao Nguyen Thi, and Duc Hoa Tran

Hanoi University of Technology, Hanoi, Vietnam

Abstract— Breast cancer is the second most common type of cancer and also one of the leading cause of cancer death worldwide. Mammography, which uses X-ray technology to image the breast, is currently the method of choice of early detection of breast cancer. This paper introduces a method for detecting suspicious masses on mammograms, which are efficient applicable for circumstances in Vietnam. The method consists of three steps: background subtraction, template matching and region growing. The method has been tested on the Mammography Image Analysis Society (MIAS) database. A relatively high detection rate and low false positive per image implies that the method can be a quite effective tool in diagnosing breast cancer.

Keywords— Breast cancer, template matching, region growing, mass detection.

I. INTRODUCTION

Breast cancer is the most common cancer and continues to be a significant public health problem among women around the world. Mammography, making images of the breast using X-rays, is the most widely used modality to detect and characterize breast cancer [7]. Mammography has high sensitivity and specificity, even small tumors and microcalcifications can be detected on mammograms. The breast is compressed between two plexiglas plates to flatten and immobilize it. Mammograms show a projection of the breast that can be made from different angles. The two most common projections are medio-lateral oblique and cranio-caudal. Both of these projections should include as much breast tissue as possible in the image as shown in Figure 1.

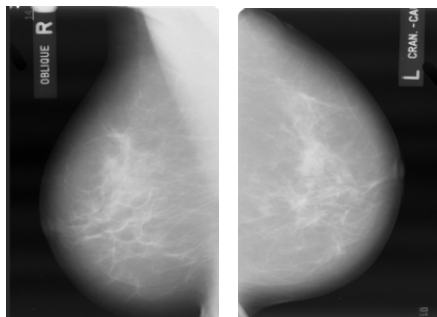


Fig. 1 Medio-lateral oblique and cranio-caudal films

Mammography does have a number of drawbacks. It is an invasive technique because the women is exposed to a (low) radiation dose. Also, the compression of the breast can be a painful experience.

Approximately 10% of all malignant abnormalities is radiographically occult and therefore not visible on mammograms. If palpable lesions are found that cannot be made visible using mammography, ultrasound or magnetic resonance imaging (MRI) can be used to further examine the breast. Ultrasound has rather low sensitivity and specificity and is not useful for screening, but has proven to be a useful modality for discriminating solid and cystic lesions [2]. Contrast-enhanced magnetic resonance imaging has shown to be useful for discriminating benign and malignant lesions, and due to its high sensitivity it is able to show a large number of lesion that are radiographically occult [1]. MRI is not a useful modality for screening, because of its low specificity and high cost. Mammography is the only image modality suited for screening programs because of its high performance and low costs.

Breast cancers can be described as being *in situ* (i.e. they have not spread from their originating duct or lobule). The only sign that may appear on mammograms are microcalcifications. Microcalcifications appear as small, bright objects that stand out from the surrounding tissue. Microcalcification can stand alone or in cluster.

Alternatively, breast cancers can be described as being *invasive* (i.e. they have broken into the surrounding fatty tissue of the breast). They can appear on mammograms as a mass or architectural distortion (referred as “mass” in the rest of this paper). A mass is defined as a space-occupying lesion seen in at least two different projections [3]. Masses are described by their shape and margin characteristics.

The severity of an invasive breast cancer is related to the stage of the disease [6], which describes how far it has spread (e.g. it is confined to the breast, or surrounding tissue, or has metastasised to distant organs). At state 1, the mass is no longer than 2 cm in diameter; no lymph node;. At stage 2, the mass is between 2 cm and 5 cm in diameter, and/or lymph nodes under the armpit. At stage 3, the mass is larger than 5 cm in diameter and there are lymph nodes under the armpit. And at stage 4, the mass may be any size; the lymph nodes in the armpit are often affected; the cancer has spread to other parts of the body.

Early detection of breast cancer plays an important role in treatment and cure for patient. Many image processing techniques are applied to mammograms to help radiologists segment suspicious masses and thus help early detect breast cancer.

According to statistic data at K Hospital in Hanoi – the leading hospital in cancer detection and treatment in Vietnam, the number of Vietnamese women having breast cancer is increasing, 50% of them at stage 3 or 4. The diagnosing result depends mainly on the quality of mammograms and experience of radiologists. However, the probability of missing suspicious masses may be up to 40%. Some software programs has been used but they only have basic functions such as brightness and contrast enhancement that help radiologists intepret mammothic films more accurately. Our program has been developed in order to aid radiologists and doctors not only in enhancing quality of films but also in locating possible breast masses on mammograms.

The program provides a variety of basic functions such as reading, editing, saving images; contrast enhancement; filtering; histogram modification; edge detection; distance measurement... Nevertheless, in scope of this paper, we discuss method of locating possible masses on mammo-grams that consists of three steps: background subtraction, template matching and region growing.

II. LOCATING POSSIBLE BREAST MASSES

The method of locating possible masses on mammo-grams that employed in the program consists of three steps: background subtraction, template matching and region growing as shown in Figure 2.

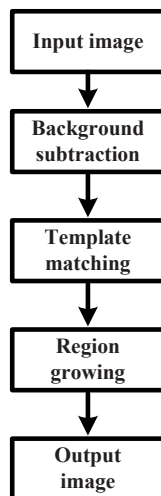


Fig. 2 Block diagram of the program

A. Input Image

Input image is digitalized mammogram and being quality enhanced if necessary.

B. Background Subtraction

As shown in figure 1, there are 2 major regions in the mammographic image: background region and breast region. The background region occupies a relative large area in the image. The masses only appear in in breast region not background region. So in order to at least reduce processing time the background should be removed or subtracted from the original image.

We can simply use a global threshold T (i.e $T=16$ as in [8]) to remove this region.

C. Template Matching

A mass in a mammogram image is either benign or malignant. Masses tend to have a greater intensity than their neighboring regions. They are somewhat circular, although they display weak or fading boundaries with neighboring tissue. Figure 3 is examples of mass.

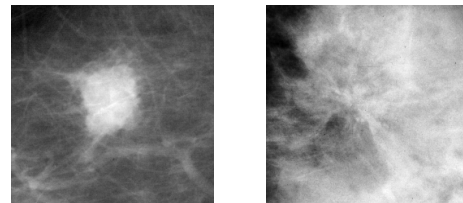


Fig. 3 Examples of mass

Objects in a mammogram image can be located and identified by comparing the image to a template. The template is constructed from a part of another image that exhibits the visual and statistical properties of the objects being sought. Several possible templates are: a sphere projected onto 2-D, a 2-D hyperbolic secant function, a simple circle.

The sphere projected onto 2-D is generated with equation (1). D is the diameter of the template.

$$F(x, y) = D^2 - x^2 - y^2 \quad (1)$$

The 2-D hyperbolic secant (sech) function is generated with equation (2) as suggested in [4]

$$F(x, y) = \text{sech}(x^2 + y^2) \quad (2)$$

There are several ways to compare a template to a mammogram image. Some use convolution or a cross-correlation based method, which is very efficient with the use of the Fast Fourier Transform (FFT). However, we found that convolution methods with the sech template can become

disordered by changes in local mammogram intensity. An alternative would be the correlation between the template and each pixel in the image, where the sub-image surrounding each pixel is the same size as the template. The correlation-based template-matching algorithm is not biased by varying intensities and is sensitive to characteristics of the shape [5]. The formula used for the correlation between the template and the sub-image is as follows

$$\text{cor}(x, y) = \frac{\text{cov}(x, y)}{\sigma_x \cdot \sigma_y} \quad (3)$$

$$\text{cov}(x, y) = \mu_{xy} - \mu_x \cdot \mu_y \quad (4)$$

where $\text{cov}(x, y)$ is the covariance of the template x , and the sub-image y surrounding the pixel. σ_x and σ_y are the standard deviations of the template and the sub-image. μ_x and μ_y are the means of the template and sub-image. μ_{xy} is the mean of each pixel in the template multiplied by each pixel in the sub-image.

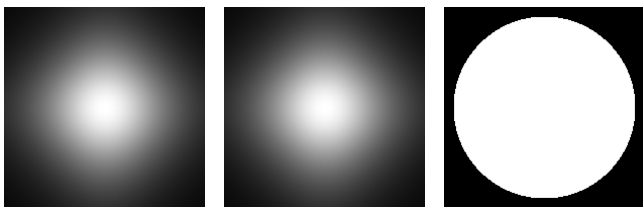


Fig. 4 Projected sphere, 2-D sech function, simple circle templates (from left to right)

The result of applying the correlation to the image returns a new image, containing values between -1 and 1. The closer the correlation value is to 1, the greater the similarity between the template and the pixel being tested. That is, pixels producing a correlation value close to 1 are similar to the mass template.

To find areas in the image, which are most likely to contain mass lesions, a threshold $T1$ is used with the correlation values. Pixels with correlation values of equal or above threshold $T1$ have a high probability of being a mass lesion. $T1$ is normally chosen in range [0.6, 1]. Figure 5 show the results with different threshold. The white areas indicate the possible mass locations in the mammograms. If $T1$ is increased, fewer detections will be produced, and if lowered more detections will be produced but many of them are false positives.

D. Region Growing

The template matching step will locate pixels that have a high probability of being a mass. However, it is very

difficult for doctors to figure out location and shape of masses if only several pixels are located and display.

To overcome this problem, we consider the pixels extracted from template matching step as “seeds” and perform region growing. Every neighbour pixel of each seed is checked. If difference between value of each neighbour pixel and that of the seed is not larger than a threshold $T2$, it will be grouped with the seed. The process continues until no neighbour pixel satisfies above condition.

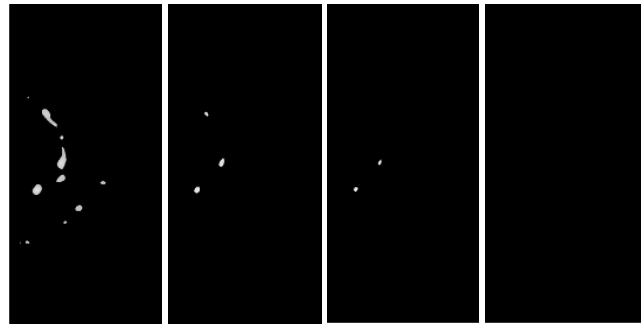


Fig. 5 Results of thresholding with $T1$ of 0.7, 0.8, 0.85 and 0.9

E. Output Image

Output image is the original image with contours of possible masses imposed on it.

III. RESULTS

The program is written using Matlab 7.0 (R14) Service Pack 2 with Image Processing Toolbox 5.0.2. The program can be installed in different computers without requiring Matlab to be pre-installed.

On the left side of figure 6 is original images that contain masses and on the right side, contours of respective masses are drawn in the images. It is noted that, even masses in images of dense glandular tissue can be detected. Beside that, area, centroid and diameter of suspicious mass are also computed and displayed.

When testing on MIAS database, we obtained the best sensitivity of about 85% and false positive per image of 0.16 with size of the template is 41×41 , $T1=0.7$ and $T2=10$.

IV. CONCLUSIONS

A relatively high detection rate and low false positive per image implies that the employed method can be a quite effective tool in aiding doctor in breast cancer diagnosing. Some of future works to improve the performance of the

method are finding more proper template; classifying detected masses as benign or malignant masses.

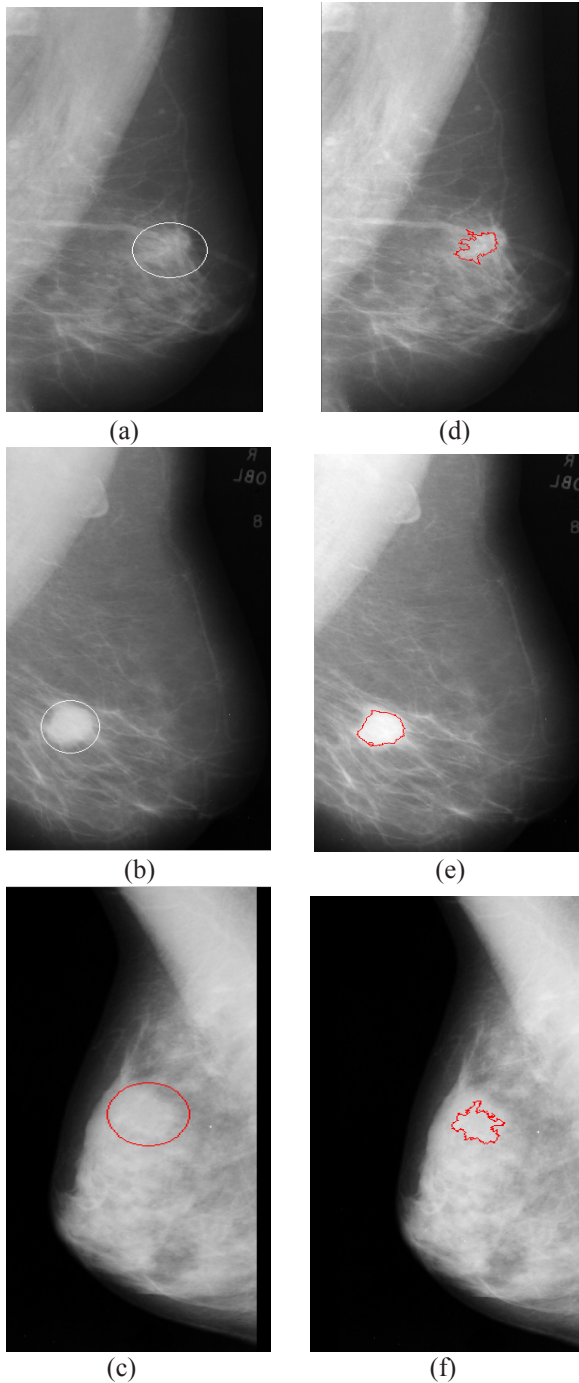


Fig. 6 (a), (b), (c) Original images. (d), (e), (f) Masses that are located by the program

ACKNOWLEDGMENT

This research is a part of Project B2008-01-156 granted by Ministry of Education and Training.

REFERENCES

1. C Boetes, J O Barentsz, R D Mus, et al (1994) Mr characterization of suspicious breast lesions with a gadolinium-enhanced turboflash subtraction technique. *Radiology* 193(3):777-781
2. V P Jackson (1990) The role of us in breast imaging. *Radiology* 177(2):305-311
3. American College of Radiology (2003) *ACR BI-RADS - Mammography, Ultrasound & Magnetic Resonance Imaging*, Fourth ed. Reston, VA: American College of Radiology
4. Morrison, Steven and Laurie M. Linnett (1999) A Model Based Approach to Object Detection in Digital Mammography. *Proceedings 1999 International Conference on Image Processing*: 182-6
5. Brake, Guido M.te, and Nico Karssemeijer (1999) Single and Multi-scale Detection of Masses in Digital Mammograms. *IEEE Transactions on Medical Imaging* 18(7):628-638
6. <http://www.cancerhelp.org.uk/help/default.asp?page=3315>
7. Bich Thuy, Hai Yen (1997) *Handbook of breast and breast cancer* (translate into Vietnamese). Medical Publishing House
8. R. Belloti, F. De Carlo, M. Castellano et al (2006) A completely automated CAD system for mass detection in a large mammographic database. *Medical Physics* 33(8): 3066-3075

Author: Viet Dzung Nguyen
 Institute: Hanoi University of Technology
 Street: 1 Dai Co Viet
 City: Hanoi
 Country: Vietnam
 Email: nvdung-bme@mail.hut.edu.vn

Retrospective Study of Biomechanical Factors Influencing Early Clinical Results of the Munting Stemless Hip Prosthesis

F. Boucher^{1,2}, P. Pouletaut¹, E. Munting^{3,4}, and M.C. Ho Ba Tho¹

¹ UMR 6600 Biomécanique et Bioingénierie, UTC, Compiègne, France

² Stryker Benoist Girard, Hérouville Saint Clair, France

³ Université de St-Luc, Hôpital de Louvain, Brussels, Belgium

⁴ Clinique Saint-Pierre, Ottignies, Belgium

Abstract— The Munting stemless hip prosthesis was developed in the early eighties by Pr E. Munting and Pr A. Vincent (UCL, Brussels, Belgium). This device was designed for young and active patients to prevent the bone loss commonly associated with femoral components having intramedullary stems. Previous in-vitro experiments and clinical densitometric follow-up confirmed that it preserved physiological loading and reduced stress shielding compared to traditional hip designs. Nevertheless, some early clinical failures were reported up to 2 years after surgery and were always related to inadequate implant positioning (varus) or partial seating of the implant on the proximal bone resection.

The aim of this study was to evaluate the relationship between the first 2 years clinical response (qualitative analysis of proximal bone remodeling) and 5 independent biomechanical factors such as patient age (A), implant position angle (IPA), pre-operative bone quality (BQ), body mass (BM) and height (H). We reviewed clinical results of a consecutive series of 103 patients operated between 1989 and 1998. Classification Tree and a Multinomial Logistic regression model (Systat.11) were used to retrospectively analyse the clinical results.

As per our hypothesis, this study confirmed the significant influence of implant position angle (IPA) to the clinical response in varus and valgus positions ($p=0.001$ and $p=0.008$). Influence of patient weight was close to statistical significance in valgus ($p=0.063$), confirming well known role of mechanical stress and strain in BMD homeostasis of the femoral bone. Rapid bone loss at the medial bone/implant interface was statistically related to varus position, 77% of which became early clinical failures.

Keywords— stemless hip prosthesis, physiological loading, bone remodeling, short term clinical results, young and active patients.

I. INTRODUCTION

The Munting stemless hip prosthesis was designed with the goal of preventing bone loss commonly associated with femoral components with intramedullary stems [1], [2]. Munting HA femoral prosthesis design has no intramedullary

stem and was developed for a distinct population of young and active patients with a life expectancy greater than 30 years where preservation of the proximal bone stock after total hip arthroplasty is beneficial as this population may need revision surgery. Clinical and experimental results confirmed expectancies whenever the implant is correctly positioned and the bone not severely osteoporotic [3], [4], [5], [6]. Nevertheless, some early clinical failures were reported up to 2 years after surgery and were always related to inadequate implant positioning (varus) or partial seating of the implant on the proximal bone resection [7].

In this study we analyse the first 2 years clinical results of a consecutive series of 103 patients operated with a Munting hip prosthesis. The objective is to evaluate the relationship between early clinical response (qualitative analysis of proximal bone remodeling) and 5 independent biomechanical factors such as patient age, implant position angle, pre-operative bone quality, body mass and height.

II. METHOD

A. Retrospective Classification of Clinical Results

We retrospectively reviewed a consecutive series of 103 patients who received a Munting hip prosthesis between 1989 and 1998. Clinical data were provided by the Université Catholique de Louvain in Brussels, (Table.1 and Table.2). Clinical failures that happened later than 2 years after surgery were excluded from the analysis, as these were mostly related to acetabular polyethylene wear.

A clinical classification matrix was created for the 103 consecutive patients. The objective was to study the relationship between a three levels dependent variable CR (clinical response) and 5 independent biomechanical factors such as patient age (A), implant position angle (IPA), pre-Op bone quality (BQ), body mass (BM) and height (H).

Table 1 Patients clinical data

Patients	103
Male	66%
Female	34%
Age	39 years (20-56)
Body mass	75 kg (42-117)
Height	172 cm (152-193)

Table 2 Patients etiology

Etiology	%
Primary Osteoarthritis	24
Avascular necrosis	20
Cortico/ethyl necrosis	14
Ankilosing spondylitis	12
Rheumatoid arthritis	8
Post-traumatic arthritis	8
Dysplasia	8
Others	6

Classification of the clinical response (CR) was based on **qualitative analysis** of bone remodeling visible on postoperative X-Rays in region of interest ROI3 (Fig.1).

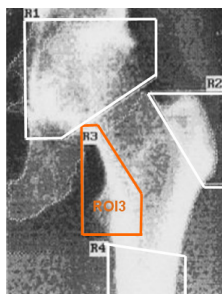


Fig. 1 Region of interest ROI3

CR1 is corresponding to a medial bone/implant interface rapid bone loss in ROI3 (Fig.2). 77% of CR1 became early clinical failures.

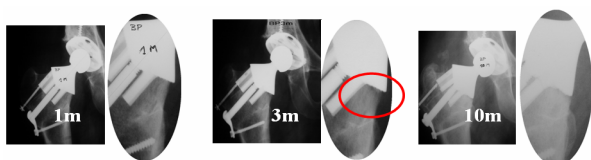


Fig. 2 CR1 from 1 month to 10 months

CR2 shows a progressive bone loss in ROI3 reaching steady state at 12 months (Fig.3).

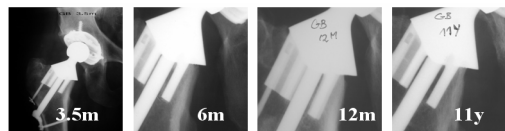


Fig. 3 CR2 from 3.5 months to 11 years

CR3 has a steady state bone density in ROI3 (Fig.4).

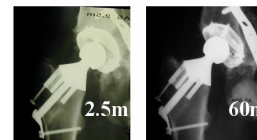


Fig. 4 CR3 at 2.5 months and 60 months

B. Pre-operative Bone Quality Assessment

In a previous DEXA study [8] we measured significant changes of bone quantity before surgery in region ROI3 of 45 patients suffering from different hip etiologies. Comparison of pre-operative BMD was found to be statistically significant between avascular necrosis and rheumatoid arthritis group of patients ($p = 0.058$ in ROI3). There was no significant difference between avascular necrosis and primary osteoarthritis ($p = 0.95$ in ROI3).

Literature review reports that patients with chronic rheumatic diseases (rheumatoid arthritis, and ankylosing spondylitis) are accompanied by focal bone destruction and progressive generalized bone loss [9], [10], [11], [12], especially when long-term corticosteroid therapy is used.

Accordingly, retrospective assessment of pre-operative bone quality (BQ) was based on patient hip etiology (Table.3).

Table 3 Pre-operative bone quality against hip etiology

BQ=1 (low bone quality)	BQ=2 (average bone quality)
Cortico/ethyl necrosis (14%)	Primary Osteoarthritis (24%)
Ankilosing spondylitis (12%)	Avascular necrosis (20%)
Rheumatoid arthritis (8%)	Post-traumatic arthritis (8%)
	Dysplasia (8%)
	Others (6%)

C. Implant Position Angle X-Rays Measurements

Post-operative implant position angle (IPA) was measured between neck axis and the femur lateral cortex on digitally stored X-Rays (Fig.5).



Fig. 5 IPA implant position angle

Measurements were carried out by a second observer to evaluate inter-observer variability (Fig.6) and repeated once again by the first observer to assess intra-observer variability (Fig.7), following the method proposed by Bland & Altman [13].

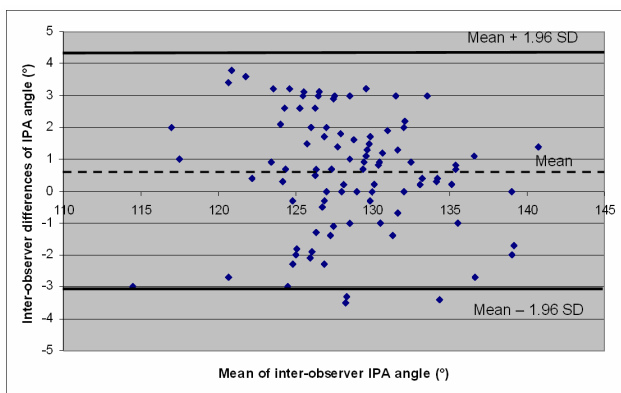


Fig. 6 95% confidence of inter-observer agreement: differences of paired measurements against the mean values of paired measurements

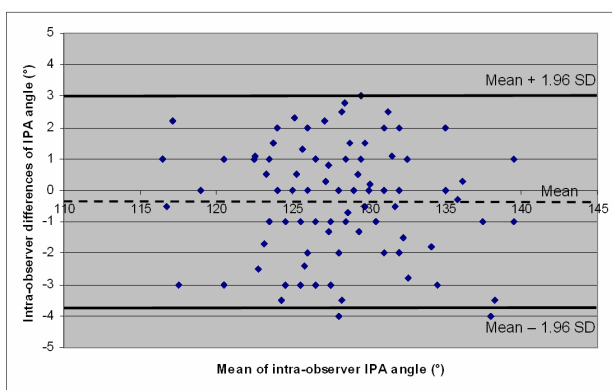


Fig. 7 95% confidence of intra-observer agreement: differences of paired measurements against the mean values of paired measurements

D. CART and Logistic Multivariate Analysis

Two multivariate analysis of the relationships between 5 biomechanical factors A, IPA, BQ, BM, H and the dependent variable CR were done using Classification Tree (CART, Systat.11) and a Multinomial Logistic regression model (Equation.1, Systat.11). Two tailed p-values of 0.05 or less was used to evaluate statistical significance of predictor variables (a, b, c, d, e and constant in Equation 1).

$$\text{Logit} \left(\frac{p(CR=i)}{p(CR=3)} \right) = a * A + b * IPA + c * BQ + d * BM + e * H + \text{constant} \quad (1)$$

III. RESULTS

From the CART analysis, only implant position angle (IPA) and body mass (BM) mainly influence the early clinical response. High-risk group (CR1, 22%) includes patients with IPA < 126° and BM > 85kg. Patients with IPA < 124° are at the highest risk of early clinical failure, independently of their body mass. Intermediate group of patients with IPA ≥ 135° (CR2, 10%) has ROI3 calcar progressive bone loss without clinical failure. Reference group (CR3, 68%) has a steady state bone density, 126° < IPA < 135° (Fig.8).

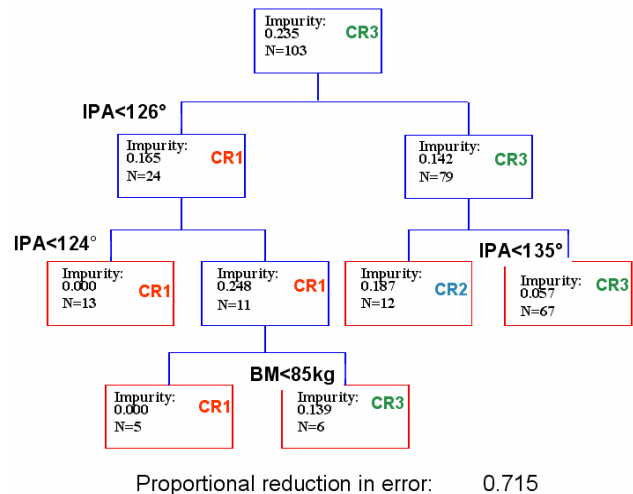


Fig. 8 CART tree results

Complementary to the CART analysis, the Multinomial Logistic regression model confirmed the significant influence of the implant position angle (IPA) to the clinical response in varus and valgus positions (p=0.001 for CR1 and p=0.008 for CR2). Influence of patient body mass (BM) was found to be close to statistical significance in valgus position (p=0.063 for CR2), confirming well known role of

mechanical stress and strain in BMD homeostasis of the femoral bone. Probabilities of CR1 (Fig.9) and CR2 (Fig.10) are plotted versus the main influencing factors IPA (120° to 145°) and BM (40kg, 75 kg, 117kg).

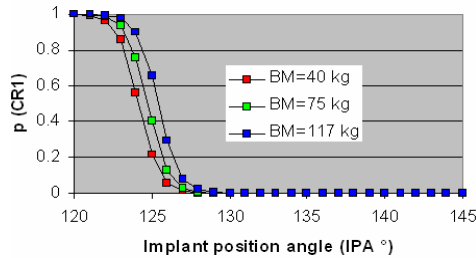


Fig. 9 Probabilities of clinical response CR1 in varus position

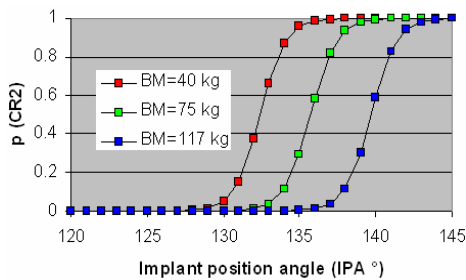


Fig. 10 Probabilities of clinical response CR2 in valgus position

IV. DISCUSSION

As per our hypothesis, this study confirmed the significant influence of implant position angle (IPA) to the early clinical response of the Munting hip prosthesis in varus and valgus positions. Varus position was statistically related to rapid bone loss at the medial bone/implant interface leading to early clinical failure for 77% of the cases reported in this series of 103 patients. A two-dimensional FEA study already explained that very high stresses developed around the most proximal and medial part of the femoral cortex with a prosthesis inserted in varus position. With the implant in valgus position the calculated stresses were significantly lower in the same region [7]. According to the Multinomial Logistic regression results, in order to avoid almost 100% of implant position angle related failures, IPA should not be less than 128° for an average body mass of 75kg and should not be less than 130° for patients heavier than 85kg. In addition to the impact of this study for the surgeon and his clinical practice, this retrospective multifactorial analysis will be used as a reference for future work to verify a bone physiological remodeling algorithm proposed to describe bone adaptation behaviour after surgery using finite element analysis.

V. CONCLUSION

The results shown in this analysis are in agreement with the work of Radcliffe et al. (2007) [14], where they found that there was a significant relationship between the implant orientation and the load transfer within the femur in the superior sections of the femoral head and neck. Our conclusions are also in agreement with several studies including work by McMinn (2003) [15], and Silva et al.(2004) [16], where it is suggested that a “valgus implant orientation is desirable whenever possible in a femoral head resurfacing”. This conclusion might also be applicable to short stem hip designs where part of the femoral neck is preserved.

ACKNOWLEDGMENT

The authors would like to thank the Saint-Luc University Hospital (Belgium) and Mrs Smitz for the collection of the clinical data.

REFERENCES

1. De Wall Malefijt & Huiskes (1993), Arch Orthop Trauma Surg
2. Kishida et al (2004), JBJS Br
3. Munting E et al (1994), Correlation between clinical and experimental observations about a stemless hip prosthesis, p. 344. In: Abstracts of the IInd World Congress of Biomechanics, Amsterdam, July 1994.
4. Munting E. et al (1995), Fixation and effect on bone strain pattern of a stemless hip prosthesis. J Biomechanics 28, 949-61.
5. Munting E. et al (1997), Effect of a stemless total hip prosthesis on the bone mineral density of the proximal femur. A prospective longitudinal study. J Arthroplasty. 12(4):373-9.
6. Ong et al (2007), ORS.
7. Munting E. (1996), development, experimental and clinical evaluation of a stemless hip prosthesis, Thesis, Université Catholique de Louvain.
8. Pouletaut et al (2008), CMBBE 2008 sup 1, 183-4;
9. Laan R F & all (1993), Bone mineral density in patients with recent onset rheumatoid arthritis: influence of disease activity and functional capacity, Ann Rheum Dis.
10. Grataco's J. & al (1999), Significant loss of bone mass in patients with early active ankylosing spondylitis, J Arthritis & rheumatism vol 42, No. 11, November 1999, pp 2319-2324.
11. Muntean L. & all (2006), Bone mineral density in patients with ankylosing spondylitis Mædica A Journal of Clinical Medicine, Volume1 No.1
12. Özlem (2008), Bone Mineral Density in Patients with Ankylosing Spondylitis, Rheumatism 2008; 23: 42-5.
13. Bland JM, Altman DG. (1986), Statistical methods for assessing agreement between two methods of clinical measurement. *Lancet* 1986;1:307-310
14. Radcliffe I.A.J. et al. (2007), Investigation into the effect of varus-valgus orientation on load transfer in the resurfaced femoral head: A multi-femur finite element analysis. *Clinical Biomechanics* 22 (2007) 780-786
15. McMinn, D., (2003), Development of metal/metal hip resurfacing. *Hip. Int.* 13, 41-53.

16. Silva, M., Lee, K., Heisel, C., Rosa, M.D., Schmalzried, T., (2004), The biomechanical results of total hip resurfacing arthroplasty. *J. Bone Joint Surg.* 86-A, 40–46.

Corresponding author:

Author: Florian BOUCHER
Institute: Université de Technologie de Compiègne
Street: Centre de Recherches de Royallieu
City: Compiègne
Country: France
Email: florian.boucher@stryker.com

Integrated Approaches for Personalised Cranio-Maxillofacial Implant Design and Manufacturing

L.C. Hieu¹, E. Bohez², J.V. Sloten³, L.T. Hung⁴, L. Khanh⁵, N. Zlatov¹, and P.D. Trung¹

¹ Cardiff School of Engineering, Cardiff University, Wales, UK

² School of Advanced Technologies, Asian Institute of Technology, Thailand

³ Division of Biomechanics and Engineering Design, K.U. Leuven, Belgium

⁴ Department of Information Technology, Hanoi University of Technology, Vietnam

⁵ Departments of Medical Imaging and Neurosurgery, Central Army Hospital 108, Vietnam

Abstract— Personalised implant design based on CT/MRI data has been developed since 1990s and commercially available in recent years. Although the technology brings in the well-recognised benefits, the number of clinical cases is still limited and the technology has not been widely applied for the treatment in hospitals due to the complexity of the technology, the high cost of implants and the lack of human resources in the area of biomodelling in hospitals. Especially, the closely multidisciplinary collaboration among radiologists, surgeons, and biomedical engineers is always needed during the design and manufacturing steps of the implant. In addition, the optimal solutions for investment of hardware and software are not easily obtained. In this paper, the integrated approaches for personalised cranio-maxillofacial implant design & manufacturing are presented. It covers the wide range of technical solutions based on the available design & manufacturing technologies. Different implant design methods based on different input data, medical image processing and geometrical modeling tools will be emphasized. Finally, the aspects related to the design for manufacturability of the implants are also discussed to utilize effectively limited hardware & software tools.

Keywords— Implant design and manufacturing, biomodelling, cranio-maxillofacial surgery.

I. INTRODUCTION

Medical image based modeling technology or Bio-modelling has been familiar with surgeons and biomedical engineers since the ends of 1990s, especially in the area of design and manufacturing of biomodels, personalized implants, surgical tools as well as medical devices [1-4]. Although the benefits are well recognised, the number of clinical cases is still limited and the technology has not been widely applied for diagnosis and treatment due to difficulties of technology transfer to hospitals. The main reasons that lead to these difficulties are as follows.

▪ R1: *The complexity of the implant design*: Modelling of the personalized implants is heavily dependent on the patient data as well as specific clinical constraints. In order to complete the design process, high skills about 3D modelling and medical image processing are needed. In addition, the

designers need to be equipped with relevant medical and engineering know-how so that the designed implant could meet well both technical and clinical requirements. These highly skilled human resources are not always available in the hospitals.

▪ R2: *Challenges about multi-disciplinary collaboration & communication*: Traditionally, most of the clinical cases come from surgeons who directly treat the patients from which the clinical requirements are established for implant design. The designers, working closely with both surgeons and radiologists, transform the medical images into 3D data which is then used as the database for designing the implant and surgical tools that are needed for diagnosis, surgical planning and operation. Depending on which biomaterials used for fabricating the implants and surgical tools, prototyping and manufacturing processes are determined. The implant model is then designed and finally checked by the surgeons before it is transferred to the manufacturing stage. The implant design and manufacturing processes involve the multi-disciplinary collaboration among different experts which are normally not in the same office and organisation. Therefore, it may lead to time-consuming or miscommunication.

▪ R3: *High cost of technology*: The high cost is still a big challenge for the biomodelling technology [2, 4], especially for patients in the developing countries. Currently, investment for hardware and software for biomodelling is quite expensive. The state of the art medical image processing software and modeling tools cost from 20,000 to 50,000 USD. The Rapid Prototyping (RP) machines that can be used for biomodelling applications are from 50,000 to 200,000 USD. In addition, the reasons R1 & R2 also strongly increase the cost of biomodelling technology.

The integrated approaches presented in this paper are aimed to solve the above emerging challenges for developing personalised implants, surgical tools and biomodels in which both technological and economic aspects of the design and manufacturing technology are taken into account.

II. METHOD

Figure 1 presents the integrated approaches for design and manufacturing of personalised implants and surgical tools in which the data flow as well as associated tools and methods from medical image processing to the final implant are described.

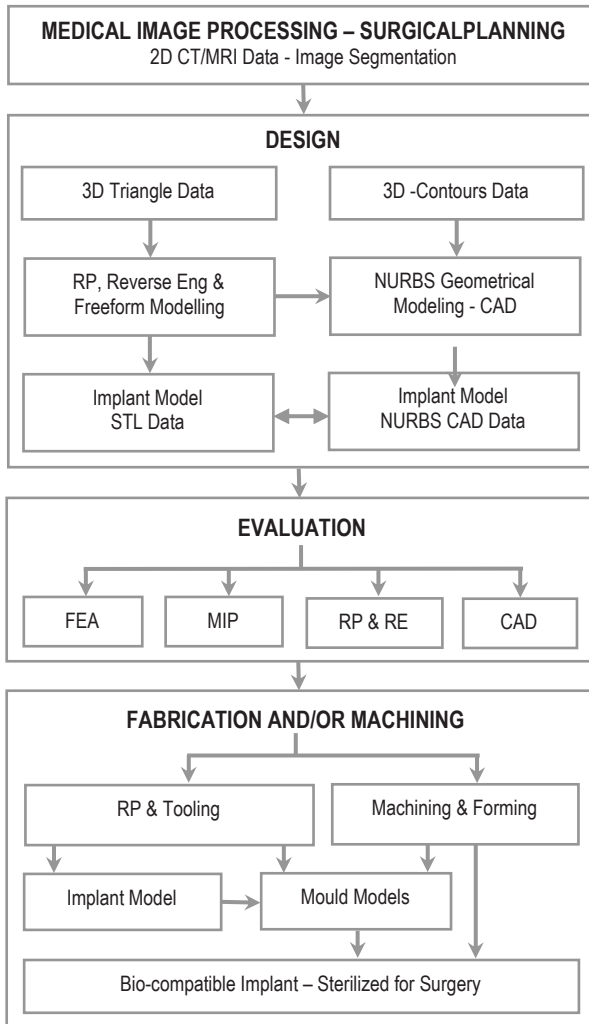


Fig. 1 Integrated approaches for implant design and manufacturing

Each design and manufacturing method has its advantage and disadvantages, it depends on the skills of designers as well as available hardware and software. There are 4 main steps: (i) Medical image processing (MIP), (ii) Design, (iii) Evaluation, and (iv) Fabrication and/or machining.

A. Medical Image Processing and Surgical Planning

CT/MRI images of the patient in the form of DICOM format are used as the input for starting implant design and

manufacturing processes. Most of the MIP packages provide the necessary tools and functions for image segmentation which refers to the process of partitioning an image into multiple sets of pixels from which Regions of Interest (ROI) can be extracted. CT data gives better results for bone reconstruction compared to MRI images which are fundamentally good for soft tissue modelling.

The output of the MIP stage is the geometry of anatomical structures in form of 3D triangle mesh models or 2D slice contours which are commonly stored as STL and IGES files respectively. These data are used for surgical planning and implant design. The most typical commercial MIP packages are MIMICS (Materialise NV), Simpleware (impleware Ltd), 3D-Doctor (Able Software Corp), and Amira (Visage Imaging GmbH). However, if we only need to reconstruct 3D models of the anatomical structures from CT/MRI data for further development, the free and open source MIP packages can be used, including 3D Slicer (Slicer), Julius framework (CAESAR Research Center) and MedINRIA (INRIA Sophia Antipolis).

B. Implant Design

Depending on the biomaterial used for an implant, manufacturing techniques which define implant design methods are determined. The methods for design and manufacturing of personalised implants based on Rapid Prototyping (RP) and CNC milling were well documented [1, 2, 3]. The most common biomaterials used for bone reconstruction in cranio-maxillofacial surgery are bone cements, PMMA and titanium (Ti). When Ti is used, the implant is normally designed in two types: (i) On-lay implant which is made from Ti sheets by hydro-forming techniques and (ii) In-lay implant which is made by CNC machining from Ti block. When bone cements and PMMA are used, it is required to apply in-lay implant design methods [3].

The design methods for on-lay implants are simpler compared to the in-lay ones. Only external surfaces of the bone structures are taken into account. Mirrored data of the intact area of the skull is used as the reference for modeling the implant from which the hard-plaster mould is made for hydro-forming process, and finally the formed Ti sheet is cut to create final boundary of the implant to fit the defect window. Meanwhile, both internal and external surfaces as well as the contact between the bone and an implant have to be carefully taken into account when designing in-lay implants. The in-lay implants have the most complex geometry. The requirements about the weight and mechanical strength of the implant have also to be satisfied. Figure 2 presents the typical in-lay implant.

There are 4 following methods for geometrical modelling of the implants, depending on the complexity of the implants and the available modelling software and tools, including RP,

Reverse Engineering (RE), freeform modelling and Computer Aided Design (CAD).

- **M1 - RP:** Most of the RP packages allow manipulating STL files as well as provide basic functions for editing 3D models. The implant is modeled based on mirrored intact area of the bone structure as well as Boolean operations. The disadvantage of this technique is the difficulty for controlling the implant thickness as well as to get the best fit implant for the defect window, because the skull is not completely symmetrical, and the tools for geometrical modelling of RP packages are quite limited. However, for the simple bone defects, this approach can provide the optimal solution in term of the cheap cost and simplicity; and when necessary, the fabricated implant can be manually corrected and refined based on the biomodel of the defect skulls. The typical RP packages include Magics (Materilise NV) and VisCAM RP (Marcam Engineering GmbH).

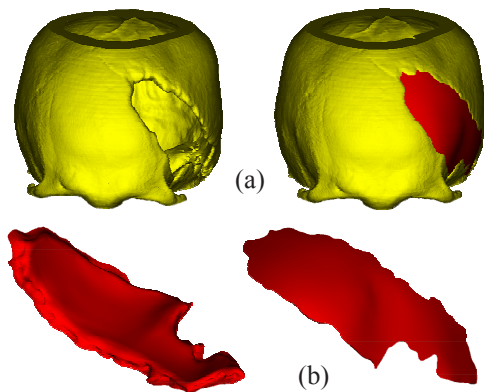


Fig. 2 (a): Defect skull and in-lay implant fitted to the defect window. (b): 3D model of the implant in different views

- **M2 - RE:** Most of the RE packages provide powerful freeform modelling tools, especially triangle mesh control and manipulations which are not commonly available in RP and CAD packages. Therefore, personalised implants can be modeled optimally. In order to model the implant based on RE tools, first of all, the defect window is filled to make it intact based on the mirrored intact area of the skull. Boolean operations are then used to create the basis shape of an implant. Finally the thickness of an implant and the contact between an implant and bone structure are controlled to get the optimal implant model. The typical RE packages are Rapidform (Rapidform, Inc.), CopyCAD (Delcam), Geomagic studio (Geomagic, Inc.), and Polyworks (InnovMetric Software Inc).

- **M3 - Freeform Modelling:** The freeform modeling techniques such as SensAble 3D modeling systems (SensAble Technologies, Inc) and ZBrush (Pixologic, Inc)

can be used for modelling the implant. However, high modeling skills and time-consuming are normally required to complete the implant design. The 3D model of the defect skull in the form of STL, VMRL, **OBJ** or 3DS format is used as the reference for modelling processes.

- **M4 - CAD:** CAD packages such as ProEngineer (PTC Inc), UG (Siemens), SolidWorks (Dassault Systèmes SolidWorks Corp) are based on Non-Uniform Rational B-spline (NURBS) modelling. Therefore, contour data of the bone structures are used as the reference for modelling the implant in CAD packages. Freeform modelling tools in CAD packages are quite limited; thus, it is difficult for modeling the complex implant, especially the ones in the zygomatic bone area (Fig. 3); and high skills are required.

When RP & Tooling techniques are used for prototyping implant models and moulds to fabricate PMMA and bone cement implants, all methods M1 to M4 can be applied. Methods M1 and M4 are normally used to design hydro-forming moulds for making on-lay implants. Although the current CAD/CAM packages allow using STL data for process planning, in order to machine complex in-lay implants from Ti blocks, method M4 is generally used for developing implant models and preparing the optimal CNC tool-paths.

C. Implant Evaluation

The designed implant needs to be carefully evaluated to assure that the technical and clinical requirements are met before it can be transferred to the prototyping and manufacturing phase. The optimal method for checking the implant geometry is to keep the coordinate system of the implant model identical with the one used for the defect skull. In this way, we could use MIP or RP & RE or CAD packages for implant evaluation by comparing the design in different cross-section views. The best option is to import the implant model into MIP packages to view the cross-sections directly on CT/MRI images. Finite Element Analysis (FEA) may need to be used for evaluating mechanical strength as well as simulating implant functions when necessary.

D. Implant Fabrication and/or Machining

There are two methods for making PMMA and bone cement implants. The first one is to use RP for making the implant prototype which is then used as the reference for making the silicon or dental plaster mould from which the implant is fabricated. The second one is to use RP for making the moulds which are directly used to fabricate PMMA or bone cement implants. With the recent progress of material development for RP applications, the current RP techniques allow fabricate biocompatible parts and the ones

with strong mechanical properties. In this way, soft-tooling techniques may not be necessary for preparation of the moulds based on implant prototypes as traditionally done.

CNC machining can be used for (i) direct milling of the implants from Ti blocks or (ii) milling the mould from which PMMA or bone cement implants are fabricated [4].

Finally, for the on-lay implants which are made by hydroforming, the moulds can be made by CNC machining, RP as well as rapid tooling techniques.

III. RESULTS, DISCUSSION AND CONCLUSIONS

More than 60 clinical cases have been conducted since 2001 based on the above presented design and manufacturing methods. Figs 2 and 3 present the typical implant design in which the geometry of the implants is complex. It took 3 to 5 working hours to complete the optimal design when all the necessary modelling tools are available.

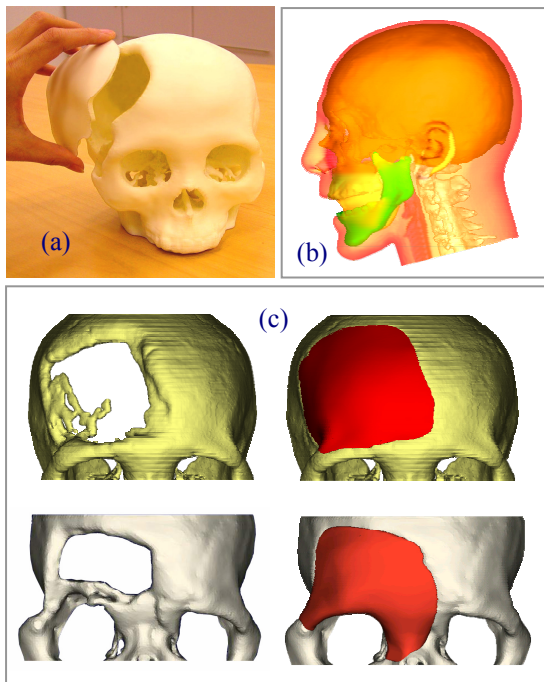


Fig. 3 (a) Biomodels of the defect skull and implant. (b) 3D modelling of the hard and soft tissues. (c) Personalised implant design

Although the personalised implants have been clinically applied for treatment of the skull defects for more than 15 years and the benefits are well documented, the technology is still currently not widely used or available in most of the hospitals, even in the developed countries. The difficulties

that limit the applications of the technology include (i) complexity of the implant design, (ii) challenges about multi-disciplinary collaboration & communication; and (iii) High cost of personalised implants and surgical tools.

There have been efforts in developing specialised software and tools that simplify the implant design processes with more and more added modelling tools as well minimising the high skill requirements. However, there have been no single package that can meet all the design requirements, and the commercial software is getting more and more expensive. In addition, each clinical case has its own clinical and technical requirements; and not all the hospital and companies can fully invest the necessary hardware and software as well as human resources. Therefore, optimal solutions need to be investigated to meet both technical and clinical requirements for personalised implants as well as to overcome obstacles about technology transfer into hospitals.

The paper presented different design and manufacturing methods with associated hardware and software options which were successfully implemented for clinical cases. Selection of the right work-flow will lead to the reasonable implant cost and effectively use the available resources. In this way, technology transfer to hospitals will be more and more convenient. Finally, the presented approaches will be useful for hospitals, universities and companies when considering investments about hardware and software which are necessary for developing BME applications for diagnosis and treatment of bone defects.

REFERENCES

1. L.C.Hieu, J.Vander Sloten, E.Bohez , L.Khanh, P.H.Binh, Y.Toshev, N.Zlatov (2005). Medical Rapid Prototyping Applications and Methods, *Assembly Automation Journal*, Vol.25, No.4., 284-292
2. Hieu L.C., Vander Sloten J., Bohez E., Phien H.N., Vatcharaporn E., An P.V., To N.C, Binh P.H. (2004). A cheap technical Solution for Cranioplasty treatments, *Technology and Health Care*, Vol.12. No.3, 281-292.
3. Hieu L.C., Bohez E., Vander Sloten J., Phien H.N., Vatcharaporn E., Binh P.H., and Oris P. (2003). Design for Medical Rapid Prototyping of Cranioplasty Implants, *Rapid Prototyping Journal*, Vol.9, No.3, 175-186.
4. Hieu L.C., Bohez E, Vander Sloten J., Oris P, Phien H.N., Vatcharaporn E., and Binh P.H. (2002). Design and manufacturing of cranioplasty implant by 3-axis CNC milling. *Technology and Health Care*, Vol.10, No.5: 413-23.

Author: Le Chi Hieu
 Institute: Cardiff University
 Street: Queen's Building, The Parade-Newport Road
 City: Cardiff CF24 3AA
 Country: UK
 Email: Le-ChiH@cf.ac.uk

Current Medical Product Development for Diagnosis, Surgical Planning and Treatment in the Areas of Neurosurgery, Orthopaedic and Dental-Cranio-Maxillofacial Surgery in Vietnam

L.C. Hieu¹, L.H. Quoc², V.V. Thanh³, T.D. Nguyen⁴, P.V. An⁵, L.T. Hung⁶, and L. Khanh⁷

¹ Cardiff School of Engineering, Cardiff University, Wales, UK

² Department of Science and Technology of Ho Chi Minh City, Vietnam

³ Ho Chi Minh City Hospital for Traumatology & Orthopaedics, Vietnam

⁴ Department of Mechanical Engineering, Ho Chi Minh City University of Technology, Vietnam

⁵ National Centre for Technology Progress, Ministry of Science and Technology, Vietnam

⁶ Department of Information Technology, Hanoi University of Technology, Vietnam

⁷ Departments of Medical Imaging and Neurosurgery, Central Army Hospital 108, Vietnam

Abstract— With the population of 86 million and good GDP growth in recent decades, the medical market in Vietnam is growing fast. However, most of the medical technology products are imported, and the number of locally manufactured ones is limited and they do not have the high competition capability in term of quality, quantity and types. In this paper, the current product development in Vietnam for diagnosis, surgical planning and treatment in the areas of Rehabilitation, Neurosurgery, Orthopaedic and Dental-Cranio-Maxillofacial surgery is presented. A roadmap for medical technology development in Vietnam is proposed.

Keywords— Product development, Neurosurgery, Orthopaedic, Dental-Cranio-Maxillofacial surgery.

I. INTRODUCTION

With a population of 86 million and a steady GDP growth about 7% as shown in Fig.1, the medical technology market in Vietnam is potentially huge. According to the Vietnam Ministry of Health (MOH), from 2005 to 2010, the government is projected to spend 1.8 billion USD for building 57 new hospitals [1]. From now until 2020, Ho Chi Minh City (HCMC) alone will spend USD \$900 million to develop the municipal medical sector, mainly for building new clinics. Table 1 presents the health care expenditure in the ASEAN region. The healthcare expenditure per capita in Vietnam is still relatively low, but it is increasing very rapidly, from 21 USD in 2000 to 45 USD in 2006 [5]. The total health care expenditure of Vietnam is estimated to be 1.5 billion USD in 2010 [2].

Most of the medical devices and equipments in Vietnam, especially the ones related to advanced medical technologies, have to be imported. Currently, there are 15 local manufacturers that make 560 products officially licensed by the MOH.

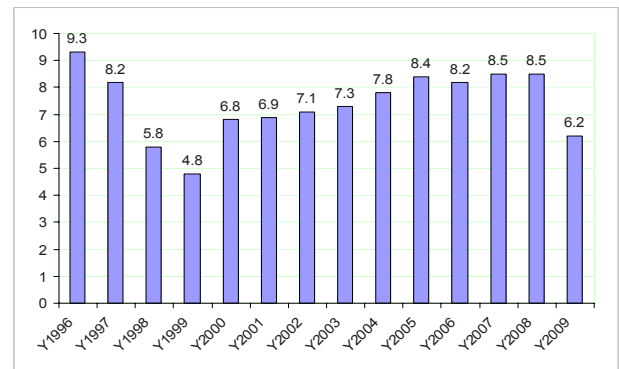


Fig. 1 Gross Domestic Product (GDP) Growth - Vietnam (%)

Table 1 Health care expenditure in the ASEAN region (Billion USD)

	2006	2007	2008	2009	2010
Indonesia	6.2	6.4	6.7	7.0	7.4
Malaysia	4.9	5.2	5.5	5.9	6.2
Philippines	2.9	3.0	3.1	3.2	3.3
Singapore	4.5	4.7	5.0	5.2	5.5
Thailand	9.8	10.4	11.1	11.8	12.5
Vietnam	1.2	1.2	1.3	1.4	1.5
Total	29.5	30.9	32.7	34.5	36.4

However, the local productions are limited to basic products, namely, plastic gloves, bandages, drips, compresses, clothes, masks, syringes and injection needles, sewing thread, surgery sutures, biomedical polymer membranes for burn therapy, lead rubber, barite powder and hospital furniture. The value of exports is low, at 81.8 million USD in 2007, with 46.4% of medical products exported to Japan.

The world market for medical technology is estimated to be 340 billion USD in 2009. It is growing steadily at an

annual average rate of 4.5%. The global orthopaedic market is estimated to have been worth approximately 40.6 billion USD in 2009. According to Research and Markets, in 2009, the Vietnamese market for medical equipment and supplies is estimated at 289 million USD, or 3 USD per capita [4]. It is expected that the medical device market in Vietnam will continue to expand at 5.9% per annum; this will take the Vietnamese market to 385 million USD in 2014, although the per capita rate will remain largely unchanged.

According to the US Commercial Service, 90% of medical supplies in Vietnam are imported [3]. An estimated 81.4% of the medical device market is supplied by imports [4]. Although the Vietnamese government established the targets to modernize the medical technology industry via the Decision 18/2005/QD-TTg issued on October 4th, 2002 about approving the national policy on medical equipments and devices for the 2002-2010 period, the current results are still very far from targets in which it is expected to meet 60 % of the medical sector's demands by 2010.

The Vietnamese medical market will rely on imports of high-end equipment in the coming years. Meanwhile, the human resources in the area of Biomedical Engineering (BME) are quite limited. Therefore, there is the emerging need for the realistic road map and effective work plans to develop BME technologies in Vietnam, especially in the areas of areas of rehabilitation, neurosurgery, orthopedics, and dental-cranio-maxillofacial surgery.

II. CURRENT DEVELOPMENT

A. Rehabilitation, Neurosurgery, Orthopedics, and Dental-Cranio-Maxillofacial Market in Vietnam

The huge need for medical technology products in Vietnam is clearly shown. According to Vietnam Orthopaedic Association, annually there are about 2,000 patients who need a hip replacement, and 20,000 to 30,000 patients who need a knee replacement. There are annually 20,000 surgeries conducted at HCMC Hospital for Traumatology & Orthopaedics. Every year, there are approximately 120,000 patients who need the surgery for treatment due to traffic accidents. For each day in Vietnam, there are about 74 traffic accidents in which the estimated number of injured persons who has to be hospitalised is 84 [6].

There are an estimated 107,000 amputees living in Vietnam. Many lost their limbs in the Vietnam War and during subsequent border conflicts with neighboring China and Cambodia. Landmines and unexploded ordnances have continued to harm children and adults alike, decades after the wars ended. In recent years, work and traffic accidents, as well as disease and untreated infections, have taken the limbs of still more of Vietnamese people.

B. Human Resources Development

One of the objectives mentioned in the Decision 18/2005/QD-TTg of the Vietnamese government is to develop human resources specialised in medical technology development to ensure successful materialization of the principal contents of the national policy on medical equipment in the 2002-2010 period.

However, education and training in the area of Biomedical Engineering (BME) at universities in Vietnam were just started since 2003. In addition, most of these Biomedical Engineering programmes focus on medical electronics or biotechnology oriented subjects. High education training about medical product development, especially in the areas of design and manufacturing, biomechanics and biomaterials, is not available and limited at a few postgraduate researches.

C. Biomaterial Research and Development

Biomaterials are crucial for medical product development. There have been big efforts of institutes and universities working on R&D of biomaterials in Vietnam since 1990s. Ministry of Science and Technology of Vietnam (MOST) funded the research project KC-DL-20-92 in 1992 which was aimed to produce stainless steels for medical applications. The project successfully produced the medical grade stainless steel, named K92, which has the similar quality compared to the imported products.

Since beginning of 1990s, Niigrafit institute, Russia, produced carbon composite materials for medical applications under the commercial names Intost-1, Intost-2 and Intost-3. The technology was transferred to National Centre for Technology Progress (Nacentech), MOST, and these biomaterial materials have been produced in Vietnam for medical applications since 1995.

The group at Hanoi University of Technology has developed the bioceramic materials, named Bioxitan, since 1996 with the financial support from MOST. The material was successfully applied for clinical cases under the project funded by MOH from 2003 to 2005.

The Institute of Chemistry, Vietnamese Academy of Science and Technology, successfully produced hydroxyapatite materials that are currently used for medical applications, including drugs for treatment of low bone density, and bone cements for orthopaedic and cranio-maxillofacial surgery.

In 2008, HCMC Institute of Physics was funded a research project to develop calcium phosphate, including hydroxyapatite and tricalcium phosphate, for medical applications.

D. Medical Technology Product Development

a) Orthopaedic Products

Most of the orthopedic products such as plates, screws, nails, hip and knee implants as well as advanced surgical

tools and devices have to be imported up to 98% in Vietnam. There are two R&D groups in Vietnam actively working on development of these orthopaedic products: (i) Central army hospital 108 (CAH108), and (ii) Nacentech.



Fig. 2 (a) Orthopaedic plates & hip implant prototype made by Nacentech. (b) Orthopaedic tools developed by CAH108

The orthopaedic products are made in Vietnam based on stainless steels and carbon composite materials which are locally produced. Figure 2 presents the typical orthopaedic plates, hip implant prototype and orthopaedic tools made by Nacentech and CAH108. There have been at least 4,000 plates produced by Nacentech for clinical applications.

Since 1993, the surgeons at Cho Ray hospital developed orthopaedic nails based on the design of Kuntscher nails; but did not success. However, surgeons at CAH108 successfully developed orthopaedic plates and tools based on the stainless steel produced in Vietnam since 2002. They also successfully conducted clinical cases using gamma nails for treatment of bone fractures, and they are currently working on the development of new gamma nails which are compatible with anatomy of Vietnamese people.

In 2008, successful development of Steeffe plates was reported by CAH108 for treatment of degenerative lumbar spondylolisthesis. The retro and postoperative study was carried out on 67 patients.

The current research in Vietnam in the area of medical product development for orthopaedic surgery is to optimize the design and manufacturing processes as well as diversify the product types and applications.

b) Dental Cranio-Maxillofacial Products

Since 1999, with the support of Belgian government and Catholic University of Leuven (K.U.Leuven), the medical technology project (MedTech) was developed and advanced medical technologies has been successfully transferred to partners in Vietnam, including Hanoi University of Technology, Nacentech, Cho Ray Hospital, HCMC University of

Technology, CAH108. The project was also aimed to develop the BME human resources for Vietnam, especially in the areas of medical product development. Medical doctors, radiologists, researchers and lectures in Vietnam were selected to attend the short training course as well as join the R&D research to develop BME products for Vietnam based on the local clinical need and resources.

Besides, HCMC University of Technology was funded the project KC 05-01 by Ministry of Science and Technology to invest Rapid Prototyping (RP) equipments for industrial and medical applications.

With the support of MedTech, there have been at least 50 clinical cases successfully conducted in Vietnam related to bone-reconstruction in which biomodels and personalised implants are used for surgical planning and treatment in the area of dental and cranio-maxillofacial surgery [8,9]. Figure 3 presents the biomodels of the implant, bone structures and grafts for surgical planning and bone reconstruction treatment at CAH108.

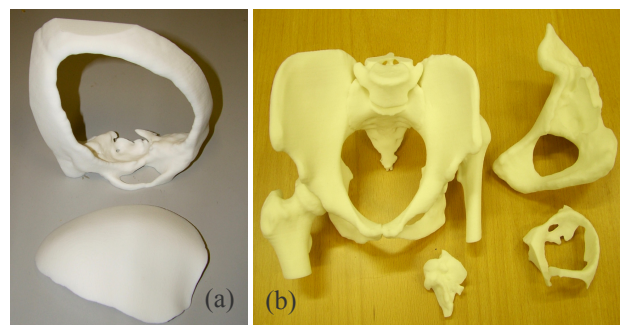


Fig. 3 (a) Biomodel of the defect window and cranioplasty implant. (b) Biomodels of the hips & bone grafts for surgical planning

Due to the high cost of personalised implants, Nacentech and MedTech successfully developed standard carbon composite templates from which cranioplasty implants are intra-operatively prepared for surgery [6]. In this way, the cost of the implant is reduced to about 30 USD. Meanwhile, the cost for one personalised implant made of PMMA materials is from 300 to 350USD. There have been at least 1,200 carbon composite templates produced by Nacentech for cranioplasty applications.

The bioceramic material, Bioxitan, developed by Hanoi University of Technology has been used for bone reconstruction since 2005. It is normally used for reconstruction of the ear bones because of difficulty in making the complex parts from bioceramic materials.

Finally, the other dental and cranio-maxillofacial products such as Ti sheet, plates and screws as well as the surgical tools and devices currently used in Vietnam have to be imported from other countries.

c) *Orthosis Products*

Rehabilitation facilities in Vietnam are technically and financially supported from other countries, including Czech Republic, Germany and USA. Since 1990, Prosthetics Outreach Foundation [7] has transferred state of the art prosthetics design and manufacturing technology to Vietnam. Carbon composites produced by Nacentech have also been used for making the orthosis and prosthetics products. There have been 1,500 artificial legs made of carbon composite materials produced by Nacentech.

III. ROADMAP FOR MEDICAL PRODUCT DEVELOPMENT

Medical product development in Vietnam is still in the beginning steps and it is clear that Vietnam lacks both technology infrastructure as well as strong BME human resource. The continuous and sustainable development strategies, supports and investments from the government are urgently needed in order to reduce the cost and meet the big need of diagnosis and treatment in Vietnam.

In order to develop successfully the high value added products for medical applications in Vietnam, the authors proposed the following short, mid and long term plans:

1. Establishing Networks of Excellence (NoE) among the R&D research centres, institutes, universities and hospitals. These networks are aimed to build up and consolidate BME human resources, including oversea Vietnamese for medical product development in Vietnam.
2. Implementing R&D activities to meet the most emerging clinical needs based on the local resources, including the human, materials, design and manufacturing facilities. Besides, technology transfer activities need to be encouraged and invested from which human resources and expertise in the area of BME are developed.
3. Promoting the international collaborations about medical product development, especially with the countries in the ASEAN region.
4. Establishment of Science and technology companies to commercialise R&D results. The successfully developed products need to be diversified about the size, type and scope of applications as well as improve the product quality with the long term support from the government.

IV. CONCLUSION

The paper presents the current medical product development for diagnosis, surgical planning and treatment in the

areas of rehabilitation, neurosurgery, orthopaedic and dental-cranio-maxillofacial surgery in Vietnam. Different aspects and R&D activities related to medical technology as well as the market in Vietnam are presented. Finally the roadmap for medical product development in Vietnam is proposed.

With the good economic growth in recent decades, Vietnam presents the big market for medical technology products. However, most of the high value added products are imported, especially the ones related to advanced medical technologies. In addition, BME human resources development in Vietnam had just been fundamentally started in recent years. Although there are big efforts from the government as well as institutes, universities and hospitals working on medical technologies, the number of medical products successfully developed and commercialised is quite limited. In order to develop medical technology products to meet the emerging need of Vietnam, and have the capability to compete with the imported products, the effective collaborations as well as NoE should be established, and the government needs to develop the effective and realistic short, mid and long term R&D programmes.

REFERENCES

1. The International Trade Administration, U.S. Department of Commerce at www.trade.gov.
2. Espicom Business Intelligence at www.espicom.com
3. Asian Now: Navigating ASEAN region – Medical equipment and supplies, the US Commercial Service at www.trade.gov.
4. The Medical Device Market: Vietnam, Research and Markets at www.researchandmarkets.com.
5. National Health Accounts 2000-06, Ministry of Health of Vietnam.
6. Hieu L.C., Vander Sloten J., Bohez E., Phien H.N., Vatcharaporn E., An P.V., To N.C, Binh P.H. (2004). A cheap technical Solution for Cranioplasty treatments, *Technology and Health Care*, Vol.12. No.3, 281-292.
7. Prosthetics Outreach Foundation at www.pofsea.org
8. L.C.Hieu, J.Vander Sloten, E.Bohez, L.Khanh, P.H.Binh, Y.Toshev, N.Zlatov (2005). Medical Rapid Prototyping Applications and Methods, *Assembly Automation Journal*, Vol.25, No.4., 284-292.
9. Hieu L.C., Bohez E., Vander Sloten J., Phien H.N., Vatcharaporn E., Binh P.H., and Oris P. (2003). Design for Medical Rapid Prototyping of Cranioplasty Implants, *Rapid Prototyping Journal*, Vol.9, No.3, 175-186.

Author: Le Chi Hieu
 Institute: Cardiff University
 Street: Queen's Building, The Parade-Newport Road
 City: Cardiff CF24 3AA
 Country: UK
 Email: Le-ChiH@cf.ac.uk

Glass Nanopipette: Fabrication and Application for Studying Living Cells

Duong Chi Dung¹, Huynh Luong Nghia¹, Veiko V.P.², Golubok A.O.², and Yakovlev E.B.²

¹ Le Quy Don Technical University -100 Hoang Quoc Viet, Hanoi, Vietnam

² Saint-Petersburg State University of Information Technologies, Mechanics and Optics - Str. Sablinskaya 14, Saint-Petersburg, Russia

Abstract— In this paper, we show fabrication of glass nanopipettes by laser heating and pulling. Then the nanopipette is used as the probe of scanning force microscope for studying living cells. We can get topographical image and mechanical properties of cells. Inside the nanopipette we can fulfill the liquid and metal wire for making an electrode. This electrode can be used for measuring ion current of channels through cell membrane by patch-clamp method.

Keywords— nanopipette, laser pulling, living cell, scanning probe microscope (SPM), patch-clamp.

I. INTRODUCTION

Nowadays, it is interesting of studying and using nano-objects of different nature. For developing of submicron and nanotechnologies, it is necessary to create the precise controlled-measuring instruments that can not only control properties of functional elements, but form and repair active structures. One of these instruments is scanning probe microscope (SPM), that is useful for studying surface properties of materials in very different conditions (in air, in vacuum, in liquid, in large interval of temperature and pressure).

The most important element of the SPM is its probe that determines the SPM solution. Laser technology allows introducing feed back control into probe fabrication process that improves the quality and the reproducibility of probe parameters. Therefore, laser assisted fabrication of probes for the SPM is an issue of the day.

In this paper we introduce the laser-based nanopipette fabrication, and show application for studying cells.

II. CONTENT

A. Laser-Based Nanopipette Fabrication

Nanopipette is a tapered glass capillary that is useful in biology, medicine, etc as an instrument for delivery of medicament and radiation into biological objects. Furthermore, nanopipette is also used in SPM as a probe. The method of nanopipette fabrication is heating the glass tube until melting state and pulling it. For heating the glass tube, it can be used gas heating, resist heating or laser radiation. In comparison

with other heating methods, heating by laser beam has some advantages: It can be turn on or turn off the heating source quickly; High temperature can be obtained in very short time; Possibility of changing the heated zone; Possibility of introducing the feed back for control the pulling process [1,2].

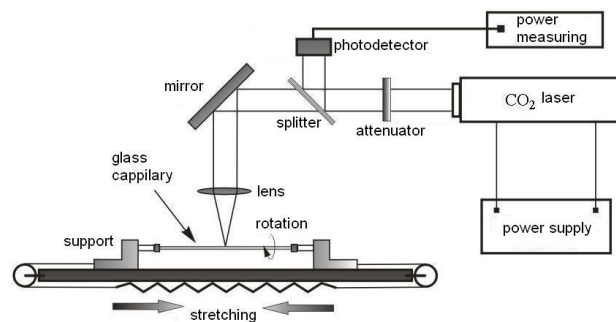


Fig. 1 Experimental setup for laser pulling nanopipettes [2]

In the figure 1 the experimental setup for laser micropipette pulling is presented. The CO₂ laser beam is directed to the lens that focuses it onto the glass tube. The glass tube is heated absorbing laser radiation and melted. For the uniform heating of glass tube surface the tube is revolved on its axis (fig. 1). Under the stretching force by using a spring or a load the glass tube is deformed and broken. As a result we receive two tapered.

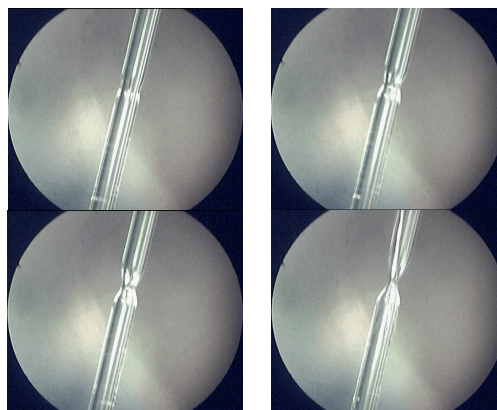


Fig. 2 Stages of nanopipette shaping by laser pulling. Photos are taken from video shooting the pulling process

For experiments we have used the borosilicate glass tubes with outer diameter 1 mm and inner diameter 0.58 mm. Kinetics of the micropipette pulling process is studied by using microfilming method. The change of the micropipette shape during pulling process is presented in the figure 2. Basing on the micropipette shaping process, we can make the dependence of the tip diameter and lengthening (elongation) on the heating time.

The parameters, which affect on the results of micropipette pulling process, are naturally the laser power, the size of heated zone and the pulling force. In the figure 3 we show the different micropipettes received at different heated zone.



Fig. 3 Change of nanopipette shape depending on heated zone (0.8 mm, 1 mm and 1.2 mm). Power density is constant -2.86 W/cm^2 . pulling force is provided by a spring -5 N

The outer diameter of micropipette tip pulled by us is about $1 \mu\text{m}$ and smaller down to 200 nm . The inner diameter is even smaller than the outer and their relation is nearly unchangeable in comparison with initial relation of the glass tube.[3]

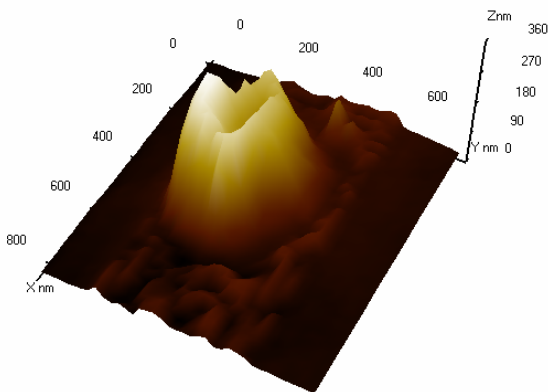


Fig. 4 3D image of nanopipette obtained by scanning test-grating TGT1 on the SPM Nanoeducator. The outer diameter of this micropipette is about 200 nm

B. Study Living Cells with Nanopipete

An interesting biomedical application is the using the nanopipettes as a multifunctional tip for many-sided

studying the cells. This includes the topographical studying of cells and bacteria in living condition (in liquid), the studying of mechanical properties of cell (e.g. hardness of cell membrane), and moreover the measurement of ion current that runs through cell membrane during its metabolic process using well-known patch-clamp method [4]. In figure 5 it is shown that the cells and bacteria are easily imaged by SPM with using nanopipettes as the probe.

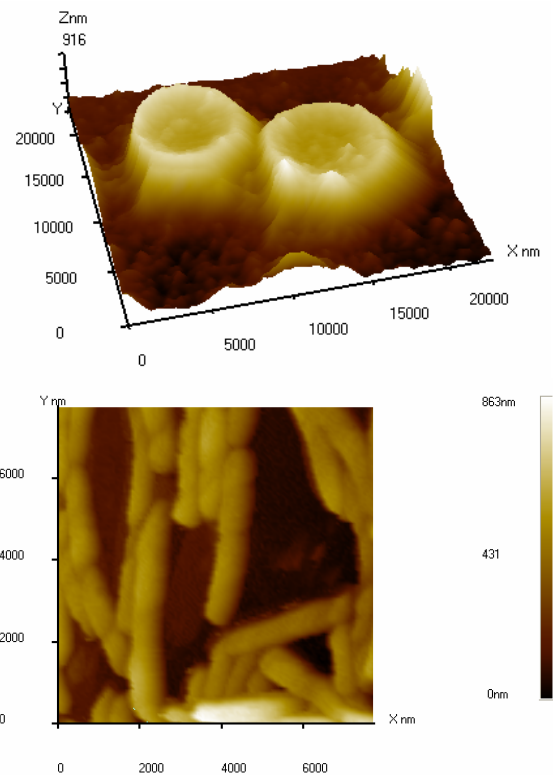


Fig. 5 3D images of blood cells and bacilli scanned by the SPM Nanoeducator using the nanopipette in force regime

SPM Nanoeducator has the function of studying the surface hardness by considering the change of amplitude of the tip oscillation in atomic force mode. In the figure 6 the changes of amplitude of tip oscillation according to the tip-sample distance at different points are shown. The red line presents the amplitude of tip oscillation by approaching the tip to the surface, and the blue line – by moving the tip away from the surface. The faster the amplitude decreases, the harder the surface. The point 1 is correspondent to the substrate surface (glass substrate), and point 2 – to the bacillus membrane. As it has been seen in figure 6, the bacillus membrane is softer than the glass substrate.

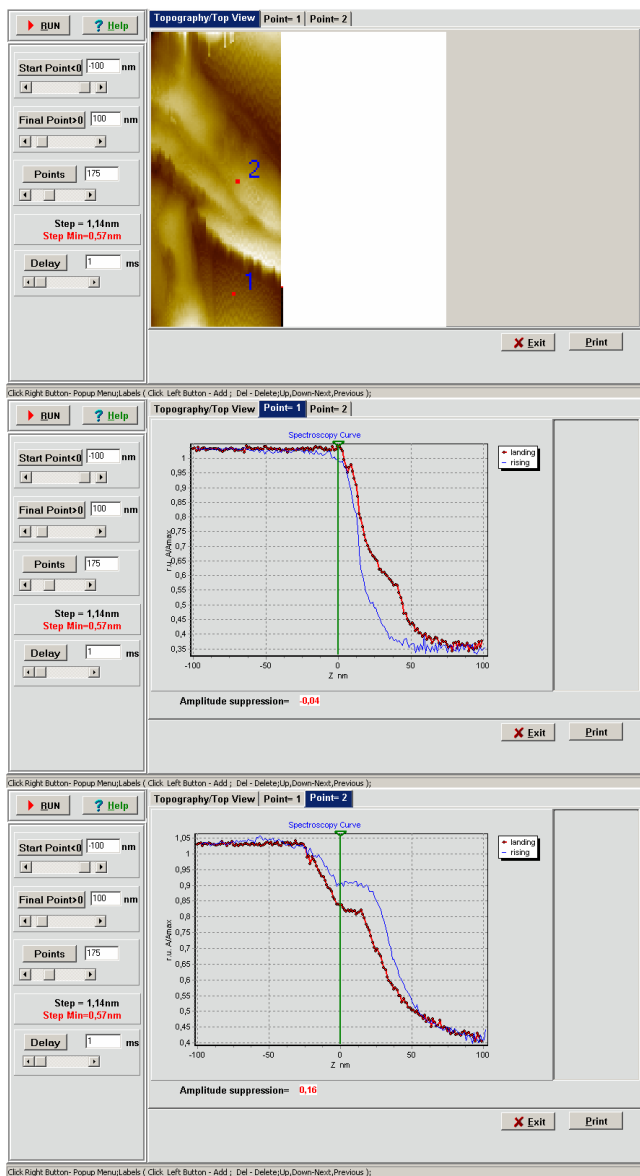


Fig. 6 The change of amplitude of tip oscillation according to the tip-sample distance

For measurement of the ion current run through bacterium membrane, the well-known patch-clamp method is useful. Inside the nanopipette there are electrolyte and an electrode. Before working with the bacillus we have designed a model from a membrane with micro-channels of about 10 μm diameter. This membrane is dipped into electrolyte. The nanopipette has outer diameter about 500 nm, and inner diameter \sim 250 nm. During scanning

nanopipette with electrode the ion current runs from metal substrate, through electrolyte, to the electrode and it will be registered. As would be expected the ion current has changed according to the topography of the modeling membrane with micro-channels. In the figure 7 the topography of one micro-hole and the corresponding ion current are shown. [5]

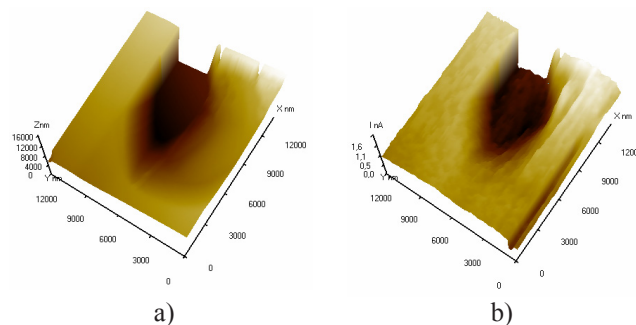


Fig. 7 a)- The topography of one micro-hole (micro-channel) and b)- the corresponding diagram of the ion current

Because of limited time, the ion current through cell membrane has not measured yet. But the model mentioned above and many works about path-clamp confirm that cell membrane potential can be registered.

III. CONCLUSIONS

Thus in this paper the laser technology for nanopipette fabrication is shown. The using of nanopipettes as the probe for SPM allows simultaneous studying different properties of cells.

REFERENCES

1. V.P. Veiko, N.B. Voznesensky, Y.M. Voronin, N.N. Voznesenskya, N.N. Markovkina, V.A. Chuiko. (2000), Laser-based micropipettes: design, technology and applications. SPIE, 4157, p.174–182
2. Zung V.Z., Markovkina N.N., Veiko V.P., Yakovlev E.B. (2004) Laser-assisted of formation micropipettes for biomedicine. Proceedings of SPIE.-2004.-Vol.5399.-P.245-252
3. Zuong Z.V, Markovkina N.N, Yakovlev E.B. (2003) Mathematical modeling of micropipette laser pulling process. Proceedings of institutes. Priborostroenie 2003, Vol.46, №6. p.42-45
4. M.G. Langer, W. Haberle et al. (1997) A scanning force microscope for simultaneous force and patch-clamp measurement on living cell tissues. Rev. Sci. instrum. 68(6), June 1977, p. 2583-2590
5. V. P. Veiko, A. O. Golubok, Z. Zuong, N. V. Varkentina, and E. B. Yakovlev. (2008) Combined nanopipettes for scanning probe microscopy: laser technology for processing and testing. Proc. SPIE, Vol. 6879, 68791W (2008); DOI:10.1117/12.762939

Resolution Study of Ultrasound Reflections in Bovine Vertebral Bones *In-Vitro*

L.H. Le^{1,2,3}, C. Zhang¹, and E. Lou^{3,4}

¹ Department of Radiology and Diagnostic Imaging, University of Alberta, Edmonton, AB, Canada T6G 2B7

² Department of Physics, University of Alberta, Edmonton, AB, Canada T6G 2B7

³ Department of Biomedical Engineering, University of Alberta, Edmonton, AB, Canada T6G 2B7

⁴ Glenrose Rehabilitation Hospital, Alberta Health Services, Edmonton, AB, Canada T5G 0B7

Abstract— Spinal fusion is the most common surgery to correct severe spinal deformities. It involves insertion of screws through the pedicles of vertebrae. Due to the serious neurological or vascular injuries caused by cortical perforation of pedicle screw insertion, an ultrasound imaging method has the potential to vision the spinal vertebrae and provide real-time guidance for the insertion. The objective of this study is to investigate the optimal frequency required to resolve the reflections from the closely-spaced layer interfaces. An immersion pulse-echo experiment was set up to study a bovine spinous process *in-vitro*. Two ultrasound frequencies (3.5 MHz and 5.0 MHz) were considered. The results of our preliminary study are very promising. All interfaces are clearly identified for both frequencies. Strong reflection signals are obtained when the beam is normal to the interface; otherwise, the echoes are weak or nonexistent. Thickness measurements between interfaces are comparable with those from the micro-CT image.

Keywords— Ultrasound, imaging, screw insertion, scoliosis, spinal surgery.

I. INTRODUCTION

Adolescent idiopathic scoliosis (AIS) is a three-dimensional deformity of the spine. It is usually detected at about age ten to skeletal maturity. This lateral curvature affects the rib cage and presents as deformities of the trunk. The spinal deformity is described by the Cobb angle that is measured between the upper and lower vertebrae that tilt most severely towards the concavity of the deformed spine. The ratio of girls to boys with small curves of 10 degrees is equal but increases to a ratio of 10 girls for every one boy with curves greater than 30 degrees. Scoliosis in girls tends to progress more often and, therefore girls more commonly need treatment than boys [1]. According to the Scoliosis Research Society, it is estimated that 0.3% adolescents will require treatment [2]. The long-term results of untreated scoliosis are still controversial [3-8], but patients with untreated curves will have a higher chance of back pain [2, 5]. In severe cases, the twisting of the spine can cause the ribs to press against the lungs, restrict breathing, and reduce oxygen levels. Spinal surgery is the most effective method to treat severe scoliosis.

The aim of spinal surgery is to stop the curve progression and correct the deformity. During surgery, pedicle screws will be inserted through pedicles into the vertebral bodies at different vertebral levels. A pre-bent rod is then secured to the screw heads to correct the deformity. The width of pedicles varies for different vertebrae. For thoracic spine, the average pedicle width ranged from 4.5 to 9.8 mm [9-11]. The available dimensions of pedicle screws ranged from 3.5 to 6.5 mm. To achieve the best curvature correction, pedicle screws should be inserted to the center of the pedicles [12]. The margin between the pedicle screw and pedicle outer boundaries is approximately 1-2 mm. Due to its closeness to surrounding neural structures, a malposition could occur if the screws penetrate the pedicle and directed into the major vessels. A malposition of a pedicle screw may result in serious neurological or vascular injuries, even death. Although the incidence of death was reported to be less than 1% [13], cortical perforation rate of the pedicle screw was reported ranging from 25% to 54.7% [9, 10, 14, 15, 16]. To minimize the malposition rate, various computer assisted navigation systems such as fluoroscopy, CT, and robot technologies have been developed. Fluoroscopy assisted technique has been widely used by orthopedic surgeons to localize pedicle screw positions for intra-operative imaging due to its real time updating images. However, the radiation exposure to both the surgeons and patients in the operation room is the major concern. Amiot et al. [17] introduced a CT assisted technique to spine surgery. They used a pre-surgical CT scan to generate a 3D spine model to assist the screw placement during surgery. However, the different lying positions will affect the vertebral rotation and orientation. Errors may exist between the pre-scanned CT images and the real vertebra during the operation. A robot-assisted method was also proposed to help surgeons during pedicle screw insertion by Ortmaier et al. [18]. The disadvantage of this system is bulky and difficult to use. Ultrasound (US)-based guidance has been successfully applied in many areas such as anesthesia [19] and has many advantages such as low cost, portability, and lack of ionizing radiation.

This study is part of our goal to investigate the potential application of ultrasound to guide screw insertion during surgery. The objective of this preliminary study is to investigate

the optimal frequency required to resolve the ultrasound echoes from the closely-spaced interfaces.

II. MATERIALS AND METHODS

A vertebral bone specimen with attached pedicles, laminae and processes was obtained by excision of bovine cervical bone. All soft tissues were removed from the specimen. The spinous process of the sample was detached from the point where laminae meet process and cut into several small pieces of about 30 mm in length. Fig. 1a shows the dimension of a process sample which is about 38 mm x 30 mm. The cross section of the sample shown in Fig. 1b reveals two approximately 3 mm thick cortical layers with a cancellous core. The sample is larger than a typical pedicle but the cancellous core is similar to that of pedicle with a maximum core thickness of 5 mm.

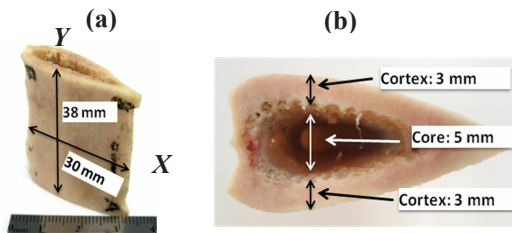


Fig. 1 (a) The dimension and (b) the cross-section of a bovine process sample. The two arrows in (a) indicate the two perpendicular scanning directions, X and Y , respectively.

Fig. 2 shows the setup for the pulse-echo experiment. The device has a fixed arm which holds the bone sample in position. Another arm, which can be adjusted and mechanically moved in the front/back, up/down, and left/right directions, holds the transducer. Two focused immersion transducers (Olympus, Waltham MA) were used in the study. The transducers have an active diameter of 6.4 mm (0.25 in) and two frequencies were considered: 3.5 MHz (V384-N-SU) and 5.0 MHz (V310-N-SU). The typical waveforms and corresponding amplitude spectra generated by the two transducers are illustrated in Fig. 3. The initial distance between the transducer and the sample was set at about the focal length of the transducer: 17.8 mm for 3.5 MHz and 25.4 mm for 5 MHz. The transducer was translated along two scanning directions (see X and Y in Fig. 1a) at a discrete 0.5 mm spatial interval. The transducer's face was perpendicular to the bone surface initially. The whole setup was immersed in distilled water at room temperature. The transducer was pulsed by a Panametrics broadband pulse/receiver 5800PR unit (Olympus, Waltham MA). The signals were recorded and digitized to 8 bits by a LeCroy

wavesurfer 422 oscilloscope (LeCroy, Chestnut Ridge, NY). Each signal was averaged more than 256 times and decimated with a time interval of $0.02 \mu\text{s}$ for off-line signal analysis by a computer. The off-line analysis included noise-filtering and time-gain compensation (TGC). The thicknesses of the bone layers were determined by the arriving times of the echoes and the known ultrasonic velocities of water (1480 m/s) and cortex (2770 m/s).

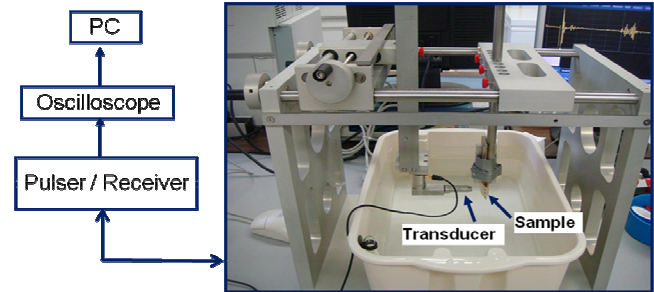


Fig. 2 Setup for the immersion ultrasound pulse-echo experiment

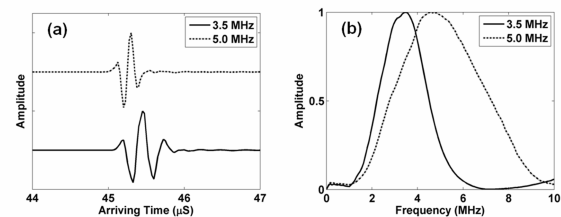


Fig. 3 (a) The typical waveforms and (b) the corresponding amplitude spectra generated by the 3.5 MHz (solid curve) and 5.0 MHz (dashed curve) transducers

III. RESULTS AND DISCUSSION

The colored B-mode ultrasound images or $(x-t)$ echograms of the bone specimen for the two scanning frequencies along the X -direction are illustrated in Fig. 4. The strength of the signals was gain-compensated for later arrivals. The time differences of the echoes between the two scanning frequencies attribute to the transducers' position at their corresponding focal distances from the sample. The box delineates our region of interest (ROI). Due to the fact that the cortex and in-filled distilled water have different acoustic impedances, four interfaces defined by the cortex and water were identified for both frequencies. As shown in the figures, the first reflection (R1) is from the water/cortex interface. The signals are strong and continuous. The second reflection (R2) from the cortex/water interface is obvious and its intensity has been enhanced by

appropriate TGC. Both the third (R3) and fourth reflections (R4) from the second cortical layer are visible but lack of continuity. The images outside and on the right of the ROI are complicated and less identifiable because the bone surface curved further away from normal incidence of the ultrasound beam, the cancellous core was getting narrower and eventually the two cortical layers merged into a single layer as the scanning position was getting closer to the edge of the bone sample (see Fig. 1b). The complication was compounded by the finite size of the transducer's active element, resulting in an overlap or superposition of the echoes from closely-spaced interfaces. Finer details could be observed by the 5.0 MHz and generally, the corresponding images show less continuous or segmented reflections because the high frequency had better sensitivity to locate small discontinuities in the sample than the low frequency.

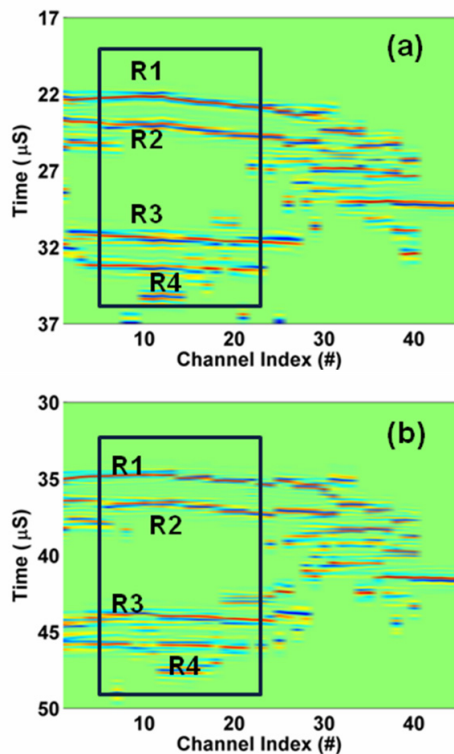


Fig. 4 The colored B-mode echograms of the bone specimen along the X-direction: (a) 3.5 MHz and (b) 5.0 MHz. The black box outlines the region of interest

Fig. 5 displays the B-mode ultrasound images of the specimen along the Y-direction for both frequencies. All the interfaces are visible and identified quantitatively as discussed above. The scanning direction was roughly parallel to the interfaces, which were approximately spaced at constant thickness. This was reflected as parallel lines in the images.

In order to further verify the accuracy of the ultrasound method, we compared the thickness of cancellous core layer measured by the two methods: US and micro-CT (μ CT). Fig. 6 depicts the μ CT cross-sectional image of the sample.

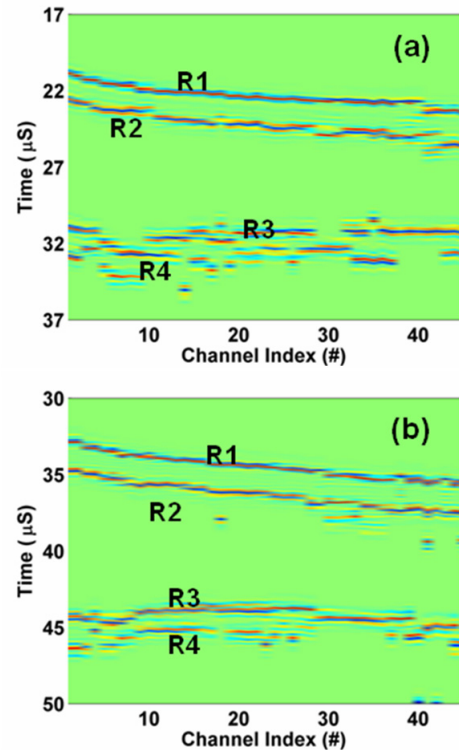


Fig. 5 The colored B-mode echograms of the bone specimen along the Y-direction: (a) 3.5 MHz and (b) 5.0 MHz

The region bounded by the two vertical lines corresponds to the ROI in Fig. 4 and is approximately 10 mm wide. The pixel size was $34.33 \mu\text{m}$. The ultrasound beam of finite thickness insonifies an area of the sample instead of a point. By assuming the insonified area 6.4 mm wide (the diameter of the transducer's element), approximate 186 pixels centred at the scanning location were averaged to provide a μ CT-thickness. Fig. 7 displays the thickness measurement of the twenty channels within the ROI obtained by the two methods. The US-thicknesses agree well for the two frequencies. For the first fifteen channels, the thickness differences between the ultrasound and μ CT images are approximately 0.31 ± 0.23 mm for 3.5 MHz, and 0.31 ± 0.16 mm for 5.0 MHz, respectively. However, the difference increases up to 1 mm for the remaining channels. The agreement deteriorates due to the surface curvature resulting in bigger ultrasonic measurement errors.

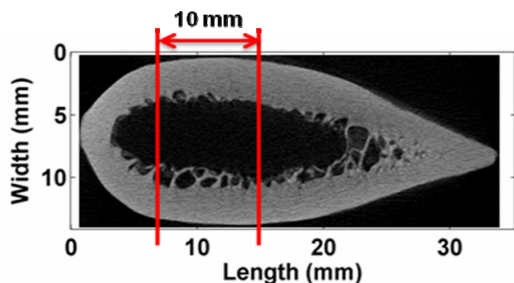


Fig. 6 The μ CT cross-sectional image of the bone sample. The region between the red vertical lines corresponds to the ROI delineated in Fig. 4

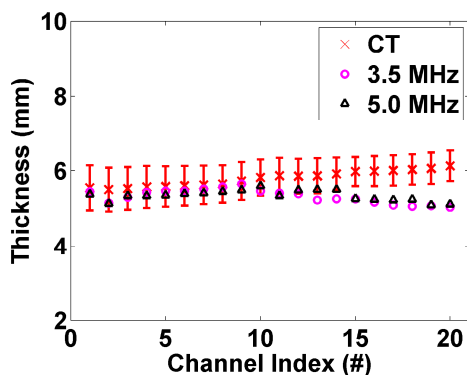


Fig. 7 Thickness comparison between the μ CT and ultrasound methods for the cancellous core layer within the ROI

IV. CONCLUSIONS

The results of our preliminary study are very promising. All interfaces are clearly identified for both frequencies. Strong reflection signals are obtained when the beam is normal to the interface but the echoes are weak or nonexistent with increased bone curvature. The thickness agreement decreases when the bone curvature increases with the inaccuracy ranging from 6% to 20%. Our future study will focus on signal and image processing techniques to enhance the signals and continuities of the reflection. Also, a phase array approach is in progress to study the problem further.

ACKNOWLEDGMENT

We would like to thank Dr. Michael R. Doschak of Faculty of Pharmacy & Pharmaceutical Sciences for his assistance with micro-CT scanning and Rick (J.D.) Zhang for preparing the bone samples. The work was supported by a Discovery Grant from the Natural Sciences and Engineering Research Council of Canada.

REFERENCES

1. Roach JW (1999) Adolescent idiopathic scoliosis. *Ortho Clinic North Am* 30: 331-341.
2. Lonstein JE (1994) Adolescent Idiopathic Scoliosis. *The Lancet*, 344: 1407-1412.
3. James JIP (1954) Idiopathic Scoliosis. The prognoses, diagnosis, and operative indications related to curve patterns and the age at onset. *J Bone Joint Surg* 36B: 36-49.
4. Nachemson A (1968) A long term follow-up study of non-treated scoliosis. *Acta Orthopaedica Scandinavica*, 39(4): 446-476.
5. Weinstein SL, Zavala DC, and Ponseti IV (1981) Idiopathic scoliosis: long term follow-up and prognosis in untreated patients. *J Bone Joint Surg* 63-A (5):702-712.
6. Weinstein SL and Ponseti IV (1983) Curve progression in idiopathic scoliosis. *J Bone Joint Surg* 65-A: 447-45.
7. Edgar MA and Mehta MH (1988) Long-term follow-up of fused and unfused idiopathic scoliosis. *J Bone Joint Surg* 70(5): 712-716.
8. Dickson JH, Mirkovic S, Noble PC, Nalty T, and Erwin RW (1995) Results of operative treatment of idiopathic scoliosis in adults. *J. Bone Joint Surg* 77(4): 513-523.
9. Vaccaro AR, Rizzolo SJ, Allardyce TJ, Ramsey M, Salvo J, Balderston RA, and Cotler JM (1995) Placement of pedicle screws in the thoracic spine. Part I: Morphometric analysis of the thoracic vertebrae. *J Bone Joint Surg* 77A: 1193-1199.
10. Vaccaro AR, Rizzolo SJ, Allardyce TJ, Ramsey M, Salvo J, Balderston RA, and Cotler JM (1995). Placement of pedicle screws in the thoracic spine. Part II: An anatomical and radiographic assessment. *J Bone Joint Surg* 77A: 1200-1206.
11. Laporte S, Mitton D, Ismael B, Fouchecour M, Lasseau JP, Lavste F, and Skalli W (2000) Quantitative morphometric study of thoracic spine. A preliminary parameters statistical analysis. *Eur J Orthop Surg Traumatol* 10: 85-91.
12. Geerling J, Kendoff D et al (2007) Navigated pedicle screw placement in lumbar spine fusion surgery. *Navigation and MIA in orthopedic surgery*, Springer Berlin Heidelberg: 540-546
13. Bradford DS, Tay BK, and Hu SS. (1999) Adult scoliosis: surgical indications, operative management, complications and outcomes. *Spine* 24:2617-2629.
14. Belmont PJ, Klemme WR, Dhawan A, and Polly DW (2001). In vivo accuracy of thoracic pedicle screws. *Spine* 26(21):2340-2346.
15. Xu R, Ebraheim NA, Ou Y et al (1998) Anatomic considerations of pedicle screw placement in the thoracic spine. *Roy-Camille technique versus open-lamina technique*. *Spine* 23: 1065-1068
16. Liljenqvist U, Halm H, and Link T (1997) Pedicle screw instrumentation of the thoracic spine in idiopathic scoliosis. *Spine* 22: 2239 - 45
17. Amiot LP, Labelle H, DeGuise JA, Sati M, Brodeur P, and Rivard CH (1995) Computer-assisted pedicle screw fixation. A feasibility study. *Spine* 20(10):1208-1212
18. Ortmaier T, Weiss H, Dobeles S, and Schreiber U (2006) Experiments on robot-assisted navigated drilling and milling of bones for pedicle screw placement. *The inter J Med Robotics Comput Assist Surg* 2: 350-363
19. Danelli G, Fanelli A, Ghisi D, Moschini M, Ortu A, Baciarello M, and Fanelli G (2009) Ultrasound vs nerve stimulation multiple injection technique for posterior popliteal sciatic nerve block. *Anaesthesia* 64:638-642.

Author: Lawrence H. Le
 Institute: Radiology & Diagnostic Imaging, University of Alberta
 Street: 8308-114 street
 City: Edmonton
 Country: Canada
 Email: lawrence.le@ualberta.ca

Light-Emitting Diodes (LEDs): An Artificial Lighting Source for Biological Studies

Duong Tan Nhut and Nguyen Ba Nam

Tay Nguyen Institute of Biology, VAST, 116 Xo Viet Nghe Tinh, Dalat, Lam Dong, Vietnam
duongtannhut@yahoo.com

Abstract— Light-emitting diodes (LEDs) have been demonstrated to be a artificial flexible lighting source which has significant effects on biological processes. LEDs are not only the solution for biological studies but also for health caring projects. Numerous studies have been conducted in order to investigate the effects of LEDs on plants such as elongation, axillary shoot formation, leaf anatomy, and rhizogenesis as well as on animals such as cellular proliferation, collagen synthesis, growth factor metabolism in cells, cell growth enhancement, and cancer treatment. These studies have lead to many satisfactory results. The use of LEDs has a wide range of applications, such as a radiation source for plant production, investigations on animal nerve system and cell growth, and other applications for fishery and creative nature photographing, etc.

Keywords— Light-emitting diodes (LEDs), photomorphogenesis, photobiomodulation, photodynamic therapy.

I. EFFECTS OF LEDS ON PLANT GROWTH AND DEVELOPMENT

The importance of light quality on several morphologic characteristics such as plant elongation, axillary shoot formation, leaf anatomy and leaf size, and rhizogenesis have been reported (Fig. 1a,b,h,i,j,k,l,m). LEDs are a promising electric light source even for space-based plant growth chambers and bioregenerative advanced life support because of their small mass and volume, solid state construction, safety and longevity. The new superbright blue LEDs makes it possible to evaluate the effectiveness of a total LED irradiation system involving both the superbright blue and red LEDs on *in vitro* plantlet growth (Fig. 1c,d,e,f,g). The high photon level of blue and red LEDs and their wavelength specificity have certainly given the new system and added advantage.

It has early been reported that red LEDs affect stem elongation, leaf expansion, and chlorophyll synthesis [1], photosynthesis [2], and morphogenesis [3; 4]. The decrease in total fresh and dry weight of plantlets under red LEDs was less than that of plantlets under blue LEDs, while there was a noticeable decrease in root weight under red or blue LEDs alone, particularly under blue LEDs as compared to under the control (PGF). The present studies have indicated that plantlets of some species were elongated under only red LEDs while some other species showed normal growth [5]. The elongated plantlets under red LEDs had a thin stem and yellowish leaves, explaining why the plantlets had the smallest chlorophyll content, and their photosynthetic rate and top and root fresh weight were lower as compared to those cultured

under red plus blue LEDs. Some researches also showed that the normal growth of plants was obtained under red LEDs without any support of blue LEDs and that was a characteristic used for successfully growing lettuce plants. The decrease in root weight under red LEDs alone could be accounted for the decrease in shoot/root ratio as reported earlier.

The responses of plantlets cultured under different blue to red LED ratios were considered for commercial applications. These responses are depended on the plant species. And it is important to clarify the optimum blue to red LED ratio for plantlet growth is the most important new finding in this study. This work is the key to evaluating in detail the demand of the blue to red LED ratio [5]. Several studies showed that 1% supplemental blue fluorescent (BF) lamp light appeared to have little effect on final shoot dry matter accumulation and seed yield when compared to red LEDs alone, whereas the addition of 10% BF light to red LEDs consistently produced shoot dry matter and seed yield close to that of white light, despite the fact that white light had a slightly lower photochrome photostationary state and a higher amount of blue light. This might suggest that there is a minimum threshold level for blue light for optimal wheat development under a red-based light source.

It was found that shoot lengths under either blue or red LEDs were greater than under mixed LED or fluorescent lamps, the plantlets overgrew and appeared fragile, but that plantlets under mixed LED or fluorescent lamps were healthy without elongation. There are many studies attempting to find the relationship between red and blue light ratios for these purposes in light quantity like these reports, but they were not clear. It was suggested that plantlet growth under superbright blue and red LED were affected by blue LEDs. In the absence of blue LEDs, plantlets were abnormal, elongated petioles or stem. Normal plantlet growth was clearly related to the presence of blue LEDs and plantlet quality was a function of the amount of blue LEDs. Red LEDs promoted leaf growth but decreased chlorophyll content. Blue light appears to interact with the phytochrome system or through a blue light receptor, which elicits plant responses. It has been shown that without the blue LEDs, an imbalance during the growth and development of the plantlets occurs in every plant species. The better explanation by differences in various red to blue LED ratio is preferred to that by B:R [blue (not LED):red], B:FR [blue (not LED):far-red], R:RF [red:far-red] or B:R [blue (not LED):red (not LED)] ratios.

However, blue LEDs are expensive and they could not be used practically for micropropagation yet. Micropropagation cost reduction could be achieved by culturing shoots under different irradiation levels in which red to blue LED ratio was 90% red + 10% blue LED.

Lower photosynthesis in plants under red LEDs may be associated with lower stomatal conductance, for stomata have been shown to be controlled more by blue than by red light. It has also been suggested that the narrow peak emission of red LEDs leads to an imbalance of photons available to photosystem I and photosystem II, thus altering the ratio of cycle to whole chain reaction transport, and causing a reduction in net photosynthesis. Moreover, red LEDs produced less non-photosynthetic radiation than conventional lamps, which implicates differences in photosynthesis utilization efficiency of photons emitted from LEDs relative to broad-spectrum lamps.

Acclimatization is the final step in a successful micropropagation procedure. During this stage, plants have to adapt to the new environmental conditions of the greenhouse or the field. Hyperhydricity as well as a poor development of the photosynthetic apparatus are the major constraints for promoting acclimatization. Low photosynthetic rates for plants *in vitro* have been reported. This is due to depletion of carbon dioxide (CO₂) in the vessel during the light period, low irradiance and high sugar content. Increasing photosynthetic capacity *in vitro*, by lowering sucrose in the medium and increasing light intensity and ambient CO₂ concentration, can give shorter and more successful acclimatization. However, this depends on species and cultivars. It was demonstrated that high sucrose levels during *in vitro* culture facilities acclimatization of rose plantlets compared to photoautotrophic growing conditions.

The subsequent growth of strawberry plantlets cultured on MP-RW ('Miracle Pack'-Rockwool) systems under LED after transferring to soil was enhanced as compared to that under PGF. LEDs were suggested to be used for improving the quality of plantlets, which can then be used as mother stock for shoot multiplication. The results might be concerned with the same or better photosynthetic ability of plantlets cultured under LEDs as compared to the ability under PGF (plant growth fluorescent) lamps.

It was reported that the growth and development in the rooting stage of plantlets of some horticultural plants were remarkably improved by using novel film culture systems processing thermally stable, high light transmittant and gas-permeable film material [6]. The RW was shown to be the best substrate for *in vitro* growth at the rooting stage. The film culture and LED systems were effective for *in vitro* growth of plantlets and subsequent growth after transferring to soil.

The use of the film culture and total irradiation system by using superbright red and blue LEDs can be applied for micropropagation of several plant species. Plantlets cultured under LED were vigorous and adapted well under *ex vitro* conditions. With further improvements to be made, it is reasonable to expect that the total irradiation system using

superbright red and blue LEDs will be a major light source for a wide range of plant culture systems in the future.

Case studies: In vitro growth and physiological aspects of some horticultural plantlets cultured under red and blue LEDs.

The use of LEDs as a radiation source for plants has attracted considerable interest and attention in recent years because of its vast potential for commercial application. Some significant studies were carried out to examine the effects of the superbright red and blue LEDs applied singly or in combination on the growth of *in vitro* horticultural plantlets. Physiological and morphological aspects were also examined to clarify factors of enhanced growth and development of plantlets under LEDs as compared to those under normal light, plant growth fluorescent lamps (PGF). Shoots of strawberry (*Fragaria* spp.), *Eucalyptus*, *Phalaenopsis*, *Cymbidium*, banana and *Spathiphyllum* were cultured in the 'Culture Pack'-Rockwool (CP-RW) or 'Miracle Pact'-Rockwool (MP-RW) systems under superbright LED or PGF by using CO₂ enrichment with sugar-free medium.

The effects of superbright red and blue LEDs on the plantlet growth of strawberry, *Eucalyptus*, *Cymbidium*, *Phalaenopsis*, banana and *Spathiphyllum* were first studied. Under blue LEDs, plantlet growth was inhibited while the plantlets elongated under red LEDs. On the other hand, plantlet growth was enhanced under red and blue LEDs, comparable to growth under PGF showing the usefulness of the total irradiation system using superbright LEDs for the micropropagation of many plant species.

To clarify the optimal blue to red LED ratio for the growth of plantlets, shoots were cultured under four ratios at 45 $\mu\text{mol}\cdot\text{m}^{-2}\cdot\text{s}^{-1}$: (1) 100% red LED, (2) 90% red + 10% blue LED, (3) 80% red + 20% blue LED, and (4) 70% red + 30% blue LED. The growth of *Eucalyptus*, *Cymbidium*, *Phalaenopsis*, banana (*Musa* spp.) and *Spathiphyllum* plantlets were enhanced under 80% red + 20% blue LED while strawberry plantlet growth was enhanced under 70% red + 30% blue LED. These results show that the optimal blue to red LED ratio for plantlet growth varies among different plant species (Fig. 1n,o,p) [5; 7].

The *in vitro* growth of plantlets cultured under 90% red + 10% blue LED at 45, 60, and 70 $\mu\text{mol}\cdot\text{m}^{-2}\cdot\text{s}^{-1}$, of which ratios were adopted to reduce the product cost because of high cost of the superbright blue LEDs. The results showed that the growth of plantlets was enhanced under 60 $\mu\text{mol}\cdot\text{m}^{-2}\cdot\text{s}^{-1}$ and was better than that under PGF.

The results of physiological experiments showed that the photosynthetic rate of *Cymbidium* plantlets was higher under 80% red + 20% blue LED as compared to those of the other LED ratios and PGF, and that of *Phalaenopsis* plantlets was equal under both LED (80% red + 20% blue) and PGF. Stomatal morphology did not differ in these two species cultured under either LED or PGF. The differences of stomatal morphology between *Eucalyptus* plantlets obtained from the

sugar-free CP-RW system under LED and those under PGF were not observed, while those grown on a sugar-free Bottle•Agar (BO•AG) system showed some abnormal stomata. These results suggested that LED irradiation had no problem and was effective for *in vitro* physiological behaviors and morphogenesis, causing the enhanced growth *in vitro*.

Attempts were also made to examine whether the irradiation source during *in vitro* culture affects the subsequent growth of strawberry, *Eucalyptus*, banana and *Spathiphyllum* plantlets transferred to soil. The *ex vitro* growth of *Eucalyptus*, banana and *Spathiphyllum* plantlets cultured under 80% red + 20% blue LED *in vitro* was enhanced as compared to that under PGF, while the *ex vitro* growth of strawberry plantlets was enhanced when those were cultured under 70% red + 30% blue LED *in vitro*. This showed that LED irradiation source used for the *in vitro* culture of strawberry, *Eucalyptus*, banana and *Spathiphyllum* plantlets affects not only the growth of plantlets *in vitro*, but also the *ex vitro* growth of these plants after transferring to soil (Fig. 1q,r,s).

The studies presented here demonstrated the effectiveness of a total irradiation system by using superbright red and blue LEDs for plantlets of many plant species grown *in vitro* and their subsequent growth after transferring to soil. From the results and a lot of attractive feature of LEDs, it is reasonable to expect that the total LED irradiation system will be a major light source for a wide range of micropropagation systems in the future with further improvements to be made.

II. EFFECTS OF LEDS ON BIOLOGICAL PROCESSES IN HUMAN AND ANIMALS

Rapid Healing of Laser Eye Injuries with LED Technology

At the cellular level, photoirradiation at low fluencies can generate significant biological effects including cellular proliferation, collagen synthesis and the release of growth factors from cells. Photobiomodulation by light in the red to near infrared (NIR) range (630 – 1000 nm) using low energy lasers or LED arrays has been shown to accelerate wound healing, improve recovery from ischemic injury in the heart and attenuate degeneration in the injured optic nerve. Several studies have demonstrated that LED photoirradiation at 670 nm stimulates cellular proliferation in cultured cells and significantly improves wound healing in genetically diabetic mice.

The therapeutic effects of red to near infrared result, in part, from intracellular signaling mechanisms triggered by the interaction of NIR light with the mitochondrial photoacceptor molecule cytochrome oxidase which culminate in improved cellular mitochondrial energy metabolism and antioxidant production.

It was demonstrated that NIR-LED treatment can heal poisoned neurons by stimulating cytochrome oxidase activity,

protect against retinal damage and improves the recovery of retinal function in a rodent model of mitochondrial poison-induced blindness, and promote retinal healing and improved visual function following high intensity laser-induced retinal injury in adult non-human primates.

Various biological processes in cell culture of animal models can be modulated by low energy photon irradiation by light in the far red to near infrared spectral range (630 – 1000 nm) using low energy lasers or light emitting diode arrays. This phenomenon of photobiomodulation has been applied clinically in the treatment soft tissue injuries and to accelerate wound healing. The mechanism of photobiomodulation by red to near infrared light at the cellular level has been ascribed to the activation of mitochondrial respiratory chain components resulting in initiation of a signaling cascade which promotes cellular proliferation and cytoprotection. A comparison of the action spectrum for cellular proliferation following photoirradiation with the absorption spectrum of potential photoacceptors lead to suggest that cytochrome oxidase is a primary photoreceptor of light in the red to near infrared region of the spectrum [8].

Studies conducted in primary neuronal cultures have shown that 670 nm LED photobiomodulation reversed the reduction in cytochrome oxidase activity produced by the blockade of voltage-dependent sodium channel function by tetrodotoxin and up-regulated cytochrome oxidase activity in normal neurons. Additional studies have extended these investigations to an *in vivo* system to determine if 670 nm LED photobiomodulation would improve retinal function in an animal model of format-induced mitochondrial dysfunction. Results demonstrated the therapeutic benefit of photobiomodulation in the survival and functional recovery of the retina *in vivo* after acute injury by the mitochondrial toxin, formic acid generated in the course of methanol intoxication. *In vivo* evidence were provided that three brief post-methanol-intoxication treatments with 670 nm LED photoirradiation promotes the recovery of retinal function in rod and cone pathways and protects the retina from the histopathologic changes induced by methanol-derived format. These findings provide a link between the actions of red to near infrared light on mitochondrial oxidative metabolism *in vitro* and retinoprotection *in vivo*.

Low energy laser irradiation has promoted benefits in enhancing the healing of hypoxic, ischemic, and infected wounds. However, lasers have limitations in beam width, wavelength capabilities, and size of wounds that can be treated. Heat generated from the laser light can damage biological tissues, and the concentrated beam of laser light may accidentally damage the eye. LED arrays were developed for NASA manned space flight experiments. In comparison to lasers, the patented LED technology generates negligible amounts of heat, is clinically proven to be safe, and has achieved non-significant risk status for human trials by the FDA.

The prolonged effect of 3 brief LED treatments in mediating the cytoprotective actions in cultured retinal cells and the retinoprotective actions in methanol intoxication suggests that 670 nm LED photostimulation induces a cascade of signaling events initiated by the initial absorption of light by cytochrome oxidase. These signaling events may include the activation of immediate early genes, transcription factors, cytochrome oxidase subunit gene expression and a host of other enzymes and pathways related to increased oxidative metabolism. In addition to increased oxidative metabolism, red to near infrared light stimulation of mitochondrial electron transfer is also known to increase the generation of reactive oxygen species. These mitochondrially generated reactive oxygen species may function as signaling molecules to provide communication between mitochondria and the cytosol and nucleus and thus play an important signaling role in the activation of retinoprotective processes following LED treatment. Results of several studies and others suggest that photobiomodulation with red to near infrared light augments recovery pathways promoting neuronal viability and restoring neuronal function following injury [9]. Importantly, there was no evidence of damage to the normal retina following 670 nm LED treatment. Based on these findings, it is suggested that photobiomodulation may represent an innovative and novel therapeutic approach for the treatment of retinal injury as well as the treatment of retinal diseases, including age-related macular degeneration, glaucoma, diabetic retinopathy, and Leber's hereditary optic neuropathy.

LED-Enhancement of Cell Growth

Studies on cells exposed to microgravity and hypergravity indicate that human cells need gravity to stimulate growth. As the gravitational force increases or decreases, the cell function responds in a linear fashion. This poses significant health risks for astronauts in long-term space flight. The application of light therapy with the use of NASA LEDs will significantly improve the medical care that is available to astronauts on long-term space missions. NASA LEDs stimulate the basic energy processes in the mitochondria (energy compartments) of each cell, particularly when near-infrared light is used to activate the color sensitive chemicals (chromophores, cytochrome systems) inside. Optimal LED wavelengths include 680, 730 and 880 nm and the healing of wounds has been improved in laboratory animals by using both NASA LED light and hyperbaric oxygen. Furthermore, DNA synthesis in fibroblasts and muscle cells has been quintupled using NASA LED light alone, in a single application combining 680, 730 and 880 nm each at 4 Joules per centimeter squared.

Muscle and bone atrophy are well documented in astronauts, and various minor injuries occurring in space have been reported not to heal until landing on Earth. An LED blanket device may be used for the prevention of bone and muscle

atrophy in astronauts. The depth of near-infrared light penetration into human tissue has been measured spectroscopically. Spectra taken from the wrist flexor muscles in the forearm and muscles in the calf of the leg demonstrate that most of the light photons at wavelengths between 630 – 800 nm travel 23 cm through the surface tissue and muscle between input and exit at the photon detector. The light is absorbed by mitochondria where it stimulates energy metabolism in muscle and bone, as well as skin and subcutaneous tissue.

Long term space flight, with its many inherent risks, also raises the possibility of astronauts being injured performing their required tasks. The fact that the normal healing process is negatively affected by microgravity requires novel approaches to improve wound healing and tissue growth in space. NASA LED arrays have already flown on space shuttle missions for studies of plant growth and FDA has proven human trials. The use of light therapy with LEDs can help prevent bone and muscle atrophy as well as increase the rate of wound healing in a microgravity environment, thus reducing the risk of treatable injuries becoming mission catastrophes. Space flight has provided a laboratory for studying wound healing problems due to microgravity, which mimic traumatic wound healing problems here on Earth. Improved wound healing may have multiple applications that benefit civilian medical care, military situations and long-term space flight. Laser light and hyperbaric oxygen have been widely acclaimed to speed wound healing in ischemic, hypoxic wounds [9].

Lasers provide low energy stimulation of tissues resulting in increased cellular activity during wound healing including increased fibroblast proliferation, growth factor synthesis, collagen production and angiogenesis. Lasers, however, have some inherent characteristics that make their use in a clinical setting problematic, such as limitations in wavelength capabilities and beam width. The combined wavelengths of light optimal for wound healing cannot be efficiently produced, and the size of wounds that may be treated by lasers is limited. LEDs offer an effective alternative to lasers. These diodes can be made to produce multiple wavelengths, and can be arranged in large, flat arrays allowing treatment of large wounds. Potential benefits to NASA, military, and civilian populations include treatment of serious burns, crush injuries, non-healing fractures, muscle and bone atrophy, traumatic ischemic wounds, radiation tissue damage, compromised skin grafts, and tissue regeneration. Combat casualty cares in special operations already have adopted the NASA LED technology for submarines deployed in training with risk of injury. Special operations are characterized by lightly equipped, highly mobile troops entering situations requiring optimal physical conditioning at all times. Wounds are an obvious physical risk during combat operations. Any simple and lightweight equipment that promotes wound healing and musculoskeletal rehabilitation and conditioning has potential merit.

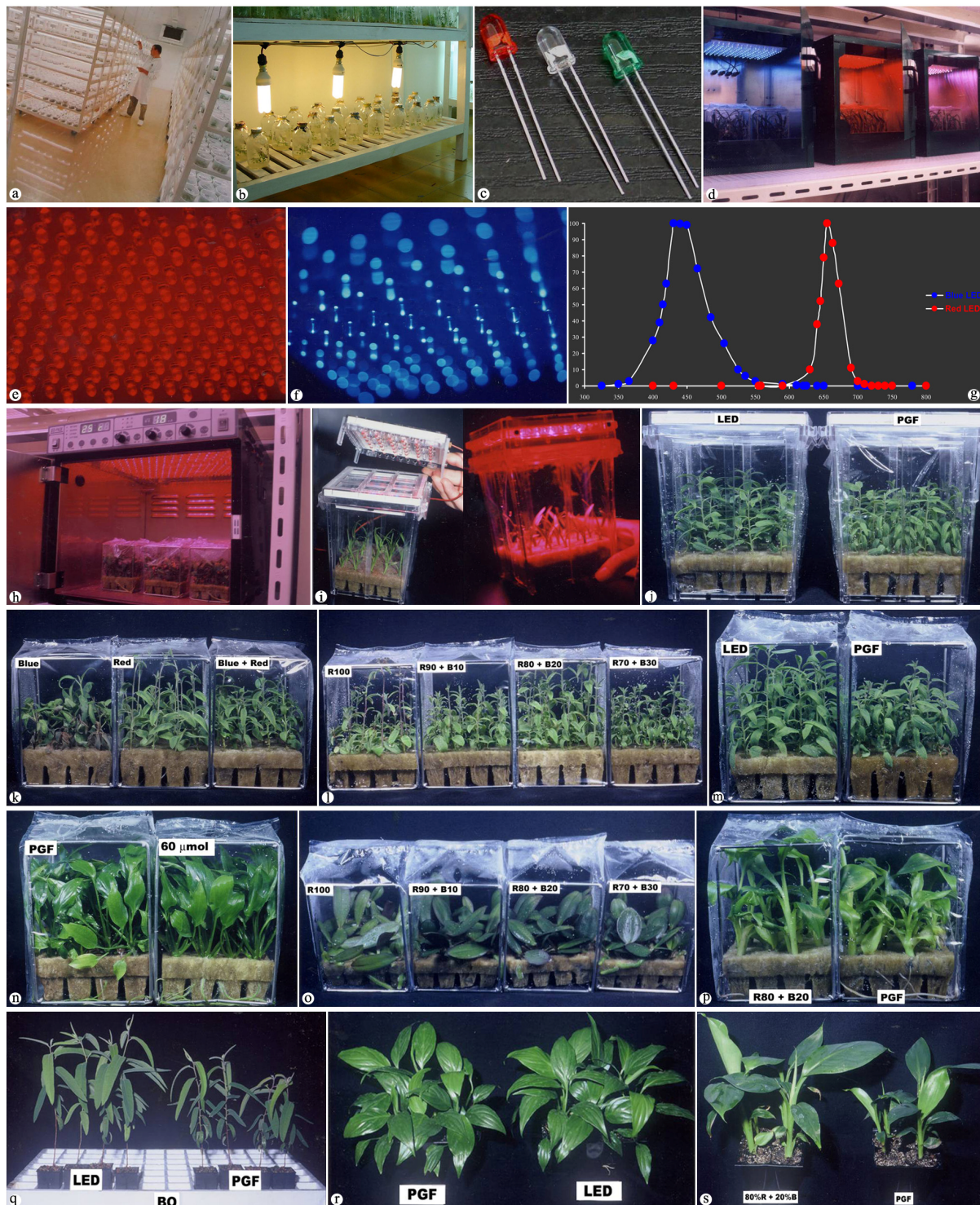


Fig. 1 Some artificial lighting sources using for plant growth and development cultured *in vitro*. a: Neon light; b: Compact 3U light; c, d: LED light; e: Red LED; f: Blue LED; g: Spectral energy distribution of blue and red LED; h: LED PACK 3; i: LED CAP; j, k, l, m: *Eucalyptus citriodora* cultured under LED CAP and Neon light (PGF); n, o, p: *Spathiphyllum*, *Phalaenopsis* and Banana plantlets cultured under LED light; q, r, s: *Eucalyptus*, *Spathiphyllum* and Banana plantlets derived from LED and PGF light acclimated in greenhouse

NASA LEDs have proven to stimulate wound healing at near-infrared wavelengths of 680, 730 and 880 nm in laboratory animals, and have been approved by FDA for human trials.

The NASA LED arrays are light enough and mobile enough to have already flown on the space shuttles numerous times. LED arrays may be used for improved wound healing and treatment of problem wounds as well as speeding the return of deconditioned personnel to full duty performance. Examples include: (1) promotion of the rate of muscle regeneration after confinement or surgery; (2) personnel spending long periods of time aboard submarines may use LED arrays to combat muscle atrophy during relative inactivity; (3) LED arrays may be introduced early to speed wound healing in the field [10].

LED-Photodynamic Therapy for Cancer

Astronauts in deep space are subjected to increased levels of radiation, compared to low-earth orbit environments. Cancer protection strategies are therefore a subject of the NASA-LED photodynamic therapy program. Photodynamic therapy (PDT) is a cancer treatment modality that recently has been improved using LED space technology. PDT consists of intravenously injecting a photosensitizer, which preferentially accumulates in tumor cells, into a patient and then activating the photosensitizer with a light source. This results in free radical generation followed by cell death. LEDs are an effective alternative to lasers for PDT. Laser conversion to near-infrared wavelengths is inherently costly and inefficient. LEDs have been frequently used to emit longer wavelength broad spectrum nearinfrared light of 25 – 30 nm bandwidths. LED lamps traditionally consist of an array of semiconducting LED chips.

In recent years, improvements in semiconductor technology have substantially increased the light output of LED chips. A novel type of LED chip is based on the semiconductor Aluminum Gallium Arsenide (AlGaAs). These LED chips have been manufactured to emit light with peak wavelengths of 680 and 730 nm, which are optimal wavelengths for the absorption spectrum of the new photosensitizers used for cancer PDT.

The development of more effective light sources for PDT of brain tumors has been facilitated by applications of space LED array technology; thus permitting deeper tumor penetration of light and use of better photosensitizers. Lutetium Texaphyrin (Lutex) and Benzoporphyrin Derivative (BPD) are new, second generation photosensitizers that can potentially improve PDT for brain tumors. Lutex and BPD have major absorption peaks at 730 nm and 680 nm respectively, which give them two distinct advantages. First, longer wavelengths of light penetrate brain tissue easily so that larger tumors could be treated; and second, the major absorption

peaks mean that more of the drug is activated upon exposure to light. In deep space, the LED-PDT technology may be capable of early cancer surveillance and treatment before radiation-induced tumors can develop in astronauts [11].

III. CONCLUSION

The LED-based light source, with the newly developed capability and the trends of brighter intensity and lower price, has made it a promising light source for studies on biological processes. With current studies and further investigations to be made, LEDs have been increasingly applied for promoting cell research, plant production. It is also considered as a feasible alternative for lasers in human health caring.

ACKNOWLEDGEMENT

The author would like to thank Prof. Michio Tanaka (Kagawa University, Japan) for permission of using the photos.

REFERENCES

1. Tripathy B C, Brown C S (1995) Root-shoot interaction in the greening of wheat seedlings grown under red light. *Plant Physiol* 107: 407–411
2. Tennessen D J, Singasas E L, Sharkey T D (1994) Light-emitting diodes as a light source for photosynthesis research. *Photosynthesis Research* 39: 85–92
3. Hoenecke M E, Bula R J, Tibbitts T W (1992) Importance of “blue” photon levels for lettuce seedlings grow under red-light-emitting diodes. *HortScience* 27: 427–430
4. Robin C, Hay M J M, Newton P C D (1994) Effect of light quality (red:far-red ratio) and defoliation treatments applied at a single phytomer on axillary bud outgrowth in *Trifolium repens* L. *Oecologia* 100: 236–242
5. Nhut D T (2002) *In vitro* growth and physiological aspects of some horticultural plantlets cultured under red and blue light-emitting diodes (LEDs). Doctoral thesis, Kagawa University, Japan
6. Tanaka M, Nhut D T, Takamura T et al. (1998) *In vitro* growth of strawberry plantlets cultured under superbright red and blue light-emitting diodes (LEDs). Abstract of the XXVth International Horticultural Congress 407
7. Nhut D T, Takamura T, Watanabe H, Tanaka K (2000) Light-emitting diodes (LEDs) as a radiation source for micropropagation of strawberry. In: Kubota C, Chun C (Eds.) *Transplant Production in the 21st Century*. Kluwer Academic Publishers, 2000, pp 114–118
8. Karu T (1999) Primary and secondary mechanisms of action of visible to near-IR radiation on cells. *J Photochem Photobiol* 49: 1–17
9. Conlan M J, Rapley J W, Cobb C M (1996) biostimulation of wound healing by low-energy laser irradiation. *J Clin Periodont* 23: 492–496
10. Whelan H T, Buchmann E V, Whelan N T et al. (2001) NASA light-emitting diode medical applications from deep space to deep sea. In: El-Genk M S (Ed.) *Space Technology and Applications International Forum*, 2001, pp 35–45
11. Schmidt M H, Meyer G A, Reichert K W et al. (2004) Evaluation of photodynamic therapy near functional brain tissue in patients with recurrent brain tumors. *J Neuro-Oncology* 67: 201–207

A Novel Electronic Cervical Range of Motion Measurement System

E. Lian¹, J. Hachadorian¹, Ngo Thanh Hoan², and Vo Van Toi²

¹ Electrical and Computer Engineering Department, Tufts University, Medford Massachusetts, USA

² Biomedical Engineering Department, International University of Vietnam National Universities, Ho Chi Minh City, Vietnam

Abstract— In this article we describe the design of a novel, portable, head-mounting, electronic system to measure the ranges of motion of the cervical spine (CROM). The device used monolithic integrated circuits such as: accelerometers, gyroscopes and a single-chip 12-bit data acquisition system. This Electronic Cervical Range of Motion measurement system is connected to a personal computer interface that allows for efficient and reliable data transfer, thereby limiting the potential for human calculation and transcription errors. Overall, the system is accurate, reliable, portable, low-cost, and user-friendly. Furthermore, the system displays specific instructions to the user, in order to insure proper measurement technique and to limit inter-user error.

Keywords— Cervical Range of Motion, Accelerometer, Gyroscope, Single-chip Data Acquisition System.

I. INTRODUCTION

Neck pain is a common musculoskeletal disorder, for which large numbers of patients receive medical treatment every year. The diagnosis and the evaluation of treatment success in patients with neck pain often require a continuous physical assessment of the range of motion of the cervical spine (CROM). Therefore it is significant to have a portable device that patient could use themselves to follow up how the treatment evolves.

Measuring CROM consisted of determining the maximum angles that a subject can perform using his/her head alone without pain in 3 plans: frontal (tilt left/right), sagittal (flexion/extension) and transverse (rotation left/right).

There are many methods and devices for measuring cervical range of motion that are currently in use such as: dual inclinometers, bubble goniometers, radiographs, compass technology, visual estimation, ultrasound, geometric methods, the Fastrack, digital optoelectronic instruments, computerized kinematic analysis using passive markers and infrared TV cameras, MRI, and CROM device [1-5].

All of these methods have some success in accurately determining cervical range of motion. The ideal cervical range of motion measurement system would be: accurate, precise, portable, low-cost, electronic, intuitive, and user-friendly. The system would have a personal computer interface that allows for efficient and reliable data transfer, thereby

limiting the potential for human calculation and transcription errors. Furthermore, the system would be able to print specific instructions to the user, in order to insure proper measurement technique and to limit inter-user error. A survey of the background literature has revealed that no existing method of measuring cervical range of motion meets all of the aforementioned criteria.

Table 1 Range of Motion System Performance Comparison

SYSTEM	Axial Rotation Capable	Electronic	Portable	Performance	Low-Cost	Ease of Use
CROM	X		X	X	X	
Digital Optoelectronic		X		X		
Fastrack						
Dual Inclinometers			X	X	X	
Bubble Goniometer			X		X	X
Radiographs				X		
Ultrasound						
Geometric Methods	X		X		X	

The matrix in Table 1 indicates that very few current cervical range of motion measurement systems provide axial rotation measurement capability. This paper describes a novel Electronic Cervical Range of Motion Measurement System (ECROM). This electronic system provides accurate measurements, increases quality of documentation, and enhances measurement simplicity.

II. MATERIALS AND METHODS

The ECROM was built using a three-axis accelerometer, ADXL330, used as tilt sensor to measure both the Frontal and Sagittal CROM, a resonator gyroscope, ADXRS150, used as a rotation sensor to measure the Transverse CROM and a MicroConverter® ADuC841, a single-chip 12-bit data acquisition system that includes precision A/D and D/A converters, an 8052 Flash microcontroller, multiplexers, buffers, a temperature sensor, a voltage reference, a watchdog timer, a time-interval counter, serial interface ports, and a post-microprocessor that processed data that can be fit into the monitoring screen, typically a computer terminal for data display and further calculations (Fig.1). These are the monolithic IC from Analog Devices Inc. (Massachusetts, USA) [6].

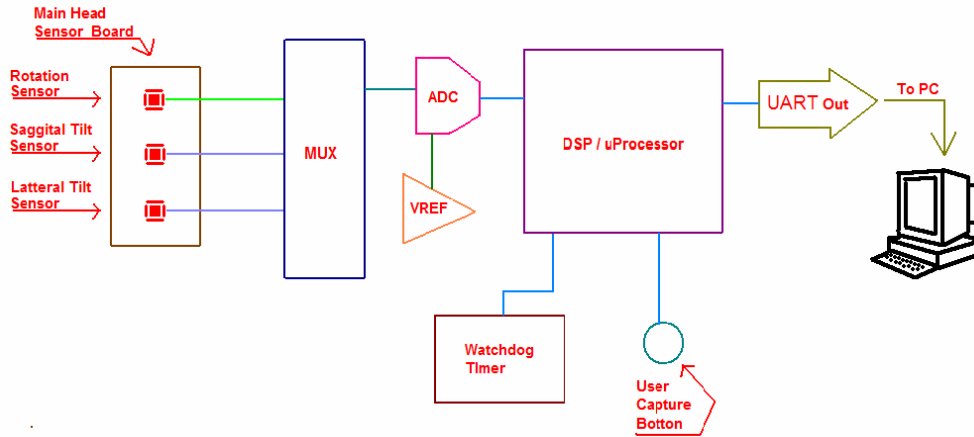


Fig. 1a Portable ECROM Device Block Diagram

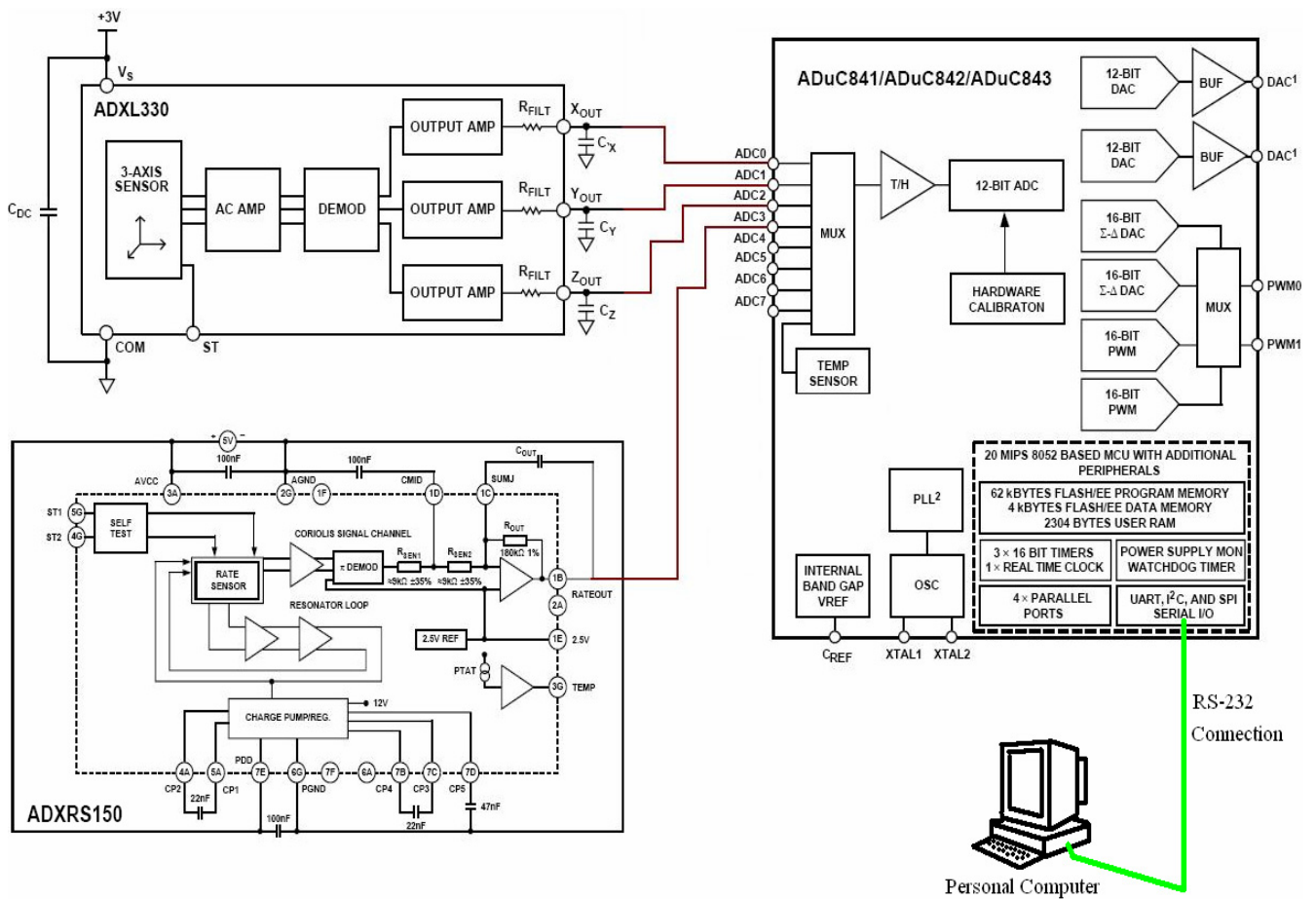


Fig. 1b ECROM System Integration

The ADXL330 outputs X, Y, Z analog voltages depending on the tilting in respective X, Y, Z directions. We will exclusively examine the X-output; the Y-output and the Z-output follow the same underline principle. The analog output voltage from the ADXL330 is fed into AIN1 of the ADuC841. After the analog voltage passes through a MUX, it is propagated into the ADuC841's integrated 12-bit ADC. The output of the ADC is in digital format, which is processed after going into 8052 MCU. The output of the Micro-Converter propagates through a RS-232 connecting cable to the personal computer, where it is displayed in the Hyper-terminal in Hex format. An algorithm for calculating tilting, or flexion and extension, of the head with the ADXL330 tilt-sensor is listed below:

1. ADXL330 acquires the initial position of the head. After MUX and ADC, the digital form of this voltage is stored as the 1st voltage in ADuC841 memory location for calibration purposes.
2. The INTO button on ADuC841 evaluation board is pressed to send the 1st voltage to the PC UART screen for system validation purposes.
3. After subject's head is finished turning, the INTO button is pressed again to record the 2nd voltage-the voltage associated with the final head position. Similarly, this voltage is stored in the ADuC841 memory location and then output onto the PC UART screen.
4. After the absolute difference of these two voltages is calculated by the MicroConverter, it is displayed in the PC's UART window in Hex format. This Hex output is manually entered into the appropriate Microsoft Excel worksheet.
5. The Hex output is converted into decimal format by using an Excel formula. The following equation is used to translate the decimal output into a voltage reading.

$$Voltage = \frac{Output_decimal \times System_reference_voltage}{1 + 2^{Bit_ADC}}$$

6. The degree of axial rotation of the head is then calculated in Excel with the following formula:

$$Degree_turned = \frac{\arcsin(delta_output)}{AccelerometerSensitivity \times 1g}$$
7. A screen shot of Accelerometer Excel worksheet is shown below.

Accelerometer		
Enter delta (in hex format) from UART:	a1	
Degree tilted	40.9159177	degree
CALCULATION TABLE AND OUTPUT VOLTAGES		
delta in hex	a1	
delta in decimal	161	
delta in voltage	0.196485233	
degree tilted	40.91591771	
Note: DEGREE=ASIN(delta output/0.31*180/pi())		

Fig. 2 illustrates how the tilt sensor's outputs behave as the tilting angle changes. At 0° tilting, the accelerometer is at its default position, which correlating to analog voltage of around 1.5V, half way between 3V power supply and ground. At 75° tilting, the analog voltage decreases linearly to about 1.2V. Approaches 90° tilt, the nonlinearity of the device starts to show. After resetting the device to the initial 0° tilt position, analog voltage of around 1.5V is reestablished. For both clockwise and counter clock tilting, the accelerometer behaves similarly. To measure cervical strength of motion, 75° of linearity is sufficient because the human neck can rarely turn more than 75°. Accelerometer can be safely used in this application.

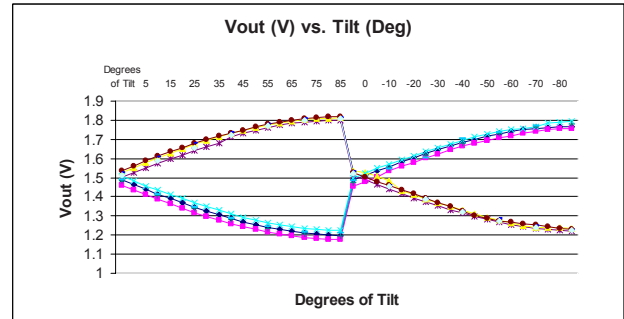


Fig. 2 ADXL330 Accelerometer Characterization Data Plot (see text)

Similarly, the output of the resonator gyroscope ADXRS150 can be converted into the neck rotation angle according to the following formula:

$$Neck_rotation_in_degree = \frac{Initial_voltage - Ave_voltage}{12.5mV / degree / second} \times total_time_in_second$$

The whole circuit (5x5cm) was attached on the top of a hard hat that can fit securely on the subject's head and provide a stable platform (Fig. 3). The hat was light and comfortable enough to allow unencumbered and unrestricted movement of the neck. A software program was written to treat the signals and display in an appropriate form in a user-friendly way.



Fig. 3 ECROM system mounted on a hard hat

III. RESULTS AND DISCUSSIONS

The accuracy and precision of the measurement system were assessed by mounting the device sensors upon a testing apparatus capable of titling and rotating to pre-set angles.

The test apparatus was designed to reliably simulate the frontal, sagittal and transverse motions. The performance capabilities of the measurement system were determined by comparing the measured angles of flexion, extension, and rotation, to the pre-set angles of the testing apparatus.

System accuracy was characterized by recording the system output for angles varying from -90° to $+90^{\circ}$ of tilt, in 5° increment. The precision of the tilt sensing system was characterized by setting the test apparatus to various angles of tilt, and performing multiple measurements at each angle setting.

Tilt Sensor repeatability was studied for 38° tilt angles in both the clockwise and counter-clockwise directions. The maximum measurement error in this case was less than 2.0° , with a mean error of 0.73° . The mean measurement system result after ten trials was 37.27° , with a standard deviation of 0.63° . This implies that 90% of measured tilt for an actual tilt of 38° is in the range of $37.27+3 \times 0.63$ and $37.27-3 \times 0.63$ which is from 35.38 to 39.16° .

Gyroscope repeatability was studied for 55° rotation angles in both the clockwise and counter-clockwise directions. The maximum measurement error in this case was less than 4.0° , with a mean error of 3° . The mean measurement system result after ten trials was 51.9° , with a standard

deviation of 0.52° . This implies that 90% of measured tilt for an actual tilt of 38° is in the range of $51.9+3 \times 0.52$ and $51.9-3 \times 0.52$ which is from 50.36 to 53.45° .

IV. CONCLUSIONS

We developed an Electronic Cervical Range of Motion measurement system that is accurate, reliable, portable, low-cost, and user-friendly. The system connected to a personal computer interface that allows for efficient and reliable data transfer, thereby limiting the potential for human calculation and transcription errors. Furthermore, the system is able to display specific instructions to the user, in order to insure proper measurement technique and to limit inter-user error.

ACKNOWLEDGMENT

We would like to thank Professor Noshir Mehta, Tufts School of Dental Medicine for his valuable assistance.

REFERENCES

1. Carpaneto J., Micera S., Galardi G., Micheli A., Carboncini M.C., Rossi B., Dario P. (2004) A protocol for the assessment of 3D movements of the head in persons with cervical dystonia. *Clin Biomech* (Bristol, Avon). 19 (7):659-63.
2. Tousignant M., Smeesters C., Breton A.M., Breton E., Corriveau H. (2006) Criterion validity study of the cervical range of motion (CROM) device for rotational range of motion on healthy adults. *Journal of Orthopedic Sports Phys Ther.* 36 (4):242-8.
3. Strimpakos N., Sakellari V., Gioftos G., Papathanasiou M., Brountzos E., Kelekis D., Kapreli E., Oldham J. (2005) Cervical spine ROM measurements: optimizing the testing protocol by using a 3D ultrasound-based motion analysis system. *Cephalalgia.* 25(12):1133-45.
4. Jordan K., Haywood K.L., Dzedzic K., Garratt A.M., Jones P.W., Ong B.N., Dawes P.T. (2004) Assessment of the 3-dimensional Fastrak measurement system in measuring range of motion in ankylosing spondylitis. *Journal Rheumatol.* 31(11):2207-15.
5. Chiarello C.M., Savidge R. (1993) Interrater reliability of the Cybex EDI-320 and fluid goniometer in normals and patients with low back pain. *Arch Phys Med Rehabil.* 74(1):32-7.
6. Analog Devices Technical Reference Books: Practical Design Techniques for Sensor Signal conditioning. *Prentice Hall 1994.*

Author: Vo Van Toi

Institute: Biomedical Engineering Department, International University of Vietnam National Universities, Ho Chi Minh City, Vietnam

Street: Linh Trung Ward, Thu Duc Dist.

City: Ho Chi Minh

Country: Vietnam

Email: vvtoi@hcmiu.edu.vn

Measurement of the Range of Neck Motion: A Comparative Study

J. Hachadorian¹, A. Lugo², E. Lian¹, Truong Quang Dang Khoa³, and Vo Van Toi^{1,2,3}

¹ Electrical and Computer Engineering Department, Tufts University, Medford, Massachusetts, USA

² Biomedical Engineering Department, Tufts University, Medford, Massachusetts, USA

³ Biomedical Engineering Department, International University of Vietnam National Universities, Ho Chi Minh City, Vietnam

Abstract— Neck pain is a common musculoskeletal disorder. The diagnosis and the evaluation of treatment success in patients with neck pain often require a continuous physical assessment of the cervical range of motion (CROM) of the cervical spine. Several devices allowing the measurements of ROM have been reported in literature. In this study we measured the frontal, sagittal, transverse CROM using a novel Electronic Cervical Range of Motion (ECROM) System and compared the obtained results with those reported in literature using other devices and methods such as: Bubble Goniometry, Digital Inclinator, Radiograph, Digital Optometric Device, Spin T and Laser Headset. We found that the average values and standard deviations of Tilt Left were $43.2 \pm 8.1^\circ$, Tilt Right were $39.9 \pm 7.4^\circ$, Flexion were $54.4 \pm 8.1^\circ$, Extension were $58.3 \pm 7.2^\circ$, Rotation Left were $72.3 \pm 7.1^\circ$, Rotation Right were $59.1 \pm 8.1^\circ$ and Sagittal were $112.7 \pm 12.3^\circ$. Both average values and standard deviations were compatible with values reported in literature with one exception from the Spin T. The number of subjects participated apparently was not an influential factor to the results. In addition, our results suggested that the increase in *physical activity* increased the Lateral Motions and the Right Rotation; the *Body Mass Index* did not influence or weakly influenced the CROM, the increase in *sleep duration* decreased the Lateral motions and the *sleeping in prone position* seemed influenced the Rotation Left motion.

Keywords— Cervical spine; Neck motion; Measurements of Cervical Range of Motion; Neck pain.

I. INTRODUCTION

Many delicate and vital structures pass through the cervical spine which not only supports the entire head, but also allows enormous maneuverability and range of motion. Measuring the Cervical Range of Motion (CROM) is an important clinical issue and consisted of determining the maximum angles that a subject can perform using his/her head alone without pain in 3 plans: frontal (tilt left/right), sagittal (flexion/extension) and transverse (rotation left/right) (Fig. 1). Several devices have been described in literature that allow measuring part or all of these 3 head's movements.

In this paper we report the experimental results obtained on healthy subjects using the Electronic Cervical Range of Motion (ECROM) device which was described in detail

elsewhere. The ECROM consists of an electronic circuit board secure on a hat worn by a subject. The circuit board consists of a three-axis accelerometer, a resonator gyroscope and a single-chip 12-bit data acquisition system (Lian et al., 2010)[2]. When the subject moves his/her head, those motions will be recorded and displayed. The ECROM allowed measuring all 3 motions: Frontal, Sagittal and Transverse.

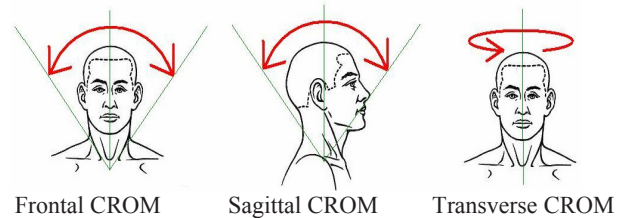


Fig. 1 Cervical Range of Motion consists of maximum angles that a subject can perform using his/her head alone without pain in 3 plans: frontal (tilt left/right), sagittal (sagittal flexion/extension) and transverse (rotation left/right)

The results obtained with the ECROM were compared to those obtained with other measurement methods and devices reported in literature such as:

Bubble Goniometry, which consists of measuring CROM using a protractor attached to a hinged ruler or a floater (Wolfenburger 2002).

Digital Inclinator, which consists of harnessing the subject's head to a helmet that is attached to a series of electric drives. As the subject's head moves, the movement in the electric drives is analyzed to obtain displacement reading for the angle (Wolfenburger 2002).

Radiograph, which consists of taking pictures of subject necks with an X-ray machine and measuring the angles between the vertebrae (Wolfenburger 2002, Bogduk 2000, Stitzel 2003).

Digital Optometric Device, which consists of a series of reflective sensors attached to the head of a subject. A receptive device can calculate the relative distance between each of the sensors (Burns 2006, Carpaneto 2004, Ferrario 2002, Koerhuis 2003 [9]).

Spin T (Haynes 2002)[10] which consists of harnessing the subject's head to a helmet and the evaluator uses a set of long rulers to draw a line when the subject is in resting

position and then again when the subject moves to the target position. Using both positions, an angle can be measured from the drawn lines.

Laser Headset (Lugo et al., 2010)[1] consists of a rotating Laser source (similar to that of a Laser pointer) secured on a headset worn by a subject. When the Laser rotates fast enough the lighted dot trail is perceived by the eyes as a line. The motion of the head changes the positions of the line which can be tracked and the angles can be calculated.

II. MATERIALS AND METHODS

Ten healthy subjects participated in this study. Their ages ranged from 25 to 50 years old (age average and standard deviation: 35.6 ± 4.5 years old). Two were females 8 were males, 7 were Asians and 3 were Caucasians. All of them were free of any medication and didn't complain of any kinds of muscle pains at the time of the experiments. The tenets of the Declaration of Helsinki were followed; the local Institutional Review Board approved the study protocols and experimental procedures. Also, informed consent was obtained for all subjects. Before the experiment each subject filled out a questionnaire, which was kept confidential and included patient's identification, age, ethnicity and gender.

During the experiments the subjects wore the ECROM and sat in an upright chair with adjustable armrests (Fig. 2).

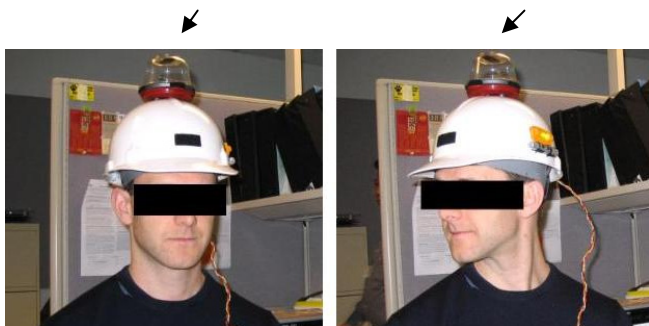


Fig. 2 A snapshot of the Transverse CROM Measurement: initial position is shown at the left figure, right rotation shown at the right figure. The ECROM device (arrow) was secured on top of a hard hat

They had their feet on the ground, with the knees and elbows fixed at 90° . They were asked to assume a natural head and neck position by looking in a mirror positioned 2m in front of them at the eye level. In the Frontal CROM measurements, the subject was asked to tilt as much as possible his/her head to the left then to the right using only his/her neck and without rotating the head. In the Sagittal CROM measurements the subject was asked to bend as much as possible his/her neck forward then backward without moving

the torso. In the Transverse CROM the subject was asked to rotate as much as possible his/her head to the right then to the left without moving the torso. The subject remained at the extent of his/her range of motion for 10 seconds before performing the next motion. The movements of other body parts were restricted. The subjects were allowed to familiarize with the experimental apparatus and procedures, and performed some test movements before the actual data collection. For each movement, three repetitions were performed at natural speed. The averages and standard deviations were computed. Statistical methods were performed.

III. RESULTS

Fig. 3 shows the Sagittal CROM obtained from 10 healthy subjects. The average and standard deviation were $112.7 \pm 12.3^\circ$. Although there is no target CROM measurement to be considered healthy (Bogduk 2000, Koerhuis 2003 [9]), it is unclear while there was a difference among the healthy subjects.

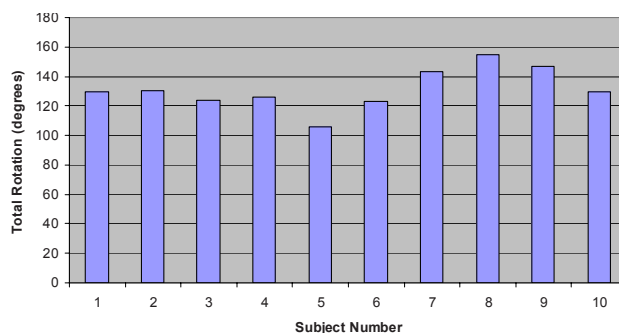


Fig. 3 Sagittal CROM obtained on 10 healthy subjects

Fig. 4 shows the Sagittal CROM obtained using the ECROM on those 10 healthy subjects in comparison with the results obtained from other methods and devices.

Table 1 below shows the values of left tilt and right tilt movements, flexion and extension movements, left and right rotation movements and Sagittal CROM obtained using the ECROM on those healthy subjects. For comparison, we also indicated the corresponding values reported in literature, obtained from other methods and devices such as: Bubble Goniometry, Digital Inclinator, Radiograph, Digital Optometry, Spin T and Laser Headset.

We found that beside the results obtained with the Spin T, the difference between our results and those of other studies was not statistically significant ($p > 0.05$). The standard deviations in our study were also at the same magnitude as those in other studies. Furthermore, based on the number of subjects participated in all studies we found that

this factor did not influence the results. In other words, the experiments can be carried with a small number of subjects.

correlation coefficient yielded positive correlation in the lateral motions and right rotation but not in the left rotation (Tilt Left $r = 0.3$; Tilt Right $r = 0.4$; Right Rotation $r = 0.3$, Rotation Left $r = 0.0$).

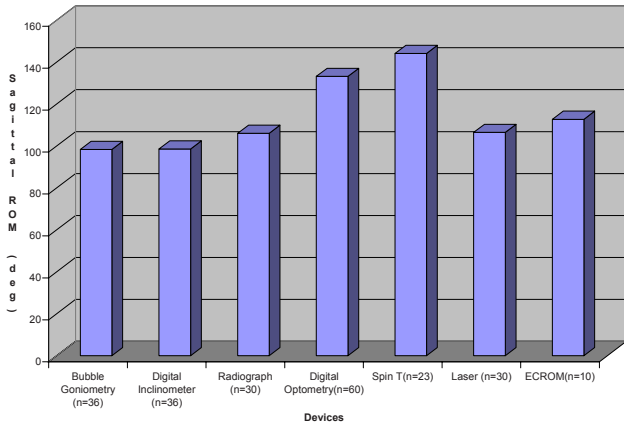


Fig. 4 The Sagittal ECROM obtained with ECROM (last bar) in comparison with results from other methods and devices

Body Mass Index

Since the neck is surrounded by muscle, it has been suggested that there may be a difference between the body frame characteristics of subjects (Bogduk 2000). To study this possible influence we determined the correlation between the CROM and the “body mass index” (BMI) of each subject. The BMI is defined as the individual's body weight divided by the square of his or her height. The BMI average of our subjects was $22.9 \pm 2.6 \text{ kg/m}^2$. Using the Pearson's correlation coefficient we found that there was a small correlation for lateral and rotation movements, and extension (Tilt Left, $r = -0.1$; Tilt Right, $r = -0.1$; Rotation Left $r = -0.2$; Rotation Right $r = -0.1$; Extension $r = 0.2$). There was however a stronger positive correlation on Flexion movement ($r = 0.3$); the reason for this correlation is unclear.

Table 1 Measurements using ECROM on 10 healthy subjects in comparison with other methods

Device/method	Tilt Left (degree)	Tilt Right (degree)	Flexion (degree)	Extension (degree)	Rotation Left (degree)	Rotation Right (degree)	Sagittal CROM (degree)
Bubble Goniometry (n= 36)							98.3 ± 12.9
Digital Inclinator (n=36)							98.5± 12.3
Radiograph (n=30)							106.0 ± 12.8
Digital Optometry (n=60)	40.9 ± 9.3	43.1 ± 8.9	59.5 ± 10.9	73.7 ± 13	77.7 ± 8.0	80.8 ± 7.4	133.2± 11.9
Spin T (n=23)	48.7 ± 9.3	49.4 ± 9.4	61.1 ± 7.1	83 ± 14.5	79.9 ± 13.0	90.9 ± 17.2	144.1± 10.8
Laser (n=30)	45.3 ± 8.3	45.0 ± 8	47.9 ± 8.3	58.5 ± 7.3	69.3 ± 8.4	65.1 ± 8.3	106.4± 7.8
ECROM (n=10)	43.2 ± 8.1	39.9 ± 7.4	54.4 ± 8.1	58.3 ± 7.2	72.3 ± 7.1	59.1 ± 8.1	112.7 ± 12.3

It has been reported in literature that factors such as physical activity, body mass index and sleep habits influenced the CROM values. In the following, using the ECROM we investigated the possible influences of these factors on our subjects.

Physical Activity

The effect of physical activity such as stretching on CROM is subjected to controversy (McCarthy 1997, Anderson 1991, Burns 2006). The average of stretching activity of our subjects was 3.7 ± 1.9 times per week. The Pearson's

BMI and Physical Activity

In order to determine whether the combination of BMI and Physical activity may yield better correlation we implemented the following relationship of adjusted BMI which took into account not only the height and weight but also the physical activity index which is the number of exercise per week. It basically attempts to define how much of a person's BMI is due to the amount of exercise.

$$\text{Adjusted BMI} = \text{BMI} / [\text{Activity Index}(0-7 \text{ times per week})]$$

We found that the CROM in the lateral plane was weakly positively related (Tilt Left $r = 0.3$; Tilt Right $r = 0.4$). In the sagittal and transverse planes, there was little or no relation (Flexion $r = 0.2$; Extension $r = 0.1$; Rotation Left movement $r = 0.0$; and Rotation Right $r = 0.3$).

Sleep Habits

Sleeping position and duration account for neck-muscle stretching that might affect CROM. Our subjects slept 7.2 ± 1.1 hours per night.

The correlation between sleeping time and the CROM indicated a negative value between increasing sleeping time and the Tilt Left ($r = -0.5$), as well as the Tilt Right movement ($r = -0.3$). No correlation was found between sleep time and other movements ($|r| < 0.3$).

Four subjects were side (lateral) sleepers, 3 were stomach (prone) sleepers and 3 were back (supine) sleepers.

Figure 5 shows the relationship between CROM and sleep habit. An ANOVA suggested that only rotation left seemed to be affected by sleep position ($p = 0.043$).

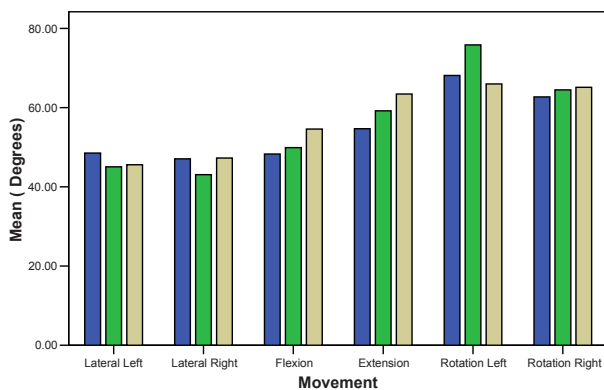


Fig. 5 CROM at different sleeping positions (1st bar: lateral, 2nd bar: prone, 3rd bar: supine). An ANOVA suggested that the selected sleeping positions and their data were not sufficient evidence to demonstrate that the selected sleeping positions affect five of the studied movements. Rotation Left was apparently affected by different sleeping positions ($p = 0.043$)

IV. CONCLUSIONS

We evaluated the functions of ECROM in measuring the Frontal, Sagittal and Transverse CROM of 10 healthy subjects. We found that the average values and standard deviations of Tilt Left were $43.2 \pm 8.1^\circ$, Tilt Right were $39.9 \pm 7.4^\circ$, Flexion were $54.4 \pm 8.1^\circ$, Extension were $58.3 \pm 7.2^\circ$, Rotation Left were $72.3 \pm 7.1^\circ$, Rotation Right were $59.1 \pm 8.1^\circ$ and Sagittal were $112.7 \pm 12.3^\circ$. Both average values and standard deviations were compatible with values reported in

literature with one exception from the Spin T. The number of subjects participated apparently was not an influential factor to the results. In addition our results suggested that the increase in *physical activity* increased the Lateral Motions and the Right Rotation; the *Body Mass Index* did not influence or weakly influenced the CROM, the increase in *sleep duration* decreased the Lateral motions and the *sleeping in prone position* seemed influenced the Rotation Left.

REFERENCES

1. A. Lugo, A. V. Tran, H. M. T Nguyen and Vo Van Toi. (2010) A Laser Headset for Measuring Cervical Range of Motion (In press in the Proceeding of the Third International Conference on the Development of Biomedical Engineering in Vietnam).
2. E. Lian, J. Hachadorian, T. H. Ngo and Vo Van Toi. (2010) A Novel Electronic cervical Range of Motion Measurement System, (In press in the Proceeding of the Third International Conference on the Development of Biomedical Engineering in Vietnam).
3. N. Strimpakos, V. Sakellari, G. Gioftos, M. Papathanasiou, E. Brontzos, D. Kelekis, E. Kapreli, J. Oldham. (2005) Cervical spine ROM measurements: optimizing the testing protocol by using a 3D ultrasound-based motion analysis system. *Cephalalgia*; 25(12):1133-45.
4. M. Tousignant, L. de Bellefeuille, S. O'Donoghue, S. Grahovac. (2000) Criterion validity of the cervical range of motion (CROM) goniometer for cervical flexion and extension. *Spine*;25(3):324-30.
5. A.L. Morphett, C.M. Crawford, D. Lee. (2003) The use of electromagnetic tracking technology for measurement of passive cervical range of motion: a pilot study; 26(3):152-9.
6. V. Feipel, B. Rondelet, J. Le Pallec, M. Rooze. (1999) Normal global motion of the cervical spine: an electrogoniometric study. *Clin Biomech (Bristol, Avon)*; 14(7):462-70.
7. S. Agarwal, G.T. Allison, K.P. Singer. (2005) Validation of the spin-T goniometer, a cervical range of motion device. *Journal of Manipulative Physiol Ther.*; 28(8):604-9.
8. N. Strimpakos, V. Sakellari, G. Gioftos, M. Papathanasiou, E. Brontzos, D. Kelekis, E. Kapreli, J. Oldham. (2005) Cervical spine ROM measurements: optimizing the testing protocol by using a 3D ultrasound-based motion analysis system. *Cephalalgia*; 25(12):1133-45.
9. C.L. Koerhuis, J.C. Winters, F.C. van der Helm, A.L. Hof. (2003) Neck mobility measurement by means of the 'Flock of Birds' electromagnetic tracking system. *Clin Biomech (Bristol, Avon)*; 18(1):14-8.
10. M.J Haynes, S. Edmondston. (2002) Accuracy and reliability of a new, protractor-based neck goniometer. *Journal of Manipulative Physiol Ther.*; 25(9):579-86.
11. M. Tousignant, N. Boucher, J. Bourbonnais, T. Gravelle, M. Quesnel, L. Brosseau. (2001) Intratester and intertester reliability of the Cybex electronic digital inclinometer (EDI-320) for measurement of active neck flexion and extension in healthy subjects. *Man Ther.*; 6(4):235-41.

Author: Vo Van Toi

Institute: Biomedical Engineering Department, International University of Vietnam National Universities, Ho Chi Minh City, Vietnam

Street: Linh Trung Ward, Thu Duc Dist.

City: Ho Chi Minh

Country: Vietnam

Email: vvtoi@hcmiu.edu.vn

Extract an Irregular Structure of an Echinocytes Using Morphological Operations

Hoang Manh Ha and Thai Thanh Nga

College of BioMedical Instrumentations/Department of Lab Equipments, Hanoi, Vietnam

Abstract— Most of disease information of the Echinocytes is often carried by irregular structure. The diseased characterization of an echinocytes with shape is explained. An abnormal shape cells separation are reviewed that recognise a irregular structures from images of an Echinocytes. In this paper, these irregular structures are mesured from the top hat transform. It has been shown numerically that a specific characteristic of an echinocytes can be reconstructed, with good approximation, from the procedures of dilation and erotion. As an application, an algorithm is developed that not only improve diseased informations of cells but also removes speckle noise from images. Finally, the results are compared and contrasted with a well-known methods namely, the extraction of a specific characteristic using wavelet transform. The results show improved accuracy of an extraction.

We use a binary image of an echinocyte for evaluating practical designs in improving accuracy.

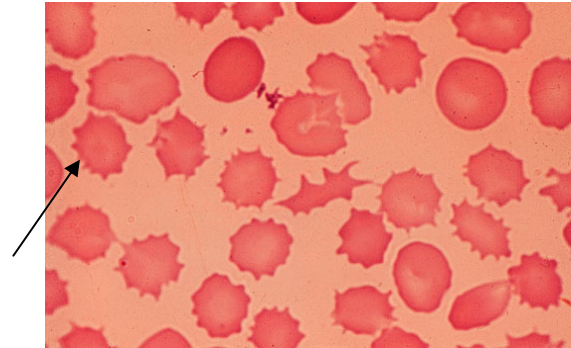


Fig. 1 Image of the echinocyte

I. INTRODUCTION

Echinocytosis is observed in uremia, liverisease, hypomagnesemia, hypophosphatemia, post-chemotherapy, and in athletes after heavy physical exercise [1]. So the recognition of an echinocytes from of the blood cells images has been an interest research topic for the last few years. The normal resting shape of the human red blood cell (RBC or erythrocyte) is a flattened biconcave disc (discoocyte) $8\mu\text{m}$ in diameter (see [1]). A spur cells, are red cells with multiple irregularly shaped and randomly distributed cytoplasmic projections (see Figure 1). As we know, the mathematical characterization of irregular with lipschitz exponent is explained. Theorems are reviewed that estimate local lipschitz exponent of function evolution across scales of their wavelet transorm ([6], [7]). Additional areas of mathematics recently have developed interactions with biology. Three-dimensional topology and low-dimensional differential geometry are two examples. Theorems about the global topological invariants of curves and ribbons in two-dimensions have been instrumental in studying the structural of closed circular. The biological problems to be solved become more accuracy ([3], [4], [5]).

Choosing a top hat transform minimize the error of irregular extraction and could avoid the undesired effect on images of normal blood cells.

II. EXTRACT AN IRREGULAR STRUCTURE OF AN ECHINOCYTE USING MORPHOLOGICAL OPERATONS

A. Morphological Operations

Morphological operations have to do with processing shape [2]. The two most common morphological operations are dialation and erosion. In dialation the rich get the richer and in dialation, the center or active pixel is set to the maximum of its neighbors, and in erosion it is set to the minimum of its neighbors. Since these operations aer often performed on binary images, dilation tend to expand border or region, while erosion tend to decrease or even eliminate small region. The size and the shape of the neighborhood used will have a very strong influence on the effect produced by eigther operation.

The two processes can be done in tandem, over the same area. Since both dilation and erosion are nonlinear operations, they are not invertible transformation; that is, one followed by the other will not generally result in the orginal image. If erosion is followed by dilation, the operation is termed opening. If the image is binary, this combined operation will tend to remove small objects without changing the shape and size of larger objects ([2], [3]). Basically, the initial erosion tends to reduce all objects, but some of the smaller objects will disappear altogether. The subsequent dilation will restore those objects that were not eliminated by erosion. If the order is reversed and dilation is performed

first followed by erosion, the combined process is called closing. Closing connects objects that are close to each other, tends to fill up small holes, and smooths an object's outline by filling small gaps. As with the more fundamental operations of dilation and erosion, the size of objects removed by opening or filled by closing depends on the size of the neighborhood that is selected.

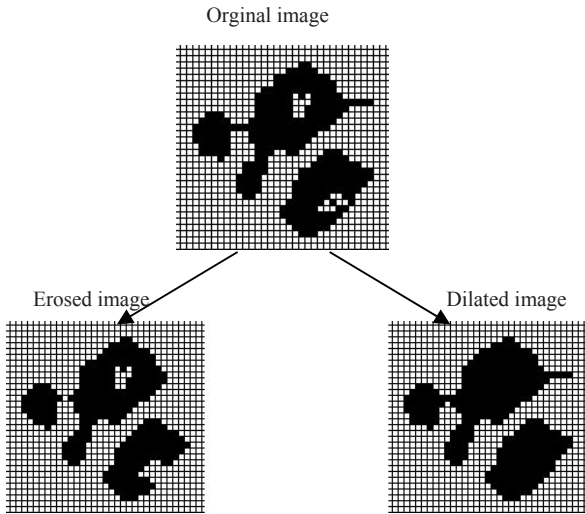


Fig. 2 Example of morphological operations

If an image is represented as a set I and a structuring element as a nother set B , the result of the dilation of image A by structuring element B can be thought of as showing those areas where the structuring element B hits the set I . Informal, set theoretic terms([2], [3], [4]). The basic mathematical morphological operators are dilation and erosion, derived from these, opening and closing operations are also defined. Dilation of a grey-scale image $I(x, y)$ by a grey-scale structuring element $B(s, t)$ is denoted by

$$(I \oplus B)(x, y) = \max \{ I(x-s, y-t) + b(s, t) \} \quad (1)$$

The domain of $I \oplus B$ is the dilation of the domain of I by the domain of B . Erosion of a grey-scale image $I(x, y)$ by a grey-scale structuring element $B(s, t)$ is denoted by

$$(I \ominus B)(x, y) = \min \{ I(x+s, y+t) - b(s, t) \} \quad (2)$$

The domain of $I \ominus B$ is the erosion of the domain of I by the domain of B . Opening of a grey-scale image $I(x, y)$ by a grey-scale structuring element $B(s, t)$ is denoted by

$$I \circ B = (I \ominus B) \oplus B \quad (3)$$

Closing of a grey-scale image $I(x, y)$ by a grey-scale structuring element $B(s, t)$ is denoted by

$$I \bullet B = (I \oplus B) \ominus B \quad (4)$$

Dilation is the maximum pixels set union when structuring element overrides image, while erosion is the minimum pixels set union when image is overlapped by structuring element. Dilation expands image set and erosion shrinks it. Opening is erosion followed by dilation and closing is dilation followed by erosion. Opening generally smooths the contour of an image, breaks narrow gaps. As opposed to opening, closing tends to fuse narrow breaks, eliminates small holes, and fills gaps in the contours. The small feature of image I , denoted by $F_d(I)$, is defined as the difference set of the opening of an image $I(x, y)$ and the domain of I . This is also known as dilation residue edge detector:

$$F_d(I) = (I \circ B) \oplus B - I \quad (5)$$

B. Echinocyte Feature Extraction Using Morphological Operations

Fig. 1 is an original blood cell image, there are some small features on all abnormal cells in this image, these are logical and morphological characters of blood cell image and these features make it possible to recognise a echinocyte. These features are extracted with the method suggested here. First, the cell image is filtered with laplacian filter and then changed into binary image with the mean of filtered image as its threshold. The original image is changed into binary image in the same way. Here the morphological operations erode of fig 3 in equation (2) then morphological operations dilate in equation (1).

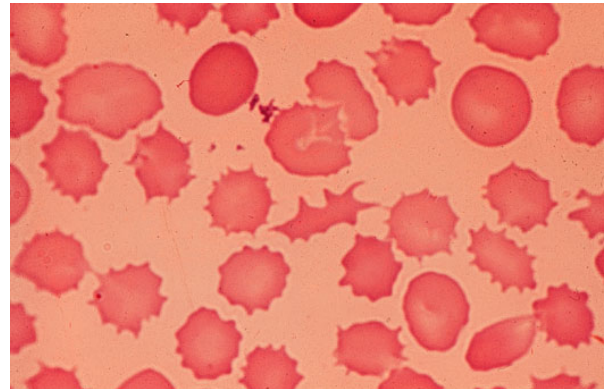


Fig. 3 Blood cells image

A different between a dilated image and orginal image makes it possible to extract the feature of echinocyte from the blood cells binary image, an irregular feature of the echinocyte is reflected in fig 4

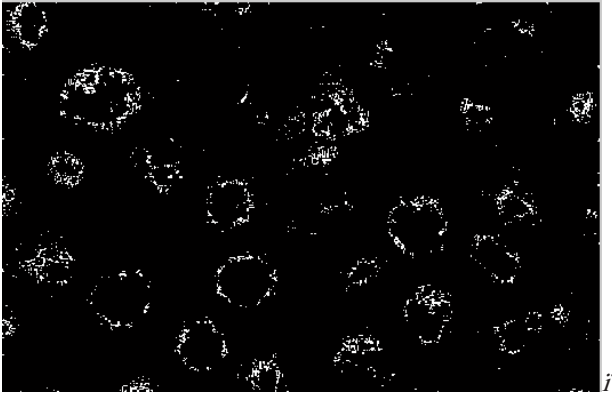


Fig. 4 A binarized feature extracting image of an echinocyte

All of normal blood cells are disappeared in fig 4. This result will help observer focus on echinocyte.

C. Comparison of a Feature Extraction Using Morphological Operations and Using Wavelet Transform

For the case an irregular feature extraction using wavelet transform, the normal blood cells are remained remarkably (see fig 5). Fig 4 and fig 5 are processed images from a same original image (fig 3). The remaining normal blood cells are undesired informations. They prevent the recognition of echinocyte.

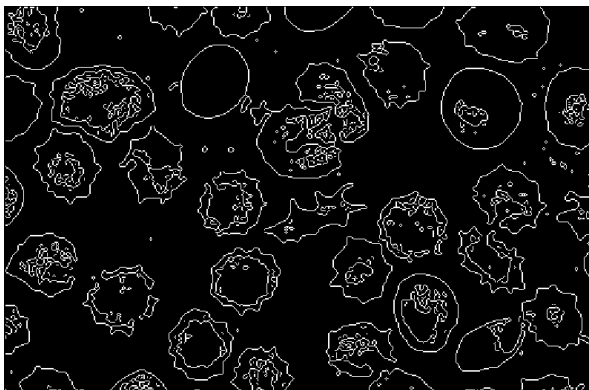


Fig. 5 A binarized feature extracting image of an echinocyte (using wavelet transform)

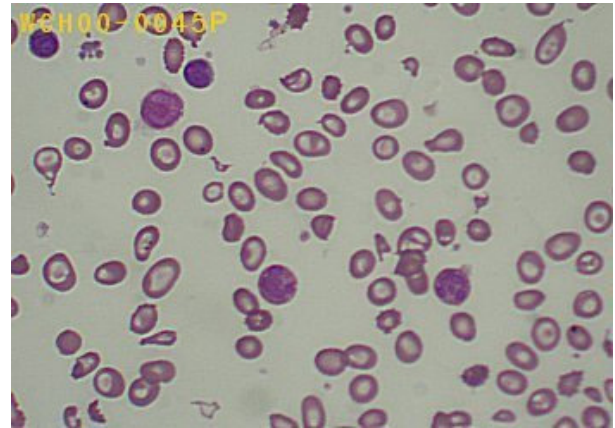


Fig. 6 Blood cells image



Fig. 7 A binarized feature extracting image of an echinocyte

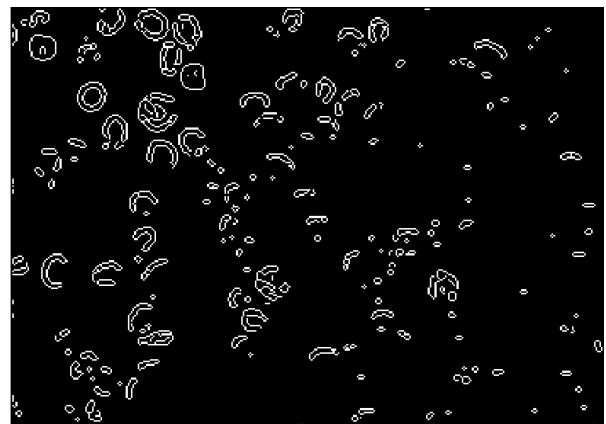


Fig. 8 A binarized feature extracting image of an echinocyte (using wavelet transform)

Fig 6 shows the original blood cells image. Fig 7 reflects result of the extraction, obtained with the morphological

operations. A feature extraction using wavelet transform reflected in fig 8. We can see in fig 8 that a lot of normal RBCs became abnormal RBCs after perform detect a irregular.

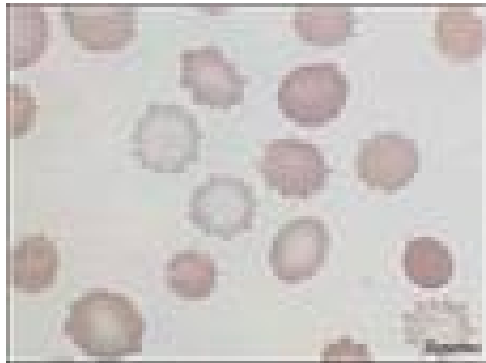


Fig. 9 Blood cells image

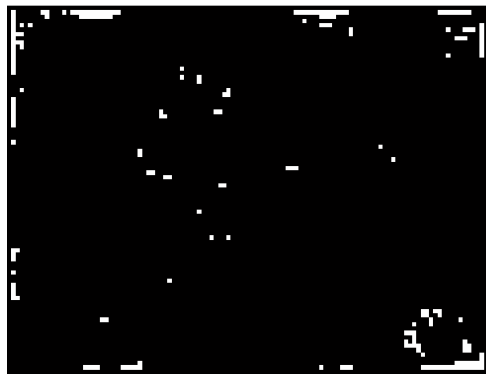


Fig. 10 A binarized feature extracting image of an echinocyte

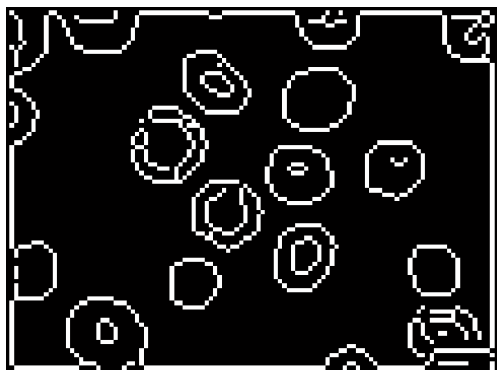


Fig. 11 A binarized feature extracting image of an echinocyte (using wavelet transform)

By comparing these figures, we can see that when the approach of the wavelet transform chosen, after processed

there is distortion on the fig 11. An echinocyte look like normal RBC.

To introduce more advantage of using morphological operations, let see and compare figures 9, 10 and 11. Fig 9 is microscopic image. There is only echinocyte in that. Fig 10 shows after processed image in case we use morphological operations. Fig 11 give us result of an implementation of the wavelet transform for the same aim. In case we use morphological operations, an irregular feature of echinocyte kept perfectly. An echinocyte can be recognised easily. It usefull with a location of the abnormal RBCs. for an observation on electronics microscopes.

III. CONCLUSIONS

A feature irregular extraction using morphological method of for the blood cell image is suggested in this paper, it uses the image processing toolbox of MATLAB 7.0 and gets the desirable results. The method is very simple and reliable for human cell image in this paper.

ACKNOWLEDGMENT

The authors are very grateful to Dr. Pham Canh Duong for his lectures of a pretopo and top-hat transform. Research described in this article was supported by Dr of Sci Pham Tran Nhu.

REFERENCES

1. Robert V. Pierre. (2002) Red cell morphology and the peripheral blood film. *Clinics in Laboratory Medicine*, Volume 22, Issue 1, Pages 25-61.
2. M. Ranzato et al. (2007) Automatic recognition of biological particles in microscopic images. *Elsevier, Pattern Recognition*.31-39
3. Milan sonca et al. (1993) *Image processing, analysis and machine vision*. Chapman & Hall Computing.
4. John L. Semmlow. (2004) *Biosignal and biomedical image processing Matlab-based applications*. Marcel Dekker Inc.
5. Ranjan Mukhopadhyay, Gerald Lim H. W., and Michael Wortis. (2002) Echinocyte Shapes: Bending, Stretching, and Shear Determine Spicule Shape and Spacing. *Biophysical Journal* Volume 82. 1756-1772
6. Stephane Mallat, Wen Liang Hwang. (1992) "Singularity detection and Processing with Wavelets", *IEEE Transactions on information Theory*, vol 38, No 2.
7. John J. Benedetto.(1994) *Wavelets: Mathematics and Applications*, CRC Press,

Author: Hoang Manh Ha
 College: College of BioMedical Instrumentations
 Street: 1/89 Luong Dinh Cua – Phuong Mai – Dong Da
 City: Hanoi
 Country: Vietnam
 Email: hidden_ha@yahoo.com

Study on Artificial Scaffold from Cancellous Bone

To Minh Quan, Thai Tu Thanh, Phan Kim Ngoc, and Tran Le Bao Ha

Laboratory of Stem Cell Research and Application, University of Science, Viet Nam National University, Ho Chi Minh, Vietnam

Abstract— This study aims to create bone graft from porcine's cancellous bone. Cancellous bone is one of the commonly used materials due to its natural porous structure. However, it can arise a serious of immune responses. So we decellularized it to take out all cells inside. Cancellous blocks ($3 \times 4 \times 4 \text{ mm}^3$) were first treated with Tris-HCl for 6 hours to remove all soft tissues. Then, they were partially demineralized in 0,6M HCl, and were further treated in a decellularizing solution (acetone or chloroform/methanol). The treated blocks were stained with hematoxylin and eosin to assess efficiency of decellularization. Umbilical cord blood-derived cells (UCBDCs) were seeded on the acellular cancellous bone and cultured for some of days to evaluate biocompatibility *in vitro*. The result shows that cancellous bone blocks treated by using two decellularizing solutions have none cell; the most efficiency of cell seeding into scaffold were carried out at 2000 rpm in 1 minute and repeat 4 times. After 7 days culturing *in vitro*, cells adherent, spread and are capable of migrating and proliferating. The adhesion and spread of UCBDCs into scaffold were imaged with SEM. In this way, we made successfully a porous scaffold from porcine's cancellous bone and this scaffold support the cell attachment.

Keywords— Artificial porous scaffold, demineralized cancellous bone, decellularization, biocompatibility, Umbilical cord blood-derived cells (UCBDCs).

I. INTRODUCTION

Bone graft is frequently transplanted, second only to blood, with about 500,000 bone grafts performed annually in the United States. With the critical bone defects, nonunion fractures, cancer, the patients have to suffer pain for a long time. It waste time and money of the patients and they will get a lot of problems in their life. Thus, bone grafts were used to speed up bone healing, for example HA, coral, cancellous, compact bone. Cancellous bone is one of the commonly used materials due to its natural porous structure.

Autologous cancellous grafts have been used in the treatment so for orthopedic problems. Such as: bone defects, nonunion fractures, and spinal fusion. Their limitations are significant, such as insufficient supply, an additional surgical procedure, and postsurgical pain associated with the donor site. In order to minimize these, allografts and xenografts have been developed. Allograft also carries several disadvantages, including low osteogenicity, risk infection, low quantity.

Xenografts have some advantages, including its structure is similar to human bone the quantity is high, and the price is cheap. Thus, xenologous cancellous grafts are interested in [3], [7]. However, xenografts evoke a serious of immune responses. To decrease immune responses, porcine cancellous bone blocks were decellularized to make some porous grafts. These grafts retain almost proteins of cancellous and have none of cell [1].

II. MATERIAL AND METHODS

A. Preparation of Cancellous Bone Graft by Decellularizing Method

Cancellous bone is derived from pocrine spine. Cancellous bone was divided into small pieces ($3 \times 4 \times 4 \text{ mm}^3$). These pieces were washed with Tris-NaCl solution for 6 hours to clean all blood cells. Tris-NaCl treated cancellous blocks were partially demineralized in 0,6M HCl for 15 minutes, and were further treated in a decellularizing solution (acetone or chloroform/methanol) for a few hours (2 or 18 hours) to take out all cells inside [1], [8]. The efficiency of decellularization was evaluated by HE (Hemotoxyline and Eosin) staining.

The pore size of specimens was estimated by SEM (scanning electron microscope). Some pictures of acellular specimens were imaged by SEM. Based on this pictures, the average size of the pores was calculated.

B. Culturing of UCBDCs

The UCBDCs were provided by Laboratory of Stem cell Research and Application. To isolate mononuclear cells (MNCs), UCB was loaded onto Ficoll-Hypaque solution. After density centrifugation at 3000 rpm for 10 minutes at room temperature, MNCs were removed from the interphase and washed by centrifugating two to three times in PBS. MNCs were set in culture into T25 Roux in DMEM/F12 medium containing 10% FBS in 37°C , 5% CO_2 . Medium was changed every three days. Cells harvested with 0.25% trypsin EDTA solution in phosphate-buffered saline (PBS, pH 7.4) from cell culture flasks were resuspended in culture medium and seeded onto others flasks. UCBDCs at passage 5 were cryopreserved in DMEM/F12 containing 10%FBS, 10% DMSO [5], [6], [2].

C. Seeding UCBDCs into Acellular Cancellous Blocks

Prior to cell seeding, the scaffolds were pre-wet in the spin tubes using 1.5ml of the appropriate DMEM/F12 medium and incubated overnight at 37°C. Tubes containing the pre-wet scaffolds received 1 ml of a suspension containing 2x10⁴ cells. The tubes were then loaded into the centrifugation machine and spun at the 2000 rpm for 1 minute. The process was repeated 10 times to move the cells into the scaffold interiors. The centrifugation time tested included 0, 2, 4, 6, 8, 10 minutes. At that time, 10 µl suspension was collected for evaluating the concentration of viable and dead cells [4], [9].

III. RESULT

A. Decellularized Cancellous Blocks

The result of HE staining shows that cancellous blocks don't have any cells. All blood and bone cells are removed. The control specimens are red because they contain some kinds of cells including blood cells such as erythrocytes, leukocytes and bone cells such as osteoblasts, osteocytes, osteoclasts. HE staining show clearly that cancellous bone contain bony trabeculae and cells including blood cells around bony trabeculae and bone cells on bony trabeculae.

After washing with Tris-NaCl solution for 6 hours, cancellous specimens are white. This proved that almost blood cells were cleaned. HE staining show that the decellularized specimens have no cells, they don't have blood and bone cells. They contain only bony trabeculae, so they are absolutely white.

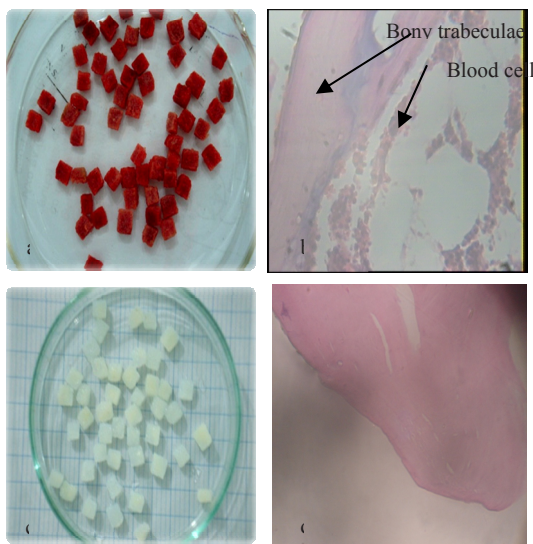


Fig. 1 Pocrine cancellous bone; (a) control group, (b) HE staining of control group (x100); (c) experiment group, (d) HE staining of experiment group (x100)

However two kinds of decellularizing solution acetone and chloroform/methanol are differently effective. Acetone solution is more effective in decellularization than chloroform/methanol solution. In a little cases, chloroform/methanol treated grafts have a few of cells while acetone treated grafts are not.

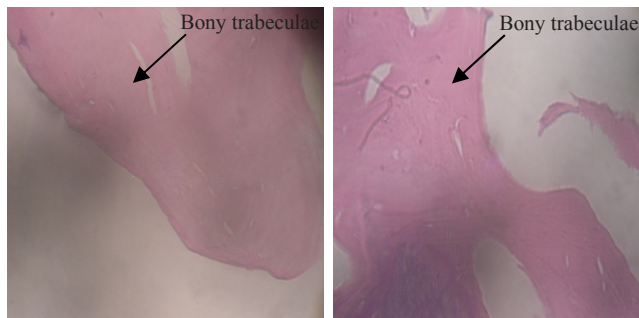


Fig. 2 Pocrine cancellous blocks were decellularized by chloroform/methanol (a) and by acetone (b) (x100)

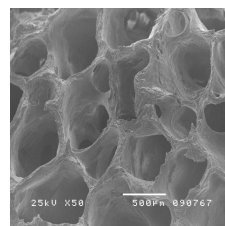


Fig. 3 Acellular blocks was imaged by SEM

The pictures were taken by SEM show that cancellous bone is a porous structure consisting of an interconnected network of the large pores. Pore size ranges from 250 µm to 1000 µm (1 mm) in diameter. It shows that cancellous blocks are high porosity. Pore with large size as partially demineralized cancellous support vascular in growth assisting a convenient condition for cell infiltration.

B. UCBDCs Culture

UCBDCs thawed in DMEM/F12 containing 20% FBS were cultured in DMEM/F12 containing 10% FBS. After 2 hours, UCBDCs attached to substrate, and 7 days later, UCBDCs reached 80% flask surface.

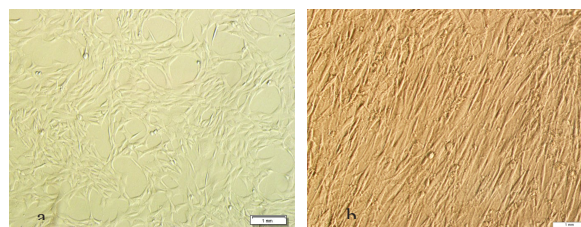


Fig. 4 UCBDCs after (a) 7 days culturing and (b) 10 days culturing

C. Optimization of Rotational Duration

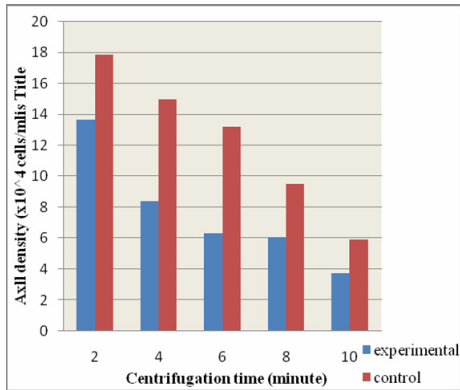


Fig. 5 The quality of alive cells after centrifugation

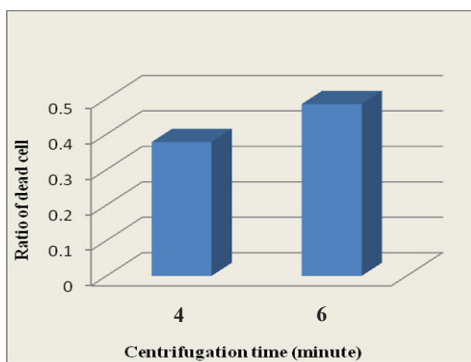


Fig. 6 The ratio of dead cell after four and six minutes centrifugation

The number of the cells moved into scaffold is the gap between a number of viable cells of control groups and experimental groups at one point time (0, 2, 4, 6, 8, 10 minutes). At the time of 4, 6 minutes, this gap is higher than other times. A number of cells seeded into scaffold at the times of 4, 6 minutes aren't statistical different. Thus, we compared the death rate of the cells between 4 and 6 minutes. It founds that, at 4 times, death rate is lower.

After seeding into scaffold 7 days, UCBDCs attached and spread on scaffold surface.

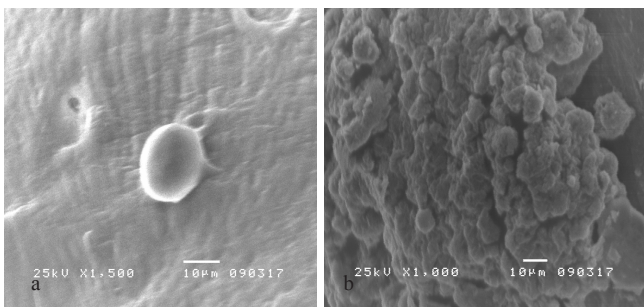


Fig. 7 UCBDCs attached to scaffold surface were imaged by SEM after 2 week culturing ((a): one cell, (b): cell cluster)

IV. CONCLUSION

We have succeeded in creating a scaffold from porcine's cancellous bone, and it was completely removed cell by the process of decellularizing solution. Moreover, we also have demonstrated that the centrifugation is a promising strategy for constructing tissue engineered bone by seeding UCBDCs cells into cancellous scaffold due to its simplicity and efficacy. In addition, the porous scaffold works *in vitro* as biomaterial scaffold, allowing the UCBDCs cell attachment, and it is harmless to this cell. For that reasons, artificial scaffold from porcine's cancellous bone can be applied in the creation of artificial bone in near future.

REFERENCES

- Guangpeng Liu, Jian Sun, Yulin Li, Heng Zhou, Lei Cui, Wei Liu and Yilin Cao (2008) Evaluation of Partially Demineralized Osteoporotic Cancellous Bone Matrix Combined with Human Bone Marrow Stromal Cells for Tissue Engineering: An In Vitro and In Vivo Study. *Calcif Tissue Int* 83:176–185.
- Inga Drossea, Elias Volkmera, Rodolfo Capanna, Pietro De Biase, Wolf Mutschlera, Matthias Schiekera (2008) Tissue engineering for bone defect healing: An update on a multi-component approach. *Injury, Int. J. Care Injured* 39S2:S9–S20
- PeibiaoZhang, Zhongkui Hong, TingYu , XuesiChen , XiabinJing (2009) Chemical, Structural Properties, and Osteoconductive Effectiveness of Bone Block Derived from Porcine Cancellous Bone. *Biomaterials* 30:58–70.
- Marcio Mateus Beloti, Paulo Tambasco de Oliveira and Adalberto Luiz Rosa (2008) Seeding Osteoblastic Cells into a Macroporous Biodegradable CaP/PLGA Scaffold by a Centrifugal Force. *Jouranal of Biomaterials Applications* 1.00.
- N.M.Ocarino, J.N.Boeloni, A.M.Goes, J.F.Silva, U.Marubayashi, R.Serakides (2008) Osteogenic differentiation of mesenchymal stem cells from osteopenic rats subjected to physical activity with and without nitric oxide synthase inhibition. *Nitric Oxide* 19:320–325.
- Sandra Hofmann, Henri Hagenmuller, Annette M. Koch, Ralph Müller, Gordana Vunjak-Novakovic, David L. Kaplan, Hans P. Merkle and Lorenz Meinel (2007) Control of in vitro tissue-engineered bone-like structures using human mesenchymal stem cells and porous silk scaffolds. *Biomaterials* 28:1152–1162.
- Seth Greenwald, Scott D. Boden, Victor M. Goldberg, Yusuf Khan, Cato T. Laurencin and Randy N. Rosier (2001) Bone-graft substitutes: Facts, Fictions and Applications. *The Journal of Bone and Joint Surgery* 83:98-103.
- Ulrich Kalus, Helga Muller, Hans Baudisch, Hans-Jürgen Birkhahn, Rüdiger von Versen, Arne Hansen and Axel Pruss (2005) A method for the determination of the residual chloroform in defatted cancellous bone transplants. *Cell and Tissue Banking* 6:71–75.
- W.T. Godbey, B.S. Stacey Hindy, Matthew E. Sherman and Anthony Atala (2004) A novel use of centrifugal force for cell seeding into porous scaffolds. *Biomaterials* 25:2799–2805.

Report Case: Cultured Keratinocyte Autograft on Collagen from Amniotic Membrane for Treatment the Injured Human Skin

Tran Le Bao Ha¹, Huynh Minh Tuan², Tran Thi Thanh Thuy², Tran Cong Toai², and Hoang Nghia Son³

¹ University of Natural Sciences, Vietnam National University, HoChiMinh City, Vietnam

² Pham Ngoc Thach University of Medicine, Vietnam

³ Institute of Tropical Biology, Vietnam

Abstract— Cell therapy is an emerging therapeutic strategy aimed at replacing or repairing severely damaged tissues with cultured cells. The epidermis is a major site of self-renewal in which there is constant replacement of cells lost by desquamation in the superficial layers by cell division in the basal layers – epidermal stem cells and transit amplifying cells. These cells are amenable to *in vitro* expansion and constitute a major area of research in regenerative medicine, tissue engineering, and skin grafting. In this research, cells from patient skin were collected, cultured, amplified in serum free medium. The multilayered structure was made by using insert dishes lined collagen membrane derived from human amniotic membrane and air-lifting. Then, the cells were evaluated by karyotyping and immunohistochemistry. The result shows that the keratinocyte sheet is composed of 4 to 5 layers which the proliferating cells are closely lying on the basal layer. The cells have a normal karyotype. Keratinocyte sheet is easy to strip off from the flask surface by using collagen as a scaffold. After graft, the result indicates that the diminution of scar in the region which skin is taken off, the relief of pain, the low infection risk, the same effect for split-thickness autograft case.

Keywords— Epidermis, epidermal stem cell, transit amplifying cell, serum free medium, amniotic membrane, basal layer.

I. INTRODUCTION

The demand in burn wound treatment, skin and muscle loss in traffic and work accidents, diabetic ulcers, cardiovascular diseases, radiation induced ulcers... is currently popular. The most difficult problem for the treatment of massive full-thickness wounds is the lack of skin for autograft. Thus, a large number of various methods have been developed such as CEA (Cultured Epidermal Autograft) (Ariane et al., 2006). Its advantages have been determined by the use of a small intact skin area (2-3 cm²), we could initiate the culture in order to obtain a big number of keratinocytes which were ready to use for autograft (James et al., 2009).

The first CEA case for adult autograft so as to treat major burn wound was reported by O' Connor and his colleagues in Boston in 1981. Then, in 1986, Cuono et al. reported a CEA case to save an adult who presented 55% TBSA burn wound, 80% burn wounds were degree III (Cuono et al., 1986). Similarly, in 1988, Bettex-Galland et al. studied

CEA on a child's burn wound degree III in thigh. The result showed that CEA method was naturally more esthetical than the others which used the meshed skin (Bettex-Galland, 1988). In 2000, Loss et al. have used an alternative method that they treated a 26-year old male who sustained a 93% TBSA burn injury (60% full-thickness burn, 33% partial-thickness burn) with artificial skin, split – thickness autograft and CEA in combination (Loss, 2000).

Afterwards, the benefit of the use of CEA has been changed, from “a useful factor” to “an inexplicable effect acting to the large burn wound patient” (Wood, 2006).

Consequently, we studied and experienced the cultured keratinocyte sheet autograft for the purpose of application in cell engineering in order to contribute on improving the quality of treatment for the patient.

II. MATERIALS AND METHODS

A. Research Object: intact skin from patient having skin autograft indication, 1,5 – 2 cm² area.

B. Isolation, Culture and Amplification of Keratinocytes (Susan, 2003)

In sterile condition, the skin pieces was washed three times in PBS and the fatty tissue was removed. After that, skin was cut into small pieces and incubated in Trypsin-EDTA (GIBCO) in 18h, at 4° C. The detachment of epidermis and dermis was produced by mechanically dissociation, the keratinocytes were obtained from the epidermis by using a pipette to suspend. The cell density, the percentage of viable cells was determined after using blue trypan dye (Sigma).

The keratinocytes were cultured in primitive medium: DMEM supplemented FBS (Fetal Bovine Serum), EGF (Epidermal Growth Factor), hydrocortisone, cholera toxin (Sigma) with the density 3 x 10⁵ cells/cm², 37° C, 5% CO₂.

After 2 days, the primitive medium culture was replaced by Serum Free Medium (SFM – GIBCO) specially reserved for keratinocytes.

When the cells approximately reached 70% - 80% confluence of the flask culture, we initiated the subculture.

C. Elaboration of Keratinocyte Multilayers on Collagen Membrane

Collagen membrane obtained from epithelial removed amniotic membrane by using Trypsin-EDTA in combination with the mechanically dissociation. Amniotic membranes from pregnancy were negatively tested with HIV, HBV, HCV, syphilis.

Collagen membrane spread onto the bottom of the insert dishes.

Keratinocytes subculture on collagen membrane with the cell density 3×10^4 cells/cm², incubated 37° C, 5% CO₂.

SFM medium inside and outside of the insert dish was changed once/ every 2 day.

Once the keratinocytes proliferated all over the collagen surface, we aspirated all medium inside of the insert dish and we continued to change the medium outside of the insert dish every day, in 7 days.

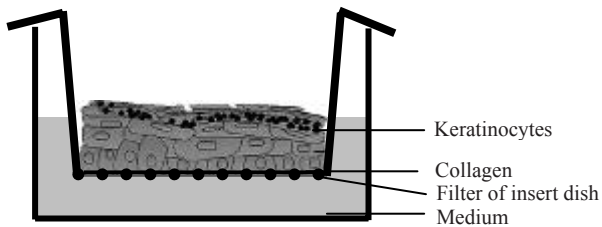


Fig. 1 The picture illustrates the keratinocyte culture method into the insert dish. The keratinocytes were exposed to the air-liquid surface, the nutrition was supplied from the inside medium throughout the filtrating spores of the insert dish

D. Cell Culture Evaluation

Karyotype: Cells were treated with 0,1 µg Colcemid in 20 minutes and incubated in KCl 0,075M. Following this, cells were fixed in fixative's solution (methanol : acetic acid). **G banding technique:** Slides were treated in 0,5% Trypsin and then in 5% staining Giemsa's solution in 5 minutes. The results were analyzed by Cytovision, Nikon 600 karyotyping analysis system.

Immunohistochemistry staining: the potentially proliferating keratinocytes in cell sheet were used for immunohistochemistry staining with p63 marker. After the cells were layered, the cell sheet was cut into small slices and stained with p63 antibodies clone 4A4. Finally, the results were observed under Olympus optic microscopy.

E. Cultured Keratinocyte Sheet Autograft on Patient

Patient is male, 15 years old, hospitalized due to traffic accident with skin defect wound degree IIb, wound care whilst waiting for cultured keratinocyte sheet autograft.

Skin biopsy is taken off and the keratinocyte culture was established.

Clinical follow-up in 7 days, 2 weeks, 6 weeks and 8 weeks.



Fig. 2 Skin is taken off for cell culture

III. RESULTS – DISCUSSION

A. Result of Keratinocyte Culture and Proliferation

Cells were isolated and cultured in serum – free medium, the keratinocytes commenced to form cell clusters in the third or the fourth day. Then, these clusters became more and more big and associated to form a single cell layer onto culture dish surface (the seventh day). The population double time is 36h.



Fig. 3 Keratinocytes formed colonies (a) and monolayer onto culture dish (b) (200X)

B. Multilayered Keratinocytes on Collagen Membrane

Following the second subculture, the keratinocytes were placed onto collagen membrane in the insert dish.

The cells were exposed to the air – liquid interface in seven days, then the tissue sample was stained HE in order to determine the potentially layering capacity of the cells.

The result showed that the cells formed 4 – 5 layers onto collagen membrane.

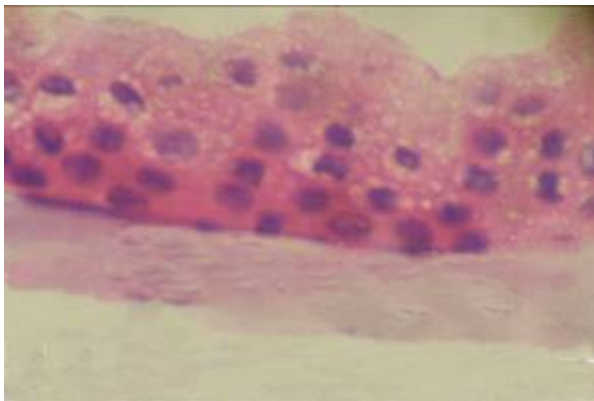


Fig. 4 Result of HE staining of the cell sheet, the cells were exposed to the air in seven days (400X)

C. Cell Culture Evaluation

Keratinocyte Karyotype

Human cultured keratinocyte karyotype in our conditions possessed a normal karyotype: 46, XX: Each cell contained a lot of diploid 46 chromosomes, 44 autosomes and two gonosomes XX.

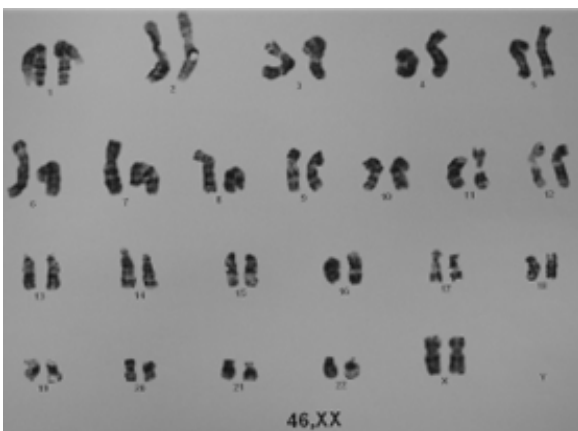


Fig. 5 Karyotype of cultured keratinocytes

Immunohistochemistry Staining

Cultured keratinocyte sheet was used for immunohistochemistry staining. Control case was intact skin.

Both samples were positive to p63 undifferentiated marker. Cell samples *in vitro* consisted of 4 – 5 keratinocyte layers, the positive cells to p63 undifferentiated marker were closely stratifying on the collagen membrane, the upper cells were differentiated.

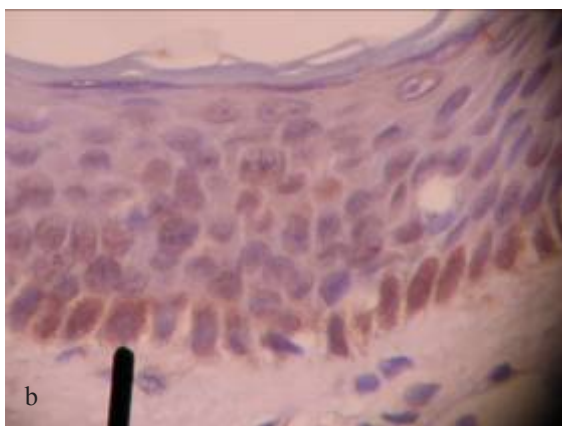
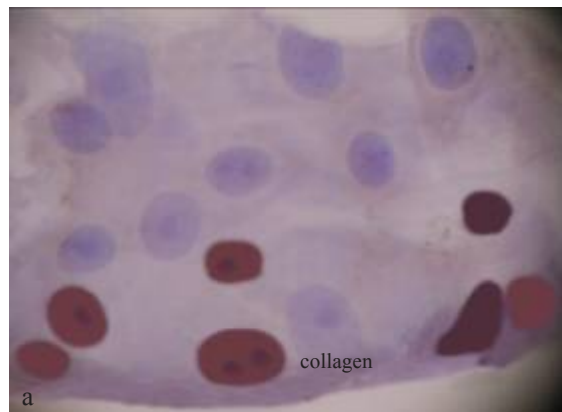


Fig. 6 Immunohistochemistry result with p63 antibody: keratinocytes on collagen membrane (a) and control skin (b). The brown cells were positive to p63

The cells formed multilayer on the collagen membrane were easily split from the culture dish surface by separating the collagen membrane from the dish surface.

D. Cultured Keratinocyte Sheet Autograft on Patient

Three weeks after the skin was taken off, the patient was grafted with cultured keratinocyte sheet which had a 45 cm² area in combination with the split-thickness autograft.

Eight weeks later, the result of cultured keratinocyte sheet autograft was similar to the case of split thickness autograft.

As a matter of fact, the advantages of cultured keratinocyte sheet autograft: the possibility of the grafting area multiplication (50 times after 3 weeks), the diminution of scarring, the relief of pain, the low infection risk, the same effect in compare to the split - thinness autograft.

However, the cultured keratinocyte sheet is absent from melanocytes (the melanocytes were hard to live and proliferate in the keratinocyte culture medium). Moreover, it is difficult to rapidly evaluate after graft, one example, the cultured keratinocyte sheet autograft couldn't give us an esthetical sense because of the lack of melanin two months after graft.



Fig. 7 Cultured epidermal autograft on patient: a – 3 days before graft, b – 5 days after graft, c – 7 days after graft, d – 9 days after graft, e – 45 days after graft, f – 60 days after graft

IV. CONCLUSIONS

Cultured keratinocyte sheet are composed of 4 – 5 layers, the proliferating cells are lying on the collagen membrane. They present a normal karyotype under our strictly standard culture conditions. The keratinocyte sheet is easy to split from the culture dish surface owing to the use of amniotic membrane as carrier.

The application in graft treatment on the patient, the result shows: the reduction of scarring, the relief of pain, the low infection risk and the same treatment result in comparison to the split-thickness autograft.

REFERENCES

1. Ariane R., Yann B. (2006) Essentials of stem cell biology. Elsevier, 440 – 444
2. Loss M., Wedler V., Kunzi W., Meuli-Simmen C., Meyer V.E. (2000) Artificial skin, split-thickness autograft and cultured autologous keratinocytes combined to treat a severe burn injury of 93% of TBSA. *Burns* 26: 644 – 652
3. Bettex-Galland M., Slongo T., Hunziker T., Wiesmann U., Bettex M. (1988) Use of cultured keratinocytes in the treatment of burn wounds and burn scars. *Z Kinderchir* 43: 224–228
4. Cuono C., Langdon R., McGuire J. (1986) Use of cultured epidermal autografts and dermal allografts as skin replacement after burns injury. *Lancet* i8490: 1123–1124
5. Wood FM., Kolybaba ML., Allen P. (2006) The use of cultured epithelial autograft in the treatment of major burn wounds: Eleven years of clinical experience. *Burns* 32: 538 – 544
6. Susan SY. (2003) Current Protocols in Cell Biology. John Wiley & Sons, Inc., 155 – 160
7. James SE., Booth S., Dheansa B., Mann DJ., Reid MJ., Shevchenko RV., Gilbert PM. (2009) Sprayed cultured autologous keratinocytes used alone or in combination with meshed autografts to accelerate wound closure in difficult-to-heal burns patients. *Burns* 35: 215-220

Corresponding author:

Tran Le Bao Ha
University of Natural Sciences
Vietnam National University
HoChiMinh City
Vietnam
Email: tlbha@hcmuns.edu.vn

Doxorubicin Delivery by Copolymeric Nanoparticle for Treatment of Breast Cancer

N.V. Cuong^{1,2}, J.L. Jiang¹, and M.F. Hsieh¹

¹ Department of Biomedical Engineering and R&D Center for Biomedical Microdevice Technology, Chung Yuan Christian University, 200, Chung Pei Rd., Chung Li, Taiwan 32023

² Department of Chemical Engineering, Ho Chi Minh City University of Industry, 12 Nguyen Van Bao Rd, Ho Chi Minh City, Vietnam

Abstract— Amphiphilic polymeric nanoparticles have been attracted much attention in various pharmaceutical, biological and medical fields because they can use as carriers for anticancer drugs with sustained release, prolong the circulation time, prevent multidrug resistance and uptake by reticuloendothelial system. Here, we report a triblock copolymer as Doxorubicin (DOX) delivery system for treatment of breast cancer cells. Triblock copolymers of monomethoxy poly(ethylene glycol) (mPEG) and ϵ -caprolactone were prepared with varying lengths of poly(ϵ -caprolactone) (PCL) compositions and a fixed length of mPEG segment. These amphiphilic linear copolymers based on PCL hydrophobic core and hydrophilic mPEG ending, which can self-assemble into nanoscopic micelles with their hydrophobic cores, encapsulated doxorubicin in an aqueous solution. The particle sizes of prepared micelles were around 73.5-123.2 nm. The DOX loading content and DOX loading efficiency were from 3.7-7.4% and 26.4-49.2%, respectively. DOX-released profile was pH-dependent and faster at pH 5.4 than pH 7.4. The safety evaluations showed that nanoparticle did not induce hemolysis and NO production. Additionally, the cytotoxicity of DOX-loaded micelles was found to be similar with free DOX in drug-resistant cells (MCF-7/adr). The greater amounts of DOX and faster uptake accumulated into the drug-resistant cells from DOX-loaded micelles suggest a potential application in cancer chemotherapy.

Keywords— Nanoparticles, micelles, drug delivery systems, multidrug resistance, doxorubicin.

I. INTRODUCTION

Doxorubicin (DOX), an anthracycline drug, has been found very effective for the treatment of breast cancers as well as tumors of ovarian, prostate, brain, cervix and lung. Nevertheless, drawbacks such as cardiac toxicity, short half-life, and low solubility in aqueous solution have hindered its applications. Also, multidrug resistance (MDR) has been found in some tumor cells and has been attributed to the P-glycoprotein (P-gp) efflux pump on the plasma membrane. To overcome these obstacles, there is a need for the development of alternate formulation of DOX having good aqueous solubility, free of side-effects and overcoming MDR in tumor cells. Several strategies have been employed to

deliver DOX by new formulations including, liposomes, nanoparticles, mixed micelles, microspheres, water-soluble prodrugs, and conjugates, and polymeric micelles, etc [1-3].

Amphiphilic copolymers are self-assembled into spherical nano-sized micelles. There are two regions of a copolymeric micelle. The hydrophobic micelle core acts as a drug reservoir. The hydrophilic corona provides a protective interface between the core and the aqueous environment. The use of block copolymer micelles for the targeted delivery of DOX has proven to be a promising approach for improving the therapeutic efficacy of DOX, prolonging the circulation time and reducing the side-effect. The DOX is encapsulated into the core of a polymeric micelle by chemical conjugation or physical entrapment.

Herein, we report an ABA-type triblock copolymer aiming for its application as a carrier for the delivery of DOX. The triblock copolymer is composed of two identical hydrophilic segments (A: mPEG) and one hydrophobic segment (B: PCL). The self-assembly, morphology of the polymeric micelles were also studied in an aqueous solution. To demonstrate the pharmacological application of the triblock copolymers as drug carriers, DOX-loaded nanoparticles composed of triblock copolymers were prepared. Additionally, the release profile of DOX, the safety evaluations including cytotoxicity, NO production and hemolytic test were demonstrated.

II. MATERIAL AND METHOD

A. Material

Monomethoxy poly(ethylene glycol) (mPEG, $M_n=5000$), ϵ -caprolactone, doxorubicin hydrochloride (DOX·HCl), dicyclohexylcarbodiimide (DCC), 4-dimethylamino pyridine (DMAP), succinic anhydride, 2-diphenyl-1,3,5-hexatriene (DPH) and dimethylsulfoxide (DMSO) were purchased from Sigma-Aldrich (St.Louis, MO, USA). Stannous 2-ethyl hexanoate (stannous octoate, SnOct) was obtained from MP Bio-medicals, Inc. The mPEG was purified by re-crystallization on the dichloromethane/diethyl ether system, and ϵ -caprolactone was dried using CaH_2 and distilled under a reduced pressure.

Triethylamine (TEA), 1,4-dioxane, dichloromethane (DCM), diethyl ether, tetrahydrofuran (THF) and other chemicals were all reagent-grade and were used without further purification.

Human breast cancer cell lines (MCF-7) were kindly provided by Dr. Y. H. Chen of the School of Pharmacy, College of Medicine, National Taiwan University. 3-(4,5-dimethylthiazol-2-yl)-2,5-diphenyl tetrazolium bromide (MTT) was purchased from Sigma-Aldrich (St. Louis, MO, USA). Dulbecco's modified eagle's medium (DMEM) and antibiotic antimycotic were purchased from GIBCO. The fetal bovine serum (FBS) was obtained from HyClone.

B. Preparation of Copolymeric Nanoparticles

For the DOX-unloaded micelles, the micelle solution was prepared by dissolving 20 mg of ABA block copolymer in 2.0 mL of THF, and then 1.0 mL of double distilled water was added under stirring. The resulting solution was placed at room temperature for 12 h, then was transferred to a dialysis bag and dialyzed against double distilled water for 24 h (MWCO: 50,000 Da, Spectrum Laboratories, USA).

For the DOX-loaded micelles, DOX was first neutralized before micelle preparation. 3.0 mg of DOX was neutralized with an excess amount of TEA in 1.0 mL of THF. The DOX solution was then added into the 2.0-mL THF solution of ABA copolymer (20 mg). This solution was added 1.5 mL of double distilled water under stirring for 6 h. To remove untrapped DOX and TEA, the mixture was next transferred for dialysis against double distilled water for 24 h to produce micelles. The water was replaced hourly for the first 3 h.

The drug loading efficiency (DLE) was defined as the weight percentage of DOX in micelles relative to the initial feeding amount of DOX. The drug loading content (DLC) was calculated from the mass of incorporated DOX divided by the weight of polymer. The amount of DOX loaded in micelles was determined by the absorption at 485 nm using UV/Vis spectrometry (UV-530, Jasco, Tokyo, Japan). The DOX solutions of various concentrations were prepared, and the absorptions of the solutions were measured to obtain a calibration curve [3].

The particle size and its polydispersity were determined by dynamic light scattering (DLS) at 25 °C using a Zetasizer 3000HSA (Malvern Instruments Ltd, UK) with an excitation of 633 nm illuminated at a fixed angle of 90°. The micellar solutions, prepared as described earlier, were diluted into a final concentration of 0.2 mg/mL and then filtered through a Millipore 0.2 µm filter prior to measurements. The average diameter was calculated by a CONTIN analytical method.

C. Measurement of Nitric Oxide (NO)

RAW 264.7 macrophage cells were seeded in a 24-well plate (1×10^5 cells/well) and incubated in 37°C, 5% CO₂ for 1 day. Micellar solution at various concentrations was added to the cells in a final volume of 0.8 mL. The supernatants were collected after 24 h and NO production was determined by Greiss reagent. Moreover, total protein extract was determined by Micro BCA Protein Assay.

D. Hemolytic Test *in vitro*

The experimental procedure described here is an adjustment of standard F-756-00 [4], which is based on colorimetric detection of Drabkin's solution. To a 0.7 mL of micellar solution at various concentrations was incubated in 0.1 mL of rabbit blood (plasma free hemoglobin of blood was lower than 2 mg/mL) at 37 °C and for 3 h. Following incubation, the solution was centrifuged at 3800 rpm for 15 min. To determine the supernatant hemoglobin, 0.5 mL of Drabkin's solution was added to 0.5 mL of supernatant and the sample was allowed to stand for 15 min. The amount of cyanmethemoglobin in the supernatant was measured by spectrophotometry at a wavelength 540 nm and, then, compared to a standard curve (hemoglobin concentrations ranging from 0.003 to 1.2 mg/mL). The percent hemolysis refers to the hemoglobin concentration in the supernatant of a blood sample not treated with micelles to the obtained percentage of particle-induced hemolysis. Finally, saline solution and double distilled water were used as negative and positive control, respectively.

E. *In vitro* DOX Release Profile

The experimental procedures were adapted from an earlier study [3]. In brief, 1.5 mL of DOX-loaded micellar solution was dissolved in 0.5 mL PBS (0.1 M, pH 7.4) and acetate buffer solution (0.1 M, pH 5.4), and was transferred into a dialysis tube (MWCO: 50,000 Da). The tube was immersed into a buffer solution of 15 mL and was kept at 37 °C. At several time intervals, 1.0 mL of the buffer solution outside the dialysis bag was withdrawn for UV-Vis analysis and replaced with fresh buffer solution. DOX concentration was calculated based on the absorbance at 485 nm as described before.

F. Cytotoxicity: MTT Assay

The *in vitro* cytotoxicity of polymeric micelles was tested against human breast cancer cell lines: MCF-7. The cell culture medium was composed of DMEM with 10% fetal

bovine serum and antibiotic antimycotic. The cell viability was determined by tetrazolium dye (MTT) assay. MCF-7 cells were seeded in 96-well plates at a density of 1000 cells/well and were incubated at 37 °C under a humidified atmosphere containing 5% CO₂ for 24 h before assay. After that, the cells were further incubated in media containing polymeric micelles of various concentrations. DMEM medium was used as a control to be compared with results obtained from micelles. After 24 hours, the medium was removed and washed twice with PBS, and then MTT solution and medium were added to each well followed by 4 hours of incubation at 37 °C. Subsequently, the medium was removed and violet crystals were solubilized with DMSO. After shaking slowly twice for 5 s, the absorbance of each well was determined using a Multiskan Spectrum spectrophotometer (Thermo Electron Corporation, Waltham, MA) at 570 nm and 630 nm. The cell viability (%) was calculated as the ratio of the number of surviving cells in drug-treated samples to that of control.

III. RESULT AND DISCUSSIONS

A. Preparation of Copolymeric Nanoparticles

The size and the size distribution of copolymeric micelles were measured with dynamic light scattering, and the results are demonstrated in Fig. 1. The effective diameter of the unloaded-micelles was 73.5 nm with narrow size distribution (polydispersity = 0.053). The size of the DOX-loaded micelles increased to 123.2 nm compared with 73.5 nm of unloaded-micelles. It was recognized that the particle size of DOX-loaded micelles increased slightly comparing to that of the DOX-free micelles. Similar results were also obtained in other report [5].

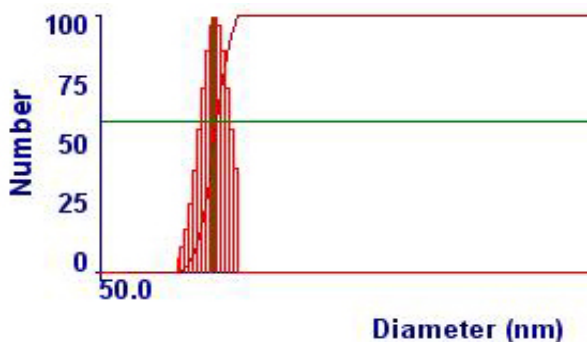


Fig. 1 Size and size distribution of prepared micelles

B. Safety Measurements

The toxicity of micelles on macrophage cells was evaluated by performing NO assay. Experimental results indicated

that micelles did not affect NO production up to 0.5 mg/mL (Fig. 2). The NO production resembled that of the control group. Conversely, the LPS (50 ng/mL) significantly increased the NO production of macrophage cells.

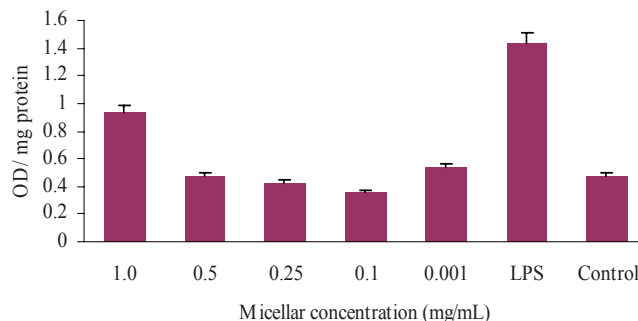


Fig. 2 Effects of micelles on the levels of nitric oxide in RAW264.7 cells

The biocompatibility of materials with blood was examined by performing a hemolytic test. According to Fig. 3, increasing the micellar concentration slightly increased the hemolysis of polymeric micelles. The hemolysis of polymeric micelle at a concentration of 2 mg/mL caused a slight hemolysis on rabbit erythrocyte comparing with that of the negative control (saline solution) and blank solution (PBS buffer).

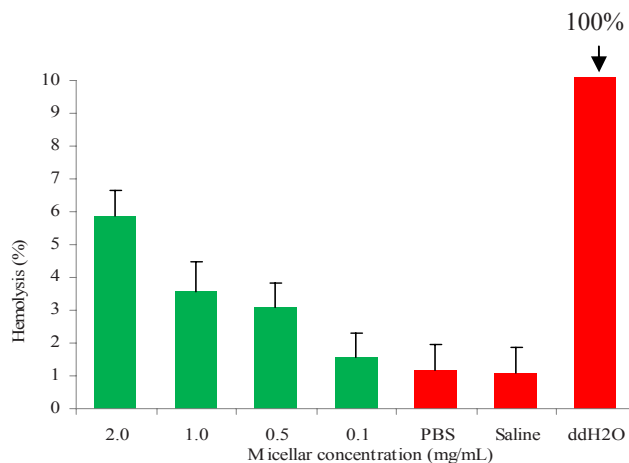


Fig. 3 Hemolytic test on polymeric micelles

C. Cytotoxicity: MTT Assay

The cytotoxicity of polymeric micelles to MCF-7 cell was evaluated using MTT assay method. Figure 4 demonstrates the cell viability after 24 hours incubation with polymeric micelles of triblock copolymer at various concentrations (0.001, 0.01, 0.1, 0.5 and 1.0 mg/mL). The results

show that the lowest cells viability was a round 75% with a concentration of 0.5 mg/mL. However, the higher cell viability was observed when the cells were cultured with a concentration of 1.0 mg/mL. The cells viability suggests that the triblock copolymeric micelle has generally low cytotoxicity to the MCF-7 cells with concentration up to 1.0 mg/mL.

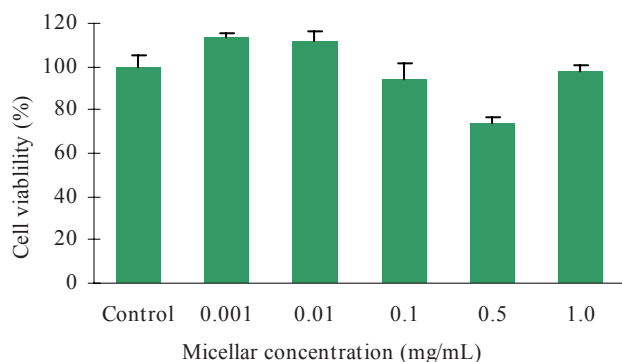


Fig. 4 The cytotoxicity of micellar solution of triblock copolymers

D. *In vitro* DOX Release Profile

The *in vitro* release profiles of DOX from the polymeric micelles was studied in in PBS (0.1 M, pH 7.4) and acetate buffer solutions (0.1 M, pH 5.4) at 37 °C. The results showed an initial burst release of DOX and followed by a sustained release for about 48 h. The initial burst release of DOX from micelles could be attributed to the diffusion of DOX located close to the surface of particles or within the hydrophilic shell [6]. The total release of DOX in a period of 48 h with pH 7.4 and 5.4 was 25% and 37% of total DOX concentration, respectively. However, the release of DOX at a pH value of 5.4 was found faster than that at a pH value of 7.4. These results could be attributed to the re-protonation of the amino group of DOX and the faster degradation of the micelle core at lower pH values. This pH-dependent release profile is of particular interest. It is expected that the greater part of DOX-loaded micelles will remain in the micelles cores for a considerable time period in plasma after intravenous administration and have the potential for prolonged DOX retention time in the blood circulation. However, a faster release may occur at low local pH surrounding the tumor site or by the more acidic environment inside the endosome and lysosome of tumor cells after cellular uptake of micelles through endocytosis.

IV. CONCLUSIONS

In this present work, the formation of nano-size micelles base on triblock copolymer has been successfully prepared. The micelles did not affect the cell viability at concentration up to 1.0 mg/mL. The DOX release profile was a pH dependent manner and the higher release rate was observed at acidic condition. Additionally, the micelles did not induce NO production and hemolytic levels compared with control group. A combination of NO production and cytotoxicity of the micelle suggested that the copolymeric micelle in this study had an extremely low toxicity and was safe for intravenous injection.

ACKNOWLEDGMENT

This work was supported by the National Science Council, Republic of China under grant 96-2221-E-033-049/97-2218-E-033-001, and project of the specific research fields in Chung Yuan Christian University under grant CYCU-98-CR-BE.

REFERENCES

1. Marchi N, Hallene K et al. (2004) Significance of MDR1 and multiple drug resistance in refractory human epileptic brain. *BMC Medicine* 2: 37.
2. Zhang Z, Huey Lee S, Feng S.S (2007) Folate-decorated poly(lactide-co-glycolide)-vitamin E TPGS nanoparticles for targeted drug delivery. *Biomaterials* 28: 1889-1899.
3. Hsieh M.F, Cuong N.V et al. (2008) Nano-Sized Micelles of Block Copolymers of Methoxy Poly(ethylene glycol)-Poly(ϵ -caprolactone)-Graft-2-Hydroxyethyl Cellulose for Doxorubicin Delivery. *J. Nanosci. Nanotechnol* 8: 2362-2368.
4. Standard practice for assessment of hemolytic properties of materials. West Conshohocken, PA: ASTM International 2000.
5. Zhang Y, Zhuo R.X (2005) Synthesis and *in vitro* drug release behavior of amphiphilic triblock copolymer nanoparticles based on poly(ethylene glycol) and polycaprolactone. *Biomaterials* 26: 6736-6742.
6. Allen C, Maysinger D, Eisenberg A (1999) Nano-engineering block copolymer aggregates for drug delivery. *Colloid Surf. B: Biointerfaces* 16: 3-27.

Corresponding author:

Author: M.F. Hsiesh
 Institute: Chung Yuan Christian University
 Street: Chung Pei Road
 City: Chung Li 32023
 Country: Taiwan, ROC
 Email: mfhiesh@cycu.edu.tw

Regeneration of Pancreatic B Cells of Type 1 Diabetic Mouse by Stem Cell Transplantation

Pham Van Phuc, Pham Le Buu Truc, Duong Thanh Thuy, Truong Hai Nhung,
Doan Chinh Chung, Nguyen Khac Toan, Ma Kien Phuc, and Phan Kim Ngoc

Laboratory of Stem cell Research and Application,
University of Science, Viet Nam National University HCM city, Vietnam

Abstract— Type 1 diabetes is the result of an autoimmune attack against the insulin-producing β cells of the pancreas. Current treatment for patients with type 1 diabetes typically involves a rigorous and invasive regimen of testing blood glucose levels many times a day along with injections of recombinant insulin. Islet transplantation is still not indicated for pediatric patients. Many recent researches have shown that stem cell therapy can be the best choice for treatment this disease. The aims of this research were investigating regeneration of pancreatic β cells of type 1 diabetic mouse after stem cell transplantation. Diabetic mice were induced by streptozocin. Some different kinds of stem cell such as mesenchymal stem cells and nucleated cells derived from human umbilical cord blood; mesenchymal stem cells and hematopoietic stem cells and mononuclear cells derived from murine bone marrow; insulin-secreting cells differentiated from mesenchymal stem cells were used to transplant into diabetic mice. Each diabetic mouse was transplanted with 5×10^6 cells by one of two ways: inject into pancreas or inject into tail portal vein. Regeneration of β cells was confirmed by decreasing blood glucose level, increasing insulin concentration in blood, body weight and the number of islets of Langerhans in the pancreas. The results showed that transplanting different kinds of stem cells as well as injection methods would give different results for regeneration of β cells. The best result achieved when transplanting insulin producing cells derived from mesenchymal stem cells into diabetic mice by directly injecting into pancreas.

Keywords— diabetic mouse, mesenchymal stem cell, bone marrow, stem cell therapy, type 1 diabetes.

I. INTRODUCTION

Diabetes mellitus, often referred to simply as diabetes—is a chronic disease in which the body either does not produce enough, or does not properly respond to, insulin, a hormone produced in the pancreas. Hyperglycemia or high blood sugar, a common condition caused by the uncontrolled diabetes, damage the body system seriously, especially the nervous system and blood vessels.

Current diabetes treatments just aim to lower the blood sugar through diet, exercise, medication with tablets and insulin. Therefore, researchers have been carrying out new diabetes treatments such as artificial CD3 antibody,

pancreas graft and pancreatic islet cell graft in order to restore the insulin production of the body. However, these therapies are expensive, low compatibility, and easy to be rejected by the receiver's immune system.

In recent researches, stem cells have brought to new hope. Bone marrow with two major stem cells (hematopoietic and mesenchymal stem cells), the adult bone-marrow derived stem cells can regenerate the β cell in diabetes animal models. These results lead to a new approach in diabetes treatment, especially type 1 diabetes.

In this research, diabetic mice were created by injection streptozocin. After that, they were treated by one of three approaches: grafting allogenic bone marrow, grafting mesenchymal stem cells, grafting insulin producing cells differentiated from mesenchymal stem cells.

II. MATERIAL-METHODS

A. Diabetic Mice Model

Diabetes models were created by intravenous infusing streptozocin (STZ) with dose 50mg/kg/day during 5 days.

B. Bone Marrow Isolation

Bone marrow from male mice were isolated by flushing via 26 G needle contacting with a 1 ml syringe. Stem cells derived from bone marrow population were enriched with lyse red blood cell techniques. This population was injected freshly into diabetic mice.

C. Mesenchymal Stem Cells From Human Umbilical Cord Blood

Human UCB was obtained from Hung Vuong Hospital, HCM city, Vietnam. UCB was collected from normal full-term and pre-term deliveries, following consent from the patient, and tested for HIV, HBV, HCV and syphilis by VDRL. To isolate mononuclear cells (MNCs), each UCB unit was diluted 1:1 with phosphate buffered solution (PBS) and carefully loaded onto Ficoll Hypaque solution (1.077 g/ml, Amersham, Freiburg Germany). After density gradient centrifugation at 800 g for 16 minutes at room temperature, MNCs were removed from the interphase, washed twice with PBS and resuspended in cryo-medium (IMDM, 10% DMSO,

bought from Sigma-Aldrich) at 10^7 - 10^8 cells/ml and seeded in T25 culture flasks (Nunc, Germany). Flasks were maintained at 37°C in a humidified atmosphere containing 5% CO₂. Medium was changed for each 4 days. The cells at the fifth passage were analyzed by flow cytometry for markers: CD13, CD14, CD34, CD45, CD166 and differentiated into adipocyte and osteoblast.

D. Differentiating Mesenchymal Stem Cells into Insulin Producing Cells

Mesenchymal stem cells were pre-inducing medium containing LG-DMEM supplemented 10 mM nicotinamide, 1 mM beta-mercaptoethanol and 10% FBS. After 48 h, medium was changed with fresh inducing medium. Inducing medium contained HD-DMEM supplemented 10 mM nicotinamide, 1 mM beta-mercaptoethanol and 10% FBS. This medium was changed continuously for 48h during 14 days.

E. Transplantation of Cells into Diabetic Mouse

The cells (bone marrow cells, mesenchymal stem cells and insulin producing cells) were grafted into mice via vein or directly into pancreas or both.

In allogenic bone marrow transplantation experiment: diabetic mice were grafted bone marrow cells via tail vein. There were two groups of mice: DC-TM group: diabetic mice were injected with PBS via tail vein and TX-TM group: diabetic mice were injected with bone marrow cells via tail vein.

In xenograft of mesenchymal stem cell experiment: diabetic mice were grafted mesenchymal stem cells via tail vein and directly into pancreas. There are four groups of mice: DC-TM group and DC-TUY: diabetic mice were injected with PBS via tail vein and pancreas respectively; MSC-TM group and MSC-TUY: diabetic mice were injected with mesenchymal stem cells via tail vein and directly into pancreas respectively.

In xenograft of insulin producing cells experiment: diabetic mice were grafted insulin producing cells directly into pancreas region near the spleen.

III. RESULTS

A. Allogenic Bone Marrow Transplantation Blood Sugar Level Recovery

DC-TM group: from 0th to 3th day, blood sugar level increased 112.00 ± 47.29 mg/dL. From 3th to 6th day, blood sugar level decreased 92.67 ± 89.76 mg/dL, then lightly increased on 12th day, suddenly increased to 419.17 ± 24.75 mg/dL on 15th day. From 15th to 30th day, the blood sugar level fluctuated stably from 419.17 ± 24.75 to 423.67 ± 110.39 mg/dL.

TX-TM group: from 0th to 9th day, blood sugar level increased greatly, particularly higher than DC-TM group (at 9th day: 410.33 ± 28.36 compared to 276.33 ± 37.07 with $P < 0.05$). From 9th to 12th day, the blood sugar level decreased, then increased from 12th to 24th day.

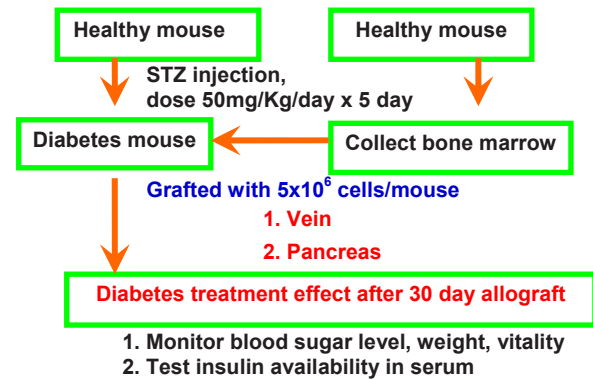


Fig. 1 Experiment procedure

Insulin production recovery

The HPLC result showed that insulin was present in the control and the TX-TM mice's serum (peak time was 29.161 minute of the control, and 29.173 minute of standard insulin sample).

In HPLC result, there was no insulin in DC-TM mice's serum (peak time was 29.306 minute of DC-TM group compared to 29.173 minute of standard insulin sample, DC-TM group's peak time was not in the standard region).

The results showed that at the portal vein group, weight and blood glucose were in turn 24.83 ± 0.71 g (18.83 ± 0.71 g of the control group) and 285.17 ± 40.31 mg/dL (423.67 ± 110.30 mg/dL of the control group).

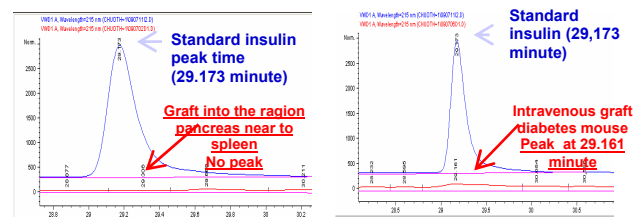


Fig. 2 Detection of insulin in peripheral blood by HPLC. There was no peak of insulin in control (DC-TM) (a) while there was a peak of insulin in TX-TM group

B. Xenograft of Mesenchymal Stem Cell Derived from Human Umbilical Cord Blood Weight

The weight mice of grafted groups were higher than the correlative control groups; lower than the normal group. The weight increased after grafting and always higher than 0th grafting day. MSC-TM group's mouse weight on 30th

day increased higher than on 0th day and was nearly the same as the normal group (MSC-TM group increased 22% compared to 27% of the normal group). Moreover, compared to MSC-TUY group, MSC-TM group's weight increased higher, especially from 9th day to 30th day. While the DC-TM group's weight decreased by time, the weight decreased 24% on 30th day. In MSC-TUY group and DC-TUY group, the weight decreased by time, on 30th day, it decreased 28%.

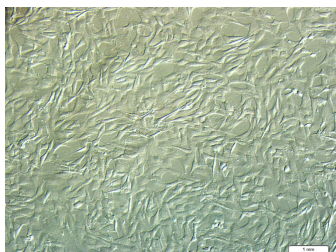


Fig. 3 Mesenchymal stem cells derived from human umbilical cord blood

Blood Sugar Level

Both grafted groups had blood sugar level higher than the normal group. However, the blood sugar level was always lower than the control group in general. The blood sugar level of two grafted groups increased greatly on the 3rd day, then decreased and were around the prior grafted day.

In MSC-TM group, the blood sugar level in 30 testing days was lower than the 0th day (259.00 ± 0.00), the lowest decrease was 37% (18th day). However, the blood sugar level was higher on some days (3th, 21th, 27th and 30th) compared to 0th day, but the highest level was only 27%. Especially, from 6th to 18th day, the blood sugar level decreased obviously, was lower than the control group and was equal to the normal group in some days (9th day was 176.00 ± 72.64 , 18th day was 164.33 ± 75.57), compared to the normal group (75.53 ± 10.84 and 98.87 ± 11.24 ; $P > 0.05$). After 30 grafted days, the blood glucose level was almost equal to the prior grafted day (30th day 293.33 ± 93.83 compared to 0th day 259.00 ± 0.00 ; $P > 0.05$). Whereas, the blood sugar level of DC-TM group was always higher than 0th day's. On 30th day, the DC-TM group's blood glucose level reached 420.00 ± 78.00 , 62% higher than of 0th day.

In MSC-TUY group, although the blood sugar level after grafted was higher than the 0th day's, the highest increase was only 50%. The blood sugar level decreased in some days (6th day 249.00 ± 49.00 , 15th day 214.00 ± 35.00), the lowest decrease was 17%. Simultaneously, the blood sugar level was always lower than the control group (except 12th day, which was 340.00 ± 900 , equal to the control group, which was 312.67 ± 55.52 , $P > 0.05$). After 30 days of graft, the blood

sugar level of MSC-TUY group increased, but it only reached 50%, whereas the DC-TUY increased up to 105%.

Insulin in serum

The insulin existence in mouse serum was evaluated by comparing with the peak time of the standard insulin sample. There was no insulin in the serum of both control groups. Both methods had the same result, in which the insulin was available in the serum, similar to the normal group. This result proved that the two MSC graft methods could help the diabetes mice regenerate the insulin in their blood. Thus, the blood sugar level and the weight was stable than the untreated mice.

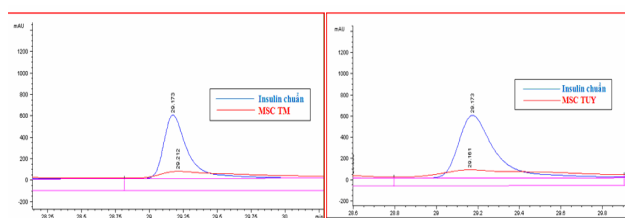


Fig. 4 Detection of insulin in peripheral blood by HPLC. (a) MSC-TM group, (b) MSC-TUY group

C. Insulin-Producing Cell Transplantation

Based on our previous studies, we were successful in differentiating MSCs into IPCs. In the differentiating process, the cell proliferation slowed down, and cell became short, round after 48 hour pre-induction in LG-DMEM differentiating medium. Then some islet pancreatic cell-like colonies appeared on 9th day, which was 200-350 μm in diameter. The islet pancreatic cell-like colonies increased by time. After 14 days, MSCs were differentiated into insulin secreting cells.

The grafted IPCs had positive effect on the diabetes treatment process of mouse model

The diabetes treatment potential of IPCs was tested *in vivo* in STZ induced diabetes mouse model. The blood sugar level of the mice was over 200mg/dL and did not decrease in 20 days after the last STZ injection. These mice were used for the next experiment.

3 diabetes mice were grafted with 5×10^6 IPCs in 0.01 ml PBS. The blood sugar level of IPCs grafted mice decreased after 3 days (3th day= 287.3 ± 31 mg/dl compared to 0th day= 306 ± 0 mg/dl); whereas the blood sugar level of PBS-injected diabetes mice continued to increase (3th day= 390.7 ± 39.4 mg/dl compared to 0th day= 306 ± 0 mg/dL). In the 30 days after graft, although the IPCs grafted mice's blood sugar level did not decrease to the normal blood sugar level (< 120 mg/dl), it did not increase like the control PBS injected diabetes mice (0th day= 306 ± 0 mg/dL compared to

30th day=577.5±39.5 mg/dL) and was stable (0th day=306±0 mg/dL compared to 30th day=342,7±33,8 mg/dL) (Fig. 2)

The normal mice's weight continued to increase and was higher than the IPCs and PBS injected diabetes mice's. The weight of control mice decreased (0th day=28±0 compared to 30th day=21.5±0.5 g), whereas the IPCs grafted's increased (0th day=28±0 g compared to 30th day=29.3±1.9 g).

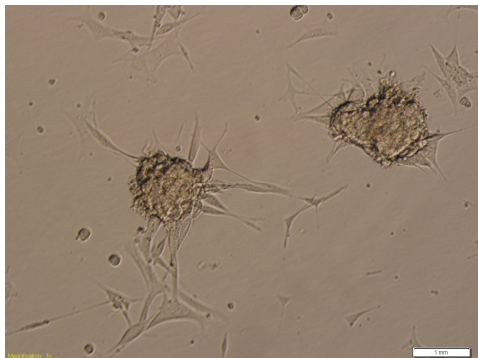


Fig. 5 Islets differentiated from mesenchymal stem cell

The HPLC result showed that there was no insulin in the control group, but there was insulin in the IPCs grafted group. In normal mouse serum, insulin was detected (peak time was 29.161 minutes of normal mice compared to 29.173 minutes of standard insulin). There was no insulin in diabetes mice (no peak time in the standard peak time region) and no insulin in the control mice. In IPCs grafted diabetes mouse serum, insulin was detected (peak time was 29.187 minutes of IPCs grafted mice compared to 29.173 minutes of standard insulin sample).

Although IPCs could keep the blood sugar level not increase much, they could not help to decrease the level. Moreover, the grafted cell dose might be small, thus, the diabetes treatment effect was not good. So that higher cell density graft studies should be carried out.

After 30 graft day, IPCs grafted mice's blood sugar level was stable. Although the blood sugar level was not decreased, it was not increased like the control mice, which tended to increase. The vitality of IPCs grafted mice increased and the insulin was presented in the serum of those mice, the DTZ dyed cells were also higher than the control. Therefore, IPCs had positive effect on the 30-day diabetes treatment process in mouse model.

IV. CONCLUSION

This study proved that the stem cell grafted method had positive effect on type 1 diabetes treatment, initially.

In the two grafted methods, intravenous injection had better result. In the three tested cell types (bone marrow cells, mesenchymal stem cells, stem cell derived insulin secreting cells), the insulin producing cell derived from mesenchymal stem cell had the best effect on recovering the insulin and blood sugar level in diabetes mouse model.

REFERENCES

1. Bo Sun, Kyung-Hwan Roh, Sae-Rom Lee, Yong-Soon Lee, Kyung-Sun Kang. Induction of human umbilical cord blood-derived stem cells with embryonic stem cell phenotypes into insulin producing islet-like structure (2007). *Biochemical and Biophysical Research Communication* 354, 919-923
2. Chao KC, Chao KF, Fu YS, Liu SH. Islet-like clusters derived from mesenchymal stem cells in Wharton's Jelly of the human umbilical cord for transplantation to control type 1 diabetes. *PLoS ONE*. 2008 Jan 16;3(1):e1451
3. Jafary H, Larijani B, Farrokhi A, Pirouz M, Mollamoha-mmadi S, Baharvand H. Differential effect of activin on mouse embryonic stem cell differentiation in insulin-secreting cells under nestin-positive selection and spontaneous differentiation protocols (2008). *Cell Biol Int* 32:278-286.
4. J.M.Ryan, F. Barry, J.M. Murphy and B. P. Mahon. Interferon- γ does not break, but promotes the immunosuppressive capacity of adult human mesenchymal stem cells (2007). *Clinical and Experimental Immunology*, doi: 10.1111/j.1365-2249
5. Jennifer M Ryan, Frank P Barry, J Mary Murphy and Bernard P Mahon. Mesenchymal stem cells avoid allogeneic rejection (2005). *Journal of Inflammation*, doi: 10.1186/1476-9255-2-8
6. Gao X, Song L, Shen K, Wang H, Niu W, Qin X. Transplantation of bone marrow derived cells promotes pancreatic islet repair in diabetic mice (2008). *Biochem Biophys Res Commun* 371:132-137
7. Gao F, Wu DQ, Hu YH, Jin GX. Extracellular matrix gel is necessary for in vitro cultivation of insulin producing cells from human umbilical cord blood derived mesenchymal stem cells.(2008) *Chin Med J (Engl)* 21:811-818.
8. Li Y, Zhang R, Qiao H, Zhang H, Wang Y, Yuan H, et al. Generation of insulin-producing cells from PDX-1 gene- modified human mesenchymal stem cells (2007). *J Cell Physiol* 211:36-44.
9. Kodama M, Takeshita F, Kanegasaki S, Ochiya T, Quinn G. Pancreatic endocrine and exocrine cell ontogeny from renal capsule transplanted embryonic stem cells in streptozocin- injured mice (2008). *J Histochem Cytochem* 56:33-44.
10. Xu X, D'Hoker J, Stange G, Bonne S, De Leu N, Xiao X, et al. Beta cells can be generated from endogenous progenitors in injured adult mouse pancreas (2008). *Cell* 132:197-207.

Corresponding author:

Author: Pham Van Phuc,

Institute: Lab. Of Stem cell Research and Application, University of Science, Vietnam National University, Street: 227 Nguyen Van Cu, HCM City, VN,

Email: pvphuc@hcmuns.edu.vn

Results of Curing Some Diseases by Stem Cell Transplantation at Stem Cell R&D Laboratory

Phan Kim Ngoc and Pham Van Phuc

Laboratory of Stem cell Research and Application
University of Science, Viet Nam National University HCM City, Vietnam

Abstract— Stem cell therapy in curing dangerous diseases usually is main target of many researches about stem cells. In the world, researching and applying stem cells to cure diseases got some great achievements while there is a few in Viet Nam. In recently years, Laboratory of Stem cell R&D, University of Science, VNU HCM city carried out some researches about pre-clinical treatment diseases using stem cell therapy. We used some different kinds of stem cells such as mesenchymal stem cells derived from umbilical cord blood to cure bone marrow failure syndrome and bone broken. The results showed that efficiency of cure was different when various methods and kinds of stem cell were applied. These results were bases for developing novel approaches and applying clinical treatment.

Keywords— Diabetic disease, bone marrow failure, bone broken.

I. INTRODUCTION

Stem cells are available in almost all tissues of the body. They have significant role in homeostatic regulation. Cell replacement therapy is concerned to be a potential treatment for irremediable diseases; these diseases have been treated well and effectively in previous decades. Some of the remarkable successes are the cornea therapy, the marketable cornea and skin replacement therapy, advantages in the pancreas replacement therapy, cord blood therapy and the potentiality in collecting large quantity of cells from the embryos, fetuses and adult bodies which give hope in curing a lot of diseases effectively, such as cardiovascular diseases, lysosomal storage diseases, migratory tumor. Stem cell therapies are commercialized and concerned greatly.

Along with the world's highly development in research for curing diseases by stem cells, Laboratory of Stem cell Research & Application (Stem cell Lab) have researched and applied some kind of stem cells in curing diseases. This report will present briefly the results of curing bone marrow failure, diabetes, broken bone by stem cells and differentiating germ cells to mature sperms for curing infertility.

II. RESULTS

A. Bone Marrow Failure

Bone marrow failure is the condition in which the bone marrow fails to produce all of blood cells or it only produces

red cell, white cell or combined two lineages. According to Botnick Le *et al.*, Busulfan (BU) and Cyclophosphamide (CY) have significant impact on hematopoietic stem cells, which cause the acute bone marrow failure. In this research, we use these chemicals to create bone marrow failure mice. Ten mice were made by the above procedure. In the 10th day after injecting with BU and CY, male mouse's bone marrow derived mesenchymal stem cells were injected to mice. The results showed that 3 in 10 transplanted mice were dead in the 25th day (10 days after transplanted) and 6/10 transplanted mice had significant weight recovery, from 19g/mouse to 29g/mouse after 20 days.

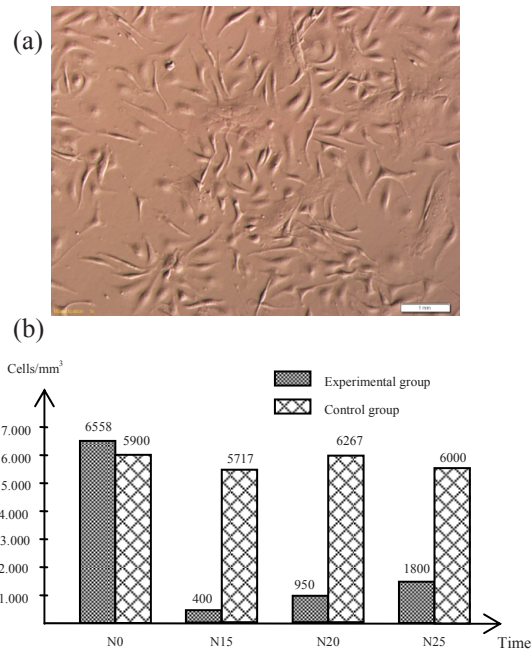


Fig. 1 (a) Bone marrow derived mesenchymal stem cells (b) The decline of total white blood cells by time induced by BU and CY treatment, comparing to the control. D0, D15, D20, D25 correspondingly after injection. The total white blood cells in the diagram are the average values of tested mice

The recovery of total white blood cell was recorded. There was 425 cells/mm³ in the 10th day before transplanted and 2508 cells/mm³ in the 10th day after transplanted (20th day).

This outcome showed that the mesenchymal stem cells had a major role in curing bone marrow failure. In the animal models, there was 33% of mice lived if they did not injected with mesenchymal stem cells. Nevertheless, when the MSCs were transplanted, this ratio came up to 70%. These MSCs could renew or regenerate a new microenvironment “niche” in the bone marrow which helped the hematopoietic stem cells live, from which the hematogenesis system can be recovered. After transplantation, MSCs could produce SCF which stimulate the remained HSC proliferate.

After 10 days of transplantation, the total white blood cells in the peripheral blood was around 2,500 cells/mm³ (increase 5 times compare to the control) and the total white blood cells in the alive mice after 10 days injection with BU and CY is 950 cells/mm³. Therefore, compare to the control, on the blood collection day (10 days after transplanted), the white blood cells increased 2.5 times compare to the alive mice that were not injected.

However, in the 20th day, in the non-grafted mice, 67% mice were dead and the white blood cell in alive mice was 950 cells/mm³ in average. If compare to the MSC transplanted mice in the same time, the amount of white blood cell was 2500 cells/mm³; but there were 3 mice died.

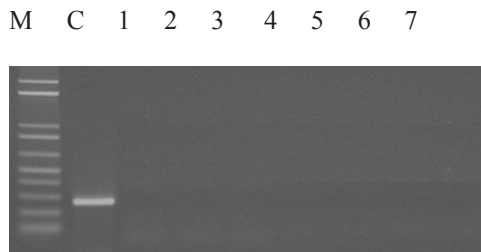


Fig. 2 Results of PCR reactions with genome DNA isolated from bone scar after MSC transplantation. M: ladder, C: positive control, 1, 2, 3, 4, 5, 6 and 7: 7 mice grafted with MSC

After 10 days transplantation, collecting the peripheral blood of alive mice for isolating DNA and carrying out PCR reaction with specific primers for gene *sry*, which is specific for male individuals. The electrophoresis result showed that all 7 mice were negative with *sry* gene. That means the transplanted MSCs were not present in peripheral blood.

MSC transplantation with a dose of 10⁶ cells/mouse improved survival rate of bone marrow failure mice from 33% to 70%; the weight of mouse increased and the total number of leucocyte cells increased 5 times compared to before transplantation and increased 2.5 times compared to

mouse surviving without transplantation on the 10th day after the transplantation and non-grafted cells.

B. Type 1 Diabetes

Mice (*Mus musculus* var. Albino) from 8 to 10 week old, same sex, weighing 20-30g were taken care in the same condition.

This research had three main stages: Modeling phase: 3 mice in the normal mouse group (BT) and 12 mice in the diabetes mouse model group (TD). Induction of diabetes by injecting a dose STZ 50mg/kg/day for 5 days to examine the concentration of blood sugar in 20 days in order to generate the diabetes mouse models.

The number of cells was chosen to be transplanted was 5x10⁶ cells/mouse. Grafted cells in diabetes mouse model by 2 methods: into the veins (TX-TM) and into pancreas region near to spleen (TX-TUY). The diabetes mouse models obtained after STZ induction were randomly put into four groups (each group had 3 individuals): Group ĐC-TM: diabetes mouse models had PBS injected into veins; Group ĐC-TUY: diabetes mouse model group had PBS injected into the pancreas region near the spleen. Group TX-TM: diabetes mouse group received bone marrow contained 5x10⁶ cells into veins; Group TX-TUY: diabetes mouse group received bone marrow suspension containing 5x10⁶ cells into pancreas region near the spleen.

The results showed that:

Weight: Group TX-TUY recovered weight from 18 to 30 days, and was slower than group TX-TM (12 day).

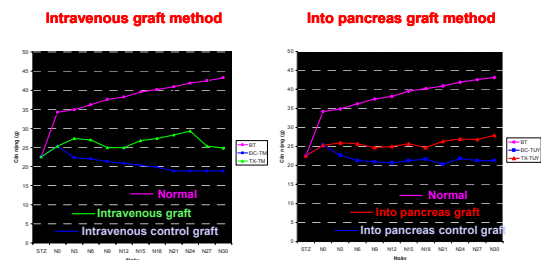


Fig. 3 The chart of weight recovery. The weight body of mice after (a) intravenous graft (b) pancreas graft of bone marrow cells

Blood sugar: Group TX-TUY had the lowest blood sugar level (on D6) compared to TX-TM group (on D30). Group TX-TUY always had blood sugar levels much lower than group TX-TM. The approaching pancreas transplantation method improved blood sugar level better than the vein grafting method.

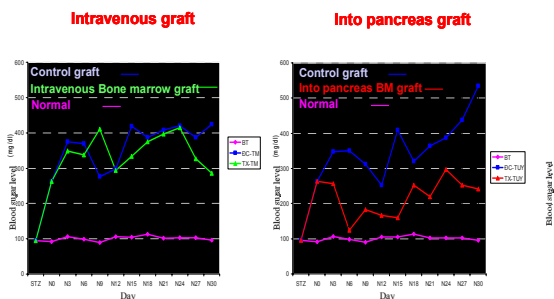


Fig. 4 Glucose peripheral blood recovery chart. Glucose peripheral blood decreased significantly in mice pancreas grafted with bone marrow (b), while this was not clearly in mice intravenous graft (a)

HPLC: Both transplantation methods had insulin in mouse serum (Peak of pancreatic grafts occurred in 29.212 minutes, peak of vein grafts was about 29.103 minutes).

Conclusion: effect of bone marrow cells transplantation into pancreas region near the spleen was better than vein: (1) Weight index: increased 10% after 30 grafted days, (2) glucose blood index: the most effective impact was after 6 grafted days, declined 8% after 30 day bone marrow graft; (3) Pancreatic recovery: two times higher than the veinal grafted method.

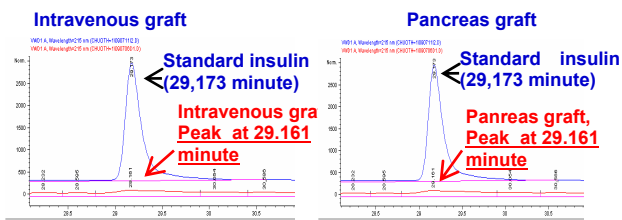


Fig. 5 Detect the existence of insulin in peripheral blood by HPLC. (a) in intravenous graft, (b) in pancreas graft

C. Broken Bone

This research aims: evaluating the effects of grafting MSC derived from human umbilical cord blood to broken bone mice. There are three doses of cells: 10^5 cells, 10^6 cells, 10^7 cells for studying the MSC ability in healing broken bone in mice.

The reason of bone fracture is much diversified and all of them are due to the effects of external forces. This experiment used forces caused by heavy objects falling from different heights. The higher the heavy object is, the greater the velocity is when the object hit the mouse leg.

Cell grafting: MSCs were prepared in 4 tubes 1.5 ml differed in cell concentrations in 0.1 ml PBS solution. Carrying out

one in three procedure with 3 different doses: 10^5 cells/individual, 10^6 cells/individual, 10^7 cells/individual.

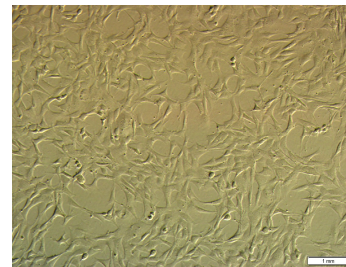


Fig. 6 Mesenchymal stem cells derived from human umbilical cord blood

In the modeling experiment: ability of controlling left hind limb was tested at day 7, 14, 21, 28 after broken bone with 1N, 2N, 3N, 4N, 5N force. The results showed that 4N force was the most suitable for making broken bone mouse.

In the graft experiment: the 10^7 cell/mouse dose was the best in 3 doses. After 21 days, all mice could control the broken hind limb by themselves as the normal hind limb. In other doses (10^5 , 10^6 cells/mouse), although mice might be recovered at day 21, their flexibility was limited (the number of footsteps and the pedal swimming frequency in water compared with normal hind limbs).



Fig. 7 Bone scar after MSC transplantation

Mouse limb bone surgery grafted with 10^7 cells/mouse showed that bone fragments attached entirely to the main bone with large scar. Thus, when grafted MSC with cell concentration of 10^7 cells/mouse, healing period was shortened compare to 10^5 cells/mouse, 10^6 cells/mouse and 7 days sooner than the control.

To determine the existence of grafted MSC at broken bone, the scar was isolated and identified the existence of HLA-A gene specified for human via PCR method from the DNA genome of scar's cells. Electrophoresis result in agarose 2% showed that there were no bands of target DNA at the broken position.

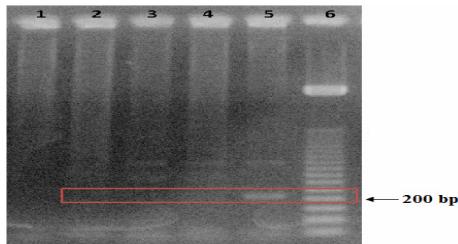


Fig. 8 Results of HLA-A gene PCR. 5: positive control, 6: ladder; 1, 2, 3 and 4: mice grafted with MSC

Thus, the MSC differentiation and availability in the healed bone site was not determined. We suggest that the grafted MSC in the broken bone site not only participate in the healing process, differentiate into bone component cells but also in the indirect healing process, in which MSCs stimulate the cytokine secretion and differentiating factors for gathering the cellulitis, mesenchymal stem cells in the initial bone healing process. The initial stage had a major role in starting the healing broken bone process. In this stage, vascular forming cells gathered to become a vascular system in order to provide nutrient for new bone, self mesenchymal stem cells were gathered and differentiated into bone tissue in the healing process. It was proven that all the MSC grafting mice had healing time shorter than the control. Therefore, MSCs did not directly participate in differentiating into mouse new bone in broken bone model after 21 days. The shorten recovery time of mouse's hind limb in this experiment can be caused by MSC indirect effect on gathering self-cells in the initial stage of healing broken bone.

After MSCs were injected into broken bone mouse models, the result showed that MSC might be able to heal broken bone. In five-week-old mice, the time of healing broken bone was reduce by MSC injection. The broken bones were healing at dose of 10^5 cells/mouse and 10^6 cells/mouse. MSC transplantation at 10^7 cell/mouse could help diminish the healing broken bone time to slighter than 7 days compare with non-transplanted MSCs.

REFERENCES

1. Burwell RG 1969 "The fate of bone grafts. In: Apley AG, editor. Recent advances in orthopaedics", London: Churchill, p 115-207.
2. Figliuzzi M, Cornolti R, Perico N, Rota C, Morigi M, Remuzzi G, Remuzzi A, Benigni A. 2009 Bone marrow-derived mesenchymal stem cells improve islet graft function in diabetic rats. *Transplant Proc.* 41(5):1797-800.
3. Leiter EL, 1999 STZ induce diabetes service, The Jackson laboratory.
4. Lin Lin, Xin Fu, Xin Zhang, Lian-xu Chen, Ji-ying Zhang, Chang-long Yu, Kang-tao Ma, Chun-yan Zhou 2006 "Rat adipose-derived stromal cells expressing BMP4 induce ectopic bone formation in vitro and in vivo", *Acta Pharmacologica Sinica*, 27 (10): 1608-1615.
5. Mardanpour P, Guan K, Nolte J, Lee JH, Hasenfuss G, Engel W, Nayernia K. 2008 Potency of germ cells and its relevance for regenerative medicine. *J Anat.* 213(1):26-9.
6. Scott R Bruder, Neelum Jaiswal, Nancy S. Ricalton, Joseph D. Mosca, Karl H. Kraus, and Sudha Kadiyala 1998, "Mesenchymal Stem Cells in Osteobiology and Applied Bone Regeneration", Lippincott Williams & Wilkins.
7. Shuichi Ashizuka, William H. Peranteau, Satoshi Hayashi, and Alan W. Flake, 2005 "Busulfan-conditioned bone marrow transplantation results in high-level allogeneic chimerism in mice made tolerant by in utero hematopoietic cell transplantation", *Exp Hematol* 34(3), pp. 359-368.
8. Sudepta Aggarwal, and Mark F. Pittenger 2005. Human mesenchymal stem cells modulate allogeneic immune cell responses. *Blood.* Vol. 105, No. 4, pp. 1815-1822.

Corresponding author:

Author: Phan Kim Ngoc,
 Institute: Lab. Of Stem cell Research and Application, University of Science, Vietnam National University, Street: 227 Nguyen Van Cu, HCM City, VN,
 Email: pkingoc@hcmuns.edu.vn

Regulations of Cell Division from Streptomyces That May Play an Important Role in Drug Resistance

Nguyen H.K. Tu

School of Biotechnology, HoChiMinh City International University, HoChiMinh City, Vietnam

Abstract— A gene *minDSL* encoding a cell division of D-cycloserine producing *Streptomyces* has been cloned and sequenced [10]. The *minDSL* gene was expressed in *E. coli*. The *minDSL* gene gives rise to a filamentous phenotype in *E. coli* when MinDSL protein was fused with His-tag in pET21a(+) construction. Scanning electron microscope analysis shows the indentations along the cells. His-tag MinDSL protein is soluble. However, the introduction of *minDSL* gene with the sequence containing 49 nucleotides at up stream of *minDSL* gene gave apparent morphological alteration into minicells when using pET28a(+) as an expressed vector. The native MinDSL protein is insoluble. In this study, we showed morphological differentiation, how to purify the insoluble MinDSL protein and D-cycloserine resistant assay. Investigation of minicell production indicates that the production of minicells is blocked when maltose was added in the culture. This is the report about the effects of *Streptomyces minDSL* gene in *E. coli* in the formation of minicell phenotype which may participate in drug resistance that is interested in cancer treatment and vaccine preparation nowadays.

Keywords— cell division inhibitor, *Streptomyces*, drug resistance, morphological change.

I. INTRODUCTION

In rod-shaped bacteria such as *Escherichia coli*, the proper placement of the cell division site is maintained by the MinC, MinD, and MinE proteins encoded by the *minB* locus [2,3]. In this system, the MinC and MinD proteins act in concert forming an inhibitor of cell division capable of blocking septum formation at all potential division sites (polar and midcell sites). The MinE protein gives topological specificity to the MinCD division inhibitor by restricting its activity to polar division sites, thus ensuring that separation is limited to the proper division site at midcell [6]. MinD is an ATPase in *E. coli* [5].

Filamentous soil bacteria, including the strains belonging to the genus *Streptomyces*, have a complex morphological differential and are well known for their ability to produce an enormous variety of bioactive secondary metabolites, such as antibiotics and immunosuppressant drugs. The entire nucleotide sequences of the *Streptomyces* genomes of *Streptomyces coelicolor* [1] and *S. avermitilis* [7] have

recently been reported. Both strains carry the MinD homolog, but not MinC or MinE. MinD homolog harbored by *Streptomyces* has not yet been well-characterized [9]. Our goal is to develop the effects of MinD homolog harbored by *Streptomyces* in morphological change, especially the minicell and filamentous morphology in *E. coli*. During the morphological change in bacteria, the MinD expression caused different solubility. Because of morphological change, the drug resistance is also effected. The minicell are anucleated cells that lack chromosomal DNA derived from the minicell producing parent cells from which they are produced. The term “minicell” encompasses derivatives of eubacterial and archaeobacterial cells that lack parental chromosomal DNA as well as anucleated derivatives of eukaryotic cells. Minicells are often smaller than their parent cells. Administration of targeted minicells containing cytotoxic drugs eliminate formerly drug-resistant tumors [8].

That is why *minD* gene is essential for cell division and the viability in *E. coli*. Significant advances have been made towards understanding the molecular role of MinD homolog harbored by *Streptomyces* in the division process.

II. MATERIALS AND METHODS

A. Bacterial Strains and Plasmids

S. lavendulae was used as a source of preparing chromosomal DNA. *E. coli*, BL21(DE3), pET21a(+), pET28a(+) were used.

B. Construction of the *S. lavendulae minDSL* in *E. coli*

To construct *E. coli* expressing the *S. lavendulae minDSL*, a PCR with primers 5'- CACCATATGACCACTCGAATCCTCCCCGC-3' and 5'-CACCTCGAGGCCCTCCCGGCCGCGC-3' was performed. The product was treated with NdeI and XhoI (sites underlined), and inserted into pET21a(+) to create pET21a(+)/*minDSL*. To amplify upregulated-*minDSL* (*minDSL* containing 49-bp upstream of *minDSL*) gene, PCR primers (5'-GGAATTCCAGTCCCACCGACCGC ACGT AC-3' and 5'-CCGCTCGAGCGGGCCACGAGC AGCAGG ATC-3') were designed. The resulting amplified product was

digested with EcoRI and XhoI (sites underlined) and inserted into pET28a(+) to create pET28a(+)/upregulated-minDSL.

C. Overexpression of His-tag MinDSL, Native MinDSL Protein in *E. coli*

Transformation the constructed plasmids in *E. coli* were performed [4]. *E. coli* BL21(DE3) harboring pET21a(+)/minDSL and pET28a(+)/upregulated-minDSL was grown at 37°C in 1 L of an LB medium to OD₆₀₀=0.5, whereupon isopropyl-β-D-thiogalacto-pyranoside (IPTG) was added to culture at the final concentration of 0.5 mM to induce the expression of MinDSL. The *E. coli* cells were grown for 5.5 h at 28°C and observed by microscope.

D. Microscopic Observation Method

Light microscope: *E. coli* cells expressing minDSL were observed directly on microscopic slide by a light microscope (OLYMPUS X172).

Scanning electron microscope (SEM): *E. coli* cells were fixed in 1% solution of tetroxide (OsO₄) after prefixed with 2% solution of mercury chloride (HgCl₂) and observed by SEM, using JEOL JSM6300 scanning electron microscope.

E. D-cycloserine (DCS) Resistance Assay

E. coli transformed by pET21a(+), pET28a(+), pET21a(+)/minDSL, pET28a(+)/upregulated-minDSL were grown in LB medium. The test was measured the turbidity after the *E. coli* were cultured with DCS at the interval time.

III. RESULTS

A. Introduction of the *S. lavendulae* minDSL into *E. coli* Cells

Introduction of pET21a(+)/minDSL into *E. coli* BL21(DE3) cell caused a filamentous shape, as observed by a light microscope (Fig. 1B) and SEM (Fig. 1D).

To facilitate further study of MinDSL, the *E. coli* BL21(DE3) carrying the pET28a(+)/upregulated-minDSL plasmid was overexpressed. Under the presence of IPTG, the transformant took a minicell phenotype (Fig. 2B), whereas the same cell transformed with pET28a(+) exhibited a normal rod-shaped morphology (Fig. 2A). The minicells are produced by a process that is similar to the normal cell division except that it occurs near one or both poles of the cell. The division process, that generates the minicells, seems to be “normal” in many ways [9,11]. In

this case, DNA is not distributed to both sides of the division plane. The production of minicells is a consequence of the unusual genetic constitution and does not require any unusual manipulation of the environment [13]. They have anticipated that the minicell phenotype will be valuable in a variety of genetic and biochemical studies [11]. The *E. coli* BL21(DE3) carrying the pET28a(+)/upregulated-minDSL plasmid was overexpressed under the presence of maltose, the cells are longer than the *E. coli* BL21(DE3) carrying the pET28a(+) (Fig. 2C, 2D).

In conclusion, the overexpression of *S. lavendulae* minDSL in *E. coli* causes the cellular shape change. That is, the minDSL gene with the fused construction results in the filamentous shape, whereas the native MinDSL corrects the minicell phenotype in *E. coli* (Fig. 2B).

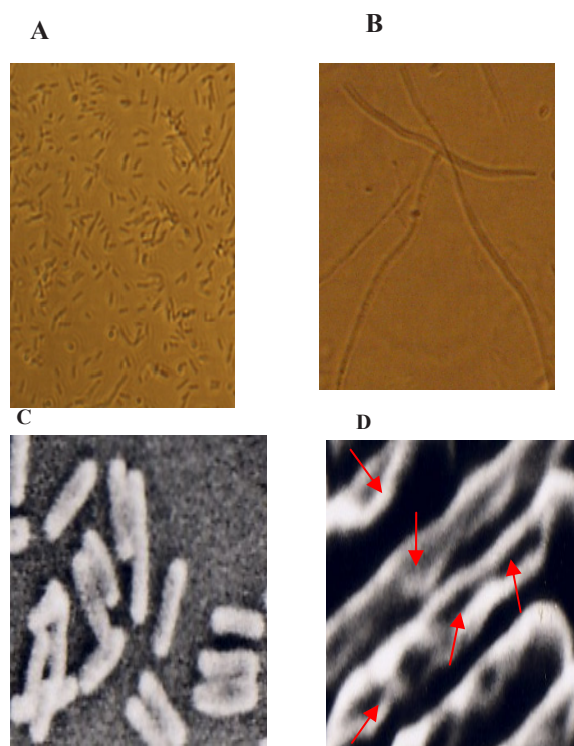


Fig. 1 The cell shapes of *E. coli* BL21 (DE3) carrying minDSL when using pET21a(+) as an expression vector. (A) and (B) are the pictures filmed by light microscope, but (C) and (D) are the picture filmed by scanning electron microscope. *E. coli* BL21 (DE3) transformed with pET21a(+) is a typical rod shape, as shown in (A) and (C). The same host transformed with pET21a(+)/minDSL exhibits a filamentous phenotype, as shown in (B) and (D). Red arrows show the indentations along the cells. Photographs of light microscope with the scale bar is 5 μm, and both figures are at the same magnification. Photographs of scanning electron microscope with the scale bar is 1 μm

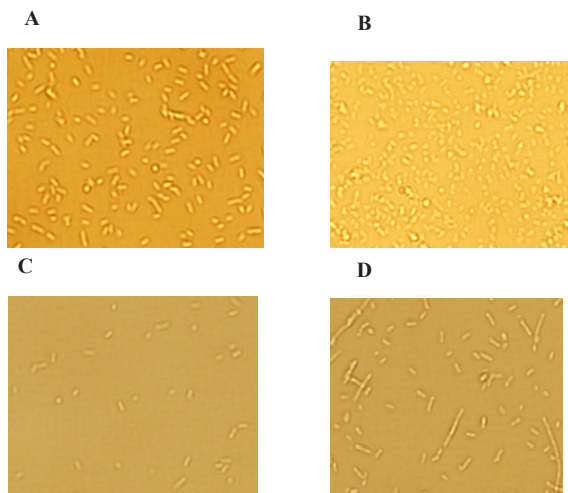


Fig. 2 The cell shapes of *E. coli* BL21 (DE3) carrying minDSL when using pET28a(+) as an expression vector. (A) *E. coli* BL21(DE3) cells were transformed with pET28a (+). (B) *E. coli* BL21(DE3) cells were transformed pET28a(+)/upregulated-minDSL. (C) Phenotype of *E. coli* BL21 (DE3) cells were transformed with pET28a (+) in LB medium supplemented with maltose (1%). (D) *E. coli* BL21(DE3) cells were transformed pET28a(+)/ upregulated-minDSL in LB medium supplemented with maltose (1%). Photographs of light microscope with the scale bar is 5 μ m, and both figures are at the same magnification. Photographs of scanning electron microscope with the scale bar is 1 μ m

B. Purification of the Native MinDSL

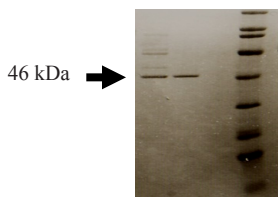


Fig. 3 Purification of MinDSL was analyzed by Tricine-SDS-PAGE [12]

Since the minicell phenotype will be valuable in a variety of genetic and biochemical studies, a native MinDSL was purified. After *E. coli* BL21 (DE3) carrying minDSL was grown, the cell mass was collected to inclusion body from the cell-free extract. Washing the inclusion body with 1% n-decyl- β -D-glucopyranoside was useful to reduce the contaminated proteins. The washed inclusion body was dissolved in a buffer containing 1% n-decyl- β -D-maltopyranoside. The MinDSL was purified from the inclusion body, as described in the experimental procedures section. The MinDSL was purified to homogeneity, as shown in Fig. 3.

C. D-Cycloserine Resistance Assay

To investigate the role of minDSL in antibiotic resistance, the D-cycloserine resistant assay was performed. The results are in fig. 4.

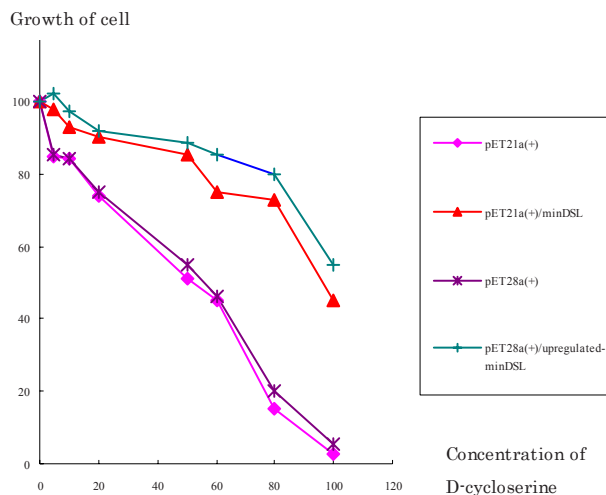


Fig. 4 D-cycloserine resistance assay in *E. coli*

IV. DISCUSSIONS

Interestingly, the data showed the role of minDSL in phenotype differentiation and antibiotic resistance. Relationship is not clear. However, by the microscopic analysis, the intantations in the cell wall reflect that minDSL may play a role in cellular mechanism. In the experiment, the construction of minDSL with pET21a(+) and pET 28a(+) with different antibiotic selection in the selective medium will be explained in further study.

V. CONCLUSIONS

Our experiment suggests the considerations that bacterial shapes are not accidental but are biologically important. In the *E. coli* system with the overexpression of MinCDE, the function of MinDSL from *S. lavendulae* was activated by means of the putative primary promoter upstream of minDSL along with the selective conditions of environment. This is the first report about the effects of *Streptomyces* minDSL gene in *E. coli* in the formation of minicell phenotype which may participate in drug resistance that is interested in cancer treatment and vaccine preparation.

REFERENCES

1. Bentley SD, Chater KF, Cerdeño-Tarraga AM, Challis GL, Thomson NR, James KD, Harris DE, Quail MA, Kieser H, Harper D et al. (2002) Complete genome sequence of the model actinomycete *Streptomyces coelicolor* A3(2). *Nature* 417: 141–147
2. de Boer PA, Crossley RE, Rothfield LI (1989) A division inhibitor and a topological specificity factor coded for by the minicell locus determine proper placement of the division septum in *Escherichia coli*. *Cell* 56: 641-649
3. de Boer PA, Crossley RE, Rothfield LI (1992) Roles of MinC and MinD in the site-specific septation block mediated by the MinCDE system of *Escherichia coli*. *J Bacteriol* 174: 63-70
4. Hanahan D (1983) Studies on transformation of *Escherichia coli* with plasmids. *J Mol Biol* 166: 557-580
5. Hu Z, Gogol EP, Lutkenhaus J (2002) Dynamic assembly of MinD on phospholipid vesicles regulated by ATP and MinD. *Proc Natl Acad Sci USA* 99: 6671-6676
6. Hu Z, Lutkenhaus J (2003) A conserved sequence at the C-terminus of MinD is required for binding to the membrane and targeting MinC to the septum. *Mol. Microbiol* 47: 345-355
7. Ikeda H, Ishikawa J, Hanamoto A, Shinose M et al. (2003) Complete genome sequence and comparative analysis of the industrial microorganism *Streptomyces avermitilis*. *Nat Biotechnol* 21: 526-531
8. Jennifer AM, Nancy BA et al. (2007) Sequential treatment of drug-resistant tumors with targeted minicells containing siRNA of a cytotoxic drug. *Nat Biotech* 27: 643-654
9. Meinhardt H., de Boer PA (2001) Pattern formation in *Escherichia coli*: a model for the pole-to-pole oscillations of Min proteins and the localization of the division site. *Proc Natl Acad Sci USA* 98: 14202-14207
10. Nguyen HKT, Kumagai T, Matoba Y, Sugiyama M (2008) Molecular cloning and functional analysis of minD gene from *Streptomyces lavendulae* ATCC 25233. *J Bioscience Bioeng* 106(3): 303-305
11. Raskin DM, de Boer PA (1999) Rapid pole-to-pole oscillation of a protein required for directing division to the middle of *Escherichia coli*. *Proc Natl Acad Sci. USA* 96: 4971-4976
12. Schagger HJ, Jagow G (1987) Tricine-sodium dodecyl sulfate-polyacrylamide gel electrophoresis for the separation of protein in the range from 1 to 100 kDa. *Anl Biochem* 166: 368-379
13. Shih YL, Rothfield L (2006) The Bacterial Cytoskeleton. *Microbiol Mol Biol Rev* 70: 729-754

Author: Nguyen Hoang Khue Tu
 Institute: School of biotechnology, HoChiMinh City International University
 Street: Quarter 6, Linh Trung - Thu Duc
 City: HoChiMinh
 Country: Vietnam
 Email: nhktu@hcmiu.edu.vn

Cellular Bio-corrosion of Metal Implants and Effects of Metal ions on Bone Cells and Immune Cells

Filgueira, E. Chan, and D. Cadosch

School of Anatomy and Human Biology, University of Western Australia, Crawley, Australia

Abstract— Metal implants have become essential therapeutic tools in cranial, dental, orthopaedic and cardiovascular surgery. In most cases, the implants are well tolerated. However, short term orthopaedic implant loosening and failure happens in 3-80% of patients, depending on implant material, location and precondition. Especially inflamed tissues like rheumatoid arthritic joints have been shown to have increased implant failure. However, the mechanisms of implant loosening are still not well understood. This study investigated cellular and immune-related mechanisms that may play a role in aseptic implant loosening.

A human *in vitro* model has been used for this study. The interaction between metal surfaces or metal ions and immune cells or bone cells was investigated. Cell culture, immune fluorescence and electron microscopy, functional tests, flow cytometry and molecular methods were applied.

The results indicate that metal surfaces made of stainless steel, aluminum or titanium are corroded by human osteoclasts (bone resorbing cells) *in vitro*. The released ions are taken up by the osteoclasts and immune cells, which are affected in various ways, including induction of metal sensitivity reactions and enhanced activation of osteoclasts.

We can conclude that human osteoclasts are able to corrode metal implants and release metal ions, which have then various effects on immune cells and possible on different organs and the whole organism.

Keywords— Metal implant, bio-corrosion, osteoclast, immune cells, peri-implant inflammation.

I. INTRODUCTION

Metal implants have become essential biomedical therapeutic tools in a variety of treatments. Metal implants are composed of a variety of metals, depending on function and location. Medical grade stainless steel, chromium-cobalt and titanium alloys are the most frequently used materials. Aluminum, chromium, cobalt, iron, manganese, molybdenum, nickel, titanium, vanadium and zirconium are the most frequent metals used for metal implants [1].

There are various applications for metal implants, including vascular and digestive stents, internal fracture treatments, face and dental surgery, and orthopedic joint replacements.

This paper focuses on orthopedic devices and related problems, as most published studies investigated orthopedic metal implants [1].

Usually, orthopedic metal implants are well tolerated. However, between 3% (e.g. hip joint replacement) [2, 3] and 80% (e.g. hand joint replacement in patients with rheumatoid arthritis) [4] of patients develop severe side effects, depending on anatomical location and medical condition.

Side effects may include toxic effects of implant derived metal ions [5, 6], inflammation and pain [7], and implant loosening [1, 3]. The cause for side effects is related to metal wear and corrosive products. However, little is known about bio-corrosion of metal implants and the resulting inflammatory processes. This study focuses firstly on osteoclasts, the only, but very potent bone resorbing cells and their role in bio-corrosion and implant loosening, and secondly on immune cells that are responsible for metal ions related inflammation and pain.

II. WRITING THE PAPER

A. Osteoclastic Bio-corrosion

A human *in vitro* model has been established to investigate the bio-corrosive potential of human osteoclasts *in vitro* and to evaluate the influence of metal ions on osteoclast maturation and function. For that purpose, peripheral blood monocytes were cultured in the presence of the cytokines M-CSF and RANK-L [8, 9]. After 1 to 3 weeks in culture, monocytes become functional bone resorbing osteoclasts with specific activity of tartrate resistant acid phosphatase (TRAP) and the typical basal actin ring that stabilizes the basal side of the polarized cells. The cells grow easily on culture plastic material and glass, as well as on medical grade stainless steel (Figure 1), aluminum and titanium [10]. In addition, the osteoclasts secrete protons and various enzymes towards the metal surface which have strong corrosive properties [11, 12]. Thus, osteoclasts corrode the metal surface and dissolve metal ions that are then taken up by the cells, to be eventually released on the other site of the cell [13]. In case of water soluble ions of iron, chromium, cobalt, nickel and manganese, those can be measured in the cell culture supernatants [10], whereas titanium ions are not well water soluble and remain in the cells after being taken up by the osteoclasts. Intracellular titanium has been shown with a

newly developed detection methods [14, 15], including fluorescence microscopy (Figure 2) and energy filtered transmission electron microscopy [15].

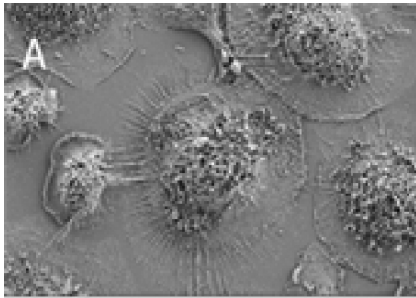


Fig. 1 Human osteoclasts were cultured for 2 weeks on glass (A) or medical grade stainless steel (B) before processed for surface scanning electron microscopy. No major difference has been found comparing cells cultured on the different surfaces

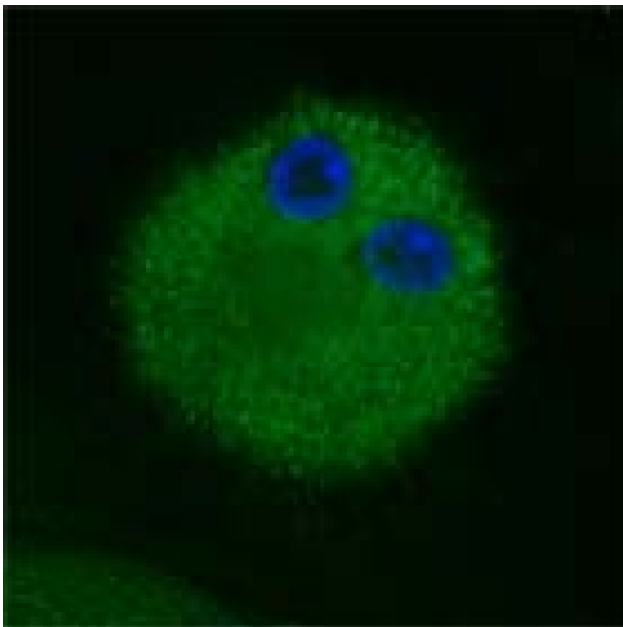
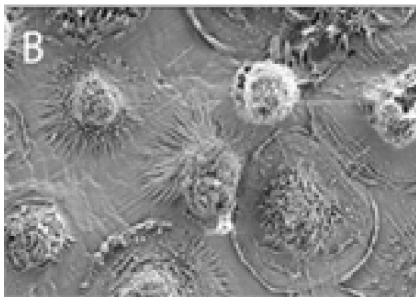


Fig. 2 Osteoclasts were cultured for 2 weeks on titanium foil before stained with Newport Green DCF and documented with confocal fluorescence microscopy [14]. Note the green stained granular areas in the cytoplasm as well as in the nucleus representing titanium distribution in the bi-nucleated cell (blue nuclear stain)

Once released, the various metal ions enhance recruitment and maturation of new osteoclasts, as shown for titanium by our group [16, 17]. Increased osteoclastic activity results in enhanced bio-corrosion and bone resorption [16].

B. Influence of Metal Ions on Immune Cells and Inflammation

Metal ions released from metal implants by osteoclastic bio-corrosion are distributed throughout the body and are eventually taken up by dendritic cells, the most potent antigen-presenting cells [14, 15, 18]. Besides changing phenotypic and functional properties of dendritic cells [18], metal ions complex with cellular proteins and peptides. In case of titanium, the ions form complexes with phosphorus-containing proteins and peptides (usually signaling molecules), nucleotides (DNA in the nucleus and RNA in the cytoplasm) and lipids (phospholipids of the cellular membranes) [15]. The new antigenic metal-peptides are presented by dendritic cells to specific T-lymphocytes that react and are activated [15]. The dendritic cells and activated T-lymphocytes accumulate in tissues with high metal concentrations, usually close to the metal implant, and form inflammatory reactions [7] that include secretion of inflammatory cytokines, such as TNF- α , TGF- β , interleukin-6 and interleukin-1 β [19]. Most important is secretion of RANK-L by the activated T-lymphocytes, an essential factor for maturation, survival and function of osteoclasts [19].

III. CONCLUSIONS

Osteoclasts play a major role in bio-corrosion of orthopedic metal implants. Implant-derived metal ions enhance osteoclastic recruitment, maturation, survival and function. The metal ions also induce a peri-implant inflammation with accumulation of various immune cells. The metal ions form complexes with cellular proteins that become new antigens inducing allergic reactions where T-lymphocytes play an essential role. Those immune cells produce various inflammatory cytokines that cause inflammation and pain. In addition, T-lymphocytes secrete RANK-L, an essential factor for osteoclast functions. Finally, the described mechanisms are probably responsible for a vicious cycle with enhanced peri-implant inflammation and pain, as well as enhanced osteoclastic bio-corrosion and peri-implant bone resorption culminating in implant loosening (Figure 3).

The reason why some patients react but others do not enter the vicious cycle is still not known and has to be the focus of future studies.

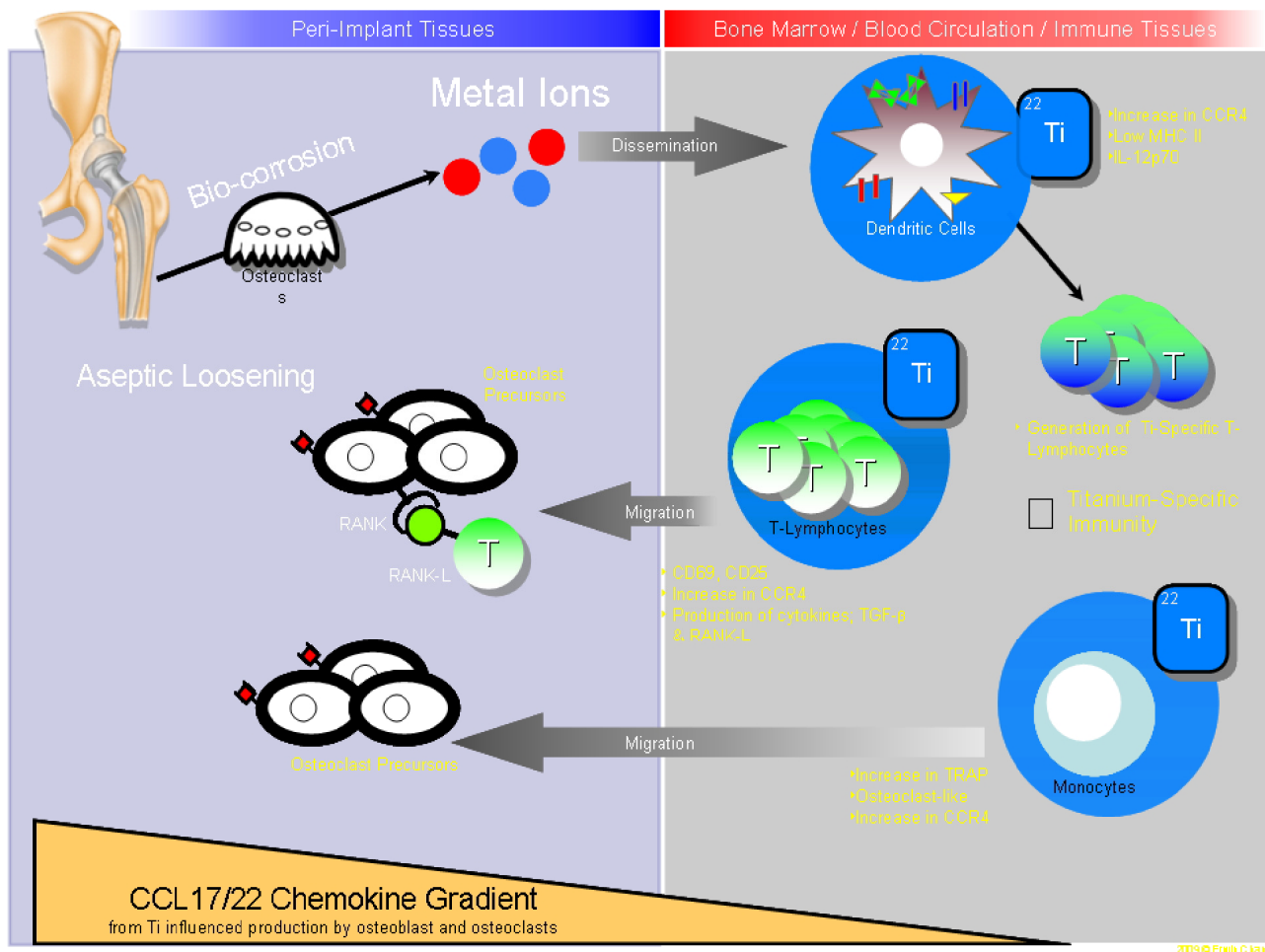


Fig. 3 Schematic summary

ACKNOWLEDGMENT

We acknowledge the facilities, scientific and technical as-sistance of the Australian Microscopy & Microanalysis Research Facility at the Centre for Microscopy, Characterisation & Analysis, The University of Western Australia, a facility funded by The University, State and Commonwealth Governments. This work was supported by National Institutes of Health Grant GM072726 and the AO Foundation Grant 05Z34Format the Acknowledgment and References headlines without numbering.

REFERENCES

The list of References should only include papers that are cited in the text and that have been published or accepted for publication. Citations in the text should be identified by numbers in square brackets and the list of references at the

end of the paper should be numbered according to the order of appearance in the text. Examples of citations for Journal articles [1], books [2], the Digital Object Identifier (DOI) of the cited literature (which should be added at the end of the reference in question if available) [3], Proceedings papers [4] and electronic publications [5].

Cited papers that have been accepted for publication should be included in the list of references with the name of the journal and marked as ‘in press’. The author is responsible for the accuracy of the references. Journal titles should be abbreviated according to Engineering Index Inc. References with correct punctuation.

1. Smith J, Jones M Jr, Houghton L et al. (1999) Future of health insurance. *N Engl J Med* 965:325–329
2. South J, Blass B (2001) *The future of modern genomics*. Blackwell, London
3. Smith J, Jones M Jr, Houghton L et al (1999) Future of health insurance. *N Engl J Med* 965:325–329 DOI 10.1007/s002149800025
4. Lock I, Jerov M, Scovith S (2003) Future of modeling and simulation, IFMBE Proc. vol. 4, World Congress on Med. Phys. & Biomed. Eng., Sydney, Australia, 2003, pp 789–792

5. IFMBE at <http://www.ifmbe.org>
 6. Tezer M, Kuzgun U, Hamzaoglu A et al. (2005) Intraspinal metaloma resulting in spinal paraparesis. *Arch Orthop Trauma Surg* 25: 417-421
 7. G Voggenreiter, S Leiting, H Brauer et al. (2003) Immunoinflammatory tissue reaction to stainless-steel and titanium plates used for internal fixation of long bones. *Biomaterials* 24:247-54
 8. Filgueira L (2004) Fluorescence-based staining for tartrate-resistant acidic phosphatase (TRAP) in osteoclasts combined with other fluorescent dyes and protocols. *J Histochem Cytochem* 52:411-414
 9. Meagher J, Zellweger R, Filgueira L (2005) Functional dissociation of the basolateral transcytotic compartment from the apical phagolysosomal compartment in human osteoclasts. *J Histochem Cytochem* 53:665-670
 10. Cadosch D, Chan E, Gautschi OP et al. (2009). Bio-corrosion of stainless steel by osteoclasts - In Vitro evidence. *J Orthop Res* 27:841-846
 11. Vaananen HK, Laitala-Leinonen T (2008) Osteoclast lineage and function. *Arch Biochem Biophys* 473:132-138
 12. Kajiya H, Okamoto F, Fukushima H et al. (2003) Calcitonin inhibits proton extrusion in resorbing rat osteoclasts via protein kinase A. *Pflugers Arch - Eur J Physiol* 445:651-658
 13. Salo J, Lehenkari P, Mulari M et al. (1997) Removal of osteoclast bone resorption products by transcytosis. *Science* 296:270-273
 14. Cadosch D, Meagher J, Gautschi OP et al. (2009) Uptake and intracellular distribution of various metal ions in human monocyte-derived dendritic cells detected Newport Green DCF diacetate ester. *J Neurosci Meth* 178:182-187.
 15. Chan E, Mhawi A, Clode P et al. (2009) Effects of Ti(IV) ions on human monocyte-derived dendritic cells. *Metallomics* 1:166-174
 16. Cadosch D, Chan E, Gautschi OP et al. (2009) Titanium IV ions induced human osteoclast differentiation and enhanced bone resorption in vitro. *J Biomed Mat Res* 91A:29-36
 17. Cadosch D, Chan E, Gautschi O et al. (2009) Titanium induced production of chemokine CCL17/TARC and CCL22/MDC in human osteoclasts and osteoblasts. *J Biomed Mat* in press DOI 10.1002/jbm.a.32390
 18. Chan E, Filgueira L (2009) Effect of vanadium on human dendritic cells. *Toxicol Environ Chem* in press
 19. Cadosch D, Sutanto M, Chan M (2009) Titanium Uptake, Induction of RANK-L Expression and Enhanced Proliferation of Human T-Lymphocytes. *J Orthop Res* in press DOI 10.1002/jor.21013
- Author: Luis Filgueira
Institute: Anatomy and Human Biology, University of Western Australia Street: 35 Stirling Hwy
City: Crawley, WA 6009 Country: Australia
Email: lfilgueira@anhb.uwa.edu.au

Chitosan Hydrogel as an Immunoisolative Barrier for Xenogeneic Islet Transplantation

K.C. Yang^{1,2}, Z. Qi¹, F.H. Lin^{2,3}, C.C. Wu^{2,4}, and S. Sumi¹

¹ Department of Organ Reconstruction, Institute for Frontier Medical Sciences, Kyoto University, Kyoto, Japan

² Institute of Biomedical Engineering, College of Engineering and College of Medicine, National Taiwan University, Taipei, Taiwan

³ Division of Medical Engineering, National Health Research Institute, Miaoli County, Taiwan

⁴ Department of Orthopedic, En Chu Kong Hospital, Taipei County, Taiwan

Abstract— Chitosan hydrogel was utilized as an immunoisolative barrier to facilitate the xenogeneic islets transplantation without immunosuppression. Rat islets were encapsulated in chitosan hydrogel and transplanted into the renal subcapsular space of diabetic mice. Non-fasting blood glucose level (NFBG), and body weight were recorded perioperatively. Mice were sacrificed at predetermined intervals and kidney transplanted with islets/chitosan hydrogel was retrieved for histologic examination. Results showed that the NFBG of mice transplanted with islets/chitosan hydrogel maintained in the range of 148-242 mg/dl for four weeks with increased body weight. Histologic sections revealed that the islets successfully engrafted at renal subcapsular space with positive insulin staining. This study indicates that the chitosan hydrogel protects encapsulated islets successfully during xenotransplantation.

Keywords— Type 1 diabetes, Xenotransplantation, Immunoisolation, Chitosan Hydrogel, Encapsulation.

I. INTRODUCTION

Pancreatic islet transplantation normalizes the metabolic control of blood glucose to prevent the development of chronic complications is an efficacious treatment for Type 1 diabetes [1]. Although limited donor sources prevent islet transplantation from becoming a major treatment option [2]. Using xenogeneic species as donor sources may solve the problem of an insufficient donor supply [3]. However, xenogeneic islets are subject to immune rejection in humans because of the extensive antigenic differences [4]. Therefore, immune rejection remains a major restriction to xenotransplantation.

Immunoisolation is an efficacious strategy which can facilitate the use of xenogeneic cell source to solve the problem of insufficient donor supply and can minimize or eliminate the need of systemic immunosuppression [5]. Injectable hydrogel is of great interest for cell encapsulation and tissue engineering [6, 7]. Chitosan is the deacetylated product of chitin and is applied in a variety of implantable applications because of its biocompatible and non-immunogenic properties [8, 9]. Chitosan solution with

glycerol 2-phosphate disodium salt hydrate (β -GP) is a thermosensitive material which is liquid in room temperature and gelation as hydrogel at 37 °C [10]. The densely reticulate structure of hydrogel may serve as an immunoisolative barrier to protect the transplanted tissues. Besides, the mass diffusion of small molecules within the hydrogel is fast due to the property of high water content [11]. These characters make the hydrogel as a promising material for immunoisolation.

In this study, a streptozotocin induced diabetic mouse model was applied to evaluate the feasibility of using chitosan hydrogel as an immunoisolative barrier for xenogeneic islet transplantation without immunosuppression. Our hypothesis was that islets could be protected from the attack of recipient immune system when encapsulated in chitosan hydrogel and the assumption was demonstrated.

II. MATERIALS AND METHODS

Preparation of Chitosan/ β -GP Solution

2.5 % chitosan (417963, Sigma, USA) was solved in 0.1 M acetic acid (017-00256, Wako, Japan), and glycerol 2-phosphate disodium salt hydrate (β -GP, G6251, Sigma, USA) was solved in deionized water (0.8 W/V). The β -GP solution was added into the chitosan solution until the pH value of the mixed solution became 7.4. The chitosan/ β -GP solution was utilized as a carrier in the following study.

Islet Isolation and Evaluation

Wistar rats aged 9-10 weeks were used as donors. The method of islet isolation was as follow. 10 ml of type XI collagenase solution was infused into the common bile duct that was ligated at the hepatic side and before the inflow to the duodenum. Then the collected pancreata were digested for 17 minutes at 37 °C in a water bath. The digested pancreata were filtered by stainless steel mash to separate the islets and were purified by the discontinuous Dextran 70 gradient solution (17-0280-02, Amersham, Sweden). The

harvested islets were cultured overnight in RPMI-1640 medium (31800-089, Gibco, USA) supplemented with 1 % antibiotic-antimycotic solution (15240-062, Gibco, USA) and 10 % fetal bovine serum (12103-78P, JRH, USA) in the incubator set at 5 % CO₂, 37 °C.

Recipient Preparation

C57BL/6 mice, aged 9-10 weeks, weighing between 23-25 grams were used as recipient. Mice were induced to diabetic by single intraperitoneal injection of 190 mg/kg streptozotocin (S0130, Sigma, USA) in the pH=4.5 citrate buffer (09127-61, Nacalai, Japan) 14 days pre-operation. Mice with non-fasting blood glucose concentration (NFBG) higher than 400 mg/dl on two consecutive measurements were chosen as recipients.

Transplantation

The animal study was divided into three groups, the first one was normal mice (Normal mice group, n=6); the second group was diabetic mice transplanted with naked islets (Naked islets group, n=6); the third group was diabetic mice transplanted with chitosan/β-GP solution containing islets (Islets/hydrogel group, n=6). For the second and third group, after adequate skin preparation and sterilization, the back of mouse was opened by scissors and the left kidney was exposed. For the second group, 500 islets were suspended in 30 μl of phosphate buffered saline and transplanted into the renal subcapsular space. For the third group, 500 islets were suspended in 30 μl of chitosan/β-GP solution and transplanted.

The NFBG and body weights of mice were recorded perioperatively.

Histologic Examinations

The kidney transplanted with naked islets or islets/chitosan hydrogel was removed for histologic examinations. Sections were stained for hematoxylin and eosin. For the immunohistochemical staining, sections were stained with primary anti-insulin antibody and further counterstained with the hematoxylin.

Statistical Analysis

Data was expressed as mean ± standard error of the mean (SEM) and analyzed by One-way ANOVA. Differences were considered significant if *p*-values were less than 0.05.

III. RESULTS

ANIMAL STUDY

The NFBG of Naked islets group was decreased from 472±34 to 163±40 mg/dl post-operation and maintained in the level of 160-300 mg/dl for 7 days; then it increased to 449±126 mg/dl on day 14 and returned to hyperglycemia thereafter (Fig. 1). The NFBG of Islets/hydrogel group was decreased from 487±56 to 148±32 mg/dl and maintained in the 150-250 mg/dl range for four weeks with significant difference (*p*<0.05) in comparison to the Naked islets group.

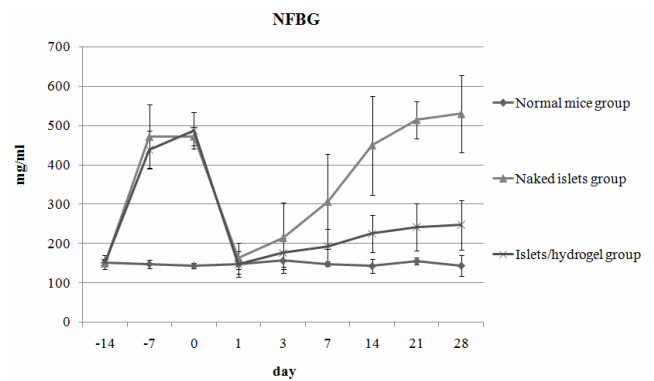


Fig. 1 Diabetes was induced in mice on day -14. Mice were transplanted with naked islets or islets/chitosan hydrogel on day 0. NFBG of Naked islets group was significantly higher than that of Islets/chitosan hydrogel group (*p*<0.01)

The changes in body weights are shown in Fig. 2. The body weights of Naked islets group decreased from 24.3±1.4 to 18.7±1.2 g. The body weights of Islets/hydrogel group increased progressively from 21.8±1.3 to 24.8±1.0 g which were significantly higher than that of Naked mice group (*p*<0.05).

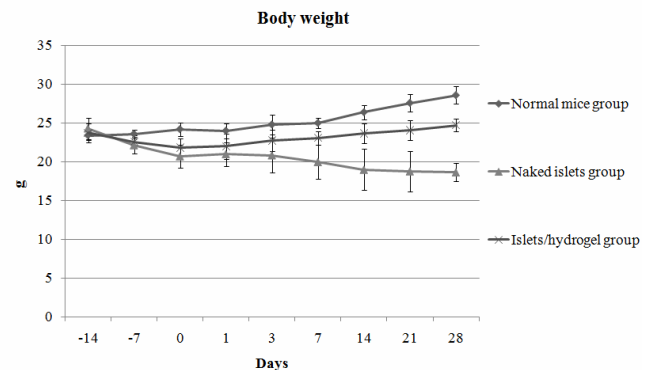


Fig. 2 Body weights of Naked islets group were significantly lower than that of Islets/chitosan hydrogel group (*p*<0.01)

Histologic Examination

The histologic sections of islets/hydrogel group reveal that the islets were located at the renal subcapsule space of mouse (Fig. 3, H&E, 40X). The immunohistochemical staining shows the islets had sufficient insulin production.

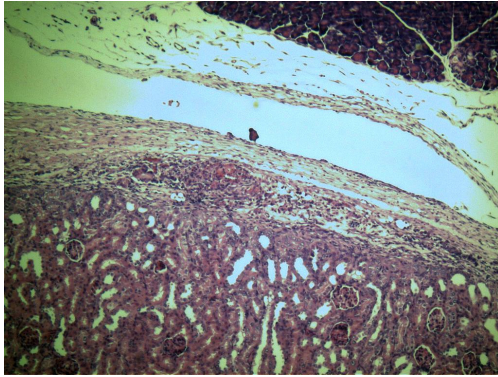


Fig. 3 Histologic section of islets/hydrogel group reveals that the islets grafted at the renal subcapsule space of mouse (H&E, 40X)

IV. DISCUSSIONS

The feasibility of use chitosan hydrogel as an immunoisulative barrier for xenogeneic islet transplantation without immunosuppression is demonstrated in this study. The NFBG of mice transplanted with naked islets decreased to euglycemia and maintained for 7 days (Fig. 1). However, the NFBG returned to hyperglycemia thereafter that attributed to the grafts rejection. The NFBG of mice transplanted with islets/hydrogel decreased from 487 ± 56 to 148 ± 32 mg/dl one day post-operation indicating the transplanted islets with hydrogel quickly released insulin into diabetic mice. The NFBG maintained in 150-250 mg/dl range for four weeks proving the continuous function of transplanted islets. These results indicate that chitosan hydrogel can protect the islets from the recipient's immune system efficaciously [12].

Body weight is also an important indicator for type 1 diabetes [13]. The body weight of diabetic mice transplanted with islets encapsulated in chitosan hydrogel increased from 21.8 ± 1.3 to 24.8 ± 1.0 g in 4 weeks. On the contrary, that of mice transplanted with naked islets decreased continuously in a similar fashion of the diabetic mice without any treatment ($p > 0.05$) (Fig. 2). Increased body weight indicates recovery of the blood glucose metabolism of diabetic mice.

Fig. 3 shows the histologic section of kidney retrieved from mouse that transplanted with chitosan hydrogel contained islets four weeks post-operatively. The section reveals that the islets were located at the renal subcapsular space; the transplanted islets were well-granulated with

insulin production. These histologic findings indicate that islets successfully engrafted at renal subcapsular space and that the chitosan hydrogel protects the transplanted xenogeneic islets from the cellular immunity successfully.

In conclusion, this study demonstrates that the injectable chitosan hydrogel can be applied in islet transplantation since islets encapsulated in hydrogel and transplanted into the renal subcapsular space are able to survive and function for 4 weeks. Moreover, the body weights and serum insulin level of mice transplanted with islet/hydrogel were better than those of mice transplanted with naked islets. We believe some further investigation of the longevity of transplanted islets should be demonstrated may provide a new treatment for type 1 diabetes in the future.

REFERENCES

1. Merani S, Shapiro AM. (2006) Current status of pancreatic islet transplantation. *Clin Sci* 110(6):611.
2. Galandiuk S, Sterioff S. (2005) The problems of organ donor shortage. *Mayo Clin Proc* 80(3):320.
3. MacKenzie DA, Hullett DA, Sollinger HW. (2003) Xenogeneic transplantation of porcine islets: an overview. *Transplantation* 76(6):887.
4. Tonomura N, Shimizu A, Wang S, et al. (2008) Pig islet xenograft rejection in a mouse model with an established human immune system. *Xeno* 15(2):129.
5. Narang AS, Mahato RI. (2006) Biological and biomaterial approaches for improved islet transplantation. *Pharmacol Rev* 58(2):194.
6. Giuseppe M, Jean-Christophe L, Jacques D, et al. (2002) Biocompatibility of thermosensitive chitosan-based hydrogels: an in vivo experimental approach to injectable biomaterials. *Biomaterials* 23:2717.
7. Hong Y, Song H, Gong Y, et al. (2007) Covalently crosslinked chitosan hydrogel: properties of in vitro degradation and chondrocyte encapsulation. *Acta Biomater* 3(1):23.
8. Khor E, Lim LY. (2003) Implantable applications of chitin and chitosan. *Biomaterials* 24:2339.
9. Berger J, Reist M, Mayer JM, et al. (2004) Structure and interactions in chitosan hydrogels formed by complexation or aggregation for biomedical applications. *European Journal of Pharmaceutics and Biopharmaceutics* 54:35.
10. Berger J, Reist M, Chenite A, et al. (2005) Pseudo-thermosetting chitosan hydrogels for biomedical application. *International Journal of Pharmaceutics* 288:197.
11. Drury JL, Mooney DJ. (2003) Hydrogels for tissue engineering: scaffold design variables and applications. *Biomaterials* 24:4337.
12. Nagata N, Gu Y, Hori H, et al. (2001) Evaluation of insulin secretion of isolated rat islets cultured in extracellular matrix. *Cell Transplantation* 10(4-5):447.
13. Takada J, Machado MA, Peres SB, et al. (2007) Neonatal streptozotocin-induced diabetes mellitus: a model of insulin resistance associated with loss of adipose mass. *Metabolism* 56(7):977.

Corresponding author:

Author: Shoichiro Sumi, MD, PhD, Ass. Prof.
 Institute: Department of Organ Reconstruction, Institute for Frontier Medical Sciences, Kyoto University.
 Street: 53 Kawahara-cho, Shogoin, Sakyo-ku
 City: Kyoto, 606-8507
 Country: Japan
 Email: sumi@frontier.kyoto-u.ac.jp

The Method to Encourage Biological Cell Division with Vibration and Circulation Technique Using Optical Manipulating

N. Watanabe and K. Taguchi

Ritsumeikan University, 1-1-1 Nojihigashi, Kusatsu, Shiga, Japan

Abstract— A dual-beam trapping method was proposed and discussed for the three-dimensional optical trapping of a micro-particle. Cycling the two laser beams from optical fiber ends which were shifted a few ($\sim 10 \mu\text{m}$) in horizontal direction, the micro-particle set into an oscillatory circular motion. This method can pick up and circulate a micro-particle against gravity. This micro-particle manipulation and analytical technology can be integrated on a Lab-on-a-Chip device. Generally it is known that mechanical stimulus influences cell growth speed.

Keywords— laser beam effects, optical fiber, optical trapping, axial trapping force, theoretical analysis, refractive index.

I. INTRODUCTION

In the past several years laser trapping has become a useful tool primarily in the fields of biology, physics and engineering. A laser beam from an optical fiber end provides a method of micro-manipulated particles [1], atoms and biological cells without the need of direct physical contact. This cell manipulation and analytical technology can be integrated on a Lab-on-a-Chip device. Generally it is known that mechanical stimulus influences cell growth speed.

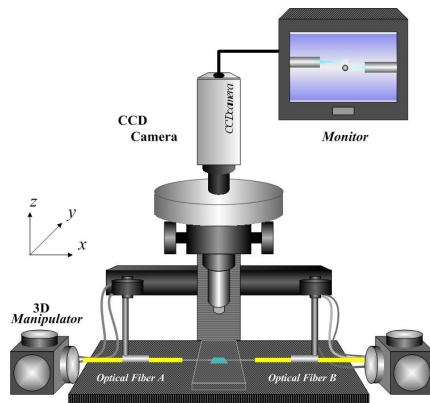


Fig. 1 Experimental setup

We proposed a novel optical circulation technique of a micro-particle using plural optical flat-top fibers, which were mounted horizontally to the bottom of a sample chamber, and verified that an optically trapped micro-particle

could be circulated by controlling laser power emerging from optical fibers without moving optical fibers. We have already demonstrated an optically circulated manipulation system (Fig.1), which was very economical and much simpler to operate micro particles. In this study, we theoretically analyzed the optical forces on a micro-particle. The output of laser light was coupled into an optical fiber, which had an optical connector at the fiber end. The fiber was attached to a xyz manipulator and was inserted horizontally to a micro particle. A microscope with liquid-immersion microscope objective was used to observe the trapped micro-particle and the trapping behavior was recorded on a VTR with a CCD camera. The fiber trap was formed using a temperature stabilized, 1300nm, cw diode laser, pigtailed with single mode fiber having a mode field diameter of $\sim 9.5 \mu\text{m}$. This laser source was chosen because it minimizes absorption effects in biological samples in the near infrared, and it is a readily available opto-electronics component.

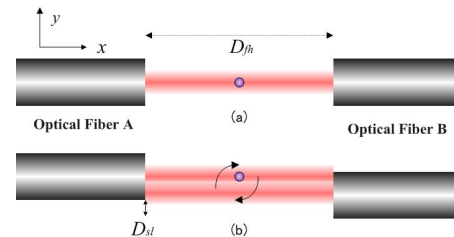


Fig. 2 (a) A dual beam trapping. (b) Optically circulated manipulation

A dual beam trapping method was proposed and discussed for the three-dimensional optical trapping of a micro particle (Fig.2 (a)). A micro-particle was gravitated toward the central beam axis, and was located at the stable point, which was equidistant between the tip of fiber A and the tip of the fiber B, below the beam axis. Our proposed optical manipulation technique was optically circulating a micro-particle to cycle two laser irradiations that was emerging from optical fiber A and optical fiber B. These optical fibers were shifted a few in horizontal direction (Fig.2(b)). A micro-particle was circulated in synchronization with the change cycle of two laser irradiations using an optical switch controlled by personal computer. The authors have examined the circular motion of a micro-particle changing

the output power of laser irradiations and the switching time of two laser irradiations.

We attempted to make a micro-particle into a continuous circular motion using the laser beams from plural optical fibers, which were mounted horizontally to a sample as shown in Fig. 1.

II. RESULT AND DISCUSSION

We calculated the optical forces on a particle by the laser beams from optical fiber end using a formulation based on the ray optics approximation analysis. For all calculations, it was assumed that the optical fiber inserted horizontally to a sample cell. In addition, only laser beam with Gaussian intensity profiles were considered. In this study, we theoretically analyzed the optical forces exerted on a micro-particle by each laser beam from plural optical fiber ends.

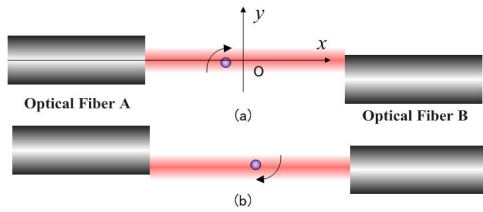


Fig. 3 (a) Laser beam was emitted from optical fiber A. (b) Laser beam was emitted from optical fiber B

Point O shown in Fig. 3 represents the point which was equidistant between the tips of optical fiber A and optical fiber B on the beam which was emerging from fiber A. The horizontal distance D_{fh} between the each tip of the optical fiber A and B was changed as shown in Fig.2.

In Fig. 3(a) the particle is trapped on the beam axis of the laser beam that was emitted from optical fiber A. On the beam axis, the total y-directed optical forces act on the micro-particle were precisely balanced and the micro-particle was pushed towards +x-direction. The difference between the x-directed and y-directed moving velocity can be understood by considering the difference of the optical forces acting on a micro-particle.

When the micro-particle is irradiated the laser from optical fiber B on the +y-side of the beam axis B, the micro-particle was pushed towards the beam axis B by the attracting force. For a micro-particle located on the beam axis B, it is pushed towards the -x-direction by the optical force.

We calculated theoretically the optical trapping force based on geometrical optics [3]. The results obtained are valid only for particles with sizes larger than the wavelength of the laser light. The optical trapping force produced by each ray is simply calculated by considering the momentum

change of the ray. The force is represented by the momentum change per unit time. The total force can be obtained by summing the forces calculated for each ray. Mathematical expression (1) and (2) shows the optical force of a single ray of power P incident on a micro-particle's surface at an angle θ . The total force from a single ray can be described by a simple formula and be divided into two components F_x and F_z .

$$F_x = \frac{n_1 P Q_x}{c} \dots(1) \quad F_z = \frac{n_1 P Q_z}{c} \dots(2)$$

n_1 : the refractive index of the surrounding medium, P: ray of power, c: the velocity of light.

Q represents an efficiency factor of the optical trapping.

$$Q_x = 1 + R \cos 2\theta_1 - \frac{T^2 \{ \cos 2(\theta_1 - \theta_2) + R \cos 2\theta_1 \}}{1 + R^2 + 2R \cos 2\theta_2} \dots (3)$$

$$Q_z = R \sin 2\theta_1 - \frac{T^2 \{ \sin 2(\theta_1 - \theta_2) + R \sin 2\theta_1 \}}{1 + R^2 + 2R \cos 2\theta_2} \dots (4)$$

θ_1 : incident angle, θ_2 : refraction angle, R: degree of reflection T: transmission factor.

The total optical force on the sphere is the sum of components expressed by equations (1) and (2) over individual rays of the laser beam.

Cycling the two beams of the optical fiber A and the optical fiber B, the micro-particle settles into an oscillatory circular motion between the beam axis A and beam axis B.

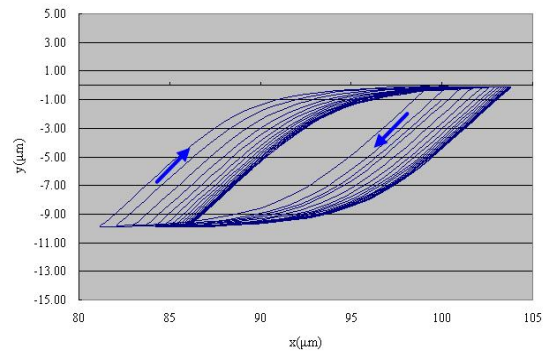


Fig. 4 The dynamic behavior of the particle

We calculated the dynamic behavior modeling of a micro-particle in laser-trapping beams, we pulsed a 20mW laser with a cycle period of 1, 10, 100, 250, 500, 1000 and 1500msec. The beam cycling process started at the laser irradiation from the optical fiber A. The micro-particle is first pushed towards the beam axis A by the attracting force. After a few seconds the micro-particle was circulated between the beam axis A and beam axis B.

The algorithm designed for computing the dynamic behavior of the micro-particle is based on obtaining the particle's next position and orientation given its previous position and orientation, the force and torque currently calculated, and previous velocity components. In computing the next velocity components the acceleration is taken as constant over the time interval dt . Similarly, the velocity is taken as constant over the time interval dt [2]. Based on the new position, the force and torque were recalculated and the displacement process repeated. The process is repeated until the desired dynamic properties are displayed.

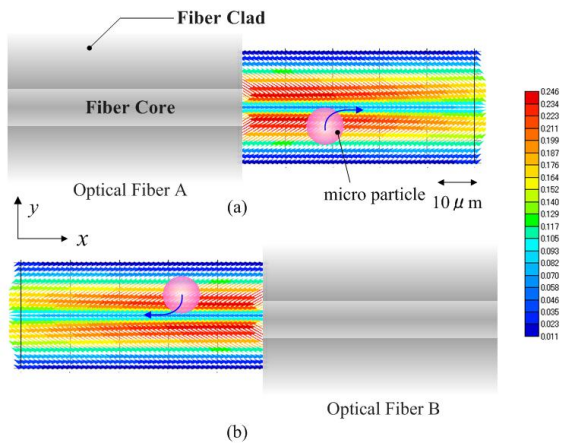


Fig. 5 Calculation results of the relative magnitude and direction of the optical forces on the micro-particle. (a) Laser beam was emitted from optical fiber A. (b) Laser beam was emitted from optical fiber B

Fig.4 shows the dynamic behavior of the particle (refractive index $n=1.59$, radius $r=5\mu\text{m}$, density $p=1.05\text{ g/cm}^3$) in 20mW laser beams with a cycle period of 250msec. In this case, the fiber trap was formed using a temperature stabilized cw diode laser, pigtailed with single-mode fiber.

Fig.5 depicts the calculated relative magnitude and direction of the total forces acting on a micro-particle dispersed in liquid as a function of the position of the particle in the x-y plane. The total forces act on the micro-particle in the direction of the beam axis and the repulsive force on the beam axis. In contrast, during radiate laser beam from the optical fiber B, the optical forces is opposite in sign to it when the micro-particle is radiated the laser beam from the optical fiber A. (Fig.5(b))

For comparison, we analyzed the optical forces acting on a particle along the x axis on beam axis in the case of a dual beam trapping method (Fig.2(a)). The axial (horizontal) optical confinement of particle depends on the value of the horizontal distance D_{fh} between the optical fiber ends. Point

O shown in Fig. 3 represents the point which was equidistant between the tips of optical fiber A and optical fiber B on the beam axis. In this case, the fiber trap was formed using a temperature stabilized cw diode laser in an optical fiber whose end had been cleaved. The optical force acting on a polystyrene particle dispersed in water. Fig.6 shows the axial (horizontal) components of an optical force on a micro-particle. When the horizontal distance $D_{fh} < 140\mu\text{m}$, the micro-particle was trapped, and it located about $140\mu\text{m} < D_{fh}$ the micro-particle was flipped.

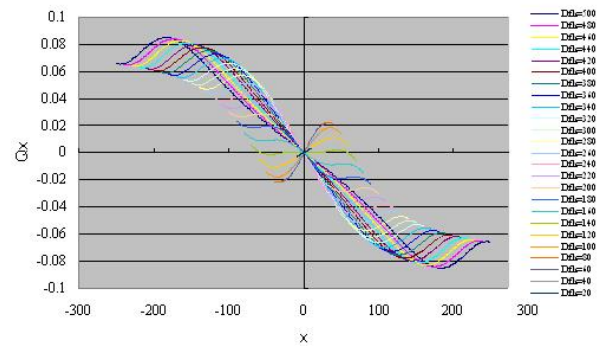


Fig. 6 The optical forces along the x axis using optical cleave fibers

But, the optically circular method can pick up and circulate a micro-particle which is located about $140\mu\text{m} < D_{fh}$ when a particle is flipped in the case of dual beam trapping.

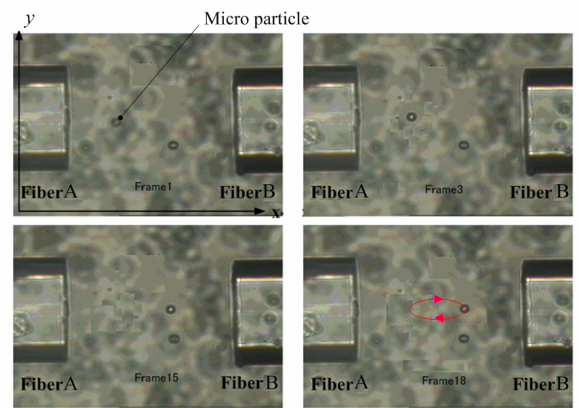


Fig. 7 Experimental results. (Top View)

Fig. 7 shows the experimental results of the optical force acting on a polystyrene particle dispersed in water. The micro-particle was circulated.

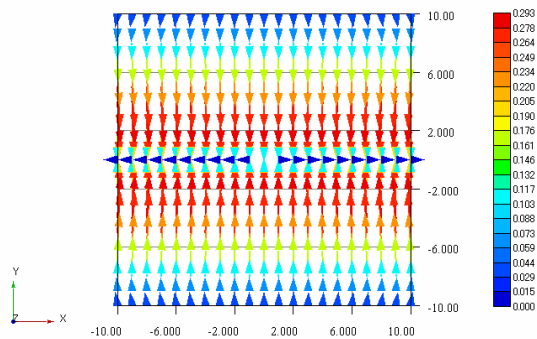


Fig. 8 Calculation results of the relative magnitude and direction of the optical forces on the micro-particle by using a dual beam trapping method on the value of the horizontal distance Dfh was $100 \mu m$

The optical force on a micro particle dispersed in liquid as a function of the position of the particle in the x-y plane (Fig.8). When the value of the horizontal distance Dfh was $100 \mu m$, the micro-particle was flipped in the case of a dual beam trapping method.

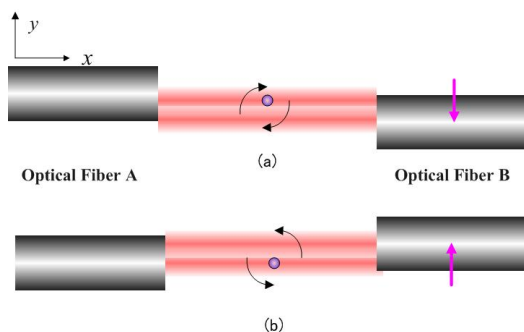


Fig. 9 (a) Optically circulated manipulation. (b) Inverse rotation method

When a micro-particle was irradiated using to cycle two lasers that was emitted from optical fiber A and optical fiber B which was shifted a few in -y-direction (Fig. 9 (a)), a micro-particle circulated in a clockwise direction. When the optical fiber B was shifted a few in +y-direction (Fig.9 (b)), the micro-particle circulated in inverse rotation. Fig.10 shows the dynamic behavior of the particle in 20mW laser beams with a cycle period of 250msec.

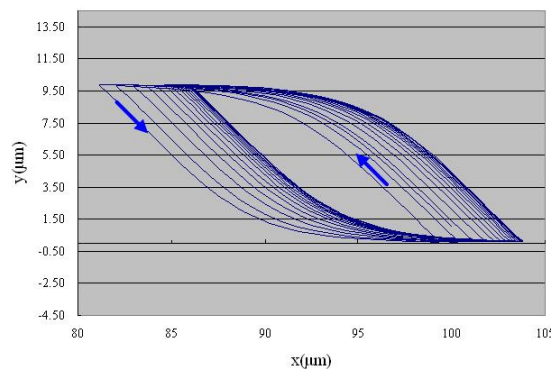


Fig. 10 The dynamic behavior of the particle using inverse rotation method (Fig.9 (b))

III. CONCLUSIONS

This technique could easily levitate and vibrate a micro particle against gravity. Our fiber trap system was formed using a temperature stabilized cw diode laser and single-mode fibers. Laser beam was changed every ΔT using an optical switch. The horizontal distance Dfh between the tips of optical fiber A and optical fiber B was set as $190 \mu m$. From theoretical results, the micro-particle vibrated on displacement amplitude $9.6 \mu m$ when the micro-particle was irradiated the laser beam at 20mW, switching time ΔT was 100msec. A manipulated micro particle was circulated when one's fiber displaced several micrometers in a horizontal direction. And the micro-particle was circulated in the opposite direction when one's fiber displaced in the other direction. From these theoretical results, we verified that our proposed optical manipulation technique was useful for the manipulation of biological cells.

REFERENCES

- [1] Kozo Taguchi, Kentaro Atsuta Takeshi Nakata Masahiro Ikeda "A Possible Manipulation of a Biological Cell by a Laser Beam Focused Through Optical Fiber" IEICE TRANS ELECTRON., Vol.E83-C, No.4 pp.664-667, April (2000)
- [2] Robert C. Gauthier and Mike Ashman, "Simulated Dynamic Behavior of Single and Multiple Spheres in the Trap Region of Focused Laser Beams" APPLIED OPTICS. pp. 6421-6431 (1998)
- [3] S.Sato H. Inaba, "Optical Trapping and Manipulation of Microscopic Particles and Biological Cells by Laser Beams" Optical and Quantum Electronics 28 pp.1-16(1996)

Adaptive Cross-Point Regions for Lossless Images Compression

T.T. Dang¹, T.D. Vu¹, and T.P. Vo²

¹ Hochiminh city University of Technology, Hochiminh city, Vietnam

² Tonducthang University, Hochiminh city, Vietnam

Abstract— This paper presents ACRIC (Adaptive Cross-point Regions for lossless Image Compression), a scheme for losslessly encoding and decoding images, especially medical images. Developed from the scheme ACRIC (Cross-point Regions for lossless Image Compression), ACRIC gives new ideas to build adaptive cross-point regions without using their fixed lengths. Based on the effect of Gray coding on cross points which have grey values around grey levels 2^n , the data bits of cross points trend to same states in cross-point regions after Gray coding, so we can optimize the probability of cross points for the step of modeling in the process of entropy coding.

Keywords— Cross point, entire cross point region, ideal cross point region, bit plane decomposition, entropy coding.

I. INTRODUCTION

This paper is based on the ideas of papers [1], [2]. It presents the effect of Gray coding on the process of calculating the probability of bits in cross point regions.

Cross points are neighbor points around the points of grey levels 2^n , and they are easily specified by [3]. The original data points whose values are less than 2^n have bit states much different from those of the data points greater than or equal to 2^n [4], [5]. The change of bit states for Gray code transformation has been studied by many authors [6]-[8], and the number of bits and the distribution of these bits of Gray codes in the regions of cross points are mentioned in [1], [2]. The real data are arbitrary, so the change of bit states is systematically developed in the form of probability of data bits in cross-point regions before and after Gray coding.

This paper has seven sections. After this introduction, Section II mentions the definition of cross-point regions and the propositions about characteristics of Gray codes of cross points. The area of cross point regions is in Section III. The change of the probability of bits in cross point regions is presented in Section IV. Section V introduces the scheme ACRIC (Cross-point Regions for Lossless Image Compression). In Section VI, some of our results obtained from using the above theory are presented. Section VII contains the conclusion and the scope for future research.

II. GRAY CODING AND ITS EFFECT ON CROSS POINTS

DEFINITION 2.1. For a set of integers from 0 to $(2^N - 1)$, where N is a positive integer representing bit length, the region of cross points $2^n A(n)$, with n from 1 to $(N - 1)$, is a set of maximally 2^n data points along the direction of encoding around the only value of 2^n , consisting of 2^{n-1} forward data points $A_f(n)$ and 2^{n-1} backward data points $A_g(n)$ (including the point of 2^n if it exists). The value 2^n is called the boundary of these two parts.

If the region of cross points A contains 2^n points with contiguous values, the least significant bits always represent the difference of these values. For example, when $n = 3$ the region $A(3)$ consists of the values 4, 5, 6, 7, 8, 9, 10, 11; the value $8 = 2^3 (= 2^n)$ is called the boundary of two small regions $A_f(3) = \{4, 5, 6, 7\}$ and $A_g(3) = \{8, 9, 10, 11\}$. In this case the boundary 2^n exists explicitly.

These cross-point regions $A(n)$ are called the *entire cross-point regions* (ECRs) to distinguish them from the *ideal cross point regions* (ICRs) in Definition 2.2.

PROPOSITION 2.1. For a data string of adjacent values from 0 to $(2^N - 1)$, where N is a positive integer representing bit length, let n be the exponent of the boundary value 2^n in the region of cross point $A(n)$, where n is from 1 to $(N - 1)$. Bits of Gray codes in the backward region $A_g(n)$ on the bit plane $n - 1$ are 1. This region $A_g(n)$ contains 2^{n-1} 1 bits; therefore, the region $A(n)$ on bit plane $n - 1$ contains 2^n 1 bits.

Proof of Proposition 2.1.

According to Definition 2.1, with a value of n in the interval 1 to $(N - 1)$, 2^{n-1} data points in the region $A_f(n)$, from $2^{n-1}, \dots, 2^n - 1$ are expanded under the form of a polynomial of radix 2 as the following:

$$0.2^{N-1} + \dots + 0.2^n + 1.2^{n-1} + x.2^{n-1} + \dots + x.2^0. \quad (1)$$

The 2^{n-1} data points in the region $A_g(n)$, from $2^n, \dots, 2^n + 2^{n-1} - 1$ are expanded by the following polynomial:

$$0.2^{N-1} + \dots + 0.2^{n+1} + 1.2^n + 0.2^{n-1} + x.2^{n-2} + \dots + x.2^0, \quad (2)$$

where x is 1 bit or 0 bit.

After Gray code transformation, (1) and (2) become (3) and (4), respectively:

$$0.2^{N-1} + \dots + 0.2^n + 1.2^{n-1} + x.2^{n-2} + \dots + x.2^0, \quad (3)$$

$$0.2^{N-1} + \dots + 0.2^{n+1} + 1.2^n + 1.2^{n-1} + x.2^{n-2} + \dots + x.2^0. \quad (4)$$

Equation (4) shows that the region $A_g(n)$ on bit plane $n - 1$ contains 2^{n-1} 1 bits. From (3), we can see a similarity to the region $A_l(n)$. By combining (3) and (4), the region $A(n)$ on the bit plane $n - 1$ contains 2^n 1 bits.

For example, when $n = 3$, $A(3) = \{4, 5, 6, 7, 8, 9, 10, 11\}$, $A_l(3) = \{4, 5, 6, 7\}$ and $A_g(3) = \{8, 9, 10, 11\}$. In the region $A(3)$ the decimal values from 4 to 11 have 1 bits on the bit plane 2 ($= 3 - 1$) in the form of Gray codes.

According to this proposition and the characteristic of real images, after Gray coding the probability of 1 bit is larger than the probability of 0 bit in $A(n)$ s and also larger than the probability of 1 bit being outside $A(n)$ s on the same bit plane.

In practice, we usually get $A(n)$ s with the width smaller than 2^n data points, because we want to get 1 bits as much as possible in the area for smaller sizes of cross point map. This leads to ECRs with adaptive widths when they are applied on real data.

DEFINITION 2.2. *Let the positive integer N be the bit length of data points. The region of cross points $A_o(n)$, with n from 1 to $(N - 1)$, is a set of data points whose grey values are from $(2^n - 2^{n-1})$ to $(2^n + 2^{n-1} - 1)$. The point of grey value 2^n (if it exists) is called the center point of the cross point region, and the grey value 2^n is called the central value. These regions are the ICRs.*

By Definition 2.2, data points in ICRs have grey values that satisfy the rule

$$V_A(n) = \{2^n - 2^{n-1}, \dots, 2^n + 2^{n-1} - 1\}, \quad (5)$$

and the ECRs contain the ICRs in real data. We will see that in this scheme for lossless image compression, the position of ICRs determine ECRs by identifying center points 2^n with cross points around the center 2^n .

PROPOSITION 2.2. *Let n be the exponent of the central value 2^n in the ICR $A_o(n)$, where n is from 1 to $(N - 1)$ and N is a positive integer representing bit length. Bits of Gray codes in the ICR $A_o(n)$ on the bit plane $n - 1$ are 1 bits.*

Proof of Proposition 2.2.

According to Definition 2.2, and Proposition 2.1, with a value of n in the interval 1 to $(N - 1)$, grey values of data points in the region $A_o(n)$ are from $(2^n - 2^{n-1})$ to $(2^n + 2^{n-1} - 1)$, so they may be expanded under the form of polynomials of radix 2 (1) and/or (2).

After Gray code transformation, (1) and (2) become (3) and (4) respectively. Both (3) and (4) always give 1 bits on the bit plane $n - 1$. This is very good for compressing real data because the probability of 1 bit in ICRs is 1, and the probability of 0 bit in ICRs is 0. This fact plays an important role in optimizing the probability of a data bit in ECRs.

III. AREA OF CROSS POINT REGIONS

To reduce the size of cross point map, we define the areas of cross point regions which are actually two dimensional sets of cross point regions. The following definition is about the area of cross point regions mentioned.

DEFINITION 3.1. *The area of cross point regions $AR(n)$ is a rectangle consisting of cross point regions so that the number of cross points in the area is maximal.*

By this definition, there are many cross point regions in the area $AR(n)$ but they may be incomplete, that means these cross point regions may not consist of enough 2^n cross points of A type. There will be some data points which don't satisfy the property of entire cross point regions but in the area of cross point regions because of the random distribution of data. This has some effect on our scheme of lossless image compression. Instead of using cross point regions on each line to optimize the probability we take areas of cross point regions on the bit planes $n - 1$.

IV. PROBABILITY OF DATA BITS IN CROSS POINT REGIONS

A. Probability of Data Bits

Define $P^A(b_{ij}^l | f_k(i, j, l))$ as the conditional probability of 1 bit ($b_{ij}^l = 1$) and 0 bit ($b_{ij}^l = 0$) in row i , column j on the bit plane l being encoded, in accordance with Proposition 2.1, where l is the significant number of the bit plane and is equal to $n - 1$. These probabilities present the k th-order estimate [9] of the image, where the function $f_k(i, j, l)$ is a set of previous neighbor bits:

$$f_k(i, j, l) = \{b_{uv}^m | (m > l, \forall u, \forall v) \cup (m = l, u < i, \forall v) \cup (m = l, u = i, v < j)\}. \quad (6)$$

The subscript k in $f_k(i, j, l)$ presents the k th-order estimate, so the number of bits b_{uv}^m in the set $f_k(i, j, l)$ is $k - 1$; their order is defined beforehand.

Define $P_{CR}^A(b_{ij}^l | f_k(i, j, l))$ as the probabilities of 1 bit ($b_{ij}^l = 1$) and 0 bit ($b_{ij}^l = 0$) in a cross point region \mathcal{A} . The term α is a real value in the range of $[0, 1)$. The probability of data bits in a specific cross point region can be changed by the following rule without affecting the coding and decoding processes [10], [11]:

$$P_{CR}^A(b_{ij}^l = 1 | f_k(i, j, l)) = P^A(b_{ij}^l = 1 | f_k(i, j, l)) + \alpha \cdot P^A(b_{ij}^l = 0 | f_k(i, j, l)), \quad (7)$$

$$P_{CR}^A(b_{ij}^l = 0 | f_k(i, j, l)) = P^A(b_{ij}^l = 0 | f_k(i, j, l)) - \alpha \cdot P^A(b_{ij}^l = 0 | f_k(i, j, l)). \quad (8)$$

The value α can be obtained by averaging the Hamming distances of data bits in cross point regions before and after Gray coding.

B. Hamming Distance in Calculating Factors α

According to Definition 2.1 and 2.2, we call the ECR i of A type on the bit plane l ECR(i, l), and similarly for ICR(i, l). Let h_i be the Hamming distance between bits before and after Gray coding in ECR(i, l), and let w_i be the width of that cross-point region, $w_i \leq 2^n$. By definition, $h_i \in [0, w_i]$. The value h_i is the quantity of bit states that are changed. From Proposition 2.1 and 2.2 these bits tend to the same states, i.e. 1 bits, but maybe there are some 0 bits in this Hamming distance in ECR(i, l) after Gray coding, we call the quantity of these 0 bits r_i . This increases the probability of 1 bits, $P_{CR}^A(1|\dots)$, and decreases the probability of 0 bits, $P_{CR}^A(0|\dots)$ in the ECR(i, l) that includes the region ICR(i, l). A larger value of h_i corresponds to a larger probability of 1 bits in that ECR. Therefore, the values α_i are a standardization of the values h_i .

The value of α_i for optimizing the probability of bits in ECR(i, l) is defined by

$$\alpha_i = \frac{h_i - r_i}{w_i}. \quad (9)$$

The value of α_{AR} in the area of cross point regions on the bit plane l being encoded is determined by

$$\alpha_{AR} = \max(\alpha_1, \alpha_2, \dots, \alpha_M), \quad (10)$$

where M is the number of entire cross points regions in the area $AR(n)$ being estimated.

The final value of α , $\alpha(l)$, on the bit plane l being encoded is a rule F that assigns the value $\alpha(l)$ based on values α_{AR} . In a general form it is

$$\alpha(l) = F_\alpha \{ \alpha_{AR1}, \alpha_{AR2}, \dots, \alpha_{ARb}, \dots, \alpha_{ART(l)} \}, \quad (11)$$

where $T(l)$ is the number of areas of cross point regions of A type on the bit plane l that are determined by the algorithm of comparison [3]. The rule F_α determines the value $\alpha(l)$ and is proposed as

$$\alpha(l) = \frac{\sum_{i=1}^{T(l)} \alpha_{ARi}}{T(l)}. \quad (12)$$

In accordance with Definitions 2.1 and 2.2, there are $N-2$ values of $\alpha(l)$, where N is the bit length for representing pixels of images, l is the number of bit plane being processed, and $l = n - 1$, where n is the exponent of the boundary value. The set of $\alpha(l)$ s is

$$S_\alpha^l = \{ \alpha(l) \mid 1 \leq l \leq N-2 \} \\ = \{ \alpha(1), \alpha(2), \dots, \alpha(N-2) \}. \quad (13)$$

The set S_α^l can be called S_α for short.

V. THE ACRIC SCHEME FOR LOSSLESS IMAGE COMPRESSION

Figure 1 presents a broad overview of the ACRIC scheme. Each step is numbered according to the sequence of the scheme, so we have 7 steps from 1 to 7. Step 1 (cross-point regions) looks for areas of cross point regions where we can optimize the probability of data bits. These areas of regions are coarsely found because step 5 (cross-point regions) will identify exactly the regions in the area where the probabilities of data bits need to be optimized by calculating factors α . Some cross-point regions satisfying step 1 but not satisfying step 5 will be canceled. Step 2 (Gray coding) carries out Gray code transformation over the original data. After that, Step 3 (Coarse probabilities) computes the probabilities of data bits with k th-order estimates. Step 4 computes the factors α . Step 5 evaluates cross-point regions. Step 5 will cancel entire cross-point regions that are not good at the encoding process; these ECRs contain very small ICRs. Step 6 optimizes probabilities of data bits in ECRs. The process of encoding at Step 7 (coding) uses Jones' algorithm [10]; it will give us the data, a compressed image.

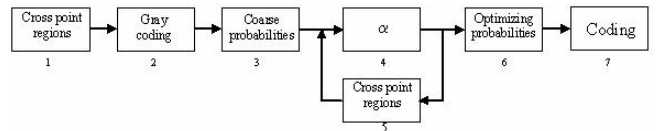


Fig. 1 The ACRIC scheme with the theory of cross-point regions for lossless image compression

Table 1 Experimental results of lossless image compression with ACRIC

Image	Size	ACRIC	AES (WinRAR 3.40) [13]	JPEG 2000 [14]
COUPLE	512 x 512	1.655 : 1	1.427 : 1	1.513 : 1
LENA	512 x 512	1.707 : 1	1.567 : 1	1.752 : 1 *
ZELDA	256 x 256	1.868 : 1	1.511 : 1	1.603 : 1
FROG	621 x 498	1.648 : 1	2.121 : 1 *	1.217 : 1
MOUNTAIN	640 x 480	1.496 : 1	1.520 : 1 *	1.177 : 1
MANDRILL	512 x 512	1.253 : 1	1.206 : 1	1.291 : 1 *

* These results are better than those of ACRIC.

VI. EXPERIMENTAL RESULTS

Table 1 presents results for images compressed by the scheme ACRIC. The compression ratio used here is the ratio between files of images, i.e. including the headers of the original image and the compressed image. With these results we can see that ACRIC is good for images that have many similar grey levels, especially medical images containing backgrounds with few different grey levels. These results are also better than those in [12], which compressed only medical images.

The algorithm for ACRIC uses $k = 4$, so there are 3 neighbor bits of the bit being coded. These are chosen beforehand. From the results in Table 1 we can see that when using ACRIC to losslessly compress images (Couple, Lena, Zelda, Frog, Mountain, Mandrill), we can obtain higher compression ratios than other schemes (AES, JPEG 2000). For images whose grey levels change a great deal in cross point regions, like Mandrill, ACRIC may give better or worse results than other methods, depending on the analyses of each method.

The encoding process here uses Jones' method [10]. This algorithm is like arithmetic coding but uses integers in the processing. At this point the program can process 8-bit grey images of bitmap file format. The restored images must be identical to the original images.

VII. CONCLUSION

The encoding scheme ACRIC and some results were presented to illustrate the use of the theory of cross-point regions to optimize the probabilities of data bits in those regions. Generally, the scheme ACRIC is a process of entropy coding. It includes two parts: modeling and coding. The cross-point region theory can be used in the first part in order to reduce interpixel redundancy; the second part uses Jones' method to reduce coding redundancy.

The basic concepts were introduced in [1], [2], which are now the foundation for the theory of optimizing probabilities of cross points with the new concept of ideal cross-point

regions. A meaningful improvement in compression ratio has been obtained, compared to other authors' methods. From this mathematically sound foundation, the problem of improving the compression ratio of image processing and transmission can be developed further in the future.

REFERENCES

1. D. T. Tin, V. D. Thanh, N. K. Sach (2004) Effect of Gray codes on data areas around cross points. Vietnamese journal of science and technology, vol 42, No 2, 2004, pp 21-26
2. D. T. Tin, V. D. Thanh, N. K. Sach, S. Higuchi (2004) Effect of Gray coding on the State and the Distribution of data bits in cross point regions. ICCEA Proc., Beijing, China, 2004, pp. 553 – 556
3. D. T. Tin (2004) Effect of Gray codes on data areas around cross points. The 2nd report of Doctor thesis, HCMUT, Vietnam, 2004.
4. C. J. Lu, S. C. Tsai (2001) A note on iterating an α -ary Gray code. SIAM J. Discrete Math vol 14, No 2, 2001, pp. 237-239
5. N. K. Sach (1997) Digital Images and video processing. Science and Technology Publisher, Vietnam
6. M. C. E (1984) On generating the N-ary reflected Gray codes. IEEE Transactions on computers, vol 33, 1984, pp. 739-741
7. W. Gilbert (1984) A cube-filling Hilbert curve. Math Intell, vol.6, 1984, pp 78-81.
8. M. B. Squire (2001) Gray codes and Efficient Generation of Combinatorial Structures. Ph.D. dissertation, Department of Computer Science, North Carolina State University, 2001
9. R. C. Gonzalez, R. E. Woods (2002) Digital Image Processing. Prentice Hall, 2002, pp 438- 440
10. C. B. Jones (1981) Efficient Coding System for Long Source Sequences. IEEE Trans. Inform. Theory, vol 27, No 3, 1981, pp 280-291
11. D. T. Tin, V. D. Thanh, N. K. Sach (2002) An improvement of Jones' method of lossless data compression, Posts and Telecommunications journal, No. 7, 2002, pp 65-69
12. D. T. Tin, S. Higuchi (2001) A lossless coding scheme for image. Medical Imaging and Information sciences journal, Japan, vol.18, No. 2, 2001, pp 75-82
13. Federal information processing standards publication 197 (2001) Announcing the Advanced Encryption Standard. National Institute of Standards and Technology (NIST)
14. T. Acharya, P.-S. Tsai (2005) JPEG2000 Standard for image compression. Wiley

Author: DANG Thanh Tin
 Institute: Hochiminh city University of Technology
 Street: 268 Lythuongkiet
 City: Hochiminh city
 Country: Vietnam
 Email: dttin@hcmut.edu.vn

Cortical Bone Microelasticity Assessed with Scanning Acoustic Microscopy: Relationship to Nanostructural Characteristics across a Human Osteon

Mathilde Mouchet^{1,5}, Aurélien Gourrier^{2,4,5}, Fabienne Rupin^{1,5}, Kay Raum³, Françoise Peyrin^{4,5,6},
Amena Saïed^{1,5}, and Pascal Laugier^{1,5,*}

¹ Univ Pierre et Marie Curie, Paris France

² Univ Paris Sud, Paris France

³ Universitätsmedizin, Berlin Germany

⁴ ESRF, Grenoble, France

⁵ CNRS, Paris, France

⁶ INSERM, Lyon, France

Abstract— Objective : Scanning acoustic microscopy derived impedance (Z) of cortical bone osteons shows a bimodal lamellar pattern of alternating high and low Z values. The goal of this study was to assess the relationship of osteon level impedance variation to the orientation and size of mineral (hydroxyapatite) platelet at one micron resolution. **Methods :** Data were acquired on a human femoral cross-section using 900-MHz SAM, synchrotron radiation micro-computed tomography (SR- μ CT to measure the local variation of HA content) and small angle X-ray scattering (SAXS). SAXS provides the relative variation of HA platelet orientation and changes in mean thickness from the analysis of the integrated SAXS intensity and pattern, respectively. **Results :** While SR- μ CT images showed a constant level of mineral, both SAM and SAXS images displayed the lamellar level modulation related to the modulation of microelasticity, orientation and thickness of the platelets. Z was strongly correlated with the SAXS intensity ($R^2=0.91$, $p<0.0001$) but much lower correlated with the platelets thickness ($R^2=0.35$, $p<0.0001$). **Conclusions :** Our study is the first one that combines SAXS, SR- μ CT and SAM to elucidate the impact of mineral platelets orientation and mean thickness on microelasticity. Our results suggest that the main factor contributing to microelasticity variations is the platelet orientation reflected in modulations of the integrated SAXS intensity.

Keywords— Acoustic scanning microscope, cortical bone, stiffness, hydroxyapatite, osteon.

I. INTRODUCTION

The osteon is one of the fundamental functional unit of human cortical bone. Each osteon consists of concentric lamellae, approximately 3 to 7 μm thick, arranged around a central Haversian canal. At the nanoscale level, these lamellae are made of mineral platelets (hydroxyapatite) with given size and orientation distributions, embedded in an organic matrix of collagen fibers.

Although the osteon has been the subject of numerous studies for decades, its detailed structure is still a matter of dispute. It is understood that the lamellar arrangement is a multilayer structure where each fibrous layer is oriented in a different direction. The correlation of the mineralized fibril structure to the lamellar mechanical properties over entire osteons is not yet fully understood.

The elastic properties of lamellae of human cortical bone have been investigated using scanning nanoindentation (1) and acoustic microscopy (2). Both the nanoindentation modulus and acoustic impedance showed a characteristic bimodal lamellar pattern of alternating high and low values. Previous reports suggested that the lamellar modulation of microelastic properties is related to the lamellar level modulation of the mineral content (1) or to variations of the lamellar orientation (2). Both assumptions are plausible, however, the orientation of mineral platelets and collagen fibers were not directly assessed for a face-to-face confrontation with microelastic measurements. Furthermore, the influence of mineral platelets thickness on tissue level elasticity has not been investigated so far. The goal of this study was to look at the osteon level variation of acoustic impedance and to assess its relationship to mineral platelet orientation and size with a micrometre resolution.

II. METHODS

Data were acquired on the same locations of cross-section of a human femoral mid-shaft. The sample were fixed and dehydrated in ethanol then embedded in polymethylmethacrylate.

We used 900-MHz scanning acoustic microscopy to assess the acoustic impedance with a micrometer resolution. Acoustic microscopy measures the amplitude of a high frequency ultrasonic pulse reflected from the surface of a material. The microscope is calibrated with a set of materials which have

known acoustic impedance. The signal reflectivity from the surface is then converted into an acoustic impedance value which is modelled as the square root of the product of the local mass density and local stiffness coefficient in the test direction.

When the density (or mineralization) is known, the stiffness coefficient can be computed. When the density remains constant, the relative variations of acoustical impedance reflect directly the variations in elasticity.

The variations of orientation as well as the mean thickness of mineral platelets were obtained from small angle X-ray scattering (SAXS) measurements. SAXS allows to image nanostructural features in the specimen within a micrometre resolution. The general principle of SAXS is based on two-dimensional scanning of a thin sample section with an X-ray microbeam, collecting SAXS patterns at every scanning step using a two dimensional detector. From the intensity measured at each pixel, it is possible to deduce two parameters: (i) the integrated SAXS intensity, which depends on the orientation of the anisotropic scattering objects. Therefore, in the case of bone, the integrated intensity depends on the orientation of the mineral platelets. The shape of the SAXS patterns was found to change in the radial direction of the osteon from circular to strongly elliptical, showing a variation of the mineral orientation. (ii) the T parameter which is related to the mean thickness of the mineral platelets.

The local variations of mineral content were determined from synchrotron radiation micro-computed tomography (SR- μ CT). By means of a monochromatic x-ray beam, SR- μ CT directly provides accurate 3-D maps of the linear attenuation coefficient within the sample. The absorption depends on the amount of mineral content which can be related to the differences in gray levels in reconstructed images. As acoustic microscopy and SAXS provide information about the surface properties, the corresponding surface is extracted from the 3D reconstruction of the bone mineral density.

III. RESULTS

The well-known lamellar level modulation was observed in SAM (Fig.1) and SAXS (Fig.2) images, but not in the SR- μ CT images (Fig. 3). While the absence of modulation on SR- μ CT images indicates a constant level of mineral in the explored region, the SAM and SAXS images indicate a modulation of microelasticity, orientation and thickness of the osteonal mineral platelets. The local acoustic impedance showed a strong positive correlation with the SAXS intensity ($R^2=0.91$, $p<0.0001$) (Fig.4) and a much lower correlation with the platelets thickness ($R^2=0.35$, $p<0.05$).

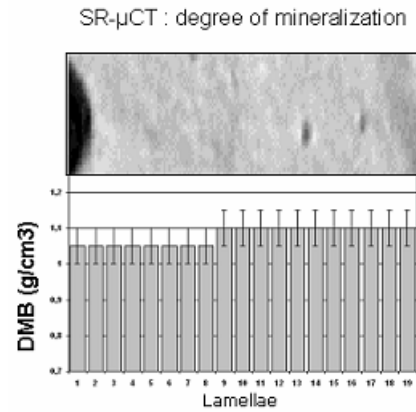


Fig. 1 Mineralization image obtained in SR-CT (top) and distribution of mineralization along across the osteon from haversian canal to outer limit

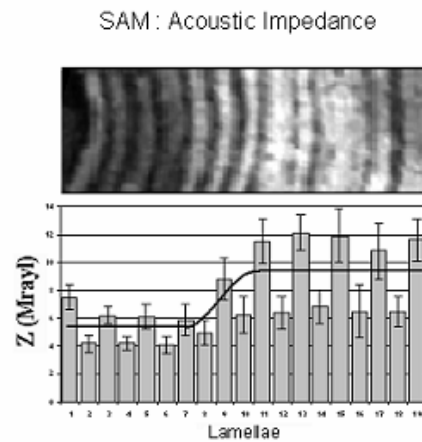


Fig. 2 The lamellar modulation of acoustic impedance can be observed in the image (top) and the distribution across the osteon (bottom)

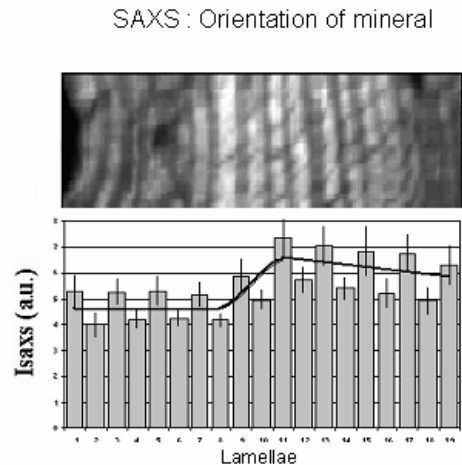


Fig. 3 The lamellar modulation of SAXS intensity (reflecting the orientation of hydroxyapatite platelets) can be observed in the image (top) and the distribution across the osteon (bottom)

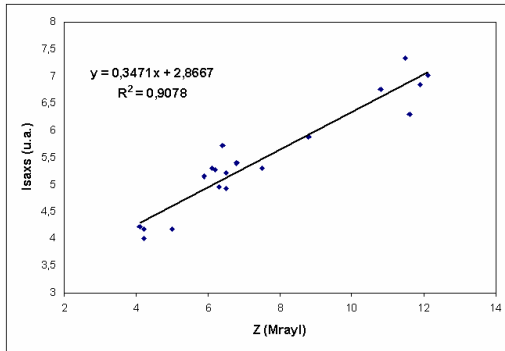


Fig. 4 Correlation between acoustic impedance and SAXS intensity

IV. CONCLUSIONS

This is the first study that combines SAXS, SR- μ CT and SAM imaging in order elucidate the impact of mineral platelets orientation and mean thickness on microelasticity. The alternating pattern of high and low impedance values across a human osteon was found in spite of a homogeneous

distribution of mineral quantity. Our results suggest that the main factor contributing to these impedance variations is the platelet orientation reflected in modulations of the integrated SAXS intensity and that the mean platelet thickness contributes only to a small extent to the variations in acoustic impedance. The paper can be published in the Proceedings. Please pay attention to the registration deadline.

Acknowledgment: This work was supported by CNRS.

REFERENCES

1. H.S. Gupta, U. Stachewicz and W. Wagermaier. J Mater Res. **21** (2006) 1913.
2. T. Hofmann, F. Heyroth, H. Meinhard, W. Fränzel and K. Raum. J Biomech. 39(2006) 2282.0001).

Author: Pascal LAUGIER
 Institute: University Pierre et Marie Curie
 Street: 15 rue de l'Ecole de Médecine
 City: Paris
 Country: FRANCE
 Email: Pascal.laugier@upmc.fr

The Overview of Tomographic Algorithms Used in Medical Imaging Equipments

Huynh Luong Nghia and Tran Anh Quang

Le Quy Don Technical University /Biomedical electronic Department -100 Hoang Quoc Viet, Hanoi, Vietnam

Abstract— The article presents the overview study of computerized tomographic algorithms. They include all of physical principles, mathematical methods and technical means used for defining the parameters of internal structures of different objects without breaking the whole of them when is measured.

Keywords— Tomography, computed tomography, algorithm, back projection, absorption coefficient.

I. INTRODUCTION

Nowadays, medical imaging equipment is more and more broadly used because they bring many benefits in diagnosis and therapeutic. These devices are based on three fundamental factors:

a/ Physical inventions as X-ray, nuclear magnetic resonance phenomenon, ultrasound wave, radioactivity....

b/ The development of hi-technologies such as specialized high-speed computers, high quality sensors, and semiconductors....

c/ Tomographic algorithms

To determine structure parameters of the body, the last one will be affected by following physical fields:

1. Roentgen rays (gamma ray, X-ray): The basic parameter measured is here the intensity of X-rays before and after they go through the body. The main structure parameter of the body is the density distribution of tissues in volume.
2. Radioactive rays: radiopharmaceuticals that have short decay half-life time, are entered into the body by injection or through the digestive system. The temporal distribution of the radiopharmaceuticals in body is a main structure factor. It's measured from the intensity of gamma rays that are released from the body. Also the gamma absorption rate of tissues in volume is defined too.
3. Electromagnetic field: This kind of affection is used in computed tomography (MRI) in the form of nuclear magnetic resonance signal.
4. Ultrasound wave: Essentially the density distribution of tissues in volume is here defined. However, this technique also allows to solve other parameters such as the rate of blood flow distribution in vessels...

5. Other physical fields: laser, light, electric field, magnetic field...

After applying physical fields on the bio-object and using proper sensors in order to receive signals responded, the most important thing remains to do is employing proper tomographic algorithm to reconstruct the object relying on received signals.

II. THE TOMOGRAPHIC ALGORITHMS

In accordance with each kind of above stated physical fields, medical imaging equipments are divided to following types:

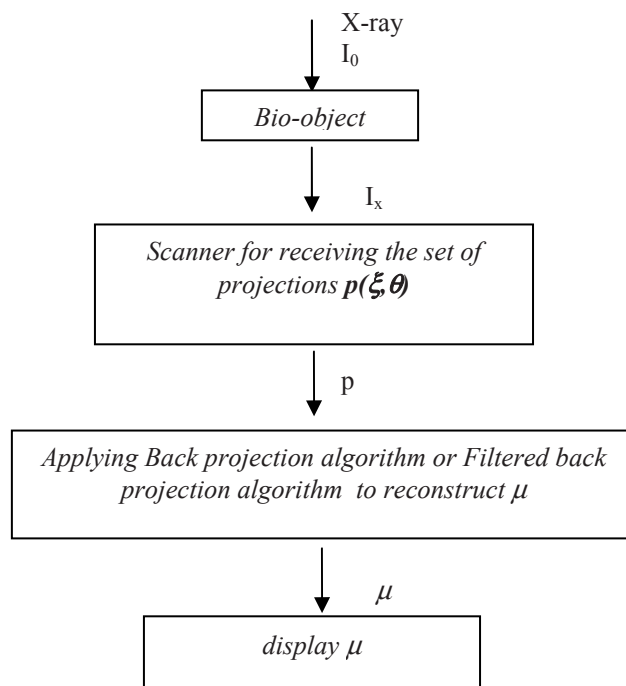


Fig. 1 The diagram of Roentgen computed tomography algorithm

- 1 Roentgen computed tomography (CT-scanner)
- 2 Radioactive computed tomography (SPECT and PET)
- 3 Magnetic resonance imaging (MRI)

- 4 Ultrasound computed tomography (Ultrasound scanner)
- 5 The devices operating on the principle of computed tomography

A. Roentgen Computed Tomography Algorithm

When the body is radiated by Roentgen rays, these rays will be partly absorbed by tissues in the body. This property is defined by a attenuation coefficient μ . Received rays form a set of projections $p(\xi, \theta)$ that are used to reconstruct the internal structure of the body. Therefore, the basic problem of Roentgen computed tomography is to represent the linear absorption coefficient $\mu(x,y)$ through a set of projections $p(\xi, \theta)$ (The diagram of Roentgen computed tomography algorithm is indicated in Figure 1). This is also the basic problem of all types of computed tomography.

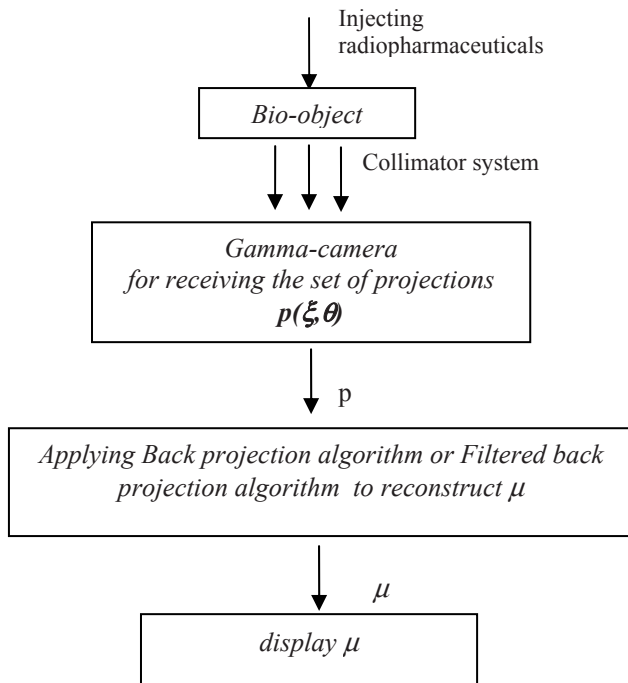


Fig. 2 The diagram of Radioactive computed tomography algorithm

B. Radioactive Computed Tomography Algorithm

In radioactive computed tomography, radio-active isotopes are injected into the body, then gamma sensors are used to receive the intensity of released radioactive rays. Cylinder and cone collimators are used to determine the absorption coefficient and the distribution of radioactive isotopes intensity in the body. Currently there are two types

of typical radioactive computed tomography: Single photon emission tomography (SPECT) and Pozitron emission tomography (PET). The diagram of radioactive computed tomography is represented as in figure 2:

C. Nuclear Magnetic Resonance Imaging Algorithm

In magnetic resonance imaging (MRI), nuclear magnetic resonance (NMR) is stimulated in tissues of the body. Then, the radiosignals released from these tissues will be received by RF coil giving information of tissue distribution. The diagram of nuclear magnetic resonance imaging algorithm is represented as:

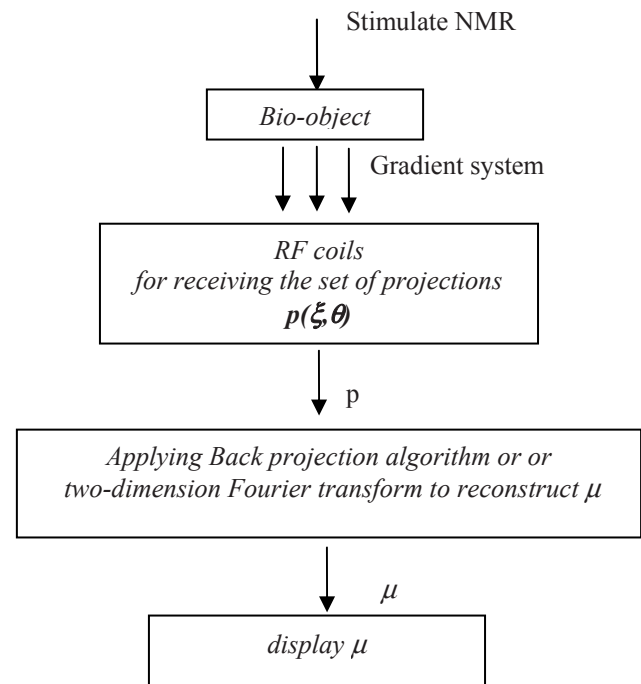


Fig. 3 The diagram of nuclear magnetic resonance imaging algorithm

D. Ultrasound Computed Tomography Algorithm

In Ultrasound computed tomography, the interaction between ultrasound wave and the body is used to determine the distribution of sound velocity c and the tissue density ρ . Ultrasound signals are stimulated and received by piezoelectric transducers. Received data is also processed by above mentioned algorithms, i.e by applying Fourier transform algorithm in order to reconstruct internal structures of the body as indicated in the following diagram:

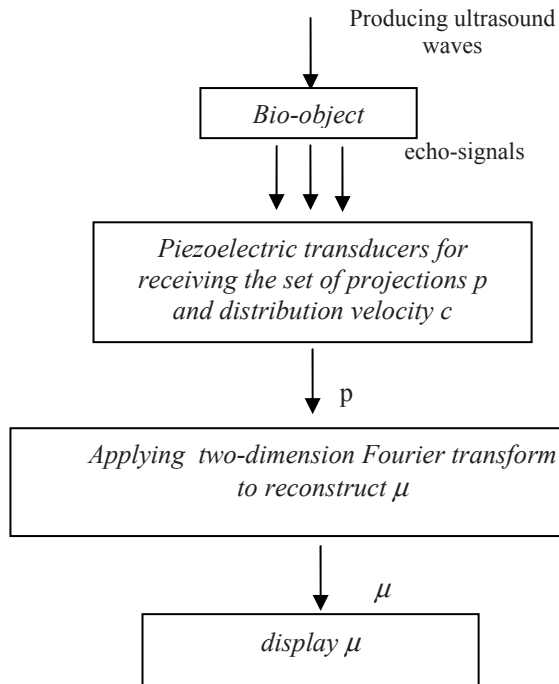


Fig. 4 The diagram of Ultrasound computed tomography algorithm

E. The Devices Operating on the Principle of Computed Tomography

Nowadays, there have been many diagnostic and therapeutic-oriented devices that are very effective such as optical-laser scanner, near-infrared spectroscopy NIS, diagnostic and therapeutic-oriented devices DDFAO/ESG... In

these devices computed tomography algorithms are applied in different aspects depending on the structural or functional diagnostic aim of the device.

III. CONCLUSIONS

This article has presented the overview of basic algorithms of currently computed tomography. While each type of the specific computed tomography algorithm is shown, the article find out their common base. It is *Applying Back projection algorithm or Fourier transform to reconstruct μ* after receiving the set of projections (raw data) by different ways. This allows constructing mathematical models and simulating algorithms in order to design and manufacture all types of medical imaging devices.

REFERENCES

1. А.С.КРАВЧУК, (1996) *Вычислительная Томография*, Москва, МГАПИ.
2. NGHIA HUYNH LUONG, " *The Algorithm for image reconstruction in CT- Scanner* ", in Proceedings 2002, REV8, Hanoi, pp 369-371.
3. NGHIA HUYNH LUONG, " *Simulating the process of image reconstruction in MRI equipment* ", in Proceedings 2005, VICA6, Hanoi, pp383 –388.
4. NGHIA HUYNH LUONG, ANH TRAN QUANG " *Modelling the activity of magnetic resonance imaging equipment* ", Poster paper, BME –1 2005, Tp HoChiMinh
5. NGHIA HUYNH LUONG, DANG TRAN HUY (2006) " *The Algorithm for Sagittal Tomoslices in Single Photon Emission Computerized Tomography (SPECT)* ", Journal of Science and Technique, 114, pp 102-108, Military Technic Academy, Hanoi.

Adaptive Complex Wavelet Technique for Medical Image Denoising

Nguyen Thanh Binh¹ and Ashish Khare²

¹ Faculty of Computer Science and Engineering, HCMC University of Technology, HCMC, Vietnam

² Department of Electronics & Communication, University of Allahabad, Allahabad, India

Abstract— Medical images are generally of poor contrast and complex types of noise and blur. So denoising of images is an important role in processing and analysis of medical image. The purpose of the paper takes advantages of the adaptive denoising filter in the wavelet domain. The filter is based on the second derivative of Gaussian filters methods, and in particular generalizes an adaptive method proposed earlier by R.Duits [2]. We propose a new method which is based on the steerable complex wavelet construction. For improving of the proposed method, we have compared the results with the other recent methods such as ForWaRD [3], WaveD [1],...

Keywords— medical image, denoising, steerable complex wavelet, Gaussian, filters.

I. INTRODUCTION

Medical images are generally of poor contrast and get complex types of noise due to various acquisitions, transmission, storage and display devices. So it is very difficult to suggest a robust method for noise removal which works equally well for different modalities of medical images.

During the last decade, several new methods have emerged for removing Gaussian random noise from medical images. The 2D dual-tree complex wavelet proposed by Kingsbury [8] satisfies these requirements very well. Unfortunately, it is less convenient for motion estimation since the motion information is related to the coefficient phase, which is a nonlinear function of translation. Neelamani [3] has given that the ForWaRD method is outperforms classical denoising methods based on the Wiener filtering. The major advantage of ForWaRD is the performance for boxcar blur with low noise levels. For other types of noise, the performance of ForWaRD is not good. Recent paper by Donoho [1] exploits both the natural representation of the convolution operator in the Fourier domain and the typical characterisation of Besov classes in the wavelet domain. The limitation of WaveD is the dependence of their performances on tuning of parameters. In almost of imaging applications, medical images are often corrupted with non-Gaussian noise and a complex nature of noise, these methods do not provide good results.

The purpose of the paper takes advantages of the adaptive denoising filter in the wavelet domain. The filter is based on the second derivative of Gaussian filters methods,

and in particular generalizes an adaptive method proposed earlier by R.Duits [2]. We propose a new method which is based on the steerable complex wavelet construction. For improving of the proposed method, we have compared the results with the other recent methods such as ForWaRD [3], WaveD [1],...

The rest of the paper is organized as follows: in section 2, we described the basic concepts of measuring noise and details of the proposed algorithm. In section 3, the results of the proposed method for denoising are shown and compared to other methods and finally in section 4, we presented our conclusions.

II. MEASURING NOISE AND THE PROPOSED MODEL

A. The Factors Affect to Noise

To find the original medical image the degraded medical images has to be denoised.

The noising, or degradation, of a medical image can be caused by many factors. Noise from instruments such as machine specifications, detector specifications, and surroundings... is further enhanced due to application of different quantization and reconstruction algorithms. Noising of edges in a medical image occurs in many different fields. This noise is often unwanted.

B. Measuring Noise

We have used the traditional measures signal to noise ratio (SNR) and Peak Signal to Noise Ratio (PSNR).

Mean Square Error (MSE) which requires two $M \times N$ gray-scale images, the original image I and the denoised image \tilde{I} , is defined as,

$$MSE = \frac{1}{MN} \sum_{i=0}^{m-1} \sum_{j=0}^{n-1} |I[m, n] - \tilde{I}[m, n]|^2$$

The PSNR is the most commonly used as a measure of quality of reconstruction in image denoising, defined as,

$$PSNR = 20 \log_{10} \left(\frac{MAX_I}{\sqrt{MSE}} \right)$$

where, MAX_I is the maximum pixel value of the image. The PSNR of the images denoised is compared using wavelet

and curvelet transform denoising for each type of noise mentioned above.

C. The Steerable Filters Model

The basis functions of the steerable pyramid are directional derivative operators of different size and orientation. Any function can be expressed as a linear combination of rotated versions of itself that is called steerable.

The fundamental idea of steerable filter is to apply basis filters that correspond to a fixed set of orientations and interpolate between each discrete response. As defined in [6] the steering constraint is formulated as:

$$f^\theta(x, y) = \sum_{j=1}^M k_j(\theta) f^{\theta_j}(x, y) \quad (1)$$

where M is the number of basis functions required to steer a function $f^{\theta_j}(x, y)$. Working in polar coordinates

$$r = \sqrt{x^2 + y^2} \text{ and } \Phi = \arg(x, y) \text{ is more convenient.}$$

Let f be a function that can be expressed as a Fourier series in polar angle Φ

$$f(r, \Phi) = \sum_{n=-N}^N a_n(r) e^{in\Phi} \quad (2)$$

The steering condition (1) holds for function f expanded in the form of (2) if and only if the interpolations $k_i(\Phi)$ are solutions of the following equation:

$$\begin{pmatrix} 1 \\ e^{j\theta} \\ \dots \\ e^{jN\theta} \end{pmatrix} = \begin{pmatrix} 1 & 1 & \dots & 1 \\ e^{j\theta_1} & e^{j\theta_2} & \dots & e^{j\theta_M} \\ \dots & \dots & \dots & \dots \\ e^{jN\theta_1} & e^{jN\theta_2} & \dots & e^{jN\theta_M} \end{pmatrix} \begin{pmatrix} k_1(\theta) \\ k_1(\theta) \\ \dots \\ k_M(\theta) \end{pmatrix} \quad (3)$$

Freeman and Adelson [4] proposed the concept of steerable filters and applied it to several problems. With a set of basis filters, one can adaptively steer a filter along any orientation. Freeman described constraints for design of the radial filters as follows:

1. Lowpass filter L_1 . Since there is a subsampling operation during the computation of transform. It create aliasing so in order to avoid aliasing, the lowpass filter L_1 should have strictly zero response above $\omega/2$
2. Lowpass filter L_0 . It should cover the frequency bound of L_1 . The response should be equal to 1 for ω between 0 and $\pi/2$ and zero at $\omega = \pi$.
3. Bandpass filter B. The constraint for the design of bandpass filter $B(\omega)$ is

$$|L_0(\omega)|^2 = |B(\omega)|^2 + |L_1(\omega)|^2 |L_0(2\omega)|^2 \quad (4)$$

4. Highpass filter H. This is obtained simply by subtracting the response of L_0 from unity.

The filter bank used to construct the pyramid is polar-separable in the Fourier domain and the orientation tuning is constrained by the property of steerability [6]. The complex filters in the pyramid provide invariance to the phase of the medical image structures. The steerability of the orientation channels allows the extraction of contrast at arbitrary orientations from only a small set of fixed-orientation basis filters.

D. The Proposed Model

To create steerable filters, we first assume that the steering of filter responses across scales can be obtained by linearly combining the responses $f_{\alpha i}^\theta(x, y)$, where $i \in \{1, \dots, N\}$, of a small set of N basis filters $G_{\alpha i}^\theta(x, y)$ as

$$f^\theta_\alpha = \sum_{i=1}^N s_{i,\alpha} f^\theta_{\alpha i}(x, y)$$

where $s_{i,\alpha}$ is the steering coefficient of filter i for scale α . To select the scales of our filter set, with the scale parameter α , the radial frequency response $G_\alpha(\omega)$ changes smoothly. The change in radial response in the frequency domain increases exponentially with α .

Spatial filters are described with similar orientation, scale and phase characteristics. Polar separable filter kernels $G_\alpha^\theta(\omega, \Phi)$ allow the radial frequency (scale) characteristic of the filters to be separately specified from the angular frequency (orientation) characteristic. It is specified in the Fourier domain by the radial frequency function $G_\alpha(\omega)$ and angular frequency function $G^\theta(\Phi)$ where α and θ are the scale and orientation of the desired filter respectively:

$$G_\alpha^\theta(\omega, \Phi) = G_\alpha(\omega) G^\theta(\Phi)$$

The inverse discrete Fourier transform of $G_\alpha^\theta(\omega, \Phi)$ yields a complex filter $g_\alpha^\theta(\omega, \Phi)$ in the spatial domain where the real and imaginary parts of the kernel are in quadrature.

In the new algorithm, medical image denoising has been demonstrated in the wavelet domain using techniques involving soft thresholding approaches. Here, we approach the problem of denoising by designing a wavelet domain algorithm which utilizes the feature complex filters suggested in above. The approach is as follows:

1. Apply the L-level steerable filter decomposition to the noisy medical image, yielding a set of bandpass channels $f_k^{(\ell)}(x, y)$ with $\ell = 1, 2, 3, \dots, L$ and $k = 0, 1, 2, \dots, K/2-1$, and a down-sampled low-pass channel at the coarsest scale.
2. Start the denoising and reconstruction process at the coarsest scale by setting $\ell = L$.
3. Filter the bandpass channels $f_k^{(\ell)}(x, y)$ with the synthesis filter bank to reconstruct the unsteered medical image channels $(f_k^{(\ell)}(x, y))_{\text{recon}}$.

$$f_s^{(\ell)}(x, y, \Phi_s) = \sum_{k=0}^{K/2-1} s_p(\phi, k) f_k^{(\ell)}(x, y) + \sum_{k=0}^{K/2-1} s_q(\phi, k) (f_k^{(\ell)}(x, y))^* \quad (5)$$

where the polynomial steering function s_p, s_q with coefficients p_k, q_k of the polynomial fits in steered angle Φ as

$$s_p(\Phi, k) = \sum_{n=1}^P p_k(n)\Phi^n \quad ; \quad s_q(\Phi, k) = \sum_{n=1}^Q q_k(n)\Phi^n$$

5. Steer the reconstructed medical image channels to obtain using Eq(5) with the dominant orientation map $\Phi_s^{(1)}(x, y)$.

III. EXPERIMENTS AND RESULTS

In this section, we show the experimental results of our algorithm. Our proposed algorithm, a complex steering algorithm applied to the steerable pyramid outputs described in the above, utilize a threshold which is a fixed fraction of the maximum magnitude at each level of decomposition. We have compared the results with the other recent methods: ForWaRD [3], WaveD [1] and Symmlet (wavelet shrinkage, based on a Symmlet 8 wavelet decomposition). The implementation of the Symmlet 8 and shrinkage rely on the WaveLab 802 package.

We implemented the method described in section 2 on many medical images with many difference medical images size and many difference cases. We see that the results of our proposed method are better than the other methods with difference medical images size.

In next the other experiments, we have given combination of Gaussian additive, speckle and impulsive noise. From many the other medical images tests show that the results of our proposed method are also better than the other methods. These results clearly demonstrate the superiority of the proposed method over others. In here, we also report our results in some medical images cases.

We now test our proposed method in several cases that medical images are corrupted Gaussian noise, Speckle noise. Table 1 and 2 show the PSNR value (in dB) of tests in several cases.

Table 1 PSNR value (dB) of different denoised images using the image sizes with Gaussian noise

Test Image	Noisy Image	Symmlet Restored	For-WaRD Restored	WaveD Restored	Proposed method
1	24.23524	25.30717	28.45245	29.42430	30.45846
2	24.45722	25.54327	28.24652	30.65305	31.23464
3	24.74727	25.55353	29.05555	30.65341	31.63560
4	26.35788	26.34525	29.00326	30.78775	31.97646
5	24.08446	25.35721	28.14572	29.56600	30.35439
6	23.78521	25.33245	27.65433	28.76784	29.25563
7	23.87634	25.65355	27.14565	29.67126	29.99906
8	22.76427	25.13518	27.76811	28.74504	29.98581
9	22.96732	24.70350	26.85370	28.26352	28.96683
10	21.43672	23.48350	26.67364	27.63476	28.68855

Table 2 PSNR value (dB) of different denoised images using the image sizes with Speckle noise

Test Image	Noisy Image	Symmlet Restored	For-WaRD Restored	WaveD Restored	Proposed method
1	15.31689	15.43456	15.56733	16.35788	16.63333
2	18.42796	18.57862	18.68332	19.45677	19.73285
3	17.61588	17.76586	17.99626	18.35780	18.83682
4	18.32145	18.44535	18.85436	19.35713	19.73362
5	17.47827	17.53330	17.86435	18.36832	18.67318
6	18.42579	18.62626	18.78764	19.36901	19.62695
7	14.63673	15.34573	15.95437	16.36900	16.82172
8	14.38945	15.05452	15.75342	16.25792	16.71389
9	18.22368	18.96432	19.85320	20.32104	20.69312
10	16.33570	16.85450	17.86425	18.38620	18.85216

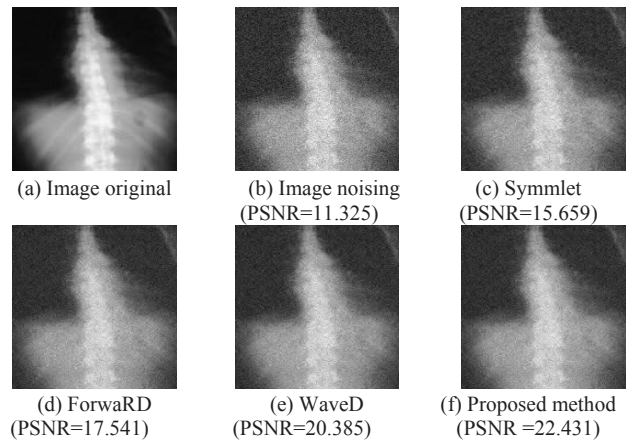


Fig. 1 Noisy ultrasound image and denoised images by different methods

From the results presented in the above table (Table 1 and 2), it is clear that the performance of the proposed method is better than the ForWaRD, WaveD and Symmlet method for medical image having any type of noise such as Gaussian and Speckle noise.

Figure 2 shows the plot of MSE of noisy medical image with MSE of medical images denoised by the proposed method as well as Symmlet, ForWaRD and WaveD method. From this figure, we see that the results of our proposed method are better than the Symmlet, ForWaRD and WaveD method.

As mention in section 1, the Symmlet, ForwaRD and WaveD method have limitations. The orientation, scale and symmetry subband of the medical images decomposition present many advantages for medical image analysis and feature extraction. This is one of the reasons which our proposed performs better than the other methods. For example, an orientation map computed at the end of a line segment will produce a bimodal response. The filters are almost always either symmetric or antisymmetric. The

symmetry (or anti-symmetry) of the filters imposes a periodicity on the orientation map, regardless of the underlying medical image structure. On the other hand, due to the properties of the transform, this proposed method is accomplished in a very intuitive manner, by the application of a nonlinear mapping in the wavelet transform domain, mediated by dimensionless measures of orientation dominance and corner strength. So almost of the cases, our proposed method is better than the other methods.

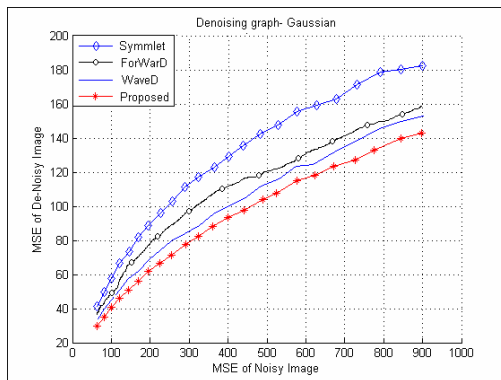


Fig. 2 MSE performance of the proposed method with Symmlet, ForWaRD and WaveD method

IV. CONCLUSIONS

In this paper, we have proposed a new de-noising method for medical images. The method is applicable to the blurred medical images corrupted by various types and amounts of noise. The proposed method is simple to implement as well.

In this work, we improved denoising algorithm that exploits polar rotation on the second derivative of Gaussian filters. The proposed method takes advantage of adaptive denoising filter in the wavelet domain. The filter is based on the second derivative of Gaussian filters methods. Our focus is on minimizing spatial noising. Our method is applicable to medical images taken under a variety of medical image,

improves the mapping between source and reference colors when there is a disparity in size of the chromatic categories, handles achromatic categories separately from chromatic categories. However, while the denoising methods described here do not in any sense challenge the performance of recently reported denoising systems using complex wavelet decompositions, the ability to integrate feature measurements directly with denoising through steering is very intriguing. It is interesting to speculate how the performance of such structure based wavelet domain methods might be improved.

REFERENCES

1. D.L Donoho, M.E Raimondo " A fast wavelet algorithm for image deblurring", IEEE Transactions on Image Processing, Vol. 16, No. 2, 2004
2. R.Duits, M.Felsberg, L.M.J.Florack, and B.Platel, "Alpha scale spaces on a bounded domain". Proc.Scale Space, Vol.2695, pp502-518, 2003
3. R. Neelamani, H.Choi, and R.Baraniuk, "Forward: Fourier-wavelet regularized deconvolution for ill-conditioned systems" IEEE Transactions on signal processing 52 pp. 418–433, 2004
4. W. T. Freeman and E. H. Adelson, "The design and use of steerable filters," IEEE Trans. Pattern Anal. Mach. Intell., vol. 13, no. 9, pp. 891–906, Sep. 1991.
5. Nguyen Thanh Binh, Ashish Khare and Moongu Jeon, "Adaptive Video Segmentation using Steerable Complex Filters", in procc. of Workshop on Image Processing and Image Understanding, 20-22 February, 2008, Jeju, Republic of Korea.
6. Nguyen Thanh Binh, Ashish Khare "Medical image deblurring in wavelet domain" 11th Conference on Science and Technology, HCMC University of Technology, 2009
7. Nguyen Thanh Binh, "Using adaptive wavelet for image de-noising", 5th Scientific Conference of the University of Natural Sciences HCMC, November 2006.
8. N. Kingsbury, "Image processing with complex wavelets," Phil. Trans.Roy. Soc. London, Ser. A, vol. 357, no. 1760, pp. 2543–2560, Sep. 1999

Author: Nguyen Thanh Binh
 Institute: Ho Chi Minh City University of Technology
 Street: 268 Ly Thuong Kiet, Dist 10
 City: Ho Chi Minh
 Country: Vietnam
 Email: ntbinh@cse.hcmut.edu.vn

Three Dimensional Medical Image Processing and Analysing Software

Tran Phan Son Giang

University of Technology, Faculty of Applied Science, Department of Biomedical Engineering, Ho Chi Minh City, Vietnam

Abstract— In recent years, three-dimensions medical image processing has been considering as a large field, which is not only a big interest of bio-medical researchers and physicians, but also a challenge in processing and making three-dimensions images useful to bio-medical researches and practically clinical applications. This thesis consists of a detailed survey of three-dimension medical images with processing methods, which are followed by several of special algorithms. Through this survey, some of algorithms are usefully applied into designing a Java 3D medical image processing software. After validation and evaluation, the results of this software are found to be significantly useful in medical research and education. By taking the advantages of multi-platform property and advanced packages of Java, this software not only work well with different platforms, but also potentially have image processing methods to be extended.

Keywords— 3D image processing, volume images, medical image software.

I. INTRODUCTION

Biomedical imaging is essential to medical research and clinical practice. Although there were lots of medical image studies belong to 2D, 3D, and 4D images, that couldn't afford to meet all different customized needs, especially is respect of 3D images.

Three dimensional image processing is a large field that has evolved in recent years, leading to a major improvement in patient care. The revolution capabilities of new 3D and 4D imaging modalities, along with computer reconstruction, visualization, and analysis of multi-dimensional medical volume image data, provide powerful new opportunities for medical diagnosis and treatment.

Until recently, 3D visualization and quantitative analysis of an image dataset could only be performed on specific workstations with expensive compatible softwares. Researchers analyze images of varied imaging modalities, such as microscopy, X-ray, CT, MRI, fMRI, and PET. If each software application is platform specific, researchers will be very difficult to analyze a single image dataset. This often reduces efficiency while simultaneously increasing lab costs.

By taking full advantage of Java, which is an object-oriented, interpreted, programming language, a medical image processing software has been designed to help researchers increase efficiency and reduce costs by providing them with a flexible tool that can operate on virtually any platform. This

software makes use of some special image processing methods to support researchers in processing and visualizing 3D medical image datasets in different ways, which is very helpful and convenient for medical studying and applications.

II. THEORY

A. 3D Image Segmentation

Extract a three-dimensional surface for each anatomic object from volumetric data. A number of image segmentation methods have been developed using fully automatic or semi-automatic approaches for medical imaging. The most used method in object-specific segmentation is based on deformable model. Such deformable models or snakes were improved by the introduction of a new class of external force, called the gradient vector flow (GVF) field, which are vector fields derived from images by minimizing an energy functional in a variation framework. Another common method is clustering, which is based on the analysis of gray level in the volume image.

B. Surface Rendering

Extract a surface from the 3D data volume as a collection of adjacent polygons and to visualize the extracted surface by appropriate algorithms. Diffusion and shading of light are exploited to increase the 3D illusion.

C. Volume Rendering

Visualizes sampled functions of 3D data volume by computing 2D projection of a semi-transparent volume from a desired point of view without the use of any segmentation procedure. At each voxel in the data volume, a color and a transparency is assigned, depending on look-up tables. Then, rays are traced into the volume and are attenuated and colored depending on the rough through the volume.

Three common methods are used in computer graphics to render 3D volume images are: volume ray casting, shear-warp factorization and texture mapping.

III. PROGRAMMING 3D MEDICAL PROCESSING AND ANALYSING SOFTWARE IN JAVA

A. 3D Image Browser Designing

The browser should have capabilities of browsing multi-dimension images (especially designed for viewing 3D

images) and processing lots of image datasets at the same time. Suitably, this browser has been designed over the size of 1024×768 pixels.

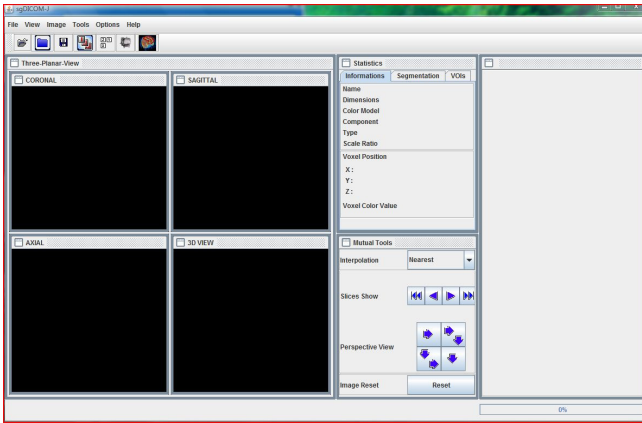


Fig. 1 Basic interface of sgDICOM-J

B. Tri-orthogonal Image Planes Viewing Function

After getting enough image information, construct the image data, which represent for the images looking from 3 principal orthogonal planes (axial, coronal, sagittal). Using some viewing-directions deformations and some tools of JAI and Java 3D to construct appropriate slices, displayed in different frames.

C. 3D Image Segmentation Tools

Building some common tools using in processing 3D images such as : Smoothing, Filtering, Shearing, Cutting, Crop, Marking...

D. Volume Image Visualization

Using specific algorithms to construct the appropriate VOIs (volume of interests) and display them in 3D space with the use of texture mapping technology. Volume images must be resized to dimensions that are power of 2 by interpolating.

IV. RESULTS

A. Browsing and Displaying 3D Image in Orthogonal Planes

Showing image information in statistic frame : name, size, type, voxel location, voxel color values...

Showing 3 image slices in Coronal, Axial, Sagittal frames respectively.

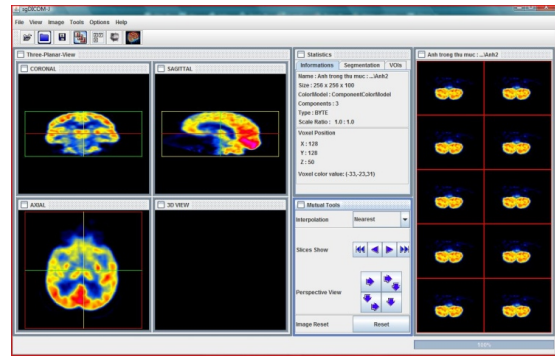


Fig. 2 Browsing 3D image

B. Segmentation Tools

Smoothing 3D images by inputting the smooth kernel size (the default size is 3).

Filtering image for visualization or post-processing conveniently. These filters are : Edge Extraction (Sobel), Sharpen, Low-pass, High-pass, Laplacian.

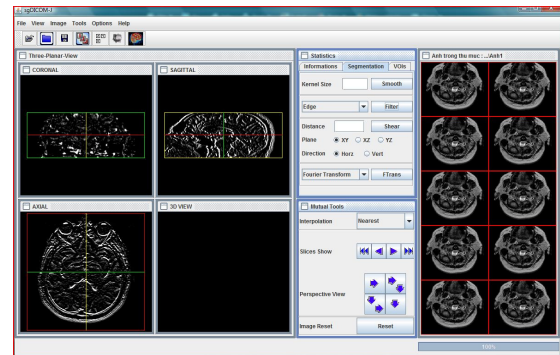


Fig. 3 Edge extracting

Shearing volume image in 3D space to recorrect image shape.

Volume of interest (VOI) : create volume images with desired size. There are some sub-functions such as cutting, cropping, and marking volume image.

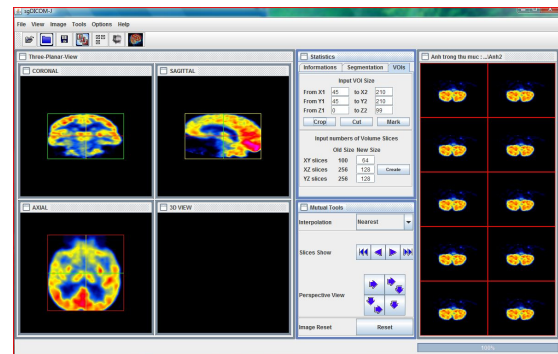


Fig. 4 Building and processing VOIs

LookupTables : include special lookup tables which is suitable for studying special human organs (brain, muscle, tissue, bone...)

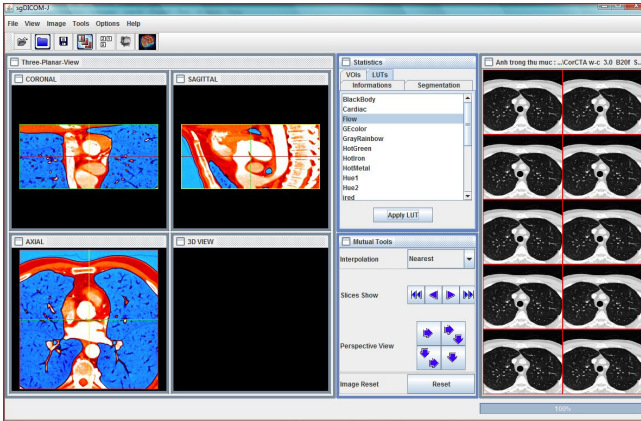


Fig. 5 Lookup tables applying

C. Visualization Function

By using texture mapping technology and Open Graphics Library to rendering volume images. The image must be in power of 2 size to viewing in Java 3D Application Programming Interface.

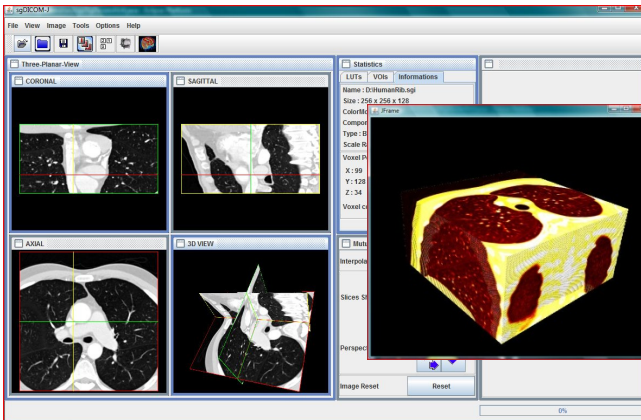


Fig. 6 Volume image visualization

V. CONCLUSIONS

For experiment, this software has some approaches in such way it processes medical images, processing 3D images, reconstructs and visualizes 3D volume images.

Along with the development of information technology and the advantage of Java program language, the applied software will be more and more efficiency and robust. Since then, there is a great perspective to enhance this software with registration routines, which will support more available tools for medical diagnosis and applications.

REFERENCES

1. D. Blythe. *Advanced graphics programming techniques using OpenGL. Texture Mapping*, Chapter 6, SIGGRAPH '99 Course, 1999 <http://www.opengl.org/resources/code/samples/sig99/advanced99/notes/node48.html>
2. D. J. Bouvier. *Getting start with the Java 3D™ API*. Tutorial 1.5, Java 3D Version 1.1.2, Sun Microsystems, Inc., 1999.
3. T. Yoo, W. Schroeder et al. *Insight segmentation & registration toolkit (ITK)*. Kitware Inc., 2009 <http://www.itk.org>.
4. E. Neri, D. Caramella, C. Bartolozzi. *Image processing in radiology – Current Applications*, Springer-Verlag, 2008.
5. National Institute of Health (USA). *Medical image processing analysis & visualization (MIPAV). Algorithms*, Vol 2, 2007.
6. P. G. Lacroute. *Fast volume rendering using a shear-warp factorization of the viewing transformation*, Stanford University, 2005.
7. R. Santos. *Java advanced imaging API : a tutorial*. Instituto Nacional de Pesquisas Espaciais, Laboratório Associado de Computação e Matemática Aplicada, 2004.
8. Sun Microsystems, Inc. *Business. Programming in Java™ Advanced Imaging*, Release 1.0.1, 1999.
9. T. McReynolds. *Programming with OpenGL : Advanced rendering. C.13 :Volume visualization with texture*, SIGGRAPH '99 Course 1999 <http://www.opengl.org/resources/code/samples/advanced/advanced97/notes/>.
10. Trần Phan Sơn Giang. *Thiết lập phần mềm xử lý và hợp nhất 3 chiều hình ảnh chẩn đoán y khoa*. Luận văn tốt nghiệp Khoa Khoa Học Ứng Dụng, Trường ĐH Bách Khoa Tp.HCM, 2007.
11. W. Rasband. *ImageJ - Image Processing and Analysis in Java*. National Institute of Mental Health, Research Services Branch, 1997.
12. W. Schroeder, K. Martin, B. Lorensen et al. *Visualization toolkit (VTK)*. Kitware Inc., 2009 <http://www.vtk.org>.

Formation of Biodegradable Copolymeric Nanoparticles for Anticancer Drug Delivery

N.T.H. Anh¹, N.V. Cuong², and N.K. Hoang²

¹ Ho Chi Minh City College of Food Industry, 140 Le Trong Tan St, Tan Phu Dist, HCMC, Vietnam

² Ho Chi Minh City University of Industry, 12 Nguyen Van Bao St, GoVap Dist, HCMC, Vietnam

Abstract— The conventional chemotherapeutic agents have often associated with limitations due to the drug's poor aqueous solubility, side effects resulting from toxicity to healthy tissues. Drug incorporated in nanosized polymeric micelles are promising nanocarrier systems for drug and gene delivery, because the polymeric micelles have several advantages, such as controlled drug release, enhanced tumor-penetrating ability, reduced side toxicity, increased stability, loading capacity and specific-tissue target ability, as well as chemical or physical stimuli-sensitivity. Thus, preparation of nontoxic polymeric micelles may ensure their effectiveness and safety in the clinical use. In this present work, we reported the preparation of nanosized micelles based on amphiphilic copolymer of poly(ϵ -caprolactone)-*b*-poly(ethylene glycol)-*b*- poly(ϵ -caprolactone). The polymeric nanoparticles were prepared in aqueous solution by co-solvent precipitation technique at room temperature. Polymeric micelles were measured by dynamic light scattering (DLS) with the size in a range of 70-90 nm and narrow polydispersity. Additionally, the toxicities of polymeric micelles were evaluated by MTT assay and nitric oxide production. These results confirmed low toxic polymeric micelles, suggest that the polymeric micelles hold a potential for anticancer drug delivery.

Keywords— Poly(ethylene glycol); poly(ϵ -caprolactone); triblock copolymer; nanoparticle, anti-cancer.

I. INTRODUCTION

The polymeric nano-sized micelles can be formed by self-assembly of amphiphilic polymer in aqueous solution. The nano-size micelle has been merged as one of the most promising nano-carrier systems for the controlled release of various hydrophobic anticancer drugs such as doxorubicin and paclitaxel [1, 2]. Since drug delivery system using nanocarriers are able to increase stability, solubility of drug and selective targeting, reduce the side-effects of anticancer drug and prolong the blood circulation time, passive targeting to the tumor tissues via the enhanced permeability and retention (EPR) effect, and improved drug bioavailability [3, 4].

Poly(ϵ -caprolactone) (PCL) is a polyester, which has been studied intensively due to its good biodegradability and biocompatibility. PCL can be prepared by ring opening

of lactone in presence of initiation and catalyst [5]. Nevertheless, PCL is a type of semicrystalline and hydrophobic polymer, which shows the melting point around 60 °C. PCL is often at rubbery state at room temperature and with low glass transition temperature.

Poly(ethylene glycol) (PEG) is a water-soluble and non-toxic material with no antigenicity and immunogenicity. PEG is considered as polymer that can prevent protein absorption and improve the biocompatibility for blood contact compound [6]. Additionally, PEG was also introduced into several polymers such as PCL, polylactide (PLA) [7], poly(glycolic acid) (PGA), or their copolyesters (PLGA) [8] to increase the biocompatibility and used as drug carriers, which allows PEG to be used for clinical applications.

In this study, biodegradable amphiphilic PCL-PEG-PCL copolymer was synthesized. In aqueous medium, this amphiphilic copolymer can form nano-sized micelles. The properties of nanoparticles as drug carriers were investigated, including CMC values and particle size. Moreover, the biocompatibility of polymeric nanoparticles was also evaluated *in vitro*. The cytotoxicity was examined in L929 mouse fibroblasts cell line. Furthermore, nitric oxide (NO) production and reactive oxygen species (ROS) generation were also demonstrated.

II. MATERIAL AND METHOD

A. Materials

Dihydroxyl-terminated poly(ethylene glycol) (PEG, $M_n=4000$) and ϵ -caprolactone were purchase from TCI Japan. Stannous 2-ethyl hexanoate (stannous octoate, SnOct) was obtained from Sigma-Aldrich (St.Louis, MO, USA). The PEG polymer was purified by extraction with ethyl ether, followed by drying through azeotropic distillation in toluene. Lipopolysaccharides (LPS), Dimethyl-sulphoxide (DMSO), 2',7'-dichlorofluorescein diacetate (DCF-DA) and 3-(4,5-dimethylthiazol-2-yl)-2,5-diphenyl-tetrazolium bromide (MTT) were purchased from Sigma (Sigma Chemical Company, St. Louis, MO, USA). All other chemicals were of analytical grade and used without further purification.

B. Preparation of Nano-sized Micelles

The nanoprecipitation method was used to prepare PCL-PEG-PCL nanoparticle [8]. In briefly, triblock copolymer PCL-PEG-PCL (5 mg) was dissolved in 2 ml of tetrahydrofuran (THF). The polymer solutions were added to 10 mL of Millipore water. The resulting solutions were stirred at room temperature for 3 h and transferred to dialysis bag (MW cut off: 50000), then dialyzed against Millipore water for 24 h. The solution was filtered through 0.45 μ m syringe filter.

C. Determination of Particle Sizes and Polydispersities

The particle size and size distributions were measured by dynamic light scattering (Malvern instruments, England) at a wavelength of 633 nm and 25 °C, and at a scattering angle of 90° at a concentration of approximately 0.4 mg/mL in water. The Z average value was recorded as the average of ten measurements.

D. Measurement of Nitric Oxide (NO) Level

RAW 264.7 macrophage cells were seeded in a 24-well plate (1×10^5 cells/well) and incubated in 37°C, 5% CO₂ for 1 day. Micellar solution at various concentrations was added to the cells in a final volume of 0.8 mL. The supernatants were collected after 24 h and NO production was determined by Greiss reagent.

E. Measurement of ROS Generation

To determine the degree of ROS generation induced by the polymeric nanoparticle, a fluorometric assay, utilizing the unique intracellular oxidation of DCF-DA, was used. RAW 264.7 macrophage cells were seeded in a 24-well plate (1×10^5 cells/well) and incubated in 37°C, 5% CO₂ for 1 day. Polymeric nanoparticles at various concentrations were added to the cells in a final volume of 0.8 mL. After 24 h, the medium was removed and incubated with 40 μ M DCF-DA for 4 hours. At the end of DCF-DA incubation, cells were washed with PBS, lysed with trypsin. The fluorescent of dichlorofluorescein (DCF), which is the oxidized product of DCF-DA, was measured using the microplate with spectrofluorometer with excitation and emission wavelengths of 485 nm and 530 nm

F. Cell Viability

Viable cells were assessed using an MTT assay. The L929 cells were seeded at densities designated as 1×10^5 cells/well into 24-well tissue plates using Dulbecco's

modified Eagle medium (DMEM) supplemented with 10% FBS, 100 U/mL of penicillin, and 100 mg/L streptomycin. The plates were incubated at 37 °C. After 24 h, the culture medium was replaced with DMEM medium plus 10% FBS, and polymeric nanoparticles of various concentrations were added into the culture medium. The DMEM medium was used as control. The cells were incubated for 24 and MTT assay was performed to evaluate cell viability. Briefly, the culture medium was removed, and the cells were washed with PBS twice. About 160 μ L of DMEM medium and 40 μ L MTT solution (5 mg/mL in PBS) were added to each well, followed by incubation at 37 °C for 4 h to allow MTT formazan formation. The medium and MTT were removed and 200 μ L of dimethylsulfoxide was added to dissolve the formazan crystals. After 5 min, the optical density (OD) at 570 nm was determined using a microplate reader. The ratios of OD₅₇₀ from each experimental group ($n=4$) to the OD₅₇₀ of control group were used to assess the cell viability.

III. RESULT AND DISCUSSIONS

A. Preparation of Copolymeric Nanoparticles

Figure 1 shows the size and the size distribution of copolymeric micelles which were measured by dynamic light scattering. The average diameter of the micelles was 92.2 nm and narrow size distribution.

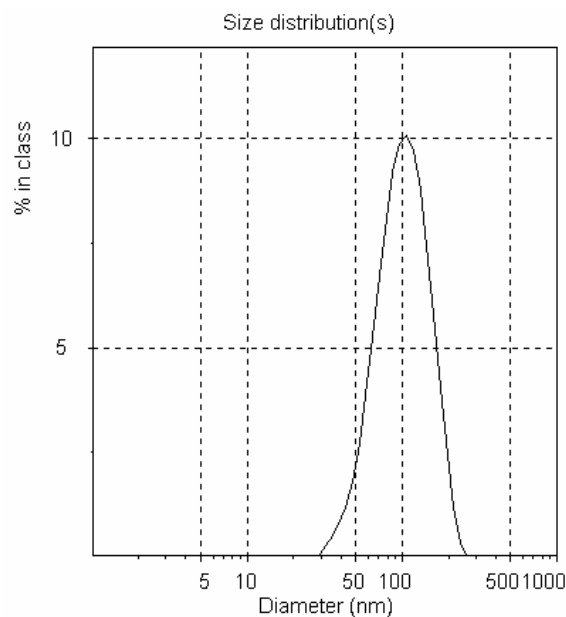


Fig. 1 Size and size distribution of prepared micelles

B. Measurement of Nitric Oxide (NO) Level

Activation of macrophages was related with the increased level of NO which is second messenger in inflammatory signal. Macrophages were cultured in 24 well-plates for 24 h and NO released from the cells to the supernatant was measured. As a result, NO was increased in a polymeric concentration-dependent manner (Fig. 2). The results indicated that micelles did not affect NO production up to 0.5 mg/mL. The NO production was similar to that of control. However, at the concentration of 1.0 mg/mL, the NO production was increased to 2-fold compared with non-treated control. Especially, at concentration of 100 ng/mL, the LPS significantly induced the NO level and was reached to 7-fold in comparison with non-treated control.

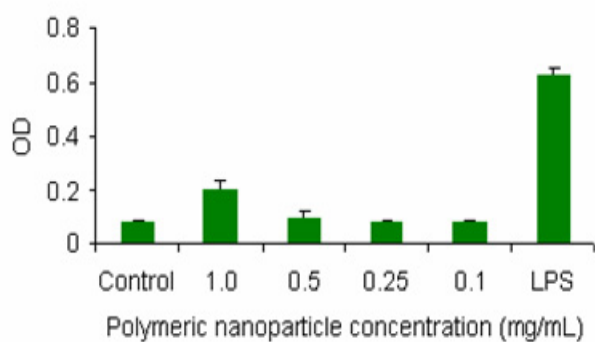


Fig. 2 Effects of micelles on the levels of nitric oxide production

C. Generation of ROS in Macrophage Cells

The level of ROS was determined in cultured RAW264.7 cells treated with polymeric nanoparticles at various concentrations of 1.0 mg/mL, 0.5 mg/mL, 0.25 mg/mL, and 0.1 mg/mL, respectively. The LPS (100 ng/mL) was used as positive control. Figure 3 demonstrates the fluorescence intensity of oxidized DCF. The ROS generation was increased with increasing of polymeric concentration in RAW264.7 cells. When cells were treated with concentration of 1.0 mg/mL, ROS generation was increased to 2-fold compared to non-treated control and similar to LPS-treated group.

D. Cell Viability

The MTT assay was performed to evaluate the cytotoxicity of polymeric micelles to L929 cells. The results of MTT indicated that the all the concentrations did not affect significantly the cell viability after 24 hours incubation with

polymeric micelles. Furthermore, the cell viability of concentration up to 0.25 mg/mL was similar to control group and 80% of cell viability was observed with concentration of 1.0 mg/mL. The cells viability suggests that the polymeric micelle has generally low cytotoxicity to the L929 fibroblast cells with concentration up to 1.0 mg/mL.

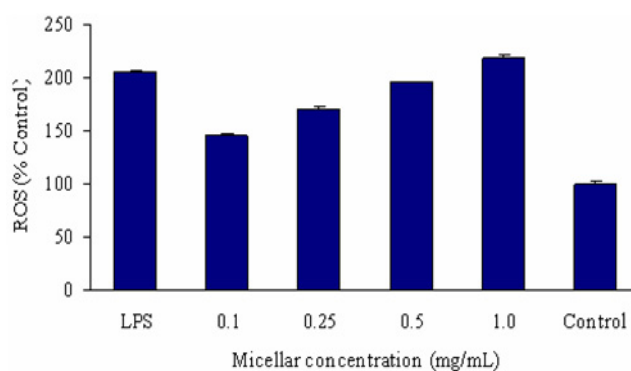


Fig. 3 Induction of oxidative stress as measured by the formation of fluorescent form of DCF against polymeric micelles

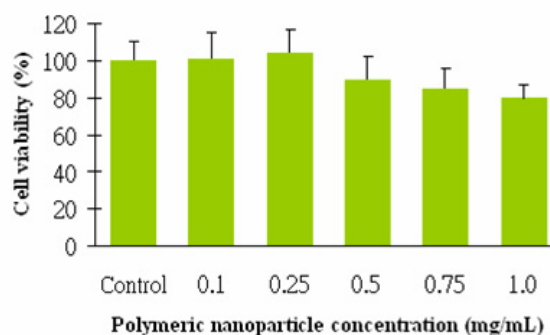


Fig. 4 The cytotoxicity of polymeric micelles to L929 cells

IV. CONCLUSIONS

We have been prepared successfully the non-toxic polymeric micelles in this work. The average diameter of polymeric micelles was 92.2 nm. The biocompatibility of polymeric micelles was evaluated. The polymeric micelles did not affect the cell viability. Additionally, NO production level in polymeric micelle-treated group was similar to non-treated group. This finding suggests that the prepared polymeric micelles hold great promise for anti-cancer drug delivery.

REFERENCES

1. Rosler A, Vandermeulen G.W.M, Klok H.A (2001) Advanced drug delivery devices via self-assembly of amphiphilic block copolymers. *Adv Drug Deliv Rev* 53: 95–108.
2. Kataoka K, Harada A, Nagasaki Y (2001) Block copolymer micelles for drug delivery: design, characterization and biological significance. *Adv Drug Deliv Rev* 47: 113–131.
3. Torchilin V.P (2007) Micellar nanocarriers: pharmaceutical perspectives. *Pharm Res* 24: 1–16.
4. Mikhail A.S, Allen C (2009) Block copolymer micelles for delivery of cancer therapy: transport at the whole body, tissue and cellular levels. *J. Contr. Release* 138: 214-223.
5. Chen H.Y, Huang BH, Lin CC (2005) A Highly Efficient Initiator for the Ring-Opening Polymerization of Lactides and ϵ -Caprolactone: A Kinetic Study. *Macromolecules* 38 5400-5045.
6. Greenwald RB, Choe YH, McGuire J, Conover C.D (2003) Effective drug delivery by PEGylated drug conjugates. *Adv. Drug. Deliv. Rev.* 55: 217-250.
7. Blanco E, Bey E.A, Dong Y et al. (2007) β -Lapachone-containing PEG–PLA polymer micelles as novel nanotherapeutics against NQO1-overexpressing tumor cells. *J. Contr. Release* 122: 365–374.
8. C. Jianjun, A. Benjamin, Teplya, S. Ines et al. (2007) Formulation of functionalized PLGA–PEG nanoparticles for in vivo targeted drug delivery. *Biomaterials* 28: 869–876.

Corresponding author:

Author: N.T.H. Anh
Institute: Ho Chi Minh City College of Food Industry
Street: Le Trong Tan
City: Ho Chi Minh
Country: Vietnam
Email: anhnth@cntp.edu.tw

Synthesis and *in Vitro* Cell Compatibility of α -Tricalcium Phosphate-Based Apatite Cement Containing Tricalcium Silicate

L.J. Cardenas¹, A. Takeuchi², K. Tsuru², S. Matsuya³, and K. Ishikawa²

¹ College of Dentistry, Iloilo Doctors' College, Timawa Ave., Molo, Iloilo City, Philippines

² Department of Biomaterials, Faculty of Dental Science, Kyushu University, 3-1-1 Maidashi, Higashi-ku, Fukuoka, Japan

³ Section of Bioengineering, Department of Dental Engineering, Fukuoka Dental College, 2-15-1 Tamura, Sawara-ku, Fukuoka, Japan

Abstract— The presence of silicate in artificial bone graft material is known to be effective in increasing bone formation rate. We previously reported the basic setting properties of α -tricalcium phosphate (α -Ca₃PO₄; α -TCP) based apatite cement (AC) with various amount of tricalcium silicate (Ca₃SiO₅; alite) addition using sodium dihydrogen phosphate (NaH₂PO₄) as the liquid phase. In this study, *in vitro* biological compatibility of pure α -TCP and 2.5-10.0 wt% alite added to α -TCP based AC is investigated in terms of cell attachment, proliferation and differentiation.

Set ACs aged for 168 hrs were used for cell studies with bone marrow cells from tibia of 4 week-old, male, SD rat. Initial cell attachment was observed after 7 hrs; cell proliferation was observed after 3, 5, and 7 days. Cell differentiation (alkaline phosphatase activity) was observed after 3, 6, and 9 days of incubation.

Cell attachment of alite added ACs were almost the same as sintered hydroxyapatite (HAp) and alite-free AC. Cell proliferation at 2.5-7.5 wt% alite added ACs were significantly higher at day 5 and 7 ($p < 0.05$). Alkaline phosphatase activity revealed that 2.5 wt% alite addition accelerated the osteogenic cell activity at day 6 and 9 ($p < 0.05$) whereas too much alite addition resulted in the decrease of osteogenic cell activity.

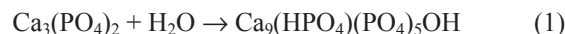
In conclusion, we found that α -TCP based AC containing appropriate amount of alite could be an improved AC since it shows suitable setting time, higher mechanical strength and possible higher osteoconductivity.

Keywords— Apatite cement, α -tricalcium phosphate, Tricalcium silicate, Silicate, Setting properties, *In vitro*.

I. INTRODUCTION

Apatite cement (AC) based on calcium phosphates offer an advantage for being freely moldable and adaptable to the surface of bone defect. In addition, they have excellent biocompatibility because of their similarity to the inorganic component of the calcified tissue of the body [1,2]. The first AC, reported by Prof. Monma and Kanazawa in 1976 was based in α -tricalcium phosphate (α -TCP, α -Ca₃(PO₄)₂), the cement converted to calcium deficient HAp (CDHAp, Ca₉(PO₄)₅(OH)₂) at a temperature below 100°C [3]. Setting

reaction of α -TCP is simple and involves only a two step reaction; the dissolution of TCP when mixed with water, and precipitation into CDHAp, in the following setting reaction:



CDHAp is a “non-stoichiometric” HAp, it is more resorbable than stoichiometric HAp (sintered HAp) [4]. Therefore, it may be incorporated to bone more readily by osteocytes.

It was reported that Si-containing bioactive materials exhibit excellent ability to induce the formation of bone-like HAp *in vitro* and *in vivo* by activating bone related bone expression and stimulate cell proliferation [5,6]. Camire *et al.* [5] had previously documented AC using Si-substituted α -TCP synthesized by solid-state reaction of various α -TCP substitution amounts (1 and 5 mol% belite (Ca₂SiO₄)) by reacting mixture of calcium carbonate (CaCO₃), calcium pyrophosphate (Ca₂P₂O₇), and silicon dioxide (SiO₂). Results showed the positive effect of Si in bone formation and integration when AC was implanted into rabbits. However, mechanical property of the AC decreased with the increase in Si content. Belite is also a good candidate as additive to improve the osteoconductivity of AC. Nonetheless, its hydration is much slower when compared with tricalcium silicates (Ca₃SiO₅, alite), which also contain Si. In our preliminary study, belite also showed limited effects. Cardenas *et al.* [7] previously investigated alite added AC with higher mechanical strength and suitable setting properties using 2.5-5.0 wt% alite as additive.

In this study, alite was used as the source of Si to α -TCP-based AC. Cements were studied with respect to its setting properties and *in vitro* biocompatibility.

II. MATERIALS AND METHODS

A. Sample Preparation and Characterization

Alite was synthesized in the same manner mentioned in our previous study [7]. Briefly, three moles of CaCO₃ (Wako Pure Chemical Industries, Ltd., Osaka, Japan) and

one mole of SiO₂ (Wako Pure Chemical Industries, Osaka, Japan) were mixed in ethanol for 4 hrs, preheated at 1000°C for 2 hrs, and air quenched. The product was subsequently heated at 1500°C for 24 hrs and air quenched. The alite powder was sieved in a 45 µm screen to eliminate the inclusion of larger particles and the resultant alite of about 10 µm was used as additive. Commercial α-TCP powder (α-TCP B, Taihei Chemical, Osaka, Japan) approximately 5 µm in size was used as base powder phase for AC. Synthesized alite powder was mixed with α-TCP powder in ratios of 2.5, 5.0, 7.5, 10.0, 20.0 wt% (e.g. 2.5 wt% alite means 0.975 g α-TCP powder and 0.025 g alite powder) using sample mill (Kyoritsu-Rikou SK-M2, Tokyo, Japan). As the liquid phase of AC, aqueous solution of sodium dihydrogen phosphate (NaH₂PO₄) was prepared by dissolving NaH₂PO₄ (Wako Pure Chemical Industries, Ltd., Osaka, Japan) in distilled water so that the concentration became 0.25 mol/L. Each powder was carefully weighed and mixed with the liquid phase at powder-to-liquid ratio of 2 using a stainless steel cement spatula and packed into split stainless mold (6 mm in diameter x 3 mm in height). Both ends of the mold were covered with glass plates and aged at 37°C and 100% relative humidity for 24 hrs. Some of the specimens aged for 24 hrs were subsequently aged in distilled water at 37°C for 144 hrs. After aging, the specimen were soaked in acetone for 3 min and dried at 60°C to arrest further reaction.

Initial setting time was measured using standard Vicat needle apparatus (Maruto Testing Company, Tokyo, Japan) based on ISO1566. Packed cements in Teflon mold were kept at 37°C and 100% relative humidity condition. Cements (n=3) were checked from time to time using testing apparatus by dropping the 1 mm diameter needle with 300 grams load. Setting time was defined as an elapsed time until the needle failed to penetrate or produce flaws on the surface of the cement. Dried fractured surface of the specimen was sputter-coated with gold and examined under the scanning electron microscope (JEOL, JSM 5400LV, Tokyo, Japan) with accelerating volt of 15kV. Dried specimen were ground to fine powder with an agate mortar and pestle and characterized under X-ray diffractometer (XRD, Rigaku, RINT2500V, Tokyo, Japan) with the CuKα radiation generated at 20 KV and 40 mA. Mechanical strength of set AC (n=5) was evaluated in terms of diametral tensile strength (DTS) at a loading rate of 1 mm/min.

B. *In vitro* Biological Study of Set AC

Bone marrow cell (BMC) culture: Bone marrow cells harvested from 4-week-old, male, SD rat were cultured in α-minimal essential medium (α-MEM; SIGMA-Aldrich Co., UK) supplemented by 20% fetal bovine serum (FBS;

Biowest, France) and 1% antibiotics (Penicillin-Streptomycin; Invitrogen Co., N.Y., U.S.A.), stored inside the incubator under 37°C with 5% CO₂ for 5 days.

Cell attachment and cell proliferation rate determination: AC specimens aged for 168 hr were utilized and were sterilized by autoclaving. Five-day-old cultured cells were rinsed with phosphate buffer solution (PBS) for 3 times to remove any adherent cells. Cultured BMC were detached by 0.25% trypsin EDTA solution and counted using haemocytometer and adjusted to 5000 cells / well using the culture medium. Cells were seeded on the specimen (n=3) with an area of 0.785 cm² and stored inside the incubator under the above-mentioned condition. After 7 hrs, 3, 5 and 7 days, the specimen were rinsed with PBS, detached with 0.25% trypsin EDTA solution and counted using haemocytometer. Cell attachment rate after 7 hrs were calculated for the percentage of attached cells.

Alkaline phosphatase (ALP) activity: ALP activity of the supernatant was measured using an ALP B-Test WAKO kit (Wako, Japan) based on the Bessey-Lowry method. ALP activity was normalized by samples total protein production measured with a Bicinchoninic Acid Assay (BCA, BCA™ Protein Assay Kit, Pierce Biotechnology, U.S.A.).

III. RESULTS

A. *Setting Properties and Characterization of AC*

Table 1 shows the initial setting time of the AC containing 0.0, 2.5, 5.0, 7.5, 10.0, 20.0 wt% alite and their DTS after 24 hrs and 168 hrs. Initial setting time of alite-free AC (0.0 wt%) was approximately 7 min and increased to 11-16 min when the amount of alite addition was increased up to 10.0 wt%. The addition of 20.0 wt% alite significantly extended the setting time at approximately 180 mins. DTS values of 2.5 and 5.0 wt% alite (14.4±1.9 MPa and 12.3±1.7 MPa, respectively) after 24 hrs were higher than that of alite-free AC. AC containing 7.5 wt% alite shows quite lower DTS at 24 hrs compared to alite-free AC but drastically increased thereafter and reached its maximum after 168 hrs. While AC containing 10.0-20.0 wt% alite obtained the lower DTS values compared to the rest of the cements.

Figure 1 shows the XRD patterns of the set AC containing 0.0, 2.5, 5.0, 7.5, 10.0 and 20.0 wt% alite after 168 hrs of aging. The XRD pattern of pure α-TCP and commercial HAP were also shown for comparison. The transformation of cement into apatite was almost completed after 24 hrs for ACs with 0.0-7.5 wt% alite. In contrast, ACs with 10.0-20.0 wt% alite suppressed the apatite formation even after 168 hrs.

Table 1 Initial setting time of 0.0, 2.5, 5.0, 7.5, 10.0, 20.0 wt% of alite and their diametral tensile strength (DTS) after 24 and 168 hrs

Powder (wt %)		Setting Time (min)	Diametral Tensile Strength (MPa)	
α -TCP	alite		24 hr	168 hr
100.0	0.0	7 \pm 1	9.3 \pm 0.6	10.7 \pm 1.8
97.5	2.5	11 \pm 0	14.4 \pm 1.9	13.8 \pm 1.7
95.0	5.0	12 \pm 0	12.3 \pm 1.7	12.0 \pm 1.3
92.5	7.5	16 \pm 1	7.1 \pm 0.8	11.8 \pm 0.8
90.0	10.0	16 \pm 1	2.3 \pm 0.4	2.4 \pm 0.6
80.0	20.0	176 \pm 7	0.9 \pm 0.4	0.9 \pm 0.1

B. In vitro Biological Study

Cell attachment rate of all AC samples showed no significant difference after 7 hrs of incubation. However, during the 5th day of incubation, cell proliferation rate of most of the alite-containing ACs showed significant difference ($p < 0.05$) when compared to 0.0 wt% alite AC (graph not shown).

Figure 2 shows the result of the total ALP activity value per total protein unit on each specimen after 3, 6 and 9 days of culturing. ALP activity during 3 and 6 days among specimen were quite limited. However, on the 9th day of culturing, ALP activity of 2.5 wt% alite added AC is more than twice the value ($p < 0.05$) of sintered HAp and pure α -TCP cement.

IV. DISCUSSION

Recently, studies about the incorporation of Si to ceramics and ACs have been seriously undertaken by many scientists because of the biomimetic effect of Si and the enhanced osteoconductivity of the material [8]. However, appropriate source and amount of Si for implant materials is still not established.

Alite in α -TCP has some roles in the setting properties of AC. Silicate ion is known to promote apatite nucleation in certain bioactive glasses and ceramics [6,8]. In this study, silicate ion from alite may also promote the nucleation of apatite and entanglement of the crystals as well. Thus, final DTS of set ACs with 2.5-7.5 wt% alite were improved (Table 1). Another reason may be the formation of calcium silicate hydrogel, which could provide core-matrix structure in the apatite formation (however, the present of silicate hydrogel is not yet proven in our study). Unfortunately, dissolution of alite produced an alkaline circumstance and

suppressed the apatite crystal formation resulting to low mechanical strength. Due to promoted apatite nucleation as mention earlier and the presence of alkaline circumstance, nucleation of apatite proceeds competitively and therefore setting properties of AC with alite seemed to be complex.

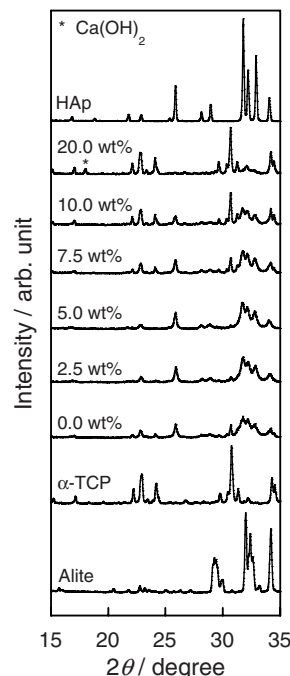


Fig. 1 XRD patterns of different ACs after 24 hrs of incubation. The XRD pattern of pure alite, α -TCP and HAp are also shown for comparison

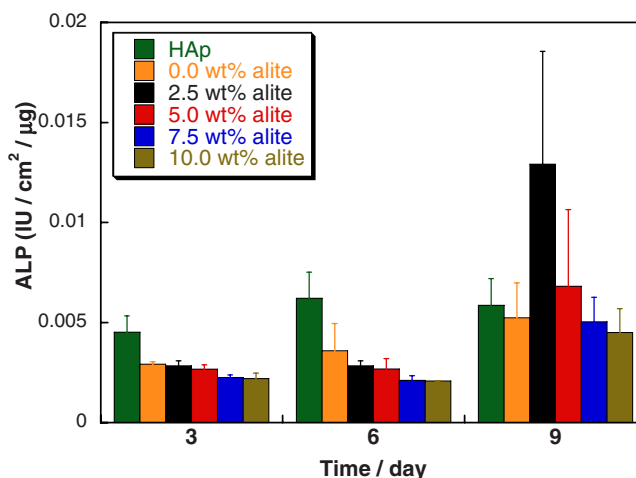


Fig. 2 The ALP activity of AC containing 0.0, 2.5, 5.0, 7.5 and 10.0 wt% alite is shown. Sintered HAp is also indicated for comparison

Previous studies revealed that Si is found on the growth front during early bone formation in higher animals and in

bioceramics by enhancing mesenchymal cell differentiation and osteoblast activity [8,9]. In this study, presence of alite as the source of Si improved the osteoconductivity of α -TCP based AC. In cell proliferation analysis, most of the alite-containing ACs (2.5-7.5 wt%) obtained higher proliferation rate ($p < 0.05$) as early as 5 days of culturing when compared against alite-free AC and HAp. During the 7 days of culturing, cell proliferation rate increase in number with increasing alite content up to 7.5 wt% (graph not shown). This result indicates that only an optimum amount of alite should be added to improve the initial osteogenic cell biocompatibility of AC. The cell differentiation assay (in terms of ALP) showed that 2.5 wt% alite AC ($p < 0.05$) obtained the highest ALP activity in contrast to the rest of the tested samples (Fig. 2).

The *in vitro* results suggest that only a small amount of alite or Si is deemed necessary to improve the osteoconductivity of α -TCP based AC. Other researchers already noticed that some higher level of Si compounds might cause other diseases such as urolithiasis, lung fibrosis and Balkan nephropathy [10,11]. Therefore, too much Si is also harmful to the health of individuals. Even up to date, the ideal Si level in the body remained undefined.

V. CONCLUSIONS

In conclusion, we found that α -TCP based AC containing appropriate amount of alite could be an improved AC since it shows suitable setting time, higher mechanical strength and possible higher osteoconductivity. Based on the findings in our present study, further *in vitro* and *in vivo* biological studies are now in progress.

ACKNOWLEDGMENT

This study was supported in part by a grant-in-aid for Scientific Research from the Ministry of Education, Sports, Culture, Science and Technology, Japan.

REFERENCES

1. Constantino PD, Hiltzik DH, Sen C, Friedman CD et al. (2001) Sphoethmoid cerebrospinal fluid leak repair with hydroxyapatite cement. Arch Otolaryngol Head Neck Surg 127:588-593
2. Ros DA, Marentette LJ, Thompson G, Haller JS. (1999) Use of hydroxyapatite bone cement to prevent cerebrospinal fluid leakage through frontal sinus. Neurosurgery 45:401
3. Monma H, Kanazawa T. (1976) The hydration of α -tricalcium phosphate. Yogyo-Kyokai-Shi 84:209-13
4. Wei X, Urgurlu O, Akinc M. (2007) Hydrolysis of α -tricalcium phosphate in simulated body fluid and hydration behavior during the drying process. J Am Ceram Soc 90:2315-2321
5. Camire CL, Saint-Jean SJ, Mochales C et al. (2006) Material characterization and *in vivo* behavior of silicon substituted α -tricalcium phosphate cement. J Biomed Mater Res B Appl Biomater 76B:424-431
6. Kokubo T, Ito S, Huang ZT et al. (1990) Ca-P-rich layer formed on high-strength bioactive glass-ceramics A-W. J Biomed Mater Res 74:331-343
7. Cardenas LJ, Takeuchi A, Matsuya S, Ishikawa K. (2008) Effects of tricalcium silicate addition on basic properties of α -tricalcium phosphate cement. J Ceram Soc Jap (116)83-87
8. Hench LL. (1991) Bioceramics: from concept to clinic. J Am Ceram Soc 74:1487-510
9. Carlisle EM. (1970) Silicon a possible factor in bone calcification. Science 167:279-280
10. Leusmann DB, Pohl J, Kleinhans G. (1986) Urolithiasis in a patient injecting pure silica: a scanning electron microscopy study. Scan Electron Microsc 2:757-60
11. Lugowski SJ, Smith DC, Lugowski JZ et al. (1998) A review of silicon and silicone determination in tissue and body fluids – a need for standard reference materials. Fresenius J Anal Chem 360:486-488

Corresponding author: Lester Joseph G. Cardenas
 Institute: College of Dentistry, Iloilo Doctors' College
 Street: Timawa Ave., Molo
 City: Iloilo City 5000
 Country: Philippines
 Email: lester_cardenas@yahoo.com

In Vitro Culture and Differentiation of Osteoblasts on Coral Scaffold from Human Bone Marrow Mesenchymal Stem Cells

C. Gargiulo¹, H.D. Thao¹, H.M. Tuan¹, T.T.T. Thuy¹, P.H. Van³, L. Filgueira², and T.C. Toai¹

¹ Pham Ngoc Thach Medical University, department of Histo-pathology, Embryology, Genetics and Biotechnology for tissue transplants, Ho Chi Minh city, Vietnam

² University of Western Australia School of Anatomy and Human Biology

³ The Central Lab of the University of Medicine and Pharmacy, Ho Chi Minh City, Vietnam

Abstract— Biomaterial such as corals is an excellent osteoconductive material to be used to bone human derived stem cells for clinical regenerative intent. Bone regeneration is often needed for multiple clinical purposes for instance in aesthetic reconstruction and regenerative procedures. In this paper we describe an approach that aim to provide fundamental information allowing a scientific biomechanical basis for use of natural coral scaffold to initiate mesenchymal stem cells into osteogenic differentiation process for transplant purposes. Isolated MSCs from human bone marrow were induced into osteoblasts by using an osteogenic medium enriched with two specific growth factors FGF9 and vitamin D2. Eventually, part of cultured MSCs were directly transferred and seeded onto coral scaffolds and induced to differentiate into osteoblasts and part were cultured in apposite flask for mesenchymal stem cell medium. Finally, our data indicated that hBM is a very reliable source of MSCs and that these cells may be easily differentiated into osteoblast and seeded into coral as optimal device for clinical application.

Keywords— osteoblast, mesenchymal stem cell, human bone marrow, coral, transplantation.

I. INTRODUCTION

Bone graft replacements are essential for multiple clinical purposes and worldwide the need of bone graft procedure is extremely high second only to bone transfusion (1). Numerous are the condition require bone graft replacement such as regeneration of damaged bone caused by disease, trauma or infection, unsolved fracture healing caused by failure of the highly specific response of body to restore the bone integrity or simply to enhance the bone reconstruction around surgically implanted devices to maintain a correct alignment of bone after rupture or crack (10, 15). The use of bio-material could be an alternative solution to avoid those problems due to their high tolerability by the host with almost null impact on host immune system (3). Bio-material should possess specific mechanical properties compatible with the anatomical area into which they are to be inserted, and should have enough volume fraction with high surface area to carry a high

number of cells within the scaffold and the surrounding host tissues allowing its in-growth and vascularization (9). There are available several bio materials such as sea-coral, fibrin, hydroxyapatite and demineralized bone matrix from cadaver and are used as scaffold in implant procedure (2, 4, 5, 16). In this project we propose the use of sea-coral as bio-osteoconductive material of osteoblast cells obtained from hBM MSCs for implant in individuals with bone defection, the plan is to deliver osteoprogenitor cells with scaffold right onto damaged site allowing a better bone regeneration.

II. MATERIALS AND METHODS

BM MSCs Collection and Culture

1.5 to 2.0 ml of bone marrow was collected from iliac crest and tested for exclusion of infection, including HIV, HBV, HCV and VDRL. After one week in culture, the average cell density was of 4.4×10^7 /ml. A total of 40.5 ml of BM blood (range $1-16 \times 10^7$) was measured with an average of 79.95 ± 8.31 CFU-Fs (range: 29-156 colonies). Mononuclear cells from BM were isolated by centrifugation at room temperature, in a density 1×10^7 cells/ml by using Ficoll-Paque (Amersham, Freiburg Germany) and PBS and centrifuged at 300g for 10 minutes. Suspended cells have been collected and counted by using trypan blue, 300 μ l suspended cells plus 3ml IMDM (IMDM, Gibco), plus 20 % FBS v/v (Gibco USA). Mononuclear cells were cultured in IMDM medium plus 15% FBS and 500 μ l penicillin-streptomycin and incubated at 37°C with in a humidified atmosphere with 5% CO₂. Non-adherent cells were removed by medium change performed every 3 days and washed by using PBS twice. Primary mononuclear cells started to attach average at day 2, they were passaged at day 8 at 70-80% confluence by using a solution of Trypsin-EDTA 2 (Gibco) and seeded in new flasks at density of cells 10^5 /ml.

Osteoblast Culture

Primary BM derived MSC were cultured in a medium solution composed of IMDM containing antibiotics, 15%

FBS, 10^{-7} M dexamethasone (Sigma Aldrich), $50\mu\text{g/ml}$ ascorbic acid (Sigma-Aldrich), 10mM/ml β -glycerol phosphate (Sigma Aldrich) and the additional combination of vitamin 10^{-7} M D2 and 10ng/ml FGF9.

Fluorescence Electronic Microscope

Either hBM MSCs or Osteoblast have been tested by fluorescence microscope for actin, desmin, vimentin, Runx2 and osterix (OSX). RUNX2 (Santa Cruz Biotechnology inc. USA) from purified goat polyclonal antibody raised against a peptide mapping at the C-terminus of RUNX2 of human origin. OSX (Santa Cruz Biotechnology inc. USA). Monoclonal Anti-Desmin antibody produced in mouse (Sigma-Aldrich) and monoclonal Anti-Vimentin antibody produced in mouse, (Sigma-Aldrich). Slides used are SuperFrost from Menzel, Filter Cards from Thermo Shandon, and Cytospin 3 centrifuge from Shandon together with holders and containers.

Fluorescence Staining Procedures

The reagents used are PBS, permeabilisation reagent 0.1% tritonX in PBS, staining solution 1 containing primary antibody, $100\mu\text{l}$ for each specimen, staining solution 2 containing secondary antibody with green fluorescence (FITC), phalloidine-Alexa fluor 546 stains for actin filaments and DAPI nuclear stain, $100\mu\text{l}$ for each specimen, glass jar, Dako mounting medium and cover slips. Slides were washed once in PBS in jar for 3 minutes, dried it was added $100\mu\text{l}$ of permeabilisation reagent per slide to cover all sections for 1 minute. Slides were washed in Jar with PBS for other 3 minutes, once dried it was added $100\mu\text{l}$ of staining solution 1 per slide to cover all sections for 1 hour. Slides were washed 3 times for 1 minute in PBS in a jar, by changing PBS and it was added $100\mu\text{l}$ of staining solution 2 per slide to cover all sections for 1 hour. Slides were dried and it has been mounted the tissue by using Dako mounting medium and seal the cover slips with nail varnish.

MSCs and Osteoblast Karyotyping

MSCs and osteoblast were harvested at approximately 70-80% confluence in culture flask T25cm2 and treated with colcemid for mitotic arrest. Then, cell pellet was suspended in KCl hypotonic solution and fixative's solution methanol: acetic acid (3:1). After that, cells were dropped onto cold wet slides and allowed to air-dry. Slides were denaturated in heat at least 40 minutes at 80°C . Following slides were colored in Giemsa staining's solution and wash in tap. Finally, twenty to 30 metaphase cells per slide were analyzed, the karyotype of each culture is representative of >80% cell confluence.

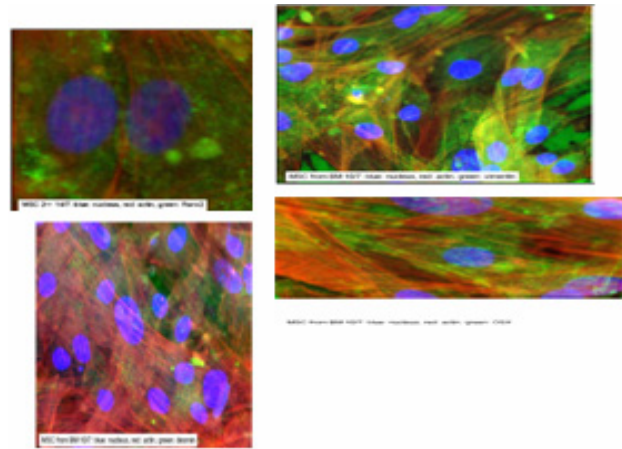


Fig. 2 MSCs stained for actin red color; runx2 green color

Fig. 3 MSCs stained for vimentin, green color; actin, red color

Fig. 4 MSCs stained for desmin, green color; actin, red color

Fig. 5 MSCs stained for osterix, green color; actin, red color

Coral Seeding and Preparation

One natural porous coral was selected, *Porites Lutea*. The coral was washed in 0.9% distilled water, lyophilization and sterilized gamma ray 25Kgy. MSCs were centrifuged five times with coral scaffold in osteogenic medium at 1000 rpm and consecutively collected and seeded in culture flask with new 5ml osteogenic up to 21 days. Osteoblast destined for fluorescence analysis by electronic microscope was harvested at day 7 while cells destined to be tested by AP were harvested after 21 days.

RT-PCR

Total RNA extraction of the tested cell culture was carried-out including the positive control using the Trizol LS reagent (Invitrogen). The supernatant was removed without losing the precipitated RNA at the bottom or on one side of the bottom of the tube.

The cDNA synthesis was carried-out using the inscript cDNA synthesis kit (Biorad).

Finally, the multiplex PCR was carried-out for osteocalcin and actin. Osteocalcine forward primer (5'-CGC AGC CAC CGA GAC ACC AT-3') 25pm/reaction, Osteocalcine reverse primer (5'-GGG CAA GGG CAA GGG GAA GA-3') 25pm/reaction, Actin forward primer (5'-CCA AGG CCA ACC GCG AGA AGA TGA C-3') 25pm/reaction, Actin reverse primer (5'-AGG GTA CAT GGT GGT GCC GCC AGA C-3') 25pm/reaction; Results were read under agarose gel electrophoresis with #600bps band for actin expression, and #400bps band for osteocalcin expression.

III. RESULTS

In vitro culture of MSCs from hBM and their morphology. To investigate and confirm the potential of hBM derived stem cells our team has isolated low density mononuclear cells from BM, and cultured under appropriate condition by using IMDM plus 15%FBS. In appropriate culture condition, at day 4 mononuclear cells started to form few adherent, fusiform and elongated fibroblast like cells clusters, each of which derived from a distinct precursor cell, the CFU-F. MSCs have been tested for actin, vimentin, desmin, runx2 and OSX by fluorescence electronic microscope (fig.2-5). Eventually, MSCs from hBM were tested for karyotype (fig.1), chromosome preparations from primary MSC cultures at passage 4 were tested by conventional staining and G-banding techniques.

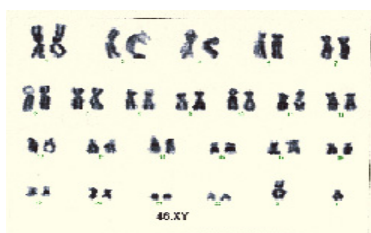


Fig. 1 MSCs Karyotype, cells are 30 days c.ca and 2nd generation

MSCs showed normal diploid karyotypes with no chromosome structural alteration, 46 XY or 46 XX, without aneuploidy or polyploidy, eventually these results indicate that the in vitro cultured MSCs are able to retained normal cytogenetics before and after being differentiated into osteoblasts.

By Fluorescence Electronic Microscope

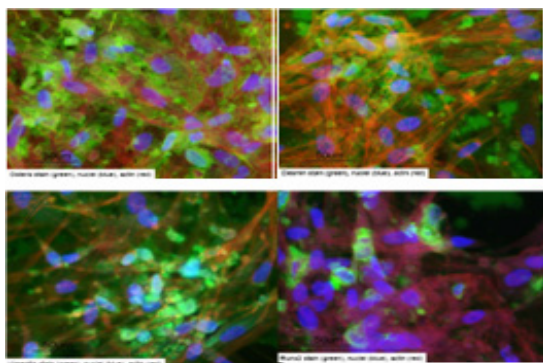


Fig. 6 Osteoblasts stained for osterix, green color; actin, red color, by fluorescence electronic microscope

Fig. 7 Osteoblasts stained for desmin, green color; actin, red color, by fluorescence electronic microscope

Fig. 8 Osteoblasts stained for Runx2, green color; actin, red color, by fluorescence electronic microscope

Fig. 9 Osteoblasts stained for Vimentin, green color; actin, red color, by fluorescence electronic microscope

IV. CHARACTERISTIC OF OSTEOBLAST CULTURES FROM BM AND THEIR MORPHOLOGY

In the presence of osteogenic inducers human BM mesenchymal like cells started to change shape, together with a continuous increase of AP and a high presence of typical nodules of hydroxyapatite. The morphology was assessed by inverse microscope and compared with cells from published studies. Osteogenesis was evaluated by classic cytochemical stain AR, AP and VK, by RT-PCR for osteocalcin markers by after a period of 21 days (fig.12), assessed for Runx2 and OSX by fluorescence electronic microscope (fig.6-9). Overall, osteoblast like cells from BM MSCs revealed an average high grade of homogeneity, and it was observed that all cell lines acquired their typical round-cuboidal shape within few days and showed to have a strong adherence capacity with a fast growth rate. At the beginning of week 2 cells started to produce a strong, compact matrix with high presence of calcium deposits. MSCs seeded on a coral scaffold began to adhere on scaffold surface just after a week, newly osteoblast colonies homed deep inside the porous and interstitial spaces of the coral and were tested for actin by fluorescence electronic microscope (fig.11) and also stained by HE, Giemsa and AP (fig. 10). Osteoblasts at second passage (60 day c.ca) tested for karyotype showed normal diploid karyotypes, 46 XY with no chromosomal defect, these results confirm that osteoblast may retain normal cytogenetics after a long period of in vitro culture.

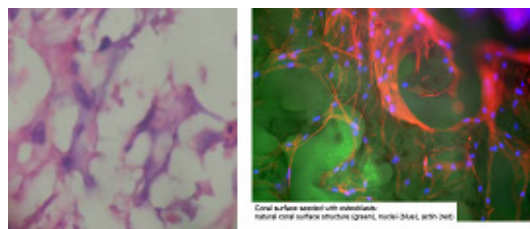


Fig. 10 Osteoblast like cells from hBM stained with AP, inverse microscope x400 at day 15

Fig. 11 Osteoblasts from hBM seeded on coral stained by fluorescence microscope for actin, red color; blue color are nuclei

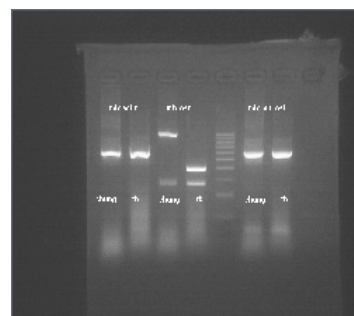


Fig. 12 The BM-MSCs osteoblast phenotype was evaluated by the expression of osteocalcin at day 15 by using RT-PCR following the manufacturer instruction

V. DISCUSSION

The results of our study show a behavior in vitro of BM derived MSCs and osteoblasts which are in line with data from published studies. After a relatively critical first phase of seeding we have successfully obtained without any substantial loss (less than 1%), cultures up to the 3rd generation, over a dozen samples of MSCs and osteoblasts from a single cell culture. The results have confirmed the ability of BM derived MSCs and osteoblast to adhere and proliferate on a coral scaffold, *Porites Lutea*, homing in the deepest interstices within a short time period (6, 7). These data are to be considered crucial because it has demonstrated that the coral scaffold may be used as an ideal osteoinductor and osteoconductor that can be eventually used in clinical procedure in treatment of complicate bone reconstructive procedures. Furthermore, our results showed two additional facts, first there is no apparent correlation between the donor's age and primary cells density and quantity of primary CFU-Fs collected from BM, second there is no correlation between donor's age and the survival rate of BM MSCs and osteoblast which survived over the third generation for more than three months. If we compare the data from the youngest donor, who is 18 years old, the density of his primary cells and the quantity of CFU-Fs is far more less than those from the oldest donor, who is 78 years old, with a ratio of 2.2/ml of cell density against 8.0/ml and a quantity of CFU-Fs of 34 against 110. Although, all osteoblasts from MSCs were positive for traditional stain as AR, AP, VK and HE our study has confirmed the relevant need of two additional growth factors in osteogenic medium such as vitamin D2 and FGF9 in order to obtain positive results for osteocalcin marker by RT-PCR. (5, 17), result that may be explained by the fact the expression of osteocalcin is not directly correlated with the results of cytochemical stains like AR, AP and VK (3). Vitamin D3 and D2, have the capacity to induce the presence of mRNA for osteopontin and reduce the level of FGF9 conversely the presence of FGF9 induces the level of CBFA1, osteopontin and collagen type1 (16). A fact, that was lately corroborated by other studies that confirmed how in vitro differentiation of embryonic stem cells (ES) and MSCs need specific inducers as ascorbic acid, dexamethasone and 1,25 dihydroxyvitamin D3, all essential factors for matrix deposition and mineralization (5, 7, 11). The importance of vitamin D3 and FGF9 in the new bone tissue formation it has been also confirmed by a different clinical studies that reported how atherosclerotic plaque formation recall the osteogenesis process and 1,25

dihydroxyvitamin D3 is deeply responsible of calcium influx into vascular smooth muscle cells as great inhibitor of their proliferation (19), while FGF9 has been demonstrated as critical factor for skeletal development especially in limb bud, in fact mice lacking of this factor show a defection known in humans afflicted with achondroplasia (18). As some author warns expansive subcultivation may eventually impair the cell functionality, by affecting their karyotype and telomerase activity, which consequently induces an earlier senescence and apoptosis (17). In fact, in vitro culture may alter the phenotypic stability of stem cells that means once they are re-injected in vivo they may start to differentiate into different cell lineage responding to specific micro-environmental signals (1, 8, 14). In addition, although there has been an extensive use of MSCs either in vitro or in vivo, still missing a conclusive understanding on the possible different behavior of fresh or non-manipulated versus expanded MSCs within the tissue microenvironment in vivo (11, 13). Therefore, it is essential to get clear the effective role and function between the progenitor cell lineage and the terminally committed progeny and the biological identity of the different types of MSCs (12). Some scientists speculate that some form of osteoporosis may be due to an abnormal tendency of osteoblast precursors to differentiate into adipocytes (19).

VI. CONCLUSIONS

hBM MSCs from our study showed homogenous characteristics and morphology and very distinctive traits and all can be easily cultured and seeded into coral scaffold. BM cells revealed an initial remarkable adherent capacity, a very fast proliferation, high versatility and a high growth rate, in addition these cells maintained their multipotential capability indeed osteoblasts were re-differentiate into MSCs presenting a great proliferation ability. In addition, results obtained by RT-PCR are in line with the observation that osteocalcin is completely expressed only when osteogenic medium is enriched of two additional factors as vitamin D2 and FGF9. To conclude, at the present one fact is well consolidated, the future of stem cells and their effective use in clinical field still require time. As some author diligently warns, we still have to solve a few crucial issues before considering their definitive use in clinical treatments for human diseases, it is critical to know the final fate of stem cells once they are transfused in a new environment and their specific involvement either in tissue healing or as aetiopathogenic agents.

REFERENCES

1. Bari C de, F Dell'Accio; Mesenchymal stem cells in rheumatology: a regenerative approach to joint repair; *Clinical Science* 2007, 113:339-348.
2. Bodine PVN; Wnt signaling control of bone cell apoptosis; *Cell research* 2008, 18:248-253.
3. Chamberlain G, J Fox, B Ashton, J Middleton; Mesenchymal stem cells: their phenotype, differentiation capacity, immunological features and potential for homing; *Stem Cells* 2007, 25:2739-2749.
4. Chang YJ, DTB Shih, CP Tseng, TB Hsieh, DC Lee, SM Hwang; Disparate mesenchymal lineage tendencies in mesenchymal stem cells from human bone marrow and umbilical cord; *Stem Cells* 2006, 24:679-685.
5. Chao NJ, SG Emerson, KI Weinberg; Stem Cell Transplant; *Journal of Hematology* 2004, 1: 354 – 371.
6. Chen F, S Chen, K Tao, X Feng, Y Liu, D Lei, T Mao; Marrow derived osteoblasts seeded into porous natural coral to prefabricate a vascularized bone graft in the shape of human mandibular ramus: experimental study in rabbits; *Journal of Oral and Maxillofacial Surgery*, 2004, 42:532-537. Chun Y, TM Lee, KH Chiu, SY Shaw, CY Yang; A comparative study of the physical and mechanical properties of three natural corals based on the criteria for bone-tissue engineering scaffold; *J. Mater. Sci.: Mater Med*, 2009 20:1273-1280.
7. Hilton MJ, X Tu, X Wu, S Bai, H Zhao, T Kobayashi, HM Kronenberg, S Teitelbaum, P Ross, R Kopan, F Long; Notch signaling maintains bone marrow mesenchymal progenitors by suppressing osteoblast differentiation; *Nature Medicine* 2008, 14:3, 306-312.
8. Holick MF, RM Biancuzzo, TC Chen, EK Klein, A Young, D Bibuld, R Reitz, W Salameh, A Ameri, A D Tannenbaum; Vitamin D2 Is as Effective as Vitamin D3 in Maintaining Circulating Concentrations of 25-Hydroxyvitamin D; *Journal of Clinical Endocrinology & Metabolism* 2008 3:677-681.
9. Hung SC, NJ Chen, SL Hsieh, H Li, HL Ma, WH Lo; Isolation and characterization of size-sieved stem cells from human bone marrow; *Stem Cells*, 2002, 20:249-258.
10. Jono S, Y Nishizawa, A Shioi, H Morii; 1,25 dihydroxyvitamin D3 increases in vitro vascular calcification by modulating secretion of endogenous parathyroid hormone-related peptide; *Journal of the American Heart Association-Circulation* 1998, 98:1302-1306.
11. Lee HS, GT Huang, LL Chiou, MH Chen, CH Hsieh, CC Jiang; Multipotent mesenchymal stem cells from bone marrow near site of osteonecrosis; *Stem Cells* 2003, 21:190-199.
12. Silva L da, AI Caplan, NB Nardi; In search of the in vivo identity of mesenchymal stem cells; *Stem Cells* 2008, 26:2287-2299.
13. Song L, RS Tuan; Transdifferentiation potential of human mesenchymal stem cells derived from bone marrow; *FASEB Journal* 2004, 18:980-985.
14. Toai TC, HD Thao, NP Thao, C Gargiulo, PK Ngoc, PH Van, DM Strong; In vitro culture and differentiation of osteoblasts from human umbilical cord blood; *Cell Tissue Bank*, 2009, .
15. Tsai MS, SM Hwang, KD Chen, YS Lee, LW Hsu, YJ Chang, CN Wang, HH Peng, YL Chang, AS Chao, SD Chang, KD Lee, TH Wang, HS Wang, YK Soong; Functional network analysis on the transcriptomes of mesenchymal stem cells derived from amniotic fluid, amniotic membrane, cord blood and bone marrow; *Stem Cells Express* 2007, 25:10, 2511-2523.
16. Waese EY, R Kandel; Application of stem cells in bone repair; *Skeletal Radiology* 2007, 37:7, 601-608.
17. Winter EA de; What is the future of stem cells?; *Cytotechnology* 2003, 43:133-138.
18. Yavrapoulou MP, JG Yovos; The role of the Wnt signaling pathway in osteoblast commitment and differentiation; *Hormones* 2007, 6:4, 279-294.

Evaluation of Novel Carbon Nano-tube Particles in the Bacterial and Viral DNA and RNA Extraction from the Clinical Samples

S.T. Pham¹, K.C. Nguyen², D.X.A. Vo⁴, H.N. Hoang³, L.T.T. Ho⁴, and H.V. Pham³

¹ University of New South Wales, Sydney, Australia

² University of Medicine and Pharmacy, Hochiminh city, Vietnam

³ Nam Khoa Biotek Co., Ltd., Pty., Hochiminh city, Vietnam

⁴ Saigon High Tech Park, Hochiminh city, Vietnam

Abstract— Molecular techniques have become the most important methods of detecting bacterial and viral pathogens. However, current genomic extraction methods are currently limited in term of automation. In this study, carbon nano-tube was used as the vector to trap DNA and RNA molecules. The capability of carbon nano-tube to trap DNA and RNA was evaluated using samples (TB and HBV for DNA extraction and HCV for RNA extraction) with known quantities and compared to the previously established BOOM method for DNA extraction and Trizol-LS method for RNA extraction. No log difference was observed between the two methods of extraction. Carbon nano-tube is a novel material with potent for automation in molecular diagnosis.

Keywords— carbon nano-tube, DNA extraction, RNA extraction, molecular techniques, diagnosis.

I. INTRODUCTION

BOOM extraction technique was developed by Boom et al. in 1990 (1). This method has been long a method of choice in many diagnostic laboratories due to its rapidness, simplicity and performance (1, 2, 6, 7) Nevertheless, the limitation of this method was its limited automation capability and lack of high throughput. Current commercially available high throughput protocol, utilizing BOOM, was developed by Roche (3-5, 8) However, this product is limited to the current status of science in Vietnam due to the cost and machinery requirement.

The spiral structure of the carbon nano-tubes make this particle owns two essential characters: (1) trap the DNA and RNA molecules; (2) act like nano magnetic bar. Thank to these two characters, the carbon nano-tube particles can be used as the vehicle to trap and extract the DNA and RNA of the bacterial and viral pathogens from the clinical samples for PCR and qPCR testing.

In this study, we developed and set up the DNA/RNA extraction method using carbon nano-tubes as vehicle to trap, isolate, and purify the DNA/RNA of the bacterial and viral pathogens from the clinical samples ready for the PCR and qPCR testing. The object of this study is to evaluate the potential applications of the novel carbon nano-tube in a modern diagnostic laboratory.

II. MATERIAL AND METHODS

A. Material

Samples: Clinical samples were collected through a network of hospital in Hochiminh city. Samples were previously diagnosed with either HBV, HCV or TB by available PCR and qPCR methods.

DNA and RNA Extraction reagents and kits: BOOM¹ reagents for DNA extraction and Trizol-LS for RNA extraction were provided by Nam Khoa Co., Ltd. Pty (Nam Khoa, Hochiminh city, Vietnam).

Carbon nano-tube: Carbon nano-tube were constructed at Saigon High Tech Park (Hochiminh city, Vietnam) under the supervision of Prof. Nguyen KC (confidential protocol). We also develop the Extraction buffer (EB) for working with the carbon nano-tube to carry out the DNA/RNA extraction of the tested samples (the formula of EB is confidential).

B. Method

The novel carbon nano-tube based extraction: The extraction buffer (EB) was mixed with the carbon nano-tubes and added into samples. Sample genomic materials (RNA or DNA) were trapped on the carbon nano-tubes. The RNA/DNA bound carbon nano-tubes were then attached on the wall of the test tube under the magnetic field provided by the magnetized tube holder. The attached carbon nano-tube pellet was washed with the washing buffers and then with ethanol. After drying with heat, the DNA or RNA trapped on the carbon nano-tubes was eluted into the Tris-EDTA (TE) 1X buffer (concentration not shown).

Extraction DNA and RNA: Same samples were treated with Trizol-LS reagents and method for RNA extraction and BOOM reagents and method for DNA extraction. The methods were carried out according to the manufacturer's instruction. In brief, the BOOM method is relied on the lysis activity and nuclease activity properties of the chaotropic agent guanidine thiocyanate (GuSCN), and the DNA-binding properties of the silica particles in the

presence of this reagent. The Trizol-LS method is relied on the homogenization of the tested samples in the solution of guanidine 14M, urea, phenol and other detergents to lyse the cells and to denature the protein in the sample leaving the DNA dissolved in phenol and the RNA dissolved in water, then precipitate and collect the RNA in the water phase.

Detection and quantification of the extracted genomic materials by PCR and qPCR methods: Extracted genomic materials of each clinical samples were quantified by the available PCR and qPCR kits provided by Nam Khoa Co. Ltd. Pty. according to the manufacturer's instruction, specific for the diagnosed pathogens. PCR was performed in the iCycler machine and qPCR was performed in IQ5 PCR machine, both are from BioRad. Quantity in copies per mL of starting material was calculated based on the obtained Ct values.

Evaluation of the novel carbon nano-tube method: the capability of the novel carbon nano-tube extraction method was evaluated qualitatively and quantitatively by comparison the results of PCR that were carried out on the extracted genomic samples get from the novel carbon nano-tube based extraction and from the BOOM for DNA or Trizol-LS for RNA extraction. The PCR's limit of detection (LOD) of the target pathogen in the serial dilutions of the bacterial suspension (*M. tuberculosis*) and the strong positive samples (HBV positive sera) was also applied to evaluate quantitatively the capacity of the novel carbon nano-tube extraction method.

III. RESULTS

Automation is a need for future advancement in diagnosis. Carbon nano-tube's capability of attracting and retain nucleic acid material is an important property for development of a novel extraction method which can then be used in high-throughput isolation of genomic materials from viral and bacterial pathogens in diagnostic laboratories. Genomic materials from 39 sputum for *M. tuberculosis* detection by PCR, 157 sera and 16 sera for HBV-DNA and HCV-RNA, respectively, for detection and quantitative by PCR and qPCR ten samples of each HBV, HCV and *M. tuberculosis* were extracted by both the novel carbon nano-tube extraction method and the BOOM/Trizol-LS method. The performance of the novel carbon nano-tube extraction method was evaluated by comparing the quantitative results from the Real-time PCR.

The LOD (limit of detection): Testing on the serial dilution of the *M. tuberculosis* suspension and the serial dilution of the HBV-DNA positive sera, the LOD of BOOM method versus carbon nano-tubes method were the same: (figure 1).

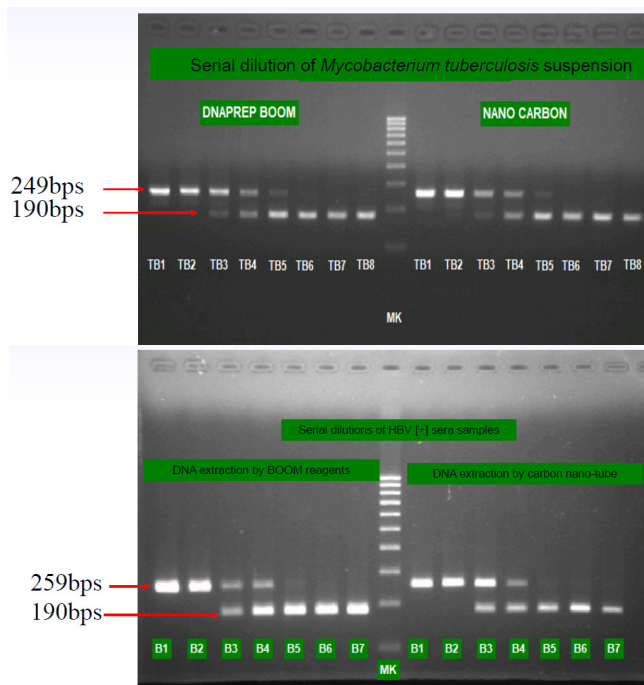


Fig. 1 Agarose gel electrophoresis the PCR products amplified from the DNA extraction done by BOOM reagents and done by carbon nano-tube of the serial dilution of the suspension of *M. tuberculosis* (upper picture) and of the serial dilution of the sera strong positive with HBV-DNA (lower picture). The result show no difference between the LOD of both methods. In the detection of *M. tuberculosis*, 249bps is the specific product amplified from the MTB genome and 190bps is the product amplified from the internal control DNA. In the detection of HBV-DNA, 259bps is the specific product amplified from the HBV genome and 190bps is the product amplified from the internal control DNA

Detection of the *M. tuberculosis*, HBV-DNA and HCV-RNA from the real samples by PCR: 39 sputum collected from patients with suspected pulmonary tuberculosis, 157 sera collected from patients with HBV infection, and 16 sera collected from patients with HCV infection were selected in this study. The sputa for *M. tuberculosis* detection and the sera for HBV-DNA detection and quantification were treated by BOOM reagents and by carbon nano-tube for DNA extraction. The sera for HCV-RNA detection and quantification were treated by Trizol-LS reagents and by carbon nano-tube for RNA extraction. The PCR was carried out for *M. tuberculosis* detection. The PCR and the qPCR were carried out for detection and quantification of HBV-DNA and HCV-RNA. The obtained results demonstrated that the BOOM method, Trizol-LS versus carbon nano-tubes have given no difference: 6/39 sputum were positive with *M. tuberculosis*, 103/157 sera were positive with HBV-DNA, 15/16 were positive with HCV-RNA. In qPCR, no difference more than 1 log was detected between carbon nano-tube method versus BOOM method and Trizol-LS

method. *Figure 2* demonstrated one result that showed no difference between the DNA extraction capacity of BOOM reagents with carbon nano-tube.

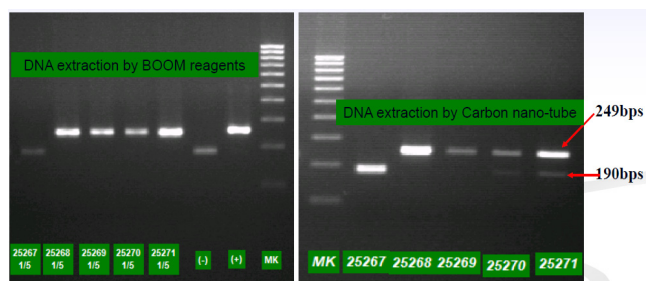


Fig. 2 Agarose gel electrophoresis the PCR products amplified from the DNA extraction done by BOOM reagents and done by carbon nano-tube of the sputa samples. The result show no difference in the detection of *M. tuberculosis* between both methods. The 249bps is the specific product amplified from the MTB genome and 190bps is the product amplified from the internal control DNA

IV. DISCUSSION AND CONCLUSIONS

From these results, the authors have believed that DNA/RNA extraction method using carbon nano-tubes is as sensitive as all methods that are currently using in most of the clinical laboratory where the available PCR and qPCR testing. This study is the primer for the development of the automated procedure for DNA and RNA extraction.

ACKNOWLEDGMENT

The project was funded by Nam Khoa Co., Ltd., Pty. under the RD fund and by the Saigon High Tech Park. All carbon nano-tube procedure and final products were provided by Dr. Nguyen KC. Samples were collected and delivered by Nam Khoa Co., Ltd., Pty. All technical work were performed at Nam Khoa Co., Ltd., Pty.

REFERENCES

1. Boom R, Sol CJ, Salimans MM, Jansen CL, Wertheim-van Dillen PM, van der Noordaa J. Rapid and simple method for purification of nucleic acids. *J Clin Microbiol* 1990 Mar;28(3):495-503.
2. Chomczynski P. A reagent for the single-step simultaneous isolation of RNA, DNA and proteins from cell and tissue samples. *Biotechniques* 1993 Sep;15(3):532-534, 536-537.
3. Cook L, Ng KW, Bagabag A, Corey L, Jerome KR. Use of the MagNA pure LC automated nucleic acid extraction system followed by real-time reverse transcription-PCR for ultrasensitive quantitation of hepatitis C virus RNA. *J Clin Microbiol* 2004 Sep;42(9):4130-4136.
4. Espy MJ, Rys PN, Wold AD, Uhl JR, Sloan LM, Jenkins GD, et al. Detection of herpes simplex virus DNA in genital and dermal specimens by LightCycler PCR after extraction using the IsoQuick, MagNA Pure, and BioRobot 9604 methods. *J Clin Microbiol* 2001 Jun;39(6):2233-2236.
5. Kessler HH, Muhlbauer G, Stelzl E, Daghofer E, Santner BI, Marth E. Fully automated nucleic acid extraction: MagNA Pure LC. *Clin Chem* 2001 Jun;47(6):1124-1126.
6. Kingston RE, Chomczynski P, Sacchi N. Guanidine methods for total RNA preparation. *Curr Protoc Mol Biol* 2001 May;Chapter 4:Unit4 2.
7. Ribaudo R, Gilman M, Kingston RE, Chomczynski P, Sacchi N. Preparation of RNA from tissues and cells. *Curr Protoc Neurosci* 2001 May;Appendix 1:Appendix 1I.
8. Stevens MP, Rudland E, Garland SM, Tabrizi SN. Assessment of MagNA pure LC extraction system for detection of human papillomavirus (HPV) DNA in PreservCyt samples by the Roche AMPLICOR and LINEAR ARRAY HPV tests. *J Clin Microbiol* 2006 Jul;44(7):2428-2433.

Corresponding authors:

Author: Pham ST (full name: Son Truong Pham)
 Institute: University of New South Wales
 Street: Biological Science Building, Lab 262, Gate 2, High Street, UNSW, Kensington.
 City: Sydney, NSW
 Country: Australia, 2052
 Email: s.pham@student.unsw.edu.au

Author: Pham HV (full name: Van Hung Pham)
 Institute: University of Medicine and Pharmacy
 Street: 793/58 Tran Xuan Soan, W. Tan Hung, Dist. 7,
 City: Hochiminh city
 Country: Vietnam
 Email: phhvan.nkbiotek@gmail.com

Stem Cell Origin and Microenvironment Contribution for NF1-Associated Neurofibromas

L.Q. Le^{1,2}, T. Shipman¹, D.K. Burns³, and L.F. Parada^{1,4}

¹Department of Developmental Biology, ²Department of Dermatology, ³Department of Pathology
The University of Texas Southwestern Medical Center, Dallas, Texas 75390-9133, USA

Abstract— The tumor predisposition disorder Neurofibromatosis type I (NF1) is one of the most common genetic disorders of the nervous system. It is caused by mutation in the *Nf1* tumor suppressor gene, which encodes a GTPase Activating Protein (GAP) that negatively regulates p21-RAS. The development of malignant nerve tumors and neurofibromas, the most frequent tumors in NF1, is a serious complication of the disease. However, little is known about the molecular mechanisms mediating the initiation and progression of these complex tumors, as well as the identity of the specific cell type that gives rise to dermal or cutaneous neurofibromas. In this study, we identify a population of neural crest related stem cells residing in the dermis termed Skin Derived Precursors (SKPs) that, through loss of *Nf1*, form neurofibromas. We propose that SKPs, or their derivatives, are the cell of origin of dermal neurofibroma. We also provide evidence that additional signals from the non-neoplastic cells in the tumor microenvironment play essential roles in neurofibroma tumorigenesis. These new findings provide a novel approach to gain a greater understanding of the molecular pathogenesis of neurofibroma and exploit innovative therapeutic approach in clinical trial to treat NF1-associated neurofibromas.

Keywords— neurofibromin, tumor microenvironment, dermal neurofibroma, NF1, SKPs.

I. INTRODUCTION

Neurofibromatosis type I (NF1) patients have a wide spectrum of clinical presentations, including developmental, pigment or neoplastic aberrations of the skin, nervous system, bones, endocrine organs, blood vessels and eyes. The cardinal features of NF1 are café au lait macules, axillary and groin freckling, combined with multiple peripheral and central nerve tumors [1, 2].

The development of neurofibromas, the most frequent tumor in NF1, and malignant nerve tumors represent a serious complication of NF1. These are unique and complex tumors that contain proliferating Schwann-like cells and other local supporting elements of the nerve fibers, including perineurial cells, fibroblasts, and blood vessels, as well as infiltration of mast cells. Neurofibromas are classified into three subtypes: cutaneous (dermal), subcutaneous and plexiform

neurofibromas. Dermal forms are exclusively in the skin and occur in virtually all individuals with NF1. They initially appear at puberty and increase in number with age and during pregnancy implicating a requisite hormonal component [3, 4]. Although similar to dermal neurofibromas at the cellular and ultrastructural levels, plexiform neurofibromas develop along a nerve plexus. They occur in about 30% of NF1 individuals and are virtually pathognomonic of the disease [3]. Unlike their dermal counterparts, plexiform neurofibromas are thought to be congenital and progressively enlarge throughout life. The temporally and spatially distinct clinical presentation of dermal vs. plexiform neurofibromas supports the hypothesis that these neurofibromas may originate from distinct progenitor cells. However, little is known about the molecular mechanisms mediating the initiation and progression of these complex tumors, as well as the identity of the specific cell type that gives rise to dermal or cutaneous neurofibromas. Recently, we identify a population of stem/progenitor cells residing in the dermis termed Skin Derived Precursors (SKPs) as the cell of origin of NF1-associated dermal neurofibromas. We show that *Nf1*-deficient SKPs can give rise to classic plexiform or dermal neurofibromas contingent on their local microenvironment and exhibit the same properties as the embryonic Schwann cell progenitors that give rise to plexiform neurofibromas. Furthermore, we show that loss of *Nf1* in SKPs is required but not sufficient to induce tumors and pointing to the essential role for the tumor microenvironment, including neurons and hormones, in neurofibroma development [5].

II. RESULTS

A. Isolation and Differentiation of Multipotent Neural Precursors from the Skin

We cultured mouse SKPs that were isolated from either back, neck or ear skin using a standardized neurosphere-forming assay [6]. Importantly, under the same conditions, we did not observe any sphere formation when we cultured bone marrow cells, indicating that these culture conditions have some specificity for neural stem/progenitor cells. As

previously demonstrated by Miller and colleagues, SKPs can be propagated *in vitro* under “undifferentiated” conditions for more than five passages and exhibit a surface marker expression profile similar to that of adult neural stem cells derived from brain dentate gyrus or subventricular zone, including nestin and glial fibrillary acidic protein (GFAP). In addition, SKPs also expressed fibronectin as previously reported [7]. We also confirmed their ability to generate neural crest derivatives including Schwann cells, neurons and adipocytes. These results are consistent with an adult stem/progenitor cell nature of SKPs.

B. *Ex vivo* Ablation of *Nf1* in SKPs to Induce *in vivo* Neurofibroma in Mice

NF1-associated plexiform and dermal neurofibromas always develop in close association with peripheral nerves whether it is a plexus in the former case, or dermal twigs in the latter. We implanted the *Nf1*^{-/-}; *LacZ*⁺ SKPs into the same animal, i.e., as an autograft, to avoid immunological rejection and to maintain a heterozygous microenvironment. When implanted intradermally/subcutaneously, we observed no tumor/neurofibroma formation over the course of seven months. We reasoned that one possible explanation for failure of tumor engraftment might be technical, caused by ineffective association of the mutant SKPs with terminal peripheral nerve projections. The sciatic nerve, a much larger nerve than those found in dermis, is a common site of plexiform neurofibromas in NF1. We therefore next reimplanted the SKPs into the sciatic nerves where close proximity to the nerve could be achieved. The autologously transplanted *Nf1*^{-/-}; *LacZ*⁺ SKPs gave rise to sciatic plexiform neurofibromas within two months post implantation 100% of the time, whereas the transplanted heterozygous (*Nf1*^{+/-}) SKPs showed no signs of tumor growth. The neurofibromas exhibited the characteristics of human plexiform neurofibromas (Fig. 1), being poorly circumscribed, composed primarily of spindle cells, and expressing the Schwann cell marker S100 β . We also observed excess collagen deposition and heavy infiltration of mast cells into these plexiform neurofibromas, a critical component of tumor initiation that is commonly observed in human neurofibromas. These data indicate that when placed in a favorable microenvironment (in proximity to a peripheral nerve), *Nf1*-deficient SKPs can give rise to *bona fide* plexiform neurofibromas. As such, these results show that SKPs have the full potential to generate neurofibromas and suggest that they may be the cell of origin of dermal neurofibroma.

C. *In vivo* Ablation of *Nf1* in the Skin to Induce Dermal Neurofibromas

Although we achieved neurofibroma formation by transplantation of purified, *Nf1*-ablated SKPs, we wished to

identify whether endogenous SKPs undergo neurofibromagenesis *in situ* in response to *in vivo* *Nf1* LOH. To address this issue, we applied tamoxifen onto the back and neck skin of neonatal *CMV-CreER*^{T2}; *Nf1*^{fllox/-} mice to ablate *Nf1* expression in SKPs *in vivo*. Six to seven months post tamoxifen application, we observed cutaneous nodules similar to human dermal neurofibromas at the application site on these mice. These tumors were analyzed histopathologically and all results indicated that these nodules were, in fact, dermal neurofibromas. Analyses included H&E staining, S100 β expression as well as other markers of Schwann cells, and Leder staining for mast cell infiltration (Fig. 2). These results further indicate that the cells of origin for dermal neurofibroma likely reside locally in the skin, since neurofibromas only developed at the site of tamoxifen application on the back and not at distant sites. Moreover, because the latency period is 6-7 months from the time of initiation to visible tumor development, it also suggests that the cells of origin of dermal neurofibroma are likely stem/progenitor cells and that other genetic/microenvironmental events, in addition to loss of *Nf1*, participate in dermal neurofibroma development.

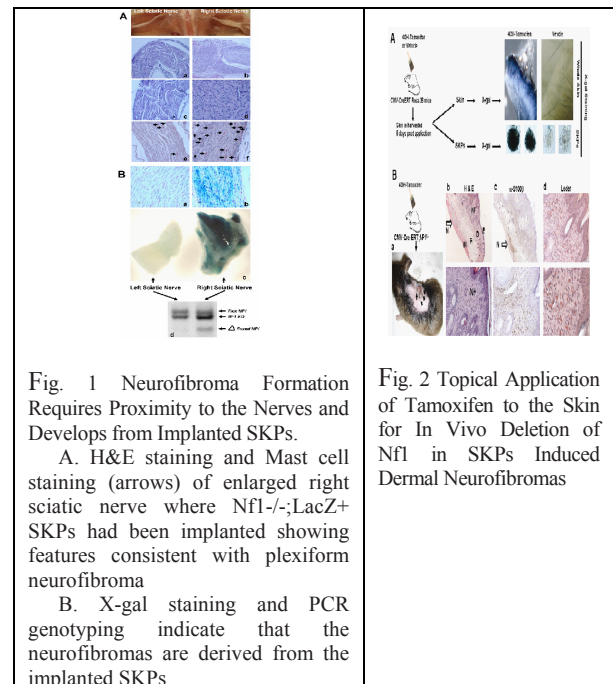


Fig. 1 Neurofibroma Formation Requires Proximity to the Nerves and Develops from Implanted SKPs.

A. H&E staining and Mast cell staining (arrows) of enlarged right sciatic nerve where *Nf1*^{-/-}; *LacZ*⁺ SKPs had been implanted showing features consistent with plexiform neurofibroma

B. X-gal staining and PCR genotyping indicate that the neurofibromas are derived from the implanted SKPs

Fig. 2 Topical Application of Tamoxifen to the Skin for *In Vivo* Deletion of *Nf1* in SKPs Induced Dermal Neurofibromas

D. *Nf1*-Deficient SKPs Give Rise to Classic Dermal Neurofibromas

In patients with Neurofibromatosis type I, dermal neurofibromas typically first appear around puberty and, subsequently continue to appear with time. These tumors have also been shown to increase in number and size during

pregnancy and, in certain cases, regress after delivery [8, 9]. These observations indicate that altered levels of certain hormones at puberty or during pregnancy may provide an important trigger to initiate or enhance dermal neurofibroma formation. Therefore, we next tested whether the hormonal milieu during pregnancy can facilitate induction of dermal neurofibroma development from *Nf1*^{-/-} SKPs in the skin. We again harvested skin from the backs and necks of male and female *CMV-CreER*^{T2};*Nf1*^{fllox/-};*ROSA26* mice for SKP isolation. We then exposed the *CMV-CreER*^{T2};*Nf1*^{fllox/-};*ROSA26* SKPs *ex vivo* to 4OH-tamoxifen to induce *NF1* deletion and dermally reimplanted the *Nf1*^{-/-};*LacZ*⁺ SKPs back to the same animals. The reimplantations were placed in the dorsal/sacral area to prevent the mice from scratching at the site of implantation. Both male and female mice were then housed in the same cage prior to reimplantation to facilitate breeding and all female mice eventually became pregnant. Strikingly, only the female mice, but not the male mice, developed cutaneous nodules at the graft site within three to four months post SKP implantation. Because the SKPs are LacZ-positive and the hosts are not, we performed X-gal staining on the tumors, which turned blue, indicating that the tumors derived from the transplanted SKPs. These results indicate that loss of *Nf1* expression in a permissive environment can effectively induce SKPs to form dermal neurofibromas. Moreover, as in the human condition, pregnancy accelerates and enhances tumor appearance, presumably due to hormonal influence. We conclude from these data that SKPs, or their derivatives, can be the cell of origin for NF1-associated dermal neurofibromas.

III. DISCUSSION

We undertook this study to test the hypothesis that SKPs were in fact the source of dermal neurofibromas in the context of *Nf1* deletion. Initially we did not observe neurofibroma formation when *Nf1*-nullizygous SKPs were implanted intradermally. However, in the human condition, dermal and plexiform neurofibromas are always physically associated with peripheral nerves and indeed when *Nf1*^{-/-} SKPs were implanted in proximity to the sciatic nerve, they always gave rise to neurofibromas. SKPs have the capacity to myelinate unmyelinated peripheral nerves *in vivo* [10, 11]. We therefore hypothesize that the microenvironment established by neurons and their associated cells may influence SKPs to preferentially differentiate toward the Schwann cell lineage creating a “window of opportunity” in which *Nf1* deficient progenitors become neurofibromas (Fig. 3).

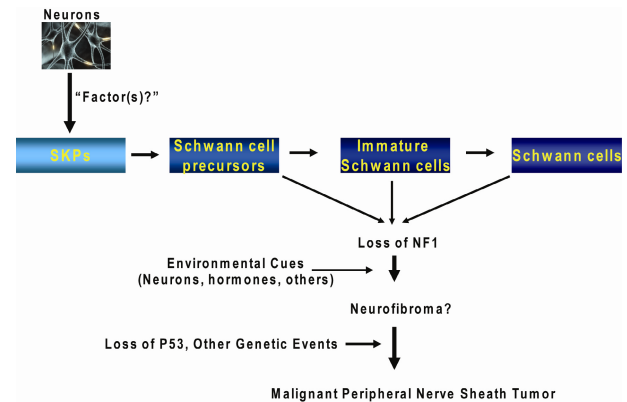


Fig. 3 Interaction between SKPs and Neurons is Required for Neurofibroma Formation.

Neurons may produce certain “physiologic factors” that preferentially induce SKPs (in the case of dermal neurofibroma) or NCSCs (in the case of plexiform neurofibroma) to differentiate toward the Schwann cell lineage. During this process of Schwann cell differentiation, loss of *Nf1* expression, in addition to other microenvironmental cues (such as hormones, neurons, inflammation, etc.), leads to neurofibroma formation. Subsequently, as the neurofibromas progress, they may acquire additional genetic alterations, such as loss of *P53*, amplification of *EGFR*, etc. that eventually lead to malignant peripheral nerve sheath tumor formation.

IV. CONCLUSIONS

Our data reveal a remarkable similarity of SKPs to embryonic neural crest precursors, apparently including the capacity to engender plexiform or dermal neurofibromas. The identity of the tumor cell of origin and the facility for isolation and expansion provides fertile ground for the continued analysis to identify additional factors and signals within the tumor microenvironment that likely play essential roles in neurofibroma genesis.

REFERENCES

1. Cichowski, K. and Jacks, T. 2001. NF1 tumor suppressor gene function: narrowing the GAP. *Cell* 104(4): 593-604.
2. Ward, B.A. and Gutmann, D.H. 2005. Neurofibromatosis 1: from lab bench to clinic. *Pediatric neurology* 32(4): 221-228.
3. Ferner, R.E. 2007. Neurofibromatosis 1. *Eur J Hum Genet* 15(2): 131-138.
4. Lakkis, M.M. and Tennekoon, G.I. 2000. Neurofibromatosis type 1. I. General overview. *Journal of neuroscience research* 62(6): 755-763.
5. Le, L.Q., Shipman, T., Burns, D.K., Parada, L.F. (2009). Cell of origin and microenvironment contribution for NF1-associated dermal neurofibromas. *Cell Stem Cell* 4 (5): 453-463.
6. Biernaskie, J.A., McKenzie, I.A., Toma, J.G., and Miller, F.D. 2006. Isolation of skin-derived precursors (SKPs) and differentiation and enrichment of their Schwann cell progeny. *Nat Protoc* 1(6): 2803-2812.

7. Toma, J.G., McKenzie, I.A., Bagli, D., and Miller, F.D. 2005. Isolation and characterization of multipotent skin-derived precursors from human skin. *Stem Cells* 23(6): 727-737.
8. Dugoff, L. and Sujansky, E. 1996. Neurofibromatosis type 1 and pregnancy. *Am J Med Genet* 66(1): 7-10.
9. Roth, T.M., Ramamurthy, P., Muir, D., Wallace, M.R., Zhu, Y., Chang, L., and Barald, K.F. 2008. Influence of hormones and hormone metabolites on the growth of Schwann cells derived from embryonic stem cells and on tumor cell lines expressing variable levels of neurofibromin. *Dev Dyn* 237(2): 513-524.
10. McKenzie, I.A., Biernaskie, J., Toma, J.G., Midha, R., and Miller, F.D. 2006. Skin-derived precursors generate myelinating Schwann cells for the injured and dysmyelinated nervous system. *J Neurosci* 26(24): 6651-6660.
11. Biernaskie, J., Sparling, J.S., Liu, J., Shannon, C.P., Plemel, J.R., Xie, Y., Miller, F.D., and Tetzlaff, W. 2007. Skin-derived precursors generate myelinating Schwann cells that promote remyelination and functional recovery after contusion spinal cord injury. *J Neurosci* 27(36): 9545-9559.

Author: Lu Q. Le, M.D., Ph.D.

Institute: The University of Texas Southwestern Medical Center

Street: 5323 Harry Hines Blvd

City: Dallas, Texas 75390-9069

Country: USA

Email: Lu.Le@UTSouthwestern.edu

Green Tea Epigallocatechin Gallate Exhibits Anticancer Effect in Human Pancreatic Carcinoma Cells via Inhibition of Both FAK and IGF-1R

H.A. Vu^{1,2,3}, Y. Beppu⁴, H.T. Chi^{2,5}, K. Sasaki⁴, H. Yamamoto⁴, P.T. Xinh^{2,3}, T. Tanii⁴, Y. Hara⁶,
T. Watanabe⁵, Y. Sato², and I. Ohdomari⁴

¹Consolidated Research Institute for Advanced Science and Medical Care (ASMeW), Waseda University, Tokyo, Japan

²Division of Ultrafine Structure, Department of Pathology, Research Institute of International Medical Center of Japan, Tokyo, Japan

³University of Medicine and Pharmacy – Ho Chi Minh City, Vietnam

⁴Faculty of Science and Engineering, Waseda University, Tokyo, Japan

⁵Department of Medical Genome Sciences, Graduate School of Frontier Sciences, the University of Tokyo, Tokyo, Japan

⁶Tea Solutions, Hara Office Inc, Food Research Lab, Miyabara, Fujieda City, Japan

Abstract— Objectives: Green tea epigallocatechin gallate (EGCG) has been shown to exhibit a growth-suppressive effect on human pancreatic cancer cells; however, the exact molecular mechanism by which EGCG suppresses cell proliferation is unclear. We hypothesize that interference with cell adhesion might be one mechanism. **Methods:** The effect of EGCG on cell adhesion and proliferation was examined using pancreatic cancer cells. **Results:** EGCG-treated pancreatic cancer cells AsPC-1 and BxPC-3 decrease cell adhesion ability on micro-pattern dots, accompanied by dephosphorylations of both focal adhesion kinase (FAK) and insulin-like growth factor 1 receptor (IGF-1R), whereas retained the activations of mitogen-activated protein kinase and mammalian target of rapamycin. The growth of AsPC-1 and BxPC-3 cells, when cultured at low density, can be significantly suppressed by EGCG treatment alone in a dose-dependent manner. At a dose of 100 μ M that completely abolishes activations of FAK and IGF-1R, EGCG suppresses more than 50% of cell proliferation without evidence of apoptosis analyzed by PARP cleavage. Finally, the MEK1/2 inhibitor U0126 enhances growth-suppressive effect of EGCG. **Conclusions:** Blocking FAK and IGF-1R by EGCG could prove valuable for targeted therapy, which can use in combination with other therapies, for pancreatic cancer.

Keywords— EGCG, FAK, N-cadherin, IGF-1R, pancreatic carcinoma.

I. INTRODUCTION

Focal adhesion kinase (FAK) is a non-receptor cytoplasmic tyrosine kinase that plays an important role in several different cell processes including cell proliferation, migration, and survival [1]. Importantly, FAK is overexpressed in cancers and inhibition of FAK activity sensitizes cancer cells to apoptosis [2], suggesting that FAK plays a role in carcinogenesis. Very recently, Liu et al have shown that FAK and insulin-like growth factor 1 receptor (IGF-1R) interact to provide survival

signals in pancreatic cancer cells [3]. IGF-1R is one of the major receptor tyrosine kinases to trigger several key molecules for cell proliferation and survival. Overexpression of IGF-1R has been detected in many different types of cancers including pancreatic cancer [4, 5], making it a potential target for therapy. In the present study, we have shown for the first time that epigallocatechin gallate (EGCG) from natural green tea effectively inhibited phosphorylations of both FAK and IGF-1R in human pancreatic cancer cell lines AsPC-1 and BxPC-3, accompanied by suppression of cell adhesion and proliferation.

II. MATERIALS AND METHODS

A. Cell Lines and Culture Conditions

The human pancreatic cancer cell lines AsPC-1 and BxPC-3 were grown in RPMI supplemented with 10% fetal bovine serum (FBS; JRH Biosciences, Lenexa, KS, USA), 100 U/ml penicillin, and 0.1 mg/ml streptomycin (Nacalai Tesque, Tokyo, Japan) in a humidified incubator of 5% CO₂ at 37°C.

B. Fabrication of Octadecylsilane Pattern for the Evaluation of Cell Adhesion

Micro-pattern coverslips composed of cell-adhesive region and cell-repellent region were fabricated on a glass surface by electron-beam lithography. Circular cell-adhesive regions of 15 μ m in diameter were covered with an amino-terminated self-assembled monolayer (SAM) and arranged with an interval of 50 μ m with a backdrop of an octadecylsilane (ODS) SAM that prohibited the cell adhesion. AsPC-1 and BxPC-3 cells were plated in the presence or absence of EGCG onto micro-pattern coverslips for 24 hours. Cells attaching to single dots were photographed under microscope.

C. Reagents

A purified preparation of EGCG was generously provided by Dr. Yukihiro Hara, Mitsui-Norin (Shizuoka, Japan). U0126 (MEK1/2 inhibitor) was purchased from Cell Signaling Technology (Danvers, MA, USA). EGCG and U0126 were dissolved in dimethylsulfoxide (DMSO). The concentration of DMSO was kept under 0.1% throughout all the experiments to avoid its cytotoxicity.

D. Proliferation Assays

Cells were seeded in quadruplicate in 96-well plates, in 100 μ l of culture media in the presence of various concentrations of EGCG. After incubation for 48 hours, 10 μ l of TetraColor ONE reagent containing tetrazolium monosodium salt (Seikagaku Corporation, Tokyo, Japan) was added to each well and cells were incubated for additional 4 hours. Absorbance at 450 nm was measured with the Biotrack II plate reader (Amersham Biosciences, Uppsia, Sweden). Results were enumerated as the percentage of the values measured when cells were grown in the absence of EGCG.

E. Western Blot Analysis

Cells were plated onto 6-cm dishes in the presence of various concentrations of EGCG. After incubation for indicated times, cells were collected by trypsinization and washed twice in phosphate-buffered saline (PBS). Total cell lysates were collected for western blot analysis as described previously [6].

F. Immunofluorescence Staining and Confocal Microscopy

Cells were plated onto coverslips and allowed to attach for 24 hours. After treated with 100 μ M EGCG for 6 hours, cells were fixed in 4% paraformaldehyde for 10 min and permeabilized with 0.1% Triton X in PBS for 5 min. Cells were then washed with PBS, blocked with 2% bovine serum albumin for 30 min and incubated with p-FAK antibody for 1 hour at room temperature. After washing three times with 0.05% Triton X in PBS, cells were subsequently incubated with Alexa fluor 488 goat anti-rabbit secondary antibody for 1 hour at room temperature, and nuclei were stained with Topro 3 before mounting. The slides were viewed using a Zeiss LSM 510 laser confocal microscope (Carl Zeiss, Jena, Germany).

III. RESULTS

A. EGCG Suppresses Cell Adhesion

Cell adhesion to other cells or extracellular matrix is of great importance in the development and disease of

multicellular organisms. We developed a micro-patterned substrate where adhesion of single cells can be observed in order to quantify the effect of EGCG on cell adhesion capacity (Fig. 1). In the absence of EGCG, approximately 60% of dots were occupied by single cells. Cell adhesion was significantly reduced at 40 μ M EGCG (approximately 20% of dots were occupied by single cells), and nearly abolished at 80 μ M EGCG.

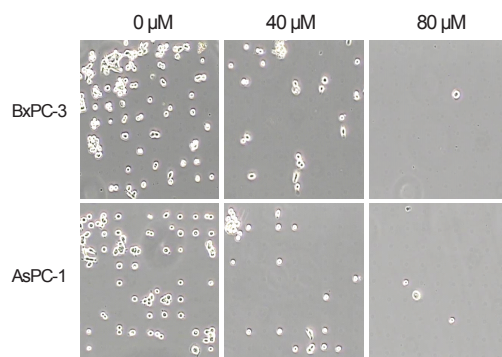


Fig. 1 EGCG suppresses cell adhesion by micro-pattern assay. AsPC-1 and BxPC-3 cells were plated at a density of 0.8×10^5 cells/ml in the presence of indicated doses of EGCG onto micro-pattern coverslips. After 24 hours, cells attaching to single dots were photographed under microscope

B. EGCG Inhibits FAK and IGF-1R Activations and the Expression of Target Molecule N-Cadherin

EGCG at 100 μ M completely abolished phosphorylation of FAK, while expression of total FAK was unchanged (Fig. 2A). In BxPC-3 cells, EGCG inhibits the phosphorylation of FAK in a dose-dependent manner. In consistent with western blot results, confocal microscopy analyses confirm that EGCG blocks FAK activation in pancreatic cancer cells (Fig. 2B).

Quite similar to FAK, IGF-1R was strongly phosphorylated in BxPC-3 cells, and lower level of phosphorylation was observed in AsPC-1 cells (Fig. 2A). As expected, 100 μ M EGCG was enough to abolish phosphorylation of IGF-1R in both cell lines, whereas it had no affect on expression of total IGF-1R.

Since FAK upregulates N-cadherin expression in pancreatic cancer cells, we ask whether inhibition of FAK by EGCG can downregulate N-cadherin expression. As shown in Fig. 2A, BxPC-3 cells, but not AsPC-1 cells, express N-cadherin. In consistent with FAK activity, N-cadherin expression is abrogated in BxPC-3 cells treated with 100 μ M EGCG.

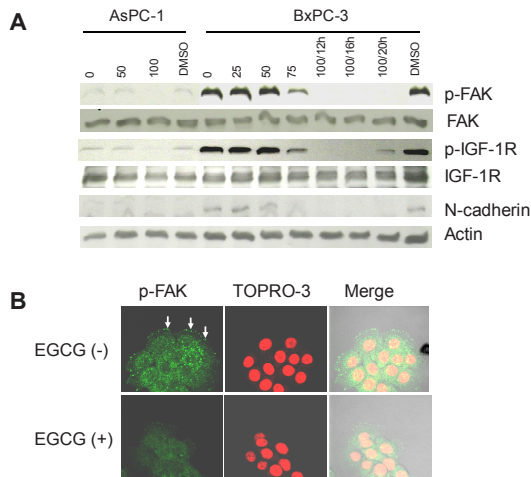


Fig. 2 EGCG inhibits FAK activity. (A) Cells were plated in the presence of various concentrations of EGCG for 12 hours. Total cell lysates were subjected to western blot analysis. (B) Immunofluorescence staining for p-FAK (green) in BxPC-3 cells in the absence or presence of 100 μM EGCG. Staining with TOPRO-3 (red) visualizes nuclei

C. Inhibition of FAK and IGF-1R Activity by EGCG Suppresses Cell Growth

EGCG inhibited the cell proliferation in a dose-dependent manner, with an IC₅₀ value of approximately 72 μM and 64 μM for AsPC-1 cells and BxPC-3 cells, respectively (Fig. 3A). However, the cell growth inhibition by EGCG diminished dramatically with increasing cell densities, similar to phenomena reported in colorectal carcinoma cells [7]. It is noteworthy that at a density of approximately 2 x 10⁵ cells/ml, EGCG at 100 μM is able to suppress more than 50% cell growth (Fig. 3B) and abolish phosphorylation of FAK and IGF-1R as well as N-cadherin expression (Fig. 2A and 2B), but fails to cleave PARP, a sign of caspase-dependent apoptosis, in AsPC-1 and BxPC-3 cells (Fig. 3C). In EGCG-treated BxPC-3 cells, nuclear integrity but not any apoptotic nuclear alterations [8] was visualized by TOPRO-3 staining (Fig. 2B).

D. MEK1/2 Inhibitor Increases the Antiproliferative Response to EGCG

Since EGCG exhibits antiproliferative effect in AsPC-1 and BxPC-3 cells without evidence of caspase-dependent apoptosis, we suspect that EGCG-treated pancreatic cancer cells retain activation of pathways important for cell survival. As shown in Fig. 4A, EGCG up to 100 μM fails to inhibit phosphorylation of MAPK and mTOR in both AsPC-1 and BxPC-3 cells. As expected, MAPK inhibitor

potentiated the EGCG-induced antiproliferative response in BxPC-3 cells (Fig. 4B).

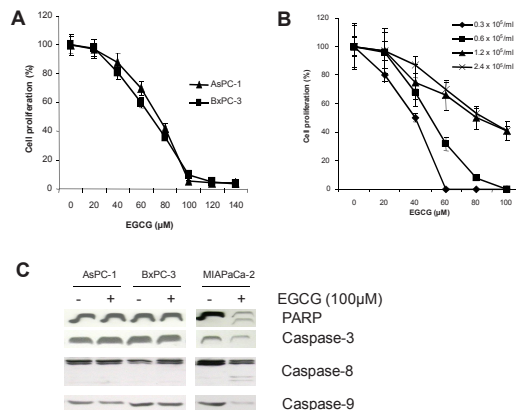


Fig. 3 EGCG suppresses cell proliferation. (A) AsPC-1 and BxPC-3 cells at a density of 0.8 x 10⁵ cells/ml were seeded in quadruplicate in 96-well plates. (B) Cell proliferation assays for BxPC-3 cells at different cell densities. Values were obtained from experiments conducted in triplicate. (C) EGCG fails to cause apoptosis in AsPC-1 and BxPC-3 cells

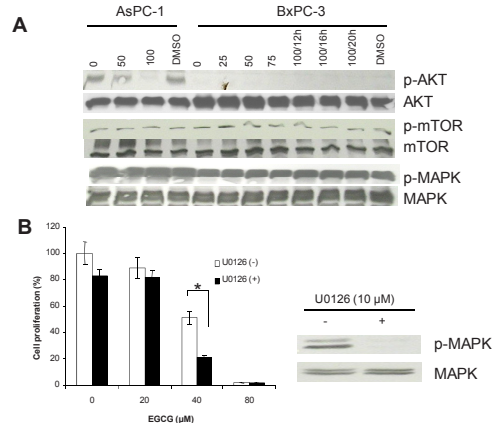


Fig. 4 (A) EGCG fails to inhibit phosphorylation of MAPK and mTOR in AsPC-1 and BxPC-3 cells. (B) MAPK inhibitor enhances EGCG-induced antiproliferative response in BxPC-3 cells. Asterisk indicates significant difference. Inhibition of phosphorylation of MAPK by U0126 at 10 μM was confirmed with western blot analysis

IV. DISCUSSION

Pancreatic cancer is a lethal disease possessing a strong tendency of metastasis. Advances in pancreatic carcinogenesis have provided more novel promising targets for prevention and treatment. Among them, upregulation of N-cadherin expression plays a key role in tumor progression

and metastasis [9]. Even though it was reported that EGCG downregulated N-cadherin expression and suppressed migration of bladder carcinoma cells [10], the molecular mechanism underlying downregulation of N-cadherin expression was not addressed. Recently, Shintani group have demonstrated that FAK upregulated N-cadherin expression in pancreatic cancer cells [11]. In agreement with their findings, we have shown here for the first time that EGCG abolished N-cadherin expression in pancreatic cancer cells via inhibition of FAK activation (Fig. 2). The inhibition was accompanied by blocking activation of IGF-1R, which interacts with FAK to provide survival signals in pancreatic cancer cells [3]. Indeed, EGCG was shown to be a highly potent inhibitor of IGF-1R tyrosine kinase activity [12]. On the other hand, in human colon carcinoma cells, inhibition of FAK activity by EGCG was reported to alter invasive phenotype [13]. Whether inhibition of FAK by EGCG in pancreatic cancer cells can actually prevent metastasis requires further animal study. However, at least, the inhibition of both FAK and IGF-1R could lead to cell growth inhibition (Fig. 3A and 3B). The fact that cell growth inhibition depends on cell density, where cell population with low density but not those with high density could be killed completely by EGCG (Fig. 3B), predicts that metastasis prevention by EGCG can achieve only if it is used at very early stage, before metastasis has been set in by large numbers of metastatic cancer cells.

With respect to therapeutic aspect, our findings do not support the application of EGCG alone for pancreatic cancer, because of its limited effect on cell growth inhibition, without evidence of apoptosis (Fig. 3B and 3C). Instead, combination of EGCG with other inhibitors such as MAPK inhibitor should be tested for this dismal cancer, since MAPK inhibitor enhanced the EGCG-induced antiproliferative response in cancer cell lines (Fig. 4B). Pancreatic cancer is an aggressive disease with aberrant activations of numerous signaling pathways. Among them, activation of MAPK by KRAS or BRAF mutation promotes the survival and growth of cancer cells [14, 15]. A phase I trial of BAY 43-9006/sorafenib, a specific inhibitor of RAF, in combination with gemcitabine for patients with pancreatic cancer indicated that the therapy was well tolerated [16]. Together, current findings warrant a combination of MAPK inhibitor such as sorafenib and EGCG for pancreatic cancer.

In conclusion, our study shows that EGCG inhibits cell proliferation and adhesion in pancreatic cancer cells by blockage of phosphorylations of FAK and IGF-1R, ultimately downregulates N-cadherin expression in cancer cells, which may help to explain the chemopreventive and therapeutic effect of EGCG on some types of cancer.

REFERENCES

1. Hecker TP, Gladson CL. Focal adhesion kinase in cancer. *Front Biosci* 2003;**8**:s705-14.
2. Golubovskaya VM, Gross S, Kaur AS, Wilson RI, Xu LH, Yang XH, *et al.* Simultaneous inhibition of focal adhesion kinase and SRC enhances detachment and apoptosis in colon cancer cell lines. *Mol Cancer Res* 2003;**1**:755-64.
3. Liu W, Bloom DA, Cance WG, Kurenova EV, Golubovskaya VM, Hochwald SN. FAK and IGF-1R interact to provide survival signals in human pancreatic adenocarcinoma cells. *Carcinogenesis* 2008;**29**:1096-107.
4. Bauer TW, Somcio RJ, Fan F, Liu W, Johnson M, Lesslie DP, *et al.* Regulatory role of c-Met in insulin-like growth factor-I receptor-mediated migration and invasion of human pancreatic carcinoma cells. *Mol Cancer Ther* 2006;**5**:1676-82.
5. Hakam A, Fang Q, Karl R, Coppola D. Coexpression of IGF-1R and c-Src proteins in human pancreatic ductal adenocarcinoma. *Dig Dis Sci* 2003;**48**:1972-8.
6. Vu HA, Xinh PT, Masuda M, Motoji T, Toyoda A, Sakaki Y, *et al.* FLT3 is fused to ETV6 in a myeloproliferative disorder with hypereosinophilia and a t(12;13)(p13;q12) translocation. *Leukemia* 2006;**20**:1414-21.
7. Inaba H, Nagaoka Y, Kushima Y, Kumagai A, Matsumoto Y, Sakaguchi M, *et al.* Comparative examination of anti-proliferative activities of (-)-epigallocatechin gallate and (-)-epigallocatechin against HCT116 colorectal carcinoma cells. *Biol Pharm Bull* 2008;**31**:79-84.
8. Pyrzynska B, Serrano M, Martinez AC, Kaminska B. Tumor suppressor p53 mediates apoptotic cell death triggered by cyclosporin A. *J Biol Chem* 2002;**277**:14102-8.
9. Shintani Y, Hollingsworth MA, Wheelock MJ, Johnson KR. Collagen I promotes metastasis in pancreatic cancer by activating c-Jun NH(2)-terminal kinase 1 and up-regulating N-cadherin expression. *Cancer Res* 2006;**66**:11745-53.
10. Rieger-Christ KM, Hanley R, Lodowsky C, Bernier T, Vemulapalli P, Roth M, *et al.* The green tea compound, (-)-epigallocatechin-3-gallate downregulates N-cadherin and suppresses migration of bladder carcinoma cells. *J Cell Biochem* 2007;**102**:377-88.
11. Shintani Y, Fukumoto Y, Chaika N, Svoboda R, Wheelock MJ, Johnson KR. Collagen I-mediated up-regulation of N-cadherin requires cooperative signals from integrins and discoidin domain receptor 1. *J Cell Biol* 2008;**180**:1277-89.
12. Li M, He Z, Ermakova S, Zheng D, Tang F, Cho YY, *et al.* Direct inhibition of insulin-like growth factor-I receptor kinase activity by (-)-epigallocatechin-3-gallate regulates cell transformation. *Cancer Epidemiol Biomarkers Prev* 2007;**16**:598-605.
13. Weyant MJ, Carothers AM, Dannenberg AJ, Bertagnolli MM. (+)-Catechin inhibits intestinal tumor formation and suppresses focal adhesion kinase activation in the min/+ mouse. *Cancer Res* 2001;**61**:118-25.
14. Almoguera C, Shibata D, Forrester K, Martin J, Arnheim N, Perucho M. Most human carcinomas of the exocrine pancreas contain mutant c-K-ras genes. *Cell* 1988;**53**:549-54.
15. Calhoun ES, Jones JB, Ashfaq R, Adsay V, Baker SJ, Valentine V, *et al.* BRAF and FBXW7 (CDC4, FBW7, AGO, SEL10) mutations in distinct subsets of pancreatic cancer: potential therapeutic targets. *Am J Pathol* 2003;**163**:1255-60.
16. Siu LL, Awada A, Takimoto CH, Piccart M, Schwartz B, Giannaris T, *et al.* Phase I trial of sorafenib and gemcitabine in advanced solid tumors with an expanded cohort in advanced pancreatic cancer. *Clin Cancer Res* 2006;**12**:144-51.

Application of Shrimp Chitosan Solution as Additive and Supplementing Ingredient in Culturing 3T3 Fibroblast Cells

Nguyen Van Toan and Nguyen Duc Tam

School of Biotechnology, International University-Vietnam National University, Vietnam

Abstract— In the present study we show that the improved proliferation of the 3T3 fibroblast cell line and the cells attachment could be obtained when applied a suitable chitosan solution as additive and supplementing ingredient in the cell culture medium of DMEM with 10% FBS, 50 U/ml Penicillin, 50 µg/ml Streptomycin, 50 µg/ml Neomycin. In addition, the 3T3 Fibroblast cells formed clear cell colonies in the cultured medium. By applying a concentration of chitosan solution of 35ppm with a volume ratio of 1: 3 to the standard cell culture medium, the cell growth of the 3T3 cell line was increased up to about 33.33% comparing to medium without chitosan solution.

Keywords— cell line, chitin, chitosan, DMEM, shrimp shells, 3T3 fibroblast cells.

I. INTRODUCTION

Chitosan (CTS)-an excellent biopolymer has been the potential choice for various applications in drug delivering, scaffolds for tissue engineering^{1,2} and wound healing management³ because of its biological, physical and chemical properties which can be quite easily controlled⁴. In those fields, wound healing has been received many interests from researchers because of its importance in the treatment of burns and prevention of surgical adhesions and cosmetic surgery⁵.

Though, the processes of making chitosan films and chitosan fibers have been well studied and reported, only few laboratories can successfully achieve and use these techniques. On the other hand, CTS solution can be prepared easier, faster comparing to CTS fibers and CTS films. Thus, using CTS solution in exploring its possible applications is an alternative way in cell culture, especially in researches related to fibroblast³.

Efforts has been made to look for applicability of CTS solution by using it in cell culture as an additive and a supplementing ingredient in culturing medium of the 3T3 fibroblast cell line. Scientifically, it is necessary to investigate the effect of chitosan solution in cell culture and applying to 3T3 fibroblast cell line is as a good example. In this paper successful application of chitosan solution is reported.

II. MATERIALS AND METHODS

3T3 fibroblast cell lines (provided by the Laboratory of Research and Applied Stem Cells, University of Natural Sciences, Ho Chi Minh City).

- Dulbecco's Modified Eagles Medium (DMEM) (Sigma#D5796)
- Fetal Bovine Serum (Sigma#F2442)
- 0.25% Trypsin/10mM EDTA (Sigma#59418C)
- Penicillin, Streptomycin, Neomycin (Sigma#P4083)
- Trypan Blue
- Sodium Bicarbonate
- 35mm-diameter disc (Jet Biofil)
- Haemocytometer
- Incubator with CO₂ supplies

High quality shrimp chitosan powder was prepared using Nguyen Van Toan's Method⁶, of which, the shrimp shells were preconditioned using Benzoic acid. Characteristics of the chitosan powder and its powder sample are shown in the Table 1.

Table 1 Characteristics of chitosan powder

Characteristics of chitosan sample	
Ash content (%)	0.52 ± 0.15
Protein content (%)	0.56 ± 0.22
Solubility (%)	99 ± 0.1
Degree of deacetylation (%)	88 ± 0.3
Turbidity (NTU)	20 ± 5.0
Viscosity (cps)	4500 ± 300

Preparation of Stock Chitosan Solution

The high quality shrimp chitosan powder was used to make stock solution in 1% acetic acid for making dilution into different doses of 20ppm, 25ppm, 30ppm, 35ppm, 40ppm, 45ppm for various experiments.

Preparation for 3T3 Fibroblast Cells Culture

The 3T3 fibroblast cell line was provided by the Lab of Stem Cell at the University of Natural Sciences which was originated from the Sigma supplier (Sigma#93061524). Cell at passage of 4-6 was used for the experiments. The cells were already sub-cultured in flask containing of DMEM (plus 10% FBS), 50U/ml Penicillin, 50µg/ml Streptomycin and 50µg/ml Neomycin.

Assays of Cell Viability and Cell Number

Two methods were used to determine the total number of cells in a given culture. The first method was adopted from Peter A. Steck, Patricia G.Voss and John L.Wang7. Alternatively, the cell density was adjusted to 1-2×104 cells/ml/35mm-disc in DMEM containing 10% FBS at the start of each experiment. To determine the number of adhered cells, haemocytometric counting was performed. The medium was aspirated and the adhered cells were trypsinized, then centrifuged and resuspended into new cell suspension for counting with Trypan. Only adhered cells were counted. Viable cells were recognized by Trypan blue exclusion.

Testing Effects of Chitosan Solution

In order for testing effects of CTS on 3T3 cell line, the 3T3 cells were first transferred into 35mm diameter culturing disc for further experiments.

Testing and Finding Out an Appropriate Volume Ratio of Chitosan Solution

The appropriate volume ratio of CTS solution versus the cell suspension solution was firstly tested. The test was carried in triplicate.

The cell was transferred to 35mm-diameter disc (35mm disc). Each disc was added with cell suspension solution and CTS solution at different concentrations was tested. The total solution volume in each disc was set to 2ml and the volume ratio (CTS/cell suspension) in each tested discs was varied from 1:1; 1:2; 1:3; 1:4 and 1:5.

Testing discs were incubated at 37oC, 5% CO2 for 48 hours. Status of the cells was checked after each 24 and 48 hours, respectively.

Testing of Suitable Chitosan Solution

The suitable concentration of CTS solution was tested after achieving the appropriate volume ratio between CTS solution and cell suspension solution. The test was carried in triplicate.

The cells were transferred to 35mm-discs for the test. Total volume in each disc was 2ml. Each disc contained CTS solution and cell suspension solution in appropriate volume ratio. The concentration was varying in each disc: 20ppm; 25ppm; 30ppm; 35ppm; 40ppm; 45ppm.

Testing discs were incubated at 37oC, 5% CO2 for 48 hours. The status of the cells was checked after each 24 and 48 hours respectively.

Experimental Design for a Suitable Replication

After having the appropriate concentration and volume ratio of CTS for putting into the cell culturing medium determined, effects of CTS on 3T3 cell line were tested in multiple test batches. Each batch contained different control sample and 5 testing samples. 6 test batches (30 testing samples) were made.

Data Analysis

All data are expressed as means ± standard deviation of representative of similar test carried out in triplicate. Statistical differences in cell number were determined by student’s t-test in which, p<0.005 was considered statistical significant.

III. RESULTS AND DISCUSSIONS

Volume Ratio Test

The volume ratio test was carried in triplicate. The cells were checked for cell adhesion at 24 hours after the start of incubation. after 48 hours of incubation, cell number was counted using Trypan cell exclusion counting method.

CTS solution at highest testing concentration was used in this test. The volume ratios between CTS solution and cell suspension solution were set into 5 ratios in 5 different 35mm-disc: 1:1, 1:2, 1:3, 1:4, and 1:5. The resulted data are shown in the Table 2.

Table 2 Cell density after 48h of incubation when tested with different volume ratio*

	Control+	1:1++	1:2	1:3	1:4	1:5
Initial Density	1	1	1	1	1	1
1st test	2	0	0	4	2	1
2nd test	1	0	0	3	1	1
3rd test	2	0	0	3	2	2
Mean value**	1.67	0	0	3.33	1.67	1.33

*Cell density counted in cell x104/ml, total volume in each disc=2ml.

** SD=±0.5

+: Control=only cell suspension solution.

++: CTS solution/cell suspension solution volume ratio.

The cells in 3 tests had shown out the result that the appropriate volume ratio for using CTS on 3T3 cell line is 1:3. The ratio 1:1 and 1:2 was not lethal for the cells since they could not grow in such media. 1:4; 1:5 did not express significant differences comparing to the control samples. Therefore, the ratio of 1:3 was chosen for later experiments.

Concentration Test

After determining the appropriate volume ratio for culturing the 3T3 cell line with CTS solution, the suitable concentration for the attachment and proliferation of the cell line is tested next. CTS solution with separated concentration was put into the cell suspension solution with volume ratio 1:3; total volume was set at 2ml.

The cells was observed for changing of status at 24 hours after incubation, and after 48 hours the attached cells was detached and counted using Trypan blue exclusion method. The test was carried in triplicate. The mentioned differences are figured in the Table 3.

Table 3 Cell density after 48h of incubation when tested with different CTS concentration at volume ratio CTS/cell suspension=1:3*

	Initial Density	1st test	2nd test	3rd test	Mean value**
Control+	1	2	2	2	2
20 ppm++	1	2	3	2	1.33
25ppm	1	2	2	2	2
30ppm	1	3	2	3	2.67
35ppm	1	4	4	3	3.67
40ppm	1	2	3	2	2.33
45ppm	1	2	2	2	2

* Cell density counted in cell x104/ml, total volume in each disc=2ml.
 ** SD = ± 0.58
 + Control=only cell suspension solution
 ++ ppm =part per million

From the collected data, it can be seen that only CTS at 35ppm concentration had the significant different with the 3T3 cell line at ratio 1:3 between CTS solution and cell suspension solution.

Replicating Tests

Experiment of 3T3 cells with CTS solution at 35ppm concentration, 1:3 volume ratio with cell suspension was replicated for confirming the achieved information.

Six test batches were conducted of which consisted of 1 control sample and 5 testing samples in each test batch. The counted cell number after 48h was taken mean value and compared with the cell number of control sample in its test batch. The data are figured in the Table 4.

Table 4 Mean cell number after 48h of incubating with CTS solution 35ppm added, volume ratio CTS/cell suspension=1:3*

Test batch number	Initial density	Control+	Sample++
1	2	3	3.40
2	2	3	4.20
3	1	2	3.60
4	1	2	3.60
5	1	2	3.60
6	1	2	3.60
Mean value**	1.33	2.33	3.67

* Cell density counted in cell x104/ml, total volume in each disc=2ml.
 ** Mean value of 5 test batch=30 sample + control sample. SD=±0.66, p<0.005
 + Control=only cell suspension solution
 ++ Mean cell number value of 5 testing samples in each test batch. SD=±0.55

Culturing the 3T3 cell line in medium with CTS solution 35ppm, volume ratio CTS/cell suspension=1:3 had shown more supportive information about the effects of CTS solution on this cell line. The mean cell number of 5 test samples in each batch after 48h of incubation was bigger than the cell number of the control sample taken with the same condition in every test batches. The appearance of the cells in the discs with CTS solution added was also significantly different from the cells in added in control disc.

The resulted data from culturing the 3T3 fibroblasts in 35mm-disc containing CTS solution at different concentration as shown in Table 3 brought about that all data had shown out the fact that at concentration of CTS of 35ppm, the number of adhered cells after 48 hours of incubation was significantly higher than those at other CTS concentration values. At 20ppm, the cell density after 48 hours of incubation was lower than the one of the control disc. The cell density increased from concentration value 25ppm to 30ppm and reached highest value at 35ppm, then decreased at 40ppm and 45ppm concentration values. It is necessary to mention that the cell proliferated at highest rate in the medium containing CTS solution at concentration value of at 35ppm.

IV. CONCLUSIONS

The study demonstrated that the improved proliferation of the 3T3 fibroblast cell line and the cells attachment could be obtained when applied a suitable chitosan solution as

additive and supplementing ingredient in the cell culture medium of DMEM with 10% FBS, 50 U/ml Penicillin, 50 µg/ml Streptomycin, 50 µg/ml Neomycin. In addition, the 3T3 Fibroblast cells formed clear cell colonies in the cultured medium.

REFERENCES

1. Chung, T.W., Yang, J., Akaike, T., Cho, K. Y., Nah, J.W., Kim, S. I., and Cho, C. S, Preparation of alginate/galactosylated chitosan scaffold for hepatocyte attachment, *Biomaterials*, 2827–2834, (2002).
2. Ma, J., Wang, H., He, B., and Chen, J., A preliminary in-vitro study on the fabrication and tissue engineering applications of a novel chitosan bilayer material as a scaffold of human neonatal dermal fibroblasts, *Biomaterials*, 331–336, (2001).
3. Risbud, M. V., Hardikar, A. A., and Bhone, R. R., Growth modulation of fibroblasts by chitosan-polyvinylpyrrolidone hydrogel: implication for wound management, *Journal of Biosciences.*, 25–31, (2000).
4. Somerman, M. J., Archer, S.Y., Imm, G.R., Foster, R.A., and Dent, J., Culturing and characterization of human periodontal ligament fibroblasts-a preliminary study. *Materials Science and Engineering*, 77-83, (1998).
5. Mariappan, M. R, Alas, E. A., Williams, J. G., Prager, M. D., Chitosan and chitosan sulfate have opposing effects on collagen-fibroblast interactions, *Wound Repair and Regeneration - Official Publication of the Wound Healing Society and the European Tissue Repair Society*, 400-406, (1999).
6. Toan, N.V, Ng, C., Aye, K. N., Trung, T.S , and Stevens W.F. , Production of high-quality chitin and chitosan from preconditioned shrimp shells, *Journal of Chemical Technology and Biotechnology*, 1113-1118, (2006).
7. Peter A. S., Patricia G.V., and John L.W. , Growth control in cultured 3T3 Fibroblasts- Assays of Cell Proliferation and Demonstration of a Growth Inhibitory
8. Activity, *Journal of cell biology*, The Rockefeller University Press, 562-575, (1979)

Author: Nguyen Van Toan
 Institute: School of Biotechnology, International University-Vietnam
 National University,
 Street:
 City:
 Country: Vietnam
 Email: nvtoan@hcmiu.edu.vn

Preparation of Size-Controlled BSA Nanoparticles by Intermittent Addition of Desolvating Agent

Hoang Hai Nguyen¹ and Sanghoon Ko²

¹Department of Food Science and Technology, Sejong University, Seoul, Korea

²Department of Food Science and Technology, Sejong University, Corresponding author, Seoul, Korea

Abstract— In order to see functionality and toxicity of nanoparticles in various food and drug applications, it is important to establish procedures to prepare nanoparticles of a controlled size. Desolvation, a thermodynamically driven self-assembly process for polymeric materials such as bovine serum albumin (BSA), is a commonly used method to prepare nanoparticles. The polymeric molecules form particles of different sizes depending on the preparation conditions such as protein content, pH, ionic strength, concentration of cross-linking agent, agitation speed, amount of desolvating agent such as ethanol, etc. In general, a desolvating agent, acetone or ethanol, is added dropwise continuously in the aqueous BSA solution until that the solution becomes just turbid to form nano-sized particles. However, in many cases the particle sizes from repeated experiments are fluctuating even if the preparation conditions are the same. As a result, standard deviation of average particle size is relatively large. Herein, we suggest that the intermittent addition of desolvating agent can improve reproducibility of BSA nanoparticle preparation. In addition, BSA nanoparticles of a controlled size can be manufactured with narrow particle size distribution. In our study, ethanol was added intermittently into 1% BSA solution at different pHs under stirring at 700 rpm. Amount of ethanol added, intermittent timeline of ethanol addition, and pH of solution were considered as process parameters to be optimized. Effect of the process parameters on size and optical density of the fabricated nanoparticles were studied. The results indicated that the size control of BSA nanoparticle was achieved by adjusting pH. The standard deviation of average size of BSA nanoparticles at each preparation condition was minimized by adding ethanol intermittently. The intermittent addition in polymeric aqueous solution at different pH can be useful for size control for food or drug applications.

Keywords— BSA nanoparticle, coacervation method, dynamic light scattering, drug delivery.

I. INTRODUCTION

Recently, nanotechnology has become a popular term in the current science and technology. Nanotechnology received a lot of attention because of application in many field in the future potential. Nanotechnology, which is still not a mature technology usually, refers to research at the scale of 100 nm or less. Nanotechnology has been introduced for the food and drug industry, including encapsulations and delivery systems. They can be formed with different compositions and biological properties such as nanoparticles, dendrimers,

nanocages, micelles, liposomes and so on [1]. Drug delivery is one of the important roles of nanotechnology by using nanoparticles as a deliver a wide range of drug to all the areas in the body [2]. Hence the efficient intracellular delivery of nanoparticles is one of main factors in enhancing the efficacy of the encapsulation therapeutic agent. For application of nanoparticles in drug industry, different nanosized carriers have been developed such as nanoparticles [3] [4], surface modified nanoparticles [5] and solid lipid nanoparticles [6]. Nanoparticles can be fabricated from proteins, polysaccharides and synthetic polymers, among them proteins based nanoparticles play an important role [7]. Commonly, serum albumin from human and bovine have been used.

In drug carriers system, the particles should be small enough to penetrate through the capillary bed. Bioactive ingredients such as nutrients, phytochemicals, nutraceutical, and drugs may be incorporated into nanoparticles to maximize delivery efficiency and increase desirable benefits [8]. Nanoparticles commonly are prepared by emulsification, or desolvation methods [9][10][11]. But this method required the organic solvent for removal the oily and surfactant for emulsion stability. Recently, desolvation process has been successful to prepare nanoparticles. In 1993, desolvation method for preparation of nanoparticles was described by Lin et al [12]. Particle size around 100 nm was prepared by adjusting pH of solution. Factors affecting properties as well as preparation conditions of nanoparticles were indicated by Soppimath et al [13], Arnedo et al [14], Langer et al [9], Krimm and Bandekar [15], Rahimnejad et al [16], and Jahanshahi et al [17]. However, up to now these methods are non-reliable. Variability in the particle size at the same preparation conditions has been large. The objective of this study is the optimization of the desolvation procedure for fabrication BSA nanoparticle with narrow particles size distribution.

II. MATERIALS AND METHODS

Materials

BSA was commercially supplied by Daisco Foods International Inc. (Eden Prairie, MN, USA). Analytical grade and high purity ethanol, and other chemicals were supplied from Sigma Aldrich (St.Louis MO, USA).

Preparation of BSA Nanoparticles

BSA nanoparticles were prepared using a desolvation method [9][12][18][19][20]. In previous study, we set up a condition to prepare 200 nm sized BSA nanoparticles. BSA powder was added to distilled water. Ethanol was added continuously or intermittently into 1% BSA solution at pH 7 under stirring at 700 rpm at room temperature until the solution became just turbid. Ethanol was added continuous in the solution with rate addition about 1.0 to 2.0 ml per min for continuous method and the rest time for each mL of ethanol addition was 5 min for intermittent method.

Measurement of Particle Size

Size, number, and volume distribution of BSA nanoparticles were measured by commercial particle size analyzer (DelsaNano, Beckman Coulter, Inc., Fullerton, CA, USA). The particle size was measured at 25°C with a scattering angle of 165°.

III. RESULTS AND DISCUSSION

Effect of Intermittent Method on Average Particle Size

In BSA nanoparticle preparation, particle size was commonly controlled by adjusting the pH and amount of added desolvating agent. In this study, we controlled them by method for adding ethanol at a given pH. In Fig. 1 particles size prepared by both intermittent and continuous addition methods were indicated. In same preparation condition, particle size fabricated by intermittent method was more stable than that fabricated by continuous method. The particle size prepared by the intermittent method was relatively small and close to 200 nm. The target particle size of 200 nm was achieved at 1% BSA aqueous solution at pH 7 by the intermittent method. The pH was the most important factor to control the coagulation of BSA molecules during the desolvation process. The isoelectric point (pI) of BSA is about 4.7. When the pH of solution was closed to the pI, the enhanced of protein-protein reaction lead to increase coagulation among BSA molecules. At pH 7, BSA molecules possessed a negative charge and coagulation of BSA molecules reduced which allowed the formation of small particles [21]. On the other hand, at low pH value (close to pI), which was electrostatic repulsive, increased coagulations among BSA molecules; as a result, larger BSA particles could form. In addition, at basic pH, an increase in hydrogen bonding results in decrease in the hydrophobicity [15]. This result supports our hypothesis with regards to control hydrophobic interaction as a means for controlling the size of BSA nanoparticle. But more important than that intermittent ethanol added method can control the size distribution and particle size of BSA nanoparticle. Maybe intermittent addition give more time for desolvation process and more stable size was formed.

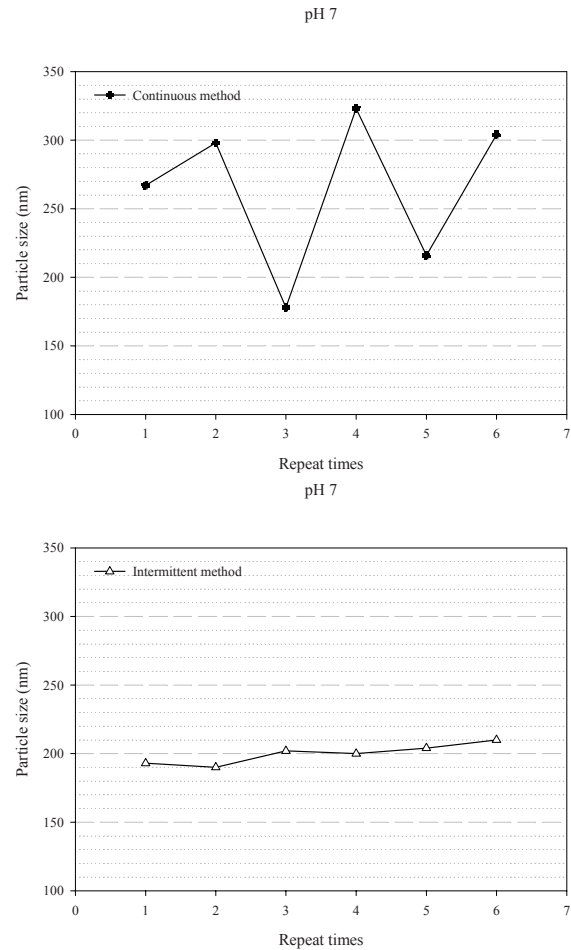


Fig. 1 Particles size of preparation conditions of BSA nanoparticle by continuous and intermittent methods

Effect of Intermittent Method on Standard Deviation of Particle Size

BSA nanoparticles were fabricated many times to check the reliability of the intermittent ethanol addition method. The reliability of the preparation was represented by standard deviation of the particle size. Fig. 2 indicates that the standard deviation of the average particle size fabricated by continuous ethanol addition method was larger than that formed by the intermittent method. In the earlier study, they tried to find out the method to control particle size, but the variability in the size at given conditions was large. Some authors have indicated that the particles size was fabricated which was independent of desolvating agent flow rate [17]. Other described that this variability probably can be attributed to the manual performance of the desolvation process, characterized by a drop by drop addition of the desolvating agent [9]. But in the present study the results were also not more improved, while even manual desolvation was replaced by a pump

controlled system which enabled nanoparticle fabrication at a defined rate of sovalting agent addition.

The similar problems were occurred in our research for BSA nanoparticle fabrication with continuous ethanol addition. Herein, we suggest that the intermittent addition of desolvating agent can improve reproducibility of BSA nanoparticle preparation.

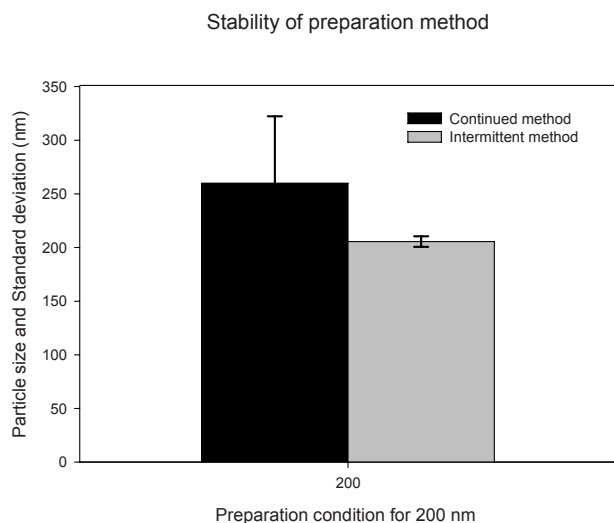


Fig. 2 Standard deviation of average particle size

IV. CONCLUSIONS

Nowadays, food-grade materials have been used to fabricate nanoparticles for various food and pharmaceutical industry applications. Here BSA nanoparticles with controlled-size were prepared using the intermittent ethanol addition method. Our study may provide the protocol method for the fabrication protein nanoparticle. The particle size range was controlled with narrow size distribution and minimum standard deviation of average size. Therefore, the intermittent addition in polymeric aqueous solution can be useful for size control for food or drug applications. Further study would be focused on the control of particle size at different pH, effect of amount of desolvating agent addition following the intermittent method, and the stability of nanoparticle through zeta potential, heat denaturation, and number of available amino group on the surface of BSA nanoparticle.

ACKNOWLEDGEMENT

This work was supported by the Korea Research Foundation Grant funded by the Korean Government (MOEHRD, Basic Research Promotion Fund) (KRF-2008-331-F00047).

REFERENCES

- Labhasetwar V. (2005) Nanotechnology for drug and gene therapy: the importance of understanding molecular mechanisms of delivery. *Current Opinion in Biotechnology*, 16(6), 674-680.
- Hans M.L, Lowman A.M. (2002). Biodegradable nanoparticles for drug delivery and targeting. *Current Opinion in Solid State and Materials Science*, 6(4), 319-327.
- Leroux JC, Cozens R, Roesel JL, Galli B, Kubel F, Doelker E, Gurny R (1995) Pharmacokinetics of a novel HIV-1 protease inhibitor incorporated into biodegradable or enteric nanoparticles following intravenous and oral administration to mice. *J. Pharm. Sci.* 84: 1387-1391.
- Couvreur P, Vauthier C (1991) Polyalkylcyanoacrylate nanoparticles as drug carrier: Present state and perspectives. *J. Contr. Release*. 17(2): 187-198.
- Araujo L, Lobenberg R, Kreuter J (1999) Influence of the surfactant concentration on the body distribution of nanoparticles. *J. Drug Target*. 6: 373-385.
- Muller RH, Wallis KH (1993) Surface modification of i.v. injectable biodegradable nanoparticles with poloxamer polymers and poloxamine 908. *Int. J. Pharm.* 89: 25-31.
- Kumar PV, Jain NK (2007) Suppression of Agglomeration of Ciprofloxacin- Loaded Human Serum Albumin Nanoparticles, *AAPS Pharm.Sci. Technol.* 8(1): Article 17.
- Rhaese S, Von Briesen H, Rübsem-Waigmann H, Kreuter J, Langer K. (2003) Human serum albumin-polyethylenimine nanoparticles for gene delivery. *Journal of Controlled Release*, 92(1-2), 199-208.
- Langer K, Balthasar S, Vogel V, Dinauer N, Von Briesen H, Schubert D. (2003) Optimization of the preparation process for human serum albumin (HSA) nanoparticles. *International Journal of Pharmaceutics*, 257(1-2), 169-180.
- Gallo JM, Hung CT, Perrier DG. (1984) Analysis of albumin microspheres preparation. *International journal of pharmaceutics*, Elsevier, 22:11, 63-74
- Müller B.G, Leuenberger H, Kissel T, (1996) Albumin Nanospheres as Carriers for Passive Drug Targeting: An Optimized Manufacturing Technique. *Pharmaceutical Research*, 13(1), 32-37.
- Lin W, Coombes A, Davies M, Davis S, Illum L, (1993). Preparation of Sub-100 nm Human Serum Albumin Nanospheres Using a pH-Coacervation Method. *Journal of Drug Targeting*, 1(3), 237-243.
- Soppimath K.S, Aminabhavi T.M, Kulkarni A.R, Rudzinski W.E. (2001) Biodegradable polymeric nanoparticles as drug delivery devices. *Journal of Controlled Release*, 70(1-2), 1-20.
- Arnedo A, Espuelas S, Irache J.M. (2002) Albumin nanoparticles as carriers for a phosphodiester oligonucleotide. *International Journal of Pharmaceutics*, 244(1-2), 59-72.
- Krimm S, Bandekar J. (1986) Vibrational spectroscopy and conformation of peptides, polypeptides, and proteins. *Advances in Protein Chemistry* 38, 181-364.
- Rahimnejad M, Jahanshahi M, Najafpour GD (2006a) Production of biological nanoparticles from bovine serum albumin for drug delivery. *Afr. J. Biotechnol.* 5(20): 1918-1923.
- Jahanshahi M, Najafpour G, Rahimnejad M. (2008) Applying the Taguchi method for optimized fabrication of bovine serum albumin (BSA) nanoparticles as drug delivery vehicles. *Afr. J. Biotechnol.* 7(4), 362-367
- Marty JJ, Oppenheim RC, Speiser P (1978). Nanoparticles - a new colloidal drug delivery system. *Pharm Acta. Helv.* 53(1): 17-23.

19. Weber C, Coester C, Kreuter J, Langer K. (2000) Desolvation process and surface characterisation of protein nanoparticles. *International Journal of Pharmaceutics*, 194(1), 91-102.
20. Ko S, Gunasekaran S. (2006) Preparation of sub-100-nm β -lactoglobulin (BLG) nanoparticles. *Journal of Microencapsulation*, 23(8), 887-898.
21. Schmidt R.H, (1981) Gelation and coagulation. In: Pour-El, A., Editor. *Protein Functionality in Foods*, Am. Chem Soc., Washington, DC, pp. 131-148

Author: Sanghoon Ko

Institute: Department of Food Science and Technology

Street: 98 Gunja-dong, Gwangjin-gu

City: Seoul 143-747

Country: Korea

Email: sanghoonko@sejong.ac.kr

Mechanical Properties of a Single Trabecula in Bovine Femur by the Three Point Bending Test

Kazuto Tanaka, Yusuke Kita, Tsutao Katayama, and Mami Matsukawa

Faculty of life and Medical science, Doshisha University, Kyotanabe city, Kyoto, Japan

Abstract— Research in bone diseases like osteoporosis is motivated by its immense of social health care costs. While there are many researches about the influence of bone mineral density and microarchitectural properties on the mechanical properties of cancellous bone, there are a few studies about the bone matrix material properties for trabecular bone. This is due to the difficulty to evaluate mechanical properties of trabeculae in complicated shape and micro size. Studying the bone matrix material properties on a microstructural level is important for understanding the mechanical behavior of bone. Therefore it is necessary to measure the mechanical properties of single trabecula directly. In this study, micro three point bending tests of single trabecula in bovine distal femur are conducted. Three dimension images of trabeculae specimens obtained from distal femur cancellous bone were evaluated by using X-ray μ CT, and elastic modulus of trabeculae specimens were measured.

Keywords— X-ray μ CT, Single trabecula, Three point bending test, Elastic modulus.

I. INTRODUCTION

The rising incidence of osteoporosis in the aging society is becoming a major public concern. At present the clinical assessment of osteoporosis is mainly on bone mineral density (BMD) measurements, such as dualenergy X-ray absorptiometry (DXA), quantitative X-ray computed tomography (QCT) and others [1]. As was pointed out by the National Institute of Health (NIH) in 2000, however osteoporosis is recognized as a skeletal disease characterized not only by low bone mass but also other factor such as bone matrix material properties. Therefore, it is necessary to measure the mechanical properties of bone tissue. While there are many researches on the mm scale such as influence of bone mineral density and microarchitectural properties on the mechanical properties of cancellous bone, there are a few studies on single trabecula using three point bending test or indent test. Elastic modulus and fracture properties can be obtained in a bending test, only elastic modulus can be obtained in a indentation test. Elastic modulus of single trabecula measured by micro bending test was reported to range from 1GPa to 7GPa [2-5]. One reason for this wide range of elastic modulus seems to come from the imperfect evaluation of three dimensional geometry of the specimen.

The sample geometry of trabecula had been determined by using 2D image of optical microscopy or micrometer. Due to the difficulty in processing trabeculae with complicated shape and micro size, it is contemplated that the sample geometry of trabecula needs to be determined by using 3D image. With the developments of X-ray computed tomography (X-ray CT) technique in spatial resolutions of μm order; X-ray μ CT have been applied to bone material observation [6]. In this study, 3D images of trabeculae specimens obtained from distal femur cancellous bone were evaluated by using X-ray μ CT, and elastic modulus of trabeculae specimens were measured by three point bending test.

II. EXPERIMENTAL METHOD

A. Specimen

Cancellous bone specimens were obtained from the right distal bovine femur. Bone marrow involved in cancellous bone specimens was removed by water jet. Single trabecula specimen was extracted from the cancellous bone in length of 2mm to 3mm and in diameter of $200\mu\text{m}$ to $500\mu\text{m}$. Specimens were polished with Speed Lap (Maruto ML-521-d) at diamond lapping (#600) to a thickness of $100\mu\text{m}$ and with emery paper (#400) on side surface.

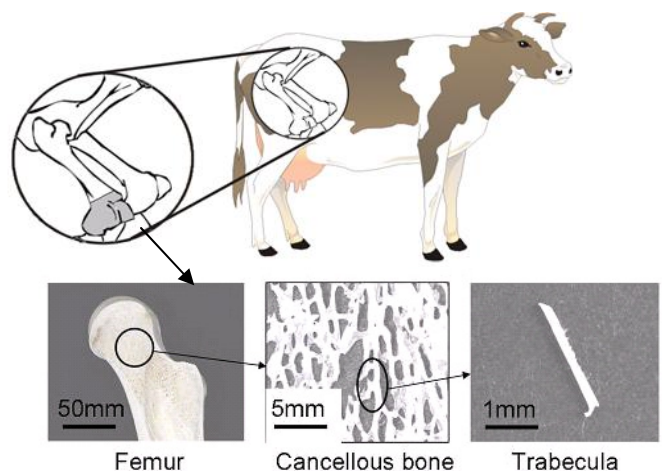


Fig. 1 Specimen from bovine femur

B. Micro Three Point Bending Test

Mechanical tests were performed by using Micro Material Tester (Shimadzu, MMT-11NV-2) with a load cell capacity of 10N. Elastic bending test below the elastic limit strain and cyclic bending test with cyclic loading and unloading with increasing maximum displacement were performed. Each specimen was placed on the jig as shown in Fig.2 and span length was set to 1.1mm. Knife-edge indenter of 0.1mm in tip radius was used for indenter in three point bending test. The positioning of specimen was conducted by XY stage in resolution of 0.01mm. Elastic bending test was carried out at a cross head speed of 0.001mm/sec for five specimens. The following equation was used to calculate the elastic modulus for each specimen.

$$E = \frac{(P/\delta)L^3}{4bh^3} [1 + 2.85(h/L)^2 - 0.84(h/L)^3]$$

E : Elastic modulus

P/δ : Gradient of the load-displacement curve

L : Span length

b : Width of specimen

h : Height of specimen

Cyclic bending test was carried out at a cross head speed of 0.01mm/sec, and the maximum displacement was increased with a ramp up rate of 0.01mm or 0.02mm.

C. X-ray μ CT and SEM Observation

Three dimension re-formation images of each cancellous bone specimen (3D images) was obtained by using micro focus X-ray system (Shimadzu, SMX-160CTS) with a voxel size of 4 μ m. Measurement of specimen geometry such as width and height was obtained from the average value of nine points of 3D image. After unloading at a cyclic bending test at displacements of 0.1mm, 0.13mm, 0.16mm and 0.2mm, 3D and SEM images of each specimen were obtained. 3D images of some specimens were obtained with a voxel size of 0.6 μ m.

III. RESULTS AND DISCUSSION

A. Bending Properties

Figure3 shows the load-displacement curve obtained from elastic bending test. The gradient of first loading curve was different from the gradient of second loading curve. The gradient of first unloading curve and second unloading curve were similar, furthermore the gradient of second loading curve and third loading curve were also similar. Therefore, it is thought that the difference of first loading curve is

evoked from minute space between the jig and specimen or irregularity of specimen surface. Since first loading eliminated these defects, gradient of linear part of the second load-displacement curve is employed in the calculating of elastic modulus. Figure4 shows the load-displacement curve obtained from cyclic bending test. After the load-displacement curve reached its maximum load at displacement of 0.1mm, local maximum value of each load-displacement curve decrease as the maximum displacement increase. Figure5 shows the SEM image of compression side surface obtained after unloading at displacement of 0.1mm, 0.13mm, 0.16mm and 0.2mm. No cracks were found on the SEM images of compression side. Figure6 shows the SEM image of tensile side in bending test obtained after unloading at displacement of 0.1mm, 0.13mm, 0.16mm and 0.2mm. Some cracks were observed in the SEM images of tensile side at maximum displacement of 0.16mm and 0.2mm. Figure7 shows the 3D image of tensile side obtained after unloading at displacement of 0.1mm, 0.13mm, 0.16mm and 0.2mm. The 3D image at a maximum displacement of 0.13mm, whose maximum load is smaller than that of 0.1mm, did not show any cracks. However 3D image at maximum displacement of 0.16mm shows some cracks at the tensile side surface in bending test, and 3D image at maximum displacement of 0.2 mm shows longer cracks throughout the full width. Figure8 shows the extracted crack surfaces of 3D image at maximum displacement of 0.16mm and 0.2 mm observed from longitudinal direction of specimen. Crack formation has been started from tensile side in bending test. 3D image at maximum displacement of 0.2mm shows that cracks do not reach the compression side in bending test. From this observation, compression strength of a single trabecula is considered to be higher than tensile strength of a single trabecula.

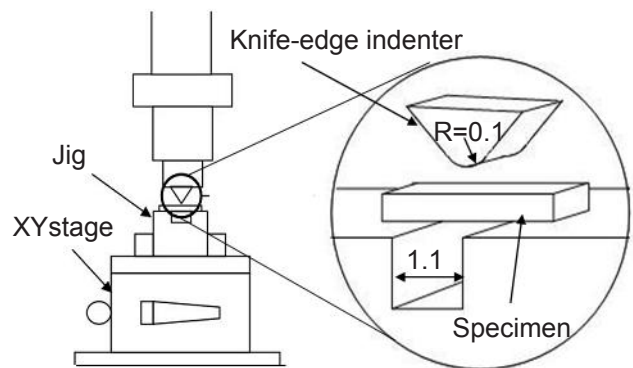


Fig. 2 Micro three point bending test

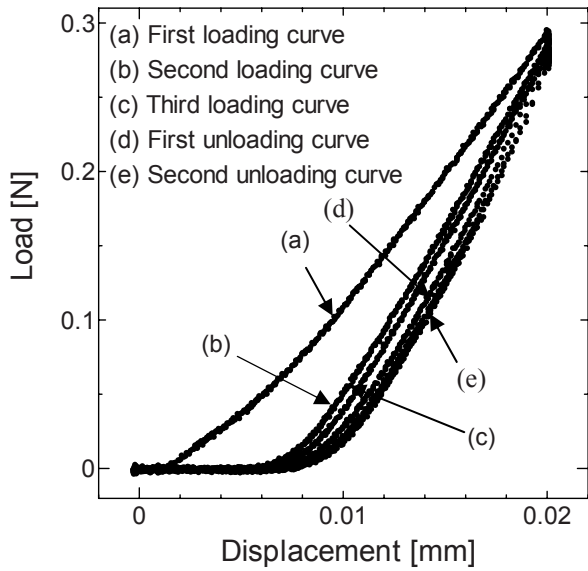


Fig. 3 Typical load displacement curve obtained by three point bending test below the elastic limit

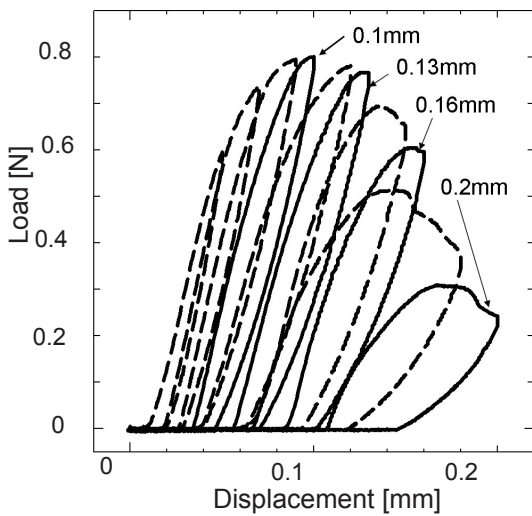


Fig. 4 Cyclic load-displacement curve obtained by three point bending test

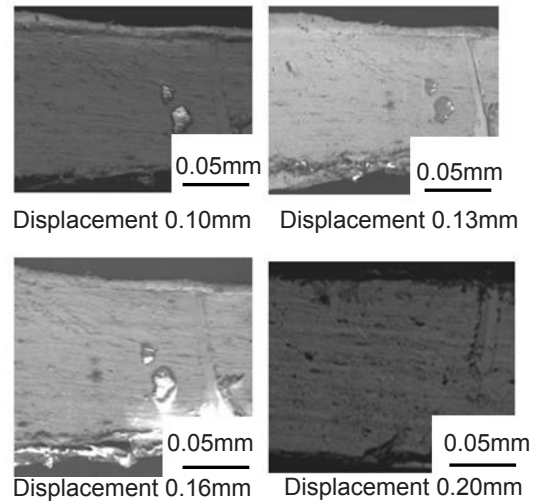


Fig. 5 SEM images for compression side of trabecula specimen after unloading at displacement of 0.1, 0.13, 0.16 and 0.20mm

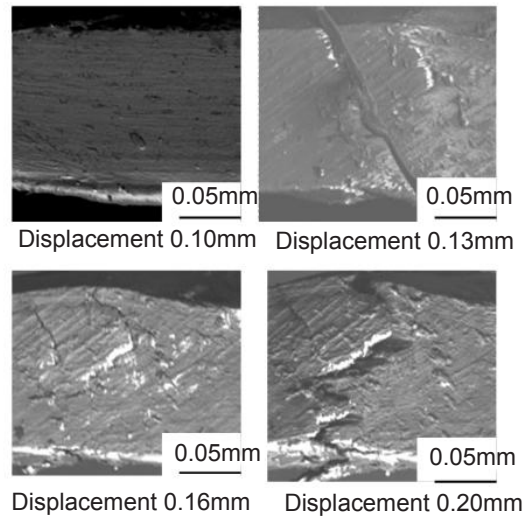


Fig. 6 SEM image for tensile side of trabecula specimen after unloading at displacement of 0.1, 0.13, 0.16 and 0.20mm

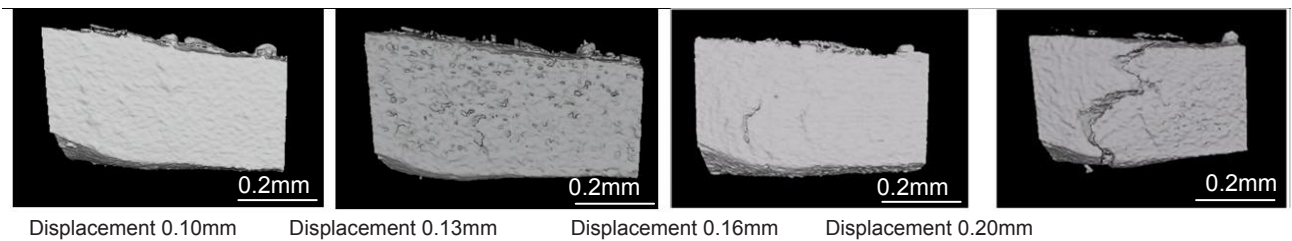
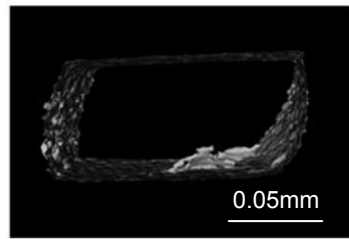
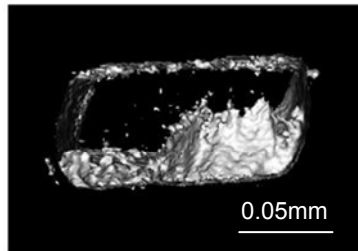


Fig. 7 3D images for trabecula specimens after unloading at displacement of 0.10, 0.13, 0.16 and 0.20mm



Displacement 0.16mm



Displacement 0.20mm

Fig. 8 Extracted crack surface of 3D image at maximum displacement of 0.16mm and 0.2 mm observed from longitudinal direction of specimen

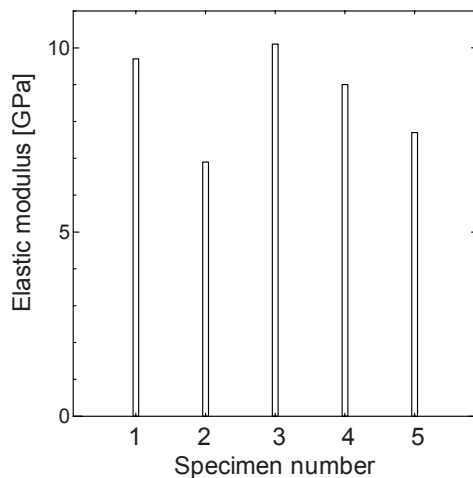
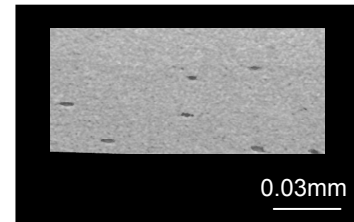


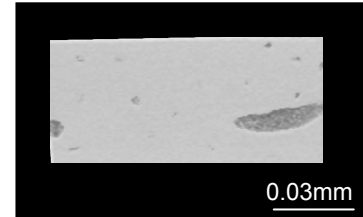
Fig. 9 Elastic modulus obtained by bending test

B. Elastic Modulus of Trabecula

Figure 9 shows elastic modulus of all trabeculae specimens. The average elastic modulus of five specimens was 8.7GPa, meanwhile the elastic modulus scattered widely. Figure 10 shows 3D image of specimen No.1 (elastic modulus: 9.5GPa) and No.2 (elastic modulus: 6.9GPa) observed with voxel size of 0.6 μ m. Specimen No.2 has bigger defect than specimen No.1. Therefore, these defects are thought to be one reason for the smaller elastic modulus of specimen No.2.



Specimen No.1 (Elastic modulus 9.5GPa)



Specimen No.2 (Elastic modulus 6.9 GPa)

Fig. 10 Inside porosity of trabecula specimen

IV. CONCLUSIONS

In this study, elastic modulus of a single trabecula obtained from cancellous bone in the distal part was measured by using the three point bending test, and the gradual changes of the specimen during the bending test was observed by using SEM and X-ray μ CT. The investigation yielded the following conclusions

- 1) While cracks of trabecula are observed in tensile surface due to the bending test, cracks of trabecula are not observed in compression surface. From this observation, compression strength of single trabecula is considered to be higher than the tensile strength of a single trabecula.
- 2) The average measured elastic modulus from bending tests was 8.7GPa.

REFERENCES

1. C. F. Njeh, C. M. Boiven et. al. (1997) The role of ultrasound in the assessment, Osteoporosis int, pp.7-22.
2. K. Choi, J.L. Kuhn (1990) The elastic moduli of human subchondral, J. Biomechanics. Vol.23, No.11, pp.1103-1113.
3. J. L. Kuhn, S.A. Goldstein et. al. (1989) Compression of the trabecular, J.orthopaedic research, pp.876-884
4. P. L. Mente, J. L. Lewis (1989) Experimental method for the mesurment, J.orthopaedic research, pp.456-461.
5. Jungmann, R., Schitter, G., (2007) Real-time Microdamage and Strain Detection during Micromechanical, Proceedings of the SEM Volume 1, pp.55-65.
6. P. J. Thurner, P. Wyss et al (2006) Time-lapsed investigation of three-dimensional, Bone 39, pp.289-299.

Author: Kazuto Tanaka E-mail: ktanaka@mail.doshisha.ac.jp
 Institute : Faculty of life and Medical science, Doshisha University
 Address: 1-3 Miyakodani, Tatara, Kyotanabe city, Kyoto, 610-0321, JAPAN

Ultrasonic Characterization of Bovine Bone Marrow

Tomohiro Kubo, Nicolas Cazier, Takashi Saeki, and Mami Matsukawa

Doshisha University, Laboratory of Ultrasonic Electronics, Kyotanabe, Japan

Abstract— Longitudinal wave in cancellous bone separates into fast wave and slow waves depending on the structure of trabeculae. The fast wave mainly propagates in the trabecular part, whereas the slow wave mainly propagates in the soft tissue. This means that slow wave is influenced by the properties of bone marrow. In this study, we have investigated the ultrasonic wave properties in bone marrow. The measured frequency range was from 3 to 10 MHz, and temperature range was from 20 to 40°C. The marrow was obtained from the shaft of a bovine femur. The measured velocity values were similar to those in water. The attenuation values were much higher than those in water. Both measured velocity and attenuation tended to decrease as the increase of temperature, showing the softening of the properties. The decreasing tendency of both velocity and attenuation changed around 33°C, where we could find a transition by the differential scanning calorimetry (DSC). This tells us that ultrasonic properties clearly revealed the temperature which was more outstanding as changes in wave attenuation. At temperatures higher than 33°C, the decreasing tendency of attenuation became smaller, telling the clear change of material properties. Bone marrow is a composite material and mainly composed of fat and soft fiber tissues. This interesting change around 33°C probably shows the transition of the fat part.

Keywords— Bone marrow, Wave velocity, Wave attenuation, Longitudinal wave.

I. INTRODUCTION

Osteoporosis is a skeletal disease causing loss of bone mass and micro-architectural deteriorations. The current gold standard for the assessment of osteoporosis is the dual-energy X-ray absorptiometry (DXA). DXA enables the measurement of bone mineral density (BMD). DXA has, however, several problems, for example, high cost, ionizing radiation and unsuitable for group screening.

On the other hand, quantitative ultrasound (QUS) has many advantages such as the portability, low cost, suitable for group screening and free ionizing radiation, which are considered to be especially suitable in the assessment of children and pregnant women. In addition, QUS techniques can evaluate the elastic properties of bone *in vivo* by the two parameters, the speed of sound (SOS) and the broadband ultrasound attenuation (BUA, slope of the linearly frequency dependent attenuation). These parameters can

provide important information related to the bone elasticity and strength. [1,2]

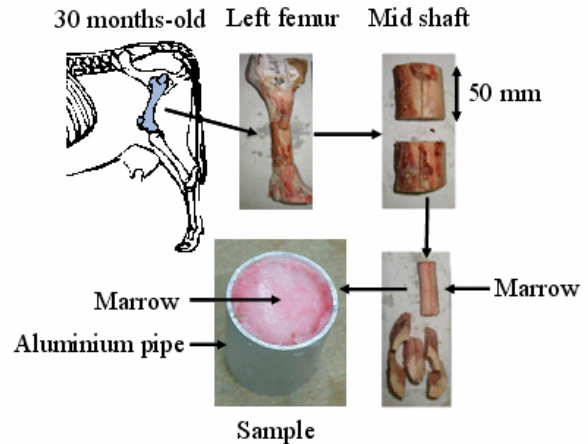


Fig. 1 Preparation steps of the marrow sample

QUS, however, has still disadvantages of the measurement accuracy, which results from the complicated structure and elastic properties of bone. Actually, bones are usually heterogeneous and anisotropic. Therefore several studies focused on the effect of bone structure on ultrasonic properties for the improvement of measurement accuracy. [3-5]

Cancellous bone, which might be affected by osteoporosis, is a porous medium composed of an inter-connected network of solid rods and plates (called as trabeculae) filled with marrow. One interesting phenomenon is that the longitudinal wave in cancellous bone separates into fast wave and slow waves depending on the trabecular structure. [6-8] The fast wave mainly propagates in the trabecular part, whereas the slow wave propagates in the bone marrow, which indicates that slow wave is influenced by the properties of soft tissue. The potential measurements of the two-wave phenomenon open new perspective for *in vivo* assessment of bone status.

In order to understand the two wave phenomena, it is necessary to understand the acoustic properties of soft tissue (bone marrow). However, there are a few researches of bone marrow. The objective of this study is then to investigate ultrasonic properties in the bone marrow, using an ultrasonic pulse technique.

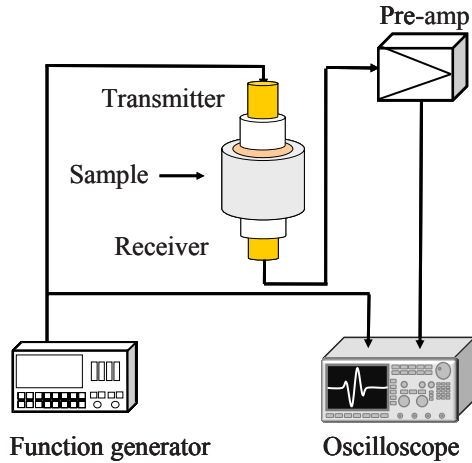


Fig. 2 Ultrasonic measurement set-up

II. MATERIALS AND METHODS

A. Bone Marrow Preparation

Figure 1 shows the preparation steps of the samples of bone marrow. 4 marrow samples were taken from 2 bovine femurs. A left femur was obtained from a 30-months-old female bovine. Cylindrical bone marrows were obtained from each part of shaft of bovine femur, proximal, middle, and distal part. The mean size of cylindrical columns was about 30 mm in diameter. In the measurement, aluminium pipe (inner diameter 23mm) was filled with marrow to prevent collapse by compression.

B. Ultrasonic Measurement

As shown in Fig. 2, a conventional pulse measurement was performed using a self-produced polyvinylidene fluoride (PVDF) transmitter and receiver (diameter 10 mm). The measured frequency range was from 3 to 10 MHz, and temperature range was from 20 to 40°C. A function generator (Agilent 33250A) delivered electrical pulses to the transmitter, which was converted into ultrasonic waves. Several sinusoidal signal (3-10 waves) with amplitude of 10 V_{p-p} was applied to the transmitter. The longitudinal wave propagated through bone marrow. The other transducer received the wave and converted it into an electrical signal. The signal was amplified by a 40-dB preamplifier (NF BX-31) and visualized with an oscilloscope (Tektronix DPO7054).

Before measurements, the samples were degassed for 15 min to remove air bubbles trapped in bone marrow.

For the temperature control, we used the water loop from a thermostatic water bath, which goes around the marrow

sample. A temperature of the sample was measured by a thermocouple.

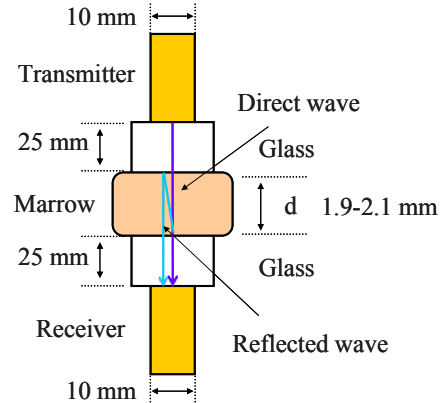


Fig. 3 Propagation of ultrasonic wave between transducers

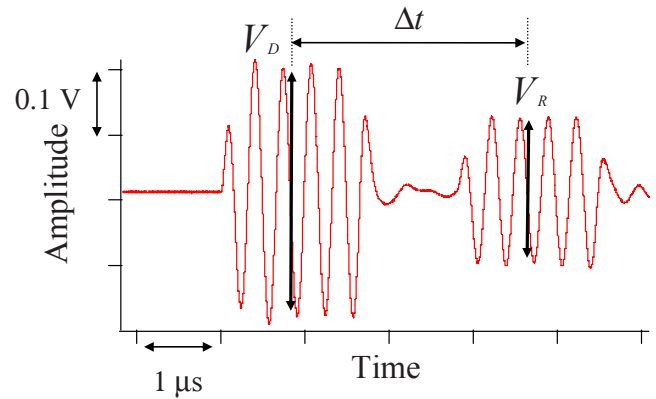


Fig. 4 A typical propagated waveform in the marrow at 3MHz

The transmitter and receiver were connected to the cylindrical glass (diameter 19 mm) for the purpose to protect the transducers from heat, and the improvement of parallelism, as shown in Fig. 3. During measurements, we observed direct wave and reflected wave which reflected twice at the interfaces between the transducer and marrow. In this case, the wave velocity values were obtained from the time difference between direct and reflected waves. The detection of the difference in arrival time (Δt) between the direct wave and reflected wave is shown in Fig. 4. The wave velocity in the marrow was derived from Δt as

$$v = 2d / \Delta t, \quad (1)$$

where d is the distance between transducers (sample thickness). The wave attenuation was obtained from the amplitude difference between the direct and reflected waves. The amplitudes of both waves were determined by the peak-to-peak amplitude of the wave signals, as shown in Fig. 4.

The wave attenuation in the marrow was derived from,

$$\alpha = \frac{1}{2d} \ln \left\{ \frac{V_D}{V_R} \left(\frac{Z_G - Z_M}{Z_G + Z_M} \right)^2 \right\}, \quad (2)$$

where d is the distance between transducers, V_D is the peak-to-peak amplitude of direct wave signal, V_R is the peak-to-peak amplitude of reflected wave signal, Z_G is the acoustic impedance of connected glass, and Z_M is the acoustic impedance of bone marrow. The used velocity and density values for acoustic impedance Z_G were 5980 m/s and 2200 kg/m³, respectively. The density is the averaged value of the samples used. For Z_M , we used density value of 900 kg/m³ and the velocity value that was obtained from the measurements.

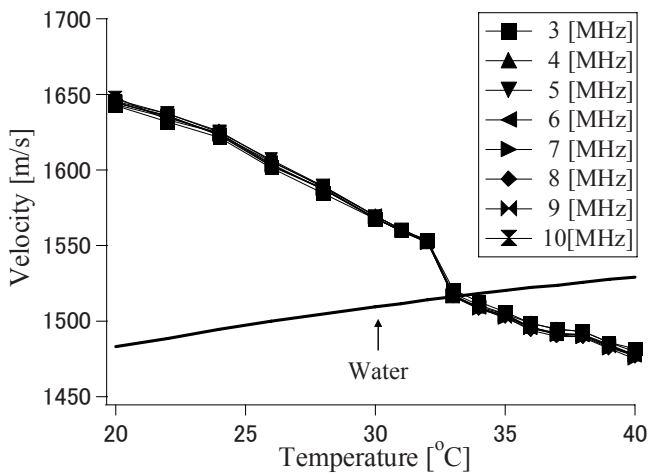


Fig. 5 Wave velocity in the bovine bone marrow in the proximal part

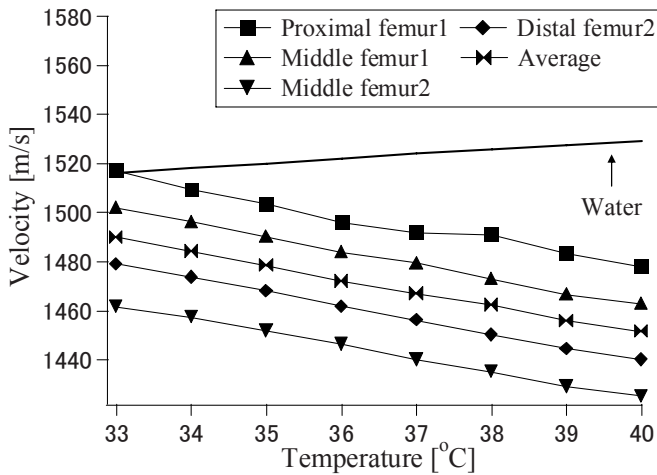


Fig. 6 The wave velocity of the bovine bone marrow from 33 to 40°C

III. RESULTS AND DISCUSSION

We measured the velocity and the attenuation in bone marrow in the range from 3-10MHz and in the range from 20-40°C. 4 marrow samples were taken from 2 bovine femurs. Figure 5 shows the velocity data of a marrow sample obtained from the proximal part of a bovine femur. The frequency dispersion was few. Figure 6 shows the mean velocity data at each part of bovine femur in the range of 33-40°C. Figure 7 shows the attenuation data of a marrow sample obtained from the proximal part of bovine femur. The attenuation increased as the increase of frequency. Figure 8 shows the attenuation data at each part of bovine femur at 5MHz and in the range of 33-40°C. Both velocity and attenuation were not shown large difference between each part of shaft of bovine femur. Almost all sample showed the similar tendency with the data in Fig. 7, except for one sample from middle part of femur.

Both measured velocity and attenuation tend to decrease as the increase of temperature, showing the softening of the properties. This decreasing tendency is in good agreement with the data of El-sariti et al. [9] The measured velocity values were similar to those in water. The temperature effect, however, was different. The attenuation values were much higher than those in water. The decreasing tendency of both velocity and attenuation changed around 33°C, where we could find the transition point of marrow, by the differential scanning calorimetry (DSC). This tells us that ultrasonic properties clearly revealed the melting temperature which was more outstanding as changes in wave attenuation. At temperatures higher than 33°C, the decreasing tendency of attenuation became weak, telling the clear change of material properties. Bone marrow is a composite material and mainly composed of fat and soft fiber tissues. This interesting change around 33°C should be investigated in detail.

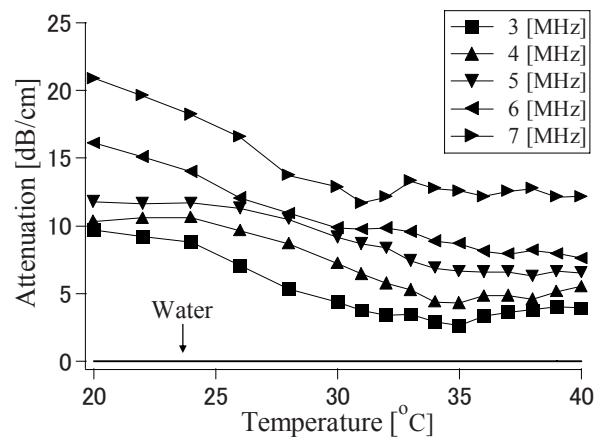


Fig. 7 Wave attenuation in the bovine bone marrow in the proximal part

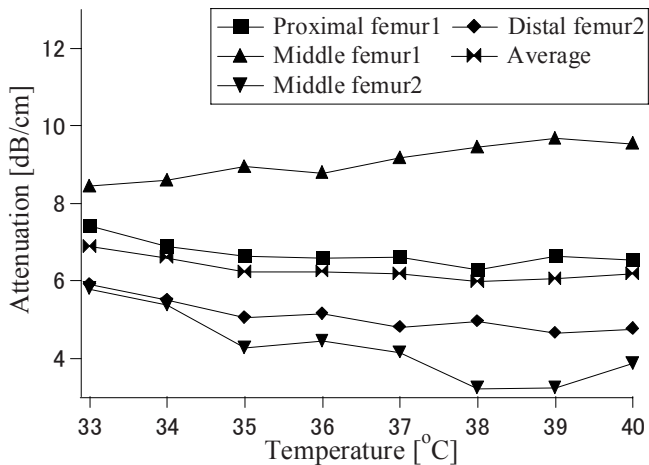


Fig. 8 Wave attenuation in bovine bone marrow samples at 5MHz

IV. CONCLUSION

Ultrasonic properties in bovine bone marrow were investigated. Both wave velocity and attenuation in marrow tended to decrease as the increase of temperature. The decreasing tendency of both velocity and attenuation changed around 33°C. From differential scanning calorimetry (DSC), transition point was found near this temperature.

The measured velocity values were similar to those in water and the attenuation values were much higher than those in water.

In this study, the number of samples was small and the obtained positions were different. The differences between samples possibly come from the positions and the interindividual difference of the femur. These discussions should be carefully investigated in the future studies.

ACKNOWLEDGMENT

This study was partly supported by the bilateral joint project between JSPS and CNRS, in addition to the Academic

Research Frontier project of Doshisha University and Ministry of Education, Culture, Sports, Science and technology in Japan.

REFERENCES

1. Nieh C F, Kuo C W, Langton C M, Atrah H I, and Boivin C M. (1997) Prediction of human femoral bone strength using ultrasound velocity and BMD. *Osteoporosis Int.* 7:471-477.
2. Han S, Medige J, Davis J, Fishkin Z, Mihalko W, and Ziv I. (1997) Ultrasound velocity and broadband attenuation as predictors of load-bearing capacities of human calcanei. *Calcif. Tissue Int.* 60:21-25.
3. Padilla F, Bossy E, and Laugier P. (2006) Simulation of ultrasound propagation through three-dimensional trabecular bone structures: comparison with experimental data. *Jpn. J. Appl. Phys.* 45:6496-6500.
4. Yamato Y, Matsukawa M, Otani T, Yamazaki K, and Nagano A. (2006) Distribution of longitudinal wave properties in bovine cortical bone in vitro. *Ultrasonics* 44:233-237.
5. Mizuno K, Matsukawa M, Otani T, Takada M, Mano I, and Tsujimoto T. (2008) Effect of structural anisotropy of cancellous bone on speed of ultrasonic fast waves in the bovine femur. *IEEE Trans. Ultrason. Ferroelectr. Freq. Control* 55:1480-1487.
6. Hosokawa A, and Otani T. (1997) Ultrasonic wave propagation in bovine cancellous bone. *J. Acoust. Soc. Am.* 101:558-562.
7. Hosokawa A, and Otani T. (1998) Acoustic anisotropy in bovine cancellous bone. *J. Acoust. Soc. Am.* 103:2718-2722.
8. Fella Z E, Chapelon J Y, Berger S, Lauriks W, and Depollier C. (2004) Ultrasonic wave propagation in human cancellous bone. *J. Acoust. Soc. Am.* 116:61-73.
9. El-Sariti A et. al. (2006) The temperature dependence of the speed of sound in bovine bone marrow at 750 kHz. *Ultrasound in Med & Biol.* 32 6:985-989.

Author: Tomohiro Kubo

Institute: Doshisha University, Laboratory of Ultrasonic Electronics

Street: 1-3, Tatara Miyakodani

City: Kyotanabe

Country: Japan

Email: dtj0119@mail4.doshisha.ac.jp

Tribological Response of Cobalt-Chromium Femoral Head under Lubrication of Bovine Serum Albumin

Cong-Truyen Duong and Seonghun Park

School of Mechanical Engineering, Pusan National University, Busan, Korea

Abstract— Micro/nano-scale tribological properties of engineering and biological materials have been investigated through Atomic Force Microscopy (AFM) by measuring surface roughness and frictional coefficient. At the micro-scale, the effect of lubricants on the tribological properties of cobalt-chromium (CoCr) femoral head has not been well identified, although a number of previous studies have reported the effect of lubricants on friction and wear of other hip implant materials at the macro-scale. Therefore, the objective of the current study is to investigate the role of bovine serum albumin as a boundary lubricant in the lubrication of CoCr femoral head by measuring its frictional coefficients with Atomic Force Microscopy (AFM) techniques. In the present study, the average value of the surface roughness (R_q) over the $25\mu\text{m}\times 25\mu\text{m}$ scanned area of the CoCr femoral head were 58.801 ± 14.277 nm ($n=12$). The frictional coefficients (μ) of the CoCr femoral head through AFM were 0.248 ± 0.029 ($n=12$) in PBS, 0.195 ± 0.014 ($n=12$) in BSA of 10 mg/ml, and 0.073 ± 0.014 ($n=12$) in BSA of 30 mg/ml. The Student t-test revealed statistically significant differences in μ of the CoCr femoral head between PBS and BSA of 10 mg/ml ($p<0.0001$) as well as between PBS and BSA of 30 mg/ml ($p<0.0001$). There was also statistically significant differences in μ between BSA of 10 mg/ml and BSA of 30 mg/ml ($p<0.0001$). These results suggest that μ of CoCr femoral head is dependent on the protein concentration of BSA, and BSA plays a significant role as an effective boundary lubricant for the friction of CoCr femoral head.

Keywords— Atomic Force Microscopy (AFM), Tribological Property, Frictional Coefficient, Surface Roughness, Cobalt-Chromium Femoral Head.

I. INTRODUCTION

Micro/nano-scale tribological properties of engineering and biological materials have been investigated through Atomic Force Microscopy (AFM) by measuring surface roughness and frictional coefficient [1-4]. In order to evaluate the likely frictional conditions in artificial joints, frictional coefficients between diverse hip implant materials such as combinations of metals, ceramics and ultra high molecular weight polyethylene (UHMWPE) have been studied through hip simulator by many researchers at the macro-scale [5-9]. It has been found that either boundary or mixed lubrication occurs when bovine serum albumin were used as a lubricant [5, 8]. When lubricants contain proteins

of albumin or globulin, the tribological properties of the rubbing surfaces are affected by the adsorption of these constituents on the bearing surfaces of the prostheses [7, 8]. In this study, we focus on albumin which is the most abundant protein in bovine serum as well as in synovial fluid. At the macro-scale, previous studies in the literature have reported the effect of albumin on friction and wear through pin-on-disk measurements, and there has been the general agreement that albumin plays an important role as an effective lubricant in the tribological behavior of hip implant materials [10, 11]. At the micro-scale, Park et al. have used AFM to study the frictional coefficient of articular cartilage [4]. Although micro-scale AFM measurements are highly suitable for exploring frictional effectiveness of boundary lubrication for diverse lubricants without being affected by the surface roughness of bearing materials in joint implants, the effect of boundary lubrications of bovine serum albumin (BSA) on hip implant materials has not been well identified. Therefore, the objective of the present study is to investigate the role of BSA as a boundary lubricant in the lubrication of cobalt-chromium (CoCr) femoral head by measuring its frictional coefficients with AFM techniques.

II. MATERIALS AND METHODS

A. Sample Preparation

One sample with length, width, and thickness of 10 mm, 10 mm, and 5 mm, respectively was machined from the main wear region of a cobalt-chromium (CoCr) femoral head which was retrieved from hip joints for a revision surgery in the context of total hip arthroplasty (THA) due to aseptic loosening after ten years of usage. Prior to the AFM measurements with lubricants, the CoCr femoral sample was cleaned in an ultrasonic bath for five minutes and then glued on top of the cylindrical flat plates (1 mm thickness and 19 mm diameter) using a small amount of cyanoacrylate glue. In this study, two types of solutions were prepared as lubricants: PBS (Phosphate Buffered Saline, Sigma-Aldrich, No. P5493) as a control solution, and BSA (Bovine Serum Albumin, Sigma-Aldrich, No. A2153) at different protein concentrations (10 mg/ml and 30 mg/ml) in PBS. All lubricants were stored at a temperature of 4 °C.

B. Frictional Measurements through AFM

For frictional measurements with lubricants through AFM, the sample was imaged at room temperature using an AFM device (XE 70, Park Scientific Instruments, South Korea) which was placed in a sealed box and equipped with software (XEI version 1.6.5) for image processing and the calculation of the surface roughness. A standard rectangular silicon cantilever with a normal spring constant of $K_N=0.95$ N/m that was integrated with a square-pyramid conical tip (curvature less than 10 nm) was used for the AFM measurements. The friction force (F_L) was calculated by the multiplication of the lateral deflection voltage signal (V_{LFM} in V), the lateral spring constant (K_L in N/m), and the lateral sensitivity (S_L in mm/V). In the present study, the friction force was calculated from the whole image of $25\mu\text{m}\times 25\mu\text{m}$ scanned area, and the lateral sensitivity (S_L) is proportional to the normal sensitivity ($S_N=61.14$ nm/V) by the following equation [12]:

$$S_L = \frac{3h^2}{2L^2} \frac{\Delta V_{LFM}}{\Delta V_{A-B}} S_N \tag{1}$$

where h is the tip height, L is the cantilever length, and V_{LFM} and V_{A-B} are the lateral and vertical voltage signals of the scanned image, respectively. The lateral spring constant (K_L) for the rectangular silicon cantilever adopted in the experiments was calculated by the following equation [13-15]:

$$K_L = \frac{Gwt^3}{3Lh^2} \tag{2}$$

where G is the shear modulus of the cantilever, w is the cantilever width, and t is the cantilever thickness. The cantilever that was used in our measurements was etched from single-crystal silicon (with integrated tips) with the following manufacturer’s specifications as determined by a

scanning electron microscope: $h=15\mu\text{m}$; $L=110\mu\text{m}$; $w=35\mu\text{m}$; $t=1\mu\text{m}$; and $G(110)=0.617\times 10^{11}$ Pa [13]. The value of the lateral spring constant calculated in this study was $K_L=29.084$ N/m.

The measurements of the frictional forces were repeated for six values of normal forces in increments of 5 nN at each position. The mean values of the root mean squared (RMS) surface roughness (R_q) (Fig. 1), the normal force (Fig. 2), and the lateral deflection voltage signal images (Fig. 3) were simultaneously measured over the same scanned area of $25\mu\text{m}\times 25\mu\text{m}$, at a scanning frequency of 1 Hz. The plot of the frictional force against the normal force was fitted with a straight line, whose slope was the frictional coefficient (Fig. 4).

C. Statistical Analyses

The Student t-test was performed to investigate statistical differences between the frictional coefficients of the CoCr femoral head obtained from different lubricants, and the significance level was set at $p<0.05$.

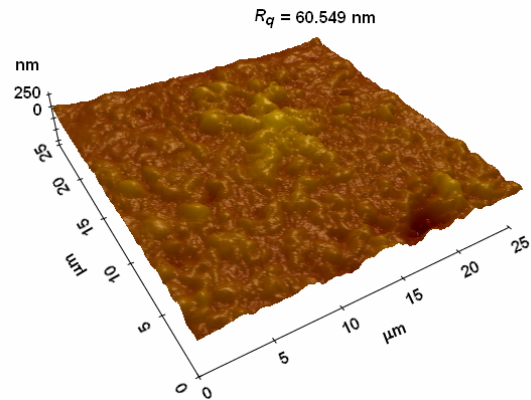


Fig. 1 Three-dimensional AFM image of the typical surface topography which is used to calculate its surface roughness value (R_q)

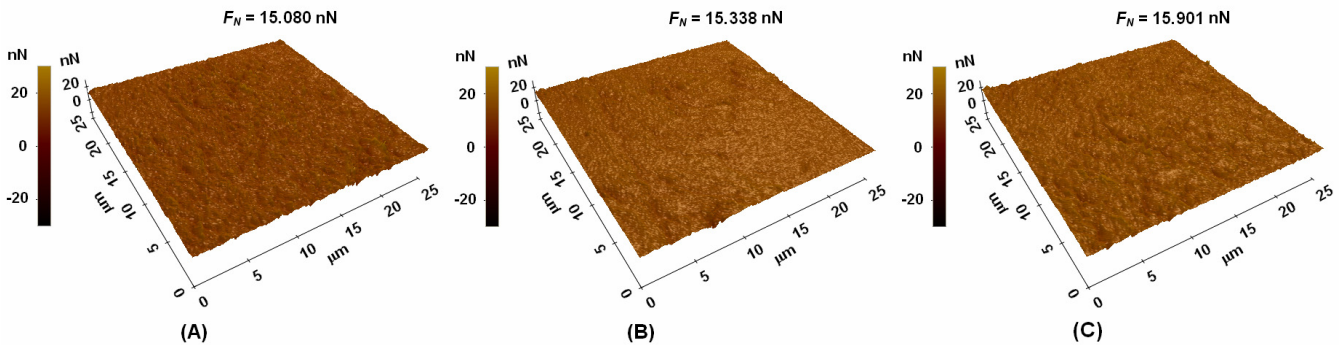


Fig. 2 Three-dimensional AFM images of the typical normal forces (F_N) for the lubricants of (A) PBS, (B) BSA of 10 mg/ml, and (C) BSA of 30 mg/ml

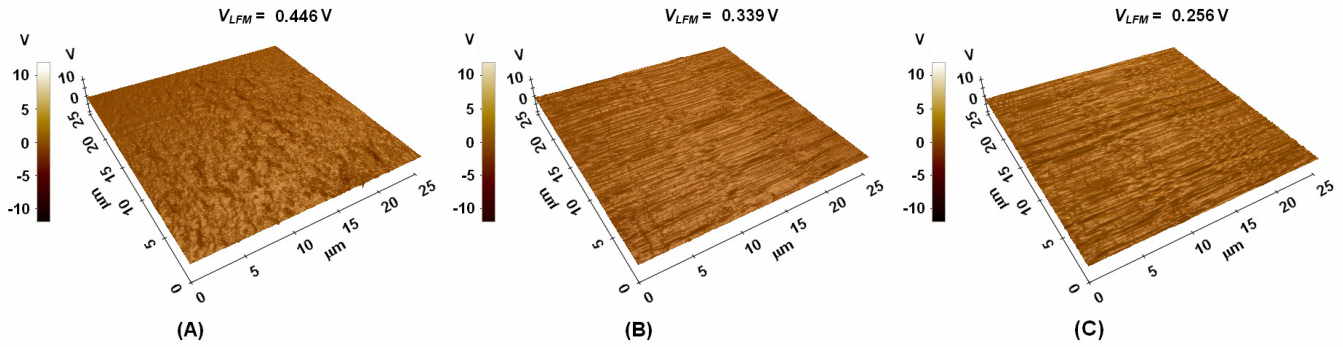


Fig. 3 Three-dimensional AFM images of the typical lateral deflection voltage signal (V_{LFM}) for the lubricants of (A) PBS, (B) BSA of 10 mg/ml, and (C) BSA of 30 mg/ml

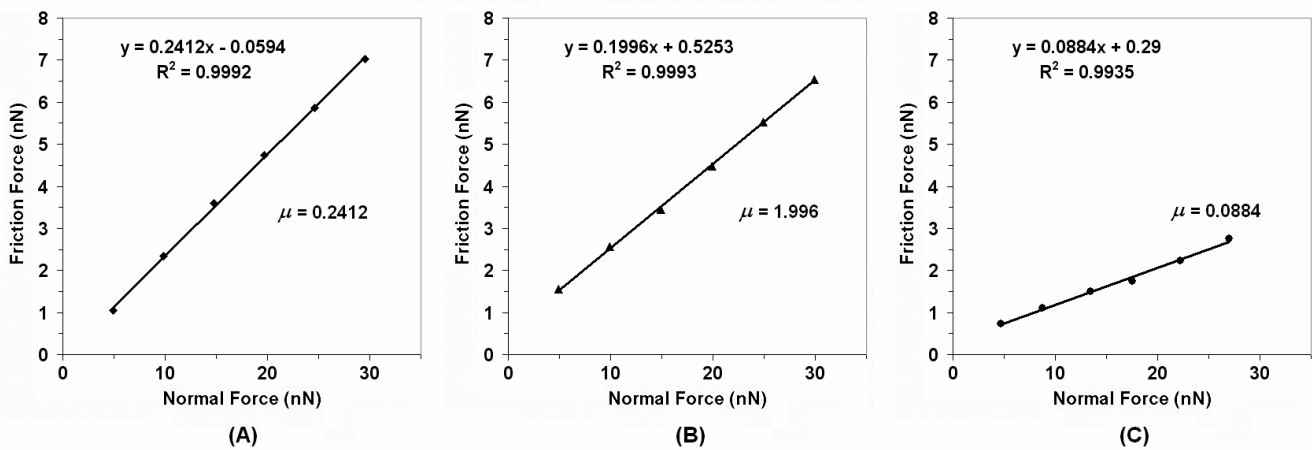


Fig. 4 Typical plots of the frictional force vs. the normal force, measured over six incremental values of the AFM normal forces for the lubricants of (A) PBS, (B) BSA of 10 mg/ml, and (C) BSA of 30 mg/ml

III. RESULTS

The average value of root mean squared (RMS) surface roughness (R_q) over the $25\mu\text{m}\times 25\mu\text{m}$ scanned area of the main wear region of the CoCr femoral head was 58.801 ± 14.277 nm ($n=12$). The frictional coefficients (μ) of the CoCr femoral head through AFM were 0.248 ± 0.029 with an R^2 of 0.997 ± 0.005 ($n=12$) in PBS, 0.195 ± 0.014 with an R^2 of 0.998 ± 0.001 ($n=12$) in BSA of 10 mg/ml, and 0.073 ± 0.014 with an R^2 of 0.997 ± 0.007 ($n=12$) in BSA of 30 mg/ml. The Student t-test revealed statistically significant differences in μ of the CoCr femoral head between PBS and BSA of 10 mg/ml ($p<0.0001$) as well as between PBS and BSA of 30 mg/ml ($p<0.0001$). Similarly, between different protein concentrations of BSA, there was

statistically significant differences in μ ($p<0.0001$) between BSA of 10 mg/ml and BSA of 30 mg/ml. The controlled normal forces (F_N) generated similar surface asperity profiles and similar average values between PBS ($F_N=15.080$ nN), BSA of 10 mg/ml ($F_N=15.338$ nN) and BSA of 30 mg/ml ($F_N=15.901$ nN) over the scanned area of $25\mu\text{m}\times 25\mu\text{m}$ as shown in Fig. 2. However, values of V_{LFM} decreased with increases in the concentrations of BSA (Fig. 3). Decreases in V_{LFM} in the order of PBS ($V_{LFM}=0.446$ V) > BSA of 10 mg/ml ($V_{LFM}=0.339$ V) > BSA of 30 mg/ml ($V_{LFM}=0.256$ V) led to decreases in μ (Fig. 4) in the order of PBS ($\mu=0.248\pm 0.029$) > BSA of 10 mg/ml ($\mu=0.195\pm 0.014$) > BSA of 30 mg/ml ($\mu=0.073\pm 0.014$), because μ is computed by dividing the average frictional force (calculated through the image of V_{LFM}) by the average normal force (calculated through the image of F_N).

IV. DISCUSSIONS

The surface roughness and frictional coefficient (μ) of the CoCr femoral head which was retrieved from hip joints for revision surgery of total hip arthroplasty (THA) due to aseptic loosening were measured successfully through AFM techniques at six different locations of its main wear region with different lubricants. It is important to accurately quantify the effects of lubricants on the tribological properties of CoCr femoral head, since such an understanding may help to optimize the bearing surface to minimize friction and wear.

The main results in the current study is that μ of the CoCr femoral head for the lubricants of PBS, BSA of 10 mg/ml, and BSA of 30 mg/ml were 0.248 ± 0.029 , 0.195 ± 0.014 , and 0.073 ± 0.014 , respectively. In the literature, AFM measurements with different lubricants of the frictional coefficients on the surface of a CoCr femoral head have not been reported. Regarding the macro-scale frictional coefficients of a CoCr alloy with lubricants through pin-on-disk measurements, Mishina et al. have reported that μ between CoCr and CoCr with human serum albumin (HSA) was ~ 0.08 [11], while Gispert et al. have reported that μ between CoCr and UHMWPE with Hank's balanced salt solution (HBSS) was ~ 0.24 [10]. Jin et al. have also reported that μ between CoCr and UHMWPE through hip simulator with the lubricant of BSA solution lie between 0.06 and 0.08 [5].

Another important result in the present study is that the amount of BSA protein concentration significantly affected reducing μ of CoCr femoral head ($p < 0.0001$); μ was higher at smaller BSA protein concentration ($\mu \sim 0.195$ for BSA of 10 mg/ml) and smaller at higher BSA protein concentration ($\mu \sim 0.073$ for BSA of 30 mg/ml). These results suggest that μ of CoCr femoral head is dependent on the protein concentration of BSA, and BSA plays a significant role as an effective boundary lubricant for the friction of CoCr femoral head. These results could be explained by the fact that albumin in BSA enhances lubricity through adsorption on the surface of CoCr femoral head and also consistent with some studies at the macro-scale [8-10]. In the case of combination of CoCr-on-CoCr and CoCr-on-UHMWPE, adsorbed protein effectively decreases the frictional coefficient in BSA measured from hip simulator [8, 9], with higher protein concentration leading to lower frictional coefficient [9].

V. CONCLUSIONS

In this study, the effect of BSA on the frictional coefficient of CoCr femoral head was examined through the AFM

techniques. The result showed that frictional coefficient of CoCr femoral head is dependent on the protein concentration of BSA, and BSA played a significant role as an effective boundary lubricant for CoCr femoral head because albumin in BSA enhances lubricity through adsorption on the surface of CoCr femoral head. In future study, efficiencies of other lubricants such as globulin and hyaluronic acid for boundary lubrication of CoCr femoral head will be elucidated through AFM frictional measurements.

ACKNOWLEDGMENT

This study was supported by the fund from the Korea Research Foundation Grant funded by the Korean Government (Basic Research Promotion Fund of MOEHRD: KRF-2007-331-D00593).

REFERENCES

1. Bhushan, B. (2001) Nano- to microscale wear and mechanical characterization using scanning probe microscopy. *Wear* 250 1105-1123.
2. Bhushan, B. (2008) Nanotribology, nanomechanics and nanomaterials characterization. *Philos T R Soc A* 366 1351-1381.
3. Fang, T. H., Chang, W. J. and Tsai, S. L. (2005) Nanomechanical characterization of polymer using atomic force microscopy and nanoindentation. *Microelectron J* 36 55-59.
4. Park, S., Costa, K. D. and Ateshian, G. A. (2004) Microscale frictional response of bovine articular cartilage from atomic force microscopy. *J Biomech* 37 1679-1687.
5. Jin, Z. M., Stone, M., Ingham, E., et al. (2006) Biotribology. *Curr Orthopaed* 20 32-40.
6. Hall, R. M. and Unsworth, A. (1997) Friction in hip prosthesis. *Biomaterials* 18 1017-1026.
7. Scholes, S. C., Unsworth, A. and Goldsmith, A. A. J. (2000) A frictional study of total hip joint replacements. *Phys Med Biol* 45 3721-3735.
8. Scholes, S. C., Unsworth, A., Hall, R. M., et al. (2000) The effects of material combination and lubricant on the friction of total hip prostheses. *Wear* 241 209-213.
9. Brockett, C., Williams, S., Jin, Z. M., et al. (2007) Friction of total hip replacements with different bearings and loading conditions. *J Biomed Mater Res B* 81B 508-515.
10. Gispert, M. P., Serro, A. P., Colaco, R., et al. (2006) Friction and wear mechanisms in hip prosthesis: Comparison of joint materials behaviour in several lubricants. *Wear* 260 149-158.
11. Mishina, H. and Kojima, M. (2008) Changes in human serum albumin on arthroplasty frictional surfaces. *Wear* 265 655-663.
12. Arias, D. F., Marulanda, D. M., Baena, A. M., et al. (2006) Determination of friction coefficient on ZrN and TiN using lateral force microscopy (LFM). *Wear* 261 1232-1236.
13. Liu, Y., Wu, T. and Evans, D. F. (1994) Lateral force microscopy study on the shear properties of self-assembled monolayers of dialkylammonium surfactant on mica. *Langmuir* 10 2241-2245.
14. Kageshima, M., Ogiso, H., Nakano, S., et al. (1999) Atomic force microscopy cantilevers for sensitive lateral force detection. *Jpn J Appl Phys* 38 3958-3961.
15. Cannara, R. J., Eglin, M. and Carpick, R. W. (2006) Lateral force calibration in atomic force microscopy: A new lateral force calibration method and general guidelines for optimization. *Rev Sci Ins* 77 -.

VEF-Sponsored HUT Biomechanics Course

B.S. Kelley¹, B.R. Rigby¹, and H.D. Vu²

¹ Baylor University, School of Engineering and Computer Science, Waco, Texas, USA

² Hanoi University of Technology, Department of Electronics Technology and Biomedical Engineering, Hanoi, Vietnam

Abstract— The Vietnamese Ministry of Education and Training (MOET) is targeting over twenty *Advanced* programs to elevate to international standards. The U.S. government, through the Vietnam Education Foundation (VEF), also supports technology capacity building and in 2008 initiated the U.S. Faculty Scholars Program for faculty members to teach in English at Vietnamese universities. The focus of one such program is biomedical engineering (BME) at the Hanoi University of Technology. The teaching efforts were conducted during the spring 2009 semester using both onsite classroom instruction as well as interactive internet video conferencing. Because the expertise of the HUT BME faculty lies predominately in the area of biomedical instrumentation, the need for course support is in non-electronics areas, for example, engineering biomechanics. The topics of the biomechanics course were centered on the design of an orthopedic implant, including specifications, a design report, and team presentations. A customized textbook included content targeted toward the design project, student assignments, and key PowerPoint slides. The American professor and students established a strong rapport including exposure to fresh learning approaches, engineering practices, and cultural and language experiences. There was a wide variability among the assigned grades, with several being highly competitive. Student evaluations indicated the course was well received and appreciated.

Keywords— biomechanics, engineering education, Vietnam.

I. INTRODUCTION

Created by the U.S. Congress in 2002 as a federal government agency, the Vietnam Education Foundation (VEF) began operations in 2003. The VEF mission is to *further the process of reconciliation and to build the bilateral relationship between the United States and Vietnam, thus serving the interests of both countries through education in science, medicine, technology, engineering and mathematics.*

The VEF Scholarships and Grants Programs are comprised of three initiatives. Since 2003, the VEF Fellowship Program has sponsored nearly 300 Vietnamese for graduate study in the U.S. The VEF Visiting Scholar Program was established in 2007 to support Vietnamese already holding a doctorate to improve their professional and research skills through visiting appointments at a U.S. university.

Beginning with the 2008-09 academic year, the VEF U.S. Faculty Scholars Grant Program was established whereby four U.S. professors were selected through an

application process to teach a course in English for a Vietnamese university. The goals of this program are:

1. To help build capacity in science and technology in Vietnam through teaching and related research.
2. To help Vietnamese institutions address specific education needs, including curriculum development, research, student learning outcomes, and evaluation.
3. To build positive relationships between U.S. and Vietnamese higher education institutions and faculty members that may lead to sustainable partnerships.

U.S. Faculty Scholars have the option of teaching courses either onsite in Vietnam or by interactive, real-time video-conferencing. As a part of this program the first author taught a Biomedical Engineering (BME) course in Engineering Biomechanics for the Hanoi University of Technology (HUT), using both onsite instruction and synchronous internet delivery during the spring 2009 semester.

II. ENGINEERING BIOMECHANICS COURSE

A. Pre-course Activities

Prior to the initiation of this project and as a result of communications between the first and the third authors, a BME faculty member at HUT, pertaining to preparing a VEF U.S. Faculty Scholar proposal, cooperative efforts were instigated. The most significant of these was to serve as the connector on behalf of HUT BME to each of six U.S. universities that HUT identified as potential partners. HUT was awarded an Advanced BME program by the MOET, and this was one of the proposed stipulations. On behalf of HUT, the author contacted each of the six U.S. universities, first with an introductory email communication, and then through a subsequent phone call. HUT selected the University of Wisconsin as their partner university.

It was also during these pre-proposal conversations that the details of the biomechanics course were birthed. HUT's existing BME program is targeted toward preparing graduates to serve in hospital and related institutions where primary responsibilities include maintaining and specifying hospital instrumentation. [1] As such, much of the BME curriculum was targeted in that direction. And because the author's expertise lies in the mechanical engineering side of

BME, it first appeared there was little opportunity to collaborate. However, with the award of the Advanced BME program there became a need to offer broader BME courses, including biomechanics, but for which the HUT faculty had little expertise. It was this combination of need by HUT, and desire by the author, that combined for a winning VEF U.S. Faculty Scholar proposal.

The timing was not perfect, as the first class of Advanced BME students entered during fall 2008, and therefore were not required to take a course in biomechanics (a third→fifth year course) during the 2008–09 academic year. This permitted the course to be offered as an elective to continuing BME students, and thus allowing the course to be offered on an experimental basis in this new format before it is integrated into the HUT Advanced BME curriculum.

B. Course Content

The first author has taught an undergraduate course in biomechanics to American students many times. However, that course was not readily adaptable to the HUT/Vietnamese environment. It was not feasible to spend an entire semester in Vietnam, and so the option to teach a portion of the course via interactive video conferencing was selected. The primary consideration here was to use course materials that easily permitted the students to comprehend and learn.

Second, because the course was taught in English, it was necessary for the pace of the course to be adjusted to allow the students to sufficiently understand. This meant altering the scope of the course to provide an array of biomechanics topics at a depth that was manageable for the students.

Third, previous studies have shown there are elements of engineering education in Vietnam that do not fully match the skills students are expected to demonstrate after graduation. [2, 3, 4] This factor led to the incorporation of a design project. With this facet the students applied theory toward application, in addition to working on teams, preparing a design report, and making a final oral presentation.

The combination of these and other factors, led to the realization that there was no sufficient existing textbook that would reasonably satisfy the expectations of the course. For this reason, a Baylor University BME graduate student (second author) and author assembled a customized “textbook” designed specifically for this course. This resource was divided into lessons/chapters, and included PowerPoint slides and readings that were either used by permission¹ or taken from open-source resources. The resulting textbook, whose cover is shown in Figure 1, was printed at Baylor, transported in a box as a piece of the author’s luggage, and a copy was given to each of the students in the course.

¹ Especially Dr. Brian Garner, Associate Professor of Mechanical Engineering at Baylor University.

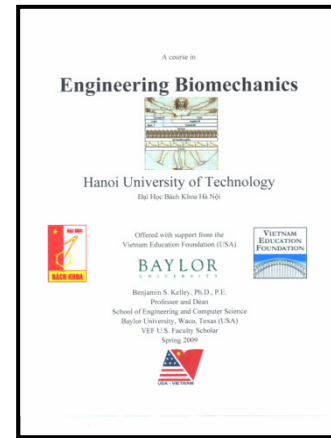


Fig. 1 Customized textbook cover

The specific topics to be included in the course were predicated on both basic biomechanics topics, time availability, student exposure and preparation, and those specifically needed to accomplish the design project. For example, within the HUT biomechanics curriculum, students are required to take several semesters of mechanics. Therefore, it was not necessary to teach basic mechanics concepts, yet it was desirable to review concepts within a BME context. Further, it did not appear the students had extensive exposure to the iterative engineering design process or technical communication. Thus summaries of these topics were inserted into the course curriculum and instruction.

A comprehensive list of the topics planned for coverage in the course was included within the course materials so that students had a full understanding of what topic would be covered on what date, and what format would be use (onsite or online). Each day consisted of two consecutive class periods and thus two lessons, or the equivalent to two chapters in the course book. During the onsite portion, the class met three times each week. And because each session lasted for two academic hours, the pace was twice that of a normal three-credit class. This was tempered, however, by the somewhat slower pace of the course to account for English language comprehension of the students. Then for the online portion, the class met for one session each week, each lasting two academic hours, thus the pace was $\frac{2}{3}$ that of a normal three-credit course. With this combination of course scheduling, approximately one half of the course was offered onsite and one half offered online. This schedule sufficed for the initial onsite portion of the course, but it had to be modified and adjusted later to accommodate extra time needed for some topics.

The scheduled topics were selected specifically to introduce the students to new matter for which they had little experience. For each of these days, the lessons covered two distinct topics. This included topics such as the iterative

engineering design process and final design presentation. These new topics were complimented during the other academic hour with matter familiar to the students, but whose applications were distinctively BME related. These included for example, bio-examples of statics and kinematics.

It was also during this initial onsite component of the course that the students were introduced to the homework expectations. Because the students were already familiar with free body diagrams, it was “communications” of what they turned in that was the greatest challenge. This included stating the problem, providing narrative of their approach, and clearly identifying their answer. Homework assignments were returned the following class period.

Because of the difficulty the students would have submitting their solutions to engineering analysis homework assignments during the online portion of the course, the homework assignments changed in nature. Therefore, the assignments focused around teamwork, components of their design report, and the final design presentation. With this approach, the students still had to perform engineering calculations, but they were targeted toward their design of an orthopedic bone plate, and in a format that could eventually be incorporated into their engineering design report. This made it simpler for the students to email their solutions.

While this approach worked well, it was also this portion of the course that identified a shortcoming. Students and teams struggled with both the engineering evaluations required for the design analysis, as well as writing the various sections of the design report. The design-analysis concern was not due to a lack of the student’s knowledge or understanding, but rather inexperience in applying that knowledge to a design scenario. Supplemental material within the course book addressed specifically this type of design, and the course lecture schedule was altered to highlight further the steps needed for the design analysis.

With regards to the design report itself, it was observed that additional student exposure to design writings was needed. This took the form of example report sections, written by the second author, that were shared with the students. While these helped, they did not alleviate the experience shortfall or the students’ apprehension with preparing the design report. New possibilities will be explored before the course is offered again.

Student teams performed well during their final design presentation. Each team forwarded a copy of their preliminary presentation, to which comments and suggestions were added. Later, each team rehearsed with the author their presentation and received further feedback.

C. Onsite Teaching

Originally 17 students were enrolled in the class, which was later adjusted to 14 students. On a typical class day

10-12 students attended. The class lectures and discussions generally followed the PowerPoint slides contained in the course book. Students were asked to review the slides and associated readings before class. To help facilitate class participation, when a student asked a good question, she/he picked a piece of candy from a bag. Students’ reactions during class and their responses on the course evaluations indicate that they enjoyed and leaned from the lectures.

D. Online Teaching

The online portion of the course was conducted using Elluminate Live[®]. This software package uses a relatively small bandwidth, and thus was adaptable to the limited internet system in Vietnam. And because it is a resource supported by Baylor, it was available at no additional cost or service fee. The Elluminate Live[®] system permits PowerPoint slides to be downloaded, students to ask questions using their microphone/headphone or via a chat box, and for the professor to be viewed and heard, and other features. [5]

From the perspective of a teacher, this system was easy and convenient to use. It was first anticipated that all of the HUT students would be in the same classroom during the online session. However, all of the computers in the assigned classroom could not simultaneously access the internet. Therefore, a second location within the HUT BME unit was utilized, but this room contained only six computers, and the students had to share computers and monitors. After several of the online lectures, the steady-state response became that some students would use the computers in the BME unit, while some would use their home computers or one in an internet cafe. In general, the attendance for online sessions was about the same, but not higher than, the onsite sessions. Many of the online sessions were also recorded, and students could access those recordings.

E. Grades

The grade each student received in the course consisted of his/her performance on 1) homework assignments, 2) midterm exam, 3) design presentation, 4) design report, and 5) final examination. In the U.S., grades are most frequently recorded on a percentage basis with a grade of A indicating 90-100%, grade of B indicating 80-90%, etc. The same grading approach was predominately applied for the HUT students. However, in the Vietnam grading system uses a 10-point scale, where a grade below 4 indicates failure (compared to a grade below 60% in the U.S.). So there are commonalities and differences between the two systems. Student grades were directly converted from the percentage system, to the 10-point-scale system, and that

was the students' final mark. No student failed the class, and some performed at a very high level.

F. Course Evaluation

Students were asked to evaluate their course experience and learning. The Baylor course-evaluation system was used, which consist of students responding to each of fifteen statements. Within Baylor's School of Engineering and Computer Science (ECS), student responses to six of those statements are particularly scrutinized. Possible student responses to each statement include:

- Strongly Agree
- Agree
- Slightly Agree
- Slightly Disagree
- Disagree
- Strongly Disagree

The six statements whose responses are most closely scrutinized are:

1. The instructor explained material clearly.
2. The instructor had an effective of presentation.
3. The instructor treated students with respect
4. The instructor was well prepared for class.
5. The course was well organized.
6. The requirements of the class were clearly explained.

For analysis and comparisons purposes, ECS generally examines the percentage of students who respond with either "Strongly Agree" or "Agree" and consider those favorable evaluations. Further, for individual faculty members, those responses are compared to those received for a broader set of similar courses (level, department, etc). For the HUT biomechanics course, it is not feasible to provide a definitive comparison to similar Baylor courses, because of the obvious differences between the student population, mode of instruction, language and cultural challenges, etc. Furthermore, Dr. Brian Garner (a very fine teacher) is the most frequent teacher of undergraduate biomechanics at Baylor, and therefore the comparison below involves the biomechanics course he teaches. Figure 2 compares data of Baylor student responses for a) a recent similar courses, b) recent offerings of undergraduate biomechanics at Baylor, c) the most recent offering of biomechanics at Baylor, and d) the HUT biomechanics course.

As can be seen from the observation of the data presented in Figure 2 the HUT biomechanics course was well received and considered by the students to be of high quality. For three of the six statements, students evaluated the HUT biomechanics equal to or higher than the other comparison groups. Again, because of all the differences embedded in these comparisons, at best, basic generalities can be drawn. Identified course improvements should enhance student experiences and learning in future offerings.

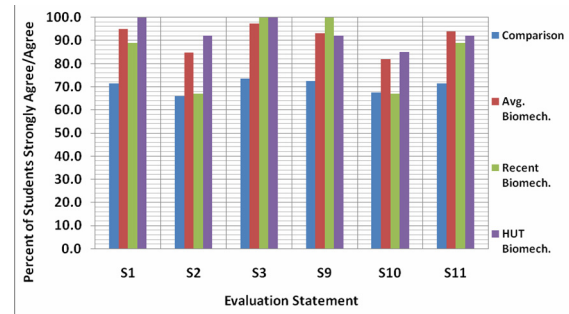


Fig. 2 Comparison of Student Evaluations of HUT Biomechanics Course to Baylor Offerings

III. CONCLUSIONS AND SUSTAINABILITY

Throughout this project sustainability continued to be an important consideration. Course improvements, including online social networks, will make that participation even richer. There may also be the opportunity to involve other Vietnamese universities since a portion of the course is offered online and the entire set of course materials have been posted to the Vietnam OpenCourseWare system.

ACKNOWLEDGMENT

This project was sponsored through a U.S. Faculty Scholars grant from the Vietnam Education Foundation, Washington DC and Hanoi, Vietnam.

REFERENCES

1. Vo, T Childress, D Jaeger, R Kaplan, D Loew, M Vungak-Novakovic, G, Webster, J (2005) Biomedical engineering in Vietnam today, IEEE Engr. in Med. & Bio. 24:1 pp 7-11.
2. Alfen, N Angle, J Gamble, H, Hashimoto, A Wang, J McNamara, L Nguyen, P (2007) Observations on the current status of education in the agricultural sciences in Vietnam, Vietnam Education Foundation and the National Academies of the United States, Washington DC
3. Petrochenkov, M (2007) Opportunities for enhancing STEM education in Vietnam, Vietnam Education Foundation and the National Academies of the United states, August, Hanoi, Vietnam.
4. Director, S Doughty, P Gray, P Hopcroft, et al. (2006) Observations on undergraduate education in computer science, electrical engineering, and physics at select universities in Vietnam, Washington DC.
5. Kelley, B Rigby, B Vu, H (2009) Teaching engineering biomechanics in Vietnam ASEE GSW Proc. Waco, Texas, 2003 TD1-3

Author: Benjamin S. Kelley
 Institute: Baylor University
 Street: One Bear Place #97356
 City: Waco, Texas 76798
 Country: United States
 Email: ben_kelley@baylor.edu

Building an Elearning Website for Biomedical Engineering Education

H.Q. Huy, N.D. Thuan, and V.D. Hai

Department of Electronic Technology and Biomedical Engineering, Hanoi University of Technology, Hanoi, Vietnam

Abstract— This paper introduces the process of constructing the elearning website for Biomedical Engineering (BME), including the process of building electronic lectures and online examinations for the course.

Biomedical Engineering is a new discipline in Vietnam, there were only three universities offer undergraduate degrees in 2005. In addition, this field requires a relatively extensive amount of knowledge of different areas such as informatics, electronics, biology, physics.. and it is growing rapidly, it is required to apply new method in education.

In this paper, we introduce the process of building the elearning website, including selecting appropriate elearning technology; apply it to form some electronic lectures; online student assessment; conduct surveys and collect feedback about website and courses.

This website is based mainly on open source softwares, a becoming popular trend in education . It has proved appropriate and successful in terms of educating biomedical engineering, especially in the advanced programme carried out at Department of Electronic Technology and Biomedical engineering, Hanoi University of Technology for the first time, in cooperation with the University of Wisconsin-Madison, USA.

Keywords— elearning, biomedical engineering, education.

I. INTRODUCTION

Biomedical engineering is only available at just some big universities such as Hanoi University of Technology, Vietnam National University – Hochiminh city (University of Technology, International University), Institute of Military Technology ... and at some related departments such as biomedical informatics biomedical engineering physics, biochemistry, biomaterials at some other universities and colleges. At Hanoi University of Technology, Biomedical Engineering was first implemented in 1999, with the aim of meeting the essential demand from society, especially from the Ministry of Health, of which Department of Electronic Technology and Biomedical Engineering is in charge. [1]

Because it is a new discipline and its lecturing materials and references are limited, it is necessary to take measure to share lectures, materials between lecturers and students, as well as to exchange experience in educating and researching among Vietnamese education institutions or with foreign universities which have cooperation in training and education (such as in advanced programme) [1].

Elearning for biomedical engineering is not a new concept [2] but elearning has just been implemented at Hanoi University of Technology through internet by accessing to elearning website. This website enable lecturers to provide lessons intergrating multimedia such as image, audio, video..in order to facilitate education and study: exploiting, sharing material, lectures; presenting and illustrating complicated problems such as definitions, operating principles of biomedical equipment, biological processes, medical image systems...

The website also assists lecturers and students with doing research through meeting and communicating domestic and foreign specialists and professors in the form of online – training or video – conferencing.

II. CONTENT

1. General Information about Elearning

Elearning (electronic learning): This term indicates a variety of applications and processes like learning via the website, learning on the computer, virtual classes and digital connection including delivering course contents, documents to attendants via the internet, intranet/ extranet (LAN/WAN), audio and video tapes, interactive television, CD-ROM, and other forms of electronic learning materials.[2]

Today, with the convergence of computer and communication, elearning is defined more directly as learning via the internet and web technology.

For Learners:

- Elearning supports the process of individual studying which allows learners to have their own studying timetable and studying methods. Learners can actively adjust the study pace to ease tension and increase efficiency. Furthermore, interaction and exchanging ideas improve the study efficacy.

For Lecturers:

- Lecturers can easily monitor students. Elearning allows the automatic saving of data on the host computer. The data will be updated when learners access the programme. Lecturers can assess learners by requiring them to answers exam questions and considering the amount of time taken to finish the exam. This helps lecturers evaluate fairly learners' performance.

2. Structure of Elearning System

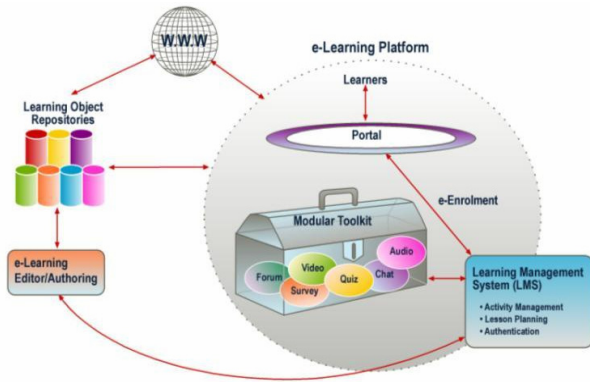


Fig. 1 Elearning system model

Including :

- * Learning is mostly via the internet, using World Wide Web (WWW) such as elearning website.
- * A very important element of the system is the Learning Management System (LMS), including various modules, making the studying convenient and easily, exploiting the advantages of the internet, like: forum to exchange ideas among class members, module to carry out a survey of an issue, testing and evaluation module, online chatting module, flash module...

3. Construction of Elearning Website

Since school year 2007-2008, Hanoi University of Technology has swiftd from education on a yearly basis to the one on a credit-based, meanwhile, carried out the advanced programme of biomedical engineering. Subject contents are based on those of US universities having the discipline of biomedical engineering [3], especially the University of Wisconsin-Madison.

Biomedical engineering students are educated in basic knowledge of the general programme, basic knowledge of the discipline of Telecommunication Electronics and Information Technology and specialistic knowledge of Biomedical engineering

Many approaches, softwares can satisfy the requirement of such elearning website but we choose Moodle [4] because:

- Moodle is an open source software: the university does not depend on any commercial software. [5] [6]
- Moodle support SCORM : SCORM is one of the greatest achievements elearning community has gained over years, ensuring the inheritance and reusing resources.
- Moodle is free.

At present, Moodle has 804,806 users officially registering at the host website, roughly 50,000 websites with

30,036,963 users from 209 different countries over the world, among them Open University – the biggest with over 452,483 learners and 19.223 courses. Moodle has supported 79 languages including Vietnamese.

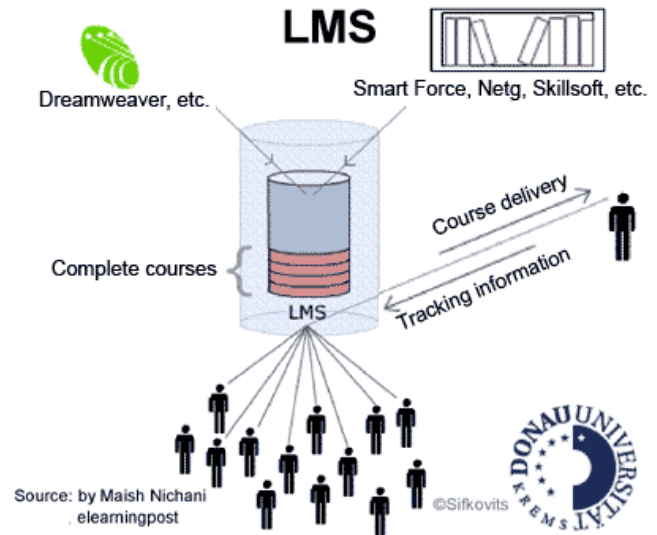


Fig. 2 Hệ quản trị học tập LMS

LMS is intergrated in the elearning website called BME Elearning Website . It has the following functions:

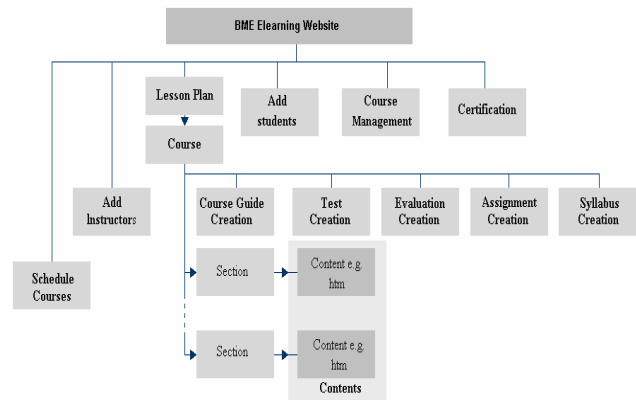


Fig. 3 Function of LMS

The technology used to contract Moodle is the script language PHP, an open source language running on different operating system like: Windows, Linux, Mac OS X... Moodle can run on various web services such as Apache, IIS (Internet Information System), Tomcat, Personal Web Server... Moreover, it supports different database systems like MySQL Server, PostgreSQL, Oracle, MS SQL Server... However, Apache and MySQL are more encouraged because they can run on many operating systems like: Linux, Windows... and they are free.

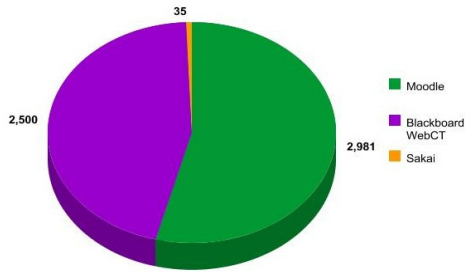


Fig. 4 Moodle holds the largest LMS segment in the world (www.zacker.org)

Moodle is designed to facilitate the principle of social education (*social constructionist*). Moodle has a large amount of flexible functions to help tele-education, and allow Vietnamese students to learn from or listen to foreign professors.

4. Building Electronic Lectures and Online Tests

The content of electronic lectures will be built by lectures based on the requirement of the subject and upload to elearning website.

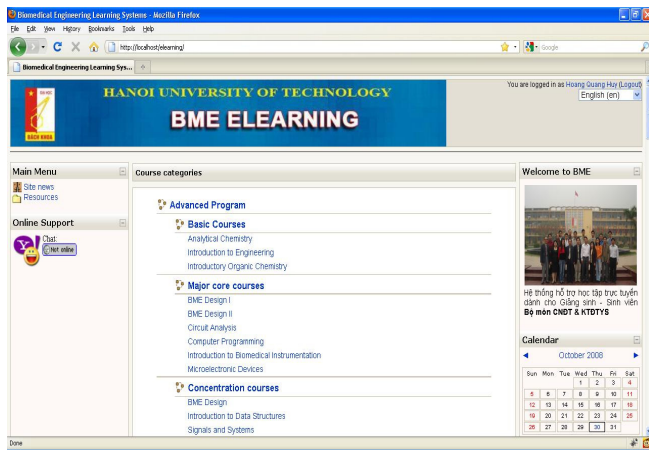


Fig. 5 Home page of BME Elearning Website

This process will be supported by available attached tools of the web. In addition, lecturers can use other softwares like Reload (<http://www.reload.ac.uk/scormplayer.html>) , eXe (<http://exelearning.org>) to create and pack lectures in accordance with SCORM [10].

This paper will not describe the process of constructing in details, but the subsequent tools will be very good to create electronic lectures:

- Slides (in the form of ppt, pdf.)
- Html pages, audio , video, flash file, SCORM package...

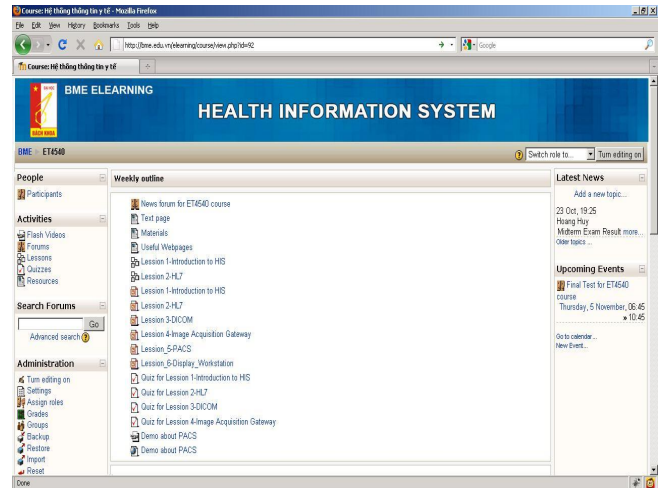


Fig. 6 Home page Medical Imaging System course

In the home page on each course, there are link to lectures and resources of the whole course such as slides, files, quizzes, assignments... and other activities like forum, chat, wiki...

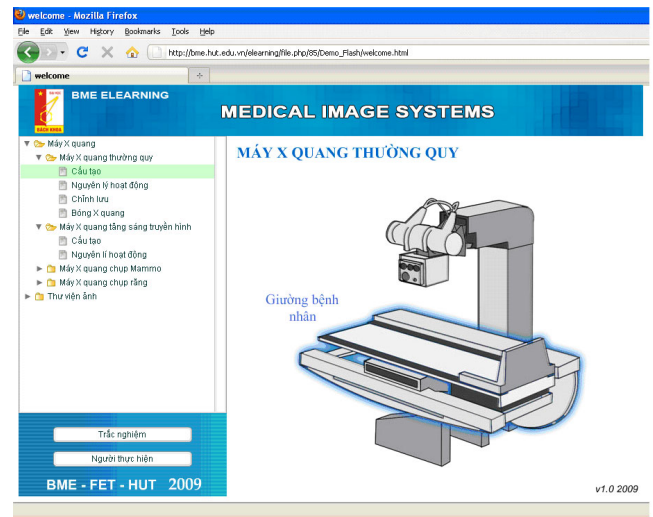


Fig. 7 A lecture in Medical Imaging Systems course

For example, in the above lecture flash which is developed by students majoring in biomedical engineering under the guidance of relative lecturer to simulate structure and operation of X-ray machines.

The elearning website will allow teleeducation via video conference in the same way applied to the subject of Biomechanics by Professor Benjamin S. Kelly (Baylor University, USA). During the studying period, professor and students were at classroom in Vietnam for the first and

last two weeks and studying in virtual class via the internet for the twelve middle weeks.

To create online tests, lecturers can use Moodle or other softwares like Reload, Hot Potatoes... The online test can be taken via the Internet or LAN (in this case LAN is LAN of the computer room). Tests include questions in the following forms:

- Multiple choices, one right choice; multiple choices, multiple right choices,
- Filling in the blank; Matching (compare)
- Calculation, description (writing answers) ...

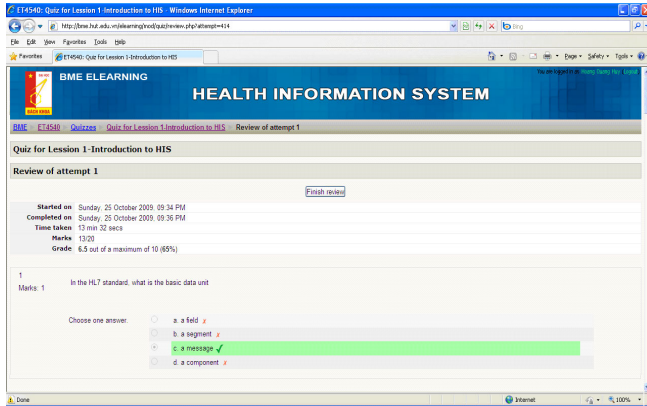


Fig. 8 Quiz in Health Information System course

After learners finish the test, the result will be informed, extracted and saved in the form of excel, text, html, xml... file. The grading is automatic and correct. This kind of test can combine with oral test, project reporting or paper test.

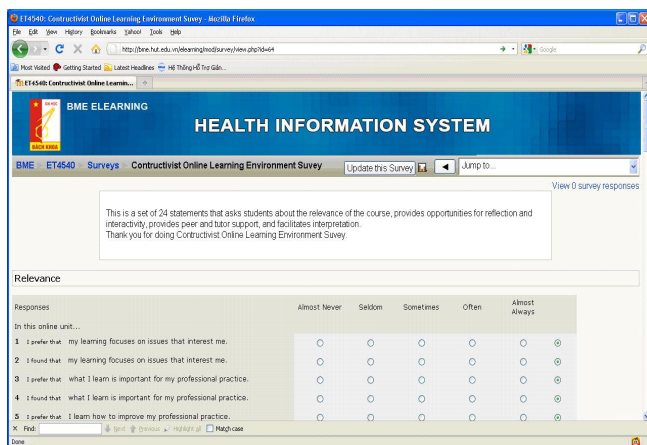


Fig. 9 Survey about Health Information System course

In each subject, lecturers can create survey forms to collect assessment ideas and comments from students in terms of subject contents and teaching methods.

III. CONCLUSIONS

1. The elearning website has already constructed and used by Department of Electronic Technology and Biomedical Engineering, bringing tremendous efficiency to education process: contents of some main subjects have been finished. Students can evaluate their studying performance everytime, everywhere, regardless of studying timetable, and increase the probability of interaction between them and lecturers.

2. The website needs constantly developing and upgrading in order to promote advantages of elearning as well as to meet the specific educational demand of this discipline.

REFERENCES

1. N. D. Thuan et al. (2004) Method to build and develop a new discipline in university, Science and Technology Journal, ISSN 0868-3980
2. Alfred C. H. Yu, Billy Y. S. Yiu Towards (2009) Integrative Learning in Biomedical Engineering
3. ABET Accredited Engineering Programs, http://www.abet.org/accredited_programs.shtml
4. Moodle at <http://moodle.org>
5. European Virtual Campus for Biomedical Engineering EVICAB at <http://www.evicab.eu>
6. Marvin Croy, Ron Smelser. (2009) LMS Evaluation: Moodle Pilot Faculty Response, UNCC, USA.
7. P. Inchingolo, F. Londero, and F. Vatta (2007) The E-HECE elearning Experience in BME Education, Medicon 2007, IFMBE Proceedings 16, pp. 1107–1110
8. William H. Rice IV (2006) Moodle elearning course development. Packt Publishing, UK
9. Jason C (2005) Using Moodle, : Teaching with the Popular Open Source Course Management System. O'Reilly, USA
10. M.J. Smith, G. Salvendy. (2007) Efficient Creation of Multi Media elearning Modules, Human Interface, Part II, HCII, LNCS 4558, pp. 457–465.
11. J. Flacke. (2009) Combining Synchronous and Asynchronous elearning tools in distance education-experiences from a course for developing countries, ISPRS 2009 : Workshop commissions VI land 2, Potsdam, Germany.
12. Horton, W. K. (2000) Designing Web-Based Training: How to Teach Anyone Anything Anywhere Anytime. Wiley

Author: H.Q Huy
 Institute: Hanoi University of Technology
 Street: No 1, Dai Co Viet Street
 City: Hanoi
 Country: Vietnam
 Email: hqhuy-fet@mail.hut.edu.vn

Ethnic Differences in Dietary Intake and the Association between Dietary Intake and Gastric Cancer Risk in Chinese Subjects Resident in Malaysia

D.M. Ha^{1,2}, D. Forman³, K.L. Goh⁴, K.M. Fock⁵, and H.M. Mitchell¹

¹ School of Biotechnology and Biomolecular Sciences, the University of New South Wales, Sydney, Australia

² Ho Chi Minh City International University- National University, Ho Chi Minh City, Vietnam

³ School of Medicine, University of Leeds, Leeds, United Kingdom

⁴ Department of Medicine, Faculty of Medicine, University of Malaya, Kuala Lumpur, Malaysia

⁵ Changi General Hospital, Singapore

Abstract—**Introduction:** Non-cardia gastric cancer (GC) is a multi-factorial disease. Currently it is believed that *Helicobacter pylori* infection, host genetic and dietary factors play a role. **Aim:** This study determined the influence of dietary factors in the etiology of GC in Chinese subjects resident in Malaysia and differences in dietary intake in 3 ethnic groups resident in Malaysia and Singapore. **Subjects and Methods:** 317 subjects with functional dyspepsia (FD) including 123 Chinese, 110 Indians and 83 Malays and 54 Chinese with GC resident in Malaysia and 127 Chinese FD subjects resident in Singapore were included in the study. Genotyping of *IL-1B-511* and *IL-1B-1473* was conducted by PCR-RFLP. *H. pylori* infection status was evaluated by ELISA. The dietary questionnaire explained by a nurse, was completed by each patient. **Results:** Significant differences were observed in the intake of alcohol, salted fish, shrimp paste, salted vegetables and fresh fruit and vegetables for the three main ethnic groups in Malaysia and between Malaysian Chinese FD and Singaporean FD patients. A significant association was observed between alcohol intake, fresh fruit and vegetables intake and shrimp paste intake and the risk of GC in Chinese resident in Malaysia. When a combination of specific host genetic factors, dietary factors and *H. pylori* infection were considered there was a significantly increased risk of GC; these factors being the C/C genotype of *IL-1B-511*, the G/G genotype of *IL-1B-1473*, low fresh fruit and vegetable intake and *H. pylori* (+). **Discussion:** In this population, *H. pylori* infection, host genetic and dietary factors are significantly associated with GC development. Beside the differences in *H. pylori* infection and host genetic factors, the differences between different ethnic groups in dietary factors may also contribute to different frequencies in GC.

I. INTRODUCTION

There is strong evidence to support the view that dietary factors play an important role in the development of gastric cancer. In particular the consumption of fresh fruit and vegetables has been proven to have a protective role in gastric cancer. More than 30 case-control studies have been conducted in different populations around the world, the majority of which have shown that consumption of fruit and

vegetables reduces the risk of gastric cancer by approximately one half [1-2].

To date there have been numerous case-control studies examining the association between host genetic factors alone or environmental factors alone and the risk of gastric cancer. However, few studies have examined the combined effect of host genetic factors and environmental factors on the risk of gastric cancer. In this study, in addition to examining the relationship between specific environmental factors and gastric cancer in the Malaysian Chinese population, the combined effect of high risk host factors, high risk environmental factors and *H. pylori* positivity on gastric cancer risk was also investigated.

II. SUBJECTS AND METHODS

A. Study Subjects

Study subjects were recruited from 01/2004 to 04/2007 in Singapore and Malaysia. All study subjects were patients presenting for upper gastrointestinal endoscopy at the Department of Medicine, University Hospital of Malaysia, Kuala Lumpur and the Changi General Hospital, Singapore. All patients prescribed anti-microbial agents, non-steroidal anti-inflammatory drugs or acid suppressants in the two month period prior to recruitment, and patients known to be infected with HIV (Human Immunodeficiency Virus) were excluded. In Malaysia, three ethnic groups, Chinese, Indians and Malays with functional dyspepsia (FD) were recruited. FD was defined as patients with dyspeptic symptoms but no gastric lesions at endoscopy. Subjects diagnosed with non-cardia gastric cancers (ICD9-151) were selected from all gastric cancer cases. Diagnosis of non-cardia gastric cancer (GC) was based on histological assessment. Control subjects for the GC study were selected from the Malaysian Chinese (FD) patients. Three hundred and seventeen subjects with FD including 123 Chinese (median age-MA: 55, 46% male), 110 Indians (MA: 50, 41% male) and 83 Malays (MA: 44, 37% male) and 54 Chinese (MA: 68, 61%

male) with GC. In addition the study included 127 Chinese FD subjects (MA: 58, 43% male) resident in Singapore.

B. Methods

DNA was isolated from whole blood using the DNA Blood Mini kit (Qiagen, Australia). Genotyping of *IL-1B-511* and *IL-1B-1473* were conducted by PCR-RFLP using the restriction enzyme *AvaI* and *StyI* respectively. *H. pylori* infection status was evaluated by ELISA and Immunoblotting (Helicoblot 2.1). On the day of endoscopic examination each patient was asked to complete a dietary questionnaire. The questions were explained to each patient by a member of the nursing staff, who completed the questionnaire with the patient. The criteria used for the classification of dietary and environmental factors into 2 groups, yes and no are described in table 1.

Statistical analysis: SPSS for Chi square test, GraphPad InStat 3 for two-sided Fisher’s Exact test.

Table 1 Criteria used to assess intake of dietary factors

Factor	Criteria
Smoking	
Yes	Current smoker or Ex-smoker
No	Never smoking
Alcohol drinking	
Yes	Current drinker or Ex-drinker daily to weekly
No	Never drinking alcohol or ex-drinker occasionally
Fresh fruit	
Yes	Weekly to daily consumption of fresh fruit
No	Never or occasional consumption of fresh fruit
Fresh vegetables	
Yes	Weekly to daily consumption of fresh vegetables
No	Never or occasional consumption of fresh vegetables
Salted vegetables	
Yes	Weekly to daily consumption of salted vegetables
No	Never or occasional consumption of salted vegetables
Salted fish	
Yes	Weekly to daily consumption of salted fish
No	Never or occasional consumption of salted fish
Shrimp paste	
Yes	Weekly to daily consumption of shrimp paste
No	Never or occasional consumption of shrimp paste

III. RESULTS

A. Significant Differences Were Observed in the Intake of Specific Dietary Factors in FD Patients from the 3 Ethnic Groups Resident in Malaysia

Comparison of alcohol intake in these groups showed that only 3.6% of Malays drank alcohol as compared with 34.1% of the Chinese and 25.5% of the Indians (p<0.001).

Intake of salted fish was also found to be significantly different (p<0.001) between the three ethnic groups, Indians (33.6%), Malays (53%) and Chinese (9.8%). Intake of shrimp paste was also significantly different in the 3 ethnic groups with only 3.6% of Indians eating shrimp paste as compared with 18.7% of Chinese and 45.8% of Malays (p<0.01) (Table 2).

Table 2 The number and percentage of Chinese, Indians and Malays with FD resident in Malaysia consuming or exposed to a range of dietary and environmental factors

Factors	FD Malaysian Chinese n(%)	FD Malaysian Indians n(%)	FD Malaysian Malays n(%)	P value (Two-sided Pearson χ^2 test)
Total number	123	110	83	
Smoking				0.42
Yes	34(27.6)	23(20.9)	18(21.7)	
No	89(72.4)	87(79.1)	65(78.3)	
Alcohol drinking				<0.001
Yes	42(34.1)	28(25.5)	3(3.6)	
No	81(65.9)	82(74.5)	80(96.4)	
Fresh fruit				0.52
Yes	109(88.6)	94(85.5)	69(83.1)	
No	14(11.4)	16(14.5)	14(16.9)	
Fresh vegetables				0.05
Yes	97(78.9)	81(73.6)	73(88.0)	
No	26(21.1)	29(26.4)	10(12.0)	
Salted vegetables				0.92
Yes	7(5.7)	5(4.5)	4(4.8)	
No	116(94.3)	105(95.5)	79(95.2)	
Salted fish				<0.001
Yes	12(9.8)	37(33.6)	44(53.0)	
No	111(90.2)	73(66.4)	39(47.0)	
Shrimp paste				<0.01
Yes	23(18.7)	4(3.6)	38(45.8)	
No	100(81.3)	106(96.4)	45(54.2)	

B. Significant Differences Existed in the Intake of Specific Dietary Factors between Malaysian Chinese FD and Singaporean Chinese FD

The percentage of Malaysian Chinese FDs who smoked or drank alcohol was higher than in Singaporean Chinese FDs [27.6% vs 17.3% (p=0.05), and 34.1% vs 21.3% (p=0.02) respectively]. In addition, the percentage of Malaysian Chinese FDs who consumed fresh fruit or fresh vegetables was lower than in the Singaporean Chinese FDs [88.6% vs 97.6% (p=0.05) and 78.9% vs 98.4% (p<0.001) respectively]. In contrast, the percentage of Malaysian Chinese FDs who consumed salted vegetables, salted fish or shrimp paste was higher than in the Singaporean Chinese FDs [5.7% vs 0% (p=0.006), 9.8% vs 0% (p<0.001), and 18.7% vs 5.5% (p=0.001) respectively].

C. The Association between Dietary Factors and the Risk of Gastric Cancer in the Chinese Resident in Malaysia

Subjects who did not drink alcohol, did not consume fresh fruit, fresh vegetables and shrimp paste were shown to be 6.6, 3.0, 3.5 and 12.2 times respectively more likely to develop GC than subjects who did consume these dietary factors (Table 3).

Table 3 Comparison of the dietary intake and alcohol and tobacco use in Chinese FD controls and GC cases resident in Malaysia

Factor	FD controls n(%)	Non-cardia GC cases n(%)	OR (95%CI)	P value (Two-sided Fisher's exact test)
Total number	123	54		
Smoking				0.5
No	89(72.4)	36(66.7)	1	
Yes	34(27.6)	18(33.3)	1.3(0.7-2.6)	
Alcohol drinking				<0.001
Yes	42(34.1)	4(7.4)	1	
No	81(65.9)	50(92.6)	6.6(2.3-19.6)	
Fresh fruit				0.01
Yes	109(88.6)	39(72.2)	1	
No	14(11.4)	15(27.8)	3.0(1.3-6.8)	
Fresh vegetables				<0.001
Yes	97(78.9)	28(51.9)	1	
No	26(21.1)	26(48.1)	3.5(1.7-6.9)	
Salted vegetables				0.2
No	116(94.3)	48(88.9)	1	
Yes	7(5.7)	6(11.1)	2.1(0.7-6.5)	
Salted fish				0.8
No	111(90.2)	48(88.9)	1	
Yes	12(9.8)	6(11.1)	1.2(0.4-3.3)	
Shrimp paste				0.002
Yes	23(18.7)	1(1.9)	1	
No	100(81.3)	53(98.1)	12.2(1.6-92.8)	

D. A Synergic Effect Was Observed When a Combination of Dietary Factors Were Examined

When intake of fresh fruit and fresh vegetable was analyzed together, the OR increased in subjects who were in the "NO" category for both fresh fruit and fresh vegetables intake, resulting in a 10.2 times increased risk of GC as compared with those in the "Yes" category (Table 4).

Table 4 The effect of various combinations of fresh fruit and fresh vegetable intakes on GC risk

Factors combined	FD controls n(%)	Non-cardia GC cases n(%)	OR (95%CI)	P value (Two-sided Fisher's exact test)
Total number	123	54		
Yes-fruit/yes-vegetables	88(71.5)	26(48.1)	1	
Yes-fruit/no-vegetable OR No-fruit/yes-vegetables	30(24.4)	13(24.1)	1.5 (0.7-3.2)	0.4
No-fruit/no-vegetables	5(4.1)	15(27.8)	10.2 (3.4-30.6)	<0.001

E. Synergic Effect Observed between Host Genetic Factors and Dietary Factors

In previous studies of the role of genetic factors and GC risk in this same study population, subjects carrying a combination of the C/C genotype of *IL-1B-511* and the G/G genotype of *IL-1B-1473* were shown to have a 5.4 times increased risk of GC than those carrying a combination of the T/T and C/C genotypes respectively. To examine the combined effect of host genetic factors and dietary factors, the results for both host and dietary factors were analyzed together. This showed that subjects who carry the C allele of *IL-1B-511* and the G allele of *IL-1B-1473* and are in the "No" category with respect to fresh fruit and fresh vegetables intake were 24.2 times more likely to get gastric

Table 5 The combined effect of genetic and dietary factors on GC risk in Chinese FD and GC subjects from Malaysia

Factors combined	FD Controls n(%)	Non-cardia GC cases n(%)	OR (95%CI)	P value (Two-sided Fisher's exact test)
Total number	123	54		
TT*/CC^/yes-fruit/yes-vegetables	22(17.9)	2(3.7)	1	
Others#	96 (78.1)	41(75.9)	4.7 (1.1-20.9)	0.03
C carriers*/G carriers^/no-fruit/no-vegetables	5(4.0)	11(20.4)	24.2 (4.0-145.4)	<0.001

* Genotype of *IL-1B-511*

^ Genotype of *IL-1B-1473*

The remaining possible situations including TT/CC/no-fruit/no-vegetables, TT/CC/yes-fruit/no-vegetables, CT/CG/no-fruit/yes-vegetables

C carriers*: C/C and C/T genotype carriers of *IL-1B-511*

G carriers^: G/G and C/G genotype carriers of *IL-1B-1473*

cancer than subjects who do not carry these alleles and are in the "Yes" category for fresh fruit and fresh vegetables intake ($p < 0.001$) (Table 5).

F. Synergistic Effect Observed between *H. pylori* Infection, Host Genetic Factors and Dietary Factors

When the same analysis as above was conducted in *H. pylori* (+) subjects only; the ORs were observed to increase from 4.7 and 24.2 (Table 5) to 9.1 and 37.3 ($p < 0.001$) (Table 6).

Table 6 The combined effect of *H. pylori* (+), genetic and dietary factors on GC risk in Chinese FD and GC subjects from Malaysia

Factors combined	FD Controls n(%)	Non-cardia GC cases n(%)	OR (95%CI)	P value (Two-sided Fisher's exact test)
Total number	72	38		
TT*/CC^/yes-fruit/yes-vegetables	16(22.2)	1(2.6)	1	
Others#	53(73.6)	30(79.0)	9.1 (1.1-71.8)	0.02
C carriers*/G carriers^/no-fruit/no-vegetables	3(4.2)	7(18.4)	37.3 (3.3-424.8)	<0.001

* Genotype of *IL-1B-511*

^ Genotype of *IL-1B-1473*

The remaining possible situations including TT/CC/no-fruit/no-vegetables, TT/CC/yes-fruit/no-vegetables, CT/CG/no-fruit/yes-vegetables

C carriers*: C/C and C/T genotype carriers of *IL-1B-511*

G carriers^: G/G and C/G genotype carriers of *IL-1B-1473*

IV. DISCUSSION

While all the subjects in this study would be classified as Asian, and the three groups live in the same country, Malaysia, significant differences were found to exist in the dietary, alcohol and smoking profiles of the Chinese, Indians and Malay ethnic groups. The finding that there was a significant difference in dietary intake between ethnic groups suggests that in case-control studies examining the effect of dietary and environmental factors on gastric cancer, matching for ethnicity is essential. Differences in dietary factors between Malaysian Chinese and Singaporean Chinese may be explained by different living conditions and cultural attitudes that exist between the two countries.

The consistently reported reverse association between consumption of fresh fruit and fresh vegetables and gastric cancer was confirmed in the Malaysian Chinese examined in this study. The finding that subjects who consumed fresh

fruit or vegetables had a 3 times lower risk of developing gastric cancer than those who did not consume fresh fruit or vegetables is higher than that in previously reported studies where the risk was generally accepted as a 2 times decreased risk [1-2].

In the Malaysian Chinese, drinking alcohol had a protective effect against gastric cancer, 92.6% (FD) vs 65.9% (GC) ($p < 0.001$) (Table 3). Analysis of the group that answered "Yes" to drinking alcohol revealed that the majority of subjects only drank alcohol occasionally (80%). Thus the majority of drinkers in the current study were not heavy drinkers. This result is consistent with previous studies that have shown that a moderate intake of alcohol may have a protective effect against gastric cancer. It has also been suggested that alcohol may have an antimicrobial effect on *H. pylori* [3-4].

The observed synergistic effect of *H. pylori*, dietary factors and host genetic factors on the risk of developing gastric cancer suggests that gastric cancer pathogenesis is, as previously suggested [5] a multifactorial disease, which includes *H. pylori* infection, host genetic factors and environmental factors.

ACKNOWLEDGMENT

This work was supported by The Cancer Council of New South Wales, Australia (REF 66/04).

REFERENCES

- [1] K. A. Steinmetz and J. D. Potter, "Vegetables, fruit, and cancer prevention: a review," *Journal of the American Dietetic Association*, vol. 96, pp. 1027-39, Oct 1996.
- [2] P. Correa, *et al.*, "Review article: Antioxidant micronutrients and gastric cancer," *Alimentary Pharmacology & Therapeutics*, vol. 1, pp. 73-82, 1998.
- [3] H. Brenner, *et al.*, "Alcohol as a gastric disinfectant? The complex relationship between alcohol consumption and current Helicobacter pylori infection," *Epidemiology*, vol. 12, pp. 209-14, Mar 2001.
- [4] B. Barstad, *et al.*, "Intake of wine, beer and spirits and risk of gastric cancer," *European Journal of Cancer Prevention*, vol. 14, pp. 239-43, Jun 2005.
- [5] D. M. Pritchard and J. E. Crabtree, "Helicobacter pylori and gastric cancer," *Current Opinion in Gastroenterology*, vol. 22, pp. 620-5, Nov 2006.

The address of the corresponding author:

Author: Hazel M Mitchell

Institute: School of Biotechnology and Biomolecular Sciences, the University of New South Wales,

Street: High Street

City: Sydney, Randwick NSW 2031

Country: Australia

Email: h.mitchell@unsw.edu.au

Phylogenetic Analysis the 5'-Noncoding Sequences of the Hepatitis C Virus Detected from the Patient with HCV Infection

Nguyễn Thái Sơn^{1,2} and Phạm Hùng Văn^{1,2}

¹ University of Medicine and Pharmacy At Ho Chi Minh City

² Nam Khoa Biotek

Abstract— BACKGROUND/AIMS: Several strains of the hepatitis C virus exist; distinct genotypes and subtypes can be identified by sequence comparison of the viral genomes. Recent evidence that the genotype/subtype of hepatitis C virus may influence the clinical course of chronic hepatitis C and the response to interferon-alpha therapy for this disease suggests that methods to identify the genotype may become clinically useful. In the present study we evaluated a recently introduced method for identifying genotype HCV based on sequencing 5'UTR region. METHODS: HCV-RNA was isolated from serum samples from 209 plasma patients with HCV infection, the 5'-UTR region was amplified by RT-PCR and subsequently sequenced in the 5'-noncoding by the dideoxynucleotide chain termination method. HCV-genotyping was performed by the blast search of the sequences with the HCV genotype gene bank. The phylogenetic analysis were used to differentiate the separate clusters of the identified HCV genotypes. RESULTS: The result of genotypes using blast search shows the proportions of patients with HCV subtype types 1a, 1b, 1c were 24.1%, 45%, 1.9% respectively, and other genotypes were genotype 2a 11.4% (24/209), 2b 0.48% (1/209), 2c 0.96% (2/209), 3a 0.96% (2/209), 6a 15.68% (31/209). However, among the genotype 1, the subtypes 1a, 1b and 1c are merged together demonstrated by the phylogenetic analysis. These results said that the differentiation of hepatitis C virus subtypes in genotype 1 was possibly insufficient in the phylogenetic tree analysis. CONCLUSIONS: Our results suggest that HCV 5' NC-region genotyping methods give sufficient information for clinical purposes, but the phylogenetic tree analysis could not differentiate the separate cluster of the subtypes among type 1.

Keywords— Hepatitis C virus, 5'UTR, Enter up to five keywords and separate them by commas.

I. INTRODUCTION

Variations in the HCV genome sequence of change is very large, up to 30-35% across the entire genome (3). HCV genome has 5' noncoding (5'UTR) and the 3' noncoding (3'UTR), and two regions: the structure region (core, E1, E2) and the non-structural region (NS2, NS3, NS4, NS5). Based on the analysis of genome sequences and regions, the 2nd international conference on HCV and virus similar in 1994 agreed to classify HCV genotype 6 are marked by

numbers (1,2,3, ...,), about 80 subtype marked by letters (a, b, c, d, ...) (4) Meaning of the determination of genotype and subtype plays an important role in monitoring the epidemiological, the change of the virus hepatitis C. Recently a number of treatment guidelines, recommendations identified genotype before treatment to select appropriate treatment regimen (1) for economic efficiency and response result.

Until now various technology is applied to determine the genotype. Two main methods are widely accepted, basing on the analysis of the 5'UTR. They are hybridization probe for the specific genotype (HCV-InoLIPA) and sequenced approach on Trugene. For InoLIPA kit, procedure don't need equipment sequencing, but we must require strict conditions for hybridization to have best result, the concentration of virus must be greater than 104 copies, so the result can correct, distinct. On the other hand, Trugene, a closed system, is high cost, the results just only show genotype of HCV, we can't retrieve the sequence, can't access easily to conduct further research (2).

Objective of this research is to analyze the 5'UTR, phylogenetic tree construction, compare results with local libraries in the blast of euHCVdb. Results will be applied in genotyping routinely for clinical purpose.

II. PATIENTS AND METHODS

A. Patients

In this study, serum of patients from multiple centers is sent to the NamKhoa biotek's laboratories in February 2009 to March 2009 period with the requirements of HCV genotype.

B. Methods

a) Extraction of ARN:

RNA was extracted from serum using the extraction RNAPREP kit of Nam Khoa Biotek in accordance with the formula Chomczynski, following manufacturers instructions. Finally, the RNA pellet was diluted in 40µl water-treated DEPC, and then, solution reserves temperature-80oC.

b) cDNA Synthesis with Random Primer :

15µl products,obtained from RNA extraction, was dissolved in the 5µl of RT-mix reagents cDNA synthesis by Nam Khoa biotek based on formula and chemical Promega (included RT enzyme, Mn, RNAsin, RNaseH, dNTP, random primer). The reaction tube runs in thermocycle instrument with the cycle (25 ° C / 5 ' , 42°C/30' , 85°C / 5 ').

c) PCR Amplification:

PCR amplification by using the 5'UTR specific primer: 25µl PCR included: 1X PCR buffer, 1.5mm MgCl₂, 10MM dithiothreitol (DTT), 200µM dNTP, 0.5µM primer HCV1F (5`-GCAGAAAGCGTCTAGCCAT-3`) and 0.5µM HCV2R (5`- CTCGCAAGCACCTATCAGG - 3`), 1.5 U Taq polymerase and 5µl cDNA sample. Thermal cycle includes: 40oC for 10 min, 94oC for 5 minutes, 40 cycles (each cycle 94oC in the 30s, 60oC in the 30s, 72oC in the 60s), the last 72 oC for 10 minutes.

PCR product 244bp in length, from positions 66 to 311 (strain H77 - Los Alamos National Security).

d) Sequencing:

Sequencing is done on ABI 3130XL with its ABI BigDye kit. Sequenced process is conducted in accordance with the instructions of the manufacturer of equipment and chemicals (ABI).

PCR products after purification were mixed with primers sequencing,in the ratio of the DNA : primer (ng: pmol) was 1: 0.7. Complete sequencing was performed in cycle sequencing: 96°C for 1 minute, 25 rounds (96 oC in the 10s, 50°C in 5 seconds, 60°C for 4 minutes). Product was purified by ethanol / EDTA / sodium acetate with cold Beckman Allegra centrifuge speed of 1650 rpm for 45 minutes at 4oC. Product precipitated at bottom tube, using for sequencing reation.

e) Phylogenetic Tree Construction:

Alignment

Sequence of 5'UTR region is entered into Molecular Phylogenetic Genetics Analysis software (MEGA version 4.1) and aligned by CLUSTAL W method in MEGA 4.0. And then, compare with reference sequence of identified genotype and subtype.

Phylogenetic tree construction:

Using neighbor-joining algorithm of the MEGA4 and p-distance calculation of differences on each nucleotid sequence. Bootstrap 1000 times resampling of phylogenetic trees was carried out test the robustness of the observed major clades.

III. RESULT AND DISCUSS

Gene sequences will be compared to gene libraries from the HCV Los Alamos National Security. Analysis based on 209 samples showed that the proportion of blast in turn is genotype 1a (24.1%), 1b (45%), 1c, 2a 11.4% and 1.9% (24/209), 2b 0.48 % (1 / 209), 2c 0.96% (2 / 209), 3a 0.96% (2 / 209),6a 15.68% (31/209).(Figure 1) Thus, in the form of study, genotype 1, genotype 2, genotype 6 are majority. However, objective's study doesn't aim to conclude in the epidemiological result, samples which taken in this study may include treated-patients, different sources, various regions. Therefore,it's difficult to have epidemiological conclusion.

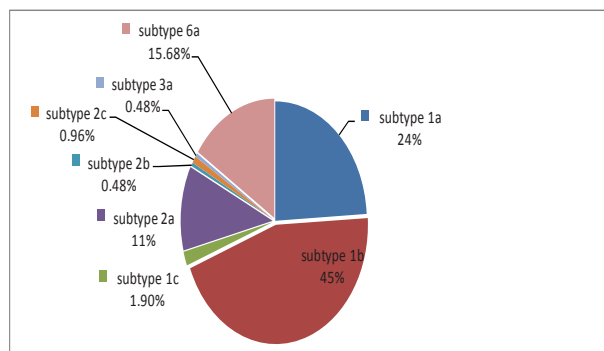


Fig. 1 Distribution of HCV Genotypes and Isolates in 209 Patients Studied as Determined by the sequencing of 5'UTR

Based on sequencing analysis by MEGA 4, 209 sequences were analyzed by comparison of each base pairs. Results showed that genotype difference from 4.5% to 13%, median 7.1 ± 1.18 , subtype from 0.6% to 4.4% with a median 1.3 ± 1 , 15 (Figure 2).

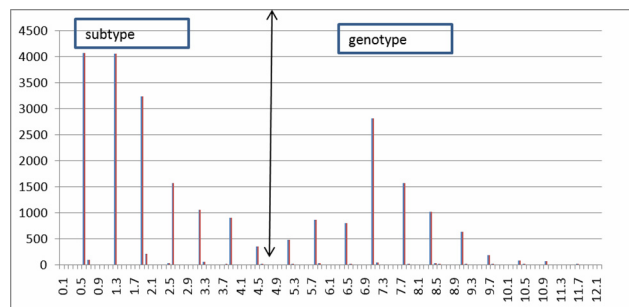


Fig. 2 Distribution of percentage sequence similarities upon pairwise comparison of 209 nucleotide sequences of HCV variants in the 5'UTR region. Number of observed sequence differences (in increments of 1%) recorded on the y-axis. Mean + 3 S.D. for each distribution shown by horizontal bar

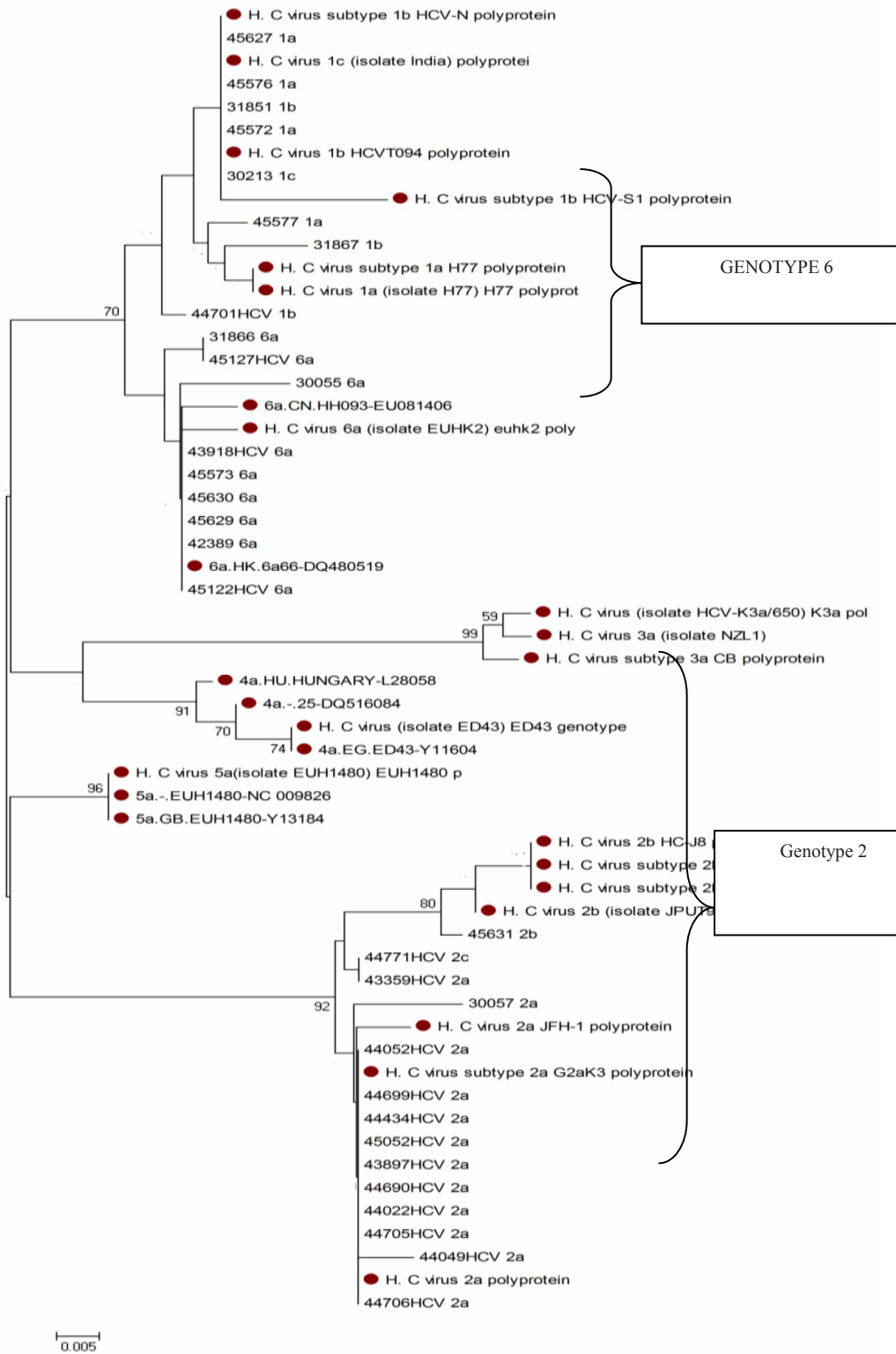


Fig. 3 Phylogenetic tree

Phylogenetic tree is made up from 209 samples, using neighbor-join method with the P-distance analysis tested by bootstrap 1000 times, the results of local blast are placed in end of each name. The reference sequence, obtaining from Alamos, is marked in red. Results showed that the samples of Nam Khoa biotek's laboratory can be divided into three main group genotype genotype 1, 2, 6. (Figure 3).

Based on analysing the phylogenetic tree revealed that the 5'UTR may be less sensitive to subtype in group 1. Because the subtypes of a genotype 1 mixed together, make it difficult for grouping of subtype distribution. The other genotypes can be grouped precisely into genotypes and subtypes. In the 5'UTR region of genotype 1, only just 2 bases vary between subtype located at 137 and 176 (position based on strains isolated H77 - ID: NC_004102), so subtypes in genotype 1 mingle with each others.

IV. CONCLUSIONS

5'UTR region of HCV could completely distinguish between genotype and subtype of HCV. Our results suggest that HCV 5' NC-region genotyping methods give sufficient information for clinical purposes, but the phylogenetic tree analysis could not differentiate the separate cluster of the subtypes among type 1. For separating subtype purpose, we recommend to sequencing other region for accurate result.

REFERENCES

1. Ghany, M. G., D. B. Strader, et al. (2009). "Diagnosis, management, and treatment of hepatitis C: an update." *Hepatology* 49(4): 1335-1374.
2. Nolte, F. S. (2001). "Hepatitis C virus genotyping: clinical implications and methods." *Mol Diagn* 6(4): 265-277.
3. Okamoto, H., Y. Sugiyama, et al. (1992). "Typing hepatitis C virus by polymerase chain reaction with type-specific primers: application to clinical surveys and tracing infectious sources." *J Gen Virol* 73 (Pt 3): 673-679.
4. Simmonds, P., E. C. Holmes, et al. (1993). "Classification of hepatitis C virus into six major genotypes and a series of subtypes by phylogenetic analysis of the NS-5 region." *J Gen Virol* 74 (Pt 11): 2391-2399.

A Study of Mean Glandular Dose during Diagnostic Mammography in Hospitals in Hanoi, Vietnam

Nguyen Thai Ha, Nguyen Duc Thuan, and Nguyen Thu Van

Department of Electronic Technology and Biomedical Electronic Engineering - Hanoi University of Technology, Hanoi, Vietnam

Abstract— A mammography examination facilitates the early detection of breast cancer. However, the potential risk of radiation-induced carcinogenesis is also increased with such a procedure. The objective of this research was to determine the mean glandular dose (MGD) from mediolateral oblique (MLO) views in each breast and the total dose per woman (for both breasts) from the exposure factor in patients undergoing mammography in some hospitals in Hanoi, Vietnam. The secondary objective was to evaluate some of the factors affecting MGD. The values of compressed breast thickness (CBT), as well as the MGD calculated from the exposure and tube voltage both mAs and target/filter combination, were collected from over 350 women ranging in age from 24 to 79 year olds. The MGD for the phantom was in range 1.0269–2.052 mGy, while the MGD for patient was in range 0,418 mGy to 2,72 mGy for the mediolateral oblique views. The mean MGD per woman was 1.45 mGy. They are quite far from the limitation of ACR recommendation, 3mGy. This may ensure that the mammography examination in some main hospitals in Hanoi Vietnam was capable of achieving acceptable dose levels for patient safety.

Keywords— Mean glandular dose, Half Value layer, Compressed breast thickness, Mammography.

I. INTRODUCTION

In Vietnam nowadays, breast cancer is the most common malignancy in women according to the statistical number of Hanoi Cancer Hospital – K - in year 2000. Early detection of breast cancer is the key to successful long-term control of the disease and good prognosis, while mammography of excellent quality is a fundamental prerequisite. However, the breast is a radiosensitive organ [1]. Hence, the potential risk of radiation-induced carcinogenesis is increased with such a procedure [2]. Because the glandular tissues of the breast are more radiosensitive than adipose tissues, the estimation of mean glandular dose (MGD) has become an area of concern [3]. The two main methods for the assessment of MGD from mammography are the use of a standard breast phantom and patient-based measurement. Standard breast or phantom measurement is utilized to define MGD limits [4–6] and is well suited for quality control and inter-system comparison to ensure that all units are capable of

achieving acceptable doses. Such measurements, however, do not indicate the actual dose received by the individual woman. The method for estimating the MGD to the breast of a patient consisted of collecting the data on compression breast thickness for each breast with an indication of the tube voltage, and mAs and target/filter combination for each patient. As direct estimation of the MGD is not feasible, it is often estimated from the measurements of the incident air kerma and converted to MGD by applying conversion factors [9]. The American College of Radiology (ACR) specifies that the MGD should not exceed 3 mGy per view for screen-film image receptors.

The primary objective of this study was to determine the MGD during diagnostic mammography in some hospitals in Hanoi, Vietnam. The secondary objective was to evaluate some of the factors affecting MGD, such as half value layer (HVL) of the X-ray beam, compressed breast thickness (CBT) and age. Such information is necessary in order to formulate recommendations to minimize radiation doses without compromising image quality.

II. MATERIALS AND METHODS

A. Standard Breast Phantom Method

In this method, the Radiation Measurements Inc. (RMI) phantom, model 156 (Radiation Measurements Inc., Middleton, WI) or equivalent, described as equivalent to 50% glandular tissue and 50% adipose tissue with CBT of 45 mm [10], is required. The method involves measuring the incident air kerma, without backscatter to the phantom and applying conversion factors determined by Wu et al [9].

B. Patient-Based Method

This study collected data from over 350 women attending mammography examinations in two mammography units, at cancer hospital – K - in Hanoi and one in Thainguyen province, in two periods, May 2007 and August 2009. Characteristics and radiographic parameters for the three mammography units are given in Table 1. Only mediolateral oblique (MLO) view was included in this study.

Table 1 Characteristics and radiographic parameters for the three mammography units

	A equipment	B equipment	C equipment
Model	Metaltronica	Planmed Sophie	Melody
SID (mm)	650	650	600
Target	Mo	Mo	Mo
Filter	Mo	Mo	Mo
kV range	20-35	20-35	24-35
mAs range	1-640	100 - 500	1-640

For each woman, data on age, weight and compression breast thickness (CBT) were also recorded. CBT was measured using a ruler, at a distance of 4 cm from the chest wall, as the distance between the bottom of the compression plate and the table upon which the breast plated. Measurement of MLO views, however, measurement was made at only one side of the compression plate, opposite to the woman's arm. For each breast, the force applied was also recorded. Thereafter, incidence air kerma was measured by using the ionization chamber placed in the x-ray field. The ionization chamber systems employed in this research was SOLIDOSE 300 with an electrometer. The exposure measure (mGy) was converted to the MGD according to ACR recommendations [10]. Figure 1 shows the measurement setting.

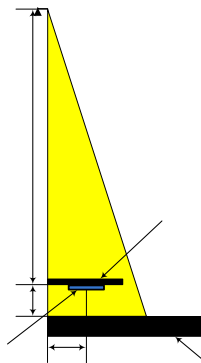


Fig. 1 Measurement of the incident air kerma at the relevant tube loading using a diagnostic dosimeter

III. RESULT

A. Mean Glandular Dose of Standard Breast Phantom

The anode/filter combination of two surveyed mammography is Molybdenum/Molybdenum, focus to image distance is 650mm. The MGD for phantom after calculated was in range 1.0269–2.052 mGy with tube voltage is 25 kV and 30 kV in respectively (as shown in Table 2).

Table 2 MGD of breast phantom PMMA 45mm

Proj	Tube voltage (kV)	Tube loading (mA·s)	Incident Air Kerma (K _i) (mGy)	HVL (mmAl)	Mean Glandular Dose (D _G) (mGy)
CC	25	55	5.491805	0.32	1.026968
CC	28	55	7.8936	0.358	1.62103
CC	29	55	8.71805	0.368	1.826955
CC	30	55	9.56285	0.38	2.052188

B. Mean Glandular Dose of Patients

The value of breast thickness and MGD were collected from over 350 patients (each patient took two MLO projections, one for left breast and one for right breast). The mean glandular dose per breast was in range 0,418 mGy to 2,72 mGy for the mediolateral oblique views. The mean MGD per breast was 1,45 mGy.

The MGDs per MLO films are significantly related to the compressed breast thickness (CBT), tube voltage and tube loading. The MGD and CBT in MLO views are show in Fig. 2.

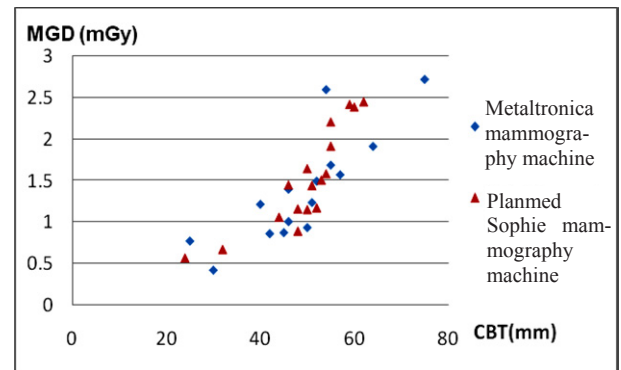


Fig. 2 The MGD for MLO projection according to compressed breast thickness (CBT)

Doses for MLO projections according to the CBT are shown in Fig. 3.

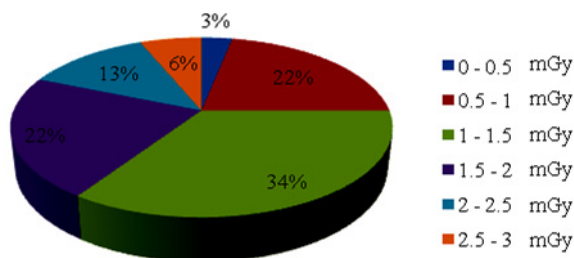


Fig. 3 The distribution of MGD on patient's breasts

The results indicated that doses for 34% of films of MLO projections were in range from 1 to 1.5 mGy, 22% of films of MLO projections were in range from 1.5 to 2 mGy, 13% of films of MLO projections were in range from 2 to 2.5 mGy and only 6% of films of MLO projections were in range from 2.5 mGy to 3 mGy, all was less than 3.0 mGy. The ACR recommends that the MGD should not exceed 3 mGy per view and the result from this research showed that all MGD of the films of MLO projections were lower than the standard dose.

This may ensure that the mammography x-ray generators in some main hospitals in Hanoi are capable of achieving an acceptable dose for patient safety. However, the measurement of breast thickness might vary because there was no standard method for measuring the thickness of the breast and the values were obtained from individual practice by each radiation technician.

In this study, the result shown that the MGD per breast was 1.45 mGy for the MLO view with mean CBT was 49.22mm. The MGD estimation in this study were based on the assumption that all breasts had a standard 50:50 ratio of adipose to glandular composition.

IV. CONCLUSIONS

The MGD for the phantom was in range 1.0269–2.052 mGy, while the MGD for patient was in range 0.418 mGy to 2.72 mGy for the mediolateral oblique views. The mean MGD per woman was 1.45 mGy. They are quite far from the limitation of ACR recommendation, 3mGy. This may ensure that the mammography examination in some main hospitals in Hanoi Vietnam was capable of achieving acceptable dose levels for patient safety.

On the multivariate test two factors, namely half value layer of the X-ray beam and compressed breast thickness, had a significant effect on MGD per woman. No significant relationships were seen between MGD per woman with respect to body mass index or age.

ACKNOWLEDGMENT

This study was supported by the Radiation Safety Center of Institute for Nuclear Science and Technology, K- hospital in Hanoi and BME Department of Faculty of Electronics and Telecommunications at Hanoi University of Technology.

REFERENCES

1. IAEA, Recommendations of the International Commission on Radiological Protection (ICRP) 1990, Springer Berlin / Heidelberg, 10.1007/BF00184120.
2. European Commission, Nuclear Science and Technology - Radiation quantities, units and measurements, Final report, 2007.
3. Beckett JR, Kotre CJ. Dosimetric implications of age related glandular changes in screening mammography. *Phys Med Biol* 2000;45:801–13.
4. Institute of Physical Sciences in Medicine. Commissioning and routine testing of mammographic x-ray systems Report 59(2). York, UK: IPSM, 1994.
5. International Atomic Energy Agency. International basic safety standards for protection against ionising radiation and for the safety of radiation sources. Safety Series no. 115–1. Vienna, Austria: IAEA, 1996.
6. American College of Radiology Committee on Quality Assurance in Mammography. Mammography quality control manual, medical physicist's section. Reston, VA: ACR, 1999
7. Report of a co-ordinated research programme jointly organized by the IAEA and the Commission of the European Communities, Radiation doses in diagnostic radiology and methods for dose reduction, 1995.
8. Gary T. Barnes, G. Donald Frey, Screen film mammography – Imaging considerations and medical physics responsibilities, proceeding of SEAAPM Spring Symposium, Wisconsin, 1990.
9. Wu X, Barnes GT, Tucker DM. Spectral dependence of glandular tissue dose in screen-film mammography. *Radiology* 1991;179:143–8.
10. International Atomic Energy Agency, Dosimetry in Diagnostic Radiology: An international Code of Practice, Technical report series No. 457, Vienna, 2007.
11. Marvin Rosenstein, Linda W. Andersen, Gordon G. Warner, Handbook of Glandular Tissue Doses in Mammography, U.S. Department of Health and Human Services, Public Health service Food and Drug Administration, Reprinted May, 1987.

Author: Nguyen Thai Ha, Nguyen Duc Thuan, Nguyen Thu Van.
 Institute: Hanoi University of Technology
 Street: Dai Co Viet
 City: Hanoi
 Country: Vietnam
 Email: thaiha-fet@mail.hut.edu.vn; thaiha_bk@yahoo.com

Relationship between Dental Occlusion and Arm Strength

Lê Minh Hòa¹, Đặng Nam Huân¹, Nguyễn Hồng Thảo², Ngô Thanh Hoàn¹, Trương Quang Dang Khoa¹, Nguyễn H.M. Tâm¹, and Võ Văn Tới¹

¹ Biomedical Engineering Department, International University of Vietnam National Universities, Ho Chi Minh City, Vietnam

² Biomedical Engineering Department, Drexel University, Philadelphia, Pennsylvania, USA

Abstract— It has been thought that imbalance in the jaws may cause loss in arm strength. However to the best of our knowledge there has been no study on this topic. In this pilot study we quantified this phenomenon. A pool of 34 healthy subjects (ages from 19 to 21 years old; average age: 19.8 ± 0.9 years old) participated in this study. They were randomly selected to participate in different experimental paradigms. Most of them were naïve to the study. All signed the consent forms. The subjects were asked to stand straight and extend their arms and legs in frontal plan. The ratio of the distance between the 2 feet and their heights was the same to all subjects and equal to 0.25. The goal of this investigation was to record the maximum forces that the subjects can resist against a pull-down force on their hands while biting a spacer of adjustable height in the left or right or both sides of their jaws or using the incisors. The control group consisted of data obtained without using spacer and on the other side of the arm. The experimental protocol consisted of several paradigms. The order of executing the paradigms was random. The results showed that (1) Imbalance bite induces contralateral loss of arm strength; (2) The loss is approximately a linear function of the height of the spacers; (3) The loss leveled when the spacer was higher than 2mm; (4) The slopes of the linear function were similar in both arms and independent to the gender; and (5) The arm strength of male was higher than that of female subjects. This investigation may be interesting in sport medicine to study the effects of the mouth guards on the athlete arm strength.

Keywords— Jaw Imbalance, Bite Imbalance, Loss of Arm Strength, Contralateral Effects, Sport Medicine.

I. INTRODUCTION

It has been reported in literature that there is a strong relationship between mouth, cranium, face, temporomandibular joint, neck and arm muscles, and respectively nerves. Bakke [1] suggested that the extent of occlusal contacts affected the electromyographic activity, bite force magnitude, masticatory efficiency and the performance of jaw movements. Van Spronsen et al. [2] suggested that the muscles of mastication depended on different factors including age and gender as other skeletal muscles. Linderholm et al. [3] who investigated the relationship between bite force magnitude and forces produced by several skeletal muscle groups in children suggested that there was a relationship between bite forces and other forces, and maximal bite force

correlated with elbow flexion force and hand grip force. Raadsheer et al. [4] found that the size of the jaw muscles was significantly related to the size of the limb muscles; however, maximal voluntary bite force moments were not significantly related to the moments of the arm flexion and leg extension forces. It has been thought that imbalance in the jaws may cause loss in arm strength. To the best of our knowledge this relationship has not been reported in scientific literature. In this article we report the results of a pilot study that suggested a strong relationship between dental occlusion and the loss of strength in the arms.

II. MATERIALS AND METHODS

A pool of 34 subjects whose ages ranged between 19 to 21 years old (average and standard deviation: 19.8 ± 0.9 years old) participated in the investigation. Most of them are naïve to the study. All participants were healthy and showed no musculoskeletal restrictions or diseases. They had a complete dentition, i.e. no premolar or molar was missing in a quadrant. There were no signs of severe malocclusions and no facial malformations. All subjects were free of any medication and didn't complain of any kinds of muscle pains at the time of the experiments.

This study comprised different experimental paradigms. We selected randomly a number of subjects in the pool to participate in those paradigms. Before the experiments each subject filled out a questionnaire, which was kept confidential and included patient's identification, age and gender. His/her height (H) was measured and recorded. The tenets of the Declaration of Helsinki were followed; the local Institutional Review Board approved the study and informed consent was obtained for all subjects.

The goal of the experiments was to determine the relationship between the bite and the arm strength. The subject was asked to stand with their arms and legs extended in frontal plan (Fig. 1) in such a way that the ratio $D/H = 0.25$. This ratio was chosen based on the fact that many subjects felt comfortable and stable. The subject was then asked to resist to a pull-down force F on one of his/her hand (with the palm turned toward the ground) without moving his or her body. The maximum value of F when the subject can no longer resist was recorded. The pull-down force consisted

of a load in kilogram that can be adjusted in the increment of one half of a kilogram and converted into Newton.

The experimental protocol consisted of asking the subject first to hold the handle of a load which was at rest i.e. the load did not apply any force on the subject arm. Second, at a warning signal the load was released at once; therefore it generated a pull-down force on the subject's arm. The subject must hold the load for a maximum of 5 seconds without moving his/her body. If the subject couldn't hold the load for this period of time the load was removed and lightened incrementally. If the subject could hold the load for this period of time, the load was removed and added incrementally. Third, the subject relaxed for 5 minutes and the measurement restarted. In the end, the maximum load the subject could hold was recorded as the strength of his/her arm.

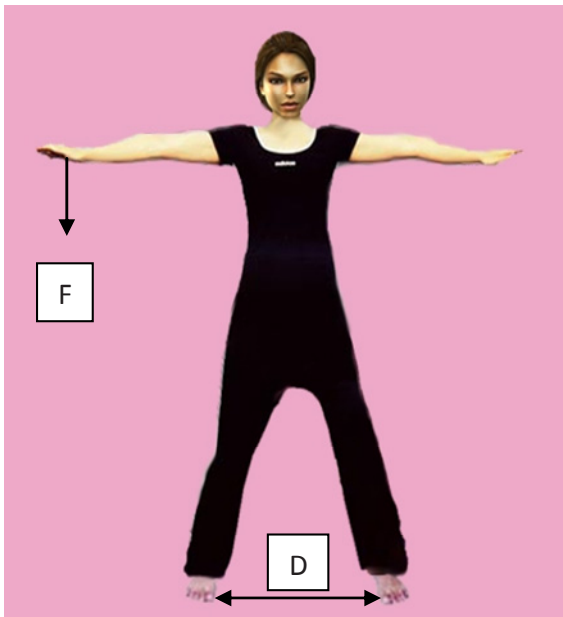


Fig. 1 During the experiment, the subject stood with the arms and legs extended in frontal plan in such a way that the ratio $D/H = 0.25$ (D is the distance between the feet and H is the subject's height measured when their heels were joined together). This ratio was chosen based on the fact that many subjects felt comfortable and stable. The subject was then asked to resist to a pull-down force F on one of his/her hand (with the palm turned toward the ground) without moving his or her body. The maximum value of F when the subject can no longer resist was recorded as his/her arm strength (see text)

During the measurements the subject kept the eyes open and was asked to look straight in front of him/her. When the final results were obtained the experiment was performed with the other arm or concluded. These values constituted the control data before the experiments continued with different paradigms. In these paradigms the subject was asked to bite on a spacer using either his/her central incisors or premolar and molar teeth. The spacers had different

heights: 0.6, 1.3, 2.0, 2.7, 3.4 and 4.1mm and were applied in a random order. The spacers were made out of a firm material to assume a good occlusal support. While the subject was biting a spacer a pull-down force was applied on the subject's arm as aforementioned.

Three paradigms were performed:

Paradigm 1: Unilateral occlusion. The subject held a spacer placed on one side of the jaw using premolar and molar teeth. The heights of the spacers were 0.6, 1.3 and 2.0 mm; however, they were applied in random order. Ten males (age: 20 ± 0.9 years old) and 10 females (age: 19.8 ± 0.9 y.o.) participated.

Paradigm 2: Bilateral occlusion. The subject held a spacer placed on both side of the jaw using premolar and molar teeth. The heights of the spacers were 0.6, 1.3 and 2.0 mm; however, they were applied in random order. Ten males (age: 19.4 ± 0.7 y.o.) participated.

Paradigm 3: Frontal occlusion. The subject bit on spacers using central incisors. The heights of the spacers were 0.6, 1.3 and 2.0 mm; however, they were applied in random order. Ten males (age: 19.9 ± 0.9 y.o.) participated.

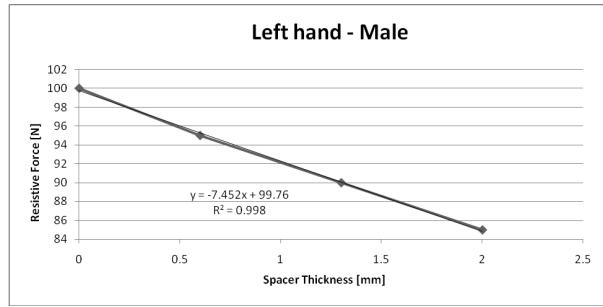
In addition, to determine whether the loss of arm strength is continual or eventually leveled we repeated the paradigm 1 with 5 male subjects. The heights of the spacers were 0.6, 1.3, 2.0, 2.7, 3.4 and 4.1mm, and applied in random order.

III. RESULTS

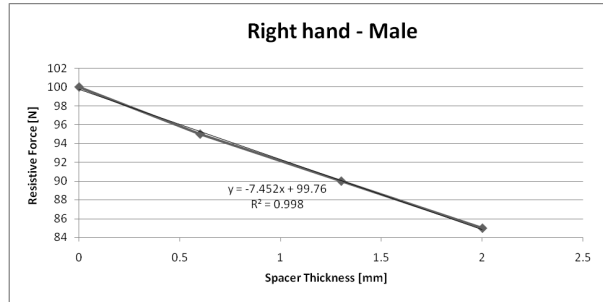
Paradigm 1: We found that when the spacers were put in the left side of the jaw the loss of arm strength occurred on the right side of the arms and the strength of the arm on the same side was intact. Similarly, when the spacers were put in the right side of the jaw the loss occurred on the left side of the arm while the strength of the arm on the same side was intact. This suggested that the bite imbalance causes a contralateral loss of strength in the arm. Although the cause of this effect was not clear its impact may be important in sport medicine where the athletes wear dental protection. Fig. 2 shows the results obtained from 2 subjects.

In addition we found that:

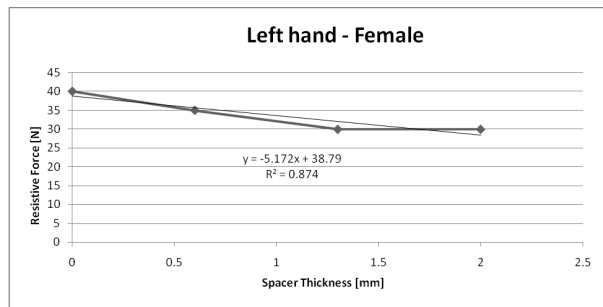
1. There was a strong correlation between the loss of strength in the arms and the heights of the spacers (typically, the correlation coefficient r^2 was about 0.9).
2. The loss is inversely linear to the height of the spacers. Table 1 indicates the averages and standard deviations of the slope a and y -intercept b of male and female subjects when the spacers were placed in the left jaw and the measurements were done in the right arms and when the spacers were placed in the right jaw and the measurement were done in the left arm.



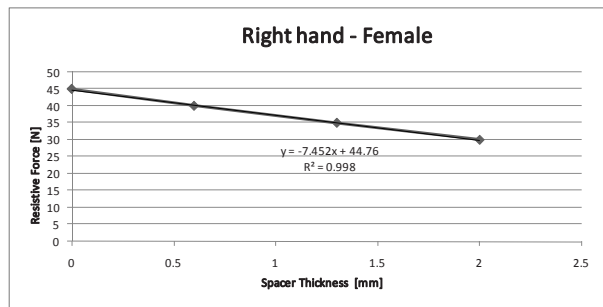
(a)



(b)



(c)



(d)

Fig. 2 Results from paradigm 1 of one male and one female subject measured on their left arms and right arms. We found that when the spacers were put in the right side of the jaw the left arm lost strength (Fig. 2a and 2c), while the right arm's strength was intact. When the spacers were put in the left side of the jaw the right arm lost strength (Fig. 2b and 2d), while the left arm's strength was intact. They suggested that the bite imbalance caused a contralateral loss of arm strength. The loss was linear and the coefficients of correlation r^2 of the fitting were high (see text)

3. Within the male or female groups, the differences of the slopes a and the y -intercepts b obtained in the right arms and in the left arms were not statistically significant ($p > 0.05$).
4. The difference between the slopes a of male group and female group was not statistically significant ($p > 0.05$). However, the difference between the y -intercepts b of male group and female group was statistically significant ($p < 0.05$). This difference can be explained by the fact that male subjects were generally stronger than female subjects.

Table 1 Averages and standard deviations of the slope a and y -intercept b obtained with male and female subjects when the spacers were placed in the left jaw and the measurements were done in the right arms and when the spacers were placed in the right jaw and the measurement were done in the left arm

	Right Arm		Left Arm	
	Male	Female	Male	Female
a [N/mm]	-5.2 ± 1.9	-3.4 ± 2.6	-4.4 ± 2.0	-3.3 ± 1.7
b [N]	78.7 ± 19	37.9 ± 4.3	71.7 ± 16.7	35.2 ± 3.9

Paradigm 2: When subjects held the spacers evenly on both sides of the jaw, we found that both arms lost their strength. The loss behaviors were the same as in the previous paradigm. The coefficients a and b are indicated in table 2. In comparison with the results obtained in paradigm 1 the differences in the coefficients were not statistically significant.

Table 2 The coefficients a and b of the loss of arm strength when the subjects held the spacers evenly on both sides of the jaw. Both arms lost their strength

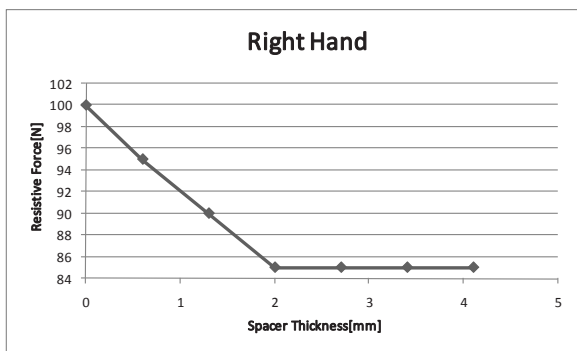
	Right Arm	Left Arm
a [N/mm]	-3.6 ± 2.1	-4.1 ± 1.8
b [N]	63.6 ± 13.5	60.9 ± 12.5

Paradigm 3: When subjects held the spacers using the central incisors we found that both arms lost their strength. The loss behaviors were the same as in the previous paradigm. The coefficients a and b are indicated in table 3. In comparison with the results obtained in paradigm 1 the differences in the coefficients were not statistically significant.

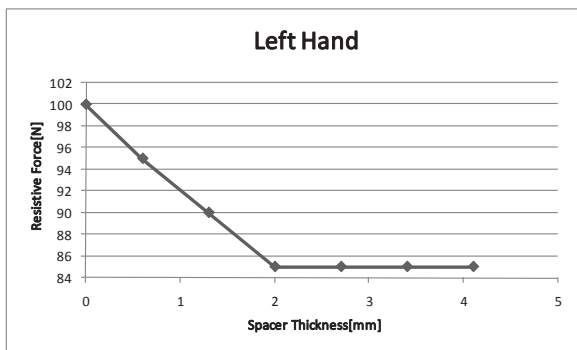
Table 3 The coefficients a and b of the loss of arm strength when subjects held the spacers using the central incisors. Both arms lost their strength

	Right Arm	Left Arm
a [N/mm]	-4.5 ± 2.3	-4.2 ± 1.2
b [N]	78.8 ± 13.6	71.0 ± 13.0

In the experiment to determine whether the loss is continual or leveled, we found that the loss hit a bottom when the spacer height was about 2mm. Fig. 3 shows the results of this experiment.



a



b

Fig. 3 Results obtained with one subject measured on his right arm when the spacers were placed on the left side of his jaw. The right arm first lost strength then the loss was leveled (Fig. 3a). The left arm strength was intact. When the spacers were put in the right side of his jaw, the left arm first lost strength then leveled (Fig. 3b) while the right arm’s strength was intact (see text and table 4)

Table 4 shows the corresponding coefficients a and b of the decreasing part. They are compatible with those found in previous experiments.

Table 4 The coefficients a and b of the loss of arm strength when subjects held the spacers using the opposite site of molar and premolar teeth. Both arms lost their strength

	Right Arm	Left Arm
a [N/mm]	-6.4 ± 1.5	-4.9 ± 2.4
b [N]	89 ± 18	77 ± 19.3

IV. CONCLUSIONS

We investigated the relationship between the bite and the loss of arm strength on a pool of 34 young and healthy subjects. The subjects stood with arms and legs extended in the frontal plan. While they bit on a firm spacer of different heights we applied a pull-down force on one of their arms. The obtained results showed that (1) Imbalance bite induced contralateral loss of arm strength; (2) The loss was approximately a linear function of the height of the spacers; (3) The loss leveled when the spacer was higher than 2mm; (4) The slopes of the linear function were similar in both arms and independent to the gender; and (5) The arm strength of male was higher than that of female subjects. This investigation may be interesting in sport medicine to study the effects of the mouth guards on the athlete arm strength.

ACKNOWLEDGMENT

We would like to thank Professor Noshir Mehta and Albert Forgione, Tufts School of Dental Medicine for their valuable introduction to the phenomenon.

REFERENCES

- Bakke M. (1993) Mandibular elevator muscles: physiology, action, and effect of dental occlusion. *Scand J Dent Res*; 101: 314–331.
- Van Spronsen P.H., Weijs W.A., Van Ginkel F.C., Prah-Andersen B. (1996) Jaw muscle orientation and moment arms of long-face and normal adults. *J Dent Res*; 75: 1372–1380.
- Linderholm H, Lindqvist B, Ringqvist M, Wennström A. (1971) Isometric bite force and its relation to body build and general muscle force. *Acta Odont Scand*; 29: 563–568.
- Raadsheer M.C., van Eijden T.M.G.J., van Ginkel F.C., Prah-Andersen B. (2004) Human jaw muscle strength and size in relation to limb muscle strength and size. *Eur J Oral Sci*; 112: 398–405

Author: Vo Van Toi
 Institute: Biomedical Engineering Department, International University of Vietnam National Universities, Ho Chi Minh City, Vietnam
 Street: Linh Trung Ward, Thu Duc Dist.
 City: Ho Chi Minh
 Country: Vietnam
 Email: vvttoi@hcmiu.edu.vn

Eyestrain, Blink Rate and Dry Eye Syndromes of Video Display Terminal Users

B. Dumery¹, P.A. Grounauer², and Vo Van Toi³

¹ Electrical and Computer Engineering Department, Tufts University, Medford, Massachusetts, USA

² Clinique Ophthalmologic Universitaire, Lausanne, Switzerland

³ Biomedical Engineering Department, International University of Vietnam National Universities, Ho Chi Minh city, Vietnam

Abstract— We investigated whether the eyestrain, often experienced by subjects using a video display terminal (VDT) for an extended period of time, is due to the decrease of blink rate or to the temporarily dry eyes. Thirty-seven subjects with no dry eyes but experienced eyestrain participated in a series of experiments. The 1st experiment was performed without using VDT to obtain the control data and subsequent experiments were performed with a VDT. In those experiments we established the base line for the eyestrain, increased the blink rate and supplied the eyes with eyedrops. Blink rate, visual acuity, temporal modulation transfer function and degree of severity of eyestrain were recorded before and after each experiment. The obtained results suggested that, using the VDT causes the decrease of the blink rate that in turn produces dry eyes which causes the eyestrain.

Keyword— Blink rate, Eyestrain, Dry eye, Temporal modulation transfer function, Video display terminal.

I. INTRODUCTION

Frequent users of video display unit (VDT) often experience eyestrain which also known as visual fatigue or asthenopia. It consists of subjective symptoms of the eyes and covers a wide range including burning, itching, tiredness, aching, and soreness of the eyes¹⁻⁴. Other investigations suggested that the use of VDT decreased the blink rate and increased the tear evaporation rate, consequently causing dry eyes[5]. On the other hand, Lowenstein[6] suggested that the eyestrain was simply due to the decrease of blink rate. In an investigation unrelated to VDT, Toda et al.[7] found that there was a strong relation between dry eyes and eyestrain.

From these investigations we hypothesize that people blink less when they use a VDT than when they do not use it. The decrease of blink rate will cause dry eye, which, in turn, leads to eyestrain. To test this hypothesis we performed four experiments. The first experiment was performed with subjects who were not using a VDT to obtain the control data. The 3 subsequent experiments were conducted with the same subjects who were using VDT. Thus, the 2nd experiment established the base line for the subject's eyestrain along with others parameters. In the 3rd experiment puffs of air were used to increase the blink rate. In the 4th experiment saline droplets were used, instead, to increase the blink rate and, at

the same time, moisten the eyes. If the treatment in the 3rd experiment eliminates the eyestrain we would then conclude that the eyestrain is due solely to the decrease of blink rate; by contrast if only the treatment in the 4th experiment eliminates eyestrain we would then conclude that dry eyes would be the cause of the eyestrain. This study may lead to improvements in working conditions.

Regarding the methods to assess the relationship between eyestrain and dry eyes, Toda et al.[7] proposed a questionnaire that included several aforementioned factors. In investigating the methods to quantify the visual fatigue of VDT users, Saito[8] found that the critical flicker frequency (CFF), after five hours of intensive eye efforts, decreased about 8%. On the other hand, studies of the sensitivity to the flickering light showed that the Temporal Modulation Transfer Function (TMTF) is more sensitive than the CFF values⁹. Furthermore, it has been reported that prolonged VDT work led to impairment of visual acuity¹⁰. From these investigations, in the present study, the eyestrain will be assessed based on the TMTF curve, visual acuity chart and questionnaire.

II. MATERIALS AND METHODS

Thirty-seven subjects (21 males and 16 females, ages: 28 ± 12 years old), who were under no medication at the time of the experiments, participated in the study. All except two were naive to the experiments. They were not diagnosed with chronic dry eyes syndrome or other eye diseases; however, they had experienced eyestrain while working with computers.

Each subject participated in a series of 4 experiments: the 1st experiment was performed without using VDT to establish the control data; the 2nd was performed with a VDT to establish the base line for the eyestrain; the 3rd was performed with a VDT and a device that stimulated blink rate and the 4th, was performed with a VDT and a device that ejected saline droplets to the subject's eyes.

Blink rate, visual acuity, TMTF curves and eyestrain were recorded before and after each experiment. The differences were computed and statistical analyses were used (level of significance was 0.05). All data are indicated by their average and standard deviation values.

The tenets of the Declaration of Helsinki were followed, the study protocols and experimental procedures were approved by the local Institutional Review Board, and informed consent was obtained for all subjects. They also filled a questionnaire regarding identification and clinical information, which were kept confidential.

The blink rate (expressed as blinks per minute, bpm) was determined with the Blink Rate Recorder, described in detail elsewhere¹¹.

The visual acuity was determined using the standard Snellen chart.

The TMTF curves were established using a visual stimulator, described in detail elsewhere¹². It generates a stimulus of the form $L = L_0 (1 + m \cos 2\pi ft)$, where L is the instantaneous luminance, L_0 the mean luminance, m the modulation depth (can be adjusted from 0 to 100%), f the frequency (can be adjusted from 0 to 100Hz) and t the time. In the investigation presented here the retinal illuminance was 100 trolands and the method to establish the TMTF curve was "fusion-to-flicker with preview" as described elsewhere¹⁷. Throughout the experiments presented here only one eye was tested, an achromatic stimulus was used with field of view of 40° and a dark surround.

The eyestrain was determined using a questionnaire which consisted of questions regarding working conditions with the computer, and the state of the eyes and vision to assess eyestrain and dry eyes similar to those described by elsewhere^[7]. The answers were rated from 1 to 5 with 1 as "No" and 5 as "Very Often". For the purpose of simplicity, all answers from the questionnaire were averaged and normalized with 1 as the highest value. Hereafter they will be referred to as the normalized eyestrain severity (NES) level.

To trigger the subject's blinking or to administer the droplets of saline to the subject's eyes we used an Automatic Eyedrop Dispenser, which has been described in detail elsewhere^[14]. In the study presented here, the device either contained only compressed air to stimulate the blinking rate or a 0.9% saline solution to supply additional fluid to the eyes.

The goal of the 1st experiment was to obtain the control data. The subjects wore the Blink Rate Recorder while performing, for an hour, without using a VDT, a task, which did not require intensive visual concentration (e.g., eating or relaxing). For the 3 subsequent experiments, the subjects wore the Blink Rate Recorder while playing intensely a computer game in front of a VDT for 2 consecutive hours. Furthermore, in the 3rd experiment, because its goal was to determine whether by increasing the blink rate alone the eyestrain symptoms could be eliminated, subjects wore, in addition, the Automatic Eyedrop Dispenser, which ejected a puff of air to the eye. The impulsive air pressure hence triggered spontaneous blinking. The air volume was small, to prevent it from contributing to the dry eyes. Further, only

one

eye

received the puff of air that was aimed toward the nasal corner of the upper eyelid. The ejection rate was one puff every ten seconds. In the 4th experiment, because its goal was to determine whether the dry eyes might cause eyestrain, the Automatic Eyedrop Dispenser delivered 0.9% saline droplets instead of puff of air. The droplets were of 5 μ l of volume and were ejected onto the caruncles of both eyes at the same time. The ejection rate was one drop every minute. The volume and ejection rate did not cause an overflow in the eyes.

III. RESULTS

The results from the 1st experiment showed that the blinking rate fluctuated randomly and was 21.6 ± 9.6 bpm. The TMTF curves, visual acuity and eyestrain established before and after the experiment were not different ($p > 0.05$).

The results from the 2nd experiment indicated that work with VDT induced eyestrain in all subjects. The blink rate was 8.9 ± 4.6 bpm. The visual acuities of all subjects slightly decreased after performing the task. The decrease was statistically significant ($p < 0.05$). The NES level was 0.6 ± 0.05 , i.e., the eyestrain increased drastically after performing the task. By contrast, the TMTF curves of only 3 subjects showed the difference between before and after the subjects performed with the VDT. The differences were found at the frequencies below 20Hz where the sensitivity to the flicker decreased significantly after performing the task; by contrast the difference of the CFF values was not statistically significant. The curves of other subjects showed no statistically significant differences at any frequencies.

The results from the 3rd experiment showed that the ejection of puffs of air increased the blink rate and reduced the eyestrain. The blink rate increased to 18.3 ± 8.2 bpm. The differences of the visual acuity before and after performing the tasks was 0.17 ± 0.01 i.e., a statistically significant deterioration of visual acuity. The average NES level was 0.42 ± 0.05 , which was statistically significant. By contrast, we found no difference for any subjects in the TMTF curves before and after performing the task.

The results from the 4th experiment showed that the ejection of the saline increased the blink rate and completely relieved the eyestrain. The blink rate increased to 20.5 ± 9.3 bpm. The visual acuity of all subjects before and after performing the tasks was not statistically different ($p > 0.05$). The average NES level was -0.1 . The negative value was due to an improvement of the NES levels of some subjects after performing the experiment. We found no difference for any subjects in the TMTF curves before and after performing the task.

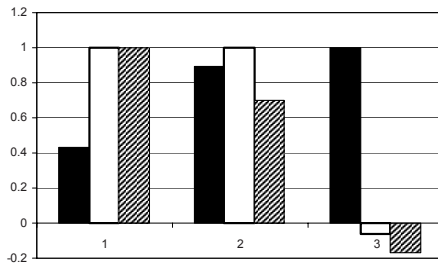


Fig. 1 Variation of blink rate (black bars), visual acuity (white bars) and severity of eyestrain (shaded bars) in 3 experiments: baseline (1), with air puff treatment (2) and with saline treatment (3). For the purpose of comparison the maximum values of blink rate, visual acuity and eyestrain were normalized with the highest values as 1. We found that when the blink rate increased the visual acuity and the severity of eyestrain improved (see text)

Fig. 1 shows blink rate, NES level and visual acuity obtained from 2nd, 3rd and 4th experiments. For the purpose of comparison, the maximum values of blink rate, visual acuity and eyestrain were normalized with the highest values as 1. We found that the difference between the blink rate obtained in the 2nd and 3rd experiments was statistically significant; by contrast the difference between the blink rate obtained in the 3rd and 4th experiments was not. The difference between the visual acuity obtained from the 3rd and 4th experiments was statistically significant and the differences among the averages of the NES obtained from the 2nd, 3rd and 4th experiments were statistically significant. We found that there is a good correlation between the averages of blink rate, NES level and visual acuity (coefficient of correlation: 0.98).

IV. DISCUSSION

Our results clearly showed that using the VDT caused blink rate decrease and eyestrain. Our goal was to investigate whether the eyestrain was solely due to the decrease in the blink rate or to the dry eyes. The results of the 3rd and 4th experiments showed that increase of the blink rate helped to reduce the eyestrain. Administration of droplet to the eyes, additionally, did relieve all of the eyestrain. Therefore, our results suggest that the eyestrain is produced by the dry eyes rather than just by the reduction of the blink rate. If the contrary were the case, increasing the blink rate alone would also completely relieve the eyestrain. Hence, we interpret the relationship among the blink rate, eyestrain and dry eyes for VDT users in the following way. Using the VDT causes the decrease of the blink rate. This decrease in turn produces the dry eyes and the dry eyes produce the eyestrain. In other words, the prolonged use of the VDT may produce dry eyes.

Another way to look at the problem is that, although the average of blink rate in the 4th experiment was slightly higher than that in the 3rd experiment (about 12%), the

difference was not sufficiently important to explain the release of all of the eyestrain as observed. Indeed, in comparison with the base line (2nd experiment), the treatment with air (3rd experiment) increased the blink rate 106% but decreased the NES only 43%; while the treatment with saline (4th experiment) increased the blink rate 130% and decreased the NES sevenfold. In comparison with the treatment with air (3rd experiment), for the treatment with saline (4th experiment) the blink rate increased only 12% but the NES decreased more than fivefold (see table 1). This suggests that eyestrain was not relieved by increasing the blink rate but mainly by increasing the eye's moisture.

Table 1 The changes (in percent) of the blink rate and normalized eyestrain severity (NES) level in different experiments. In comparison with treatment by air puff (3rd experiment), treatment by eye droplets (4th experiment) increased only slightly the blink rate (by 12%) but decreased drastically the NES (by 520%)

Experiments	2 nd vs. 3 rd	2 nd vs. 4 th	3 rd vs. 4 th
Blink rate increase	106%	130%	12%
NES decrease	43%	700%	520%

It is however, generally agreed that the blinking mechanism keeps the eye moist[15], therefore decreasing the blink rate increases the tear evaporation, and in turn, will produce dry eyes, so why do our results show that only increasing the blink rate did not relieve the eyestrain? Hence, it is not clear whether the decrease of the blink rate disturbs dominant mechanisms related to the dry eyes, such as evaporation rate of the tear film or tear break-up time, or that the eyestrain may be controlled by a higher order neuronal mechanism. Our results also suggest that exercises to increase the blinking or reduction of the palpebral fissure may not be sufficient to reduce the eyestrain, as proposed by others[5].

It has also been suggested that the blinking may be controlled by higher nervous processes[16], which decrease the blinking rate for different causes, including fatigue. In other words, fatigue would be the cause, not the consequence, of the decrease of the blink rate. To test whether this could be the case for eyestrain, we conducted an explorative experiment on three subjects to determine the transition time between not using and using a VDT. We found that the blink rate dropped almost immediately when a subject started using a VDT (Fig. 2). The decrease of the blink rate was too rapid to speculate that the eyestrain would be the cause of the reduction of the blink rate. This observation emphasizes our aforementioned suggestion.

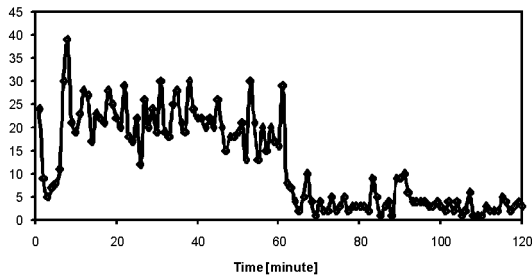


Fig. 2 Blink rate in bpm (Y-axis) of a subject during two experiments: without using a VDT (first 60 minutes) and while using the VDT (second 60 minutes). The blink rate pattern changed drastically as soon as the subject switched from one paradigm to the other (see text)

The blink rates obtained in the present investigation are compatible with results reported in the literature, e.g., Tsubota and Nakamori[5] found the blink rate in the relax conditions was 22 ± 9 bpm and while using a VDT was 7 ± 7 bpm. Our results also showed that eyestrain affected visual acuity. The higher the eyestrain the lower the visual acuity but the administration of saline improves the visual acuity. This is in agreement with reported literature[4]. On the other hand, our results showed that the TMTF curve is not sensitive enough to detect the eyestrain. Saito[8] found that the critical flicker frequency (CFF) of workers, using intensive eye efforts, after five hours of eye tracking task decreased about 8%. While our results do not confirm Saito's, it is not clear whether the type of task our subjects performed, the level of eyestrain that our subjects endured, and/or the duration of our experiment was sufficiently high to produce a detectable decrease in the CFF.

V. CONCLUSION

In summary, we found that using a VDT may cause a dramatic decrease of the blink rate. This occurs as soon as the task is begun. The decrease of blink rate causes dry eyes, which, in turn, triggers eyestrain. Artificially increasing the blink rate relieved eyestrain only partially, but supplying saline drops periodically can effectively prevent it. On the other hand, although eyestrain can be efficiently quantified by the measurements of visual acuity and responses to the questionnaire, it cannot be quantified by flicker sensitivity measurements. Further, it was unclear how eyestrain progressed during the experimental period.

ACKNOWLEDGMENTS

We would like to thank Mr. Abdullalbrahim Abdulwaheed, Mr. Kelvin Bender, Mr. Jason Hudachek, Ms. Emily Berger,

Mr. Andrew Siegel and Mr. Durwood Marshall for their assistance.

REFERENCES

1. National Research Council Committee on Vision. Video Displays, Work and Vision (1983) National Academy Press, Washington, DC, USA.
2. Scullica, L., & Rechichi, C. (1993) Is the type of VDT work important in asthenopia? *European Journal of Ophthalmology*; 3: 37-41.
3. Sheedy, J.E. (1995) Focus on computer-generated eye problems. *Occupational Health & Safety*; 64: 46-50.
4. Watten, R.G. (1994) Reinvention of visual fatigue: accumulation of scientific knowledge or neglect of scientific history? *Ophthalmic & Physiological Optics*; 14: 428-432.
5. Tsubota, K., & Nakamori, K. (1993) Dry eyes and video display terminals. *New England Journal of Medicine*; 328: 584.
6. Lowenstein, E. (1988) VDT Users: Improve comfort with the Blink of an Eye. Cambridge, MA: Polymer Technology Corporation.
7. Toda, I., Fujishima, H., & Tsubota, K. (1993) Ocular fatigue is the major symptom of dry eye. *Acta Ophthalmologica*; 71: 347-352.
8. Saito, S. (1992) Does fatigue exist in a quantitative measurement of eye movements? *Ergonomics*; 35: 607-615.
9. Guignard, C., Vo Van Toi, Burckhardt, C.W. & Schelling, J.L. (1983) Sensitivity To The Flickering Light In Digitalized Patients, *British Journal in Clinical Pharmacology*; 15: 189-196.
10. Watten, R.G., Lie, I., & Magnussen, S. (1992) VDU work, contrast adaptation, and visual fatigue. *Behaviour & Information Technology*; 11: 262-267.
11. Siegel, A., Dumery B. & Vo Van Toi (1997) Portable Blink Rate Recorder. *Investigative Ophthalmology and Visual Science (supp)*; 38: 338
12. Vo Van Toi & Grounauer, P.A. Visual Stimulator (1978) *The Review of Scientific Instruments*; 49: 1403-1406.
13. Vo Van Toi, Burckhardt, C.W., & Grounauer, P.A. (1991) Irregularities In The Flicker Sensitivity Curve. *Applied Optics*; 30: 2113-2120.
14. Vo Van Toi & Grounauer, P.A. (1998) Portable Device for Programmable, Automatic, or On-Demand Delivery of Artificial Tears. In: *Adv Exp Med Biol*; 438: 1027-1032.
15. Doane, M.G. (1980) Interaction of eyelids and tears in corneal wetting and the dynamics of the normal human eyeblink. *Am J Ophthalmol*; 89: 507-516.
16. Stern, J.A., Walrath, L.C., & Goldstein, R. (1984) The endogenous eyeblink. *Psychophysiology*; 21: 22-33.

Author: Vo Van Toi

Institute: Biomedical Engineering Department, International University of Vietnam National Universities, Ho Chi Minh City, Vietnam

Street: Linh Trung Ward, Thu Duc Dist.

City: Ho Chi Minh

Country: Vietnam

Email: vvtoi@hcmiu.edu.vn

A Laser Headset for Measuring Cervical Range of Motion

Gustavo Lugo¹, Tran Anh Vu¹, Nguyen Huynh Minh Tam², and Vo Van Toi^{1,2}

¹Biomedical Engineering Department, Tufts University, Medford, Massachusetts, USA

²Biomedical Engineering Department, International University of Vietnam National Universities, Ho Chi Minh City, Vietnam

Abstract— We developed a new device to measure the cervical range of motion (CROM) by using a diode laser as the light source and in basing on the fact that the human eyes perceive a fast-moving lighted dot as a line. The device was built as a headset that the subject can wear comfortably. The device is light, reliable and can be replicated by researchers without a strong technical support. With this device we established the CROM baseline of 24 healthy subjects and explored the effects of dental obstruction on CROM with 5 healthy subjects. The obtained results showed that the Frontal CROM was $92.53 \pm 14.6^\circ$, the Sagittal CROM was $108.12 \pm 12.93^\circ$ and the Transverse CROM was $134.0 \pm 14.71^\circ$. These results are in agreement with most reported data in literature. We also found that the differences in the results among genders and among operators were not statistically significant. The experiments with 5 healthy subjects to explore the effects of dental obstruction on CROM suggested that an imbalance in the jaw may cause an immediate imbalance in the cervical spine movements. More particularly, it may cause an ipsilateral effect on the lateral Tilt CROM.

Keywords— Cervical Range of Motion, Diode Laser, Dental Obstruction, Ipsilateral Effect, Jaw Imbalance.

I. INTRODUCTION

The Cervical Range of Motion (CROM) is the range of motion, in degrees, through which one individual can move his/her head freely and painlessly in 3 plans: frontal (tilt left/right), sagittal (flexion/extension) and transverse (rotation left/right). There is no target CROM measurement to be considered healthy [1, 2]. Therefore, a continuous investigation on one individual is an effective way to evaluate any deviation from a subject's healthy range. To that end, it is necessary to develop a simple, reliable, practical and easy to use device to measure CROM. Different devices to evaluate CROM have been reported in previous investigations [1-8]. In this article we will describe a low-cost device that we developed to maximize the accuracy and precision of CROM measurements. The device is light, reliable and can be replicated by researchers without a strong technical support. Using this novel device we investigated with healthy subjects the Frontal, Sagittal and Transverse CROM as well as the effects of dental obstructions on these values.

II. MATERIALS AND METHOD

The principle of the new device is based on the fact that human eyes perceive a fast-moving lighted dot as a line. Therefore, the core of the device is a commercial laser source (similar to the one used in laser pointer) mounted on a headset, worn by a subject. When this laser source rotates, its lighted dot traces a line on a surface perpendicular to the rotation axis. The motions of the subject's head in different corporeal planes, hence, can be tracked by the relative positions of that line.

The device (Fig.1) consists of a diode laser source (a) powered by a 3V camera battery and secured transversely on an electric dc motor (b). The laser source was placed at the center of gyration of the headset frame (c) to avoid mechanical vibrations that would disturb the comfort of the wearer. The motor is powered by a switch-enabled 1.5V battery (d) located at the base of the headset. At the top of the device, a compass (e) is placed to measure rotation of the head. Its accuracy is $\pm 2^\circ$. The frame is attached to the subject's head by an adjustable headband (g) that has a knob to allow the subject comfortably secure the headset onto his/her head. Two knobs (f) are used to adjust the frame in order to align the laser line with the horizontal plane. The total height of the device is 17.5cm. The width from one adjustable knob to the other is 28cm. The headband is adjustable from 55cm to 71cm. The total weight of the device is 0.8Kg.

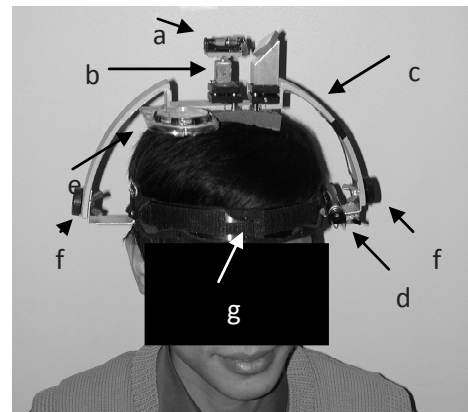


Fig. 1 Laser CROM device. a = Switch enabled diode laser; b = Motor; c = Aluminum frame; d = Switch enabled 1.5V source for motor; e = Compass; f = Adjustable knobs; g = headband

During the measurements, the subject wears the device and sits in a comfortable cushioned chair. The seat lies in the center of four translucent panels forming a cage, which measures 87cm wide, 117cm long and 207cm tall. A series of seven tape measures were placed vertically across the walls. These tapes are used to measure the changes in inclination of the line traced by the laser. The subjects sit in a cushioned chair facing one of the cage walls (Fig. 2). Any tilting angle of the head can be determined by the following formula:

$$\theta = \tan^{-1}((h_1 - h_0) / d)$$

Where θ is the tilting angle, h_1 and h_2 are the heights marked by the laser light due to the subject's head position, and d is the distance between the two related tapes. Measurements h_1 and h_2 are the point of intersection between the tape measures and the line cast by the laser. The distance d is known because of the placement of the tape measures. Therefore the operator will only record h_1 and h_2 and enters the data on a spreadsheet (Microsoft Excel) and the angle can be computed automatically.

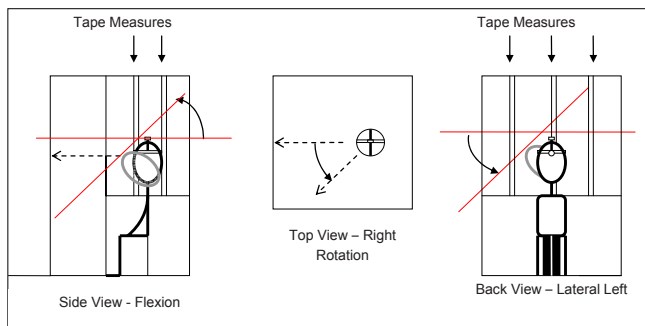


Fig. 2 Test positions of the subject. Flexion, right rotation and lateral left movement are shown with initial and final measurements

The accuracy of the device was evaluated using a 3 dimension graduated turntable. Each measurement was repeated 3 times, and then the average and standard deviation were calculated.

Table 1 indicated the preset angles and the corresponding valued obtained from the measurement with the device. Table 2 shows the range of angles in which the device can perform.

Twenty-four healthy right-handed subjects of 22.13±1.8 years old (7 females, 17 males, 9 Asians and 15 Caucasians) participated in the experiments to establish the baseline values. Five other healthy right-handed subjects of 29.6±11.5 years old (3 females and all were Asians) participated in the experiments to explore the effects of dental obstructions.

Table 1 Measured values of the accuracy testing of the laser headset device

Position (Expected Value)	Measured Value (Average ± SD) [Degrees]
Left Tilt (40°)	42.7 ± 1.1
Right Tilt (40°)	43.85 ± 1.15
Forward Tilt (40°)	39.6 ± 1.7
Back Tilt (40°)	43.6 ± 1.01
Rotation (45°)	44.6 ± 3.01

Table 2 Minimum and maximum measurements possible by the laser helmet

Position	Measured Value (min/max) [Degrees]
Left/right Tilt	-80.18/80.18
Forward/Backward Tilt	-82.6/82.6
Rotation	0/360

All of them were free of any medication and didn't complain of any kinds of muscle pains at the time of the experiments. The tenets of the Declaration of Helsinki were followed; the local Institutional Review Board approved the study protocols and experimental procedures. Also, informed consent was obtained for all subjects. Before the experiment each subject filled out a questionnaire, which included two sets of questions: one set regarding the patient's identification and clinical information, which was kept confidential. The other set of questions relate to the different behavioral patterns that may affect CROM. These characteristics were: age, ethnicity, sex and dexterity.

In the Lateral Tilt CROM measurements, the subject was asked to tilt as much as possible his/her head to the left then to the right using only his/her neck and without rotating the head. In the Flexion CROM measurements the subject was asked to bend as much as possible his/her neck forward then backward without moving the torso. In the Transverse CROM the subject was asked to rotate as much as possible his/her head to the right then to the left without moving the torso. Each measurement was repeated 3 times in a row. The averages and standard deviations were computed. Statistical methods were performed including the analysis of Variance (ANOVA) and Multivariate Analysis of Variance (MANOVA).

For the experiment to determine the effect of dental obstructions, the subject first underwent the same aforementioned protocol to obtain his/her baseline. Then an obstruction was introduced between the first and second upper left molars of the mouth. It consists of a white sterile sheet of paper of 5mm thickness. The subject was asked to

bite hard on the obstruction. Once the obstruction was in place, the same experimental protocol was performed. This procedure was then repeated with the obstruction at the right side. Each measurement was repeated 3 times in a row. The averages and standard deviations were computed. Statistical methods were performed as described above.

III. RESULTS AND DISCUSSIONS

1. CROM Baseline Experiments

Table 3 indicates the CROM results obtained with 24 subjects. Student's t-test were performed with the null hypothesis being there is no difference between the left and the right results (respectively flexion and extension results) against the alternating hypothesis being there is a difference. The statistical analysis yielded that, in all situations, the null hypothesis couldn't be rejected ($p > 0.05$). The similarity of these results may be due to the symmetry in the shape of healthy cervical spines.

Notes: Frontal CROM is the sum of lateral tilt left and right, Sagittal CROM is the sum of flexion and extension, and Transverse CROM is the sum of rotation left and right.

Table 3 Summary of collected CROM data from the Baseline Group (n=24). * = Total Frontal CROM, calculated from left plus right lateral motion; † = Total Sagittal CROM, calculated from flexion plus extension motion; ‡ = Total transverse COM, calculated from left plus right rotation motion

Movement	CROM (Average ± SD) [Degrees]
Lateral Left	46.75 ± 8.24
Lateral Right	45.78 ± 7.9
* Frontal CROM	92.53 ± 14.6
Flexion	50.13 ± 6.84
Extension	57.99 ± 7.45
† Sagittal CROM	108.12 ± 12.93
Rotation Left	70.25 ± 8.06
Rotation Right	63.79 ± 8.25
‡ Transverse ROM	134.0 ± 14.71

Although gender has been reported in literature as a CROM influencing factor [5], our data showed that the difference between the CROM of male and female subjects was not statistically significant ($p > 0.05$). The statistical analysis also showed that there was no difference in the Asian and Caucasian subjects.

Fig. 3 shows the values of sagittal CROM obtained with our device and with other devices reported in literature. We found that, besides the Spin T model, our results are within the range obtained with other devices. The devices were benchmarked on the sagittal plane since this plane is the least influenced by extra-skeletal factors [1].

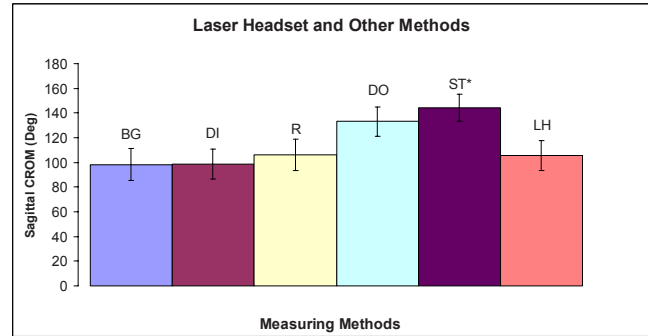


Fig. 3 Laser headset compared to other devices/methods when measuring sagittal CROM. BG = bubble goniometry (n=36); DI = digital inclinometer (n = 36); R = radiograph (n = 30); DO = digital optoelectric device (n = 60); ST = Spin T Model (n=23) and LH = Laser Headset (n = 24)

The experimental protocols were executed by an individual who instructed the subjects, performed the experiments, collected data and calculated the results; these operations may induce the inconsistency among the operators hence errors in the results. We evaluated here the possible effects due to different operators while conducting the established measurement protocol. Ten operators were participated in the study. Each of them took turns to perform identical experimental protocols on the same group of subjects. The results from these 10 operators were analyzed and compared to the baseline data presented above. An ANOVA method was performed and suggested that the influence of the operators on the results was not statistically significant ($p > 0.05$). As an example, Fig. 4 shows the sagittal data collected by the 10 operators.

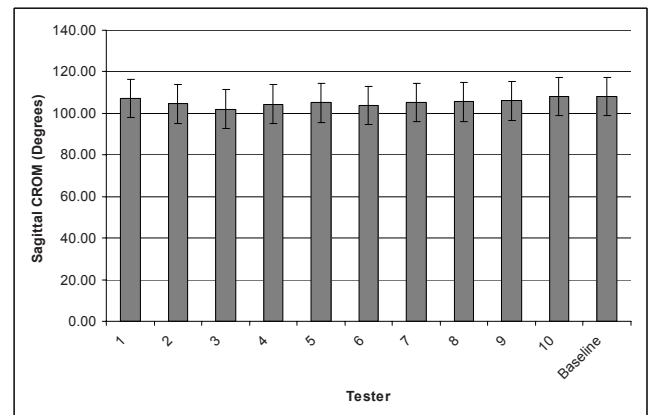


Fig. 4 Sagittal CROM data collected by 10 different operators on the same group of subjects. The study suggested that the influence of operators on the results was not statistically significant ($p > 0.05$)

2. Dental Obstruction Experiments

Table 4 showed the results of the statistical analyses in different CROM movements when the dental obstructions were introduced in the subject's mouths. These results were

inferred from the comparison for each subject between the data obtained with and without the dental obstructions. We found that the left obstruction reduced the lateral left, extension and rotation right. The right obstruction reduced lateral right, flexion, extension movements, yet increased rotation in the right motion.

Table 4 Effect of dental obstruction in the studied CROM movements. I = Increased CROM ($p \leq 0.05$); D = Decreased CROM ($p \leq 0.05$); N = No change ($p > 0.05$)

Movement	Obstruction Effect	
	Left	Right
Lateral Left	D ($p = 0.011$)	N ($p > 0.05$)
Lateral Right	N ($p > 0.05$)	D ($p = 0.028$)
Flexion	N ($p > 0.05$)	D ($p = 0.044$)
Extension	D ($p = 0.03$)	D ($p = 0.003$)
Rotation Left	N ($p > 0.05$)	N ($p > 0.05$)
Rotation Right	D ($p = 0.001$)	I ($p = 0.008$)

These results suggested the dental obstructions cause an ipsilateral effect on the lateral Tilt CROM and a possibility of cervical spine imbalances due to bite line imbalance which is in agreement with Sae-Lee suggestions [9].

In comparing the baseline results between the group of 25 and 5 subjects we found that these results were not statistically significant. This suggested that the number of patient was not an influential factor to the results. Table 5 shows those results.

Table 5 Baseline protocol results for the focus group. The data shows no difference to the baseline group ($p > 0.05$)

Movement	CROM (Average \pm SD) [Degrees]	
Lateral Left	40.14	\pm 7.8
Lateral Right	44.87	\pm 6.9
* Frontal CROM	85.01	\pm 7.4
Flexion	41.16	\pm 5.77
Extension	61.24	\pm 2.8
* Sagittal CROM	102.4	\pm 4.2
Rotation Left	64.21	\pm 12.16
Rotation Right	66.22	\pm 10.05
§ Transverse ROM	130.43	\pm 11.1

IV. CONCLUSION

We designed a Laser Headset to measure the cervical range of motion (CROM) by using a diode laser as the light source and in basing on the fact that the human eyes

perceive a fast-moving lighted dot as a line. It was mounted on a headgear that subject wore during the experiments. The device is light, reliable and can be replicated by researchers without a technical background. The results on 24 healthy subjects showed that the Frontal CROM was $92.53 \pm 14.6^\circ$, the Sagittal CROM was $108.12 \pm 12.93^\circ$ and the Transverse CROM was $134.0 \pm 14.71^\circ$. These results are in agreement with most reported data in literature. We also found that the differences in the results among genders and among operators were not statistically significant. The experiments with 5 healthy subjects to explore the effects of dental obstruction on CROM suggested that an imbalance in the jaw may cause an immediate imbalance in the cervical spine movements. More particularly, it may cause an ipsilateral effect on the lateral Tilt CROM.

REFERENCES

- Bogduk N. and Mercer S. (2000) Biomechanics of the Cervical Spine I: Normal Kinematics, *Clinical Biomechanics*. 15 pp. 633-648.
- Koerhuis C.L., Winters J.C., van der Helm F.C.T, Hof A. (2003) Neck mobility measurement by means of the 'Flock of Birds' electromagnetic tracking system, *Clinical Biomechanics*. 18: 14-18.
- Burns D.K., Wells M.R. (2006) "Gross Range of Motion in the Cervical Spine: The Effects of Osteopathic Muscle Energy Technique in Asymptomatic Subjects" *JAOA* 106: 3 pp. 137-142.
- Carpaneto J., Micera S., Galardi G., Micheli A., Carboncini M.C., Rossi B., Dario P. (2004) "A protocol for the assessment of 3D movements of the head in persons with cervical dystonia" *Clinical Biomechanics* 19 pp. 659-663.
- Ferrario V.F., Sforza C., Dalloca L.L., De Franco D.J. (2002) Active range of motion of the head and cervical spine: a three dimensional investigation in healthy young adults. *Journal of Orthopedic Medicine* 20, pp. 122-129.
- Haynes M.J., Edmoston S. (2002) Accuracy and reliability of a new protractor-based neck goniometer. *Journal of Manipulative and Physiological Therapeutics*, pp. 579-586.
- Stitzel C.J., Morningstar M.W., Paone P.R. (2003) The Effects of Bite Line Deviation on Lateral Cervical Radiographs When Upper Cervical Joint Dysfunction: A Pilot Study. *Journal of Manipulative and Physiological Therapeutics* 26(7):E17
- Wolfenberger V.A., Bui Q., Batenchuk G.B. (2002) A Comparison of Methods of Evaluating Cervical Range of Motion, *Journal of Manipulative and Physiological Therapeutics*, volume 25, number 3, pp. 154-160.
- Sae-Lee D., Wanigaratne K., Whittle T., Peck C.C., Murray C.M. (2006) A method for studying jaw muscle activity during standardized jaw movements under experimental jaw muscle pain, *Journal of Neuroscience Methods*, 157: 2, pp. 285-293.

Author: Vo Van Toi

Institute: Biomedical Engineering Department, International University of Vietnam National Universities, Ho Chi Minh City, Vietnam

Street: Linh Trung Ward, Thu Duc Dist.

City: Ho Chi Minh

Country: Vietnam

Email: vvtoi@hcmiu.edu.vn

Engineering Resistance in Brinjal against Nematode (*Meloidogyne Incognita*) Using *cryIAb* Gene from *Bacillus Thuringiensis* Berliner

Phan Dinh Phap^{1,2}, Hoang Thi Lan Xuan¹, D. Sudhakar², and P. Balasubramanian²

¹ School of Biotechnology, International University-National University Ho Chi Minh City, Vietnam

² Centre for Plant Molecular Biology, Tamil Nadu Agricultural University, India

Abstract— Transgenic brinjal plants (*Solanum melongena* cv. Co2) expressing *cryIAb* gene from *Bacillus thuringiensis* Berliner (*Bt*) were evolved by *Agrobacterium*-mediated transformation system. In the present study, 7 T₀ lines (P-Co2IAb-5, P-Co2IAb-9, P-Co2IAb-10, P-Co2IAb-12, P-Co2IAb-16, P-Co2IAb-17 and P-Co2IAb-22) harboring *cryIAb* gene were obtained. PCR and Southern blotting analyses proved the presence and integration of *cryIAb* in these lines. A polyclonal rabbit anti-CryIAb antiserum detected the expression of a 65 kDa CryIAb polypeptide in all these lines. Expression of CryIAb protein in those transgenic lines was also confirmed by lateral flow sticks (CryIAb) assay. Molecular analyses in T₁ progenies harboring *cryIAb* gene proved the presence and expression of the transgene of interest. The chi-square (χ^2) tests revealed a 3:1 segregation ratio for *cryIAb* gene in the lines viz., P-Co2IAb-5 and P-Co2IAb-9, indicating that the transgene was integrated at a single locus.

The transgenic lines thus obtained in this study were used to investigate the potential of the CryIAb protein in controlling the root knot nematode, *Meloidogyne incognita*. Bioassay for root knot nematode resistance in T₁ plants expressing CryIAb showed that there was a significant decrease in number of galls and eggmasses in *cryIAb*-transgenic lines (P-Co2IAb-5 and P-Co2IAb-9) as compared to control. In addition, there was a significant decrease in the number of eggs per eggmass on those transgenic lines tested than the non-transgenic controls. Thus, transgenic *Bt*-brinjal plants could also form a part of an integrated nematode management program.

Keywords— Transgenic brinjal, *Bacillus thuringiensis*, *cryIAb*, *Agrobacterium* transformation, *Meloidogyne incognita*.

I. INTRODUCTION

Brinjal (*Solanum melongena* Linnaeus) is an economically important vegetable crop grown in many countries in Asia, Europe and North America. It forms an important component in the diet of the people, especially in the Indian subcontinent whose diet is predominantly vegetarian in nature. Brinjal is high in nutritive value in vitamins A and C and also known as eggplant.

Brinjal is susceptible to a host of insect pests and diseases, particularly shoot and fruit borer (SFB);

Leucinodes orbonalis Guenee), Colorado potato beetle (CPB; *Leptinotarsa decemlineata* Say), aphid (*Aphis gossypii* Glover), *Fusarium* wilt (*F. oxysporum* f.sp. *melongenae*), nematodes (*Meloidogyne* spp.), etc., which reduce the marketable yield in a large measure. Resistance genes have been found in different wild *Solanum* species. However, the introduction of these genes via intergeneric crossing or asymmetric protoplast fusion is often limited, due to sterility problems [1]. Genetic transformation is a promising strategy for brinjal improvement because it overcomes the incompatibility barriers among crop species by allowing the introduction of foreign genes into plants.

Bacillus thuringiensis, a gram-positive bacterium is commonly found in soil, plant surfaces, insect cadavers and in grain storage dusts [2]. Different strains of *B. thuringiensis* produce one or more proteins, grouped as δ -endotoxins, which accumulate during sporulation to form refractile crystal bodies. The δ -endotoxins earlier were classified into four types, based on insect specificity and sequence homology, into Lepidopteran-specific (*cryI*), Lepidopteran and Dipteran-specific (*cryII*), Coleopteran-specific (*cryIII*) and Dipteran-specific (*cryIV*) [3]. The system was further extended to include *cryV* that encode for proteins effective against Lepidopteran and Coleopteran larvae. Some *B. thuringiensis* strains have also been reported to be active against mites, nematodes, flatworms, protozoa [4, 5, 6] and aphids [7].

Guri and Sink [8] were the first to report *Agrobacterium*-mediated transformation of brinjal, quickly followed by others [9, 10]. Attempts were first made to introduce a native version of Coleopteran-specific gene *cryIIIB* of *Bacillus thuringiensis* into brinjal conferring resistance to CPB, but their expression was too low for successful insect control [11]. A modified *cryIIIA* gene was developed and successfully introduced into brinjal, in which were found resistant to neonate larvae and adult CPB [12]. A synthetic *cryIAb* gene was introduced into a long-fruited (Pusa purple long) variety of brinjal. Fruits of one of the transformants were totally protected from SFB larval damage [9]. Resistance to the root knot nematode (*M. incognita*) has been engineered by inserting the *Mi-1* gene from wild tomato (*Lycopersicon peruvianum*) [10].

II. MATERIALS AND METHODS

A. *Agrobacterium* Binary Vector Containing *cryIAb* Gene

The plasmid pCAMBIA2301-*cryIAb*, harboring a 4.1 kbp *cryIAb* gene expression cassette, containing a 1.8 kbp synthetic *cryIAb* gene flanked by maize ubiquitin-1 (Ubi-1) promoter and nopaline synthase (NOS) terminator (Fig. 1; a gift from TNAU, India). The plasmid was mobilized into LBA4404 by biparental mating [13].

B. Plant Transformation

Cotyledonary leaves from 2-3 wk old seedlings of Co2 brinjal were cultured on a shoot regeneration medium (SRM; MS basal salts and vitamins, 0.044 mg/l TDZ, 2% sucrose and 0.3% phytigel). After 2 days, the explants were carefully submerged in the *Agrobacterium* inoculum for 2 min. They were blotted dry on sterile filter paper and transferred to co-culture medium (SRM supplemented with 50 μ M of acetosyringone). After 48 h co-cultivation in the dark at 26°C, the explants were washed with sterile distilled water and solution containing 500 mg/l cefotaxime. Then, they were blotted dry on sterile filter paper and cultured on the SRM medium. After 2 days, they were transferred to the selective SRM medium with 70 mg/l kanamycin. The regenerated shoots (2-3 cm in length) were excised and placed on half-strength MS hormone-free medium for 1 wk. Then, the shoots directly transferred to soil and maintained in the transgenic green house.

C. PCR Analysis

A forward primer IAB1 (5' CGTGCCAGGTGCTGGG TTCG 3') and a reverse primer IAB2 (5'GCCGCTTGACA TGGTTGCGG 3') were used to amplify a 1.5 kb-long internal fragment of *cryIAb* gene in the putative transformants as per the standard procedures [14]. Temperature profile used for amplification was as follows: pre-incubation at 95°C for 5 min leading to 35 cycles of denaturation at 95°C for 50 sec, annealing at 65°C for 50 sec and synthesis at 72°C for 50 sec followed by an extension at 72°C for 10 min.

D. Southern Blotting Analysis

Genomic DNA was isolated from plant following the CTAB methodology [15]. Ten micrograms of genomic DNA extracted from putative transformants, untransformed control plant and 10 ng of plasmid DNA (pCAMBIA2301-*cryIAb*; positive control) were digested with *Hind*III, electrophoresed on a 1% agarose gel and transferred onto a nylon membrane [14]. The blot was probed with a ³²P-dCTP-labelled 4.1 kb fragment consisting of *cryIAb* gene. The blots were subsequently analyzed by autoradiography using bio-imaging analyzer (BAS 1800) system.

E. Western Blotting Analysis

Total protein was isolated from young leaves of putative transformant and non-transformant (control) plants, fractionated by SDS-polyacrylamide gel electrophoresis according to standard procedures [16] and blotted onto a nitrocellulose membrane. The filter was probed with polyclonal rabbit anti-CryIAb antiserum and goat anti-rabbit IgG alkaline phosphatase conjugate as a secondary antibody (1:5000 dilution) in antiserum buffer [17].

F. Screening of *T₁* Transgenic Plants for RKN Resistance

Two Co2 lines (P-Co2IAb-5 and P-Co2IAb-9) expressing CryIAb were grown in plastic pots containing a sterile mixture of soil, sand and farmyard manure (1:1:1) under transgenic greenhouse. Three week old seedlings (5 plants for each line) were inoculated with J2s *M. incognita* (500 J2s per plant). Thirty days after inoculation, the number of galls, eggmasses and eggs were counted. The growth rate of nematode in the root tissue was observed by a trinocular research microscope linked to a digital CCD camera (CETI, Belgium).

III. RESULTS AND DISCUSSION

A. Transformation and Regeneration

A synthetic *cryIAb* was transferred into Co2 brinjal using cotyledonary leaves by *Agrobacterium*-mediated transformation method. The inoculated cotyledonary leaves were kept on regeneration media supplemented with 70 mg/l kanamycin. Regeneration efficiency ranged from 1.11% to 9.33% and the highest transformation efficiency was 4.0%. However, transformation efficiency was 7.5% on

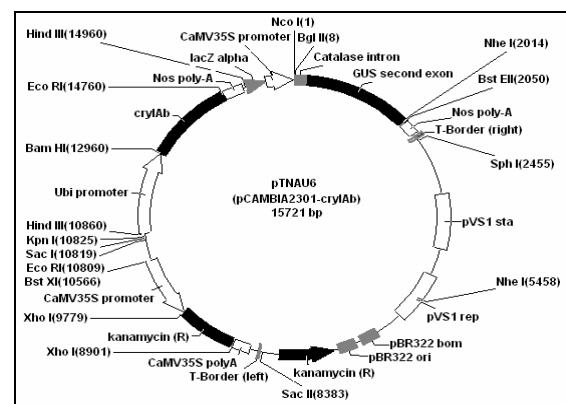


Fig. 1 Physical map of pCAMBIA2301-*cryIAb*

selection medium (50-100 mg/l kanamycin) [18] using cotyledonary leaves. It was 20.8% on selection media (50 mg/l kanamycin) [19] and 7% on selection media containing 100 mg/l kanamycin [20] using leaf explants.

B. Molecular Analysis of Putative Transgenic *T*₀ Lines

Out of 22 putative transformants, only 7 lines (P-Co2IAb-5, P-Co2IAb-9, P-Co2IAb-10, P-Co2IAb-12, P-Co2IAb-16, P-Co2IAb-17 and P-Co2IAb-22) were found stable GUS expression. With a view to confirming integration of *cryIAb* in putative transgenic *T*₀ lines, PCR analysis was performed with appropriate *cryIAb* primers on all the GUS-positive lines. All lines tested proved positive to PCR analysis (Fig. 2A). DNA extracted from these lines was digested with *Hind*III and the products were transferred onto a nylon membrane, which was probed with a radiolabelled *Hind*III fragment (4.1 kb *cryIAb*). A band of 4.1 kbp size was associated with all the putative transformants (Fig. 2B). A polyclonal rabbit anti-CryIAb antiserum detected the expression of a 65 kDa CryIAb polypeptide in all the lines. Along with the 65 kDa polypeptide, 2 to 3 last-migrating (30-40 kDa) polypeptides were also found associated with most of the putative transgenic lines tested (Fig. 2C). Cheng *et al.* [21] reported that these bands are derived from the 65 kDa CryIAb by protein degradation during boiling process in the sample.

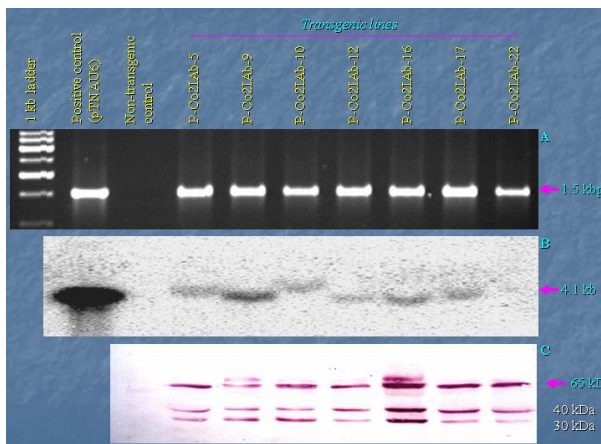


Fig. 2 Molecular analyses of *cryIAb* in putative transgenic *T*₀ lines. **A.** PCR amplification; **B.** Southern blotting analysis; **C.** Western blotting analysis to detect the expression of CryIAb in putative *T*₀ plants

C. Progeny Analysis

Out of 30 *T*₁ plants tested in each progeny, only 23 in P-Co2IAb-5 and 22 in P-Co2IAb-9 line were positive to

cryIAb by PCR analysis. To confirm the validity of observed segregation ratio of 3:1 in the progenies, χ^2 test was applied. The χ^2 test revealed that the observed ratio fitted with the expected ratio of 3:1, indicating a single locus integration in both lines. Five *T*₁ plants were randomly picked from each *T*₀ line which tested positive to *cryIAb* on PCR analysis and forwarded for performing Southern blotting analysis, when probed with a ³²P-dCTP-labelled *Hind*III fragment (4.1 kb *cryIAb*), a band of size 4.1 kb appeared with all the *T*₁ transformants tested. Eight *T*₁ plants which tested positive to *cryIAb* on PCR analysis from these *T*₀ lines were randomly selected. Western blotting analysis using polyclonal rabbit anti-CryIAb antiserum was performed on them; a 65 kDa polypeptide was associated with all the PCR-positive transformed plants.

D. Bioassays for Root Knot Nematode Resistance

*T*₁ plants expressing CryIAb (P-Co2IAb-5 and P-Co2IAb-9) were used in this study for bioassay for resistance against root knot nematode (RKN; *Meloidogyne incognita*). There was a significant decrease in number of galls and eggmasses (80-90%) found on roots of *cryIAb*-transgenic lines (P-Co2IAb-5 and P-Co2IAb-9) as compared to the control 30 d after inoculation (Table 1).

There was also a significant decrease in the number of eggs per eggmass found on *cryIAb*-transgenic lines (141.0 eggs/eggmass in P-Co2IAb-5 and 149.6 eggs/eggmass in P-Co2IAb-9) as compared to the control (Table 1; Fig. 3). Crystal proteins of *Bacillus thuringiensis* (*Bt*) are the most widely used natural insecticides in agriculture.



Fig. 3 Root knot nematode, *Meloidogyne incognita* infection assays on the transgenic and non-transgenic brinjal 30 days after inoculation

Table 1 Assessment of root knot nematode resistance on the transgenic T₁ plants expressing CryIAb protein. Values in a column followed by the same letter are not significantly different at P= 0.05 according to Duncan's multiple range test

Putative (T ₀) transgenic line	No. of galls/plant		No. of eggmasses/plant		No. of eggs/eggmass
	No.	%	No.	%	
Co2 control	90.2 ^b	100	17.2 ^b	100	339.8 ^b
P-Co2IAb-5	10.4 ^a	11.53	1.0 ^a	5.81	141.0 ^a
P-Co2IAb-9	12.2 ^a	13.53	3.4 ^a	19.77	149.6 ^a

Marroquin *et al.* [5] demonstrated that a *Bt* (Cry5B or Cry6A) toxin can target a nematode (*Caenorhabditis elegans*) and that *Bt* toxins also hold promise as nematicides. Wei *et al.* [6] reported that 4 crystal proteins (Cry5B, Cry6A, Cry14A and Cry21A) were active against several nematode species (*C. elegans*, *Pristionchus pacificus*, *Panagrellus redivivus*, *Acrobeloides* sp. and *Distobabrellus veechi*).

IV. CONCLUSIONS

Putative transgenic T₀ lines of Co2 expressing *cryIAb* (7 lines) were evolved and the integration/expression of the gene of interest were confirmed by histochemical GUS assays, PCR, Southern and western blotting analyses. Molecular analyses in 2 T₁ progenies (derived from P-Co2IAb-5 and P-Co2IAb-9) harboring *cryIAb* gene proved the presence and expression of the transgenes of interest. The χ^2 test revealed a 3:1 segregation ratio in T₁ progenies of P-Co2IAb-5 and P-Co2IAb-9 indicating that the transgene remained integrated at a single locus.

T₁ progenies expressing CryIAb were used for root knot nematode resistance, it was observed that there was a significant decrease in the number of galls and eggmasses in *cryIAb*-transgenic lines (P-Co2IAb-5 and P-Co2IAb-9) as compared to control. In addition, there was a significant decrease in the number of eggs per eggmass on those transgenic lines tested than the non-transgenic controls.

REFERENCES

- Collonnier C, Fock I, Kashyap V *et al.* (2001) Applications of biotechnology in eggplant. *Plant Cell Tissue Organ Cult* 65:91-107
- De Maagd R A, Bosch D, Stiekema W (1999) *Bacillus thuringiensis* toxin-mediated insect resistance in plants. *Science* 4:9-13
- Hofte H, Whiteley H R (1989) Insecticidal crystal proteins of *Bacillus thuringiensis*. *Microbiol. Rev.* 53:242-255
- Feitelson J S, Payne J, Kim L (1992) *Bacillus thuringiensis*: insects and beyond. *Biotechnology* 10:271-275
- Marroquin L D, Elayassnia D, Griffiths J S *et al.* (2000) *Bacillus thuringiensis* (*Bt*) toxin susceptibility and isolation of resistance mutants in the nematode *Caenorhabditis elegans*. *Genetics* 155:1693-1699
- Wei J Z, Hale K, Carta L *et al.* (2003) *Bacillus thuringiensis* crystal proteins that target nematodes. *Proc. Natl. Acad. Sci. USA.* 100:2760-2765
- Walters F S, English L H (1995) Toxicity of *Bacillus thuringiensis* d-endotoxins toward the potato aphid in an artificial diet bioassay. *Entomol. Exp. Appl.* 77:211-216
- Guri A, Sink K C (1988) *Agrobacterium* transformation of eggplant. *J. Plant Physiol.* 133:52-55
- Kumar P A, Mandaokar A, Sreenivasu K *et al.* (1998) Insect resistant transgenic brinjal plants. *Mol. Breed.* 4:33-37
- Frijters A, Simons G, Varga G *et al.* (2000) The *Mi-1* gene confers resistance to the root-knot nematode *Meloidogyne incognita* in transgenic eggplant, VIIIth Conf. "Plant and Animal Genome", San Diego, CA, USA, 9-12 Jan. 2000, Abst. No. P619
- Chen Q, Jelenkovic G, Chin C K *et al.* (1995) Transfer and transcriptional expression of Coleopteran *cryIIIB* endotoxin gene of *Bacillus thuringiensis* in eggplant. *J. Amer. Soc. Hort. Sci.* 120:921-927
- Jelenkovic G, Billings S, Chen Q *et al.* (1998) Transformation of eggplant with synthetic *cryIIIA* gene produces a high level of resistance to the Colorado potato beetle. *J. Amer. Soc. Hort. Sci.* 123:19-25
- Ditta G, Stanfield S, Corbin D (1980) Broad host range DNA cloning system for Gram-negative bacteria: Construction of a gene bank of *Rhizobium meliloti*. *Proc. Natl. Acad. Sci. USA.* 77:7347-7351
- Sambrook J, Fritsch E F, Maniatis T (1989) *Molecular cloning, a laboratory manual.* 2nd edition, Cold Spring Harbor Laboratory Press, Cold Spring Harbor, New York, USA
- Proebbski S L, Bailey G, Basun B R (1997) Modification of a CTAB DNA extraction protocol for plants containing high polysaccharides and polyphenol components. *Plant Mol. Biol. Rep.* 15:8-15
- Laemmli U K (1970) Cleavage of structural proteins during the assembly of the head of bacteriophage T4. *Nature* 227:680-683
- Gallagher S, Winston S E, Fuller S H (1995) Immunodetection. Auubel F, Bernt R, Kingston E E *et al.* (eds.) *Short protocols in molecular biology*, Wiley and Sons Inc. pp.1040-1048
- Fari M, Nagy I, Csanyi M *et al.* (1995) *Agrobacterium*-mediated genetic transformation and plant regeneration via organogenesis and somatic embryogenesis from cotyledon leaves in eggplant (*Solanum melongena* L. cv. 'Keckskemetilila'). *Plant Cell Rep.* 15:82-86
- Billings S, Jelenkovic G, Chin C K, Eberhardt J (1997) The effect of growth regulators and antibiotics on eggplant transformation. *J. Amer. Soc. Hort. Sci.* 122:158-162
- Rotino G L, Gledlie S (1990) Transformation of eggplant (*Solanum melongena* L.) using a binary *Agrobacterium tumefaciens* vector. *Plant Cell Rep.* 9:26-29
- Cheng X Y, Sardana R, Kaplan H *et al.* (1998) *Agrobacterium*-transformed rice plants expressing synthetic *cryIA(b)* and *cryIA(c)* genes are highly toxic to striped stem borer and yellow stem borer. *Proc. Natl. Acad. Sci. USA.* 95:2767-2772

Removing Noise and Artifacts from EEG Using Adaptive Noise Cancelator and Blind Source Separation

Nguyen T.K. Cuong¹, Vo Q. Ha¹, Nguyen T.M. Huong¹, Truong Quang Dang Khoa²,
Nguyen Huynh Minh Tam², Huynh Q. Linh¹, and Vo Van Toi²

¹ Applied Science Department, Ho Chi Minh city University of Technology, Vietnam

² Biomedical Engineering Department, Ho Chi Minh city International University, Vietnam

Abstract— Electroencephalography (EEG) is one of the most effective diagnostic procedure for epilepsy. However, the presence artifacts like electro-oculogram (EOG), electrocardiogram (ECG), electromyogram (EMG) and powerline noise 50hz in the EEG signal is a major problem in the study of brain potentials. A variety of algorithms have been proposed to reject these artifacts and noise including methods based on regression and blind source separation (BSS) techniques. In this study, the performances of two widely used artifact rejection techniques are presented. One based on Least Mean Square Adaptive noise cancellation (ANC) for removing ECG artifact and powerline noise. And the another is BSS technique which uses the Second Order Blind Identification (SOBI) to reject EMG and EOG artifacts. Each algorithm was applied in real EEG data and then their performance quantified in the time domain.

Keywords— EEG, noise, artifacts, ANC, BSS.

I. INTRODUCTION

EEG is one of the most effective diagnostic procedure for epilepsy. EEG records carry information about abnormalities or responses to certain stimuli in the human brain. Some of the characteristics of these signals are the frequency and the morphology of their waves. These components are in the order of just a few up to 200 μ V, and their frequency content differs among the different neurological rhythms, as the alpha, beta, delta and theta rhythms [1]. However, artifacts and noise are the outstanding enemies of high quality EEG signals. Their presence is thus crucial for the accurate evaluation of EEG signal. They fall into two major categories: technical and physiological artifacts. The most frequently seen in technical artifacts are powerline noise 50/60Hz results from poor electrode application on the scalp and transducer's artifacts. In physiological problem, artifacts are often due to ocular, heart or muscular activity; respectively are the EMG, EOG, ECG artifacts [2].

Cardiac activity: The electrical activity of the heart, as reflected by the ECG, can interfere with the EEG. Although the amplitude of the cardiac activity is usually low on the scalp in comparison to the EEG amplitude (1-2 and 20-100 μ V, respectively), it can hamper the EEG considerably at certain electrode positions and for certain

body shapes [3]. The repetitive, regularly occurring waveform pattern which characterizes the normal heartbeats fortunately helps to reveal the presence of this artifact. However, the spike-shaped ECG waveforms can sometimes be mistaken for epileptiform activity when the ECG is barely visible in the EEG.

Muscle activity: Another common artifact is caused by electrical activity of contracting muscles, measured on the body surface by the EMG [4]. This type of artifact is primarily encountered when the patient is awake and occurs during swallowing, grimacing, frowning, chewing, talking, sucking, and hiccupping [5].

Eye movement and blinks: Eye movement produces electrical activity the EOG which is strong enough to be clearly visible in the EEG. The EOG reflects the potential difference between the cornea and the retina which changes during eye movement. Another common artifact is caused by eyelid movement ("blinks") which also influences the corneal-retinal potential difference. The blinking artifact usually produces a more abruptly changing waveform than eye movement, and, accordingly, the blinking artifact contains more high-frequency components [6].

In this work, two methods Adaptive Noise Cancellation and Blind Source Separation are used to remove the 50Hz interference noise and ECG, EMG, EOG artifacts.

II. MATERIALS AND METHODS

A. MATERIALS

The experiment data derive from the Cho Ray hospital in Ho Chi Minh city, Vietnam. The scalp electrodes are allocated based on the 10-20 channel system of the international standard. In this experiment twenty one-channel EEG data and one ECG data have been acquired, its sampling frequency is 200Hz.

B. METHODS

1. ADAPTIVE NOISE CANCELLATION [7,8]

Adaptive digital filters are self learning filters, whereby an FIR (or IIR) is designed based on the characteristics of

input signals. An adaptive digital filter will therefore “adapt” to its environment. The environment will be defined by the input signals $x(n)$ and reference signal $r(n)$ to the adaptive digital filter. Adaptive noise cancellers are used in communications, signal processing, and in biomedical signal analysis, ANC can also be used to remove noise and artefacts from the EEG signals. An effective adaptive noise canceller, however, requires a reference signal. Figure 1 below shows a general block diagram of an adaptive filter for noise cancellation. The reference signal carries significant information about the noise or artefact and its statistical properties.

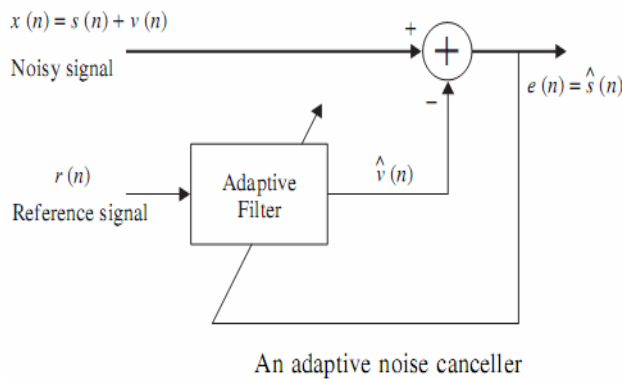


Fig. 1 Principle of Adaptive noise canceller [8]

In an adaptive filter, there are basically two processes:

- A filtering process, in which an output signal is the response of a digital filter. Usually, FIR filters are used in this process because they are simple and stable.
- An adaptive process, in which the transfer function $H(z)$ is adjusted according to an optimizing algorithm. The adaptation is directed by the error signal between the primary signal and the filter output. The most used optimizing criterion is the least mean square algorithm.

2. BLIND SOURCE SEPARATION [8]

Blind source separation (BSS) is the separation of a set of signal from a set of mixed signals, without the aid of information (or with very little information) about the source signals or the mixing process. BSS techniques have the ability to separate EEG signals to spatial components; specialists are then called to identify the artifactual components remove them and reconstruct the signal so as to be free of artifacts. BSS relies on the assumption that the source signals do not correlate with each other. For example, the signals may be mutually statistically independent or

decorrelated. BSS thus separates a set of signals into a set of other signals, such that the regularity of each resulting signal is maximized, and the regularity between the signals is minimized (i.e. statistical independence is maximized). Because temporal redundancies (statistical regularities in the time domain) are "clumped" in this way into the resulting signals, the resulting signals can be more effectively deconvolved than the original signals.

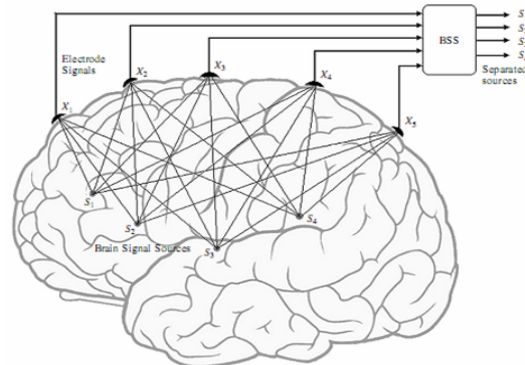


Fig. 2 BSS concept; mixing and blind separation of the EEG signals [8]

Figure 2 illustrates the BSS concept. EEG signals x_i are a linear combination of several underlying brain sources s_i . BSS techniques have the ability of finding a closest approach to the sources without a priori knowledge of them or the mixing process. The algorithm used for our study is a recently proposed algorithm that makes use of Second Order Blind Identification(SOBI) algorithm for source extraction. This algorithm makes automatic identification and removal of artifactual components using Fractal Dimension(FD). Since the EEG data collected from Cho Ray hospital are not recorded simultaneously with the EOG and EMG. Therefore we use the BSS to remove EOG and EMG from EEG.

In brief, this method consists on three basic steps. First, the original EEG data is decomposed into a set of spatial components. Second, artifactual components are identified using a suitable automatic criterion. Third, the EEG data is reconstructed by projecting back to the electrodes only the non-artifactual spatial components. Below is the example of EOG removal [9].

The EEG inverse problem:

Typically, the signal recorded at the j^{th} electrode is modeled as:

$$x_j(t) = \underbrace{\sum_{i \in r_{\text{EEG}}} a_{ji} s_i(t)}_{x_{j,\text{EEG}}(t)} + \underbrace{\sum_{i \in r_{\text{EOG}}} a_{ji} s_i(t)}_{x_{j,\text{EOG}}(t)} \quad (1)$$

In matrix form:

$$\mathbf{x}(t) = \underbrace{\mathbf{A}_{EEG}(t)\mathbf{s}_{EEG}(t)}_{\mathbf{x}_{EEG}(t)} + \underbrace{\mathbf{A}_{EOG}(t)\mathbf{s}_{EOG}(t)}_{\mathbf{x}_{EOG}(t)} \quad (2)$$

The problem we face is to estimate $\mathbf{x}_{EEG}(t)$ from $\mathbf{x}(t)$

Description of EOG correction Algorithm [9]:

INPUT

- Observed EEG data samples: $\mathbf{x}(t)$, $t = 1, 2, \dots, L$
- Analysis frame length: L_a
- Initialize frame counter: $i = 1$

while ($i \cdot L_a < L$)

- * $\mathbf{X}_{(i)} = [\mathbf{x}((i-1)L_a + 1), \mathbf{x}((i-1)L_a + 2), \dots, \mathbf{x}(iL_a)]$
- * Estimate mixing matrix \mathbf{A} from current data frame $\mathbf{X}_{(i)}$
- * Identify columns of \mathbf{A} corresponding to EOG sources
- * Remove EOG activity:
 $\mathbf{x}_{(i)} = \mathbf{x}_{(i)} - \mathbf{A}_{EOG}\mathbf{A}_{EOG}^\#(\mathbf{A}_{EEG}\mathbf{A}_{EEG}^\# + \mathbf{A}_{EOG}\mathbf{A}_{EOG}^\#)\mathbf{x}_{(i)}$
 (where $\#$ denotes the Moore-Penrose pseudoinverse).
- * $i = i + 1$

end

Description of Identifying ocular components [9]:

INPUT: Estimate spatial components in the current frame

- * Sort the components according to increasing values of FD. Let us denote the sorted components by $s^{(1)}(t), \dots, s^{(N)}(t)$ and their corresponding FDs by $\phi^{(1)}, \dots, \phi^{(N)}$.
- * Identify as EOG components $s^{(1)}(t), s^{(2)}(t), \dots, s^{(k)}(t)$ where k is the smallest integer in the range $[N/2] \geq k > 1$ such that $(\phi^{(k+1)} - \phi^{(k)}) < (\phi^{(k)} - \phi^{(k-1)})$. If there is not any k satisfying the required condition then $k = 1$.

III. RESULTS

EEG records with 22 channels, 200 Hz sampling rate, and an average recording length of 5 min have been preprocessing. For importing data to Matlab, EEGLAB software was used. The EEG records just have one ECG reference channel. Therefore, adaptive noise cancellation was used to remove powerline noise 50Hz and ECG artifacts. In figure 3, it can be found out that the data gained from channel P4 are overlapped by 50Hz noise.

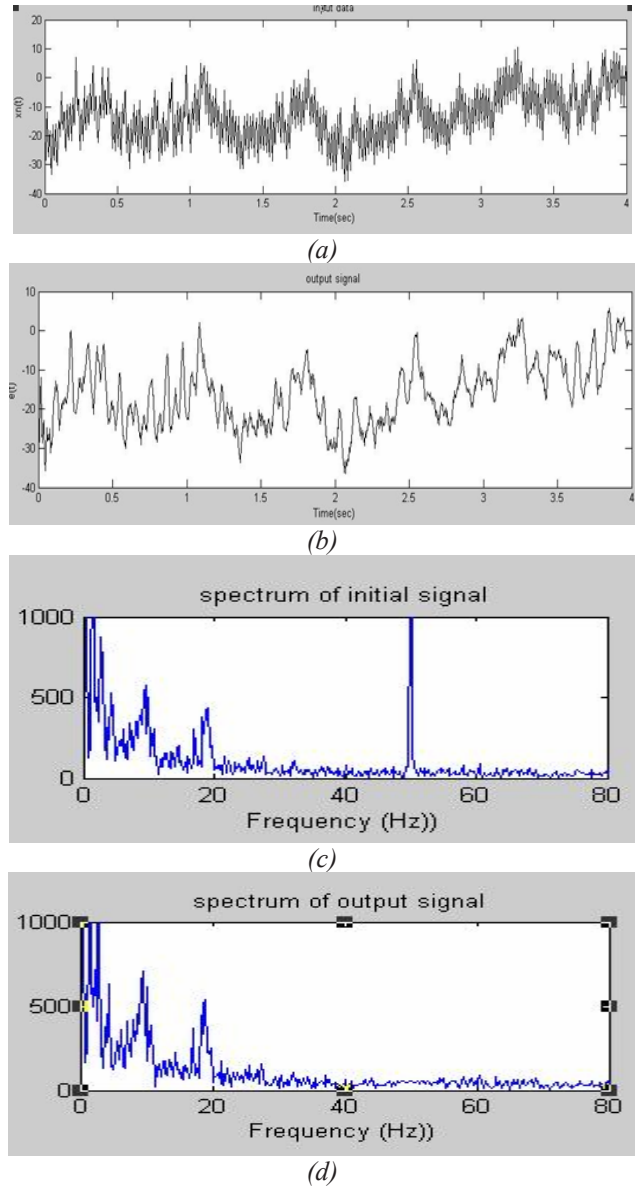


Fig. 3 Demonstration of Powerline noise 50Hz removal using adaptive filtering: (a) original P4; (b) filtered P4; (c) spectrum of original P4; (d) spectrum of filtered P4

After 50 Hz filtering, the EEG is forwarded to the second stage in order to remove ECG artifacts. The signals that recorded on channels of Cz, Pz and A2 are artifacts contain obvious ECG artifacts.

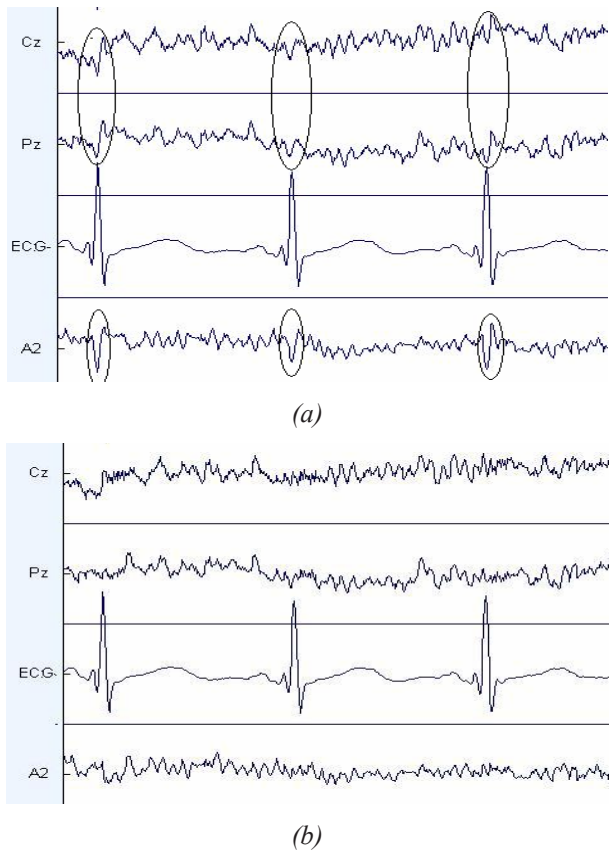


Fig. 4 Demonstration of ECG artifact minimization using adaptive filtering: (a) EEG signal contaminated with ECG artifacts; (b) filtered EEG

In the next step, EMG and EOG artifacts were removed. In figure 5 and 6, it can be seen that the signal from channels of F7, F8, T7 and T8 is disturbed seriously by muscle activities. Moreover, the signals that recorded on channels of Fp1 and Fp2 contain artifacts of eyeball movements, making it difficult in reading EEG.

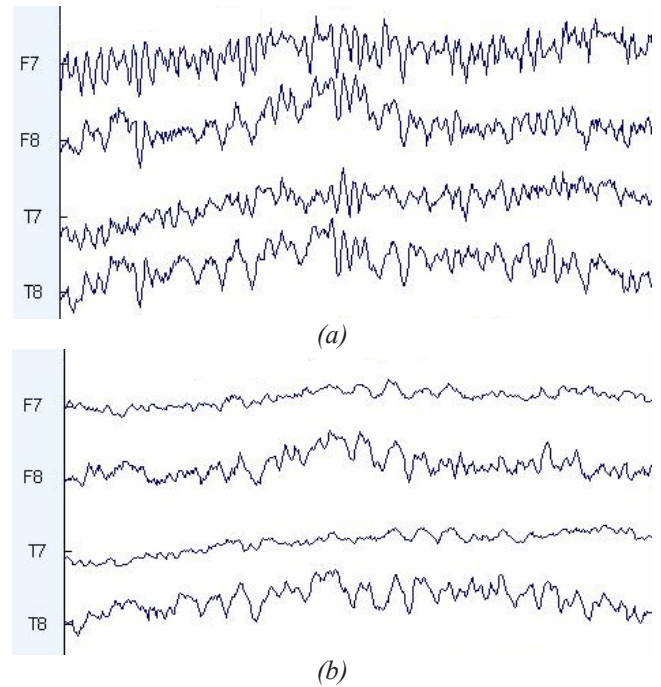


Fig. 5 Demonstration of EMG artifact reduction using Blind Source Separation: (a) EEG signal contaminated with EMG artifacts; (b) filtered EEG

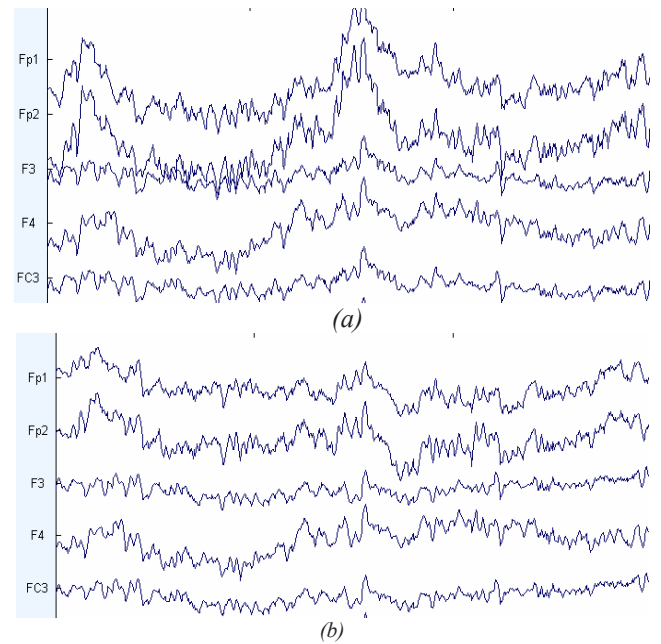


Fig. 6 Demonstration of EOG artifact reduction using BSS: (a) EEG signal contaminated with EOG artifacts; (b) filtered EEG

IV. CONCLUSIONS

This paper has presented the performance of ANC and BSS noise canceller structure for removing powerline noise, ECG, EMG and EOG artifacts to improve the quality of EEG signals. The results show that noise and artifacts were adequately attenuated in all cases. The advantage of ANC is that it very simple and can be used to eliminate a variety kinds of noise and artifacts but its disadvantage is ANC can not work if we don't have the reference signal. The BSS can overcome this problem. However, the drawback of this method is that its algorithm is more complicated and specialists should be available to recognize and reject the artifactual components.

ACKNOWLEDGMENT

This work was partially supported by Applied Science Department, HCMC University of Technology and Biomedical Engineering Department, HCMC International University, both from Vietnam. The authors would like to thank Doctor Le Tu Quoc Tuan, Mr. Huynh Huu Pho in Cho Ray hospital as well as Doctor Nguyen Thanh Luy in Postal Hospital 2, who helped on data collection and advices.

REFERENCES

1. Delay J and Verdeaux G 1967 *Electroencefalografia Clínica* (Barcelona, Toray-Masson)
2. Sörnmo L and Laguna P 2005 *Bioelectrical Signal Processing in Cardiac and Neurological Applications* (London, Elsevier Academic Press).
3. F. S. Tyner, J. R. Knott, and W. B. Mayer, *Fundamentals of EEG Technology*. Vol. 1. Basic Concepts and Methods. New York: Raven Press, 1983
4. J. V. Basmajian and C. J. De Luca, *Muscles Alive. Their Functions Revealed by Electromyography*. Baltimore: Williams & Wilkins, 1985.
5. J. S. Barlow, "Artefact processing (rejection and minimization) in EEG data processing," in *Handbook of Electroencephalography and Clinical Electrophysiology: Clinical Applications of Computer Analysis of EEG and Other Neurophysiological Signals* (F. H. Lopes da Silva, W. Storm van Leeuwen, and A. Rmond, eds.), ch. 1, pp. 15-62, Elsevier, 1986.
6. J. W. Clark, "The origin of biopotentials," in *Medical Instrumentation. Application and Design* (J. G. Webster, ed.), pp. 121-182, New York: John Wiley & Sons, 1998.
7. John L Semmlow (2004) *Biosignal and Biomedical Image Processing MATLAB based Applications* (New York, Marcel Dekker).
8. Saeid Sanei and J.A. Chambers, *EEG signal processing*.
9. G. Gómez-Herrero, W. De Clercq, H. Anwar, Egiazarian K. Kara, O.S. Van Huffel, , and W. Van Paesschen. Automatic removal of ocular artifacts in the eeg without a reference eeg channel. In *Proc. NORSIG 2006*, Reykjavik, Iceland, pages 130–133, 2006.

Removing Electroencephalographic Artifacts by Independent Components Analysis

Nguyen Thi Minh Huong¹, Truong Quang Dang Khoa², Nguyen Thi Kim Cuong¹, Vo Quang Ha¹,
Nguyen Huu Pho³, Le Tu Quoc Tuan³, Ngo Thanh Hoan², Huynh Quang Linh¹, and Vo Van Toi²

¹ University of Technology, Biomedical Engineering, HoChiMinh, Vietnam

² International University, Biomedical Engineering Department, HoChiMinh, Vietnam

³ ChoRay hospital, HoChiMinh, Vietnam

Abstract— Pervasive electroencephalographic (EEG) artifacts associated with blinks, eye-movements, muscle noise, cardiac signals, and line noise poses a major challenge for EEG interpretation and analysis. Many methods have been proposed to remove artifacts from EEG recordings, especially those arising from eye movements and blinks. In Vietnam, epilepsy analysis methods, based on the EEG, is still the visual inspection of the EEG by a highly skilled electroencephalographer or neurophysiologist. But the doctors meet with the difficulties when the obtained scalp EEG recording have not only brain activities signals but also the artifacts. Here, we use the independent components analysis (ICA) method to separate the clean data from the rest of the sources, artifacts within the brain. The separated independent components are good, we will clear the independent components is not brain activity sources and get EEG signals without the artifacts.

I. INTRODUCTION

Epilepsy is the most common neurological disorder, second only to stroke. Nearly 60 million people world-wide are diagnosed with epilepsy whose hallmark is recurrent seizures. These seizures occur at random to impair the normal function of the brain. The seizures occur at random to impair the normal function of the brain [2]. Epilepsy can be treated in many cases and the most important treatment today is pharmacological. Surgical intervention is an alternative for carefully selected cases that are refractory to medical therapy. However, in almost 25% of the total number of patients diagnosed with epilepsy, seizures cannot be controlled by any available therapy. Furthermore, side effects from both pharmacological and surgical treatments have been reported. EEG, MEG, and recently fMRI are the major neuroimaging modalities used for seizure detection. However, the number of fMRI machines is limited in each area, they are costly, and a full body scan is time consuming. Therefore, using fMRI for all patients at all times is not feasible. MEG, on the other hand, is noisy and since the patient under care has to be steady during the recording, it is hard to achieve clear data for moderate and severe cases using current MEG machines. Therefore, EEG

remains the most useful and cost effective modality for the study of epilepsy. Although for generalized seizure the duration of seizure can be easily detected using a naked eye, for most focal epilepsies such intervals are difficult to recognize. However, visual inspection of the EEG is difficult because the signal and artifacts are mixed. Many methods have been proposed to remove artifacts from EEG recordings.

Several proposed methods for removing eye-movement artifacts are based on regression in the time domain (Gratton, Coles, & Donchin, 1983; Hillyard & Galambos, 1970; Verleger, Gasser, & Möcks, 1982) or frequency domain (Whitton, Lue, & Moldofsky, 1978; Woestenburg, Verbaten, & Slangen, 1983). However, simple regression in the time domain for removing eye artifacts from EEG channels tends to overcompensate for blink artifacts and may introduce new artifacts into EEG records (Weerts & Lang, 1973; Oster & Stern, 1980; Peters 1967) [5].

Berg and Scherg (1991a) have proposed a method of eye-artifact removal using a spatiotemporal dipole model that requires a priori assumptions about the number of dipoles for saccade, blink, and other eye movements, and assumes they have a simple dipolar structure. (Lins, Picton, Berg, & Scherg, 1993). Berg and Scherg (1991b) then proposed another technique for removing ocular artifacts using principal component analysis (PCA). However, Lagerlund, Sharbrough, and Busacker (1997) showed that PCA methods cannot completely separate some artifacts from cerebral activity, especially when they both have comparable amplitudes.

Makeig, Bell, Jung, and Sejnowski (1996) proposed an approach to the analysis of EEG data based on a new unsupervised neural network learning algorithm, independent component analysis (ICA) of Bell and Sejnowski (1995). They showed that the ICA algorithm can be used to separate neural activity from muscle and blink artifacts in spontaneous EEG data and reported its use for finding components of EEG and event-related potentials (ERP) and tracking changes in alertness (Makeig et al., 1996; Jung, Makeig, Bell, & Sejnowski, 1997).

Here, we use ICA to isolate and removing a wide variety of EEG artifacts by linear decomposition using a recently developed extension of the ICA algorithm.

II. METHOD

A. Definition of ICA

We assume that we observe n linear mixtures x_1, \dots, x_n of n independent components:

$$x_j = a_{j1}s_1 + a_{j2} + \dots + a_{jn}s_n, j = \overline{1, n} \quad (1)$$

We have now dropped the time index t ; in the ICA model, we assume that each mixture x_j as well as each independent component s_k is a random variable, instead of a proper time signal [3]. Without loss of generality, we can assume that both the mixture variables and the independent components have zero mean: If this is not true, then the observable variables x_i can always be centered by subtracting the sample mean, which makes the model zero-mean:

$$\tilde{x} = x - E(x) \quad (2)$$

Let x be the random vectors whose elements are the mixtures x_1, \dots, x_n and let s be the random vector with the components s_1, \dots, s_n . Let A be the matrix containing the elements a_{ij} . The model can now be written:

$$x = As \quad \text{or} \quad x = \sum_{i=1}^n a_i s_i \quad (3)$$

The above equation is called independent component analysis or ICA. The problem is to determine both the matrix A and the independent components s, knowing only the measured variables x. The only assumption the methods take is that the components s_i are independent. It has also been proved that the

Before the application of the ICA algorithm (and after centering), we transform the observed vector x linearly to obtain a new vector \tilde{x} which is white (its components are uncorrelated and their variances equal unity).

Whitening can be performed via eigenvalue decomposition of the covariance matrix:

$$E\{xx^T\} = EDE^T \quad (4)$$

where E is the orthogonal matrix of eigenvectors of $E\{xx^T\}$ and D is the diagonal matrix of its eigenvalues, $D = \text{diag}(d_1, \dots, d_n)$. Whitening can now be done by

$$\tilde{x} = ED^{-1/2}E^T x \quad (5)$$

B. Fast ICA for n Units [3]

A unit represents a processing element, for example an artificial neuron with its weights W.

To estimate several independent components, the weights w_1, \dots, w_n must be determined. The problem is that the outputs $w_1^T x, \dots, w_n^T x$ must be done as independent as possible after each iteration in order to avoid the convergence to the same maxima. One method is to estimate the independent components one by one

Algorithms:

- i) Initialize w_i
- ii) Newton phase

$$w_i = E\{\tilde{x} g(w_i^T \tilde{x})\} - E\{g'(w_i^T \tilde{x})\} w_i \quad (6)$$

where g is a function with one of the following form:

$$g_1(y) = \tanh(a_1 y), g_2(y) = y \exp\left(-\frac{1}{2} y^2\right), g_3(y) = 4y^3$$

- iii) Normalization

$$w_i = \frac{1}{\|w_i\|} w_i \quad (7)$$

- iv) Decorrelation

$$w_i = w_i - \sum_{j=1}^{i-1} w_j^T w_i w_j \quad (8)$$

- v) Normalization (like in the step iii)
- vi) Go to step ii) if not converged.

III. RESULTS

A. Data Collection

The scalp recordings were obtained from multi-channels system, model Medtronic in ChoRay hospital. With collected data, we read it in Matlab. Then, we use the independent component analysis method to obtain independent components. The ‘‘corrected’’ EEG signals

obtained by removing the artifact independent components from the data.

B. Application of ICA to Scalp EEG

We used ICA algorithm to obtained EEG signals. The algorithm efficiently separates the underlying sources from the eye blinking artifacts and noise.

Example 1: Removing Eye Movement

Fig.1(a) shows a segment of the signals recorded by the scalp electrodes with the baseline removed. The signals are contaminated by noise and artifacts and the data is not clearly discernible. Here, 3 channel has the eye artifacts at 500-700 ms. After applying the ICA, results obtained at Fig.1 (b). The eye movement artifact between 500 and 700 s was isolated to ICA components 3. Further, components 1, and 4 evidently represent muscle noise, IC2 is the isolated muscle artifacts. The “corrected” EEG signals obtained by removing the two selected ICA components.

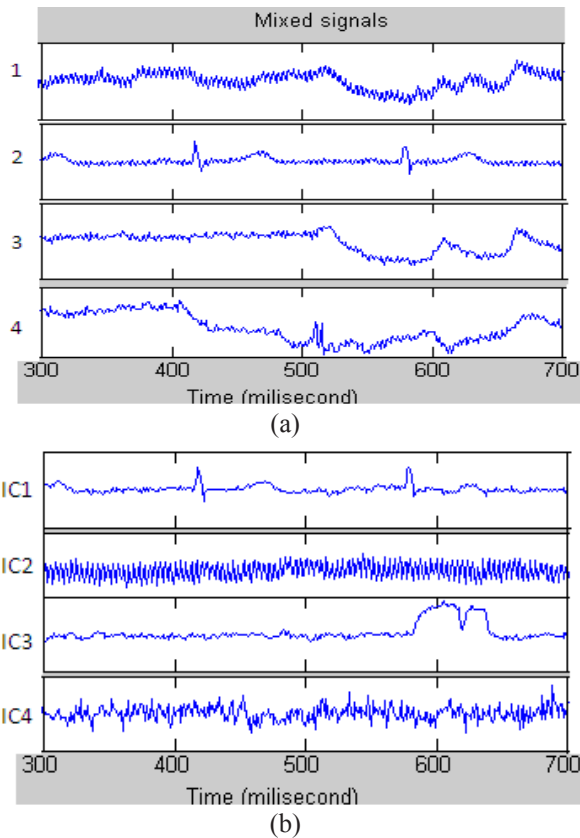


Fig. 1 Using ICA to remove the artifacts: (a) original signal- 400ms portion of an EEG time series containing a prominent eye movement, (b) independent components from original signals

Example 2: Removing Muscle Artifacts

We continue to analysis the data from ChoRay hospital. Fig.2 shows a 400ms portion of the recorded EEG time series and its ICA component activations. Fig.2 (a) is the original signals, here we observed muscle artifacts appear in 1, 3 and 2 channel have information about brain activities but it is not robusted by artifacts . Signals obtained after applying the ICA method, muscle artifact in IC3. Moreover, the other signals are clean. These help the doctor to predict the epileptic seizure exactly. We clear IC3 to obtain the clean data.

With example 1 and example 2, we obtained good results.

Muscle atifacts are isolated in specified Ics.

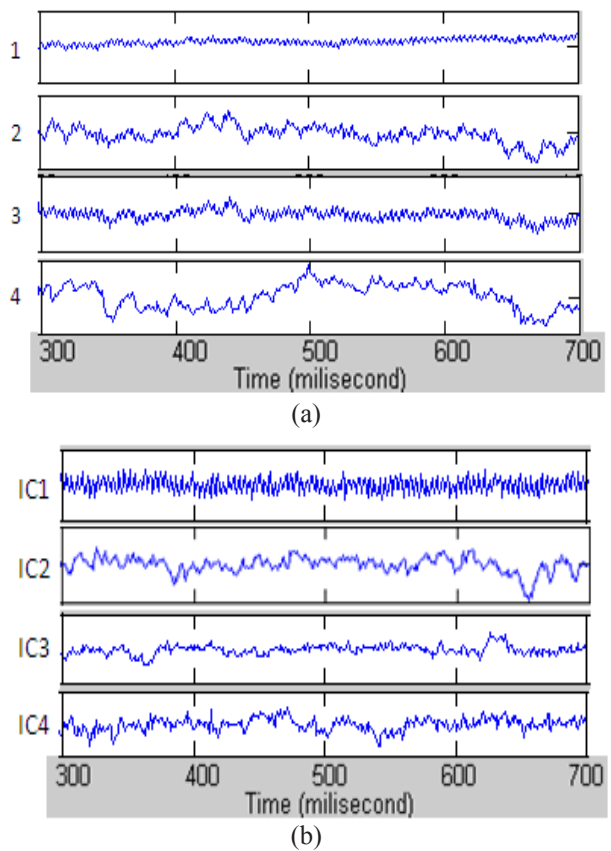


Fig. 2 Removing the muscle artifacts: (a) the original signals- 400ms portion of an EEG time series containing a prominent muscle artifact, (b) the independent components from original signals

Example 3: Removing ECG Artifact

Fig.3 shows a 400ms portion of the recorded EEG time series and its ICA component activations. Fig.3 (a) is the original signals, here we observed EEG artifacts appear in 2, 3 at about 350ms. Signals obtained after applying the ICA method, there is no EEG artifacts (Fig.3 (b)). Moreover, the other signals are clean. These help the doctor to predict the epileptic seizure exactly.

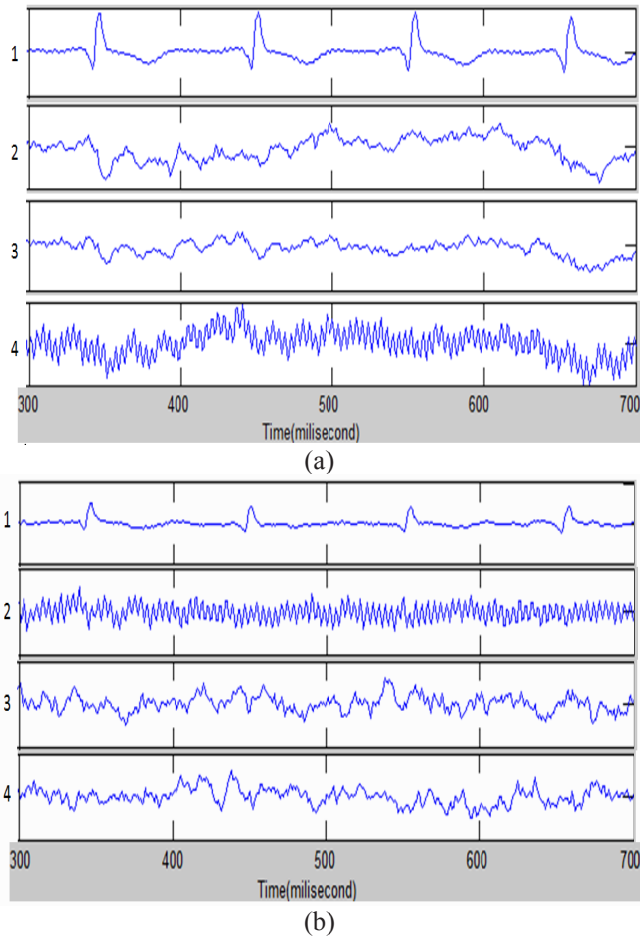


Fig. 3 Removing the muscle artifacts: (a) the original signals- 400ms portion of an EEG time series containing a prominent EEG artifact, (b) the independent components from original signals

IV. CONCLUSIONS

The results presented in our study, although limited, appear to be promising. Scalp EEG recordings seem to contain enough information about the seizure; however, this information is mixed with the signals from the other sources within the brain and it is buried in noise and artifacts. The results of the experiments clearly show that the ICA algorithm successfully separate clean data from the rest of the sources, artifacts within the brain, and independent components have information about epileptic seizure to help doctors to predict. Here, we Demonstration of electroencephalogram (EEG) artifact removal by independent component analysis –ICA. Because of limited time, we have not finished reconstructing “corrected” EEG.

REFERENCES

1. Saeid Sanei and J.A. Chambers (2007) EEG signal Processing, Cardiff University, UK. p171-191
2. Javier Corsini*, Leor Shoker, Saeid Sanei et al. (2006). Epileptic Seizure Predictability From Scalp EEG Incorporating Constrained Blind Source. IEEE transactions on biomedical engineering, Vol. 53, No. 5, May 2006. 5.
3. M. Ungureanu, C. Bigan, R. Strungaru, V. Lazarescu (2004). Independent Component Analysis Applied in Biomedical Signal Processing. Measurement science review, Volume 4, Section 2.
4. Aapo Hyvärinen and Erkki Oja (2000). Independent Component Analysis: Algorithms and Applications. Neural Networks Research Centre.
5. Tzzy-Ping Jung, Scott MakeigG (2000). Removing electroencephalographic artifacts by blind source separation. Psychophysiology, 37, 163–178. Cambridge University Press. Printed in the USA

A Trip from a Tube to a Chip Applied Micro and Nanotechnology in Biotechnology, Veterinary and Life Sciences

Dang Duong Bang¹, Raghuram Dhumpa¹, Cao Cuong¹, Laouenan Florian², Javier Berganzo², Rafal Walczak³, Yuliang Liu¹, Mingiang Bu⁴, Sun Yi⁴, Jan Dzuiban³, Jesus Miguel Rruano², and Anders Wolff⁴

¹Laboratory of Applied Micro-Nanotechnology, National Veterinary Institute, Technical University of Denmark (DTU-Vet), Denmark

²MEMS/MST Dept. Ikerlan S. Coop, Arizmendiarieta 2, 20500 Mondragon, Spain

³Institute of Electron Technology, Warsaw, Poland and Wroclaw University of Technology, Wroclaw, Poland

⁴BioLabchip group, Department of Micro and Nanotechnology, Technical University of Denmark (DTU-Nanotech), Denmark

Abstract— More than 200 known diseases are transmitted via foods or food products. In the United States, food-borne diseases are responsible for 76 million cases of illness, 32,500 cases of hospitalisation and 5000 cases of death yearly. The ongoing increase in worldwide trade in livestock, food, and food products in combination with increase in human mobility (business- and leisure travel, emigration etc.) will increase the risk of emergence and spreading of such pathogens. There is therefore an urgent need for development of rapid, efficient and reliable methods for detection and identification of such pathogens.

Microchipfabrication has had a major impact on electronics and is expected to have an equally pronounced effect on life sciences. By combining micro-fluidics with micromechanics, micro-optics, and microelectronics, systems can be realized to perform complete chemical or biochemical analyses. These so-called 'Lab-on-a-Chip' will completely change the face of laboratories in the future where smaller, fully automated devices will be able to perform assays faster, more accurately, and at a lower cost than equipment of today. A general introduction of food safety and applied micro-nanotechnology in life sciences will be given. In addition, examples of DNA micro arrays, micro fabricated integrated PCR chips and total integrated lab-on-a-chip systems from different National and EU research projects being carried out at the Laboratory of Applied Micro-Nanotechnology (LAMINATE) group at the National Veterinary Institute (DTU-Vet) Technical University of Denmark and the BioLabchip group at the Department of Micro and Nanotechnology (DTU-Nanotech), Technical University of Denmark (DTU), Ikerlan-IK4 (Spain) and other 16 partners from different European countries will be presented.

Keywords— Lab-on-a-Chip, Micro-nanotech applications, food safety.

I. INTRODUCTION

Food safety is an essential matter and taken for granted by the majority of the public. More than 200 known diseases are transmitted via foods or food products [1]. It has been shown that the presence of only small numbers of the pathogens, and in some cases, only one organism in foods, food products or water may be an effective infectious

dose [2]. The global incidence of food-borne disease is difficult to estimate, but it has been reported that in 2005 alone 1.8 million people died from diarrhoeal diseases and a great proportion of these cases can be attributed to the contamination of food and drinking water.

In industrialized countries, the percentage of the population suffering from food-borne diseases each year has been reported to be up to 30%. In the United States of America (USA), for example, around 76 million cases of food-borne diseases, resulting in 325,000 hospitalizations and 5,000 deaths, are estimated to occur each year [1].

Food contamination creates an enormous social and economic burden. In the USA, diseases caused by the major pathogens alone are estimated to cost up to US \$35 billion annually (1997). The re-emergence of cholera in Peru in 1991 resulted in the loss of US \$500 million in fish and fishery product exports that year [1]. The most common food-borne diseases are: Campylobacteriosis, Salmonellosis, Enterohaemorrhagic (causing intestinal bleeding) *Escherichia coli*, e.g. *E. coli* O157, and Listeriosis, while Cholera, a disease caused by the bacterium *Vibrio cholerae* is causing enormous economic losses and is a major public health problem in developing countries[2].

II. THE NEED OF RAPID METHODS FOR DETECTION OF FOOD-BORNE PATHOGENS

In order to comply to the demands of consumers for safe food, free of pathogens, there is an urgent need for development of rapid, efficient and reliable methods for detection and identification of such pathogens since conventional methods for detection and identification of pathogens (such as those suggested and used by the Nordic Committee on Food Analysis) often require long time [6]. In addition, these tests need to be carried out in special laboratories and require special reagents and equipment and trained technicians. By the time the conventional tests have been completed an entire community or a large part of a population may have been exposed to the pathogen in question.

The advantages of rapid testing system, which could directly give reliable results in a shorter time, are essential since appropriated measure could be taken to remove the bacterial pathogenic positive animals at the slaughter and to reduce the laborious time-consuming conventional identification tests.

III. EXAMPLES OF APPLIED MICRO-NANOTECHNOLOGY IN FOOD SAFETY, VETERINARY AND LIFE SCIENCES

A. DNA Microarrays

In 2003, Keramas *et al* [8] developed a DNA microarray for rapid detection and identification of *Campylobacter* spp. The method consists of two steps: i) Multiplex PCR with Cy5-labelled primers and ii) Hybridization of the Cy5 labelled PCR amplicons to capture probes. The method has been shown a high sensitivity since using this method *Campylobacter* spp can be detected at as low as 3 CFU – 100 times more sensitive than the conventional gel electrophoresis. Furthermore the method showed a high specificity since equal amounts of single PCR were hybridised to microarray and the individual products hybridise only to their corresponding capture probes (Fig.1). The method was successful used for detecting of *Campylobacter* spp. directly from broiler chicken faecal samples [9].

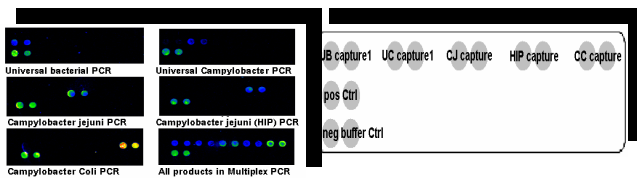


Fig. 1 The specificity of the DNA-microarray to detect of *Campylobacter* spp. in broiler chickens

Recently a Tag array suitable for rapid detection of single mutation of K-ras gene in colorectal cancer (CRC) is developed [10]. CRC is one of the most prevalent cancers causing significant mortality. CRC, however, is curable if diagnosed at early stage. It has been shown that mutations in the oncogene K-ras plays a key role in the early development of CRC. The tag-array-based hybridization method was aimed to detect Single Nucleotide Polymorphism (SNP) in codon 12 of K-ras gene in CRC. Firstly, the K-ras gene fragments containing codon 12 SNPs were amplified by multiplex PCR using 3'-SNP-specific forward primers linked with unique tags at the 5' end in combination with a Cy5-labeled reverse primer. In the PCR reaction, the Cy5-labeled reverse primer will be extended to the end of the SNP-specific forward primers and will therefore include the complimentary sequence of the tag (anti-tag). The PCR products were subsequently hybridized to the tags immobilized on different solid substrates (Fig.2.). The

fluorescently labelled primer allowed for the detection and evaluation of point mutations of K-ras derived from 12 cancer cell lines and 28 clinical patient samples containing both homozygous and heterozygous genotypes [10].

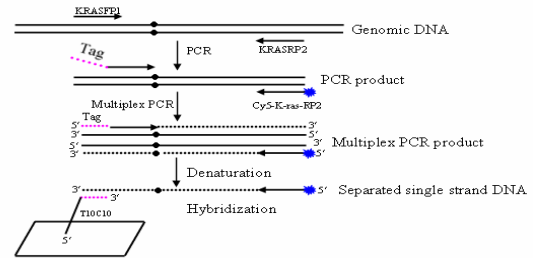


Fig. 2 Detection of K-ras gene mutations in CRC by Tag arrays

B. Bead-Based Method

Avian Influenza Virus (AIV) also called “bird flu” is a viral infection disease caused by Influenza A virus. Outbreaks of AIV cause great economic loss and started to threatening human life. Conventional methods for detection of AIV time consuming (4-6 weeks), A faster method based on RT-PCR was recently introduced. However, this method is still time consuming (2-4 working days). A novel method for isolation of AIV using magnetic beads was recently developed (Fig 3). The beads are coated with monoclonal antibody against the all AIV subtype. The viruses are captured by beads and detected by RT-PCR without RNA isolation step. Using this method it was possible to detect viruses with titre as low as 1:64 and with dilution 3×10^{-5} . So far 16 different H subtypes of AIV including high pathogenic H5N1 have been captured and detected directly from chicken faecal sample within 8 hr. [11].

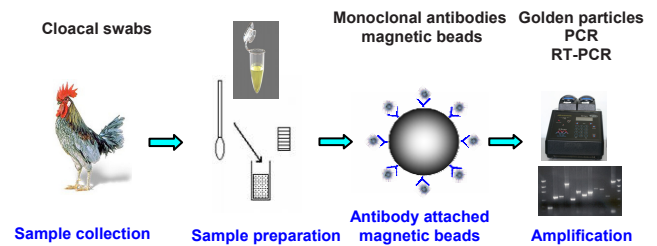


Fig. 3 Bead-based system for rapid isolation AIV directly from chicken faecal samples

C. Solid Phase PCR

More recently, a microarray-based detection technique called solid phase PCR has been developed for rapid AIV identification. In this solid phase PCR, oligonucleotide primers that are suitable for interrogating different Influenza types are covalently attached to a glass slide exactly as in DNA microarray. PCR master mixture containing RNA

genome is placed on the array and these oligos are used as nested primers for elongation. The reaction products remain covalently bound to the glass chip and can be visualized via the incorporation of Cy5 fluorescence dyes. This method exploits the high specificity intrinsic to DNA polymerases, which is much more accurate than hybridization.

D. PCR Chips

J. El-Ali *et al* (2004) [12] presented a SU8 based PCR chip with integrated platinum thin film heater and temperature sensor. The chip is fabricated in SU-8 on a glass substrate (Fig.4). The use of SU-8 provides a simple micro-fabrication process for the PCR chamber, controllable surface properties and can allow on chip integration to other SU-8 based functional elements such as sample preparation [13]. Experimental results show that the chip is capable of fast thermal cycling with heating and cooling rates of 50°C and 30°C/s respectively [12]. The chip was successful used to detect *Campylobacter* spp. directly from human clinical samples and from broiler chicken at slaughter [14].

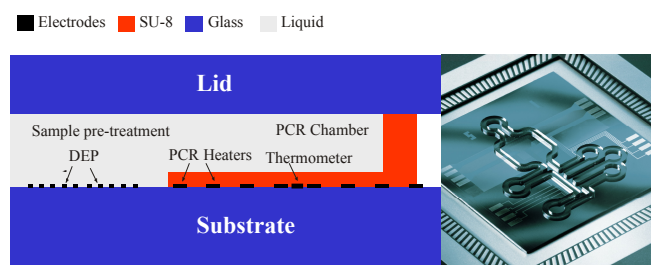


Fig. 4 A schema of the chip (left) and top view of the SU8 based PCR chip with 25µl volume PCR chamber (right)

E. Integrated Lab-on-a-Chip System for Real-Time PCR Rapid Detection of Pathogens (OPTOLABCARD System)

M. Agirregabiria *et al* (2007) described a total integrated SU-8 based Lab-on a chip system for real-time PCR rapid detection of pathogens. This SU-8 fabrication process was based on the bonding and releasing of photo-patterned SU-8 layer [15] creating a micro chamber of 2.5µl on a Pyrex substrate with a resistive Ti/Pt sensor and heaters previously fabricated (Fig. 5). The Lab-on a chip system is able to perform all the steps from sample preparation, concentration of target specific bacterial pathogens directly from faecal sample and consequently amplification of the purified DNA by real-time (also called quantitative) PCR (qPCR) [16].

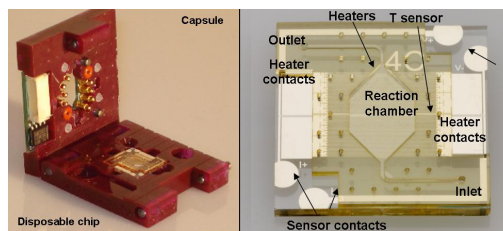


Fig. 5 Photo of a disposable chip in an open packaged device (left) and the Disposable chip with different components (right)

On chip real-time PCR detection is based on optical measurement [17]. The optical detection system (Fig. 6a) consists of: solid-state laser 636 nm, high resolution and sensitivity CCD camera (Sony 1/3”B/W SuperHAD, Japan) working as an array of VIS/NIR micro-detectors, 650 nm long-pass interference filter (ThorLabs, USA) and on-chip integrated SU8 planar waveguides ended with microlenses, made as the integral part of the PCR chamber of the microchip (Fig. 6c). Laser light is guided to the PCR chamber by direct coupling into side-wall of the planar waveguide. CCD camera, distanced a few millimeters perpendicularly to the surface of the PCR chip, collects fluorescence images (Fig. 6d). The movie-like images of the chip are processed by specialized software to give to the user fluorescence numerical data in time or PCR cycle number dependency. Using this system it has been show the detection limit of the system is about 1.5 ng/ml of DNA [17].

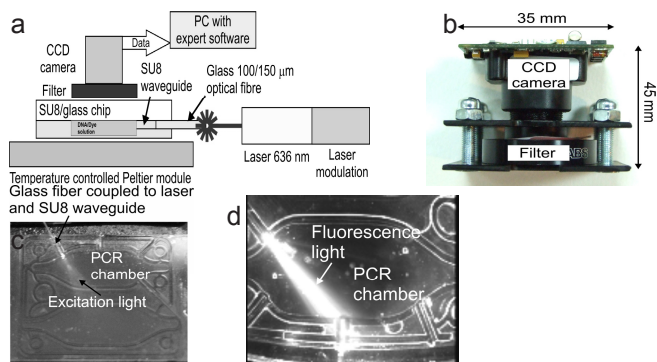


Fig. 6 CCD-based optical readout system: a) Scheme, b) Camera module with optical filter positioned above RT-PCR chip. c) Top view of the structure with mounted glass fiber illuminating detection area, d) View of the PCR chamber as collected by CCD camera/filter module – fluorescence light emitted by 2.5 ng/ml salmon sperm DNA is visible as the “light torch”

IV. CONCLUSIONS AND FUTURE OUT LOOK

In this paper an overview of food safety, food-born diseases with focus on the food-born pathogens as well as global problem of food-born illness is presented. A number of example of different micro systems with a variety of different

formats that were successfully developed from different EU and national projects from closed collaboration between the LAMINATE group at DTU-Vet and the BIOLAB CHIP group at DTU-Nanotech in Denmark and other EU project partners from Ikerlan (Spain) and ITE/PW (Poland) are also given.

Microchip-fabrication has had a major impact on electronics and is expected to have equally pronounced effects on many faces of life sciences in the years to come. By combining different functional components will create that can be realized to perform complete chemical or biochemical analyses. The so-called 'Lab-on-a-Chip' or Micro Total Analysis system will completely change the face of laboratories in a near future. With advantage of many new technologies for micro-manufacturing, with various newly developed substrates, materials and with the fast growing of successful integrating of different subcomponents with different functions and purposes without doubt a truly total integrated portable Lab-on a chip system will be created in a near future.

ACKNOWLEDGMENTS

These researches are financial sponsored by:

- The Danish Technical Research Council (Grant no. 9901659).
- The Danish Research Council for technology and production sciences (Grant no.274-05-0017.)
- The FOOD-DTU project 8, Technical University of Denmark,
- The FP-6 STREP, Project OPTOLABCARD (No 016727)

REFERENCES

1. <http://www.who.int/mediacentre>
2. <http://www.cfsan.fda.gov> May 2007
3. *Trends and sources of zoonotic agents in animals, feeding stuffs, foods and man in the European Union and Norway in 2004*. Food safety: production and distribution chain D2-biological risks. SANCO729/2004
4. EPI-NEWS 2008 No.10: <http://www.ssi.dk/sw55440.asp>
5. DFVA web. <http://www.dfvf.dk>
6. Anon (1990). *Campylobacter jejuni/coli detection in food*. Method No. 119. 2nd Ed. Nordic Committee on Food Analysis, Esbo, Finland.
7. D.D Bang Pedersen, K. Madsen, M. (2001). *Development of a PCR assay suitable for Campylobacter spp. mass screening programs in broiler production*. J. Rapid Methods Autom. Microbiology Vol 9 97-113.
8. G. Keramas, Bang, D. D. Lund, M. Madsen, M. Rasmussen, S. E. Bunkenborg, H. Telleman, P. Christensen, C. B. V (2003). *Development of a sensitive DNA microarray suitable for rapid detection of Campylobacter spp.* Molecular and Cellular Probes 17; 187-196
9. G. Keramas, Bang, D. D., Lund, M., Madsen, M., Bunkenborg, H., Telleman, P., Christensen, C. B. V. (2004). *Use of culture, PCR analysis, and DNA microarrays for detection of Campylobacter jejuni and Campylobacter coli from chicken feces*. Journal of Clinical Microbiology 42:3985-3991.
10. Yulian Liu et al. (2008). Lab on a chip World Congress conference proceeding. Barcelona, Spain 7-9 May 2008.
11. Raghuram D., K J. Handberg, A. Wolff, D. D. Bang (2008). *Isolation and identification of Avian Influenza Virus directly from chicken faecal samples using monoclonal antibody coated magnetic beads and reverse-transcription polymerase chain reaction*. Lab on a chip World Congress conference proceeding. Barcelona, Spain 7-9 May 2008.
12. El-Ali, J., I.R. Perch Nielsen, C.R. Poulsen, D.D Bang, P. Telleman and Anders Wolff (2004). *Simulation and experimental validation of a SU-8 based PCR thermocycler chip with integrated heaters and temperature sensor*. Sensors and Actuators A-Physical, 110: p. 3-10.
13. I.R. Perch Nielsen, D. D. Bang, C. R. Poulsen, J. El-Ali, A. Wolff (2003). *Removal of PCR inhibitors using dielectrophoresis as a selective filter in a microsystem*. Lab chip 3, 212-216
14. Poulsen, C. R., El-Ali, J., Perch-Nielsen, I. R., Bang, D. D., Telleman, P., Wolff, A (2005). *Detection of a putative virulence cadF gene of Campylobacter jejuni obtained from different sources using a microfabricated PCR chip*. J Rapid Methods Autom. Microbiol. Vol 9 97-113.
15. M. Agirregabiria Blanco, F. J., Berganzo, J., Arroyo, M. T., Fullaondo, A., Mayora, K., Ruano-Lopez, J. M. (2005). *Fabrication of SU-8 multilayer microstructures based on successive CMOS compatible adhesive bonding and releasing steps*. Lab chip 6, 886-895
16. M. Agirregabiria, D. Verdoy, G. Olabarria, J. Berganzo, J. Berganza, L.J. Fernandez, M. Pascual de Zulueta, K. Mayora, P. Aldamiz-Echevarria and J.M.Ruano-Lopez (2007). *μTAS 2007 Vol 1 p:584-586*
17. Rafał Walczak, Jan A. Dziuban, Jan Koszur, Anders Wolff, Dang Duong Bang, Minqiang Bu (2007). *CCD camera-based optical readout system for real-time PCR DNA analyzer: toward rapid and cheap detection of pathogens in food and clinical samples in nanograms per milliliter concentration of DNA*. *μTAS 2007 Vol 1, p:691-693*.

Au Nanoparticles for Applications in Analysis of Cellular and Biomolecular Recognitions

Cuong Cao¹, Anders Wolff², and Dang Duong Bang^{1,*}

¹ DTU-VET, Laboratory of Applied Micro-nanotechnology, National Veterinary Institute, Technical University of Denmark, DK-8200 Aarhus N, Denmark

*ddba@vet.dtu.dk

² DTU-Nanotech, Department of Micro and Nanotechnology, Technical University of Denmark, DK-2800 Kongens Lyngby, Denmark

Abstract— Au nanoparticles (AuNPs) have attracted a great interest in fabrication of various biosensor systems for analysis of cellular and biomolecular recognitions. In conjunction with vast conjugation chemistry available, the materials are easily coupled with biomolecules such as nucleic acids, antigens or antibodies in order to achieve their many potential applications as ligand carriers or transducing platforms for preparation, detection and quantification purposes. Furthermore, the nanoparticles possess easily tuned and unique optical/ physical/ chemical characteristics, and high surface areas, making them ideal candidates to this end. In this topic, sensing mechanisms based on localized surface plasmon resonance (LSPR), particle aggregation, catalytic property, and Fluorescence Resonance Energy Transfer (FRET) of AuNPs as well as barcoding technologies including DNA biobarcode will be discussed.

Keywords— Localized surface plasmon resonance, particle aggregation, catalytic property, fluorescence resonance energy transfer, biobarcode.

I. INTRODUCTION

Recently, AuNPs have been gaining considerable contributions in fundamental biological studies, food quality, safety analysis, medical diagnostics, drug delivery, and environmental monitoring. In conjunction with vast conjugation chemistry available, the nanoparticles possess easily tuned and unique optical/ physical/ chemical characteristics, and high surface areas, making them ideal candidates to those applications. By coupling with biomolecules (e.g., DNA, aptamer, protein, enzyme, etc.), AuNPs have been implemented to detect and quantify the biological interactions as optical labels, electrochemical markers, surface plasmonic amplifiers, catalytic probes, or FRET probes. In this paper, we will briefly introduce on using AuNPs as basic platforms to develop quantitative and qualitative assays for application in analysis of cellular and biomolecular recognitions, which depend on localized surface plasmon resonance (LSPR), particle aggregation, catalytic property, Fluorescence Resonance Energy Transfer (FRET) of AuNPs, and DNA biobarcode.

II. LSPR

LSPR are collective charge oscillations that occur at the interface between conductors and dielectrics of nanometer-sized metallic structures causing unique properties such as strong ultraviolet/visible absorption bands that are not present in the planar metal or brilliant colors observed for the particles in solution. It is this fascination with the optical properties that lead to their many applications in the development of biosensors.

Briefly, nanometer-sized metallic structures are ionic clusters covered by free electronic clouds. When the nanometer-sized metallic structures are excited by light, the electric field of the incoming light will induce polarization of the free electrons relative to the ionic cluster. As a result, the collective electrons of the nanoparticles oscillate with the incident photon frequency, which leads to the so-called LSPR. The excitation of free electrons of the nanoparticles by an electric field at an incident wavelength where the resonance occurs will result in strong light scattering or a strong ultraviolet/visible absorption band that is not present in the spectrum of the bulk metal [1].

To model the LSPR of spherical nanoparticles, Mie theory is the simplest calculation available for estimating the extinction of a metallic nanoparticle in a long wavelength with an electrostatic dipole limit by using [1]:

$$E(\lambda) = \left[\frac{24\pi N_A a^3 \epsilon_m^{3/2}}{\lambda (\ln 10)} \frac{\epsilon_i}{(\epsilon_r + \chi \epsilon_m)^2 + \epsilon_i^2} \right]$$

where $E(\lambda)$ is the extinction (= absorption + Rayleigh scattering), N_A is the areal density of nanoparticles, a is the radius of the metallic nanoparticle, χ is the shape coefficient or the aspect ratio of the nanoparticle (equal to 2 for a sphere and up to values of 17 for a 5 : 1 aspect ratio nanoparticle), ϵ_m is the dielectric constant of the medium surrounding the metallic nanoparticle, λ is the wavelength of the absorbing radiation, ϵ_i is the imaginary dielectric constant of the metallic nanoparticle and ϵ_r is the real dielectric constant of the metallic nanoparticle. As indicated

by the equation, the LSPR spectrum and the location of the extinction maximum of noble metal nanoparticles will strongly depend on the nanoparticle's radius a , shape χ and material (ϵ_i and ϵ_r), and the nano-environment's dielectric constant (ϵ_m); and wavelength shifts in the extinction maximum of nanoparticles can be used to detect molecule-induced changes surrounding the nanoparticles. Therefore, there are several nanoparticle-based sensing mechanisms that enable the transduction of macromolecular or chemical-binding events into optical signals based on changes in the LSPR extinction or scattering intensity shifts in LSPR λ_{\max} , or both; these mechanisms are (i) resonant Rayleigh scattering from nanoparticle labels [2], (ii) nanoparticle aggregation [3], (iii) charge transfer interactions at nanoparticle surfaces and (iv) local refractive index changes [4].

Recently, several research groups have begun to develop optical biosensors and chemosensors based on the tunable LSPR properties of noble metal nanoparticles materials such as silver and gold [3, 4]. These extraordinary optical properties of the nanostructures mean that they can be applied as materials for surface-enhanced spectroscopy[5], plasmonic devices [6] and sensors [7]. It is now well established that optical excitation of the LSPR of silver and gold nanoparticles results in absorptions with extremely large molar extinction coefficients of around $3 \times 10^{11} \text{ M}^{-1}\text{cm}^{-1}$, resonant Rayleigh scattering with an efficiency equivalent to that of 10^6 fluorophors and strong enhancement of the local electromagnetic fields near the nanoparticle surface [1]. Furthermore, the peak extinction or resonant Rayleigh scattering wavelength, λ_{\max} , intensity, and line width of these LSPR spectra are strongly dependent on their size, shape, interparticle spacing, and local dielectric environment [1]. More interestingly, Van Duyne's group has shown that the LSPR spectrum of noble metal nanoparticles is very sensitive to adsorbate-induced changes in the dielectric constant of the surrounding nanoenvironment, which provides several improvements over existing array- or cluster-based techniques; the resonant Rayleigh scattering pattern of a single silver nanoparticle can be strongly differentiated when about 60 000 molecules (or 100 zmol) of 1-hexadecanethiol or less than 100 streptavidin molecules are adsorbed on its surface [2]. Raschke *et al.* have developed a method for biomolecular recognition using light scattering of a single gold nanoparticle functionalized with biotin [8]. Additional of streptavidin and subsequent specific binding events alter the dielectric environment of the nanoparticle, resulting in a spectral shift of the particle plasmon resonance. Spectral shifts as low as 2 meV could be detected as they used single nanoparticles as sensing counterparts. Using a detection method based on resonant Rayleigh light scattering of single nanoparticles has several advantages. (i) It is a non-labeling detection; no toxic, erosive, radioactive

or invasive materials are used, making them ideal platforms for *in vivo* quantification of chemical species and monitoring of dynamic processes inside biological cells. (ii) The limit of detection will be dramatically reduced leading to very high sensitivity being achieved. (iii) The volume of reactants is greatly reduced to reduce the cost of detection. (iv) Fast detection can be performed owing to low volume and low analyte molecule detection. (v) It provides a possibility to miniaturize the instrumentation. (vi) Single nanoparticle sensing platforms offer further advantages because they are readily implemented in multiplex detection schemes. By controlling the size, shape and chemical modification of individual nanoparticles, several sensing platforms can be fabricated in which each unique nanoparticle can be distinguished from others on the basis of the spectral location of its LSPR λ_{\max} . Several of these unique nanoparticles can then be incorporated into one device, allowing for the rapid, simultaneous, label-free detection of thousands of different chemical or biological species.

III. PARTICLE AGGREGATION

Nanoparticle aggregation induced by specific biomolecular interactions is one of the nanoparticle-based sensing mechanisms; it enables the transduction of biological/chemical binding events into optical signals based on the wavelength shifts. The sensing phenomenon induces a color change of the colloidal solution from red (free particles) to blue (aggregated particles) and it has been developed as simple colorimetric assays for the detection of DNA hybridization. For example, Mirkin *et al.* developed a colorimetric DNA hybridization assay using the spectral properties of gold nanoparticles [9]. In their experiments, gold nanoparticles were coated with single-stranded DNA oligonucleotides that aggregated in the presence of target oligonucleotides with a matching sequence as indicated by a color change of the sample from red to purple. The method also has potential applications in immunoassays. For detection of antigen-antibody interaction, Thanh *et al.* have quantified the level of antibodies on the basis of the aggregation of gold nanoparticles [10]. Gold nanoparticles coated with protein A were used to determine the level of anti-protein A. The rate of aggregation of the protein A-coated gold nanoparticles in the presence of anti-protein A was monitored by measuring the absorption of the gold colloid suspension at 620 nm. Their result showed that a LOD of 1 $\mu\text{g/ml}$ of anti-protein A was observed. Another sandwich immunoassay for detection of prostate specific antigen (PSA/ACT complex) based on AuNP aggregation using two probes was developed by Cao *et al.* [11] They showed that using two probes in a sandwich immunoassay can enhance the wavelength shifts and the sensitivity of the assay. When

a target antigen is bound to its gold-tagged primary antibody, the binding event will lead to the wavelength shift to the red area due to changing in dielectric constant of the medium surrounding environment. Moreover, if a gold-tagged secondary antibody is subsequently added, a considerable aggregation will be induced because of the fact that the polyclonal antibodies contain the entire antigen-specific antibody population; one antigen molecule can form a complex with several antibody molecules. The results showed that PSA/ACT complex could be detected at concentrations as low as 1 ng/ml.

IV. CATALYTIC PROPERTY

The use of AuNPs as catalytic probes for the growth of the particles is another beneficial feature for the biosensing purpose, where the bio-recognition event is translated into AuNP growth signal. The best well-known example is silver enlargement, also called as silver staining, has been well developed and widely applied in the biological detection [12]. Silver staining utilizes AuNPs as catalytic probes to transfer biorecognition into optical signal. However, although the silver staining method allows us to directly observe the immunoassay signals on a glass chip or a nitrocellulose strip by naked eyes or specific analytical equipment, the sensitivity is much lower than those enhanced by fluorescent, radioactive, and colorimetric assays. Recently, instead of silver staining, gold salt was utilized to enlarge immune AuNPs as an alternative strategy for the catalytic growth based detection. A platform has been developed using a mixture of HAuCl_4 and $\text{NH}_2\text{OH}\cdot\text{HCl}$ to enlarge AuNPs immobilized on the nitrocellulose strip to detect human immunoglobulin G (h-IgG) [12]. The detection limit approximately achieved 10 pg/ml and rivaled conventional fluorescent, radioactive, and enzyme-colorimetric methods. On this basis, Su *et al.* developed a novel detection platform by immobilizing gold immunoprobe on glass slide and the detection limit was lowered down to 0.1 pg/ml [13]. Due to the attractive potential, this research has been applied in the detection of DNA, proteins, and cells. However, most of the studies were carried out in solid phase. The detection of protein biomarker based on homogenous growth of Au nanocrystals in solution phase has been introduced by Cao *et al.* [14]. In the solution phase, the immuno-recognition event is translated into the gold nanoparticles growth signal which can be intuitively recognized by an unaided eye, or quantitatively measured by an UV/vis spectrophotometric analysis. This assay was highly sensitive, robust, simple, and it has great potential to detect other biological interactions. Therefore, it is a significant attempt to utilize those advantages to realize a homogenous detection of pathogen

cells such as *G. lamblia* cysts. In this study, the whole experiment took advantage of centrifuge filters for cell separation and collection. During the immunoassay, target pathogen cells were captured by antibody functionalized AuNPs, and then collected and separated by centrifuge filters. Those AuNPs remained on the cells were proportional to analytic pathogen cells and furthermore played a role of color developer. The quantitative detectable color development was derived from the catalytic growth of AuNPs. All the immunoassays were completed in a homogenous liquid phase; the results demonstrated that the catalytic enlargement of AuNPs was a fast, sensitive and reliable method that might be a promising method for analogous detection of other pathogens.

V. DNA BIOBARCODE

Since the invention of polymerase chain reaction (PCR) in 1985, it has been contributing a significant impact on the revolution of medical diagnostic systems. Although very sensitive and specific, PCR is often criticized for its complicated procedure, high cost, and high false positive rate arising from cross contaminations between samples. Furthermore, it still requires a day and experienced personnel to obtain results. Bio-barcode assays, proposed by Mirkin *et al.*, is the only approach for detection of DNA and protein that can obtain PCR-like sensitivity without the enzymatic amplification [15]. Typically, to detect DNA, the method relies on two-component oligonucleotide-modified gold nanoparticles (AuNPs) (one component is single-stranded DNA complementary to the target DNA; the other one is DNA barcode strands) and single-component oligonucleotide-modified magnetic microparticles (MMPs) (also complementary to the target DNA), and subsequent detection of amplified target DNA in the form of barcode DNA. To detect protein, the bio-barcode assay utilizes two types of particles: 1) a magnetic microparticle (MMP) functionalized with antibody (primary antibody) which is to capture and isolate the target analyte from the sample solution, and 2) another particle (AuNP, polystyrene or silica microparticle) anchored with secondary antibodies, which is specific to the same target, and double-stranded DNA [16]. Only one strand of the double-stranded DNA is covalently immobilized onto the secondary particle probe, and after the sandwiching immunoreaction, the complementary DNA strand can easily be released by increasing the temperature. It surrogates for the target of interest and is therefore called DNA bio-barcode. The surrogate DNA bio-barcode can subsequently be detected by PCR, DNA microarrays, colorimetric assays, or fluorophore-based assays. Unlike other conventional sandwich immunoassays, where the signal

intensity is limited by number of antigenic valence for specific binding of reporter-tagged antibody, each particle is functionalized with a multitude of DNA strands and thus many DNA barcodes are released for each positive binding event resulting in amplification of the assay.

VI. FRET

Fluorescence Resonance Energy Transfer (FRET), also known as Förster resonance energy transfer named after the German scientist Theodor Förster, is a phenomenon where energy can be transferred nonradiatively between two dyes, a donor and an acceptor [17]. The energy transfer occurs while the donor is in the excited state and based on classical dipole-dipole mechanisms and is extremely dependent on the donor – acceptor distance. A typical example of FRET-based application is molecular beacon probes. The molecular beacons are single-stranded oligonucleotide sequences that have a stem-and-loop structure. The loop contains a probe sequence that is complementary to a target DNA while the stem is formed by the annealing of complementary arm sequences that are located on either side of the probe sequence. A fluorophore and a quencher are covalently linked to the end of each arm of the stem structure. The molecular beacons do not fluoresce when the fluorophore and the quencher stay near together. However, if the loop sequence is hybridized to a target sequence, the molecular beacons will be stretched out. Consequently, the spontaneous conformational reorganization forces the stem hybrid to dissociate and the fluorophore and the quencher to move away from each other, restoring fluorescence brightly. Recently, it is reported that AuNPs could be used as the acceptor (quencher) for the energy transfer providing several significant benefits [18]: (i) Its quenching efficiency can reach up to 100 % for both for both quantum dot and fluorescent dye; (ii) It has long distance dependence (up to 40 nm); (iii) AuNPs can quench for several dyes of different energies simultaneously; (iv) There is no need to prepare a “stem and loop” structure like molecular beacon because the backbone of single-stranded DNA is very flexible and fluorescent dyes can reversibly adsorb on the surface of gold. This will give better quenching effect and better DNA-DNA hybridization; (v) Surface adsorption of DNA-fluorophore is much less dependent on temperature than DNA melting, this is somehow better than molecular beacon in term of S/N ratio for a real-time PCR reaction.

VII. CONCLUSIONS

AuNPs are playing important roles in bioanalytical systems because of their multifunctional possibilities. With

continued advances in microsystem integration technology, the AuNPs-based sensing platforms would become important bases in the diverse biosensing market.

REFERENCES

1. Haes AJ, Van Duyne RP (2004) A unified view of propagating and localized surface plasmon resonance biosensors. *Analytical and Bioanalytical Chemistry* 379:920
2. McFarland AD, Van Duyne RP (2003) Single silver nanoparticles as real-time optical sensors with zeptomole sensitivity. *Nano Letters* 3:1057
3. Storhoff JJ, Lazarides AA, Mucic RC et al (2000) What controls the optical properties of DNA-linked gold nanoparticle assemblies? *J Am Chem Soc* 122:4640
4. Nath N, Chilkoti A (2002) A colorimetric gold nanoparticle sensor to interrogate biomolecular interactions in real time on a surface. *Anal Chem* 74:504
5. Haynes CL, Van Duyne RP (2003) Plasmon-sampled surface-enhanced Raman excitation spectroscopy. *J Phys Chem B* 107:7426
6. Maier SA, Kik PG, Atwater HA et al (2003) Local detection of electromagnetic energy transport below the diffraction limit in metal nanoparticle plasmon waveguides. *Nature Materials* 2:229
7. Mucic RC, Storhoff JJ, Mirkin CA et al (1998) DNA-directed synthesis of binary nanoparticle network materials. *J Am Chem Soc* 120:12674
8. Raschke G, Kowarik S, Franzl T et al (2003) Biomolecular recognition based on single gold nanoparticle light scattering. *Nano Letters* 3:935
9. Storhoff JJ, Elghanian R, Mucic RC et al (1998) One-pot colorimetric differentiation of polynucleotides with single base imperfections using gold nanoparticle probes. *J Am Chem Soc* 120:1959
10. Thanh NTK, Rosenzweig Z (2002) Development of an aggregation-based immunoassay for anti-protein A using gold nanoparticles. *Anal Chem* 74:1624
11. Cao C, Sim SJ (2007) Preparation of highly stable oligo(ethylene glycol) derivatives-functionalized gold nanoparticles and their application in LSPR-Based detection of PSA/ACT complex. *Journal of Nanoscience and Nanotechnology* 7:3754
12. Ma ZF, Sui SF (2002) Naked-eye sensitive detection of immunoglobulin G by enlargement of nanoparticles in vitro. *Angewandte Chemie-International Edition* 41:2176
13. Su Y (2006) A strategy for immunoassay signal amplification using clusters of immunogold nanoparticles. *Appl Surf Sci* 253:1101
14. Cao C, Li X, Lee J et al (2009) Homogenous growth of gold nanocrystals for quantification of PSA protein biomarker. *Biosens Bioelectron* 24:1292
15. Nam JM, Stoeva SI, Mirkin CA (2004) Bio-bar-code-based DNA detection with PCR-like sensitivity. *J Am Chem Soc* 126:5932
16. Nam JM, Thaxton CS, Mirkin CA (2003) Nanoparticle-based bio-bar codes for the ultrasensitive detection of proteins. *Science* 301:1884
17. Du H, Strohsahl CM, Camera J et al (2005) Sensitivity and specificity of metal surface-immobilized "molecular beacon" biosensors. *J Am Chem Soc* 127:7932
18. Ray PC, Darbha GK, Ray A et al (2007) Gold nanoparticle based FRET for DNA detection. *Plasmonics* 2:173

A Total Integrated Biochip System for Detection of SNP in Cancer

Ivan R. Perch-Nielsen¹, Monica Brivio¹, Eva Schaeffer², Klaus S. Drese², Frederica Rampf²,
Dang Duong Bang³, Henrik Bruus¹, and Anders Wolff¹

¹ Dept. of Micro- and Nanotechnology, Technical University of Denmark, DTU Nanotech Bldg. 345 East, DK-2800, Kgs. Lyngby, Denmark

² Institut für Mikrotechnik Mainz GmbH, Carl-Zeiss-Str. 18-20, D-55129 Mainz, Germany

³ Lab. of App. Micro-Nanotechnology, Nat. Veterinary Institute, Technical University of Denmark (DTU Vet), Høghøjvej 2, DK-8200 Aarhus N, Denmark

Abstract— Cancer is a leading cause of death worldwide. Resistance of tumor cells to radiation and chemotherapy is the major obstacle in cancer treatment. The serious toxicity that follows the administration of certain drugs can be associated with Single Nucleotide Polymorphisms (SNPs) of genes involved in drug metabolism and can ultimately reduce the clinical efficacy of chemotherapy. The KRAS and TP53 genes are altered in many human tumors. K-RAS point mutation appear early in the tumorigenesis pathway and can therefore be used for early cancer detection. The functional inactivation of p53 by point mutation is a hallmark of many tumors. Importantly, most anticancer agents act by inducing apoptosis and, typically, p53-deficient tumors are more resistant to drug-induced apoptosis than those carrying wild-type p53. It is therefore important to analyze such SNPs and point mutation in cancer diagnosis and treatment. In this paper, we described a total integrated BIOLABCHIP namely SMART-BioMEMS for rapid detection and identification SNPs of Kirsten-RAS (K-ras) and TP53 genes in cancer. The SMART-BioMEMS system consist of different components: An optical readout system, disposable biochip; and a reusable actuators chip that can perform all the steps from sample preparation, DNA isolation and purification, PCR amplification, Enzymatic clean up, mini-sequencing and SNP detection. The prototype of the SmartBIOMEMS system designs, detail of different components and functions will be present and discusses. It is results of great cooperation in the FP6 EU project SMART-BioMEMS.

I. INTRODUCTION

Cancer is a leading cause of death worldwide. With a total of 58 million deaths worldwide in 2005, cancer accounts for 7.6 million (or 13%) of all deaths [1]. Resistance of tumor cells to radiation and chemotherapy is the major obstacle in cancer treatment. Another important limitation of chemotherapy is the inability to predict the response of the tumor, so the choice of the treatment is often empirical. Moreover, the serious toxicity that follows the administration of certain drugs can be associated with polymorphisms of genes involved in drug metabolism so called Single Nucleotide Polymorphisms (SNPs) can ultimately reduce the clinical efficacy of chemotherapy. SNPs are common (defined as > 1%) variations that occur in human DNA in terms of changes at a single base level. It

has been estimated that the human genome contains more than 10 million SNPs [2]. SNPs within a DNA coding sequence are of particular interest to researchers because they are likely to cause genetic disorders [3, 4] and to provide information on disease susceptibility and cancer predisposition [4].

II. MUTATIONS IN K-RAS and TP53 GENES AND CANCER

The *KRAS* and *TP53* genes are altered in many human tumors including those that are defined “major killers”. The K-RAS encodes for a protein which is a key regulatory component of signal transduction pathways that transmit growth stimulatory signals from cell surface receptors to intracellular targets [5]. Activating mutations of K-RAS leads to increase and unregulated cellular proliferation, inhibition of apoptosis, and malignant transformation [6-8]. Such mutations were found to appear early in the tumorigenesis pathway [9] and K-RAS mutation detection can therefore be used for early cancer diagnosis. Mutations in TP53 gene are associated with the loss of capability to protect from tumor development. The p53 protein is a transcription factor that binds DNA at specific sequences and exerts essential and non-redundant functions in DNA replication and repair in normal and tumor cells. The functional inactivation of p53 by point mutation is a hallmark of many tumors and, perhaps, the most common genetic alteration found in cancer. Importantly, most anticancer agents act by inducing apoptosis and, typically, p53-deficient tumors are more resistant to drug-induced apoptosis than those carrying wild-type p53. Thus the determination of the p53 status is likely to become a routine analysis that may help to predict the efficacy of cancer therapy.

III. DETECTION OF SINGLE BASE ALTERATIONS IN CANCER

The detection of SNP alterations plays a central role for clinical diagnostics and for the assessment of adequate treatments of many diseases [10]. DNA sequencing [11] is the most common detection method. Other approaches

include Polymerase Chain Reaction-single strand conformation polymorphism (PCR-SSCP) [12], chemical [13] or enzymatic [14] cleavage of mismatch, allele-specific PCR [15] and denaturing gradient gel electrophoresis (DGCE) [16]. All these methods have high accuracy of detection; however, they require expensive equipment as well as laborious sample preparation, amplification, and purification steps. They are therefore time consuming, expensive, and prone to human error. Fluorescence resonance energy transfer (FRET) detection, including TaqMan genotyping [17] and molecular beacons [18], are relatively new methods that avoid the use of gel electrophoresis and have successfully been applied to real-time mutation detection. However, widespread application of these methods is limited by the high costs since each SNP requires a separate assay.

IV. BIOCHIP TECHNOLOGY

The biochip technology has emerged as a powerful tool for parallel genetic analysis [19-21] and large-scale SNP genotyping [22-24]. A number of biochip-based approaches for detecting mutations have been proposed, as recently reviewed by Bi *et al.* [25]. Chip-based technologies can have high-throughput detection capabilities, especially when using high density hybridization microarrays. However, the development of a robust microarray-based method for genotyping at the resolution of single nucleotides is a challenge [26].

V. SELECTED GENOTYPING METHOD

To fulfill the requirement of point mutation and SNP detection we first selected the minisequencing genotyping method (fig. 1). This method consists of sample preparation, DNA amplification, enzymatic cleanup, minisequencing, hybridization and detection: Tumor cells are mixed with lysis buffer, the DNA is released and binds to magnetic beads. The beads with DNA are captured by magnetic forces and PCR inhibitors are removed by washing. The DNA is amplified by PCR using specific primers for each target. After PCR amplification, all remaining primers and nucleotides are removed by an enzymatic clean up. Minisequencing follows the clean up: Primers that anneal to their template sequences immediately adjacent to the mutant nucleotide positions are added. These primers are extended with a single labeled dideoxynucleoside triphosphates (single-nucleotide primer extension) using a DNA polymerase. Finally the primers, labeled in the minisequencing reaction, are hybridized to complementary DNA probes in a DNA array and the genotype is detected

by scanning the array [27, 28]. Such protocols are already applied for genotyping in clinical settings [27, 28], but they take several days to complete and are labor intensive. It is therefore common to collect samples from several patients and then only perform it once or twice per month which can give up to several weeks waiting time for the individual patient.

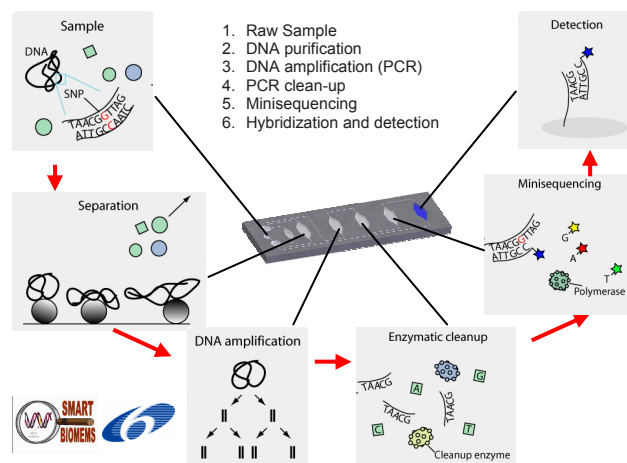


Fig. 1 Genotyping method by mini-sequencing (see text). Each step from DNA purification to hybridization and detection takes place in separate chambers on a disposable chip

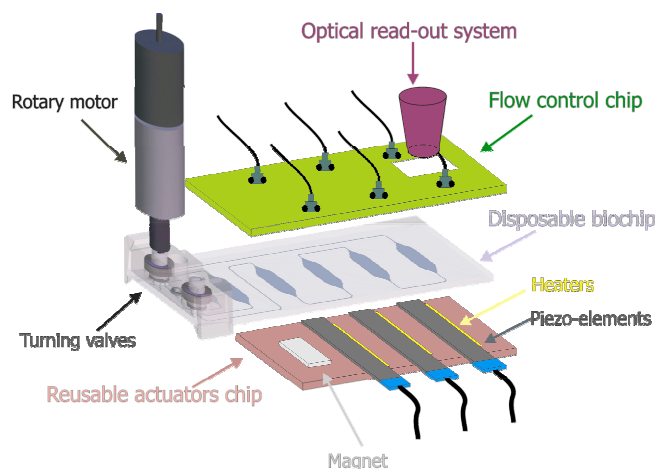


Fig. 2 Schematics of the SMART-BioMEMS system

VI. SMART-BioMEMS SYSTEM DESIGN

The total integrated SMART-BioMEMS system (fig 2) consists of two main components: 1) A disposable biochip and 2) a reusable actuator/control unit with e.g rotary motors for turning valves, a pneumatic flow control chip, a optical CCD based detection system, magnetic elements for

sample preparation and purification, and heaters for thermocycling.

VII. DEVELOPMENT OF INDIVIDUAL UNITS

Biochip with freeze-dried reagents. The injection-molded biochip is made of the polymer Topas™ with six different microchambers for sample preparation, PCR amplification, enzymatic clean up, minisequencing, and hybridization to a DNA array and detection. All the reagents (e.g. PCR mixture for PCR, enzymes for enzymatic clean-up etc.) are stored on the chip in a freeze-dried form in the respective chamber [29]. The biological genotyping protocol can therefore be performed by moving the sample from chamber to chamber. This greatly reduces the complexity of the microfluidic network, thereby simplifying both flow control and analytical procedure and are convenient for the user.

Flow control for sample preparation. Two rotary multi-position valves switch the fluidic system between the different channels used in sample injection and DNA purification.

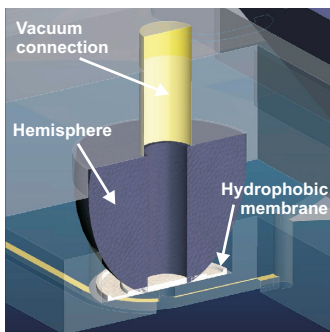
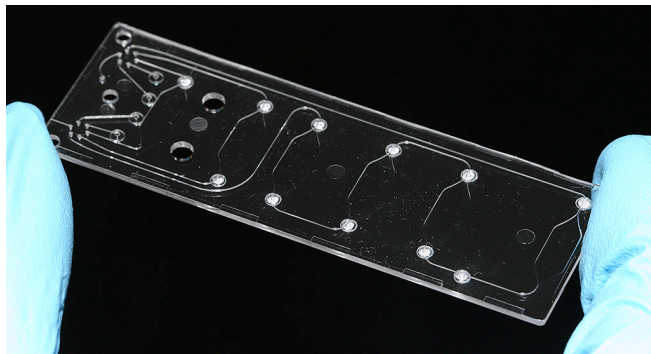


Fig. 3 A: Image of a injection molded biochip with 6 chambers. The hydrophobic Teflon membranes can be seen as white circles. B: Schematics of a hydrophobic membrane valve. The membrane is covering a air-outlet at the end of a chamber. By applying vacuum air will pass through the membrane, the pressure in the channel is lowered, and the sample is sucked into the chamber. When the sample has fully entered the chamber, it will reach the membrane which will wet and block

Flow control for the biological protocol. As described above the biological genotyping protocol is performed by moving the sample from chamber to chamber, using the reagents freeze-dried as ready to use in each respective chamber. It is therefore critical to have flow control which

can move a well defined sample volume between the six chambers. To ensure reliable operation, a passive fluidic control method was chosen. The movement of the sample is achieved by applying under-pressure to air-outlets covered by hydrophobic Teflon membranes, attached to the chip by thermal soldering (Fig 3). These membranes allow air to pass, but will block when wetted by the sample, i.e. they function as self-actuated valves. To move the sample between e.g. chamber 2 and 3, air is sucked from the air-outlet just at the end of chamber 3. Air will pass through the membrane, and the sample will follow. When the sample has fully entered the chamber, it will reach the membrane which will wet and block. This method is passive and ensures precise positional control of the sample, a thing that can be difficult to achieve by active monitoring and use of external valves.

The over- and under-pressure is provided by syringe pumps in the control unit (fig 4). Two rows of external valves direct the pressure to the desired air-outlets on chip.

Temperature control during PCR thermocycling, enzymatic cleanup, and minisequencing is achieved by means of active heaters and temperature sensors integrated in the platform underneath the chip, one heater for each chamber. A heat-sink under the heaters ensures fast cooling and that heat does not leak from one chamber to the other. The system utilizes resistive heating with integrated thermometers. Computer-controlled feedback ensures a stable temperature

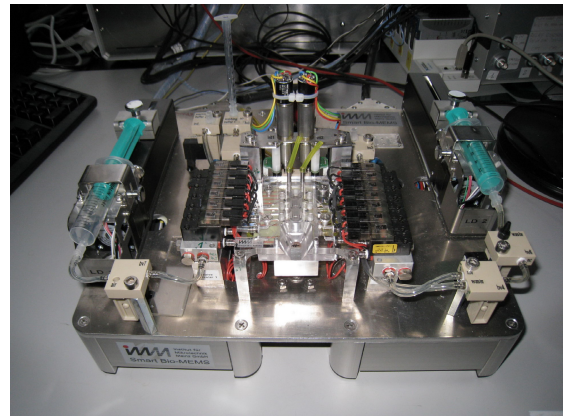


Fig. 4 Actuator/control unite for the SMART-BioMEMS system

VIII. SYSTEM INTEGRATION AND AUTOMATION

For system automation and integration we have made an actuation/control unit (fig. 4). To operate it the user will insert a biochip in the reader, place sample (with lysis buffer and magnetic beads) in the sample reservoir, and start the LabView© program SMART-BioControl™ which

automatically control the processes: The sample will be injected and magnetic elements capture beads with DNA. Rotary valve controls sample injection, the DNA washing step and addition of elution buffer. The sample, which now consist of purified DNA in elution buffer, will be moved into the chamber with reagents for the first reaction in the genotyping protocol (PCR) using the hydrophobic membrane valves. The over- and under-pressure is provided by syringe pumps in the control unite (fig 4). Two rows of externals valves direct the pressure to the desired air-outlets on chip. Individual heaters and temperature sensors under each chamber is used for temperature control and thermocycling. The unit can automatically move the sample from reaction chamber to chamber to progress the protocol. In the final chamber the labeled primers will be hybridized to a DNA array and the genotype can be read in the array reader.

IX. CONCLUSION

In this paper we report a total integrated BIOCHIP system for rapid detection and identification of SNPs in cancer. The system consists of a disposable biochip and a control/actuation unit that can realize the detection of SNPs and point mutations in K-ras and TP3 gene in an automated fashion. This means that the genotyping answer can be obtained for the individual patient in 4-5 hours compared to at present where the patient may have to wait up to several weeks since at the hospital samples from several patients are collected and the procedure only perform 1-2 times a month.

REFERENCES

1. <http://www.who.int/mediacentre/factsheets/fs297/en/index.html>.
2. Kruglyak, L. and D.A. Nickerson, *Variation is the spice of life*. Nature Genetics, 2001. **27**(3): p. 234-236.
3. Bernardino, A.L., et al., *Screening of SPINK1 mutations indicate further heterogeneity for chronic pancreatitis*. American Journal of Human Genetics, 2002. **71**(4): p. 480-480.
4. Bonadona, V. and C. Lasset, *Inherited predisposition to breast cancer: after the BRCA1 and BRCA2 genes, what next?* Bulletin Du Cancer, 2003. **90**(7): p. 587-594.
5. Hoffman, M., *GETTING A HANDLE ON RAS ACTIVITY*. Science, 1992. **255**(5041): p. 159-159.
6. Ward, R.L., et al., *Activation of the K-ras oncogene in colorectal neoplasms is associated with decreased apoptosis*. Cancer, 1997. **79**(6): p. 1106-1113.
7. Shirasawa, S., et al., *ALTERED GROWTH OF HUMAN COLON CANCER CELL-LINES DISRUPTED AT ACTIVATED KI-RAS*. Science, 1993. **260**(5104): p. 85-88.
8. Bos, J.L., *Ras Oncogenes in Human Cancer - a Review*. Cancer Research, 1989. **49**(17): p. 4682-4689.
9. Jacobson, D.R. and N.E. Mills, *A HIGHLY SENSITIVE ASSAY FOR MUTANT RAS GENES AND ITS APPLICATION TO THE STUDY OF PRESENTATION AND RELAPSE GENOTYPES IN ACUTE-LEUKEMIA*. Oncogene, 1994. **9**(2): p. 553-563.
10. Strachan, T.R., A. P., *Human Molecular Genetics*. third edition ed. 2004, London: Garland Science.
11. Losekoot, M., et al., *Denaturing Gradient Gel-Electrophoresis and Direct Sequencing of Pcr Amplified Genomic DNA - a Rapid and Reliable Diagnostic-Approach to Beta Thalassemia*. British Journal of Haematology, 1990. **76**(2): p. 269-274.
12. Orita, M., et al., *Rapid and Sensitive Detection of Point Mutations and DNA Polymorphisms Using the Polymerase Chain-Reaction*. Genomics, 1989. **5**(4): p. 874-879.
13. Cotton, R.G.H., N.R. Rodrigues, and R.D. Campbell, *Reactivity of Cytosine and Thymine in Single-Base-Pair Mismatches with Hydroxylamine and Osmium-Tetroxide and Its Application to the Study of Mutations*. Proceedings of the National Academy of Sciences of the United States of America, 1988. **85**(12): p. 4397-4401.
14. Giunta, C., et al., *P53 and Brca1 Mutation Detection Using the Enzyme Mismatch Cleavage (Emc) Method*. American Journal of Human Genetics, 1995. **57**(4): p. 342-342.
15. Bottema, C.D.K. and S.S. Sommer, *Pcr Amplification of Specific Alleles - Rapid Detection of Known Mutations and Polymorphisms*. Mutation Research, 1993. **288**(1): p. 93-102.
16. Finkelstein, J.E., et al., *Use of Denaturing Gradient Gel-Electrophoresis for Detection of Mutation and Prospective Diagnosis in Late Onset Ornithine Transcarbamylase Deficiency*. Genomics, 1990. **7**(2): p. 167-172.
17. Shi, M.M., et al., *High throughput genotyping for the detection of a single nucleotide polymorphism in NAD(P)H quinone oxidoreductase (DT diaphorase) using TaqMan probes*. Journal of Clinical Pathology-Molecular Pathology, 1999. **52**(5): p. 295-299.
18. Tyagi, S., D.P. Bratu, and F.R. Kramer, *Multicolor molecular beacons for allele discrimination*. Nature Biotechnology, 1998. **16**(1): p. 49-53.
19. Brown, P.O. and D. Botstein, *Exploring the new world of the genome with DNA microarrays*. Nature Genetics, 1999. **21**: p. 33-37.
20. Lockhart, D.J. and E.A. Winzeler, *Genomics, gene expression and DNA arrays*. Nature, 2000. **405**(6788): p. 827-836.
21. Southern, E., K. Mir, and M. Shchepinov, *Molecular interactions on microarrays*. Nature Genetics, 1999. **21**: p. 5-9.
22. Landegren, U., M. Nilsson, and P.Y. Kwok, *Reading bits of genetic information: Methods for single-nucleotide polymorphism analysis*. Genome Research, 1998. **8**(8): p. 769-776.
23. Wang, J., *From DNA biosensors to gene chips*. Nucleic Acids Research, 2000. **28**(16): p. 3011-3016.
24. Tillib, S.V. and A. Mirzabekov, *Advances in the analysis of DNA sequence variations using oligonucleotide microchip technology*. Current Opinion in Biotechnology, 2001. **12**(1): p. 53-58.
25. Bi, L.J., et al., *Biochips for detection of DNA mutations*. Current Analytical Chemistry, 2006. **2**(3): p. 323-330.
26. Syvanen, A.C., *Toward genome-wide SNP genotyping*. Nature Genetics, 2005. **37**: p. S5-S10.
27. Pastinen, T., et al., *Minisequencing: A specific tool for DNA analysis and diagnostics on oligonucleotide arrays*. Genome Research, 1997. **7**(6): p. 606-614.
28. Lovmar, L. and A. Syvanen, *Genotyping single-nucleotide polymorphisms by minisequencing using tag arrays*. Methods in Molecular Medicin, 2005. **114**: p. 79-92.
29. Brivio, M., et al., *A simple and efficient method for on-chip storage of reagents: Towards Lab-on-a-Chip system for point-of-care DNA diagnostics*. Proceedings of microTAS 2007, 2007. **1**: p. 59-61.

Author: Anders Wolff
 Institute: Technical University of Denmark
 Street: DTU Nanotech building 345east
 City: DK-2800 Kgs. Lyngby
 Country: Denmark
 Email: anders.wolff@nanotech.dtu.dk

Lab on a Chip Application in Life Sciences

N.T. Nguyen¹, Y. Sun², Y.C. Kwok², H.Y. Tan³, and W.K. Loke³

¹ School of Mechanical and Aerospace Engineering, Nanyang Technological University, Singapore 639798, Singapore

² National Institute of Education, Nanyang Technological University, Singapore 637616, Singapore

³ DSO National Laboratories, Singapore 118230, Singapore

Abstract— This paper reports examples of low-cost polymeric lab-on-a-chip (LOC) devices for life sciences, namely the detection of genetically modified organisms (GMOs) and the detection of insecticides in agriculture. As the first example, the paper presents a close-loop ferrofluid-driven LOC for rapid amplification and detection of GMOs. Polymerase chain reaction (PCR) sample was contained in a circular closed microchannel and driven by magnetic force generated by an external magnet through a small oil-based ferrofluid plug. Successful amplification of genetically modified soya and maize were achieved in less than 13 minutes. The LOC provides a cost saving and less time-consuming way to conduct preliminary screening of GMOs. As the second example, the paper reports a LOC for detection of organophosphorus insecticides for occupational hygiene in agriculture. Nerve agent sarin diluted in water was used to test the device concept. The sample was tested for trace levels of regenerated sarin using immobilised cholinesterase on the chip. Activity of immobilised cholinesterase was monitored by enzyme-assisted reaction of a substrate and reaction of the end-product with a chromophore. Resultant changes in chromophore-induced absorbance were recorded on the. Loss of enzyme activity obtained prior and after passage of the treated blood sample, as shown by a decrease in recorded absorbance values, indicates the presence of either free or regenerated nerve agent in the sample.

Keywords— Microfluidics, Lab on a chip, PCR, nerve agent.

I. INTRODUCTION

Global warming, deforestation, overutilization of natural resources are consequences of recent industrial and economic development. Future generations are at the receiving end of the irresponsibility of our generation. The concept of sustainable development involves the entire society including scientists and engineers, the environment and the economy to meet human needs while preserving the environment. With this concept, we can meet our present needs without compromising the living quality and the needs of future generations. To realize this concept, the essential needs of the world's poor should be met, while imposing limitations to the state of technology and social organization to protect the environment. Harmony between the environment, society and economy should be found.

The basic needs of living thing, including human being, are air, water and food. In contrast to other species on Earth,

human being carries out economic activities which require energy. To meet these basic needs and at the same time to protect the environment, technologies should provide and enforce clean energy, clean air, clean water and clean food. An most importantly, since the majority of the world population lives in poorer third-world countries. Making technologies available and accessible for poor nations is another key factor for the success of sustainable development. The higher living standard and the new economy created by sustainable development will also reduce the world population leading to less consumption of natural resources.

Lab on a chip technology can contribute to the development of low-cost techniques for clean energy, clean water and clean food in resource-poor setting. In this paper, we demonstrate the use of a low-cost polymeric technology for making lab on a chip for monitoring clean food and clean water. The same technology was applied to a lab-on-a-chip (LOC) for a detection concept based polymerase chain reaction (PCR). The LOC is able to distinguish different genetically modified organisms such as transgenic soybean and maize.

II. LOC FOR DETECTION OF GENETICALLY MODIFIED ORGANISMS

To meet the need on sustainable supply of food, genetically modified organisms (GMOs) with high yield and resistance against unfavorable environmental factors are one of the solution of sustainable development. GMOs have been approved for use in several countries [1]. Maize and soya are the most cultivated plants, which can be found in a wide range of products from the food industry. Polymerase chain reaction (PCR)-based detection is needed for the control and distribution of foods containing genetically modified organisms [2]. Lin et al. developed a molecular screening method based on multiplex-PCR of specific soya or maize sequences from plant DNA [3]. The PCR and the subsequent separation of the DNA samples are done in benchtop instruments. The whole detection protocol can take up a few hours or more. In resource-poor setting such as remote areas in developing countries, a lab for carrying out these tests is not available. Therefore, there is a need for developing a low-cost and fast instrument for PCR. The instrument

should be of small size and portable, so that it can be brought to and used in remote areas.

Miniaturization of LOC for PCR allows a small thermal capacity of the whole system and consequently a shorter cycle times on the order of a few minutes [4]. Microtechnologies allow the implementation of miniaturized PCR systems. In the recent years, a number of PCR devices have been reported in the literatures. These devices are based on two main concept: temporal and spatial [5]. With the temporal concept, the sample solution is kept in a small reaction chamber. Thermal cycling is realized by heating and cooling the reaction chamber repeatedly. The magnitude and the duration of each temperature cycle are determined by the requirements of the denaturing, annealing and extension processes of the to be amplified DNA. Conventional PCR systems are also based on this temporal concept. The integration of microheaters and temperature sensors into these small reaction chambers is expensive, while the cycle time is not significantly reduced by the temporal concept [6]. In spatial concept, the sample is pumped into a serpentine microfluidic channel and passes repeatedly through three spatially fixed temperature zones [7-12]. Since the temperature zones are fixed, there is no need for temporal control and thus the cycle time only depends on the thermal capacity of the sample and its flow rate. The only problem of this concept is the relatively long channel network which required a high pressure to sustain the flow. The high pressure may cause leaks and requires high-quality bonding technologies for the PCR device. Another drawback of the spatial concept with serpentine microchannels is the relatively large device footprint and the fixed number of cycles which is determined by the channel design.

As mentioned above, we intend to develop a reliable and low-cost protocol for rapid amplification of GMO. The protocol and the corresponding device should be suitable for the use in resource-poor setting of remote areas. We report here a novel close-loop magnetically-actuated microchip for rapid PCR. The PCR solution and a small oil-based ferrofluid fluid were contained in a circular loop on top of three temperature zones corresponding to the three required temperature cycles. An external permanent magnet induces a magnetic force on the ferrofluid plug which works as a piston to push the PCR sample along the channel. Since the loop is placed on the three temperature zones, the sample will experience the same thermal cycle as in traditional temporal concept or in spatial concept with serpentine microchannel. This concept combines the flexibility in cycle number of the conventional temporal concept and the short thermal cycle of the spatial concept. Furthermore, the concept allows a simple chip design with a small footprint, which allows a low-cost mass production of the device. The low driving pressure associated with pumping technique

using the ferrofluid plug leads to lower energy consumption and low cost due to the lower requirement for bonding quality of the chip.

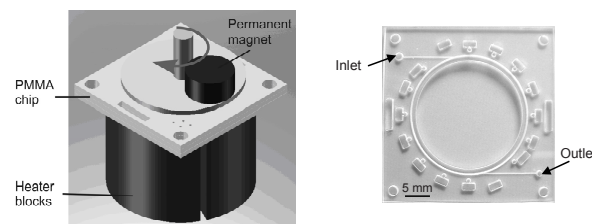


Fig. 1 Schematic concept of the T-junction with integrated microheater and temperature sensor

Figure 1 shows the basic concept of our PCR system. The LOC was made of two pieces of PMMA. The channel network was fabricated by a CO₂ laser system [13]. The microfluidic network consists of a deep close-loop circular channel for PCR reaction and two shallow straight channels tangent to the circle for sample injection and collection. The device was then sealed by a cover plate under a pressure of 20 kPa at 165 °C for 30 minutes. The PMMA device measures 30 mm × 30 mm. With a diameter of 20 mm, the circular loop was 62.8 mm long, 900 μm wide and 400 μm deep. The corresponding length of each temperature zone was approximately 21 mm. To maintain homogenous temperature distribution in each zone and to reduce heat losses, isolating thermal gaps were machined around the circular chamber. Access holes were cut into the substrate in the same machining process. Teflon tubing works as the fluidic interconnects between the chip and the external system.

The heating system consists of three copper blocks, arranged in a cylinder corresponding to the microchannel loop on the chip. Each copper block is 55 mm high and 10 mm thick. Heating cartridges are inserted into the heater blocks. The cartridges are controlled by three separate external temperature controller. The temperature of each heater block can be controlled between 25 °C and 150 °C. Each copper block is separated to its neighbors by small air gaps to ensure the temperature steps between the temperature zones.

A cylindrical neodymium magnet (15 mm high and 10 mm in diameter) coupled with a home-made stepper motor was mounted on top of the circular microchannel. Both the rotation speed and number of rotation cycles of the magnet were programmable. The magnet induces the movement of the ferrofluid plug inside the loop, allowing pumping in this closed microchannel. The circular arrangement of the three zones allows the real implementation of the sequence of denaturation, annealing and extension instead of denaturation, extension and annealing in the previous serpentine-channel system. The correct sequence prevents the denatured single-stranded DNA to re-hybridise in the extension zone. Thus,

amplification efficiency can be improved significantly with the circular configuration.

The PCR system described above was used to amplify specific soya and maize sequences from plant DNA. Certified reference Roundup Ready soybeans and Bt-176 maize materials were purchased from Sigma (MO, USA). These were freeze-dried powders with 5% GMO/non-GMO (w/w) soya and maize. The soybean and maize DNA were extracted from 100 mg of each sample using Wizard genetic DNA purification kit (Promega, WI, USA). The 172-bp 35S-promoter sequence is specific for the detection of genetic modifications in soybeans. The 118-bp lectin gene LE1 serves as a soybean control and is detectable in both transgenic and conventional soybeans. The 211-bp cryIA gene is for the specific identification of transgenic maize. The 226-bp invertase control gene serves as maize control. The details of primers were described elsewhere [14]. The 9 μL reaction mixtures contained 10 mM Tris-HCl (pH 8.3), 2 \times BSA (0.5 $\mu\text{g}/\mu\text{L}$), 50 mM KCl, 1.5 mM MgCl₂, 200 μM of each dNTP, 1 μM of each primer and 0.025 U/ μL Taq DNA polymerase. 1 μL different DNA were added separately as PCR template.

The protocol starts with the setting of the temperatures for the respective denaturation, annealing and extension zones at 95 $^{\circ}\text{C}$, 62 $^{\circ}\text{C}$ and 72 $^{\circ}\text{C}$ [14]. Next, the microchip was potioned and secured on top of the the heating blocks. Subsequently, the PCR mixture was injected using a glass syringe (Hamilton, NV, USA) through Teflon tube (Cole Parmer, Illinois, USA) fitted to the chip inlet hole. After the channel was completely filled, a small portion (2 μL) of ferrofluid (Ferrotec, CA, USA) was injected through the same inlet port. Ferrofluid is a stable colloidal suspension of sub-domain magnetic particles in a carrier fluid which can be moved through microchannels and adopt any geometry. The carrier liquid is synthetic ester oil, which is immiscible with the aqueous PCR reaction mixture. [15].

The speed of the stepper motor and of the external permanent magnet was controlled by a microcontrol (Basic24X). As the motor is switched on, the ferrofluid plug immediately moved with the rotating magnet. PCR reaction mixture was pushed around the circular channel and flowed through the three temperature zones continuously. The four DNA fragments were amplified subsequently using the PCR microchip. The magnet speed was kept constant at 2.3 mm/s, and 25 cycles were completed within 13 mins. The time was greatly reduced compared to almost 2 hours when using conventional thermal cycler. Subsequent to each run, the microchip was washed by DI water and negative control of PCR was done to make sure that there was no carryover. The amplified DNA samples were analyzed using a 1.2% crosslinked agarose gel (Sigma Chemical Co, MO, USA) stained with Ethidium Bromide (EtBr) (Sigma Chmeical

Co, MO, USA). 0.5 μg of 100 bp DNA ladder (500 $\mu\text{g}/\text{ml}$) was run together with PCR products.

The amplification products were subsequently collected from the chip and separated using gel electrophoresis. Figure 2 shows the UV image of the amplicons. It can be seen that all the four genes were successfully amplified. The products with different length were clearly distinguished in the gel from each other. As the 172 bp and 211 bp amplicons appeared only in 5% transgenic soybean and maize samples, fluorescent intensities of these two bands were much less than those for the 118 bp and 226 bp amplicons that were detectable in both transgenic and conventional samples. The results show that PCR products obtained by the ferrofluid-driven PCR microchip faithfully reflected the initial number of genome copies. To improve sample throughput, a series of concentric circles can be designed on one microchip. As the dimension of microchannel is small compared to the magnet, one magnet is adequate to drive PCR reaction mixtures in all the microchannels. For more efficient and convenient product detection, direct coupling of the device to sensitive analytical systems is feasible, and online fluorescence detection by integrating a light source and a detector with the microchip is under investigation.

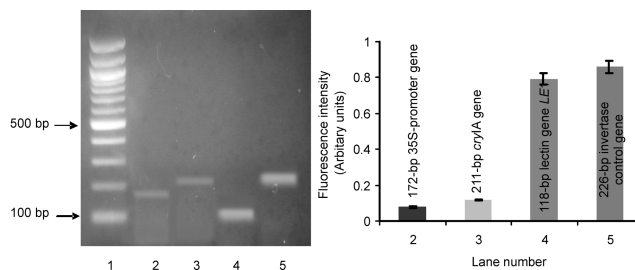


Fig. 2 UV image and relative fluorescence intensities of amplified soybean and maize samples (Lane 1: 100 bp DNA ladder. Lane 2: 172-bp 35S-promoter gene for genetic modified soybeans. Lane 3: 211-bp cryIA gene for transgenic maize samples. Lane 4: 118-bp lectin gene LE1, detectable in transgenic as well as in conventional soybeans. Lane 5: 226-bp invertase control gene, detectable in transgenic as well as in conventional maize)

III. LOC FOR DETECTION OF ORGANOPHOSPHORUS AGENTS

In countries with heavy agricultural activities, the risk of leaking insecticides into ground water is very high. Therefore, there is a need for detecting insecticides. The trace amount of this nerve agent could be found in blood of people working on the field or in contaminated water. We used sarin, a typical organophosphorus nerve agent, to test the LOC [16]. A PMMA microchip was designed and fabricated and was capable for detecting trace amounts of sarin present in a small sample volume. The detection concept is based on the inhibition reaction between the nerve agent and an enzyme. The enzyme activity was tested by hydrolysis of a

substrate. The extent of the hydrolysis reaction was measured with a chromophore.

The design of the LOC device is shown in Figure 3. The chip measures 79 mm×37.5 mm and is made of three PMMA layers. The main layer contains one side the micro-channel structures, the herring-bone patterns, the rectangular pillars and the guides for the optical fibres. The herring-bone structures in the inhibition reactor as shown in Figure 3(d) is machined on the other side of the main layer. The access holes and the opening for packing the filtration beads as depicted in Figure 3(c) and 3(f) were machined in the cover layer. The bottom layer holds the glass piece for immobilised enzyme. The three PMMA layers were bonded using the low-pressure, high temperature thermal bonding process. After bonding, the PMMA layers, the filtration beads (Merck, Darmstadt, Germany) with diameters ranging from 63 µm to 200 µm were packed into the filter chamber (Figure 3(c)) through the opening in the cover layer. The filter chamber was subsequently sealed by an adhesive (Araldite, Huntsman Advanced Materials, Utah, USA) with a PMMA sheet, Figure 3(f). Immobilization of AChE was done on a glass slide (Fisher Scientific, Pittsburg, PA, thickness of 0.1 mm) were cut into pieces measuring 15 mm×7 mm).

Three different sets of experiments were designed to assess the effectiveness of the different stages of the LOC device. In the first experiment, the inhibition reactor (Figure 3(d)) was tested with blood sample prepared outside the LOC device, bypassing the nerve gas regeneration reactor, lysis reactor and filter chamber. In the second experiment, the filter chamber and the inhibition reactor were then tested, bypassing the nerve agent regeneration reactor and the lysis reactor. In the final experiment, the whole system was tested with whole blood spiked with sarin as the input sample.

The test starts with pumping the spiked whole blood sample, KF and SAS through inlets 1, 2 and 3, respectively. As the volume ratio between spiked blood, KF and SAS is to be kept at approximately 2:9:14, we used syringes of different volumes for the respective reagents; i.e. 1-ml syringe for spiked blood, 5-ml syringe for KF and 10-ml syringe for SAS. The flow rate of the pump was set based on the 5-ml syringe as reference. For checking the effect of the residence time and the corresponding inhibition time the flow rates at inlets 1, 2, and 3 were set at 48 µl/min (3 µl/min spiked blood, 15 µl/min KF and 30 µl/min SAS) and 22.4 µl/min (1.4 µl/min spiked blood, 7 µl/min KF, and 14 µl/min SAS). Three sets of experiments were conducted to assure the repeatability of the test. The residence times were approximately 25 minutes and 65 minutes, respectively.

After the inhibition reaction, the measurement of the absorbance follows the same protocol of the first experiment.

The test of the whole LOC device in experiment 3 shows that approximately only about 5% of the enzyme was inhibited at a total sample flow rate of 48µl/min and a corresponding total residence time of 25 minutes. At this flow rate, the residence time in the regeneration reactor is about 1.5 minutes, while the protocol for the preparation outside the LOC required 3 minutes for the regeneration. Since the conditions for the filtering stage and the immobilization stage were the same as in experiments 1 and 2, the reason may be due to inefficient mixing in the first two stages or the insufficient residence time for the regeneration reaction. Fifteen measurement with a slower total sample flow rate of 22.4 µl/min and a corresponding total residence time of 65 minutes supports this hypothesis. The inhibition rate of the enzyme was increased to about 43 %.

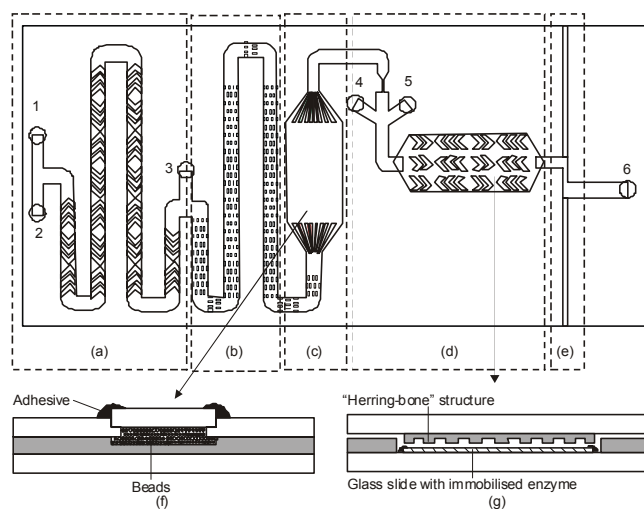


Fig. 3 Design of the lab on a chip for detection of nerve agent in blood: (a) nerve gas regeneration reactor; (b) cell lysis and filtering; (c) removal of fluoride ions; (d) inhibition reactor; (e) optical detection

Figure 4 shows the remaining enzyme activities measured in all three experiments. Despite the different levels of inhibition, all experiments show the successful detection of sarin with respect to a drop in absorbance. Experiment 2 shows clearly that the sample cleanup absorbent packed in the device was effective in removing the Fluoride ions, and more than 50% of the immobilized enzyme was inhibited. The results show that on-chip sample preparation was even better than the conventional process outside the LOC device.

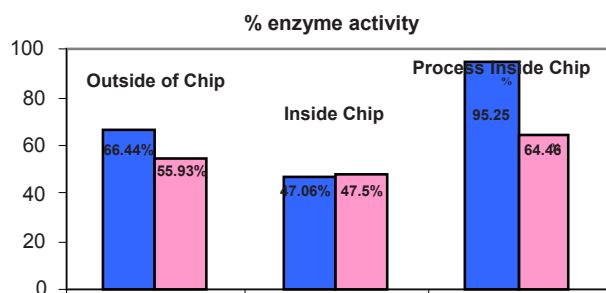


Fig. 4 Comparison of the % enzyme remained on chip for regeneration process taken place outside microchip (by passing the mixture through manifold and microchip) & regeneration process taking place within chip

IV. CONCLUSIONS

We have demonstrated two examples of low-cost polymeric LOCs contributing to sustainable development. As the first example, we demonstrated a close-loop magnetically-actuated microchip for rapid PCR amplification of GMO samples. Actuation of PCR mixtures was realized by a single button-sized external magnet through ferrofluid plugs inside the microchannels. Successful amplification of genetically modified soya and maize were achieved in less than 13 mins. This PCR microchip combines advantages of cycling flexibility and quick temperature transitions associated with two existing microchip PCR techniques, and it provides a cost saving and less time-consuming way to conduct preliminary screening of GMOs. As a second example, we report the design, fabrication and test of a LOC device for the detection of regenerated nerve agent in human blood samples. The device presented here can be extended to detection of organophosphorus insecticides. Thus, the device is suitable for other applications in occupational hygiene in agriculture.

ACKNOWLEDGMENT

The authors would like to thank the Agency of Science, Technology and Research (A*STAR) and Defence Science & Technology Agency (DSTA), Singapore for their financial support (grant number 08/1/50/19/590 "Screen-Printed Microfluidic Platform with Pneumatic Micropumps and Microvalves for Synchronized Regeneration and Detection of Nerve Agent in Human Blood Samples").

REFERENCES

- Alary R, Serin A, Maury D, Jouira HB, Sirven JP, Gautier MF, Joudrier P (2002) Comparison of simplex and duplex real-time PCR for the quantification of GMO in maize and soybean. *Food Control*, Vol. 13, 235-244.
- Lin HY, Chiueh LC, Shih DYC (2000) Detection of Genetically Modified Soybeans and Maize by the Polymerase Chain Reaction Method. *Journal of Food and Drug Analysis*, Vol. 8, 200-207.
- Forte VT, Pinto AD, Martino C, Tantillo GM, Grasso G, Schena FP (2005) A general multiplex-PCR assay for the general detection of genetically modified soya and maize. *Food Control*, Vol. 16, 535-539.
- Zhang CS, Xu JL, Ma WL, Zheng WL (2006) *Biotechnology Advances*, Vol. 24, 243-284.
- Nguyen NT, Wereley ST (2006) *Fundamentals and Applications of Microfluidics* 457.
- Lee DS, Park SH, Chung KH, Yoon TH, Kim SJ, Kim K, Kim YT (2004) Bulk-micromachined submicroliter-volume PCR chip with very rapid thermal response and low power consumption. *Lab Chip*, Vol. 4, 401-407.
- Obeid PJ, Christopoulos TK, Crabtree HJ, Backhouse CJ (2003) Microfabricated device for DNA and RNA amplification by continuous-flow polymerase chain reaction and reverse transcription-polymerase chain reaction with cycle number selection. *Anal. Chem.*, Vol. 75, 288-295.
- Curcio M and Roeraade J (2003) Continuous segmented-flow polymerase chain reaction for high-throughput miniaturized DNA amplification. *Anal. Chem.*, Vol. 75, 1-7.
- Belgrader P, Elkin CJ, Brown SB, Nasarabadi SN, Langlois RG, Milanovich FP (2003) A reusable flow-through polymerase chain reaction instrument for the continuous monitoring of infectious biological agents. *Anal. Chem.*, Vol. 75, 3446-3450.
- Chou CF, Changrani R, Roberts P, Sadler D, Burdon J, Zenhausern F (2002) A miniaturized cyclic PCR device - Modeling and experiments. *Microelectro. Eng.*, Vol. 61, 921-925.
- Chou HP, Unger MA, Quake SR (2001) A microfabricated rotary pump. *Biomed. Microdev.*, Vol. 3, 323-330.
- Sun Y, M.V.D S, Kwok YC, Nguyen NT (2008) Continuous flow polymerase chain reaction using a hybrid PMMA-PC microchip with improved heat tolerance. *Sens. Actuators B*, Vol. 130, 836-841.
- Sun Y, Kwok YC, Nguyen NT (2006) Low-pressure, high-temperature thermal bonding of polymeric microfluidic devices and their applications for electrophoretic separation. *J. Micromech. Microeng.* Vol. 16, 1681-1688.
- Jankiewicz A, Broll H, Zagon J (1999) The official method for the detection of genetically modified soybeans (German Food Act LMBG §35): A semi-quantitative study of sensitivity limits with glyphosate-tolerant soybeans (Roundup Ready) and insect-resistant Bt maize Maximized. *Eur. Food Res. Technol.*, Vol. 209, 77-82.
- Sun Y, Kwok YC, Nguyen NT (2007) A circular ferrofluid driven microchip for rapid polymerase chain reaction. *Lab Chip*, Vol. 7, 1012-1017.
- S. Y. Tan, W. K. Loke, Y. T. Tan, N.T. Nguyen (2008) A Lab on a Chip for Detection of Nerve Agent Sarin in Blood. *Lab Chip*, Vol. 8, 885-891.

Author: Nam-Trung Nguyen
 Institute: Nanyang Technological University
 Street: 50 Nanyang Avenue
 City: Singapore
 Country: Singapore
 Email: mntnguyen@ntu.edu.sg

A Lab-on-Chip for Separating and Focusing Bioparticles via Dielectrophoresis

Ngoc-Duy Dinh¹ and Cheng-Hsien Liu²

¹ Institute of Nanoengineering and Microsystem, National Tsing Hua University, Hsinchu, Taiwan 300, ROC

² Department of Power Mechanical Engineering, National Tsing Hua University, Hsinchu, Taiwan 300, ROC

Abstract— Cell sorting or cell separation and focus are an important stage in biotechnology and biomedical processing which to extract or analytic form a mixture complex and optical detect application. We present a microsystem lab chip with high throughput continuous separation cell and particle characterization and focus via dielectrophoresis (DEP). The particles are focus of hydrodynamic force by the design three inlets and will be deflected to separation and focus by control hydrodynamic drag and dielectrophoresis force. We design two electrode systems are separation electrode system and focus electrode system. The experiments are demonstrated with polystyrene (PS) beads 8 μm , 25 μm and HepG2 cells (Human Liver cells) in suspension DEP buffer solution. Under a voltage 10 V peak-peak and frequency 100 kHz suitable, different characteristic particles have different DEP force. Thus, the different distances of deflections that mean sample are separated. Then, the separated particle is focused for collection or optical detection application.

Keywords— Dielectrophoresis, Cell Separation, Cell Sorting, Cell Focus and Microfluidics.

I. INTRODUCTION

Dielectrophoresis (DEP) is a most commonly used techniques for manipulating cells or bioparticles in microfluidics devices. DEP has been known as powerful tool for cell separation because of its good cell selectivity. Presently, the published dielectrophoresis cell separation tries to separation different size of particles (three size beads) [1] or different characteristic (yeast live and dead) [2]. The focus bioparticles is presented by C-H Hsu [3]. We demonstrate a new device for separating high throughput and focus particles for detecting application. The experiment shows that the characteristic particles dominated the size of particles in dielectrophoresis effect. We mix beads 8 μm , 25 μm and HepG2 cell (around 10 μm). The cells deflected from mixture by different characterizing their electrical properties and we can separate HepG2 from sample. Previous publish presented separation different size of beads as 4 and 6 μm [4]. The ability deflect of electrical properties particle is over stronger than size of particle. Thus, we collected beads 8 μm , 25 μm in an outlet. Chip is designed operation show in Fig.1. It has three inlets (one for sample inlet, two others for DEP buffer) and three outlets (one for waste solution, one

for cell collection and one for beads). The electrode array is designed with 45° angle and it includes a system for separation and a for focus particles shown as figure 1.

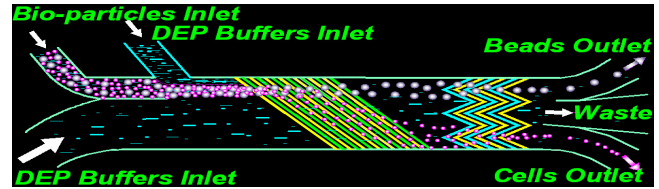


Fig. 1 The principle design

II. MATERIAL AND METHOD

The ability separation depends on hydrodynamic drag and DEP force shown as Fig2. The DEP depends on radius particles and polarizable particles in the solution under non-uniform electric fields. The time-averaged DEP force, F_{DEP} , acting on a spherical particle of radius r suspended in a medium of relative permittivity ϵ_m is given by:

$$F_{\text{DEP}} = 2\pi r^3 \epsilon_m \text{Re}[f_{\text{CM}}(\omega)] \nabla E_{\text{rms}}^2 \quad (1)$$

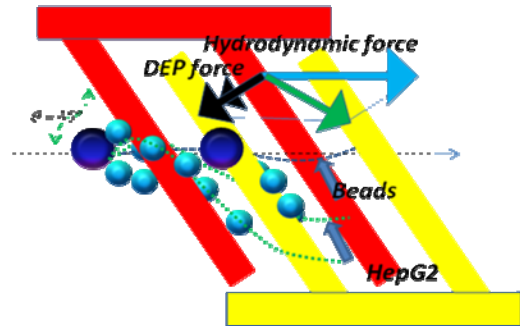


Fig. 2 The principle operation

We use CFD-ACE+ (CFD Research Corp., Huntsville, AL) for numerical simulation and use MEMS fabrication technique to fabricate the chip. The figure 3 shows 3D electric field of separation electrode system. The figure 4 shows the distribution electric field at three different positions 250 micromet, 375 and 75 micromet. Figure 5 shown as electric filed of focus electrode system.

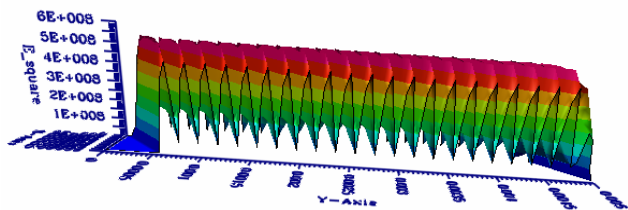


Fig. 3 3D Electric field of separation electrode system

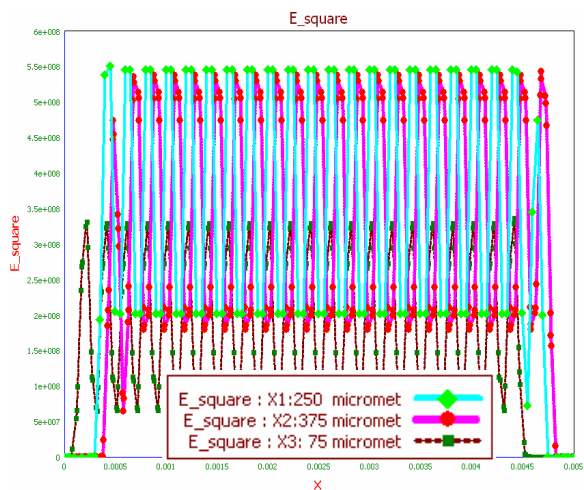


Fig. 4 The distribution Electric field at three positions X-axis

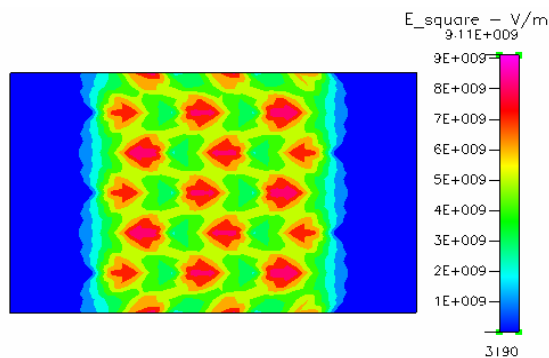


Fig. 5 2D Electric field of separation electrode system

The microfabrication process used 0.7-mm-thick Borofloat™ glass slides and the polydimethylsiloxane (PDMS) mold as the primary construction materials, along with metal evaporation and glass-to-PDMS bonding shown as the first, 3000Å titanium (Ti) is evaporated onto the glass wafer through an E-Gun evaporation process as shown in fig step1. The photo resistance, AZ 6112, is then spun onto the substrate and then patterned via a photo-lithography process by Mask#1. The Ti layer on the glass wafer is

etched by dipping in the Ti etching solution to form the bottom electrode fig step2. The negative photo-resistance, SU-8, is spun onto another silicon substrate as the micro-channel mold and then followed by another photo-lithography process via Mask#2 to define the micro-channel structure of 50 μm in height as fig step 3&4. To improve the hydrophilic of PDMS, we treat it with the O₂ plasma process. Finally, we drilled holes into the PDMS for reagent injection and sample extraction and then bonded together with the glass substrate, as shown in Fig step 5.

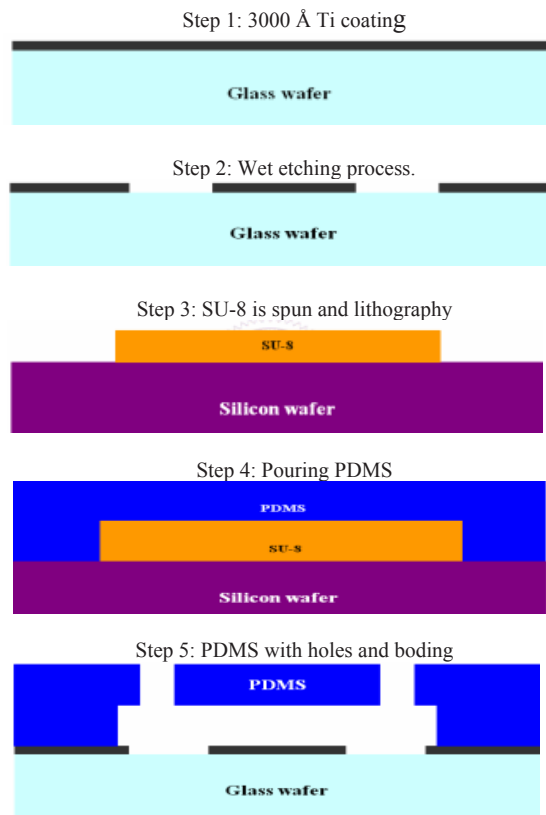


Fig. 6 The fabrication process

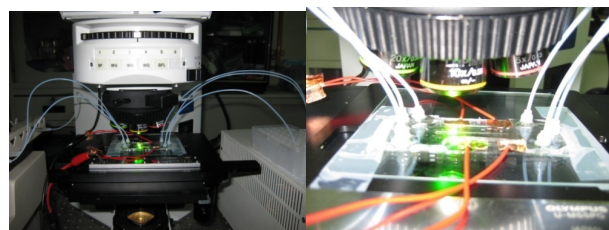


Fig. 7 Experiment setup on chip

For experiment shown as fig. 7, we used a 10-Vp-p 100-kHz sinusoidal voltage from a function generator (33120A, Agilent) to create the 1a DEP force acting on the particles,

and we used a syringe pumps (WPI, SP2301W)) to provide controlled flow through the microchannel. A gastight glass syringe (Hamilton, USA) minimized the variation in flow velocity.

III. RESULT AND DISCUSSION

The experiment with HepG2 cells (around 10 μm) and micro beads 8 μm and 25 μm are demonstrated. The sample mixture from above is put in a syringe 1 μl, DEP buffer in a syringe 1 μm and 3 μm. The figure 8a, b, c shows the deflection of HepG2 cell from the mixture.

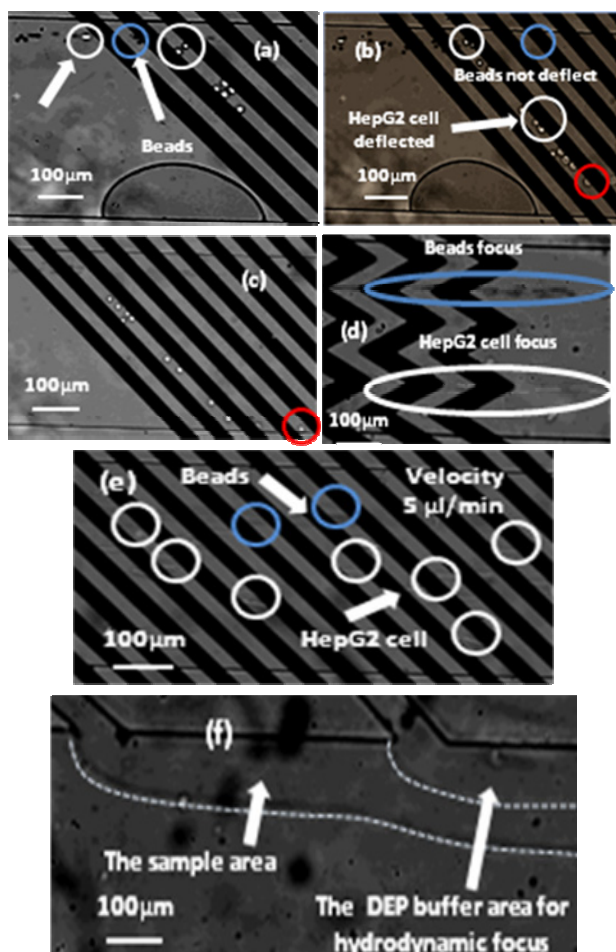


Fig. 8 Schematic illustration of the experiment with HepG2 cell and Beads, (a), (b), (c) show cell deflection from sample. Fig (d) shows the focusing of cell and beads. (e) Separation with high velocity. (f) Area hydro-dynamic focus

After across over the separation electrode system, it is focused by focus electrode system for optical detection application as fig 8d. The velocity we use 2.5μl/min. To

increasing high throughput, we work on 5 μl/min and ability deflection shown as fig 8e. With high velocity, we can overcome previous devices that published 4 μl/min [5]. We used hydrodynamic for focusing particles inlet before to electrode separation. The fig 8f shows the area sample in experiment 2.5 μl/min velocity.

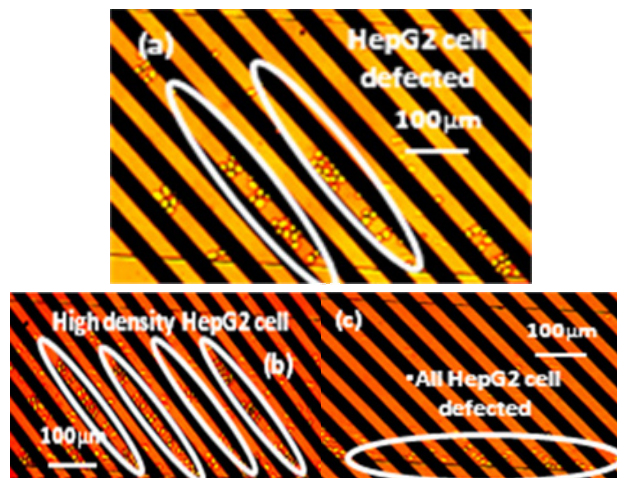


Fig. 9 a, b, c shown as high cell density separation

The ability deflection is important to separating. I decided high throughput inlet. There are several of reasons as voltage, frequency velocity but a factor mostly important that is the angle electrode. Therefore, we decrease the angle electrode in minimum suitable. Otherwise, we designed an electrode array to improve ability separation, cells will be deflected at next electrode. The figure 9b shows separation many electrodes in the same times so all of cells deflected to right side microchannel.

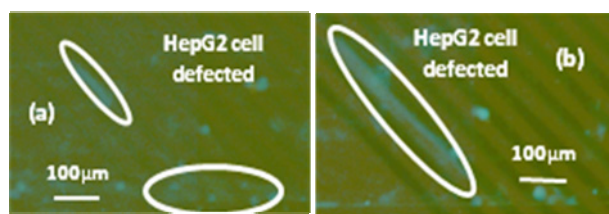


Fig. 10a, b shown as fluorescence image of cell separation

We demonstrated a separation with label HepG2 cells by Fluorescent dyes. The blue color show that the cell deflected.

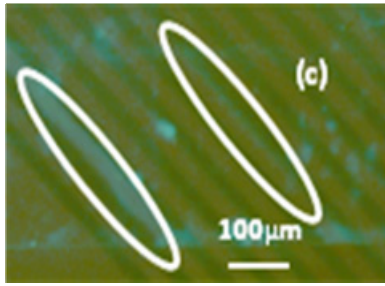


Fig. 10 c shown as fluorescence image of cell separation

Cell will be deflected on next electrode. The color fig 10c shows the cell there.

We designed a new chip high throughput separation. However, the fluorescent experiment should do more to get the better result. Chip will be improved to separating different sizes of cells. In the future, we do experiment try to separating difference sizes and different characteristic particles on a chip with high throughput.

IV. CONCLUSIONS

We designed and fabricated successful a microsystem lab chip for high throughput separation and focus bioparticle via dielectrophoresis force. The experiment demonstrated the ability separation of electric properties particle dominant the deflection of different sizes of particle or the DEP force stronger than with HepG2 cells under a frequency suitable. Compare with present devices we can separation with a higher than velocity $5 \mu\text{m}/\text{min}$. The electrode array increases the deflection of particle. With high velocity or hydrodynamic force larger, the particle will be deflected in next electrode and next electrode.

ACKNOWLEDGMENT

This research was supported by the National Science Council under grant NSC-93-2218-E-007-021 and the Nano-technology Research Program of University System of Taiwan, R.O.C.

I would like to thank professor Liu support for fabrication and Ling Yi, Meng-Yen for cells and experiment and my lab mate (Microsystem and Control Lab).

REFERENCES

1. Ki-Ho Han et al. (2009) Lateral displacement as a function of particle size using a piecewise curved planar interdigitated electrode array. *Lab Chip*, 2009, **9**, 2958-2964 DOI: 10.1039/b909753h
2. M. D. Vahey and J. Voldman (2009) High-throughput cell and particle characterization using isodielectric separation. *Anal. Chem.*, 2009, **81** (7), pp 2446–2453
3. Chia-Hsien Hsu et al (2008) Microvortex for focusing, guiding and sorting of particles. *Lab Chip*, 2008, **8**, 2128-2134 DOI: 10.1039/b813434k
4. Jason G. Kralj et al. (2006) Continuous dielectrophoretic size-based particle sorting. *Anal. Chem.*, 2006, **78** (14), pp 5019–5025
5. M. D. Vahey and J. Voldman (2009) High-throughput cell and particle characterization using isodielectric separation. *Anal. Chem.*, 2009, **81** (7), pp 2446–2455

Author: Ngoc-Duy Dinh
 Institute: Nanoengineering and Microsystem, National Tsing Hua University, Taiwan, ROC
 Street: No. 101, Section 2, Kuang-Fu Road
 City: Hsinchu
 Country: Taiwan 30013, R.O.C.
 Email: g9735581@oz.nthu.edu.tw

Nanotechnology at SHTP LABS in Vietnam

Khe Nguyen¹ and Pham Hung Van²

¹Nanotechnology Lab Director of SHTP LABS, Lot 13, N2 Street, Saigon Hi Tech Park, District 9, Ho Chi Minh City, Vietnam
Kng3328196@aol.com

²Nam Khoa Co. LTD, University of Medicine and Pharmacy in Ho Chi Minh City, Vietnam
Ho Chi Minh City, Vietnam
phhvan.nkbiotek@gmail.com

Abstract— The SHTP LABS has been formally founded in 2004, expected to spend Hochiminh City government funds. However, the lab construction and equipment purchase only completed in the mid of 2008. So every research done before this period must come out from private and personnel efforts. Today, SHTP LABS is a complex of three major units: nanotechnology lab, microelectronic labs and precision mechanic lab. So far, what we had achieved are

a) “Liquid” nano coal and its applications in microelectronic fabrications, digital fabrication, digital printing, fuel cell.

b) Solid phase synthesized carbon nano tube (SPNT) from natural products in Viet Nam.

c) Magnetic nano particles for automated diagnostic system
Up to date, 5 US patent applications have been filed and 9 proceedings have been published in the most prestigious international nanotechnology conference. Three technologies had been successfully transferred to the local industry bringing back to the labs the initial income of a half million US dollars.

I. INTRODUCTION

A. Overview of Saigon Hi Tech Park (SHTP) and SHTP’s LABS

Saigon Hi Tech Park (SHTP) is one among two national projects, namely the Saigon Hi Tech Park and the Hoa Lac Hi Tech Park that are funded by the Vietnamese government for the purpose of developing hi-tech industry in Vietnam.

In a total area of 913 hecta, Saigon Hi Tech Park (SHTP) is a governmental organization which is found in October 2002, and located in a neighborhood of The National University, and 3 major industry zones including Dong Nai, Amata and Sonadezi Industry. SHTP is also in a distance of 15 km from the International Tan Son Nhut Airport. The phase I of 300 hecta now is fully occupied by the key hi-tech foreign development investors (FDI) such as Intel, Nidec, Sonion, Jabil Circuit, with investment capital reaches up to the level of multi billions of US dollar. Besides area dedicated for hi-tech manufacturing factories, there are also some other area reserved for R&D (R&D Center or SHTP’s Research Laboratories), hi-tech work force training (SHTP’s Training Center). The SHTP’s Research Laboratories were formally established in the mid-2004’s and initially started with the Nanotechnology Laboratory and Semiconductor Laboratory reserving a national budget of USD11.5 millions covering facility building (including 600 clean room, 1400 m2 for



Fig. 1 Saigon Hi Tech Park

non-Clean room working area, and 1200m2 for waste water treatment, parking, yard etc...)

SHTP’s Research Laboratories also acquired Nagamori Center (Nidec Company).

In the next 10 years, we are planning to build a Science Park right inside the Saigon Hi-Tech Park, in which the Research Laboratories will be expanded from 4000m2 to day into a large area of about 12.8 hecta. The new plans of R&D will cover 5 laboratory systems functionalizing as Nanotechnology Lab, Semiconductor Lab, Precision Mechanics and Automation Lab, Software Lab and Nano Biotechnology Lab, prototype products factories, training center, housing and apartment complex for the Science Park’s scientists, hotel, entertainment, clinics, banking accommodations. The Science Park of SHTP will be the creative environment for fruitful research activities from fundamental researches, application researches, new talent cultivation and business partnership.

B. SHTP LABS’s Goal

The goal of SHTP LABS has been set to build new hi-technologies, which can be well developed and transferred into global market. First, SHTP LABS need to own good and enough intellectual properties (IP) in certain area where the competencies are best. The technology builders can primarily work with private investors and then with major users to bring technology to reasonable worldwide market. This goal

sounds very ambitious comparing to the capability of human power currently existing in the LABS and it would make the LABS facing with a lot of challenges in terms of immature governmental management systems in Viet Nam, and might be short vision of private investor in hi-tech business. However, these are commitments that the LABS have to accept in order to support the big growths of the entire country in the hi-tech industry.

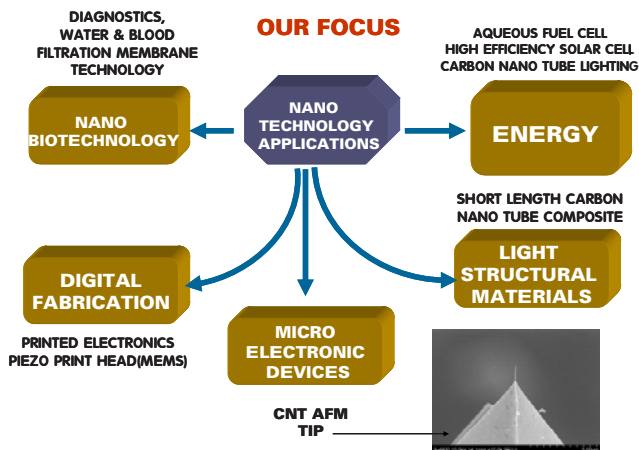


Fig. 2 Main focus of SHTP LABS

C. MAIN FOCUS

Here is our main focus (Fig. 2) for technology building: which is applications of nanotechnology in various area such as

- Renewable energy* including aqueous fuel cell, high efficiency solar cell, carbon nano tube (CNT) lighting
- Light structural materials* including short length CNT technology and its composites
- Microelectronic devices* such as CNT AFM tip
- Digital fabrication* such as printed electronics, and MEMS applications including piezo print head devices



Fig. 3 Nanotech Lab and Semiconductor Lab of SHTP's Research Laboratories spread out on a 3800m² space

- Nanobiotechnology* such as diagnostics, membrane technology for medical filtration

II. ACCOMPLISHMENTS

Next, we would discuss about our technological accomplishments during the period 2002-2009. These results can be summarized as followings

A. *RESEARCH FACILITIES* construction of the area of 3800m² (Fig 3) started at the beginning of the year 2007 and plans to be completed by the first quarter of 2008.

B. US PATENT APPLICATION PENDING

- Mask less lithography using UV absorbing nano particle, Pub. No. US2005/0250052 A1, Pub. Date Nov., 10, 2005
- Carbon nano tube print head array, Pub. No. US2006/0103694 A1, Pub. Date May 18, 2006
- Liquid nano carbon and application products, Pub. No. US2006/0112858 A1, Pub. Date June 1, 2006
- Electrolyte membrane for fuel cell utilizing nano composite Pub. No.2007/0077478 A1, Pub. Date Apr. 5, 2007
- Solid phase synthesized carbon nano fiber and tube, U.S. utility patent application No.11/555,363, filing date Nov 1, 2006

C. *PUBLIC PRESENTATIONS* at prestigious international conferences of nanotechnology:

- “The Process of Forming Micro pattern Image from “Liquid” Nano Carbon”, Khe et al DF2005 International Conferences, Sept 2005, Baltimore, proceedings p.209
- “Novel Electrolyte Membrane for Fuel Cell Utilizing Nano Composite” Khe et al, Nanotech 2006, May 2006, Boston, proceedings p.532
- “Thermal and electrical properties of “liquid” nano carbon and its applications in fuel cell technology”, Khe et al, DF2006 International Conferences , Sept 2006, Denver, Colorado, proceedings p.80
- “Novel Electrolyte Membrane for Fuel Cell Utilizing Nano Composite” Khe et al, Multifunctional Nanocomposite 2006 International Conferences, Sept 2006, Hawaii
- “Novel solid phase synthesis with tube control agent of carbon nano tube and fiber”, Khe et al, Nanotech 2007, May 2007, Santa Clara, proceedings p.61
- “Overview of “liquid” nano coals and its applications”, Khe et al, Carbon 2007 Conferences, July 2007, Seattle
- “Overview of “liquid” nano coals and its applications”, Khe et al, DF2007 , Sept 2007, Anchorage,

D) TECHNOLOGY TRANSFER

“Liquid” nano coal and water fast color ink jet ink to Thien Long Company, Viet Nam for digital printing (2007)
 “Aqueous fuel cell technology” to THLLC (2009)
 “Solid phase Carbon nano tube technology (SPNT) to THLLC (2009)

E) BUSINESS PARTNERSHIP

- 4 Wind Technologies (NASA research laboratories)
- Goodyear Usa
- Hitachi –Hitechnologies (Japan)

Let us discuss two distinguished technologies developed at SHTP's Research Laboratories

“LIQUID” NANO COAL (LNC) AND ITS APPLICATIONS

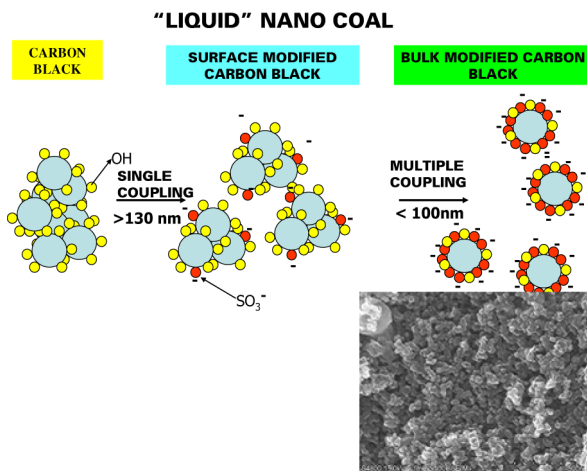


Fig. 4 “Liquid” nano coal

APPLICATIONS OF “LIQUID” NANO COALS, INVENTED AT SHTP RESEARCH LABORATORIES

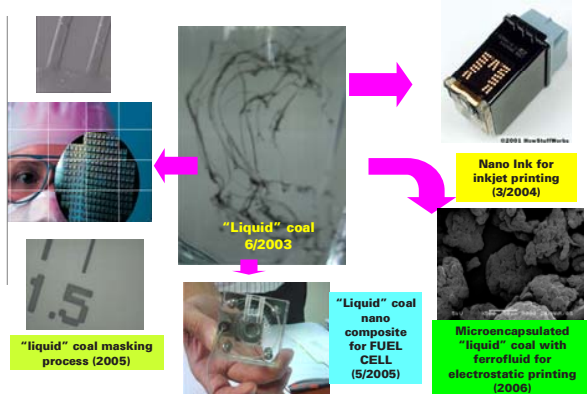


Fig. 5 LNC applications

Surface modified carbon black has been known [1] in the inkjet printing colorants by attaching a few water soluble functional groups onto it to keep hydrophobic carbon black stably dispersed in hydrophilic environment. As a result, the product shows aggregate in water having average particle size in the range of 130nm and it is not quite a nano material yet [2]. In our works, we selected the water soluble functional groups to be electrolytic so the carbon black in water can form charge of the same sign to rebel each other and reduce aggregate size. Using bulk modification which coupling electrolytic groups all over the carbon black particle by multiple coupling processes, we can obtain nano scale aggregate when the multiple coupling products touch the aqueous solvent. This product is named as “liquid” nano coal (LNC) or “liquid” coal. In the nanofabrication technique, multiple coupling processes could be considered as chemical top down. LNC is an intermediate material showing multifunctional ties that the mother material (carbon black) is not able to achieve such as

a) thin film forming properties without using vacuum technique

b) micro and nano pattern image forming useful for masking material in semiconductor wafer processing, and for thermal management in nano chip

c) Electrolytic groups exist on LNC exhibit particle repellent functionality helping to form nano scale aggregates. They also show proton transport capability as well as the capability of forming nano composite.

d) Specific nano composite between LNC and emulsion polymer does show the improvement of thermal stability of LNC itself and make it useful as proton exchange membrane for fuel cell applications [3]

SOLID PHASE SYNTHESIZED CARBON NANO TUBE (SPNT) FROM NATURAL PRODUCTS IN VIET NAM

Today, carbon nano tube (CNT) is the most typical nano material in the world, invented by Ando in 1976 and revisited by Ijima in 1991[4].

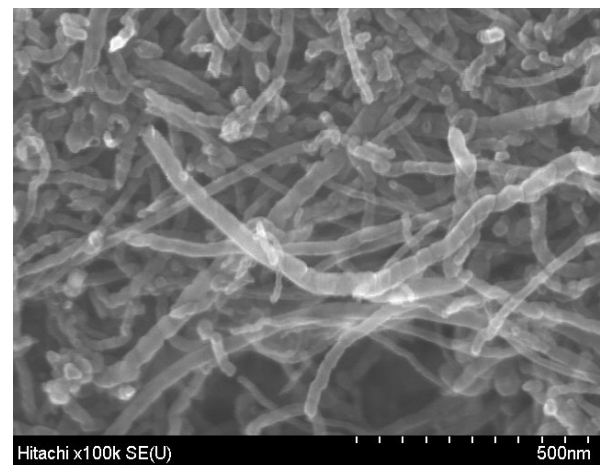


Fig. 6(A) SEM image of gas phase synthesized CNT

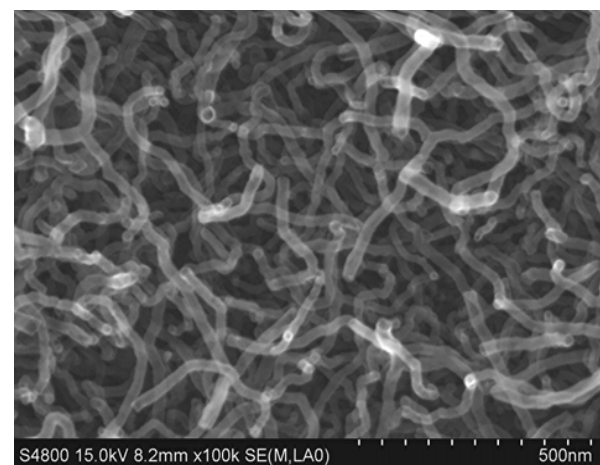


Fig. 6(B) FE- SEM image of SPNT developed at SHTP LABS

It has been known to be very light but very tough materials so it can be used as light structural materials. CNT also exhibits semi conducting & metallic properties and it does meet a lot of applications in nanoelectronics, aerospace, particularly, light structural material applications, construction. Right now, the major product of CNT is in limited production in USA, Japan, and China and still a high cost & non-uniform product, especially it is very hard to use in nano composites formulation without costly pretreatment. SHTP LABS have developed a technique to synthesize CNT using tube control agent (TCA) in a solid phase [5] using agricultural products in Viet Nam such as coffee, coconut shell, cedar wood, etc.. This technique is a novel process as it is different from laser ablation technique and arc discharge technique which do not produce large quantities. TCA is a tube forming nucleation for large quantities and different chemistry of CS. Our process can produce various kinds of CNT having different diameters, for examples, outside tube diameter = 600nm, inside diameter = 400nm tubes, suitable for chemical separation applications, average diameter ranging between 20-30nm tubes, suitable for nano composite, diameter < 1nm tubes suitable for electronic device, energy applications. Recently, our researches on CNT had been focused on very short length tube in the range of several ten to several hundred nm. The traditional synthetic process of CNT using catalytic support growth process, in general, exhibits very long tube in the range of several mm. These products need to be shortened by E-beam or X-ray, raising cost. Our SPNT products can naturally come out with short tube in the range of several ten to several hundred nm without any shortening efforts.

Our process demonstrated several advantages over the known process associated with catalytic growth plasma process such as better uniformity, purer, lower, poly amorphous structures.

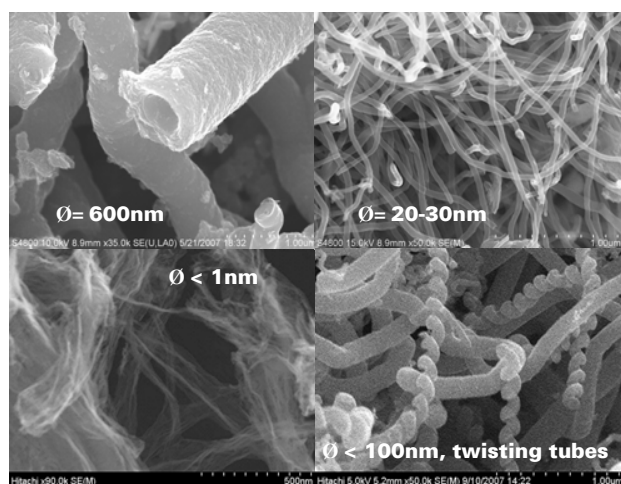


Fig. 7 FE-SEM images of various kinds of solid phase synthesized CNT produced at SHTP's Research Laboratories

Magnetic nano particles have been used as the vehicle to trap **automated diagnostic process**

This process utilizes magnetic nano particles to trap and attract the DNA and RNA of the bacterial and viral pathogens from the clinical samples. So, the main purpose of the research activities is developing and set up the DNA/RNA extraction method using carbon nano-tubes as vehicle to trap, isolate, and purify the DNA/RNA of the bacterial and viral pathogens from the clinical samples ready for the PCR and qPCR testing. The extraction buffer (EB) mixed with the carbon nano-tubes will extract the total DNA and RNA in the sample, and makes the extracted DNA/RNA trapped on the carbon nano-tubes. After that, the carbon nano-tubes will be collected on the wall of the test tube by the magnetic tube holder and will be washed with the washing buffers and then with ethanol. After drying with heat, the DNA and RNA trapped on the carbon nano-tubes will be eluted into the TE1X buffer. The authors have compared this method with BOOM method for DNA extraction and with Trizol-LS method for RNA extraction. The objects for DNA extraction are *M. tuberculosis* and HBV, and the object for RNA extraction is HCV. The method of detection of the extracted DNA is PCR and qPCR, and the method of detection of the extracted RNA is RT-PCR and RT-qPCR.

III. CONCLUSION

SHTP LABS in Ho Chi Minh City, Viet Nam have made significant progresses in nanotechnology R&D in Viet Nam, especially, its applications in light structural materials, microelectronics, digital fabrication, and renewable energy devices. We are now, moving to the 2nd phase of technology transfer and commercialization our nanotechnology products in the local market and worldwide market. There should be a lot of challenges to bring these technologies to the global market. However, we believe that our nano technologies can contribute to the world the major breakthroughs in cost and quality control, because the new frontiers of nanotechnology are always in your hands and efforts to overcome the market barrier.

REFERENCES

- [1] USP 5554739 and 5922118
- [2] Nanotech 2004 Conference, Planetary Session
- [3] Khe et al, Nanotech 2006 Conference (May 2006, Boston), Proceeding Vol.1, p.352 also see Khe et al. International Conference of Multifunctional Nano Composite (Sept 2006, Hawaii)
- [4] Endo, Proceeding of Nanotech 2006, Boston, May 2006
- [5] Khe et al, Nanotech 2007 Conference (May 2007, Santa Clara) Proceeding Vol1. p.61

Microparticle Encoding Technologies for High-Throughput Multiplexed Suspension Assays

S.W. Birtwell and H. Morgan

School of Electronics and Computer Science, University of Southampton, Highfield, Southampton, SO17 1BJ, UK

Abstract— The requirement for the analysis of large numbers of biomolecules for drug discovery and clinical diagnosis has driven the development of low-cost, flexible and high throughput methods for simultaneous detection of multiple molecular targets in a single sample (multiplexed analysis). The technique that most likely satisfies these demands is the multiplexed suspension (bead—based) assay, which offers a number of advantages over alternative approaches such as ELISAs and microarrays. In a bead-based assay, different probe molecules are attached to different beads, which are then reacted in suspension with the target sample. After reaction the beads need to be identified to determine the attached probe molecule, and thus each bead must be labelled or encoded in some way with a unique identifier. Here, we discuss some state of the art encoding methods and provide examples of how encoded particle technologies are being developed for fast multiplexed assays in a microfluidic format.

Keywords— Multiplexing, assays, microparticles, microarrays.

I. INTRODUCTION

New high throughput multiplexed technologies for analysis of large numbers biomolecules will find applications in medical diagnostics and drug discovery. For example, high-throughput immunoassays will be quicker and require lower sample volume than current diagnostic tests. Immunoassays require the identification of many different antibodies in biological fluids to identify diseases [1]; commonly achieved using sandwich assays such as an Enzyme-Linked ImmunoSorbant Assay (ELISA). Multiple assays require relatively large volumes of sample. An ELISA typically detects concentrations of target proteins in the range 1pg/ml – 10ng/ml, depending on the particular probe/target combination being used [2].

Multiplexed assays allow very large numbers of different assays to be performed in a single reaction vessel, with smaller sample volumes than traditional multiplexed ELISAs. A method allowing analysis of a larger number of targets (typically of the order of 10^4) is the protein microarray, which is used for multiplexed detection. Typically for antibody detection arrays, a glass slide is spotted with a number of different antigens. The entire surface is reacted with an antibody-containing sample and the antibodies in the sample bind only to their corresponding antigens. The signal is read using a fluorescent detector antibody that

binds to all the target antibodies. The fluorescent positions on the plate are automatically identified by analysing an image of the slide, and hence the type and quantity of antibodies present in the sample is identified. An example in which four antigens are reacted with a sample containing two different target antibodies is shown in figure 1(A) and (B). Protein-based assays have applications in detecting a variety of markers, for e.g. viral infection [3,4], cancers [5-7] and auto-immune diseases [8].

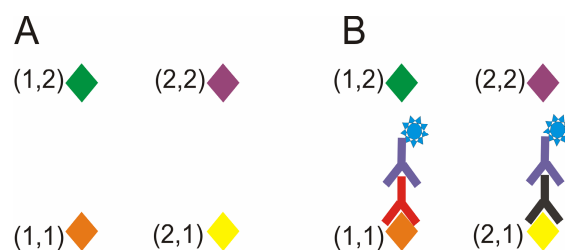


Fig. 1 Principle of antibody microarray. (A) Probe antigens attached to a glass slide. (B) Slide reacted with target antibodies corresponding to two of the antigens. A fluorescent label antibody is attached to the target antibody to indicate binding. The spatial position of the fluorescent spot identifies the antigen and hence the target antibody

Bead-based assays are being developed, where micrometre-sized beads are used to attach probe biomolecules for immunoassays. For a typical assay, a selection of different particles is used, each with a different probe attached. A suspension of such particles is reacted with the sample and the binding measured. Unlike a microarray, where the molecular probe is identified from its location in a matrix, each particle carries a unique identifier, i.e. a tag or code, as shown in figure 2. After reaction every particle is analysed for (a) fluorescence indicating binding of (for example) an antibody and (b) the unique code. The combination of these two allows identification of the probe molecule and therefore the antibodies present in the sample.

Particles can be analysed in microfluidic systems, providing a high throughput platform, which can be integrated into low-cost devices for biochemical research and point-of-care medical diagnostic applications [9,10]. Potentially particles could be directed post analysis into different reaction vessels, for split-and-mix synthesis where molecules such as a peptides or oligonucleotides are progressively and combinatorially synthesized on the beads [11].

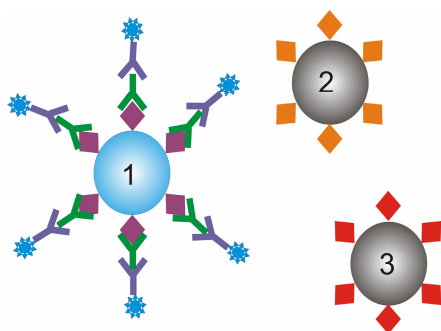


Fig. 2 Principle of a bead based assay. The assay proceeds in the same manner as microarray assay, however, instead of the probe molecules being attached to different site on a slide, each probe is attached to a different bead. Since the beads do not have a well defined position, each must have some kind of code which allows it to be identified after the reactions have taken place

The number of codes required for a bead-based assay technology depends on the assay: A few tens of code for some immunoassays [7], around $10^4 - 10^5$ for studies of biological processes such as gene expression and protein-protein interaction [12, 13] and drug discovery assays. A large number of techniques have been proposed for encoding beads, and reviews can be found in [14-16].

II. SPECTRAL ENCODING OF MICROSPHERES

The most well established encoding technique is based on spectral encoding; the code is based on the colour and intensity of light emitted from polymer microspheres doped with fluorescent dyes. Using a single dye at different concentrations, a multiplexed assay of six different cytokines has been demonstrated [17]. The code is determined from the fluorescence intensity of each particle, using a fluorescence activated flow-cytometer (FACS). A typical statistical analysis of particle fluorescence intensity is presented in the histogram in figure 3(A), demonstrating good separation between six different fluorescence intensities. Each set of beads within a band of fluorescent intensities has a unique code. The main issue with this is that there is little scope for increased multiplexing using this single-dye technology without introducing overlap in the populations.

Using multiple dyes at different concentration ratios increases encoding capacity. Beads encoded using this method are used in commercially available bead-based assay instruments, such as Luminex Corporation's xMAP technology [18]. The xMAP technology was recently approved by the US Food and Drug Administration for clinical use as part of a system to identify 12 different viruses by analysis of their genetic material [19].

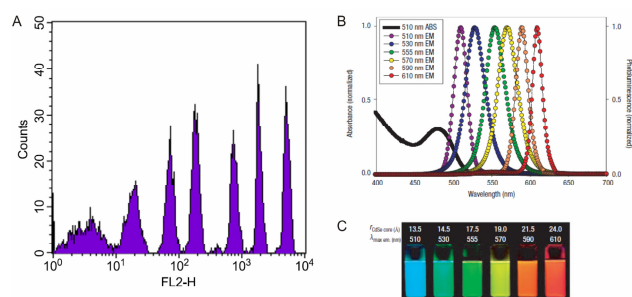


Fig. 3 (A) Fluorescence intensities from six beads containing different quantities of a fluorescent dye. The fluorescence intensity of a particular bead constitutes its identifying code. (B) Absorption spectrum (black points) and emission spectra (coloured points) of six different sized CdSe core quantum dots. (C) Fluorescence emission from the six dots, showing the QD sizes and corresponding peak emission wavelength

A similar approach uses semiconductor quantum dots rather than organic fluorophores to encode the microparticles. Encoding is provided by a combination of fluorescent wavelength and intensity, as for the xMAP technology [20-23]. The line-width of the quantum dot emission is generally narrower than organic dyes, and the peak wavelength of the emission can be fine tuned by varying the radius of the quantum dot (figure 3(B) and (C)), potentially providing a large number of individual emission wavelengths for encoding. The excitation spectrum of a quantum dot is very broad [20] (see figure 3 (B), black points), so that all the different sized quantum dots can be excited with a single wavelength, simplifying the reading optics. The quantum dots are incorporated into polymer microbeads [21,22,24], or the quantum dots themselves can be functionalized and molecules attached directly to their surface [25]. Multiple quantum dots have been embedded into a polymer microparticle in a precisely defined ratio creating a larger number of unique emission spectra [26-28].

A significant disadvantage of fluorescence-based technologies is their reliance on the fluorescence intensity of various dye/quantum dot components, which may vary between beads with ostensibly the same code. In particular, the dye-based methods are subject to variability of dye content in the beads, which causes the fluorescence intensity levels to vary. In addition, using many emission wavelengths for encoding may cause interference with the fluorescent dyes used as target binding reporters. The encoding capacity of these techniques is therefore limited to a reasonably small number ($\sim 10^2 - 10^3$) of codes.

III. STRUCTURALLY PATTERNED MICROPARTICLES – OCCLUSION CODES

One of the simplest forms of encoding particles is based on microstructuring different materials, creating patterns

which constitute a code (often binary). The earliest such technology, developed by 3D Molecular Sciences Ltd. (3DMS, Cambridge, UK), involves the patterning of SU8. Two different types of code were developed. The first, termed ImageCodes, is read on a flat plate and are relatively large ($100 \times 100 \mu\text{m}$). The codes are patterned with square array of holes, representing binary digits making up a code, figure 4 (A). The particles shown in figure 4(A) have an encoding capacity of $2^{35} \approx 10^{10}$ codes. The second type is designed to be read in a more high-throughput, flow-based system. An example is shown in figure 4(B). The codes have different patterns of ridges along both edges, constituting a binary code. During reading, the particles flow past a laser beam, and the different ridges modulate the scattered light, which is monitored by a detector. The particles shown in figure 4(B) have an encoding capacity of $2^{10} = 1024$ codes. The attachment of DNA to the flow codes was demonstrated, proving their compatibility with biochemical assays [29].

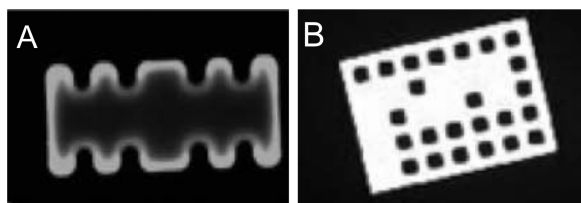


Fig. 4 (A) Optical micrograph of a 3DMS ImageCode. The L-shaped pattern of holes indicate the orientation, and the central holes constitute a binary code. (B) Optical micrograph of a 3DMS FloCode. The pattern of ridges along the edge is a binary code, read by recording the fluctuations of scattered laser light as the particle flows through a laser beam

Pregibon *et al.* [30] recently demonstrated an encoding technology where encoded PEG particle manufacture, analyte attachment and reading of the codes occurred within a microfluidic system. The particles are defined and patterned using UV light passed through a mask and a reduction lens. The particles feature a coding region on one half that is similar to the 3DMS ImageCodes. The other half of the particle has the biological probe embedded. The disadvantages of this method are the larger concentrations of probe molecules required to obtain a loading level similar to most other bead-based technologies (around 50 times larger), and the fact that the technology may be problematic for protein assays, because of the potential for UV-induced denaturation of the probes during particle formation.

A significant advantage of graphical methods of encoding compared with the spectroscopic methods is that the codes are binary, allowing for error correction. Furthermore, the capacity of these encoding methods is not restricted by competition with bandwidth from the fluorescent assay binding reporters.

IV. DIFFRACTIVE AND HOLOGRAPHIC ENCODING

One issue with occlusion-based encoding is that the encoding capacity is limited by the size of the spots and the area of the particle. To increase the encoding capacity on small ($\sim 10 \mu\text{m}$) particles, a method has been developed based on detecting the distribution of light diffracted by a miniature grating patterned on a microparticle, where information is encoded in the pitch of the grating, a [31]. Measurement of the first-order ($m = 1$) diffracted beam position when the particle is illuminated gives direct information about the pitch a . More than one grating pitch can be superimposed on a single particle to increase the encoding capacity of this technique. Using this technique, approximately 10^5 unique codes can be created on a $20 \mu\text{m}$ particle),

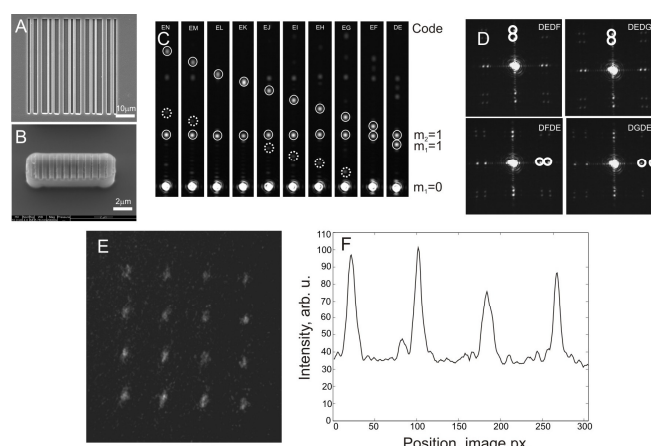


Fig. 5 (A) SEM image of a 2x superimposed encoded tag on an SU8 film nano-imprinted using an electroformed nickel imprint master. (B) A similar tag imprinted onto an SU8 microparticle. (C) Diffraction patterns in air created by nano-imprinted 1D SU8 tags containing 2 superimposed gratings. Moving from left to right shows how a progressive decrease in the pitch of one of the gratings changes the diffraction pattern. (D) Example diffraction patterns from 2D gratings. (E) An image of the reconstructed diffraction pattern from a hologram written into a $1500 \times 500 \times 35 \mu\text{m}$ SU8 particle. Image is contrast enhanced for clarity. (F) A cross section through the un-enhanced image showing the pattern signal-to-noise ratio

increasing to 10^{10} using two sets of gratings in mutually perpendicular [31].

Diffraction gratings manufactured by nanoimprinting SU8 [32] are shown in the SEM images in figure 5(A and B), whilst Figure 5(C) shows the diffraction patterns from an example set of 10 different coded particles with two superimposed gratings. Example diffraction patterns from a 2D grating are shown in figure 5(D). Methods for attaching DNA and antibodies to the SU8 particles have been developed [33]. 4-plex immunoassays and 2-plex DNA single point mutation (SNP) analyses were demonstrated using this encoding technology [33] with a sensitivity of 5nM for human IgG/anti-human IgG binding.

A significant advantage of this encoding method is the simplicity of the detection system: no microscope is required as the diffraction pattern is projected from the particle into the far field. In addition, the code is generated from the periodicity of the structure on the particle surface, making it robust with respect to particle contamination, damage and rotation [31].

An improvement on this method is based on writing holograms to encode the particles [34]. Using this technique, the diffracted pattern can be tailored to produce binary patterns in a small angular space, allowing for error correction. The hologram is written into a particle manufactured from SU8 doped with a photochromic dye. An example of a reconstructed code from such a hologram on a particle is shown in figure 19(E), together with cross-sections indicating the binary signal to noise ratio (figure 19(F)). Theoretically, around 10^{24} unique codes could be obtained on a $100\mu\text{m}$ particle (and around 4000 codes on a $20\mu\text{m}$ particle) [34]. One major advantage of this technique is that the code is non-permanent, it can be re-written several times depending on the photochromic dye used.

V. CONCLUSIONS

Suspension assays using encoded microparticles have been shown to have molecular sensitivities comparable to both ELISAs and microarrays and are realistic candidates for high throughput, low sample volume replacements for these technologies.

The graphical binary-encoding methods hold the most promise for future applications in large-scale ($>10^3$ targets) assays. Spectroscopic encoding methods will continue to be used at smaller scales because of the simplicity of code detection and because these techniques fit with existing well-proven fluorescence detection devices.

REFERENCES

1. Kindt, T.J., Goldsby, R.A., Osborne, B.A., "Immunology", 6th Edition, W.H. Freeman and Company (2007)
2. AbCam ELISA Kits specifications <http://www.abcam.com>
3. <http://www.quansysbio.com/>
4. <http://www.piercenet.com/>
5. Leffers, N., et al. (2009) *Cancer Immunology, Immunotherapy* **58**, 449-459
6. Li, F., Guan, Y. and Chen, Z. (2008) *Cellular and Molecular Life Sciences* **65**, 1007-1012

7. Qiu, M., Shi, Y., Guo, Z., Chen, Z., He, R., Chen, R., Zhou, D., Dai, E., Wang, X., Si, B., Song, Y., Li, J., Yang, L., Wang, J., Wang, H., Pang, X., Zhai, J., Du, Z., Liu, Y., Zhang, Y., Li, L., Wang, J., Sun, B. and Yang, R. (2005) *Microbes and Infection* **7**, 882-889
8. Quintana, F.J, et al., *Proc. Natl. Acad. Sci.* 105 (2008) 18889
9. Ligler, F. S. (2009) *Analytical Chemistry* **81**, 519-526
10. Yager, P., Domingo, G. J. and Gerdes, J. (2008) *Annu. Rev. Biomed. Eng.* **10**, 107
11. G. Cavalli, S. Banu, R. T. Ranasinghe, G. R. Broder, H. F. P. Martins, D. C. Neylon, H. Morgan, M. Bradley and P. L. Roach, *J. Comb. Chem.* **2007**, *9*, 462.
12. Miyazaki, K., Yamaguchi, M., Imai, H., Kobayashi, T., Tamaru, S., Nishii, K., Yuda, M., Shiku, H. and Katayama, N. (2009) *Blood* **113**, 1071-1074
13. Wong, N., et al. (2009) *International Journal of Cancer* **124**, 644-652
14. Wilson, R., Cossins, A. R. and Spiller, D. G., *Angew. Chem. Int. Ed.* **45** (2006) 6104.
15. K. Braeckmans, S. C. DeSmedt, M. Leblans, R. Pauwels and J. De-meester, *Nat. Rev. Drug Discov.* **1**, 447 (2002).
16. Birtwell, S.W. and Morgan, H., (2009) *Integr. Biol.* **1**, 337-436
17. Morgan, E., et al *Clin. Immunol.* **110** (2004) 252
18. <http://www.luminexcorp.com/technology/index.html>
19. Wu, J., Dyer, W., Chrisp, J., Belov, L., Wang, B. and Saksena, N. (2008) *Retrovirology* **5**, 24
20. Jaiswal, J. K., and Simon, S. M., *Trends Cell Biol.* **14** (2004) 497.
21. Ma, Q., Wang, X., Li, Y., Shi, Y. and Su, X., *Talanta* **72** (2007) 1446
22. Mattheakis, L. C., Dias et al., *Anal. Biochem.* **327** (2004) 200.
23. Medintz, I.L., Uyeda, H.T., Goldman, E.R., and Mattoussi, H., *Nature Materials* **4** (2005) 435
24. Han, M., Gao, X., Su, J.Z. and Nie, S., *Nature Biotechnol.* **19** (2001) 631
25. Pang, S., et al, *J. Immunol. Methods* **302** (2005) 253.
26. Ma, Q., Wang, X., Li, Y., Shi, Y. and Su, X., *Talanta* **72** (2007) 1446
27. Mattheakis, L. C., Dias, J. M., Choi, Y., Gong, J., Bruchez, M. P., Liu, J. and Wang, E., *E. Anal. Biochem.* **327** (2004) 200.
28. Han, M., Gao, X., Su, J.Z. and Nie, S., *Nature Biotechnol.* **19** (2001) 631
29. Evans, M., Sewter, C. and Hill, E., *Assay Drug Dev. Technol.* **1** (2003) 1
30. Pregibon, D. C., Toner, M. and Doyle, P. S., *Science* **315** (2007) 1393
31. S. W. Birtwell, G. S. Galitonov, N. I. Zheludev and H. Morgan, *Opt. Com.* **2008**, *281*, 1789.
32. S. Banu, S. Birtwell, G. Galitonov, Y. Chen, N. Zheludev and H. Morgan, *J. Micromech. Microeng.* **2007**, *17*, S116.
33. G. R. Broder, R. T. Ranasinghe, J. K. She, S. Banu, S. W. Birtwell, G. Cavalli, G. S. Galitonov, D. Holmes, H. F. P. Martins, C. Neylon, N. Zheludev, P. L. Roach, and H. Morgan, *Anal. Chem.* **2008**, *80*, 1902.
34. S. W. Birtwell, S. Banu, N. I. Zheludev and H. Morgan, *J. Phys. D: Appl. Phys.* in press.

Corresponding author:

Author: Sam Birtwell
 Institute: School of Electronics and Computer Science University of Southampton
 Street: Highfield
 City: Southampton
 Country: UK
 Email: s.birtwell@soton.ac.uk

Author Index

A

Afzulpurkar, N. 84
An, P.V. 123
Anderson, A.W. 1, 23
Anh, Ho Pham Huy 39
Anh, N.T.H. 203
Arlinghaus, L.R. 23
Aufaure, P. 44
Avison, M.J. 1

B

Balasubramanian, P. 278
Bang, Dang Duong 291, 295, 299
Beppu, Y. 223
Berganzo, Javier 291
Binh, Nguyen Thanh 196
Birtwell, S.W. 316
Bodhale, D.W. 84
Bohez, E. 119
Bohez, E.L.J. 51
Boucher, F. 114
Brivio, Monica 299
Brownell, A.L. 27
Bruus, Henrik 299
Bu, Mingiang 291
Burns, D.K. 219
Burrell, Robert E. 6

C

Cadosch, D. 175
Cao, Cuong 295
Cardenas, L.J. 207
Cazier, Nicolas 239
Chan, E. 175
Charleux, F. 44
Chen, L.M. 1
Chi, H.T. 223
Chivapornthip, P. 51
Cho, B.R. 67
Choi, Y.S. 67
Chung, Doan Chinh 163
Colin, A. 59, 62
Creasy, J.L. 1
Cuong, Cao 291
Cuong, N.V. 159, 203

Cuong, Nguyen T.K. 282
Cuong, Nguyen Thi Kim 287

D

Dang, T.T. 186
Dao, T.T. 44, 71
Dhumpa, Raghuram 291
Dinh, Ngoc-Duy 308
Drese, Klaus S. 299
Dula, A.N. 1
Dumery, B. 270
Dung, Duong Chi 127
Duong, Cong-Truyen 243
Dzuiban, Jan 291
Dzung, N.T. 75, 80

F

Filgueira 175
Filgueira, L. 211
Florian, Laouenan 291
Fock, K.M. 255
Forman, D. 255

G

Gargiulo, C. 211
Gatenby, J.C. 1
Giang, Tran Phan Son 200
Goh, K.L. 255
Golubok, A.O. 127
Gore, J.C. 1
Gourrier, Aurélien 190
Grounauer, P.A. 270

H

Ha, D.M. 255
Ha, Hoang Manh 148
Ha, Nguyen Thai 263
Ha, Tran Le Bao 152, 155
Ha, Vo Q. 282
Ha, Vo Quang 287
Hachadorian, J. 140, 144
Hai, V.D. 251
Han, J.-C. 90
Hara, Y. 223

Hieu, L.C. 119, 123
Hiwatari, K. 31
Ho, L.T.T. 216
Hòa, Lê Minh 266
Hoàn, Ngô Thanh 266
Hoan, Ngo Thanh 140, 287
Hoang, H.N. 216
Hoang, Huy Q. 98
Hoang, N.K. 203
Hoffman, R.E. 23
Hoffman, R.M. 31
Hong, X. 23
Hsiesh, M.F. 159
Huân, Đặng Nam 266
Hung, L.T. 119, 123
Huong, Nguyen T.M. 282
Huong, Nguyen Thi Minh 287
Huy, H.Q. 251

I

Indo, M. 102
Ishikawa, K. 207
Iwata, K. 31

J

Jeong, S.H. 67
Jiang, J.L. 159

K

Kataoka, M. 31
Katayama, Tsutao 235
Kelley, B.S. 247
Kelly, Regis B. 14
Khanh, L. 119, 123
Khare, Ashish 196
Khoa, Truong Quang Dang 144,
282, 287
Khoa, Trương Quang Dang 266
Kimura, R. 31
Kirk Shung, K. 10
Kirton, R.S. 90
Kita, Yusuke 235
Ko, Sanghoon 231
Kubo, Tomohiro 239
Kwok, Y.C. 303

- L**
- Laugier, Pascal 190
 Le, L.H. 130
 Le, L.Q. 219
 Lemaire, T. 55
 LeQuang, T. 59, 62
 Lian, E. 140, 144
 Lin, F.H. 179
 Linh, Huynh Q. 282
 Linh, Huynh Quang 287
 Liu, Cheng-Hsien 308
 Liu, Yuliang 291
 Loan, Truong Thi Hong 106
 Loi, Le Tan 39
 Loiseau, D.S. 90
 Loke, W.K. 303
 Lorprayoon, E. 51
 Lou, E. 130
 Lugo, A. 144
 Lugo, Gustavo 274
- M**
- Ma, H. 31
 Maitre, P. 59, 62
 Marin, F. 44, 71
 Masaoka, Y. 31
 Matsukawa, M. 102
 Matsukawa, Mami 235, 239
 Matsuya, S. 207
 Mégrot, F. 71
 Meltzer, H.Y. 23
 Mitchell, H.M. 255
 Morgan, H. 316
 Mouchet, Mathilde 190
 Munting, E. 114
 My, Dang Truong Ka 106
- N**
- Nadworny, Patricia 6
 Naili, S. 55
 Nakamura, K. 31
 Nakatsuji, T. 102
 Nam, Nguyen Ba 134
 Nanthavanij, S. 51
 Nga, Thai Thanh 148
 Nghia, Huynh Luong 94, 127, 193
 Ngoc, Phan Kim 152, 163, 167
 Nguyen, Duc Thuan 110
 Nguyen, Hoang Hai 231
 Nguyen, K.C. 216
 Nguyen, Khe 312
 Nguyen, N.T. 303
 Nguyen, T.D. 123
 Nguyen, Thuan D. 98
 Nguyen, Tien Dzung 110
 Nguyen, V.-H. 55
 Nguyen, Viet Dzung 110
 Nhon, Mai Van 106
 Nhung, Truong Hai 163
 Nhut, Duong Tan 134
 Nickels 35
 Nielsen, P.M.F. 90
 Nisar, A. 84
- O**
- Ohdomari, I. 223
- P**
- Parada, L.F. 219
 Park, S. 23
 Park, Seonghun 243
 Perch-Nielsen, Ivan R. 299
 Peyrin, Françoise 190
 Pham, H.V. 216
 Pham, Ngoc P. 98
 Pham, S.T. 216
 Pham, Thanh V. 98
 Pham, W. 19, 35
 Phap, Phan Dinh 278
 Pho, Nguyen Huu 287
 Phuc, Ma Kien 163
 Phuc, Pham Van 163, 167
 Phuong, Dang Nguyen 106
 Pouletaut, P. 44, 114
- Q**
- Qi, Z. 179
 Quan, To Minh 152
 Quang, Tran Anh 193
 Quoc, L.H. 123
- R**
- Rampf, Frederica 299
 Raum, Kay 190
 Rigby, B.R. 247
 Roger, T. 62
 Rruano, Jesus Miguel 291
 Rupin, Fabienne 190
- S**
- Saeki, Takashi 239
 Sahai, Nitin 48
 Saïed, Amena 190
 Sakuma, S. 31
 Sasaki, K. 223
 Sato, Y. 223
 Schaeffer, Eva 299
 Shin, S.M. 67
 Shipman, T. 219
 Shoji, Y. 31
 Singh, Lokesh 48
 Sitthiseripratip, K. 51
 Sloten, J.V. 119
 Son, Hoang Nghia 155
 Sơn, Nguyễn Thái 259
 Stringer, E.A. 1
 Sudhakar, D. 278
 Sumi, S. 179
 Sun, Y. 303
- T**
- Taberner, A.J. 90
 Tachikawa, H. 31
 Taguchi, K. 182
 Takeuchi, A. 207
 Tam, Nguyen Duc 227
 Tâm, Nguyễn H.M. 266
 Tam, Nguyen Huynh Minh 274, 282
 Tan, H.Y. 303
 Tanaka, Kazuto 235
 Tang, L. 31
 Tanii, T. 223
 Tewari, Ravi P. 48
 Thanh, Thai Tu 152
 Thanh, V.V. 123
 Thao, H.D. 211
 Thảo, Nguyễn Hồng 266
 Thi, Thom Thao Nguyen 110
 Tho, M.C. Ho Ba 44, 71, 114
 Thornton-Wells 23
 Thuan, N.D. 251
 Thuan, Nguyen Duc 263
 Thuy, Duong Thanh 163
 Thuy, T.T.T. 211
 Thuy, Tran Thi Thanh 155
 Tiep, Nguyen Van 94
 Toai, T.C. 211
 Toai, Tran Cong 155
 Toan, Nguyen Khac 163
 Toan, Nguyen Van 227
 Tran, Duc Hoa 110
 Truc, Pham Le Buu 163
 Trung, P.D. 119
 Truong, N.K.V. 67
 Tsuru, K. 207
 Tu, Nguyen H.K. 171
 Tuan, H.M. 211
 Tuan, Huynh Minh 155
 Tuan, Le Tu Quoc 287
 Tumuklu, M. 23

V

Van, Nguyen Thu 263
Van, P.H. 211
Vân, Phạm Hùng 259
Van, Pham Hung 312
Vãn Tới, Vĩ 266
Van Tới, Vo 140, 144, 270,
274, 282, 287
Veiko, V.P. 127
Viguier, E. 59, 62
Vo, D.X.A. 216
Vo, T.P. 186
Vu, H.A. 223
Vu, H.D. 247
Vu, Hai D. 98

Vu, T.D. 186
Vu, Tran Anh 274

W

Walczak, Rafal 291
Watanabe, N. 182
Watanabe, T. 223
Welch, E.B. 1
Wolff, Anders 291, 295, 299
Wu, C.C. 179

X

Xinh, P.T. 223
Xuan, Hoang Thi Lan 278

Y

Yakovlev, E.B. 127
Yamamoto, H. 223
Yamamoto, K. 102
Yamashita, S. 31
Yamazaki, K. 102
Yanagitani, T. 102
Yang, K.C. 179
Yang, Z. 31
Yano, T. 31
Yi, Sun 291

Z

Zhang, C. 130
Zlatov, N. 119

Keyword Index

α -tricalcium phosphate 207
3D image processing 200
3T3 fibroblast cells 227
5'UTR 259

A

absorption coefficient 193
Accelerometer 140
Acoustic scanning microscope 190
Agrobacterium transformation 278
algorithm 193
algorithm 94
Alzheimer's disease 23
amniotic membrane 155
ANC 282
anti-cancer 203
Anti-inflammatory 6
Antimicrobial 6
Apatite cement 207
Artifacts 282
Artificial porous scaffold 152
assays 316
Atomic Force Microscopy (AFM) 243
axial trapping force 182

B

Bacillus thuringiensis 278
back projection 193
basal layer 155
Belief Decision Tree 71
biobarcode 295
biocompatibility 152
bio-corrosion 175
bio-electroimpedance. Identify 94
Biomechanics 247
Biomechanics 51
biomedical engineering 251
Biomodelling 119
bit plane decomposition 186
Bite Imbalance 266
Blink rate 270
blood flow 27

bone broken 167
Bone marrow 163, 239
bone marrow failure 167
bone remodeling 114
Breast cancer 110
BSA nanoparticle 231
BSS 282

C

carbon nano-tube 216
Carbon-11 35
Cardiac Trabeculae Carneae 90
Cat 59
catalytic property 295
cell division inhibitor 171
Cell Focus and Microfluidics 308
cell line 227
Cell Separation 308
Cell Sort-ing 308
Cerebral Palsy 71
Cervical Range of Motion 140
Cervical Range of Motion 274
Cervical spine 144
chitin 227
chitosan 227
Chitosan Hydrogel 179
Classification 71
coacervation method 231
Cobalt-Chromium Femoral Head 243
Colonoscopy 31
color Doppler 10
Colorectal cancer 31
Compressed breast thickness 263
Computational fluid dynamic (CFD)
analysis 84
computed tomography 193
Contralateral Effects, Sport Medicine
266
coral 211
cortical bone 102
cortical bone 190
cortical bone 55
cranio-maxillofacial surgery 119

Creatinine 98
Cross point 186
cryIAb 278

D

decellularization 152
Deep reactive ion etching (DRIE) 84
demineralized cancellous bone 152
denoising 196
Dental Obstruction 274
Dental-Cranio-Maxillofacial surgery
123
dermal neurofibroma 219
Diabetic disease 167
diabetic mouse 163
diagnosis 216
Dielectrophoresis 308
Diode Laser 274
Diplegia 71
Discrimination 71
DMEM 227
DNA extraction 216
dopamine 27
dose distribution 106
doxorubicin 159
drug delivery 231
Drug delivery 84
drug delivery systems 159
drug resistance 171
Dry eye 270
DTI 23
dynamic light scattering 231

E

education. 251
EEG 282
EGCG 223
e-Hospital 98
Elastic modulus 235
elastography 10
Elearning 251
Electrosomatograph 94
EMRs 98

- Encapsulation 179
 Endoscopic imaging agent 31
 engineering education 247
 entire cross point region 186
 entropy coding 186
 epidermal stem cell 155
 Epidermis 155
 expert-like system 94
 Eyestrain 270
- F**
- FAK 223
 Fingertip 51
 finite element 55
 Flexion & Extension 48
 fluid flow 55
 fluorescence 19
 fluorescence resonance energy transfer 295
 Fluorine-18 35
 fMRI 23
 food safety 291
 Forward Dynamic Identification 39
 Frictional Coefficient 243
- G**
- Gait 44
 gait analysis 59
 gait analysis 62
 Gait cycle 48
 GAITRite® system 59
 GAITRite® system 62
 Gamma Plan 106
 Gaussian, filters 196
 Gyroscope 140
- H**
- Half Value layer 263
 healthy dog 62
 Hemiplegia 71
 Hemodialysis System 98
 Hepatitis C virus 259
 Heuristics 71
 Hill Muscle Model 48
 HL7 standard 98
 Hollow silicon microneedle 84
 human bone marrow 211
 hydroxyapatite 190
 hydroxyapatite (HAp) 102
- I**
- ideal cross point region 186
 IGF-1R 223
- Imaging 130
 im-mune cells 175
 Immunoisolation 179
 Implant design and manufacturing 119
In vitro 207
 Ipsilateral Effect 274
- J**
- Jaw Imbalance 266
 Jaw Imbalance 274
- K**
- Kinematics and Kinetics 44
- L**
- Lab on a chip 303
 Lab-on-a-Chip 291
 laser beam effects 182
 laser pulling 127
 Leksell Gamma Knife 106
 Light-emitting diodes (LEDs) 134
 living cell 127
 Localized surface plasmon resonance 295
 Longitudinal wave 239
 Loss of Arm Strength 266
 Lower Limbs 44
- M**
- Mammography 263
 mass detection 110
 MCNP 106
 Mean glandular dose 263
 Measurements of Cervical Range of Motion 144
 medical image 196
 medical image software 200
 Meloidogyne incognita 278
 mesenchymal stem cell 163
 mesenchymal stem cell 211
 metabolism 27
 Metal implant 175
 Micelles 159
 microarrays 316
 Microcalorimetry 90
 microcrack 55
 Microfluidics 303
 Micro-nanotech applications 291
 micropartic 316les
 Modeling 39
 molecular imaging 19
 Molecular Imaging 35
 molecular techniques 216
- morphological change 171
 Mouse click 51
 Mouse switch 51
 MRI 1
 MRI 23
 MRS 1
 multidrug resistance 159
 Multiplexing 316
 Muscle Energetics 90
- N**
- Nanomedicine 6
 nanoparticle 203
 Nanoparticles 159
 Nanopipette 127
 Nanosilver 6
 N-cadherin 223
 near infrared spectroscopy (NIRS) 75
 near-infrared 19
 Neck motion 144
 Neck pain 144
 nerve agent 303
 Neural MIMO NARX Model 39
 neurofibromin 219
 neuroimaging 1
 Neurosurgery 123
 NF1 219
 NIBP 98
 Noise 282
 nonlinear analysis 75
 Nonlinear Spring 51
- O**
- optical fiber 182
 optical trapping 182
 Orthopaedics 44
 Orthopaedic 123
 Orthosis 44
 Osteoblast 211
 osteoclast 175
 osteon 190
- P**
- pancreatic carcinoma 223
 particle aggregation 295
 patch-clamp 127
 Patient ID 98
 Patient Specific Model 44
 PCR 303
 Peanut agglutinin 31
 peri-implant inflammation 175
 PET 27, 35
 Photobiomodulation 134

photodynamic therapy 134
Photomorphogenesis 134
physiological loading 114
Poliomyelitis 44
Poly(ethylene glycol) 203
Poly(N-vinylacetamide) 31
poly(ϵ -caprolactone) 203
poroelasticity 55
pressure walkway 59
Pressure walkway 62
Product development 123

Q

Quality by Design 67
Quantitative ultrasound (QUS) 102

R

radiation force imaging 10
Radiochemistry 35
ratio 62
ratio fore/hind 59
receptor 27
refractive index 182
Regenerative Medicine 67
region growing 110
Rehabilitation Robot 39
Response surface methodolog 67
RNA extraction 216
Robust design 67

S

scanning probe microscope (SPM) 127
schizophrenia 23
scoliosis 130
screw insertion 130

serum free medium 155
Setting properties 207
short term clinical results 114
shrimp shells 227
Single trabecula 235
Silicate 207
Single-chip Data Acquisition
System 140
SKPs 219
spinal surgery 130
steerable complex wavelet 196
stem cell therapy 163
stemless hip prosthesis 114
stiffness 190
Streptomyces 171
Surface Roughness 243
surrogate 75

T

template matching 110
Temporal modulation transfer
function 270
theoretical analysis 182
Three point bending test 235
Time-oriented Responses 67
Tomography 193
Transdermal drug delivery (TDD) 84
Transgenic brinjal 278
transit amplifying cell 155
transplantation 211
triblock copolymer 203
Tribological Property 243
type 1 diabetes 163
Type 1 diabetes 179
Tricalcium silicate 207
tumor microenvironment 219

U

ultra-high field 1
ultrasonic imaging 10
Ultrasound 10
Ultrasound 130
Umbilical cord blood-derived cells
(UCBDCs) 152
Urea 98

V

Video display terminal 270
Vietnam 247
volume images 200

W

Wave attenuation 239
Wave velocity 239
Wound healing 6

X

Xenotransplantation 179
X-ray μ CT 235

Y

young and active patients 114

Z

Zubal head phantom 106